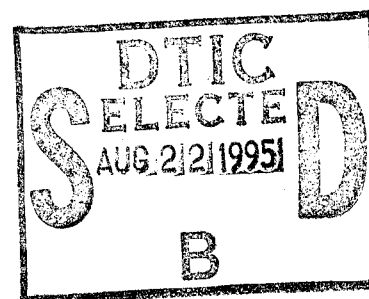


AL/CF-TR-1994-0082



**ADVANCED BIOFIDELIC COMPOSITE (ABC MAN)
DEVELOPMENT**

**Moreno White
Dan Stevenson
Christine Barker
Eric Zedelmayer
Dan Jacobson
Kenny Dang
Bernard van Leggelo**



**SPARTA, INC.
9455 TOWNE CENTER DRIVE
SAN DIEGO CA 92121-1964**

FEBRUARY 1994

FINAL REPORT FOR THE PERIOD JULY 1991 TO FEBRUARY 1994

Approved for public release; distribution is unlimited

19950821 029

**AIR FORCE MATERIEL COMMAND
WRIGHT-PATTERSON AIR FORCE BASE, OHIO 45433-6573**

**ARMSTRONG
LABORATORY**

NOTICES

When US Government drawings, specifications, or other data are used for any purpose other than a definitely related Government procurement operation, the Government thereby incurs no responsibility nor any obligation whatsoever, and the fact that the Government may have formulated, furnished, or in any way supplied the said drawings, specifications, or other data, is not to be regarded by implication or otherwise, as in any manner, licensing the holder or any other person or corporation, or conveying any rights or permission to manufacture, use or sell any patented invention that may in any way be related thereto.

Please do not request copies of this report from the Armstrong Laboratory. Additional copies may be purchased from:

National Technical Information Service
5285 Port Royal Road
Springfield VA 22161

Federal Government agencies and their contractors registered with Defense Technical Information Center should direct requests for copies of this report to:

Defense Technical Information Center
Cameron Station
Alexandria VA 22314

DISCLAIMER

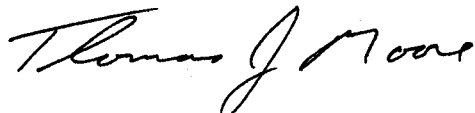
This Technical Report is published as received and has not been edited by the Technical Editing Staff of the Armstrong Laboratory.

TECHNICAL REVIEW AND APPROVAL

AL/CF-TR-1994-0082

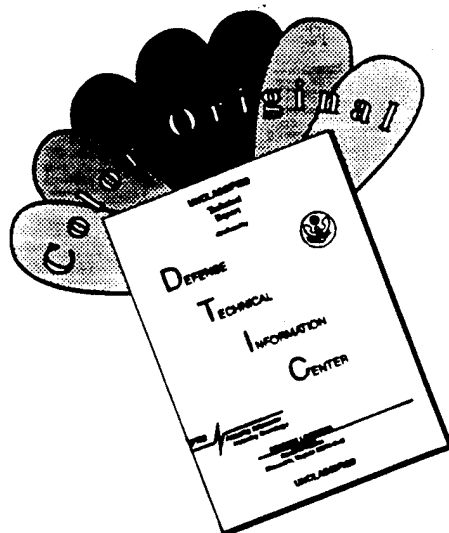
This technical report has been reviewed and is approved for publication.

FOR THE DIRECTOR



THOMAS J. MOORE, Chief
Biodynamics and Biocommunications Division
Armstrong Laboratory

DISCLAIMER NOTICE



THIS DOCUMENT IS BEST QUALITY AVAILABLE. THE COPY FURNISHED TO DTIC CONTAINED A SIGNIFICANT NUMBER OF COLOR PAGES WHICH DO NOT REPRODUCE LEGIBLY ON BLACK AND WHITE MICROFICHE.

DISCLAIMER NOTICE



THIS DOCUMENT IS BEST QUALITY AVAILABLE. THE COPY FURNISHED TO DTIC CONTAINED A SIGNIFICANT NUMBER OF PAGES WHICH DO NOT REPRODUCE LEGIBLY.

REPORT DOCUMENTATION PAGE

Form Approved
OMB No. 0704-0188

Public reporting burden for this collection of information is estimated to average 1 hour per response, including the time for reviewing instructions, searching existing data sources, gathering and maintaining the data needed, and completing and reviewing the collection of information. Send comments regarding this burden estimate or any other aspect of this collection of information, including suggestions for reducing this burden, to Washington Headquarters Services, Directorate for Information Operations and Reports, 1215 Jefferson Davis Highway, Suite 1204, Arlington, VA 22202-4302, and to the Office of Management and Budget, Paperwork Reduction Project (0704-0188), Washington, DC 20503.

1. AGENCY USE ONLY (Leave blank)		2. REPORT DATE 28 February 1994	3. REPORT TYPE AND DATES COVERED Final - July 1991 - February 1994	
4. TITLE AND SUBTITLE Advanced Biofidelic Composite (ABC Man) Development			5. FUNDING NUMBERS C F33615-91-C-0530 PE 65505F PR 3005 TA 3005B2 WU 3005B205	
6. AUTHOR(S) Moreno White Eric Zedelmayer Bernard van Leggelo Dan Stevenson Dan Jacobson Christine Barker Kenny Dang				
7. PERFORMING ORGANIZATION NAME(S) AND ADDRESS(ES) Sparta, Inc. 9455 Towne Center Dr. San Diego CA 92121-1964			8. PERFORMING ORGANIZATION REPORT NUMBER N/A	
9. SPONSORING/MONITORING AGENCY NAME(S) AND ADDRESS(ES) Armstrong Laboratory, Crew Systems Directorate Biodynamics and Bicommunications Division Human Systems Center Air Force Materiel Command Wright-Patterson AFB OH 45433-7901			10. SPONSORING/MONITORING AGENCY REPORT NUMBER AL/CF-TR-1994- 0082	
11. SUPPLEMENTARY NOTES				
12a. DISTRIBUTION/AVAILABILITY STATEMENT Approved for public release; distribution is unlimited			12b. DISTRIBUTION CODE	
13. ABSTRACT (Maximum 200 words) A study was conducted to explore the use of composites with embedded strain gages in impact testing manikins. The objectives were to improve segment mass distribution properties, allow use of more realistic flesh simulants, produce more bone-like stiffness characteristics, and provide an integral transmitted force measuring capability. A prototype Hybrid III 50th percentile manikin composite leg with strain gages embedded in the long bone skeletal segments was designed and fabricated. Two single axis accelerometers were mounted in the knee cavity and at the distal end of the tibia for measuring anterior/posterior plane accelerations and medial/lateral plane accelerations, respectively. The femur and tibia flesh coverings were fabricated from Skinflex III, a castable polyurethane elastomer with compliance and density approximately that of human flesh. A piezo film tactile foil pressure sensor grid was embedded in the skin covering to measure localized impact forces. The final composite femur weight with sensors is 20.3 lbs versus 19.6 lbs for a similar Hybrid III 50th femur. The weight of the composite tibia with sensors is 9.7 lbs versus 9.6 lbs for the corresponding Hybrid III tibia. Mechanical testing was conducted on the composite segments to verify the static design loads and to provide calibration data for the embedded strain gages. A series of horizontal sled tests were also conducted using a Hybrid III manikin with a standard Hybrid III left leg and a right leg with composite femur and tibia at peak accelerations ranging from 5 to 20 Gs to examine overall dynamic response.				
14. SUBJECT TERMS Bioengineering Composites Sensors Biomechanics Manikin SBIR			15. NUMBER OF PAGES 499	
			16. PRICE CODE	
17. SECURITY CLASSIFICATION OF REPORT UNCLASSIFIED	18. SECURITY CLASSIFICATION OF THIS PAGE UNCLASSIFIED	19. SECURITY CLASSIFICATION OF ABSTRACT UNCLASSIFIED	20. LIMITATION OF ABSTRACT UL	

THIS PAGE LEFT BLANK INTENTIONALLY

ACKNOWLEDGMENTS

This program involved a multidisciplinary effort for its successful completion. SPARTA would like to acknowledge the efforts of our team member First Technology Safety Systems (FTSS) in Plymouth Michigan for their inputs in advanced test dummy design and performance. The authors would like to particularly acknowledge Mr. Mike Salloam and Mr. Mike Beebe (formerly of FTSS) for their valuable contribution to both the long bone skeletal and flesh segment designs. The authors would also like to express their appreciation to Mr. Ric Rasmussen and Lt. Eric Spittle, contract managers at Wright-Patterson AFB OH, for their guidance and technical inputs.

Accession For	
NTIS GRA&I	<input checked="checked" type="checkbox"/>
DTIC TAB	<input type="checkbox"/>
Unannounced	<input type="checkbox"/>
Justification	
By	
Distribution/	
Availability Codes	
Dist	Avail and/or Special
A-1	

TABLE OF CONTENTS

<u>Section</u>	<u>Title</u>	<u>Page</u>
	EXECUTIVE SUMMARY	E-1
1.0	INTRODUCTION	1-1
1.1	Background	1-1
1.2	Program	1-3
1.3	Potential Future Applications.....	1-4
2.0	RESEARCH APPROACH	2-1
2.1	Program Objectives	2-1
2.2	Program Work Plan.....	2-2
3.0	PROGRAM RESEARCH RESULTS.....	3-1
3.1	Instrumentation Development.....	3-1
3.2	Structural Analysis	3-67
3.3	Long Bone Composite Design	3-200
3.4	Flesh Development	3-221
3.5	Fabrication	3-247
3.6	Validation Tests	3-253
3.7	Dynamic Sled Test	3-181
4.0	DISCUSSION OF RESULTS	4-1
4.1	Long Bone Structural Design.....	4-1
4.2	Instrumentation	4-5
4.3	Static and Dynamic Test Results	4-11
5.0	REFERENCES	5-1

LIST OF FIGURES

<u>No.</u>	<u>Title</u>	<u>Page</u>
Figure E-1	Femur and Tibia Long Bone Baseline Design Load Cases	E-2
Figure E-2	Femur and Tibia Finite Element Models	E-3
Figure E-3	Comparison of the Hybrid III, ABC Man, and Human Long Bone Segment Geometries	E-5
Figure E-4	Femur and Tibia Flesh Showing Exposed Tactical Foil and Fully Assemble Leg Segment.....	E-7
Figure E-5	Load and Acceleration Histories for the 20g Sled Test.	E-8
Figure E-6	Load and Acceleration Histories for the 20g Sled Test	E-9
Figure E-7	Finite Element Model Deformed Plot Showing Flesh Motion Relative to the Bone	E-11
Figure E.8	Comparison of Actual Femur Load History to Predicted Loads Showing Effect of Soft Flesh on Femur Load	E-11
Figure 3.1-1	Micro-Probe Applicable to Composites.....	3-3
Figure 3.1-2	Cross-Sectional View of Interferometric Sensor Mounted on Capillary Pedestal.	3-3
Figure 3.1-3	Embedded Strain Sensor Tensile Test Specimen Cutting Map	3-7
Figure 3.1-4	Embedded Resistance Foil Strain Gage Biaxial Test Specimen Description.	3-8
Figure 3.1-5	Embedded Fiberoptic Strain Sensor Biaxial Test Specimen Description	3-9
Figure 3.1-6	Embedded Fiberoptic and Foil Strain Gage Shear Test Specimen	3-10
Figure 3.1-7	Embedded Strain Sensor Concept for Cable Exit Through Bottom of Laminate	3-12
Figure 3.1-8	Installation of Embedded Strain Sensors in 3 x 12" Panel.....	3-13
Figure 3.1-9	Installation of Embedded Foil Strain Gages in 3" x 12" Panel	3-13
Figure 3.1-10.	Installation of Embedded Foil Strain Gage in 6 x 6" Panel	3-14
Figure 3.1-11	Axial and Biaxial Load Condition Test Setup	3-14
Figure 3.1-12	Test #56 Load/Pressure vs. Time	3-17
Figure 3.1-13	Test #57 Load/Pressure vs. Time	3-17

LIST OF FIGURES

<u>No.</u>	<u>Title</u>	<u>Page</u>
Figure 3.1-14.	Test #58 Load/Pressure vs. Time	3-17
Figure 3.1-15.	Test #59 Load/Pressure vs. Time	3-17
Figure 3.1-16	Test #64 Load/Pressure vs. Time	3-18
Figure 3.1-17	Test #62 Load/Pressure vs. Time	3-18
Figure 3.1-18	Test #64 Load/Pressure vs. Time	3-18
Figure 3.1-19	Test #66 Load/Pressure vs. Time	3-18
Figure 3.1-20	Test #68 Load/Pressure vs. Time	3-19
Figure 3.1-21	Test #61 Load/Pressure vs. Time, Hand Side Loading	3-19
Figure 3.1-22	Test #65 Load/Pressure vs. Time, Side Loading	3-19
Figure 3.1-23	Test #69 Load/Pressure vs. Time, Side Loading	3-19
Figure 3.1-24	Test #63 Load/Pressure vs. Time	3-20
Figure 3.1-25	Test #67 Load/Pressure vs. Time	3-20
Figure 3.1-26	Test #'s 56, 57 Load/Pressure vs. Time	3-20
Figure 3.1-27	Test #'s 59, 60 Load/Pressure vs. Time	3-20
Figure 3.1-28	Test #'s 56, 57 Load vs. Pressure, Cycles and Slopes	3-21
Figure 3.1-29a	Test #'s 56, 57 Cycle Slope Correlation	3-21
Figure 3.1-29b	Test #'s 56,57 Cycle Slope Correlation	3-22
Figure 3.1-30	Test #'s 59, 60 Load vs. Pressure, Cycles and Slopes	3-22
Figure 3.1-31	Test #'s 59, 60 Cycle Slope Correlation	3-23
Figure 3.1-32	Test #56 Strain vs. Time	3-25
Figure 3.1-33	Test #57 Strain vs. Time	3-25
Figure 3.1-34	Test #58 Strain vs. Time	3-25
Figure 3.1-35	Test #59 Strain vs. Time	3-26
Figure 3.1-36	Test #60 Strain vs. Time	3-26
Figure 3.1-37	Test #62 Strain vs. Time	3-26
Figure 3.1-38	Test #64 Strain vs. Time	3-27
Figure 3.1-39	Test #66 Strain vs. Time	3-27
Figure 3.1-40	Test #68 Strain vs. Time	3-27
Figure 3.1-41	Test #61 Strain vs. Time	3-28
Figure 3.1-42	Test #65 Strain vs. Time	3-28
Figure 3.1-43	Test #69 Strain vs. Time	3-28
Figure 3.1-44	Test #63 Strain vs. Time	3-29

LIST OF FIGURES

<u>No.</u>	<u>Title</u>	<u>Page</u>
Figure 3.1-45	Test #67 Strain vs. Time.	3-29
Figure 3.1-46	Test #56 Strain vs. Time	3-29
Figure 3.1-47	Test #57 Strain vs. Load.....	3-30
Figure 3.1-48	Test #58 Strain vs. Load.....	3-30
Figure 3.1-49	Test #59 Strain vs. Load.....	3-30
Figure 3.1-50	Test #60 Strain vs. Load.....	3-31
Figure 3.1-51	Test #62 Strain vs. Load.....	3-31
Figure 3.1-52	Test #64 Strain vs. Load.....	3-31
Figure 3.1-53	Test #66 Strain vs. Load.....	3-32
Figure 3.1-54	Test #68 Strain vs. Load.....	3-32
Figure 3.1-55a	Test #61 0° Strain vs. Load, Side Loading.....	3-33
Figure 3.1-55b	Test #61 45° Strain vs. Load, Side Loading.....	3-33
Figure 3.1-55c	Test #61 90° Strain vs. Load, Side Loading.....	3-33
Figure 3.1-56a	Test #65 0° Strain vs. Load, Side Loading.....	3-34
Figure 3.1-56b	Test #65 45° Strain vs. Load, Side Loading.....	3-34
Figure 3.1-56c	Test #65 90° Strain vs. Load, Side Loading.....	3-34
Figure 3.1-57a	Test #69 0° Strain vs. Load, Side Loading.....	3-35
Figure 3.1-57b	Test #69 45° Strain vs. Load, Side Loading.....	3-35
Figure 3.1-57c	Test #69 90° Strain vs. Load, Side Loading.....	3-35
Figure 3.1-58a	Test #'s 56, 57 Axial vs. Transverse Strain	3-36
Figure 3.1-59	Test #58 Axial vs. Transverse Strain	3-36
Figure 3.1-60	Test #'s 59, 60 Axial vs. Transverse Strain	3-36
Figure 3.1-61	Test #62 Axial vs. Transverse Strain	3-37
Figure 3.1-62	Test #64 Axial vs. Transverse Strain	3-37
Figure 3.1-63	Test #66 Axial vs. Transverse Strain	3-37
Figure 3.1-64	Test #68 Axial vs. Transverse Strain	3-38
Figure 3.1-65	Test #61 Axial vs. Transverse Strain, Side Loading	3-38
Figure 3.1-66	Test #65 Axial vs. Transverse Strain, Side Loading	3-38
Figure 3.1-67	Test #69 Axial vs. Transverse Strain, Side Loading	3-39
Figure 3.1-68	Test #'s 63, 67 Axial vs. Transverse Strain	3-39
Figure 3.1-69	Test Fabrication Coupon Schematic	3-41
Figure 3.1-69a	Post Embedded Gage (PEG) Tubes Test Specimens	3-42

LIST OF FIGURES

<u>No.</u>	<u>Title</u>	<u>Page</u>
Figure 3.1-70	Tube Specimen in Compression Test Fixture	3-43
Figure 3.1-71	Tube Specimen in Torque Test Fixture	3-43
Figure 3.1-72	Tube Torque Test Fixture Design Drawing	3-44
Figure 3.1-73	Test #4 Load vs. Time	3-45
Figure 3.1-74	Test #4 Compressive Strain vs. Time.....	3-45
Figure 3.1-75	Test #4 Gauge Strain vs. Time	3-45
Figure 3.1-76	Test #7 Load vs. Time	3-46
Figure 3.1-77	Test #7 Compressive Strain vs. Time.....	3-46
Figure 3.1-78	Test #7 Gauge Strain vs. Time	3-46
Figure 3.1-79	Test #10 Load vs. Time	3-47
Figure 3.1-80	Test #10 Compressive Strain vs. Time.....	3-47
Figure 3.1-81	Test #10 Gauge Strain vs. Time	3-47
Figure 3.1-82	Test #13 Load vs. Time	3-48
Figure 3.1-83	Test #13 Compressive Strain vs. Time.....	3-48
Figure 3.1-84	Test #13 Gauge Strain vs. Time	3-48
Figure 3.1-85	Test #16 Load vs. Time	3-49
Figure 3.1-86	Test #16 Compressive Strain vs. Time.....	3-49
Figure 3.1-87	Test #16 Gauge Strain vs. Time	3-49
Figure 3.1-88	Test #21 Load vs. Time	3-50
Figure 3.1-89	Test #21 Compressive Strain vs. Time.....	3-50
Figure 3.1-90	Test #21 Gauge Strain vs. Time	3-50
Figure 3.1-91	Test #4 Load vs. Strain.....	3-51
Figure 3.1-92	Test #21 Load vs. Strain.....	3-51
Figure 3.1-93	Test #7 Torque vs. Shear Strain	3-51
Figure 3.1-94	Test #10 Torque vs. Shear Strain	3-52
Figure 3.1-95	Test #13 Torque vs. Shear Strain	3-52
Figure 3.1-96	Test #16 Torque vs. Shear Strain	3-52
Figure 3.1.2-1	The Pendulum Impact Test Rig used for Testing and Calibrating the Piezo Sensors	3-57
Figure 3.1.2-2	The Six Configurations Employed to Test the Sensor Response.....	3-58
Figure 3.1.2-3	The Behavior of the Piezo Sensor V vs t Output Signal as a Function of Test Configuration.....	3-59

LIST OF FIGURES

<u>No.</u>	<u>Title</u>	<u>Page</u>
Figure 3.1.2-4	Sensor Voltage Output as a Function of Pendulum Impact Energy and Impulse for Five Sensor Configurations.....	3-60
Figure 3.1.2-5a	Sensor Voltage Output as a Function of Kinetic Energy of the Pendulum Impactor for an 11 lb. and a 32 lb. Pendulum.....	3-61
Figure 3.1.2-5b	Sensor Voltage Output as a Function of Momentum of the Pendulum Impactor for an 11 lb. and a 32 lb. Pendulum.....	3-61
Figure 3.1.2-5c	Sensor Voltage Output as a Function of Momentum of the Velocity of the Pendulum Impactor for an 11 lb. and a 32 lb. Pendulum	3-62
Figure 3.1.2-6	The Placement of Piezo Sensor Within the Block of Synthetic Flesh	3-63
Figure 3.1.2-7a	The Effect of Horizontal Distance Between Impact and Sensor Location on Sensor Output Peak Voltage. The data was Taken from Sensors 1 Through 6 and Impact Locations 1 Through 6 Only. The Impact Resulted from Pulling an 11 Pound Pendulum Back 12 Inches, which Generates 0.79 ft. lbs. of Energy	3-64
Figure 3.1.2-7b	The Effect of Radial Distance on the Peak Voltage Output of Piezo Sensors Embedded in PVC Elastomer. The Triangles Represent Data Between Horizontal Pairs of Impact and Sensor Locations. The Circles Represent Data from Vertical or Diagonal Pairs	3-65
Figure 3.1.2-8	A View of the Block of Synthetic Flesh After Sectioning and Disbonding to Reveal Three Damaged Sensors	3-66
Figure 3.2.1-1	Non-Linear Beam ABAQUS Femur Finite Element Model.....	3-70
Figure 3.2.1-2	Beam Stress Analysis Force-Displacement Relations and Coordinate System Definition.....	3-72
Figure 3.2.1-3	Beam Stress Analysis Maximum Bending and Shear Stress/Strain Circumferential Location	3-73
Figure 3.2.1-4	Beam Stress Analysis Local Laminate Coordinate System Used for Composite Stress Analysis.....	3-75
Figure 3.2.1-5	Composite Femur Beam Model Force and Moment Resultants (7500 lbs. Compress, $R_0 = 0.6"$ $R_i = 0.25"$, 75% 0°/25° ±45° T1000-G/Epoxy.....	3-76
Figure 3.2.1-6	Composite Femur Beam Model Laminate Stress (7500 lbs. Compress, $R_0 = 0.6"$ $R_i = 0.25"$, 75% 0°/25° ±45° T1000-G/Epoxy.....	3-77
Figure 3.2.1-7	Composite Femur Beam Model Force and Moment Resultants (7500 lbs. Compress, $R_0 = 0.6"$ $R_i = 0.25"$, 75% 0°/25° ±45° T1000-G/Epoxy.....	3-76

LIST OF FIGURES

<u>No.</u>	<u>Title</u>	<u>Page</u>
Figure 3.2.1-8	Composite Femur Beam Model Ply Fiber Direction Strains at Maximum Transverse Stress Locations (7500 lbs. Compress, $R_0 = 0.6"$ $R_i = 0.25"$, 75% $0^\circ/25^\circ$ $\pm 45^\circ$ T1000-G/Epoxy)	3-79
Figure 3.2.1-9	Composite Femur Beam Model Ply Fiber Direction Strains (7500 lbs. Compress, $R_0 = 0.6"$ $R_i = 0.25"$, 75% $0^\circ/25^\circ$ $\pm 45^\circ$ T1000-G/Epoxy)	3-76
Figure 3.2.1-10	Composite Femur Beam Model Ply Fiber Direction Strains at Extreme Bending Stress Locations (8640 lbs. Compress, $R_0 = 0.6"$ $R_i = 0.4"$, T1000-G/Epoxy)	3-82
Figure 3.2.1-11	Composite Femur Beam Model Ply Fiber Direction Strains (8640 lbs. Compress, $R_0 = 0.6"$ $R_i = 0.4"$, T1000-G/Epoxy)	3-83
Figure 3.2.1-12	Composite Femur Beam Model Ply Fiber Direction Strains at Maximum Transverse Stress Locations (8640 lbs. Compress, $R_0 = 0.6"$ $R_i = 0.4"$, T1000-G/Epoxy)	3-84
Figure 3.2.1-13	Composite Femur Beam Model Ply Force and Moment Resultants (8640 lbs. Compress, $R_0 = 0.6"$ $R_i = 0.4"$, T1000-G/Epoxy)	3-85
Figure 3.2.1-14	Composite Femur Beam Model Laminate Stress (8640 lbs. Compress, $R_0 = 0.6"$ $R_i = 0.4"$, T1000-G/Epoxy)	3-86
Figure 3.2.1-15	Composite Femur Beam Model Ply Fiber Direction Strains at Extreme Bending Stress Locations (1623 lbs. Cantilever Bending, $R_0 = 0.6"$ $R_i = 0.4"$, T1000-G/Epoxy)	3-87
Figure 3.2.1-16	Composite Femur Beam Model Ply Fiber Direction Strains (1623 lbs. Cantilever Bending, $R_0 = 0.6"$ $R_i = 0.4"$, T1000-G/Epoxy)	3-88
Figure 3.2.1-17	Composite Femur Beam Model Ply Fiber Direction Strains at Maximum Transverse Stress Locations (1623 lbs. Cantilever Bending, $R_0 = 0.6"$ $R_i = 0.4"$, T1000-G/Epoxy)	3-89
Figure 3.2.1-18	Composite Femur Beam Model Force and Moment Resultants (1623 lbs. Cantilever Bending, $R_0 = 0.6"$ $R_i = 0.4"$, T1000-G/Epoxy)	3-90
Figure 3.2.1-19	Composite Femur Beam Model Laminate Stress 1623 lbs. Cantilever Bending, $R_0 = 0.6"$ $R_i = 0.4"$, T1000-G/Epoxy)	3-91
Figure 3.2.1-20	Composite Femur Beam Model Ply Fiber Direction Strains at Extreme Bending Stress Locations (4500 in-lbs. Torsion Bending, $R_0 = 0.6"$, $R_i = 0.4"$, T1000G/Epoxy) ..	3-92
Figure 3.2.1-20	Composite Femur Beam Model Ply Fiber Direction Strains (4500 in-lbs. Torsion Bending, $R_0 = 0.6"$, $R_i = 0.4"$, T1000G/Epoxy) ..	3-93

LIST OF FIGURES

<u>No.</u>	<u>Title</u>	<u>Page</u>
Figure 3.2.1-22	Composite Femur Beam Model Ply Fiber Direction Strains at Maximum Transverse Locations (4500 in-lbs. Torsion Bending, $R_0 = 0.6"$, $R_i = 0.4"$, T1000G/Epoxy) ..	3-94
Figure 3.2.1-23	Composite Femur Model Force and Moment Resultants (4500 in-lbs. Torsion Bending, $R_0 = 0.6"$, $R_i = 0.4"$, T1000G/Epoxy) ..	3-95
Figure 3.2.1-24	Composite Femur Beam Model Laminate Stress (4500 in-lbs. Torsion Bending, $R_0 = 0.6"$, $R_i = 0.4"$, T1000G/Epoxy) ..	3-96
Figure 3.2.1-25	Femur Iges File Geometry	3-98
Figure 3.2.1-26	Solid Shaded Image of Local Titanium Insert Femur F.E. Model	3-99
Figure 3.2.1-27	Von-Mises Stress in Titanium Insert Under Compressive Load (Design Iteration I)	3-100
Figure 3.2.1-28	Axial Strain in Composite Stem under Compressive Load (Design Iteration I)	3-101
Figure 3.2.1-29	Titanium Insert Geometries (Design Iterations II and III)	3-102
Figure 3.2.1-30	Regions of Contract in Femur Insert Finite Element Model	3-103
Figure 3.2.1-31	Axial Strain in Composite Stem under Compressive Load (Design Iteration III)	3-105
Figure 3.2.1-32	Von-Mises Stress in Titanium Insert under Compressive Load (Design Iteration III)	3-106
Figure 3.2.1-33	Residual Displacement in Titanium Insert (Design Iteration III)	3-107
Figure 3.2.1-34	Femur Design Loads and Boundary Condition	3-108
Figure 3.2.1-35	ABAQUS Femur Layup Schematic (not to scale)	3-110
Figure 3.2.1-36	Femur Axial (0 Degree) Fiber Stress (psi) under 4,500 lb. Tension Load	3-111
Figure 3.2.1-37	Femur Axial (0 Degree) Fiber Strain (in./in.) under 4,500 lb. Tension Load	3-112
Figure 3.2.1-38	Femur Deformed Shape (Scale Factor = 5) under 4,5000 lb. Tension Load	3-113
Figure 3.2.1-39	Femur Deformed Shape (Scale Factor = 5) under 8,640 lb. Compression Load	3-115
Figure 3.2.1-40	Femur Axial (0 Degree) Fiber Strain (in./in.) under 8,640 lb. Compression Load	3-116
Figure 3.2.1-41	Femur Axial (0 Degree) Fiber Strain of Safety under 8,640 lb. Compression Load	3-117
Figure 3.2.1-42	6 Femur Axial (0 Degree) Fiber Stress (psi) under 8,640 lb. Compression Load	3-118

LIST OF FIGURES

<u>No.</u>	<u>Title</u>	<u>Page</u>
Figure 3.2.1-43.	Femur Axial (0 Degree) Fiber Stress (psi) Resulted from 22,700 in.-lb Lateral Bending Load	3-119
Figure 3.2.1-44	Femur Axial (0 Degree) Fiber Stress Strain (in/in) Resulted from 22,700 in.-lb Lateral Bending Load	3-120
Figure 3.2.1-45.	Femur Axial (0 Degree) Fiber Margin of Safety Resulted from 22,700 in.-lb Lateral Bending Load	3-121
Figure 3.2.1-46	Femur Deformed Shape (Scale Factor = 1) Resulted from 22,700 in.-lb Lateral Bending Load	3-122
Figure 3.2.1-47	Femur Deformed Shape (Scale Factor = 5) Resulted from 4,500 in.-lb Torsion	3-123
Figure 3.2.1-48	Femur 45 Degree Fiber Stress (psi) Resulted from 4,500 in.-lb Torsion	3-124
Figure 3.2.1-49	Femur 45 Degree Fiber Strain (in./in.) Resulted from 4,500 in.-lb Torsion	3-125
Figure 3.2.1-50	Von Mises Stress (psi) of the Titanium Insert Resulted from 4,500 in.-lb Torsion	3-126
Figure 3.2.1-51	Von Mises Stress (psi) of the Titanium Insert Resulted from 8,600 lb Compression Load	3-127
Figure 3.2.1-50	Von Mises Stress (psi) of the Titanium Insert Resulted from 22,700 in.-lb Loading Bending Load	3-128
Figure 3.2.1-51	Von Mises Stress (psi) of the Titanium Insert Resulted from 4,500 in.-lb Torsion	3-129
Figure 3.2.2-1	Preliminary Design of the Tibia Long Bone	3-131
Figure 3.2.2-2	Baseline Tibia Design Loads	3-132
Figure 3.2.2-3	Maximum Bending Induced Strains - Tension Load Case (T1000G.EPOXY 70% 0°/20% ±45 / 10% 90°).....	3-134
Figure 3.2.2-4	Maximum Bending Induced Strains - Compression Load Case (T1000G.EPOXY 70% 0°/20% ±45 / 10% 90°).....	3-135
Figure 3.2.2-5	Maximum Bending Induced Strains - Torsion Load Case (T1000G.EPOXY 70% 0°/20% ±45 / 10% 90°).....	3-136
Figure 3.2.2-6	Maximum Bending Induced Strains - Bending Load Case (T1000G.EPOXY 70% 0°/20% ±45 / 10% 90°).....	3-137
Figure 3.2.2-7	Shear Induced Strains - Tension Load Case (T1000G.EPOXY 70% 0°/20% ±45 / 10% 90°).....	3-138
Figure 3.2.2-8	Shear Induced Strains - Compression Load Case (T1000G.EPOXY 70% 0°/20% ±45 / 10% 90°).....	3-139
Figure 3.2.2-9	Shear Induced Strains - Torsion Load Case (T1000G.EPOXY 70% 0°/20% ±45 / 10% 90°).....	3-140

LIST OF FIGURES

<u>No.</u>	<u>Title</u>	<u>Page</u>
Figure 3.2.2-10	Shear Induced Strains - Bending Load Case (T1000G.EPOXY 70% 0°/20% ±45 / 10% 90°).....	3-141
Figure 3.2.2-11	Maximum/Minimum Fiber Strains - Tension Load Case (T1000G.EPOXY 70% 0°/20% ±45 / 10% 90°).....	3-142
Figure 3.2.2-12	Maximum/Minimum Fiber Strains - Compression Load Case (T1000G.EPOXY 70% 0°/20% ±45 / 10% 90°).....	3-143
Figure 3.2.2-13	Maximum/Minimum Fiber Strains - Torsion Load Case (T1000G.EPOXY 70% 0°/20% ±45 / 10% 90°).....	3-144
Figure 3.2.2-14	Maximum/Minimum Fiber Strains - Bending Load Case (T1000G.EPOXY 70% 0°/20% ±45 / 10% 90°).....	3-145
Figure 3.2.2-15	Laminate Stress - Tension Load Case (T1000G.EPOXY 70% 0°/20% ±45 / 10% 90°).....	3-146
Figure 3.2.2-16	Laminate Stress - Compression Load Case (T1000G.EPOXY 70% 0°/20% ±45 / 10% 90°).....	3-147
Figure 3.2.2-17	Laminate Stress - Torsion Load Case (T1000G.EPOXY 70% 0°/20% ±45 / 10% 90°).....	3-148
Figure 3.2.2-18	Laminate Stress - Bending Load Case (T1000G.EPOXY 70% 0°/20% ±45 / 10% 90°).....	3-149
Figure 3.2.2-19	Max Bending Induced Strain Margin of Safety - Torsion (T1000G.EPOXY 70% 0°/20% ±45 / 10% 90°).....	3-150
Figure 3.2.2-20	Max Shear Induced Strain Margin of Safety - Torsion (T1000G.EPOXY 70% 0°/20% ±45 / 10% 90°).....	3-151
Figure 3.2.2-21	Max/Min Fiber Strain Margin of Safety - Torsion Case (T1000G.EPOXY 70% 0°/20% ±45 / 10% 90°).....	3-152
Figure 3.2.2-22	Maximum Bending Strain Margin of Safety - Torsion Load Case (T1000G.EPOXY 70% 0°/20% ±45 / 10% 90°).....	3-153
Figure 3.2.2-23	Shear Induced Strains - Torsion Load Case (T1000G.EPOXY 70% 0°/20% ±45 / 10% 90°).....	3-154
Figure 3.2.2-24	Maximum/Minimum Fiber Strains - Torsion Load Case (T1000G.EPOXY 70% 0°/40% ±45 / 10% 90°).....	3-155
Figure 3.2.2-25	Maximum Bending Induced Strains - Torsion Load Case (T1000G.EPOXY 70% 0°/40% ±45 / 10% 90°).....	3-156
Figure 3.2.2-26	Maximum Shear Induced Strains - Torsion Load Case (T1000G.EPOXY 70% 0°/40% ±45 / 10% 90°).....	3-157
Figure 3.2.2-27	Maximum/Minimum Fiber Strains - Torsion Load Case (T1000G.EPOXY 50% 0°/40% ±45 / 10% 90°).....	3-158
Figure 3.2.2-28	Detailed 3-D ABAQUS Finite Element Model	3-159

LIST OF FIGURES

<u>No.</u>	<u>Title</u>	<u>Page</u>
Figure 3.2.2-29	Material Architecture Layup for the Tibia Long Bone	3-160
Figure 3.2.2-30	Tibia Axial Stress Resulting from 3000 lb Compression	3-162
Figure 3.2.2-31	Tibia Axial Fiber Strain Resulting from 3000 lb Compression	3-163
Figure 3.2.2-32	Tibia Axial Stress Resulting from 3000 lb Compression	3-164
Figure 3.2.2-33	Tibia Axial Strain Resulting from 3000 lb Compression	3-165
Figure 3.2.2-34	Tibia 45° Strain Resulting from 3000 lb Compression	3-166
Figure 3.2.2-35	Tibia 45° Fiber Strain Resulting from 3000 lb Compression	3-167
Figure 3.2.2-36	Tibia 45° Fiber Stress Resulting from 3000 lb Compression	3-168
Figure 3.2.2-37	Tibia 45° Fiber Strain Resulting from 3000 lb Compression	3-169
Figure 3.2.2-38	Axial Hoop Shear Stress Resulting from 3000 lb Compression/Tension.....	3-170
Figure 3.2.2-39	Axial Hoop Strain Stress Resulting from 3000 lb Compression/Tension.....	3-171
Figure 3.2.2-40	Tibia Total Displacement Resulting from 3000 lb. Compression	3-173
Figure 3.2.2-41	Tibia Total Displacement Resulting from 3000 lb. Tension.....	3-174
Figure 3.2.2-42	Tibia 3000 lb. Compression or Tension has High Axial Fiber Strain Margin of Safety	3-175
Figure 3.2.2-43	Tibia 3000 lb. Compression or Tension has 45° Fiber Strain Margin of Safety	3-176
Figure 3.2.2-44	Tibia Axial Stress Resulting from 5250 in-lb. Lateral Bending	3-177
Figure 3.2.2-45	Tibia Axial Strain Resulting from 5250 in-lb. Lateral Bending	3-178
Figure 3.2.2-46	Tibia 45° Fiber Stress Resulting from 5250 in-lb. Lateral Bending	3-179
Figure 3.2.2-47	Tibia 45° Fiber Strain Resulting from 5250 in-lb. Lateral Bending	3-180
Figure 3.2.2-48	Tibia Axial Hoop Shear Resulting from 5250 in-lb. Lateral Bending ..	3-181
Figure 3.2.2-49	Tibia Axial Hoop Shear Strain Resulting from 5250 in-lb. Lateral Bending	3-182
Figure 3.2.2-50	Tibia Axial Radial Shear Stress Resulting from 5250 in-lb. Lateral Bending	3-183
Figure 3.2.2-51	Tibia Radial Hoop Shear Stress Resulting from 5250 in-lb. Lateral Bending.....	3-184
Figure 3.2.2-52	Tibia Axial Stress Resulting from 4500 in-lb. Lateral Bending	3-185
Figure 3.2.2-53	Tibia Axial Strain Resulting from 4500 in-lb. Torsion.....	3-186
Figure 3.2.2-54	Tibia 45° Fiber Stress Resulting from 4500 in-lb. Torsion.....	3-187
Figure 3.2.2-55	Tibia 45° Fiber Strain Resulting from 4500 in-lb. Torsion.....	3-188
Figure 3.2.2-56	Tibia Hoop Stress Resulting 4500 in-lb. Torsion	3-189

LIST OF FIGURES

<u>No.</u>	<u>Title</u>	<u>Page</u>
Figure 3.2.2-57	Tibia Axial Hoop Stress Resulting 4500 in-lb. Torsion.....	3-190
Figure 3.2.2-58	Tibia Axial Hoop Shear Strain Resulting 4500 in-lb. Torsion	3-192
Figure 3.2.2-59	Tibia 5250 in-lb Lateral Bending has High Axial Fiber Strain Margin of Safety	3-193
Figure 3.2.2-60	Tibia 5250 in-lb Lateral Bending has High 45° Axial Fiber Strain Margin of Safety	3-194
Figure 3.2.2-61	Tibia 4500 in-lb Torsion has High Axial Fiber Strain Margin of Safety	3-195
Figure 3.2.2-62	Tibia 4500 in-lb Torsion has Moderately High 45° Fiber Strain Margin of Safety	3-196
Figure 3.2.2-63	Tibia Total Displacement Resulting from 5250 in-lb Lateral Bending.....	3-197
Figure 3.2.2-64	Tibia Total Displacement Resulting from 4500 in-lb Torsion.....	3-198
Figure 3.3.1-1	Plot of Fiber Reinforcement Physical Properties Shows the High Strength Fiber Selected for the Longbones.....	3-201
Figure 3.3.3-2	Detail Drawing of Femur Longbone	3-203
Figure 3.3.3-3	Detail Drawing of Titanium Stem.....	3-204
Figure 3.3.3-4	Detail Drawing of Titanium Ball	3-205
Figure 3.3.3-5	Instrumentation Installation for the Femur	3-206
Figure 3.2.3-6	Femur Axial (0 Degree) Fiber Strain (in./in.) under 4,500 lb. Tension Load	3-207
Figure 3.2.3-7	Femur Axial (0 Degree) Fiber Strain (in./in.) under 8,640 lb. Compression Load	3-207
Figure 3.2.3-8	Femur Axial (0 Degree) Fiber Strain (in./in.) Resulted from 22,700 in.-lb Lateral Bending Load	3-208
Figure 3.2.3-9	Femur 45 Degree Fiber Strain (in./in.) Resulted from 4,500 in.-lb. Torsion.....	3-208
Figure 3.3.4-1	Detail Drawing of the Tibia Longbone	3-210
Figure 3.3.4-2	Detail Drawing of the Titanium Tibia Ankle.....	3-211
Figure 3.3.4-3	Instrumentation Installation for the Tibia	3-212
Figure 3.3.4-4	Tibia Axial Fiber Strain Resulting from 3000 lb. Compression	3-213
Figure 3.3.4-5	Tibia Axial Fiber Strain Resulting from 3000 lb. Compression	3-213
Figure 3.3.4-6	Tibia Axial Fiber Strain Resulting from 5250 in-lb. Lateral Bending.....	3-214
Figure 3.3.4-7	Tibia 45° Fiber Strain Resulting from 4500 in-lb. Torsion.....	3-214

LIST OF FIGURES

<u>No.</u>	<u>Title</u>	<u>Page</u>
Figure 3.3.6-1	Instrumented Femur and Tibia Long Bone Segments	3-217
Figure 3.3.6-2	Femur Showing Strain Gage and Accelerometer Locations	3-218
Figure 3.3.6-3	Tibia Showing Strain Gage and Accelerometer Locations	3-218
Figure 3.3.6-4	Strain Gages are Protected by an 1/8" Thick Piece of Cellular Urethane	3-220
Figure 3.3.6-5	Foam Tape is Placed Between the Wire to Provide a Flush Surface for the Overwrap	3-220
Figure 3.3.7-1	Knee Joint Design Consists of Four Pieces	3-223
Figure 3.3.7-2	Rotation Control Block Controls Rotations of the Tibia with Respect to the Femur.....	3-224
Figure 3.4-1	Block of Cured Candidate Synthetic Flesh Material PRD-085	3-228
Figure 3.4-2	Block of Cured Candidate Synthetic Flesh Material PRD-086	3-228
Figure 3.4-3	Representative Photographs of ADAM Thigh Produced from SPARTA Synthetic Flesh.....	3-235
Figure 3.4-4	Representative Photograph of ADAM Thigh Produced from SPARTA Synthetic Flesh Indicating Areas Where Density/Uniformity Specimens Were Cut Out	3-236
Figure 3.4-5	Representative Photograph of ADAM Thigh Produced from SPARTA Synthetic Flesh Indicating Area Where Difference in Cure Temperature Produce Color Variations.....	3-237
Figure 3.4-6	Representative Micrographs of Specimens Cut From ADAM Thigh Produced from SPARTA Synthetic Flesh (30X magnification)	3-238
Figure 3.4-7	Open Mold for the Femur Flesh.....	3-243
Figure 3.4-8a	Close Up of Insert to Form Cavity for Femur Connector Access.....	3-243
Figure 3.4-8b	Close Up of Insert to Form Cavity for Femur Accelerometer	3-244
Figure 3.4-9	Raised Area in Femur Mold That will Form Cavity for Tactile Foil Array Sensor	3-244
Figure 3.4-10	Open Molds to Form Covers for Femur and Tibia Tactile Foil Array Sensor Cavities	3-245
Figure 3.4-11	Photograph of the Open Flesh Mold	3-245
Figure 3.4-12	Closed Mold for Femur Flesh	3-246
Figure 3.4-13	Closed Mold for the Tibia Flesh	3-246
Figure 3.5-1	Femur Titanium Stems and Titanium Balls	3-247
Figure 3.5-2	Tibia Titanium Ankle Insert Show 4 Different Views.....	3-248

LIST OF FIGURES

<u>No.</u>	<u>Title</u>	<u>Page</u>
Figure 3.5-3	Photographs of Partially Assembled Femur and Tibia Net Compression Molding Tools	3-249
Figure 3.5-4	Full Scale ABC Man Femur and Tibia Compared to Hybrid III and Human Femur and Tibia	3-250
Figure 3.5-5	Photograph of Fiberglass Femur and Tibia Flesh Molds Notice Bone In-Place; Flesh was Molded Around Actual Long Bone Segments to Insure Conformal Fit	3-251
Figure 3.5-6	Full Scale Molded ABC Man Deliverable Flesh Segments	3-252
Figure 3.6.1-1	Long Bone Sensor Interface Schematic	3-253
Figure 3.6.1.1-1	Schematic of Static Femur Bending Test	3-255
Figure 3.6.1.1-2	Picture of Static Femur Bending Test In-Progress	3-255
Figure 3.6.1.1-3	Plot of Load vs. Displacement for Static Femur Bending (Test 1)	3-256
Figure 3.6.1.1-4	Plot of Load vs. Displacement for Static Femur Bending (Test 2)	3-256
Figure 3.6.1.1-5	Picture of Sectioned Femur	3-257
Figure 3.6.1.1-6	Picture of Knee/Shaft Region with Wavy Fibers Indicated	3-257
Figure 3.6.1.2-1	Schematic of Static Femur Compression Test	3-259
Figure 3.6.1.2-2	Picture of Static Femur Compression Test In-Progress	3-260
Figure 3.6.1.2-3	Plot of Load vs. Displacement for Static Femur Compression (Test 1)	3-261
Figure 3.6.1.2-4	Plot of Load vs. Displacement for Static Femur Compression (Test 2)	3-261
Figure 3.6.1.3-1	Schematic of Static Tibia Bending Test	3-262
Figure 3.6.1.3-2	Picture of Static Tibia Bending Test In-Progress	3-262
Figure 3.6.1.3-3	Plot of Load versus Displacement for Static Tibia Bending	3-263
Figure 3.6.1.4-1	Schematic of Static Tibia Compression Test	3-263
Figure 3.6.1.4-2	Picture of Static Tibia Compression Test In-Progress	3-264
Figure 3.6.1.4-3	Plot of Load vs. Displacement for Static Tibia Compression	3-264
Figure 3.6.1.6-1a	Femur Strain Gage Locations and Moment and Load Notations	3-266
Figure 3.6.1.6-1b	Tibia Strain Gage Locations and Moment and Load Notations	3-267
Figure 3.6.1.6-2	Femur and Tibia Calibration Data for the Strain Gages in the Rosette Positions	3-268
Figure 3.6.1.6-3	Femur and Tibia Calibration Data for the Strain Gages in the Axial Positions	3-269
Figure 3.6.1.6-4	Calibration Data for the Femur Accelerometer A1	3-271
Figure 3.6.1.6-5	Calibration Data for the Femur Accelerometer A2	3-272

LIST OF FIGURES

<u>No.</u>	<u>Title</u>	<u>Page</u>
Figure 3.6.1.6-6	Calibration Data for the Tibia Accelerometer A1	3-274
Figure 3.6.1.6-7	Calibration Data for the Tibia Accelerometer A2.....	3-275
Figure 3.6.2-1	Photo of Tactile Foil Array Calibration Test Apparatus.....	3-276
Figure 3.6.2-2	Close-Up of Segment Being Tested.....	3-276
Figure 3.6.2-3	ABC Man Tactile Foil Layout	3-277
Figure 3.6.2-4	Flesh Instrumentation Hook-Up to DAS Schematic.....	3-279
Figure 3.6.2-5	Femur Impact Data & Calibration Curves	3-280
Figure 3.6.2-6	Tibia Impact Data & Calibration Curves	3-280
Figure 3.7-1	Wright-Laboratory ABC Man Sled Test Setup.....	3-282
Figure 3.7-2	On-Sled ABC Man Leg Prior to Testing	3-282
Figure 3.7-3	Load and Acceleration Histories for the 20g Sled Test	3-284
Figure 3.7-4	Load and Acceleration Histories for the 20g Sled Test	3-285
Figure 3.7.1-1	"Lumped Mass" Finite Element Model Depicting Segment Motion, Model is Moving from Right to Left	3-287
Figure 3.7.1-2	Acceleration and Displacement Histories for "Lumped Mass" Model in Global Coordinates	3-288
Figure 3.7.1-3	Accelerations and Rotations of "Lumped Mass" Model in Local Relative Coordinates	3-289
Figure 3.7.1-4	Comparison of Lumped Mass Accelerations and Displacement Histories with the Actual Sled Test Results.....	3-290
Figure 3.7.1-5a	Distributed Mass Flesh Finite Element Model	3-292
Figure 3.7.1-5b	Dynamic Motion of Distributed Flesh Finite Element Model (Model Motion is from Right to Left).....	3-293
Figure 3.7.1-6	Distributed Mass Acceleration and Displacement Histories.....	3-294
Figure 3.7.1-7	Distributed Flesh Mass Acceleration and Angular Rotation Histories Shown in Skeletal Local Coordinates	3-295
Figure 3.7.1-8	Comparison of Distributed Mass FEM Accelerations and Displacements to Actual Test Data	3-296
Figure 3.7.1-9	Section Forces and Moments in the Lumped Finite Element Model Compared with Actual Test Results.....	3-298
Figure 3.7.1-10	Distributed Flesh Mass Finite Element Model Section Forces and Moments Compared to Test Data.....	3-299
Figure 3.7.1-11	Comparison of Distributed Flesh Mass with Axial Sliding and Fixed Bone interface Showing an Increase in Axial Load due to the Relative Moment of the Flesh	3-300

LIST OF FIGURES

<u>No.</u>	<u>Title</u>	<u>Page</u>
Figure 4.1-1	Final 3-D Finite Element Model of the ABC Man Femur and Tibia	4-3
Figure 4.2.1-1	Photographs of Femur and Tibia On-Board Quick Disconnect Connectors	4-6
Figure 4.2.2-1	Flesh Tactile Foil Sensor Output as a Function of Impact Velocity	4-7
Figure 4.2.2-2	Layout for Flesh Sensors.....	4-8
Figure 4.2.2-3	Scaled Tactile Foil Sensor Layout	4-9
Figure 4.2.2-4	Tactile Foil Sensors Showing Folded Installation	4-10
Figure 4.2.2-5	Placement of Tactile Foil Sensors in the ABC Man Femur and Tibia Flesh	4-11
Figure 4.3.1-1	Tactile Foil Calibration Curves for the ABC Man Flesh	4-12
Figure 4.3.2-1	Comparison of Actual Acceleration Test Data with Predicted Data for Stiff Segment Mass (Ass. FEA) and Soft Flesh Distributed Mass (FEM with Flesh).....	4-14
Figure 4.3.2-2	Comparison of Femur Loads Showing the Effect of the Soft Sliding Flesh on the Stiff Bone	4-15
Figure 4.3.2-3	Comparison of Soft Flesh on the Tibia Loads with Test Loads (Not True Sledding Flesh Included in these Calculations)	4-16
Figure 4.3.2-4.	Finite Element Deformed Shape of ABC Man Leg at Full Extension with Distributed Sliding Flesh	4-16

LIST OF TABLES

<u>No.</u>	<u>Title</u>	<u>Page</u>
Table E-1	Femur and Tibia Mechanical Test Summary Results	E-4
Table E-2	Segment Mass Summary	E-6
Table 3.1-1	Embedded Strain Sensor Performance Assessment Test Matrix	3-5
Table 3.1-2	Fiberoptic Panel Fabrication Summary	3-15
Table 3.1-3	Summary of Panel to Fiberoptic Mechanical Tests	3-15
Table 3.1-4	Panel Tensile Modulus of Elasticity and Poissons Ratio Summary	3-39
Table 3.1-5	Tube Test Matrix	3-42
Table 3.1-6	Tube and Panel Measured Versus Predicted Modulus	3-53
Table 3.1-7	Types and Models of Instrumentation for the Long Bones	3-54
Table 3.2-1	Phase I Baseline Femur Design Load Cases	3-67
Table 3.2-2	Phase II Baseline Femur Design Load Cases	3-68
Table 3.2-3	Phase II Baseline Tibia Design Load Cases	3-68
Table 3.2.1-1	Preliminary Sizing Geometry for Femur and Tibia	3-69
Table 3.2.1-2	ICAN Generated Elasticities for 2-D Beam Model	3-81
Table 3.2.1-3	Femur Fiber Stress, Strain, and MS and Titanium Insert Von Mises Stress Summary Table	3-109
Table 3.2.1-4	Femur Structural Analysis Results Summary	3-130
Table 3.2.2-1	Parametric Analyses of Various Material Lay-ups of T1000G/Epoxy Pseudo-Isotropic Elastic Properties Predicted by ICAN Computer Code	3-132
Table 3.2.2-2	Maximum Stress, Strain, and Margin of Safety of the Tibia Long Bone	3-172
Table 3.2.2-3	Material Properties of T1000G/Epoxy and 6Al-4V Titanium	3-191
Table 3.2.2-4	Tibia Structural Analysis Results Summary	3-199
Table 3.3.1-1	Summary of Phase II Composite Weight Goals	3-201
Table 3.3.6-1	Femur and Tibia Pin Allocations	3-219
Table 3.4-1	Required Materials Properties for Improved Synthetic Flesh	3-226
Table 3.4-2	Amounts of Microballoons Required To Bring Synthetic Flesh Resins To Goal Density of 1.0 g/cm ³	3-230
Table 3.4-3	Summary of Density and Compressive Modulus Measurements	3-231
Table 3.4-4	Density Measurements Taken From Thigh Produced From SPARTA Synthetic Flesh Material	3-236

LIST OF TABLES

<u>No.</u>	<u>Title</u>	<u>Page</u>
Table 3.4-5	Comparison of PVC and Urethane Systems	3-240
Table 3.4-6	Summary of Polyurethane Properties	3-241
Table 3.6.1.5-1	Matrix of Various Load Cases Tested and the Corresponding Design and Load Test	3-265
Table 3.6.1.6-1	Femur Strain Gage Resistance	3-270
Table 3.6.1.6-2	Tibia Strain Gage Resistance	3-270
Table 3.6.2-1	Junction Box M Hook-Up	3-278
Table 3.6.2-2	Junction Box K Hook-Up	3-278
Table 3.7-1	Full Scale Sled Test Matrix	3-283
Table 3.7-2	Mass Breakout of ABC Man Leg Segments	3-285
Table 4.1-1	ABC Man Femur and Tibia Design Loads	4-2
Table 4.1-2	Baseline Skeletal Materials for ABC Man Long Bone Segments	4-2
Table 4.1-3	3-D Finite Element Analysis Summary for ABC Man Long Bone Segments	4-4
Table 4.2.1-1	Long Bone Sensor Summary	4-6

THIS PAGE LEFT BLANK INTENTIONALLY

EXECUTIVE SUMMARY

The objective of this Phase II SBIR program was to demonstrate the ability to develop a complete biofidelic leg structure for anthropomorphic test manikins which replicates, both inertially and geometrically, a human leg segment. The scope of the Phase II research successfully extended the Phase I results and included the analysis, design, development and fabrication of a full scale biofidelic advanced composite skeletal and polymer flesh leg segment. Both the skeletal and flesh components contained embedded sensors for real time load and impact measurements.

Current test manikins, such as the Hybrid III, can only provide gross anthropomorphic response to high dynamic accelerations and loads. The metal "bones" in the manikin skeleton limit the ability of the manikins to achieve the high degree of biofidelity required in advanced development programs such as the Crew Escape Technologies (CREST) advanced ejection seat. The metal structural members are heavier and stiffer than their human counterparts however, while they do provide adequate strength, they do not accurately replicate the segment inertial property distribution of human skeletal members. In dynamic crash or ejection scenarios, an incorrect mass distribution produces incorrect mass moments of inertia which may lead to inaccurate gross motions of the test dummy for both full body motion as well as arm and leg flail.

To achieve high inertial biofidelity, new manikin skeletal materials must be able to carry the high loads encountered during testing with greatly reduced segment mass (i.e., the skeletal material must have very high specific strength). Composites are a unique class of materials ideally suited for this application. Composites also offer the potential to directly embed the sensors into the composite structure.

SPARTA was able to successfully develop high strength biofidelic long bone segments which closely approximated human skeletal segments by using advanced composites. SPARTA also developed a flesh material with a density the same as human flesh. The flesh was a urethane polymer which was alloyed to achieve the correct density while maintaining acceptable compliance, tear strength, and handling characteristics.

A detailed structural analysis was performed to develop the composite material architecture. The design loads, shown in Figure E-1, were provided by the Air Force and corresponded to windblast exposures of a 650 knot wind. The finite element models of the femur and tibia are shown in Figure E-2. Two femur and tibia components were fabricated with embedded strain

	LOAD CASE	MAGNITUDE
1	TENSION	4500 lb
2	COMPRESSION	8640 lb
3	TORSION	4500 in-lb
4	BENDING	22700 in-lb

Baseline Femur Design Load Cases

	LOAD CASE	MAGNITUDE
1	TENSION	3000 lb
2	COMPRESSION	3000 lb
3	TORSION	4500 in-lb
4	BENDING	5250 in-lb

Baseline Tibia Design Load Cases

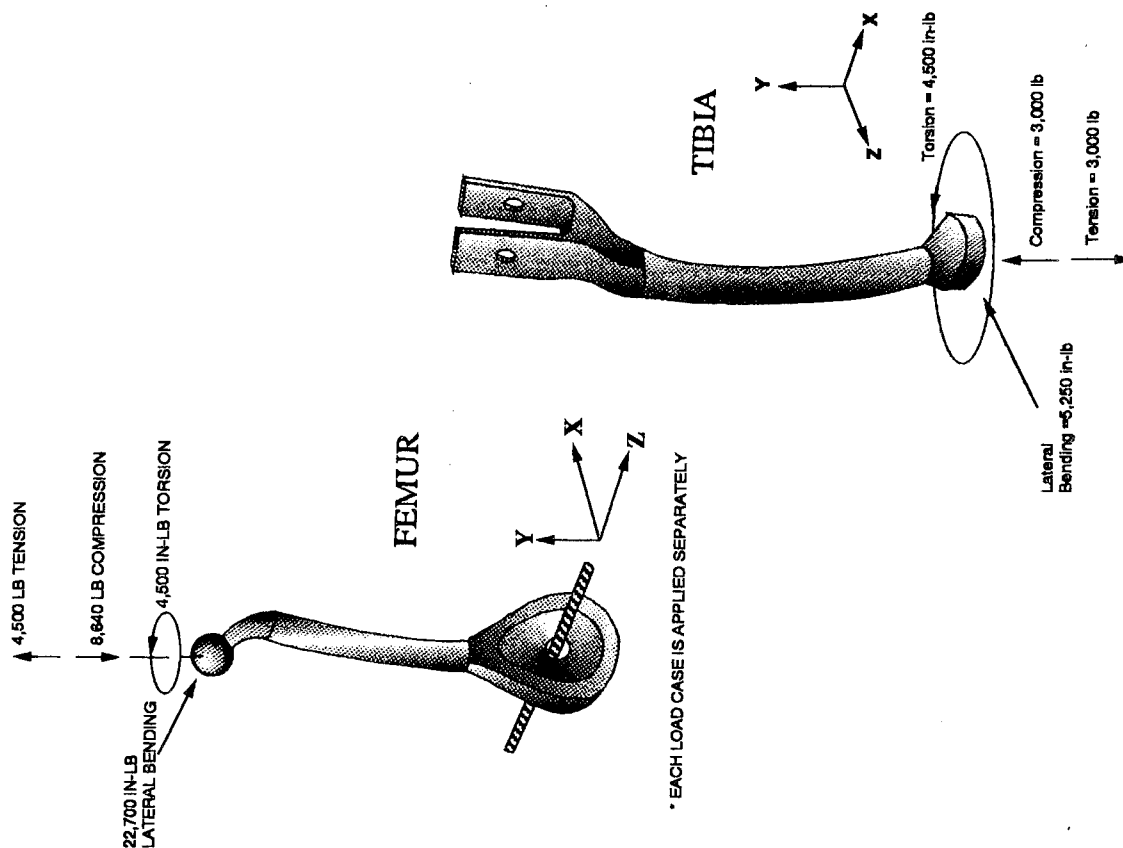
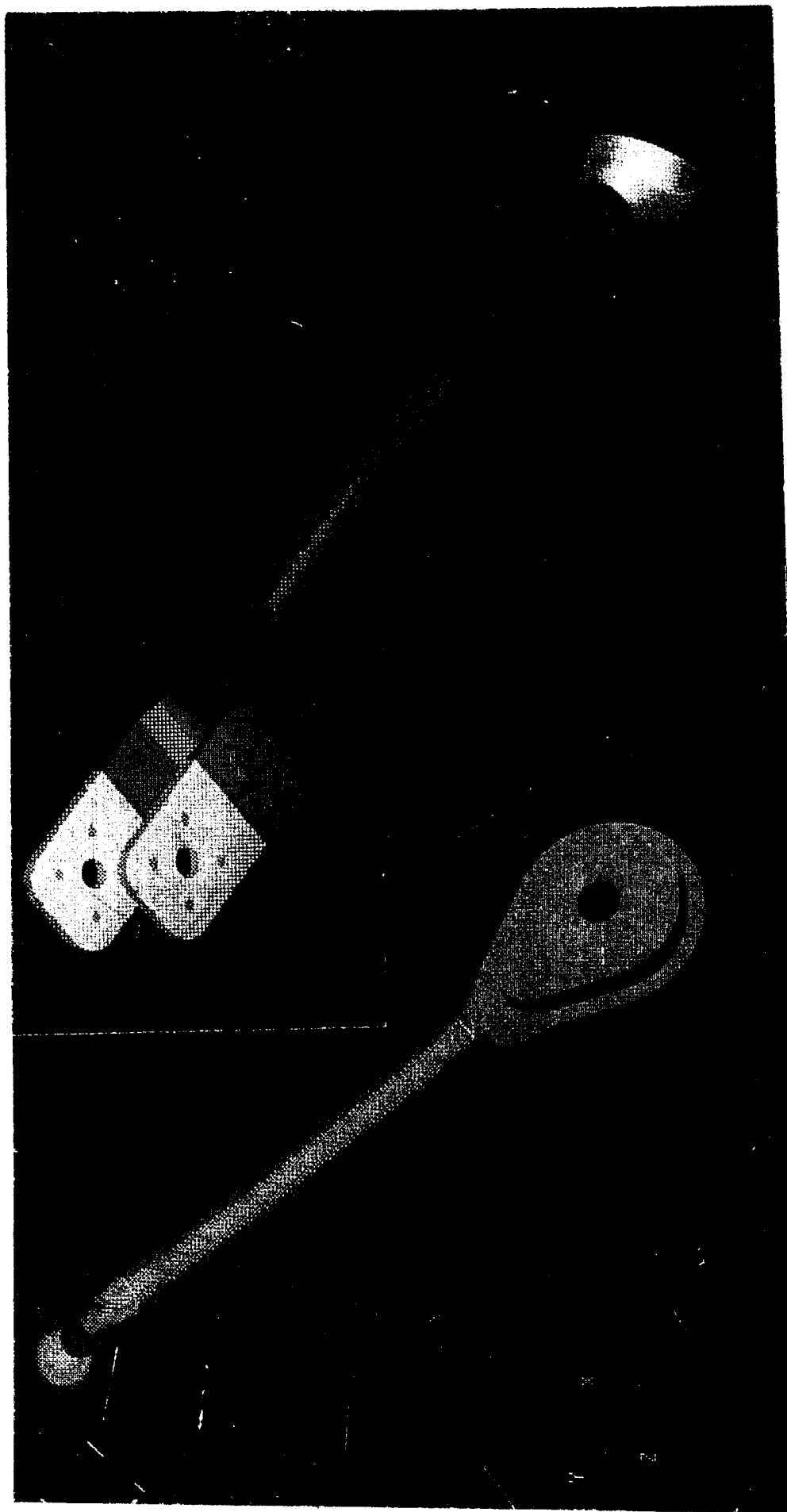


Figure E-1. Femur and Tibia Long Bone Baseline Design Load Cases.



TIBIA

FEMUR

Figure E-2. Femur and Tibia Finite Element Models.

gages and accelerometers. One set was used in the SPARTA mechanical tests and one set delivered to Armstrong Laboratory. The latter set was tested in the sled facility at the Armstrong Laboratory. Figure E-3 compares the full scale instrumented ABC Man long bone segment's anthropomorphism to the state-of-the-art Hybrid III and human long bone segments. Connectors for the embedded instrumentation can be seen on the proximal lateral portion of the femur and tibia respectively. Each long bone segment had a primary and backup (redundant) set of gages. The redundant gage set was located in the same relative position and as close as possible to the primary gage set.

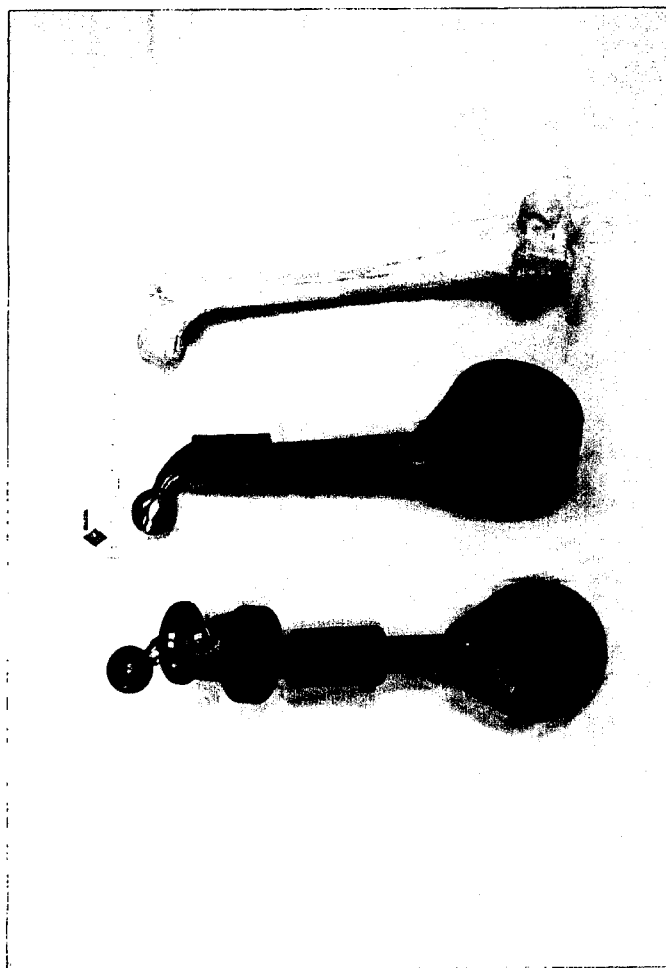
Mechanical compression and bending tests were conducted on the femur and tibia to calibrate the embedded gages and provide verification of the analytical design cases. Table E-1 gives a summary of these mechanical tests.

Table E-1. Femur and Tibia Mechanical Test Summary Results

Article	Load Case	Design Load	Test Load
Femur	Bending	(15" x 1515 lb) 22,722 in-lb	(15" x 650 lb) 9750 in-lb (excessive fiber buckling during tool closure)
Femur	Compression	8640 lb	4400 lb (no failure)
Tibia	Bending	(16" x 328 lb) 5250 in-lb	(16" x 328 lb) 5250 in-lb (no failure)
Tibia	Compression	3000 lb	3025 lb (no failure)

All tests were successful and provided calibration data for both the primary and backup strain gage sensor. All tests reached or exceeded the design load except for femur bending. The femur design load at 22722 in-lbs* (15" x 1515 lb) had a significant impact on the overall femur design. A femur bending test was performed on the first femur specimen which identified a femur fabrication problem. During the test, a crack developed at the shaft/knee interface where the maximum load was predicted. The load was increased to 650 lbs, at which point the femur was no longer able to sustain the load, and the test was halted. During the post test evaluation of the femur, the damaged area was sectioned and visual inspection of the damaged cross-sectioned revealed excessive internal fiber waviness. This misalignment caused a significant reduction in

FEMUR

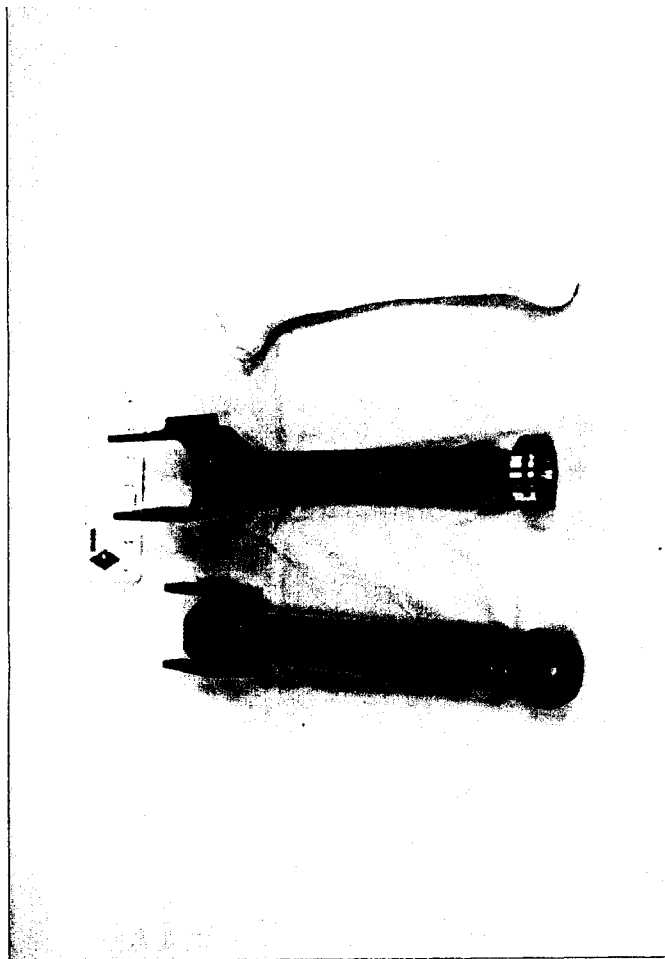


HYBRID III

ABC MAN
PHASE II

HUMAN

TIBIA



HYBRID III

ABC MAN
PHASE II

HUMAN

Figure E-3. Comparison of the Hybrid III, ABC Man, and Human Long Bone Segment Geometries.

strength and stiffness in the crack area. A modification of the femur fabrication tool can be made to maintain the correct fiber alignment. All other design strengths were verified as predicted in the analysis. Based on these data, SPARTA is confident that modification of the femur tool will result in a femur which can meet or exceed the design criteria in bending.

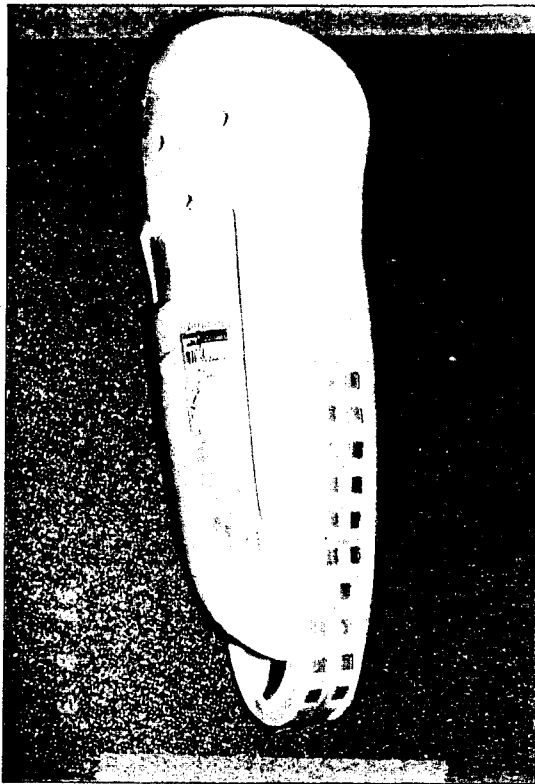
Because the large reduction in the long bone segment mass (to approximate human bone mass) a new heavier flesh was also developed. The flesh was a urethane base alloyed polymer which had a density of 1.005 gr/cc (human flesh is approximately 1.0 gr/cc). The correct density was achieved while maintaining a biofidelic compliance, good tear strength, and good environmental stability. **Figure E-4** shows the flesh with the tactical foil impact piezoelectric sensors exposed and the fully assembled leg segment.

The total upper leg and lower leg segment masses were very close to that of the 50 percentile human/Hybrid III design goal as shown in the mass data summary of **Table E-2**.

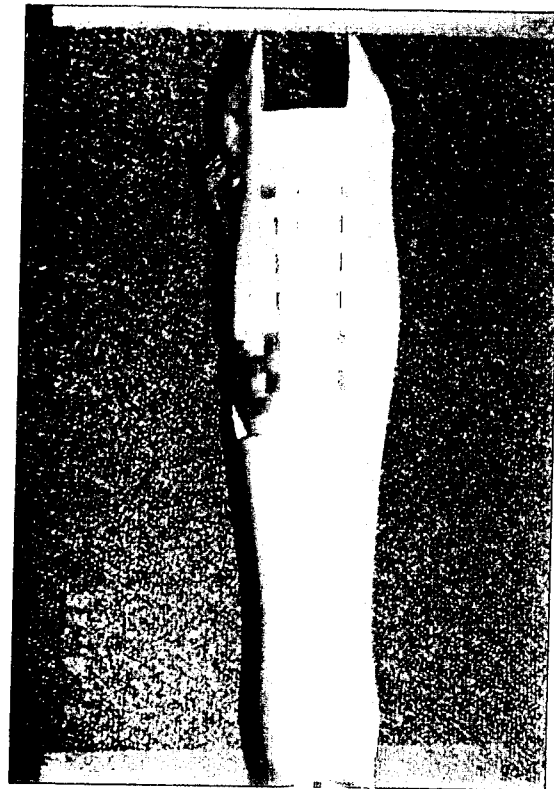
Table E-2. Segment Mass Summary

	ABC MAN	HYBRID III	DELTA
UPPER LEG	20.3 LBS.	19.6 LBS.	+3.6%
LOWER LEG	9.7 LBS.	9.6 LBS.	+1.0%

A series of sled tests were performed using a complete ABC Man femur and tibia attached to an existing Hybrid III manikin. The test accelerations ranged from 5 to 20g and measured the real-time long bone load and acceleration histories. **Figures E-5 and E-6** shows the femur and tibia response for the 20g test. As can be seen, the peak accelerations and peak loads do not occur at the same time nor do the forces necessarily correspond to what would be expected based on the accelerations. Post test analysis of the data indicated that this is due to the large difference in flesh mass and bone mass as well as the large deformations of the flesh relative to the bone segments. The accelerometers measured the accelerations of the long bones, however, because the flesh was much heavier, it produced a significant portion of the total dynamic load. The flesh compliance was much greater than that for bone and thereby provided an out of phase response and recovery time relative to the induced accelerations of the bone. This effect coupled with the fact that the heavy flesh made a significant load contribution to the bone segments produced the out of phase acceleration and load histories shown in **Figure E-5**.



**FEMUR INSTRUMENTATION
(30 PADS TOTAL)**

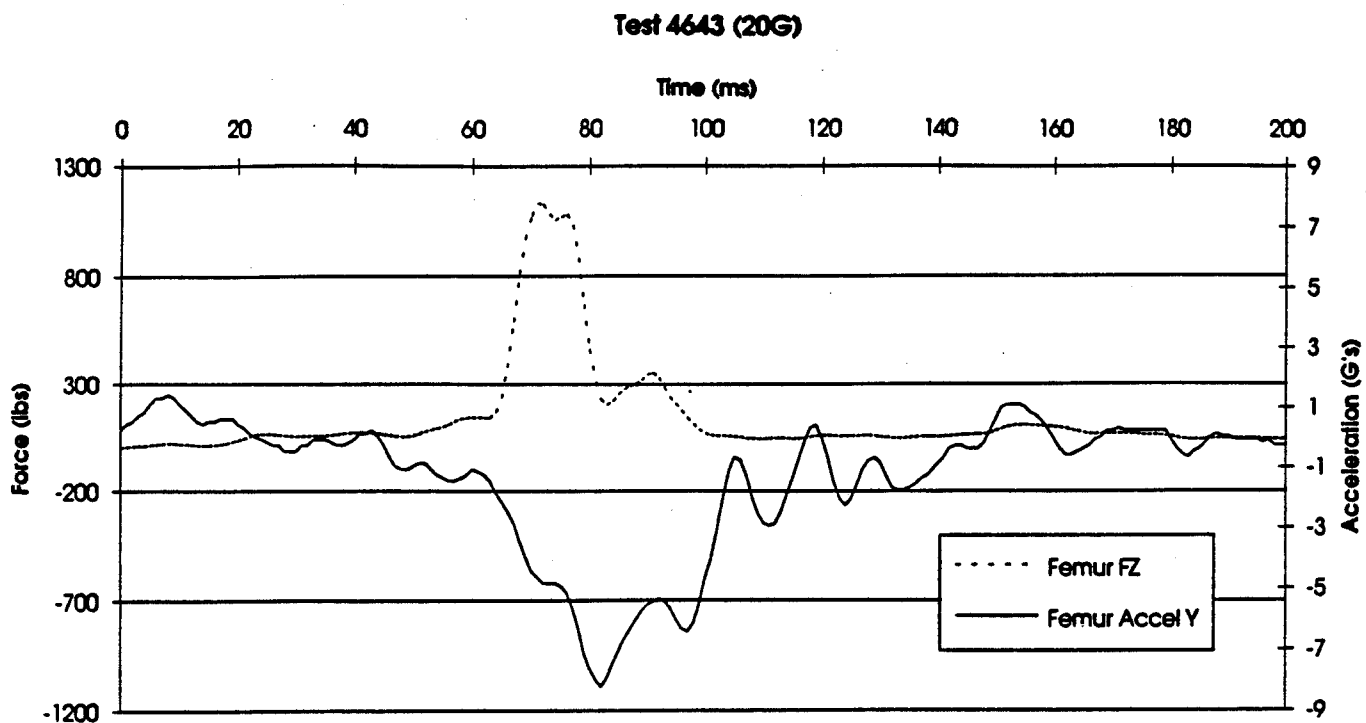


**TIBIA INSTRUMENTATION
(18 PADS TOTAL)**

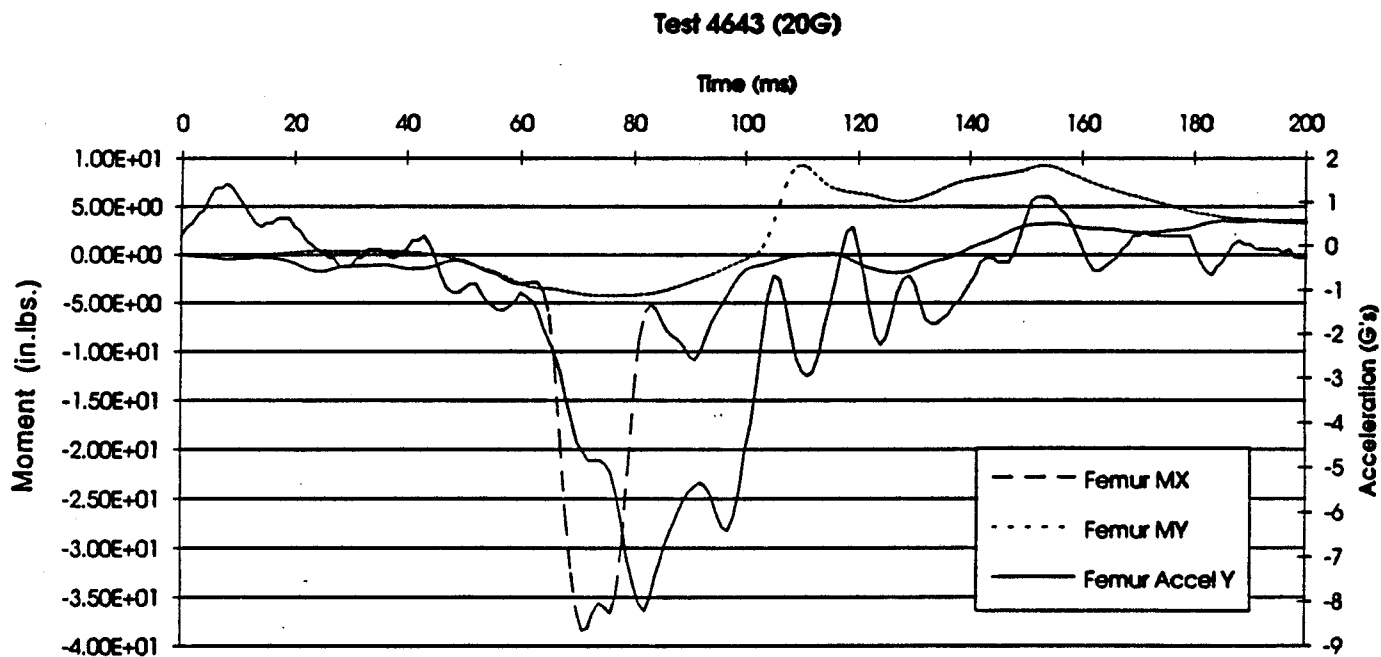


**FULLY ASSEMBLED LATERAL VIEW OF FLESH WITH LONG
BONE CONNECTION SHOWING**

Figure E-4. Femur and Tibia Flesh Showing Exposed Tactical Foil and Fully Assemble Leg Segment.



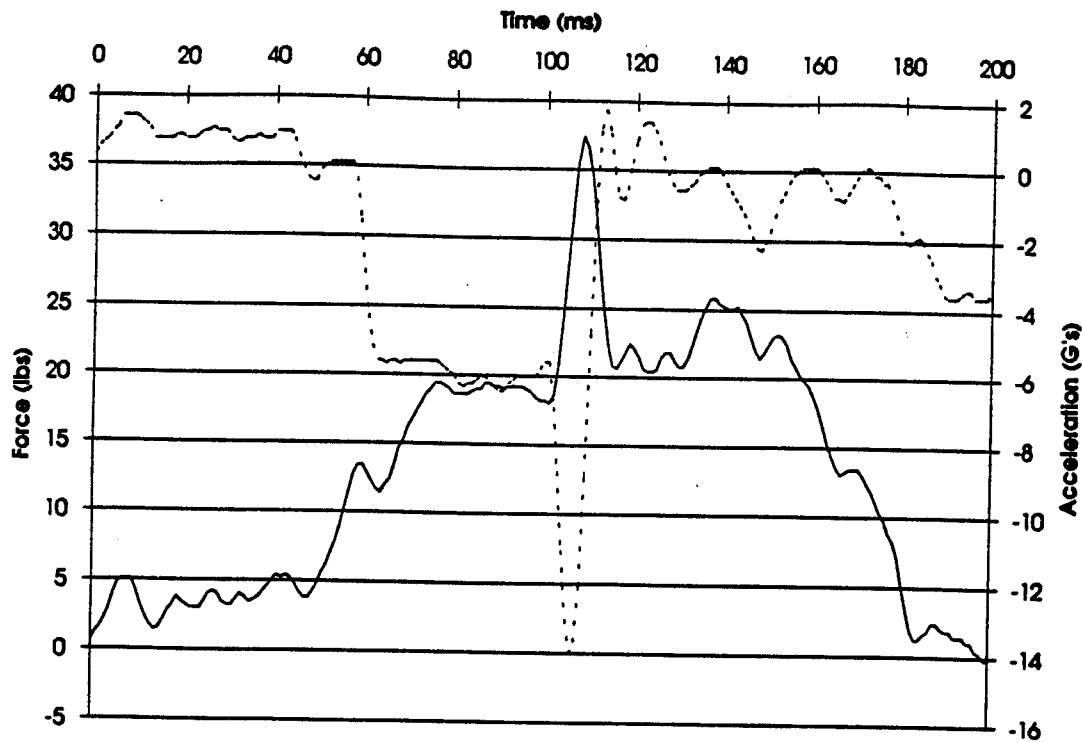
FEMUR AXIAL



FEMUR MOMENTS

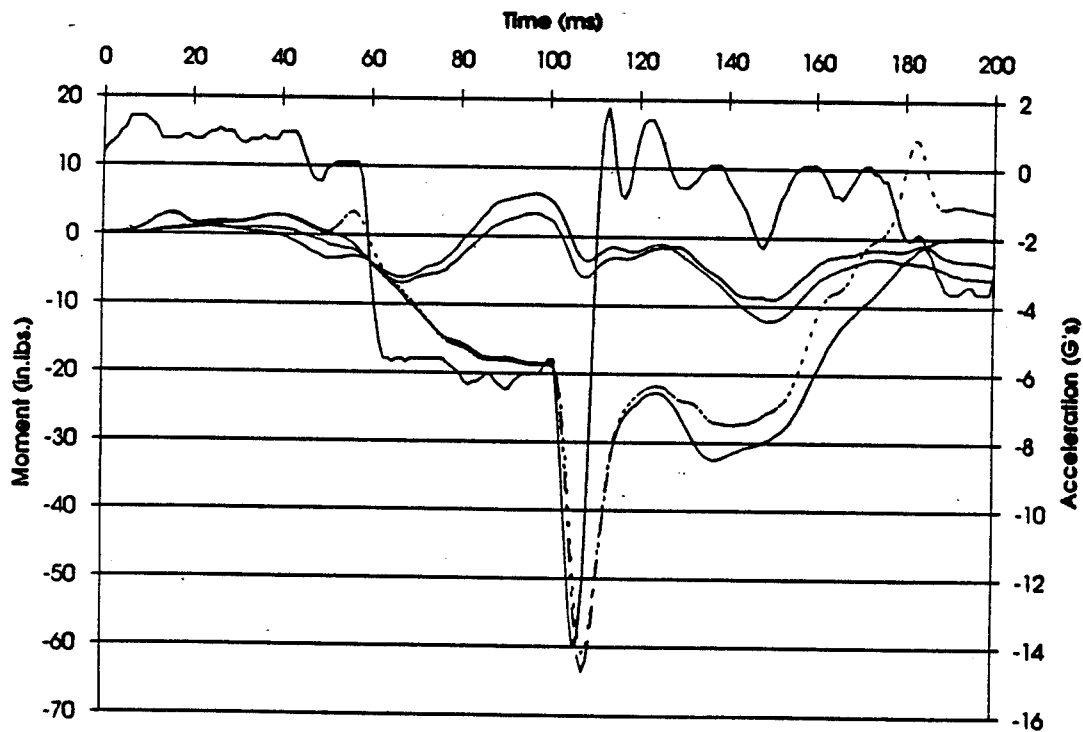
Figure E-5. Load and Acceleration Histories for the 20g Sled Test.

Test 4643 (20G)



TIBIA AXIAL

Test 4643 (20G)



TIBIA MOMENT

Figure E-6. Load and Acceleration Histories for the 20g Sled Test.

In order to assess the effects of the high mass and high compliance of the flesh on the measured bone accelerations and loads, dynamic finite element models of the ABC Man leg were developed. The post test dynamic analysis was much more complicated than anticipated. Because of this, the dynamic FEM had to incorporate some simplifying assumptions, including an assumed forcing function at the pelvis taken from the sled test video, approximate flesh and bone geometry, and sliding flesh on the femur only. However, within these limitations, the FEM showed that the dynamic response of the flesh relative to the bone had a significant effect on the overall response of the ABC Man leg and, by implication, on the response of human occupants. Figure E-6 shows a deformed plot (5x magnification) of the ABC Man leg segment at full extension. The bone was modeled with beam elements and the flesh with 2-D elements. The deformed plot shows how the flesh deforms and slides relative to the skeletal segments and induces forces which effect not only the loads in the bones but also the acceleration profile measured by the long bones. As can be seen in Figure E-7, most of the axial load is generated by the movement of the flesh and is reacted at the distal ends of each long bone respectively. Figure E-8 shows how the mass distribution and relative compliance of the flesh and bone effect the load histories. The test data show a peak load of approximately 1200 lbs, however, the dynamic finite element model with a relatively rigid lumped flesh/bone mass under predicts the peak and gives an inaccurate loading profile. When the model approximated the correct mass distribution and compliance of the flesh (distributed sliding flesh) the peak load closely approximated the measured response and showed a more reasonable load history. These data show that in dynamic environments the loads seen by the long bone segments are largely influenced by the inertial response of the flesh. Therefore, it is imperative to have the correct mass distribution and compliance of the skeletal and flesh components in anthropomorphic test manikins

The successful Phase II program demonstrated that advanced composites can be used to achieve a highly biofidelic mass distribution while maintaining the required strength and incorporating true human like anthropometry. The program demonstrated the flexibility of advanced composites to create high strength lightweight, tailorable geometric components which incorporate hybrid materials such as the synergistic integration of metals, composites and foam as well as embedded instrumentation. The development of the embedded instrumentation was achievable but was more difficult than anticipated. The ability to use co-cured instrumentation on complex net molded parts will require additional development. The post embedded gage (PEG) concept, where the gages were attached to a fully or almost fully cured substrate then overwrapped with a composite layer and postcured was an embedding technology which allowed the incorporation of active gages in the composite component. The embedded tactile foil

approach did have some problems. At very high impacted energies (≈ 17000 in-lb) the foil substrate would rupture, however, these loads may be substantially higher than would be expected to occur in localized impacts.

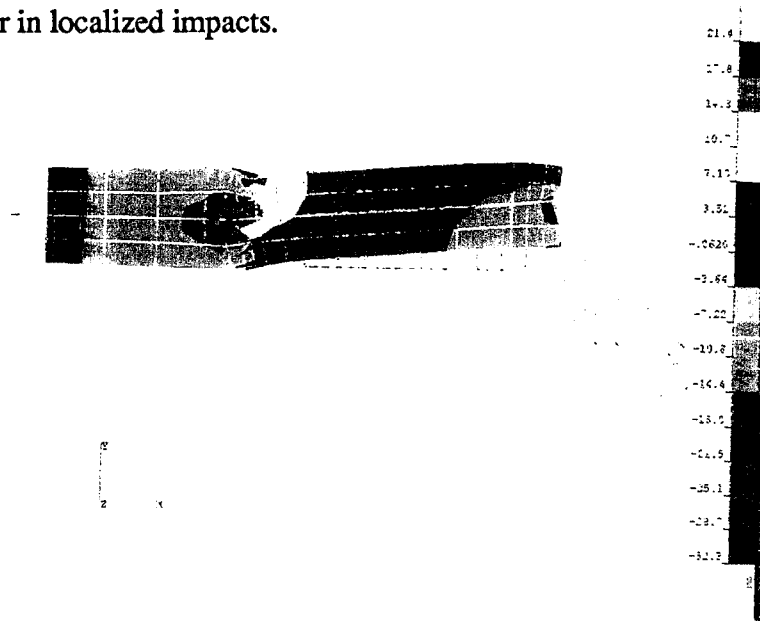


Figure E-7. Finite Element Model Deformed Plot Showing Flesh Motion Relative to the Bone.

Actual Forces vs FEA Axial Forces in Femur 20G Sled Test (4643)

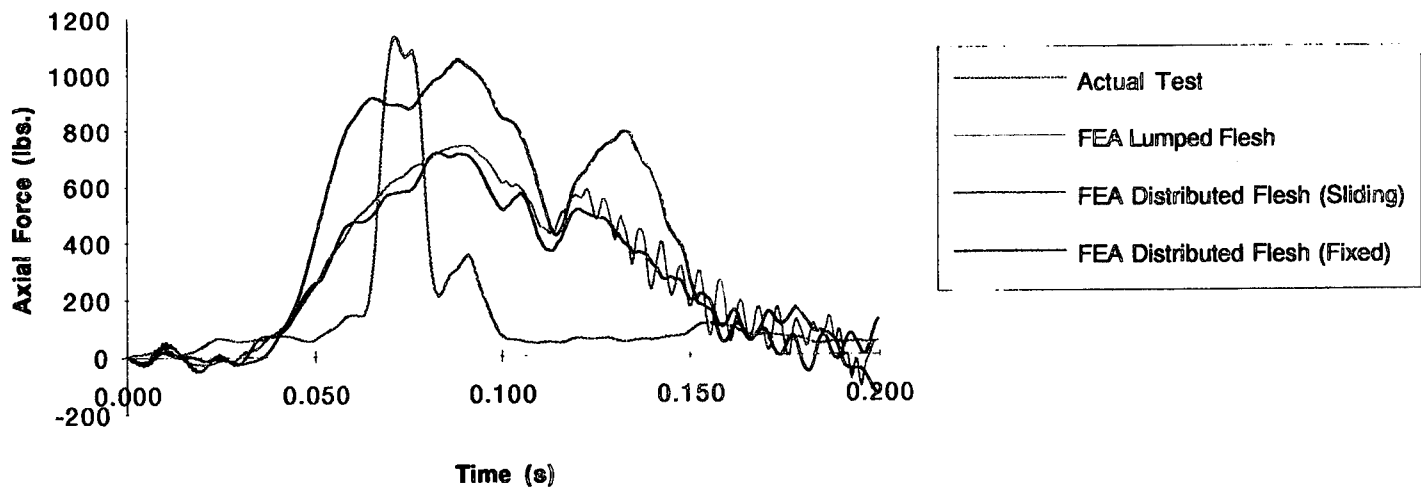


Figure E.8. Comparison of Actual Femur Load History to Predicted Loads Showing Effect of Soft Flesh on Femur Load.

1.0 INTRODUCTION

This research was performed as a Phase II Small Business Innovative Research (SBIR) program. The program was funded by Department of the Air Force, Air Force Materiel Command, Human Systems Center Brooks AFB, Texas and managed by Armstrong Laboratory (AL/CFBV), Wright Patterson AFB, OH, under contract F33615-91-C-0530. The Armstrong Laboratory point of contact was Mr. Ric Rasmussen. The technical effort period of performance for this research program was from May 16, 1991 to November 30, 1993. This research was performed by SPARTA, Inc., at their La Jolla, California office located at 9455 Towne Centre Drive, San Diego, CA 92121.

1.1 BACKGROUND

Development of modern high-fidelity anthropomorphic dummies was first stimulated by the need to simulate human response in automobile and truck crashes. General Motors led the development of a series of anthropomorphic dummies with increasing degrees of biofidelic response. The Hybrid I and II dummies provided significant improvements over previous designs (i.e., Sierra 292-1050) by standardizing parts and instrumentation and by incorporating a more anatomically correct posture and biomechanical kinematics response (1). These dummies were developed in 1971 and 1972. In 1973, General Motors initiated development of a new dummy (ATD 502) under contract to the National Highway Traffic Safety Administration (NHTSA). Improvements over the Hybrid II dummy included a more human-like seating posture, better hard surface impact response, and incorporation of biomechanically-based body response characteristics.

Advances in hardware and design concepts as well as deficiencies in the ATD and Hybrid I and II designs and their biomechanical response parameters gave the impetus for a new dummy design. The Hybrid III, which was begun in 1975 with "The primary objective... to design and build a dummy whose component response characteristics were consistent with available biomechanics data, while retaining or improving upon the best features and assets of the Hybrid II and ATD 502 designs" (1). The Hybrid III has the basic mainframe of the ATD 502 dummy with significant improvements in the neck, thorax, lower torso, and knee segments. Details of the Hybrid III and its predecessor, the ATD 502, are contained in References 1, 2, and 3.

The use of dummies to simulate human response in automotive crash scenarios lends itself naturally to the use of dummies in modeling of high performance aircraft ejection-

seat/crew-extraction phenomena. The state-of-the-art in crew extraction is being developed and implemented in the USAF Crew Escape Technologies (CREST) program. The CREST program objective is "to develop and demonstrate through full-scaled testing, new escape system technologies required to reduce fatalities and major injuries in future aircraft ejections" (4). In particular, the CREST program approach is to design an ejection seat with continuous and conditional control. In other words, crew extraction is accomplished by monitoring the crew, aircraft, and environmental conditions during the ejection process and by controlling ejection parameters (thrust, direction, etc.) to ensure that the best course of action is followed to optimize a safe escape under a unique set of conditions. The CREST program requires a very high-fidelity simulation of actual crew escape scenarios for open ejection from high performance aircraft. Integral to the program's success is a highly biofidelic, anthropomorphic dummy that can replicate and report kinematic crew response during ejection. Current manikins, such as the Hybrid III, can only provide gross anthropomorphic response to high accelerations and loads. The metal "bones" in the manikin skeleton limit the ability of the manikins to achieve the high degree of biofidelity required in an advanced development program such as CREST. The metal structural members are heavier and stiffer than their human counterparts and, while they do provide adequate strength, do not accurately replicate either the segment inertial distribution or the load-deformation properties of human skeletal members. In dynamic crash or ejection scenarios, an incorrect mass distribution will produce incorrect mass moments of inertia which lead to inaccurate gross motions of the test dummy for both full body motion as well as arm and leg flail.

To achieve high inertial biofidelity, new manikin skeletal materials must be able to carry the high loads encountered during testing with greatly reduced segment mass (i.e., the skeletal material must have very high specific strength). Composites are a unique class of materials ideally suited for this application. For example, high strength steel has a specific strength of approximately 950×10^3 in. (5) while graphite or Aramid fiber reinforced epoxies have specific strengths approaching $14,000 \times 10^3$ in. (6).

In order to demonstrate the feasibility of using advanced composites to obtain high inertial biofidelity in manikin skeletal components, SPARTA conducted Phase I and Phase II research efforts. The Phase I effort is detailed in reference 7 and developed proof-of-concept lightweight biofidelic humerus and femur designs. The Phase II program built on the successful Phase I effort to design, develop, and fabricate a total biofidelic composite leg long bone segment and flesh. The Phase II program also included embedded instrumentation in both the skeletal and flesh segments. The successful Phase II program was able to achieve total segment

mass very close to the design 50 percentile human. The upper leg mass was 20.3 lbs and the lower leg mass was 9.7 lbs which was 3.6% and 1.0%, respectively, of the 50 percentile design mass.

1.2 PROGRAM TECHNICAL OBJECTIVES

The overall Phase II program objective was to develop, fabricate, and demonstrate high biofidelic anthropomorphic manikin upper and lower leg segments that would not only have segment inertial characteristics similar to a true human response, but also incorporate embedded sensors for in-situ load measurement thereby eliminating the need for heavy secondary load cells. The Phase II program focus was to develop instrumented, highly biofidelic, complete long bone segments as well as the development of an instrumented biofidelic flesh covering to complement the high biofidelic long bone segments. The Phase II effort directly supports the Armstrong Laboratory objective of developing an advanced highly biofidelic anthropomorphic manikin for Air Force test programs. As noted in Section 1.3, this technology is directly applicable to automotive test dummies thereby supporting the SBIR objective of transferring advanced technology to private industry.

The Phase II program extended the Phase I proof-of-concept demonstration to the development of an inertially biofidelic full leg long bone skeletal and flesh segment. The Phase I effort demonstrated the analysis, design, and fabrication feasibility of using composite materials to obtain highly biofidelic, long bone segments. The focus of the Phase II program was to use composite materials to develop long bone segments that are both inertially and anatomically similar to long bones. Today's manikin long bones are fabricated from steel, are significantly heavier than human bones, have higher mass moments of inertia, and are stiffer than human in-vivo long bones. Thus, while they are extremely rugged, today's manikin long bones have, at best, first order biofidelity. The Phase II program developed long bone designs that have the total mass and mass distribution similar to that of in-vivo long bones thereby, achieving enhanced biofidelity relative to current manikin designs. The need to use external load cells was eliminated by imbedding strain sensors directly into individual long bone segments. Today's manikins also use load cells at the extremities of bone segments. These sensors are usually bulky, heavy, and are subject to bending induced load errors, and their accuracy depends on the rigidity of their mounting interface at the bone. Strain sensors embedded into a long bone segment offer the potential ability to obtain highly consistent data without recalibrating new load-cells and would also allow a consistent, highly biofidelic response to be maintained

(additional mass is not incorporated into the segment by the inclusion of a load measuring device).

An additional Phase II program objective was to develop a complimentary flesh for the long bone segment. Because of the significantly reduced mass of the long bone segments, a new high density flesh was required to maintain the mass distribution biofidelity. As with the skeletal segments, the flesh also incorporated embedded sensors at specific locations to measure blunt trauma impacts and record the energy, location and the time of the impact.

1.3 POTENTIAL FUTURE APPLICATIONS

The successful completion of the ABC Man program provides the design and concept verification of using advanced composites to develop and fabricate high biofidelic, anatomically correct bone and flesh segments for anthropomorphic test dummies. The results of this program have a wide range of applications in commercial, military, and Department of Transportation test programs involving human response to dynamic situations. The successful completion of the Phase II program provides the design and concept verification of an anthropomorphic test dummy which has high inertial and anatomical biofidelity not currently available in existing state-of-the-art test manikins. The use of embedded instrumentation provides the means to obtain consistent and accurate test data with no negative impact on the anthropomorphic static/dynamic response.

The successful results from the Advanced Biofidelic Composite Manikin (ABC Man) development program demonstrated the potential to develop a high biofidelic anthropomorphic test dummy which has near human inertial characteristics. The successful completion of the Phase II program demonstrated the ability to produce biofidelic total segment components and provides a data and experience base to extend the development to a total manikin including other skeletal areas such as the thorax, spine and neck where biofidelity is critical. The embedding of strain sensors into the skeletal segment has never been attempted (8), therefore the successful development of "smart skeletal segments" provided the proof-of-concept and experience to extend this to other skeletal segments.

The letter shown in Appendix A from a potential commercial user (shown in Appendix A) indicate the high degree of interest in using the technology developed under this research program. In addition, the use of this technology is not limited to a specific manikin but could be adapted to a wide variety of test dummies.

The inclusion of active sensors in dynamic structures is applicable not only to test dummies but can be readily extended to general structural members where "health monitoring" or in-situ measurements are required. Typical of such uses would be man rated vehicles such as aircraft and spacecraft skins/structures as well as critical but non-man rated components such as long life Strategic Defense Initiatives (SDI) orbital assets.

2.0 RESEARCH APPROACH

The program was proposed as a basic research effort to develop biofidelic long bone segments with two additional options. Option 1 was to develop a biofidelic flesh to compliment the baseline long bone segments. Option 2 was to develop an inertially biofidelic skull and cranial/mass. The baseline and option 1 proposals were funded. Option 2 was not selected due to a lack of funds. The following sections describe the program objectives and work plan for the baseline program and Option 1.

2.1 Program Objectives

The primary Phase II objectives were to develop, fabricate, and demonstrate high biofidelic anthropomorphic manikin segments that not only have segment inertial characteristics similar to a true human response, but also incorporate embedded sensors for in-situ load measurement thereby eliminating the need for heavy secondary load cells. To realize these objectives and to provide the Air Force the greatest flexibility to meet its research needs, SPARTA proposed a Phase II research effort consisting of a primary program, and two options. The proposed primary program is to develop instrumented, highly biofidelic, complete long bone segments. The two proposed program options were: (1) development of an instrumented biofidelic flesh covering to complement the high biofidelic long bone segments; and (2) development of an instrumented highly biofidelic skull that achieves human-like inertial response. The second option was not exercised by the Air Force due to a funding limitation.

The focus of the Phase II program was to achieve long bone designs that have the total mass distribution similar to that of in vivo long bones. Thus, the developed long bones will exhibit considerably enhanced biofidelity relative to current manikin designs. In addition, the program investigated the feasibility of eliminating external load cells by embedding strain sensors directly into individual long bone segments.

The primary program and its option was to investigate embedding miniature sensors into the developed biofidelic materials. Use of more recently developed sensor technologies is important in order to achieve the ultimate goal of an overall biofidelic response.

The objective of Option 1 was to develop an inertially biofidelic Hybrid III compatible flesh such that the lighter skeletal segments (Femur and Tibia) combined with the new flesh will represent an inertially correct total segment. The external flesh geometry is identical to the

existing Hybrid III geometry, however, the density and internal geometry were modified to achieve the correct segment mass distribution and skeletal fit to accommodate the new skeletal segment. There was also an expressed need for accurate blunt trauma impact force data related to human flesh (10,14). Currently flesh impact force is estimated based on secondary segment acceleration data or evaluation of "cuts" in a simulated flesh. In response to this stated need, SPARTA embedded blunt trauma sensor into the segment flesh so that a direct measurement of the impact force can be obtained. Embedding these sensors in the flesh offers several advantages:

- 1) Protection of the sensors from environmental, handling and testing damage.
- 2) Avoidance of material non uniform response due to large sensors.

The flesh developed in Option 1 is of general utility in that it approximates human flesh mass. However, a specific proof-of-concept prototype was fabricated for a specific long bone segment developed in the proposed primary program. The objective of the embedded sensors allows a detailed pressure distribution curve to be obtained at a known depth below the material surface without introducing material non-uniformities generally associated with the size of conventional pressure measurements. In order to meet these program objectives, SPARTA performed a multiphase research and development effort incorporating the work plan summarized in the task descriptions of Section 2.2.

2.2 Program Work Plan

The work plan for the program is divided into the baseline program consisting of six interrelated tasks and the flesh development (option 1) program which has 7 technical tasks.

2.2.1 Long Bone Segment Development Work Plan

Task 1 - Baseline Loads Definition

In Task 1, SPARTA defined the segment loads for each component. The Phase I loads criterion were used as the initial estimate. Additional input from the Air Force as to specific test conditions/requirements were also factored into the segment design especially as these requirements relate to data acquisition from the embedded sensors. Specific loading conditions were defined including maximum axial, lateral, bending, and torsional loads for each component.

Task 2 - Composite Constituent Selection

The material selection criteria developed in Phase I was used to establish the constituent materials in the Phase II program. An extension of the Phase I materials definition included the ability to insert active sensors in the composite as well as potential use of toughened material systems to minimize impact damage and material inhomogeneity due to the presence of the sensors.

Task 3 - Long Bone Segment Design and Analysis

In Task 3, SPARTA used the data from Tasks 1 and 2 to develop lightweight, high strength long bone segment designs. This task focused on parametric analyses of various material layups and geometries. The constituent fiber and resin materials were selected in Task 2 and were based on the requirements dictated by the structural analysis and tradeoffs between reliability/processing characteristics, weight, cost, availability, and embedded sensors impact.

Task 4 - Instrumentation Development

In this task, SPARTA developed and designed long bone segment instrumentation which was embedded in the composite part. Forces internal to the bone composite can be measured using embedded strain gages or fiberoptic sensors. Embedding the load sensors within the bone structure would provide direct bone load measurements without adding mass from an external load cell or modifying the bone joint design to accommodate an external load cell, thus allowing the long bone segment to retain its biofidelity. Both classical foil strain gages and fiberoptic sensors were investigated as candidate embedded load/strain sensors. In addition to the load sensors, SPARTA embedded bi-axial accelerometers in the long bone segments to provide discrete motion history of each individual skeletal segment.

Task 5 - Prototype Fabrication

In Task 5, the long bone segment designs developed in Task 1-4 were fabricated. As in the Phase I work, the primary fabrication method was net compression molding of the composite long bone parts. Net compression molding consists of a metal outside mold work and, in general, an inside mold made of either silicone or metal. Net compression molding provides highly consistent parts with controlled sectional dimensions and wall thicknesses and very suitable to mass production.

Prior to the fabrication of the final long bone segments, several trial subcomponent (tubes, bars, or plates) parts were fabricated with embedded instrumentation. Various previously used strain sensor embedding techniques were reviewed to determine the most appropriate one for the composite material to be evaluated. SPARTA adapted this technique to the specific material test samples. These parts allowed process-parameter development consistent with the material, structural, and sensor requirements and were used for test verification of the fabrication/instrumentation technique.

A minimum of two (2) full scale prototype leg and/or arm segments were fabricated with a minimum of one (1) full set of each fabricated segment used by SPARTA for test and evaluation. After the SPARTA test, a minimum of one (1) full scale prototype leg and/or arm segment was delivered to the Air Force.

Task 6 - Validation Tests

The instrumented long bone segments were subjected to static calibration tests in both axial and transverse loading. Data from these tests were used to calibrate the embedded load/strain sensors and verify the analytical design predictions.

Subsequent to the static load test, the full (skeletal and flesh segment) leg was dynamically tested at the Armstrong Laboratory sled test facility.

2.2.2 Flesh Development Work Plan

The objectives for developing the biofidelic flesh material were realized by following the seven tasks summarized below.

Task 1 - Flesh Characterization

In this task, SPARTA established the baseline flesh characteristics. The focus of this effort was to identify the mass and compliance (deflection under pressure) of human flesh. These data were obtained through a literature survey as well as interviews with bioengineering researchers and Armstrong - Laboratory personnel. The human flesh data were used to develop dummy flesh characteristics such that the total segment inertia and compliance was representative of that of a total human segment. During this task SPARTA selected a long bone

segment developed in the primary program as the proof-of-concept/segment to demonstrate the biofidelic flesh design as well as total long bone segment biofidelity.

Task 2 - Constituent Material Analysis/Selection

Based on the data from Task 1, SPARTA investigated candidate flesh materials. Mechanical and mass properties of polymers, such as used in the current Hybrid III flesh, can be modified by the use of particulate or fiber filled materials. Almost all solid fillers increase the strength and stiffness of the basic polymer. The mass can be increased or decreased by the selection of high or low specific gravity materials. The degree of stiffness or strength change can also be controlled by the amount, size/length, and type of filler selected. Another approach is to "alloy" one or more polymers, such as urethane and polycarbonate, to obtain a wide variation in both mechanical and thermal properties. Polymer alloys used in conjunction with fillers can provide highly tailored specific properties. SPARTA investigated both polymer-polymer alloying and polymer filling to achieve the correct mechanical and inertial properties. Candidate constituent selection was based on overall mechanical properties as well as producibility and costs.

Task 3 - Biofidelic Flesh Design

Using the data from Tasks 1 and 2, SPARTA developed a flesh design consistent with the inertial properties of the biofidelic long bone segments. Candidate polymer alloys and fillers were ranked with respect to their mass and compliance properties, producibility, availability, and costs. The most promising material candidates were selected for coupon fabrication and characterization. The compliance of the biofidelic flesh was designed to be as close as possible to that of human flesh. The flesh design also considered the material's potential for embedding sensors i.e., polymerization temperatures, filler material, and internal compliance that were compatible with candidate sensors developed in Task 4.

The flesh design task also developed the mold designs. First Technologies Safety Systems (FTSS) had the primary responsibility for the flesh mold design and attachment methodology development. The external Hybrid III flesh geometry was maintained, however the internal mold geometry was modified to fit the selected long bone segment (Task 1). Although it was anticipated that the flesh would conform to the bone, various attachment concepts were considered which would allow removable/replacement of the flesh. Candidate concepts included but were not limited to: mechanical attachment (screws/bolts); zippered segments with internal

fastening such as velcro; and interlocking slots conforming to the long bone segment. The concepts also considered the additional mass of the "new" flesh and its impact on the required strength of the attachment design.

Task 4 - Embedded Instrumentation Development

In Task 4, SPARTA investigated the use embedded sensors discussed below to measure blunt trauma impact forces. Armstrong Laboratory personnel assisted in defining the efficacy and location of candidate embedded sensors. In the case of the flesh development, interest was focused on measuring impact loads transmitted through the flesh medium. Typically impact loads are measured using accelerometers which provide only a global force estimate using a known the segment mass. However, localized load measurements are critical on head or chest blunt trauma evaluations and in some cases leg impact resulting from leg flail. This can be achieved by either using localized pressure transducers or a tactile sensor foil. Pressure transducers introduce a local discontinuity within the material. The embedded foil offers the advantage of providing a load distribution pattern which would more accurately measure blunt trauma. Localized pressure sensors would not necessarily measure the exact load peak (i.e., the impact will not occur at the sensor location) or provide a good estimate of load location within the flesh medium.

SPARTA investigated putting a pressure sensor in the flesh to measure local impact forces. Several types of sensors were evaluated in relation to load and frequency response, size, ruggedness, and accuracy. Impact forces would be measured using either combination of localized pressure transducers coupled with accelerometers or with tactile sensor technology foil embedded within the flesh material. Subminiature piezoelectric pressure transducers can be embedded at the bone/flesh interface to measure local impact loads. These sensors have a far superior frequency response bandwidth than strain gage pressure transducers which is critical in dummy testing. Segment acceleration can then be measured using Piezoresistive accelerometers and combined with pressure sensors providing a good estimate of the distribution and concentration of the impact load. However, a number of pressure transducers will have to be embedded to achieve accurate load concentration assessment and this could have a negative influence on the local system stiffness. A tactile sensor foil could instead be embedded at the bone/flesh interface and measure exact load distribution over an area of interest. This foil is 0.004 inch thick with a planar resolution of 0.05 inch and is formed of a mylar sheet covered strips of elastomeric coatings. The applied load is measured at the intersection of each of the super-imposed grid lines and the sensor can therefore be custom manufactured to meet the size

and resolution requirements of a particular application. The foil sensor can also be used to measure the damping transfer function of the flesh material around a bone structure by applying a known load and measuring the resultant bone/flesh interface load pattern and concentration ratios.

Pending the results of the sensor evaluation and analysis, SPARTA selected a sensor to be included in the flesh test specimen fabrication in Task 5.

Task 5 - Candidate Flesh Fabrication and Characterization

In this task, a minimum of two candidate flesh materials were fabricated into flat panel test coupons. These coupons were used to evaluate fabrication process methodology, material mass, compliance performance, and efficiency of the embedding active sensors from Task 4. Various embedded techniques were evaluated and tested. Flesh test coupon fabrication was performed by SPARTA to ensure conformity of fabrication with production standards for dummy manufacturing. These specimens were subjected to both static and dynamic loads to verify the candidate flesh mechanical characteristics and the embedded instrumentation performance. The dynamic tests consisted of pendulum impact tests performed at the SPARTA test facility using a series of impactor weights and sizes.

Task 6 - Prototype Flesh Fabrication

In this task, FTSS fabricated three fullscale specimens of the candidate baseline flesh materials. One specimen was used for in-house form and function evaluation, the other specimen will be delivered to the Air Force. The third was kept as a backup. The full scale candidate test specimens were fabricated to match the selected long bone skeletal segment selected in Task 1 and included the attachment mechanism developed in Task 3 and the instrumentation selected from Tasks 4 and 5.

Task 7 - Flesh Verification Tests

The objective of the verification tests was to establish the ability to fit the flesh on the long bone segment, and validate its performance (mass, compliance, and instrumentation on the actual long bone segments). SPARTA attached the flesh to the specified long bone segment for verification of the total segment for both fit and total segment mass distribution.

The fitted segment was combined with the companion segment and tested in a dynamic mode. The dynamic tests were performed at the SPARTA test facility using a pendulum impact tester to calibrate the tactile foil sensors under dynamic loading. Additional dynamic tests were performed at the Armstrong Laboratory sled test facility using a full Hybrid III 50th percentile dummy with the entire ABC Man skeletal and flesh segments.

3.0 PROGRAM RESEARCH RESULTS

3.1 Instrumentation Development

In order to achieve optimal biofidelity, the ABC Man long bone and flesh component incorporated embedded sensors to measure the deformation and acceleration of the skeletal segments and impact on the flesh segments. Load sensors and accelerometers integrated into the composite bone structure provided directional load/acceleration measurements without adding mass from an externally inserted load cell thus allowing the long bone segment to retain its mass and geometric biofidelity. The flesh also incorporated a "tactile foil" sensor to allow measurement of local impact. This capability is not currently available on crash dummy manikins.

3.1.1 Long Bone Instrumentation

The femur and tibia composite long bone segments have embedded gages to measure strain and embedded accelerometers gages to measure accelerations. The primary embedded load sensors candidates were fiberoptic gages and foil strain gages. Fiberoptic gages have a wide frequency response bandwidth which has a potential to provide a high fidelity load history during impact. They are also relatively insensitive to environmental parameters such as heat and magnetic/electric fields, and have a large signal to noise ratio. Foil gages, on the other hand have a longer experience base, are relatively inexpensive, and have a smaller profile than fiberoptic gages.

3.1.1.1 Load/Deformation Gages

Fiberoptic Strain Gages

There are two basic types of fiberoptic strain sensors in use today. The first measures the pressure on a single location cavity located at the tip of the fiber which has a diameter about 3x the size of fiberoptic strand. The second type measures the strain induced over the entire length of a uniform optical fiber. In this particular case, the first type is the preferred solution. The second type, full length measurement, would be subject to various strains experienced at the bone joint which are not directly related to the actual mid-bone forces. In addition, the fiber length from the bone to the readout device is also subject to strain during the dummy impact and would therefore introduce erroneous readings. Because of this, the single cavity fiberoptic gage was selected as the fiberoptic gage of choice.

The localized fiberoptic strain sensors have been embedded into composite material, and coupon tests have demonstrated their ability to track strain. A literature search (see references 9-24) revealed some of the results achieved with these tests. This previous work was done using uniaxial composites with strain measured only along the axis. However, the bone will experience a complex state of stress during the dummy impact which will generate a tri-axial state of strain at the fiber tip. It was not clear, based on previously performed and evaluated test results, whether the judicious placement of a fiberoptic sensor inside the bone would allow this complex state of strain to be resolved. Embedding techniques were also reviewed including the additional requirement, in this case, of the molding pressures applied during the net molding operation. Fiberoptic strand protection and routing at the bone exit point interface was also investigated with the most durable solution involving the use of small stainless steel flexible tubes embedded at the bone joint to assure full mechanical protection (the fiber has a small bending resistance). Various routings were evaluated to assure that the fiber protection sleeves were not being routed through a high strain concentration area and could easily be interfaced with the remainder of the dummy umbilical assumed to exit at the lower back.

The most promising fiberoptic sensor was a point strain sensor developed by Metacor, Inc. shown in Figure 3.1-1. In this design, a fiberoptic cable incorporates on one end an SMA-style low loss connector, and on the other, a miniature probe. A sectional view through a typical sensor probe is shown in Figure 3.1-2. This probe is composed of a central polyimide-coated optical fiber adhesively bonded into a glass or ceramic capillary, with the sensing element attached to the capillary tip using inorganic bonding techniques. The capillary is generally about 0.8mm in diameter and 10mm long, while the sensor element is a square chip 0.6mm on a side and 0.2mm high. After embedding the sensor into a composite material, distortion of the diaphragm due to strains in the composite will give a spectral shift that can be sensed and calibrated. Translation of this reading into equivalent "effective strain" of the composite is not straightforward from an analytical standpoint because the embedded probe typically has a much higher modulus than the matrix and thus disturbs the strain field locally. This can result in a 3-D stress/strain anomaly that may not be of structural concern, but could be a problem in terms of analysis and calibration.

Limited tests have been reported in the literature for fiberoptic point strain sensors. Only unidirectional composites axially loaded in the fiber direction have been reported. Neither cross-ply laminates nor off-axis loads tests have been reported. This is of concern for the ABC Man Program because the long bone designs would certainly have some angle plies (e.g., $\pm 45^\circ$) and the loads will be in combined axial and shear stress.

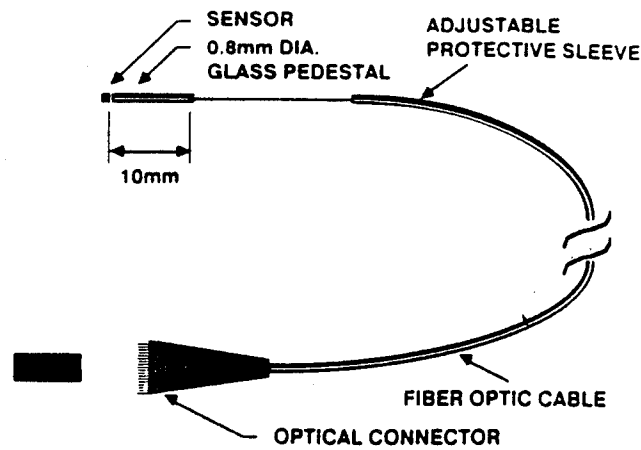


Figure 3.1-1. Micro-Probe Applicable to Composites.

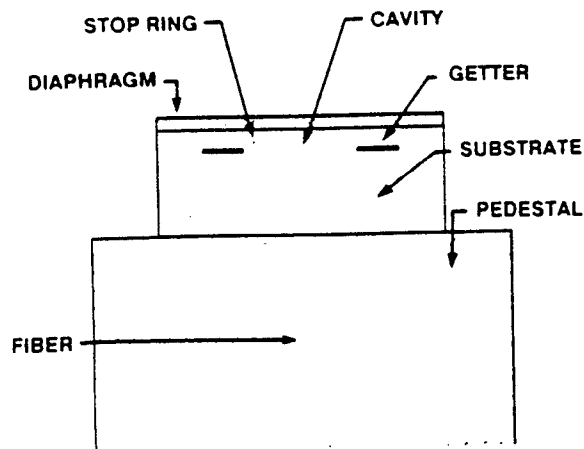


Figure 3.1-2. Cross-Sectional View of Interferometric Sensor Mounted on Capillary Pedestal.

Foil Strain Gages

Foil strain gages were an additional option for the embedded sensors. Micro-Measurement EA-06-125RD-350 gages were used in the validation experiment. These gages were fully encapsulated in a polyimide with integral 0.8" (20.3mm) long leads and a .003 in. (0.07mm) gage thickness (0.1mm thickness of the leads). The gage and lead assembly were rated to 400°F which was above the 350°F maximum processing temperature for the composite. Gage resistance was monitored prior to, and after the cure process in order to measure possible gage deformation during the pressure forming process and predict possible non-linear gage behavior. Lead wire was 24 AWG wire, 134 AWQ, with polyimide insulation rated to 600 deg F. All internal leads were inserted into a PTFE or high temperature silicone tube at the exit from

the bone segment. This tube was filled with a high temperature RTV coating such as M-Coat-C and partially embedded into a composite for mechanical strength and exited the mold with a CONAX fitting. Gage excitation was limited to around 1 Volt to reduce local gage heating. A surface foil gage was bonded to the specimen surface to provide a control strain measurement. Anticipated correlation between the surface gage and the embedded gage, as stated in the literature search data, was expected to be less than 2.5% for the in-line gage and less than 10% for the 45 degree and perpendicular gage.

An experimental effort was conducted to assess the performance and handling characteristics of embedded fiberoptic and conventional foil gages in graphite epoxy laminated composites. Flat graphite epoxy panels were fabricated with embedded gages from which mechanical specimens were machined and tested. The objective was to determine the feasibility of utilizing embedded gages for composite manikin long bone leg segments. Fully embedded sensors were located in the middle of the laminate (through the thickness) and included both fiberoptic and conventional foil. In this effort, both fiberoptic and foil gages were embedded in flat panels with both uniaxial and off axis fiber layups. Table 3.1-1 shows the test matrix used in the test program.

3.1.1.2 Fiberoptic and Foil Strain Gage Tests

As noted in Section 3.1.1.1 both fiberoptic and conventional strain gages were investigated as candidate embedded sensors. A complete tradeoff study was conducted to determine which measurement technique was most appropriate for this application. Based on design, fabrication, performance and reliability considerations, the following long bone strain sensor implementation options were considered:

- 1) Embedded Meticor Point Strain Fiberoptic Sensor
- 2) Embedded Conventional Foil Strain Sensor Gage
- 3) Post Embedded Gage (PEG) Conventional Foil Sensor
- 4) Surface Mounted Conventional Foil Sensor with Shrink Tube Overwrap

The above first two fully embedded strain sensor implementation were discussed in Section 3.1.1.1. These fully embedded sensors would be located towards the center of the composite laminate wall thickness of the long bone segments. The sensor cables (fiberoptic and

Table 3.1.1-1. Embedded Strain Sensor Performance Assessment Test Matrix

Test #	# Tests	Embedded Sensor Description					Test Type	Composite Material/Lay-up	Thickness (in)	Surface Mounted Foil Gage		
		Type ⁽⁷⁾	#	Depth from Bottom	Leads Exit Path ⁽³⁾	Orientation ⁽¹⁾				Type ⁽⁷⁾	# ⁽²⁾	Orientation ⁽¹⁾
1-2	2	Foil - Axial EA-06-125BZ-350	1	10 Plies	Side	0°	Tensile	IM7/F155 (0°) _n	0.15	Foil - Axial EA-06-125BZ-350	2	0°
3	1	Foil - Rosette EA-06-125RA-120	1	10 Plies	Bottom	0°/±45°	Biaxial	IM7/F155 (0°) _n	0.15	Foil - Rosette EA-06-125RA-120	2	0°/±45°
4	1	Foil - Rosette EA-06-125RA-120	1	10 Plies	Bottom	0°/±45°	Biaxial	IM7/F155 (0°/±45°) _m	0.15	Foil - Rosette EA-06-125RA-120	2	0°/±45°
5	1	Foil - Rosette EA-06-125RA-120	1	10 Plies	Bottom	0°/±45°	Biaxial	T300/7714 ⁽⁶⁾ (0°/±45°) _m	0.15	Foil - Rosette EA-06-125RA-120	2	0°/±45°
6	1	Foil - Rosette EA-06-125RA-120	1	10 Plies	Bottom	0°/±45°	Shear	IM7/F155 (0°/±45°) _m	0.15	Foil - Rosette EA-06-125RA-120	2	0°/±45°
7-8	2	Foil - Axial EA-06-125BZ-350	1	PEG ⁽³⁾	Side	0°	Tensile	IM7/F155 (0°) _n	0.15	Foil - Axial EA-06-125BZ-350	1	0°
9	1	Foil - Rosette EA-06-125RA-120	1	PEG ⁽³⁾	Side	0°/±45°	Biaxial	IM7/F155 (0°/±45°) _m	0.15	Foil - Rosette EA-06-125RA-120	1	0°/±45°
10-11	2	Fiber Optic Metricor 500 psi	1	10 Plies	Side	0°	Tensile	IM7/F155 (0°) _n	0.15	Foil - Axial EA-06-125BZ-350	2	0°
12	1	Fiber Optic Metricor 500 psi	2 ⁽⁴⁾	10 Plies	Bottom	0°	Biaxial	IM7/F155 (0°) _n	0.15	Foil - Rosette EA-06-125RA-120	2	0°/45°/90°
13	1	Fiber Optic Metricor 500 psi	2 ⁽⁴⁾	10 Plies	Bottom	0°	Biaxial	IM7/F155 (0°/±45°) _m	0.15	Foil - Rosette EA-06-125RA-120	2	0°/45°/90°
14	1	Fiber Optic Metricor 500 psi	1	10 Plies	Bottom	0°	Shear	IM7/F155 (0°/±45°) _m	0.15	Foil - Rosette EA-06-125RA-120	2	0°/±45°

(1) Strain Gage Element Orientations Relative to 0° Fiber Orientation
(2) Surface Mounted Gages Mounted on Both Sides (Except for PEG - Mounted on Opposite Side)
(3) Post Embedded Gage (PEG) - Surface Mounted Gage Covered With Several Layers of Cloth Fabric/Epoxy
(4) One Primary and One Redundant Fiber Optic Sensor
(5) Side - Out Side of Laminate Between Layers, Bottom - Directly Out of Bottom Layers of Laminate
(6) Fiberite Pre-preg With 0° Layers Unidirectional Tape and ±45° Layers Plane Weave Cloth
(7) All Foil Gages are Micro Measurements Gages OPTION LE: Leads Plus Polyimide Encapsulation

insulated copper wire) could be routed inside the hollow long bones and emerge through plugs at the ends. An alternate approach would be to route the sensor cables along the embedded ply layer.

The third long bone strain sensor implementation option discussed above was designated the Post Embedded Gage (PEG) approach. This approach involved mounting the gages on the outside of an initially cured bone segment using conventional surface gage bonding techniques. Then additional layers of cloth/epoxy would be cured over the gages to complete the fabrication of the segment. The wires would be routed along the surface layer of the gage. This approach was an attractive alternative to the fully embedded techniques because conventional surface gage bonding methods would be easier to control and the gages would have better resolution at the outer (high bending strain) radius location. One of the concerns of fully embedded and PEG sensors is reparability of damaged sensors or cables. If this becomes an issue, there is the option of using conventional foil surface mounted gages protected by shrink tube overwrap (option 4). The overwrap could be easily removed to repair a damaged sensor or wire. This option (4) was not addressed in the experimental program due to the success of the PEG approach (3).

The coupons for all tests consisted of flat panels with various geometries to accommodate specific tests. The embedded gages were placed at mid thickness except for the PEG sensors (Section 3.1.1). The test matrix consisted of 14 tests, shown earlier in Table 3.1-1 and included tensile, biaxial tension/compression, and in-plane shear loading conditions. The test matrix defines for each test the embedded sensor type, number, embedded depth, leads exit path and orientation; the test type (tensile, biaxial or shear); the composite material and lay-up; panel thickness; and surface mounted foil gage type, number and orientation. A typical tensile specimen is shown in Figure 3.1-3 and was machined from a 12" x 3" molded panel. The 12" by 3" panels were designed to produce 3 one inch wide tensile specimens with each of the outside specimens instrumented with the central specimen used as a tensile strength calibration reference. One 12" by 3" panel was not instrumented and was used to experiment with lead exit reinforcement techniques. Three 12" by 3" panels were instrumented with uniaxial foil gages and several curing cycle techniques were experimented with while the foil gage resistance was monitored in order to assess gage survival. Two 12" by 3" panels were instrumented with fiberoptic gages and the curing cycles were monitored as well. The fiberoptic strain gages had a measurement limit of 500 PSI. The last 12" by 3" panel was instrumented with a rosette foil gage with the solder joint on the leads outside of the panel. The biaxial foil and fiberoptic specimens are shown in Figures 3.1-4 and 3.1-5 respectively. The in-plane shear specimen is shown in Figure 3.1-6. The biaxial and shear specimens were machined from 6" x 6" molded panels. The 6" by 6" panels (see test matrix) were designed to produce to a cruciform shape to

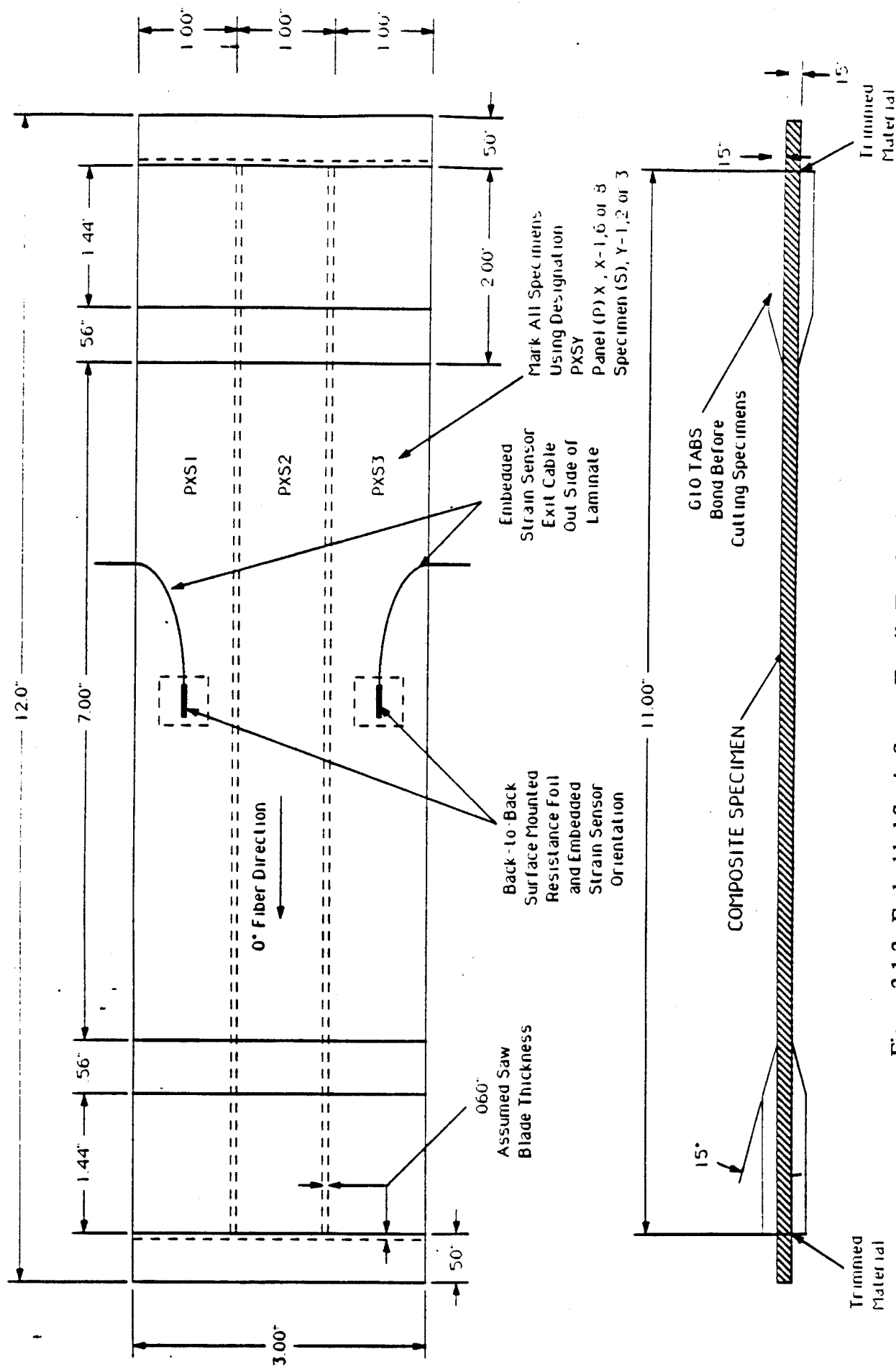


Figure 3.1-3. Embedded Strain Sensor Tensile Test Specimen Cutting Map.

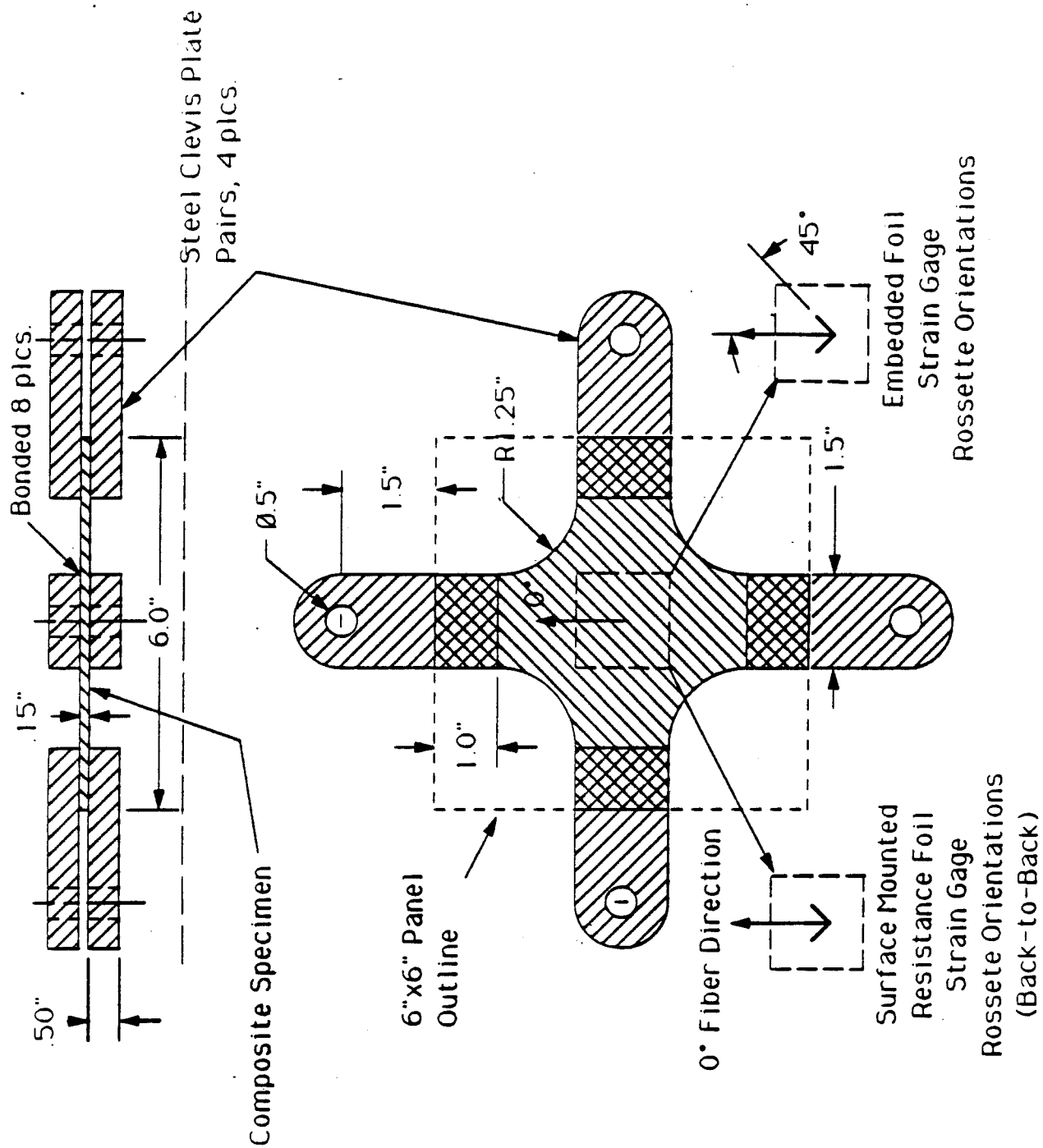


Figure 3.1-4. Embedded Resistance Foil Strain Gage Biaxial Test Specimen Description.

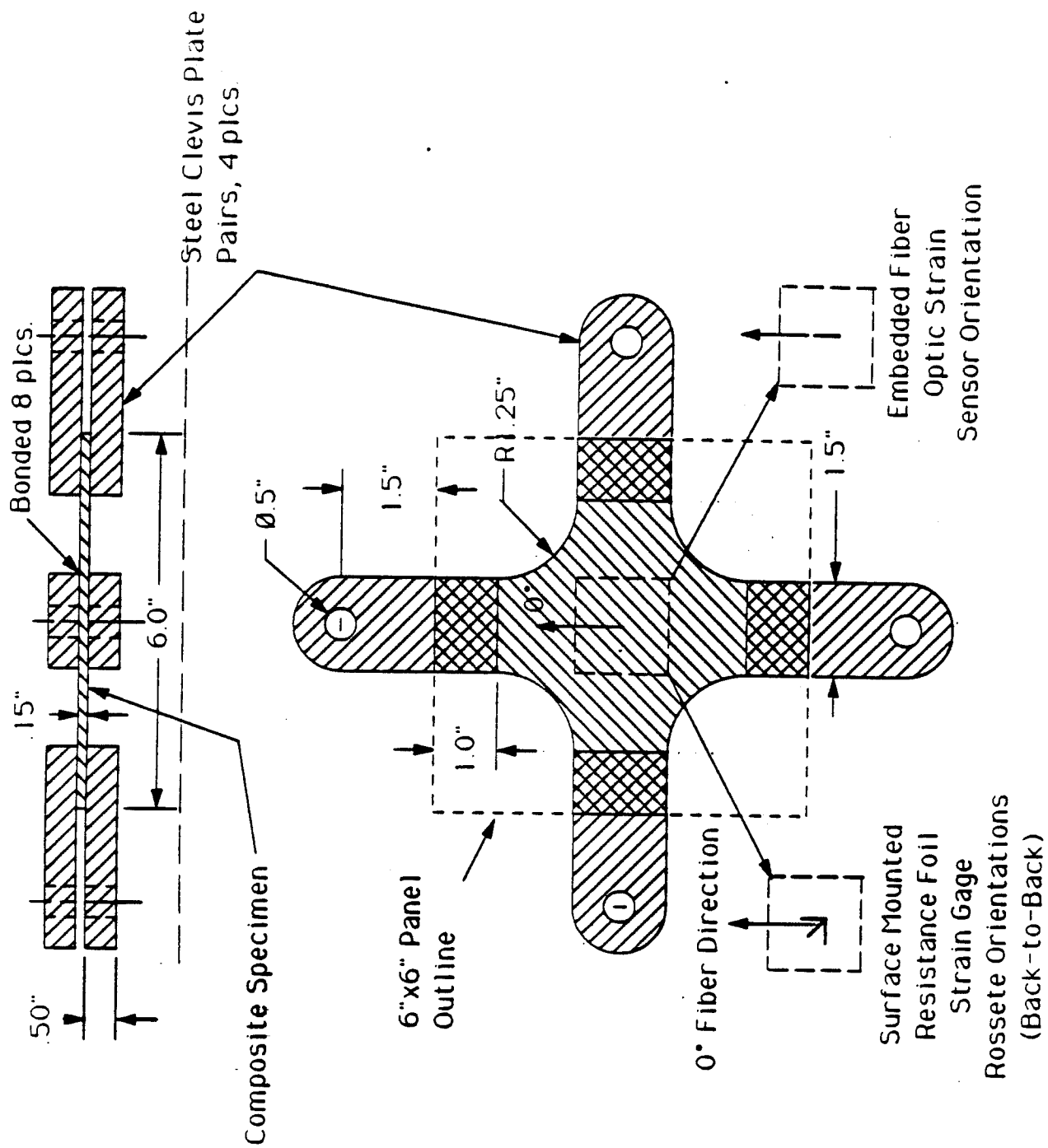


Figure 3.1-5. Embedded Fiberoptic Strain Sensor Biaxial Test Specimen Description.

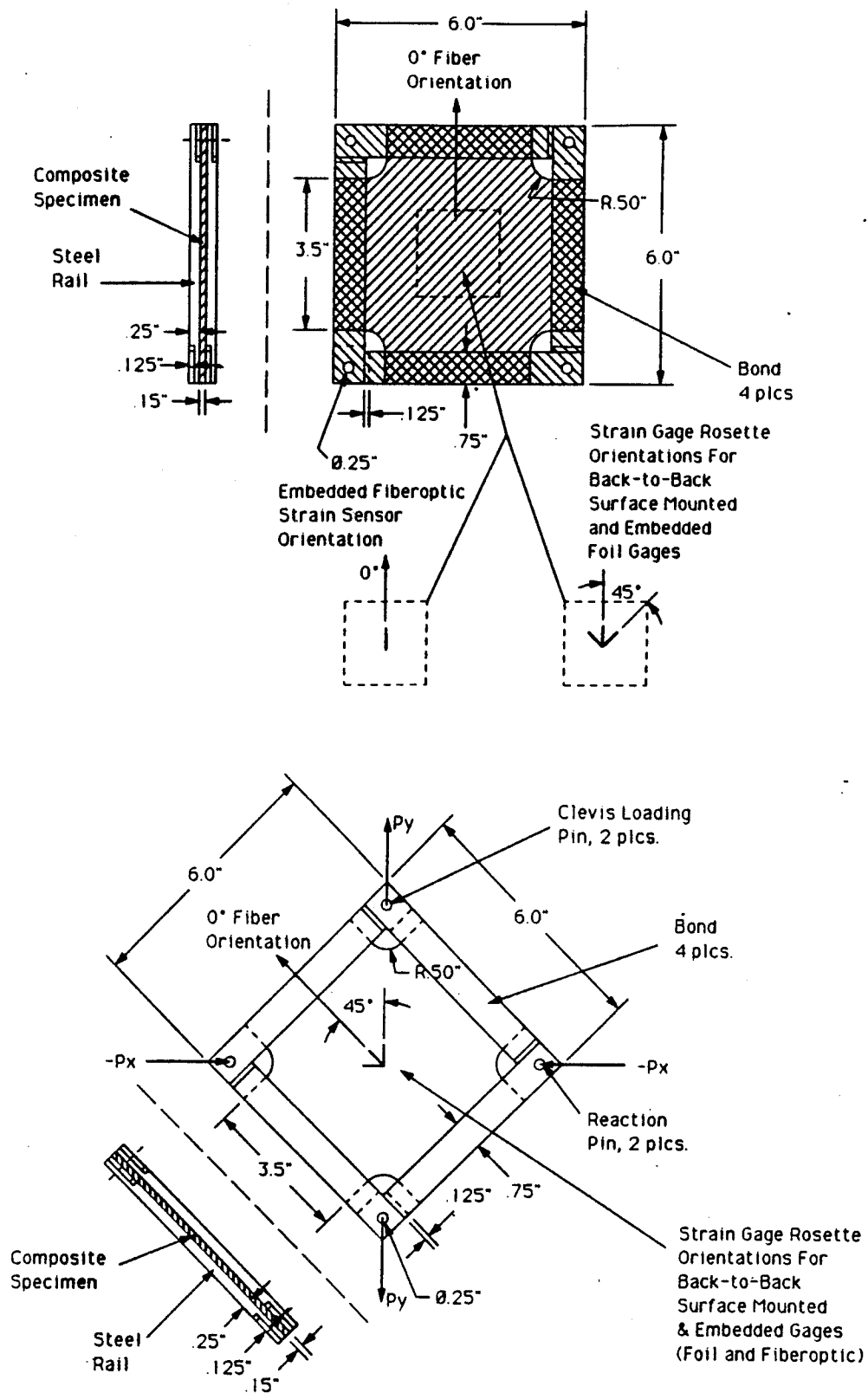


Figure 3.1-6. Embedded Fiberoptic and Foil Strain Gage Shear Test Specimen.

facilitate bi-axial load testing. One panel was made up of only 0 degree fiber and one fiberoptic gage was embedded along the fiber axis. Two panels included +/-45 degree plies and each had one fiberoptic strain sensor oriented along its main axis. One panel included +/-45 degree plies and had one rosette foil gage embedded with its leads routed along the main fiber axis. The last two panels included +/-45 degree plies and each had one rosette gage embedded with the leads routed through the bottom layers of plies. These last panels were used to assess the feasibility of running the sensor leads through the middle of the bone segment. For each embedded gage there was a surface mounted foil gage bonded directly over the embedded gage. This surface mounted gage acted as the control and was used to validate the embedded gage data. Nominally, the sensor lead wires would exit in the lamina in which the gage was embedded, however, exit through the laminent layers was also investigated to determine if routing the lead wires through the hollow center of the bone was feasible. A schematic of this layup is shown in Figure 3.1-7. Figures 3.1-8 through 3.1-10 show the installation of the embedded gages in the test panels.

3.1.1.3 Flat Specimen Test Results

All tests were performed on the SPARTA in-house MTS machine. A typical test setup is shown in Figure 3.1-11. The leads for both fiberoptic and foil gages were strain relieved in the composite prior to consolidation. Strain relief was accomplished by introducing moderate curvature bends in the leads from the gage to the composite specimen exit point. For both the fiberoptic and foil gages there was a high degree of failure during processing, post machining, and/or handling during tests. Only one fiberoptic strain gage specimen survived the panel fabrication and machining process. It was noted during layup that the fiberoptic cables as well as the fiberoptic gage/cable connection could be very susceptible high shear and breakage when transversing cross ply fibers. During processing the composite laminates are squeezed together to debulk the material. The application of pressure during debulking and consolidation causes significant movement of the composite layers. It is believed that the local differential movement between the composite laminents especially in crossply orientation introduced high local strains at the fiberoptic gage/cable connector or in the fiberoptic lead causing a local fracture of the lead or at the brittle gage/lead interface. In addition, the leads were highly susceptible to breakage at the exit point of the panel. An attempt to minimize this was done by running the lead through a small tube at the exit. While this helped, a high degree of failure was observed. Because of the low reliability of both the embedded co-processed fiberoptic and foil gage sensors, it was decided to go the PEG concept as the sensor configuration for the ABC Man program. There were, however, a significant amount of testing performed on the fiberoptic and foil gage panel coupons which survived the co-processing fabrication and handling during testing.

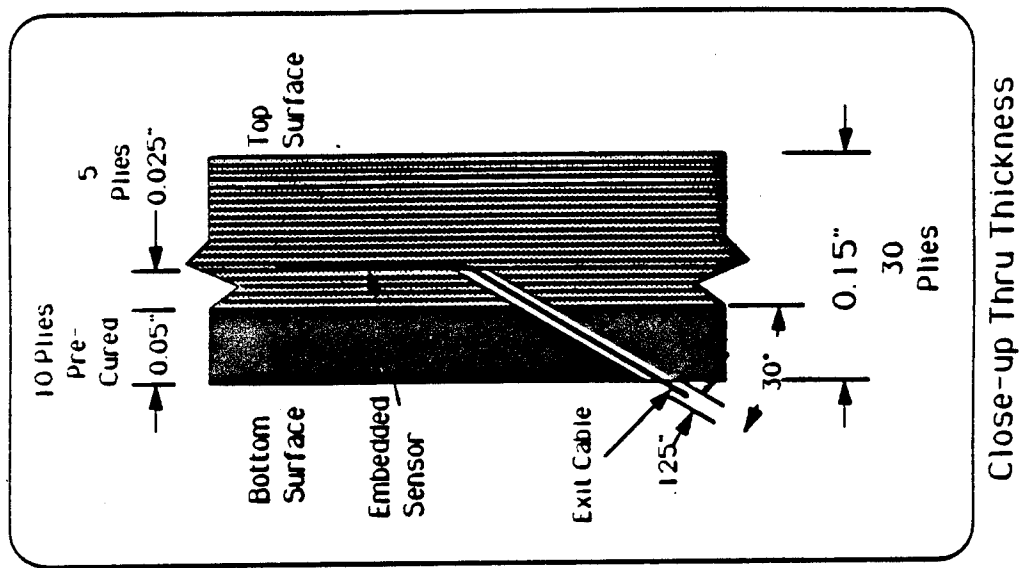


Figure 3.1-7. Embedded Strain Sensor Concept for Cable Exit Through Bottom of Laminate.

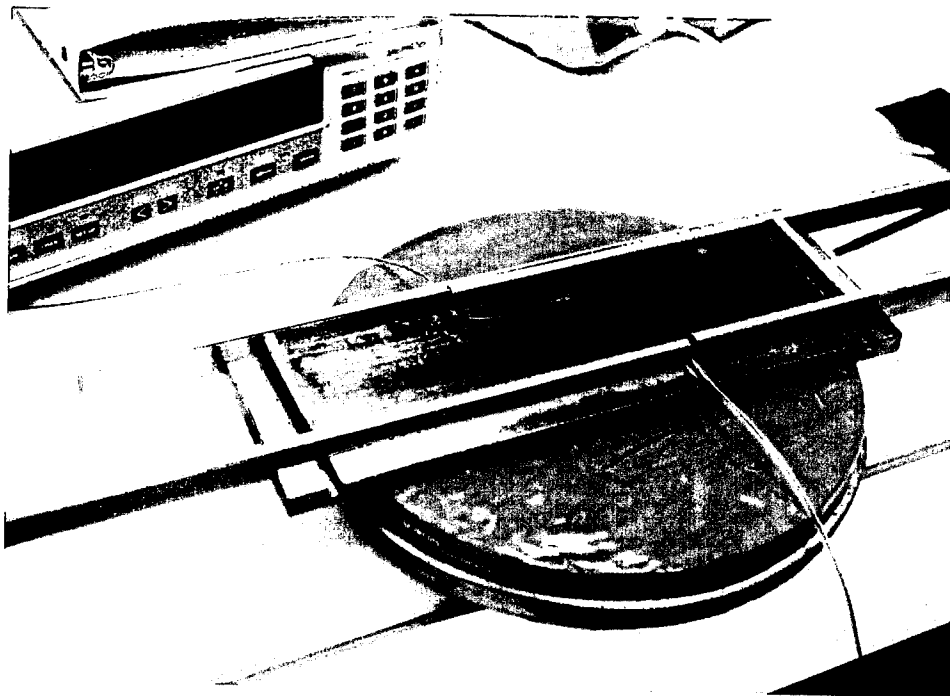


Figure 3.1-8. Installation of Embedded Strain Sensors in 3 x 12" Panel.



Figure 3.1-9. Installation of Embedded Foil Strain Gages in 3" x 12" Panel.

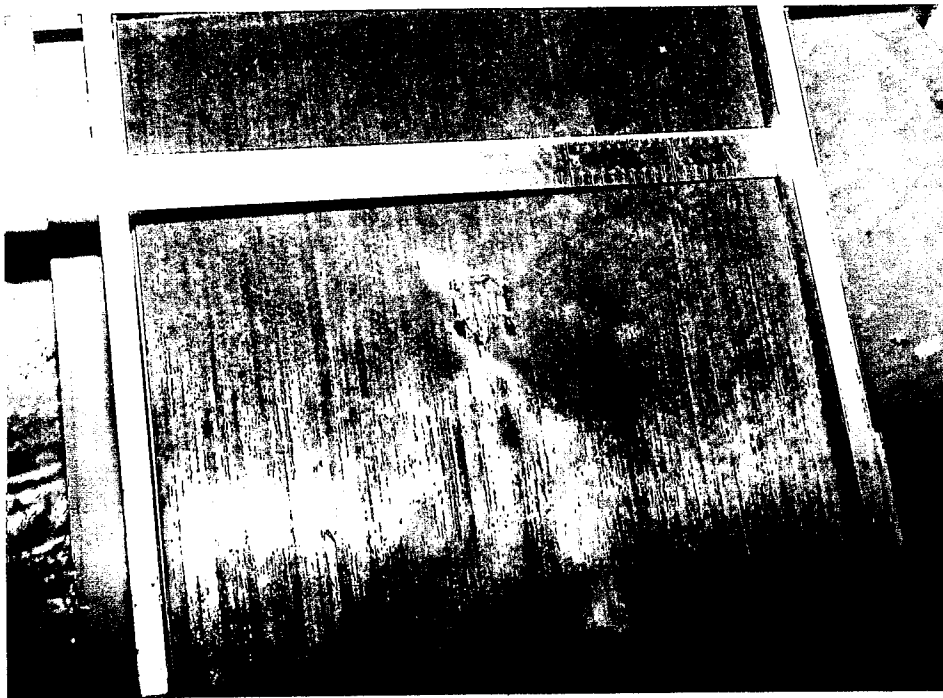


Figure 3.1-10. Installation of Embedded Foil Strain Gage in 6 x 6" Panel.

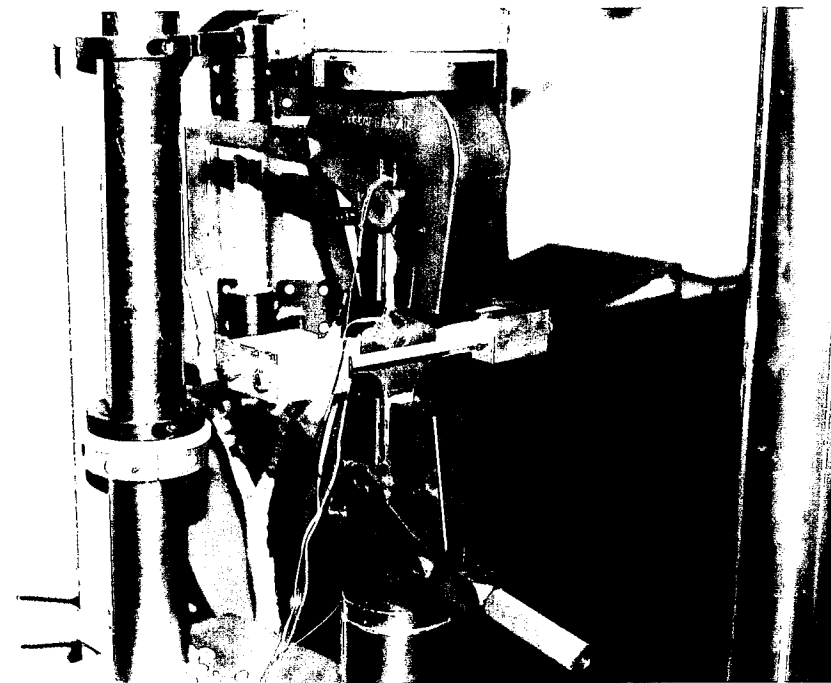


Figure 3.1-11. Axial and Biaxial Load Condition Test Setup.

Embedded Fiberoptic Test Results

Of the four panels fabricated with embedded fiberoptic gages (see Table 3.1-1) only one panel (#10) survived the processing and specimen machining as shown in Table 3.1-2. However, a series of tests were performed on the specimen cut from this panel. A summary of these tests is presented in Table 3.1-3. An expanded summary is presented below along with reduced data plots of load/response histories for each test.

Table 3.1-2. Fiberoptic Panel Fabrication Summary

ABC Man Panel #	Fabrication ID #	Fiber Optic Gauge #	Status
8	5	4100, 4101	Failed F/O gauge
8	7	4013, 3415	Failed F/O gauge
9	8	4012	Failed F/O gauge
10	9	4107	Completed
10	10	4104	Failed F/O gauge

Table 3.1-3. Summary of Panel to Fiberoptic Mechanical Tests

Test #	Test Description	Results
56	Slow axial loading, ≈ 11.1 lbs/sec	Linear strain response, sinusoidal (cyclic) pressure data
57	Slow axial loading, ≈ 15.9 lbs/sec	Linear strain response, sinusoidal pressure data
58	Moderate axial loading, then axial unloading, ≈ -28.8 lbs/sec	Linear strain response, erratic cyclic pressure data
59	Moderate axial loading, ≈ 40.3 lbs/sec	Linear strain response, sinusoidal pressure data
60	Moderate axial loading, ≈ 33.7 lbs/sec	Linear strain response, sinusoidal pressure data
61	Slow axial unloading from 12700 lbs to 10000 lbs, then hand side loading	Side loading made strain and pressure response erratic, hand side load not measured
62	Rapid axial unloading, ≈ -54.9 lbs/sec	Linear strain response, erratic cyclic pressure data
63	Calibration, very low, slow axial loading	Equipment calibrated
64	Moderate axial loading, ≈ 41.5 lbs/sec	Linear strain response, erratic cyclic pressure data
65	Moderate axial loading, ≈ 45 lbs/sec, then constant 10000 lb load with side load	Side loading made strain and pressure response erratic, hand side load not measured
66	Rapid axial unloading, ≈ -54.8 lbs/sec	Linear strain response, erratic cyclic pressure data
67	Calibration, very low, slow axial loading	Equipment calibrated
68	Moderate axial loading, ≈ 44.2 lbs/sec	Linear strain response, erratic cyclic pressure data
69	Constant 10000 lb load with side load, then rapid axial unloading, ≈ -50.8 lbs/sec	Side loading made strain and pressure response erratic, hand side load not measured

Fiberoptic Pressure Sensor - Figures 3.1-12 through 3.1-25 present the raw data from these tests. Figures 3.1-12 through 3.1-20 are plots of the axial loading tests. Figures 3.1-21 through 3.1-25 show the transverse loading tests. Figures 3.1-22 and 3.1-25 are plots of sensor calibration. Figures 3.1-26 and 3.1-27 are plots of data from two consecutive tests, tests 56 & 57 and 59 and 60, respectively. Tests 56 and 57 had relatively slow loading compared to the rest of the tests. The combined plot of the data from these two tests clearly demonstrates the cyclic pressure readings of the F/O gage. Tests 59 and 60 had a more rapid loading rate. The cyclic behavior of the F/O gage is clearly demonstrated in the plot of this data also. Figure 3.1-28 highlights the slope of these pressure cycles for tests 56 and 57. Figure 3.1-29a and 3.1-24b plot the change in the slope of these cycles. Figure 3.1-29a is a straight line curve fit and Figure 3.1-29b is a 3rd order polynomial curve fit. The change in the absolute value of the slope of these cycles is nearly linear as demonstrated in Figure 3.1-29a. Note that the correlation coefficient squared, R^2 , value is very close for both curve fits. If we can count and characterize the cycles, we could possibly use this gage to measure pressure. Figure 3.1-30 shows the slopes of the F/O gage cycles for tests 59 and 60. Under moderate loading, like tests 59 and 60, or rapid loading, like tests 64 and 68, the change in the absolute value of the pressure cycle slope is not linear. Figure 3.1-31 plots the absolute values of the pressure cycle slopes and shows a 3rd order polynomial curve fit. In this case, R^2 is not as close to 1 as the correlation for tests 57 and 58.

Due to the fragile nature of the fiberoptic gages in processing and handling, as well as the non-linear response of the fiberoptic gage under rapid loading and unloading, it was determined that the fiberoptic gage is not a viable gage for the ABC Man program. There were some very intriguing characteristics demonstrated by the fiberoptic gages, including their apparent rate dependency response and cyclic output, which are likely related to the characteristic wavelength compared to a localized material deformation. However, these investigations were beyond the scope and resources of this program especially in light of the fragile nature of the fiber optic system during processing and handling. The fiberoptic gage has demonstrated that it can likely be used for other applications if a linearizing circuit and algorithm are developed. We recommend additional analysis of this gage to assess the value of this sensor for other applications.

Embedded Foil Gage Test Results

Only uniaxial specimens with embedded foil gages survived the embedding process. The off axis gages failed mainly due to lead breakage while taking the panels from the mold and electrical shorting of the leads during panel cure.

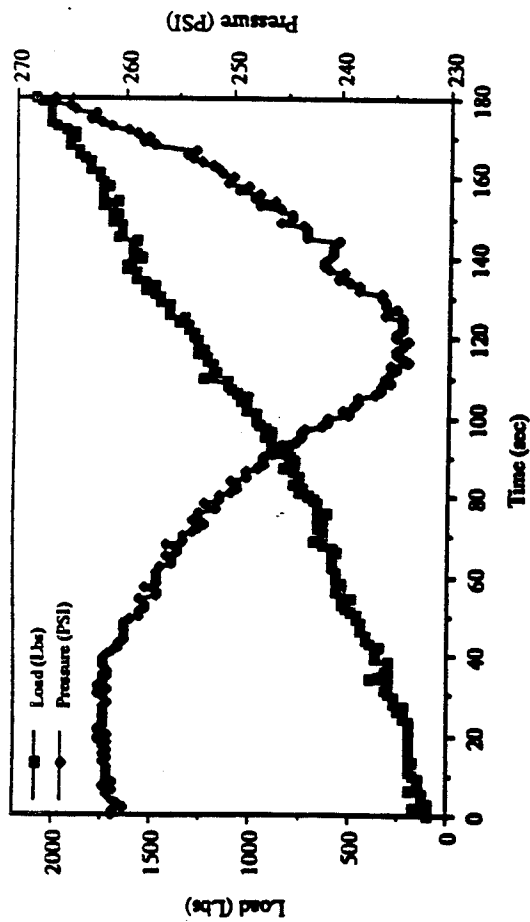


Figure 3.1-12. Test #56 Load/Pressure vs. Time.

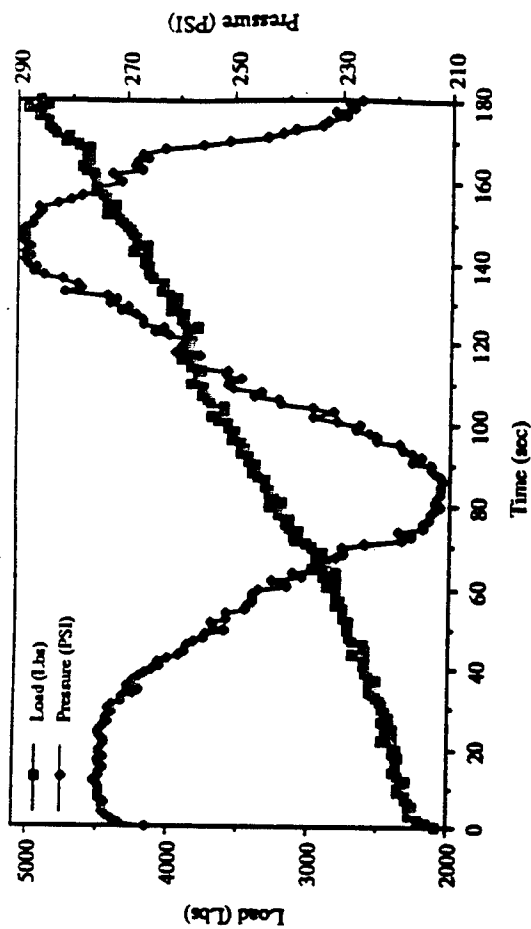


Figure 3.1-13. Test #57 Load/Pressure vs. Time.

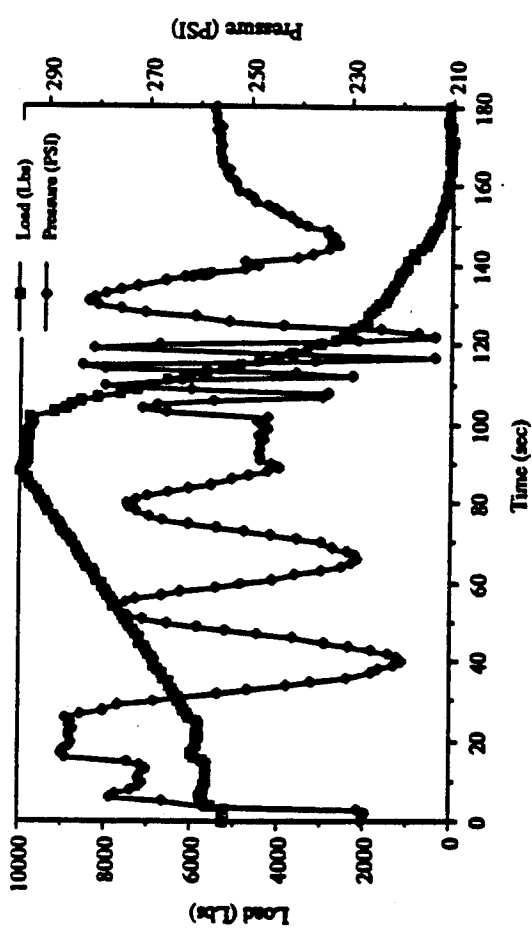


Figure 3.1-14. Test #58 Load/Pressure vs. Time.

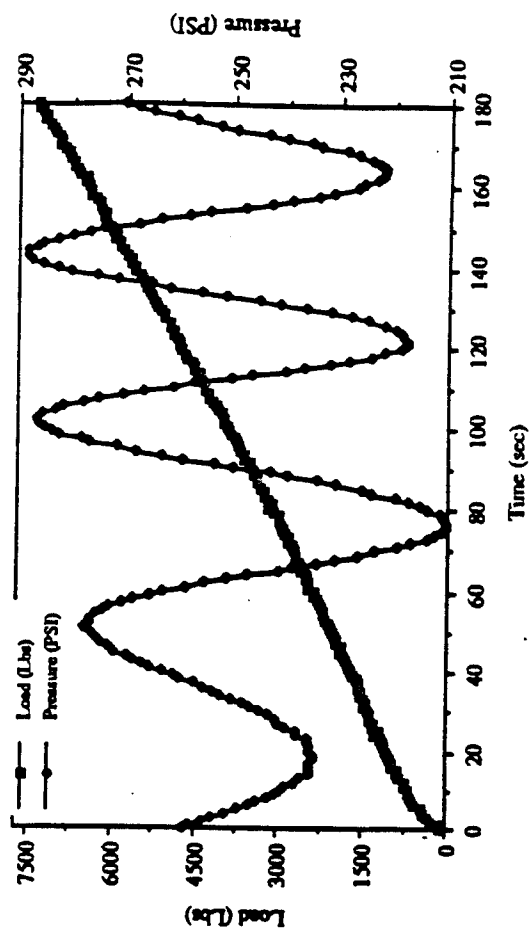


Figure 3.1-15. Test #59 Load/Pressure vs. Time.

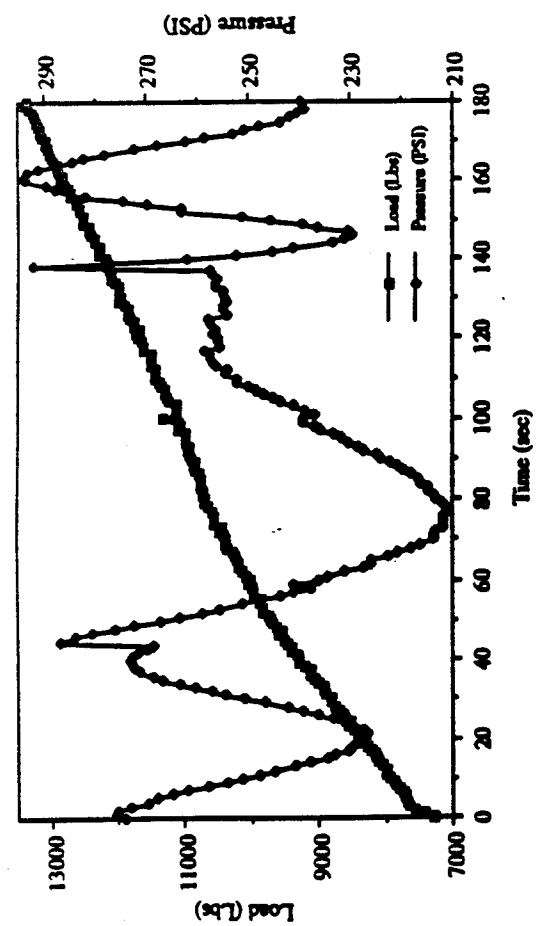


Figure 3.1-16. Test #60 Load/Pressure vs. Time.

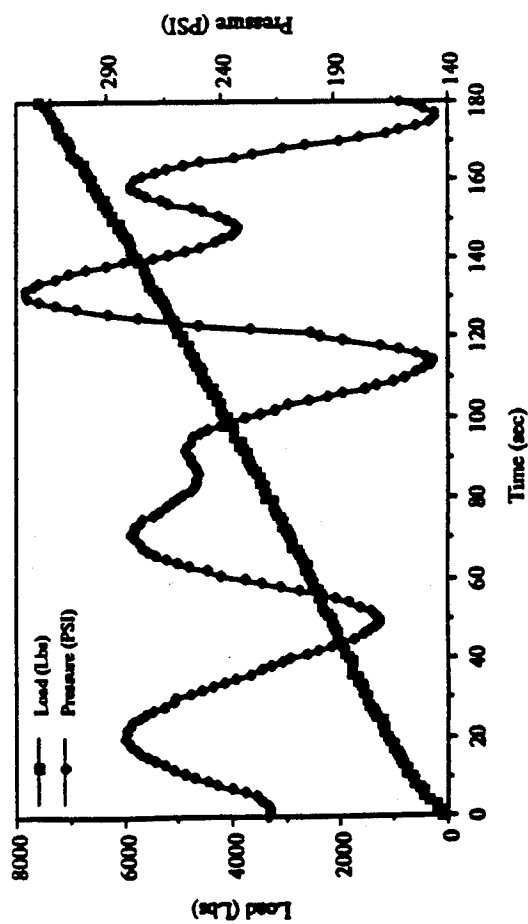


Figure 3.1-18. Test #64 Load/Pressure vs. Time.

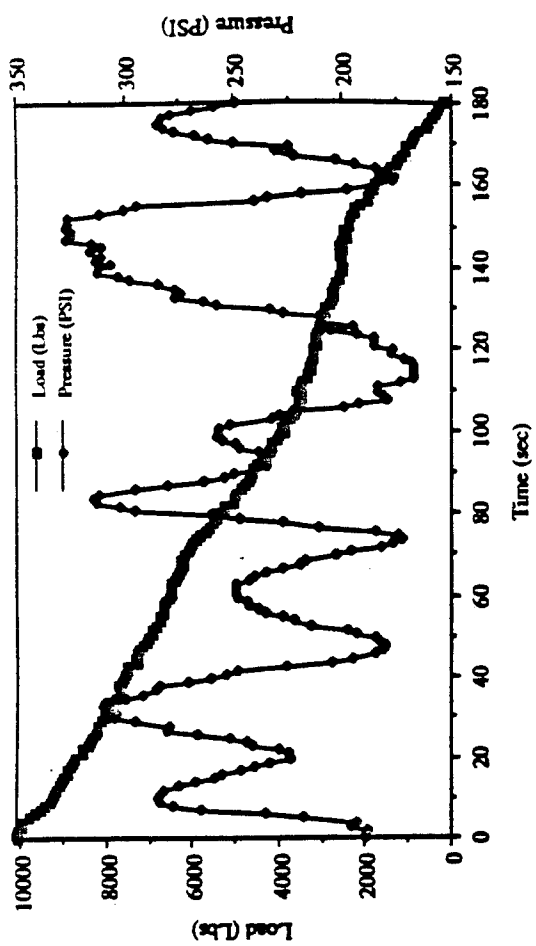


Figure 3.1-17. Test #62 Load/Pressure vs. Time.

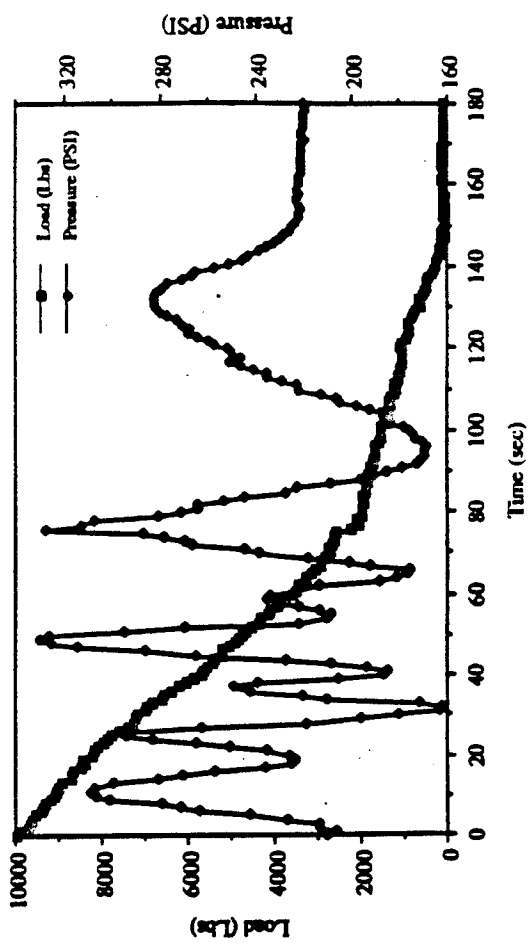


Figure 3.1-19. Test #66 Load/Pressure vs. Time.

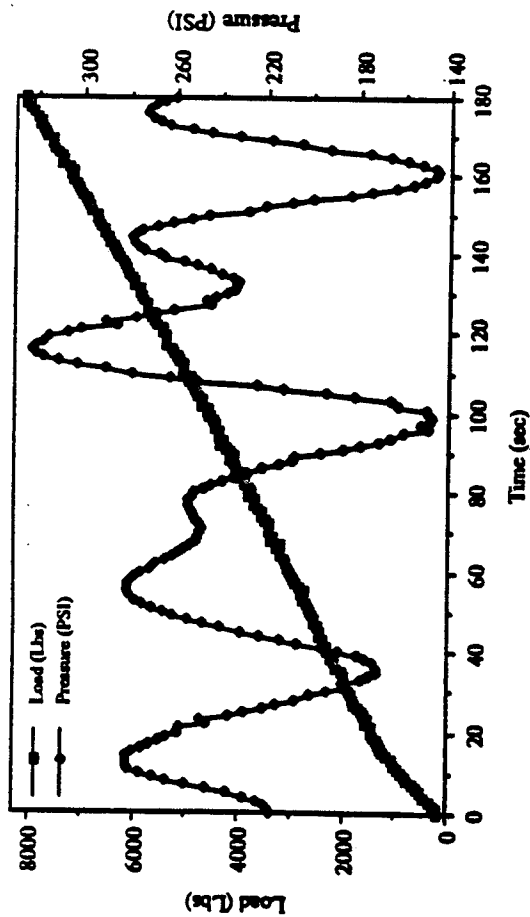


Figure 3.1-20. Test #68 Load/Pressure vs. Time.

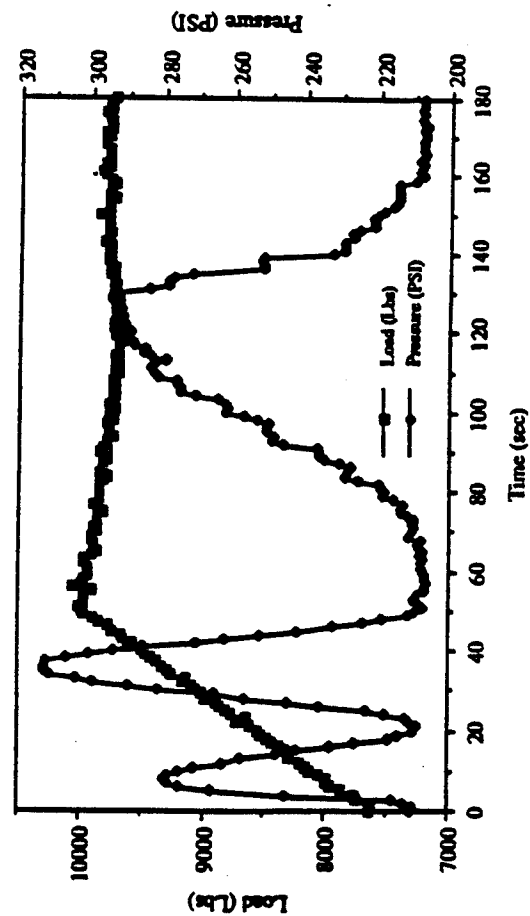


Figure 3.1-22. Test #65 Load/Pressure vs. Time, Side Loading.

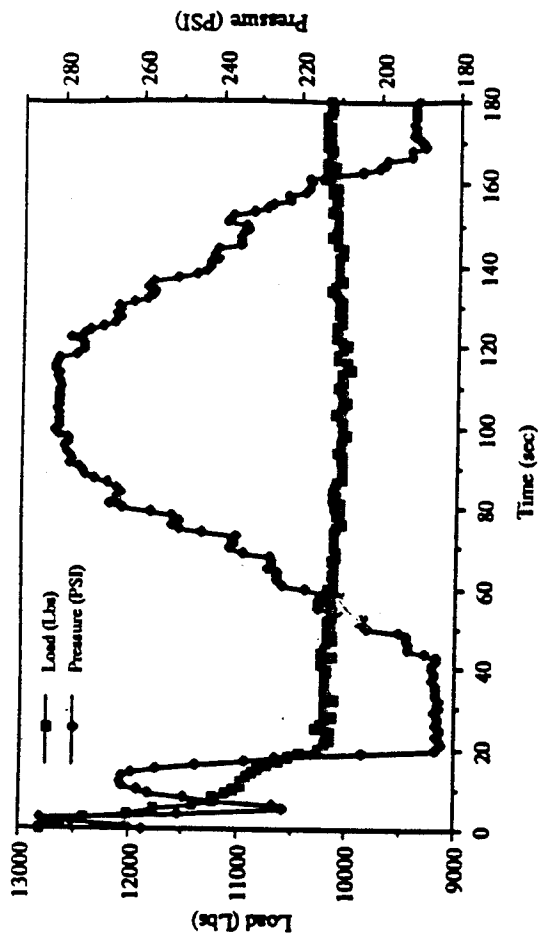


Figure 3.1-21. Test #61 Load/Pressure vs. Time, Hand Side Loading.

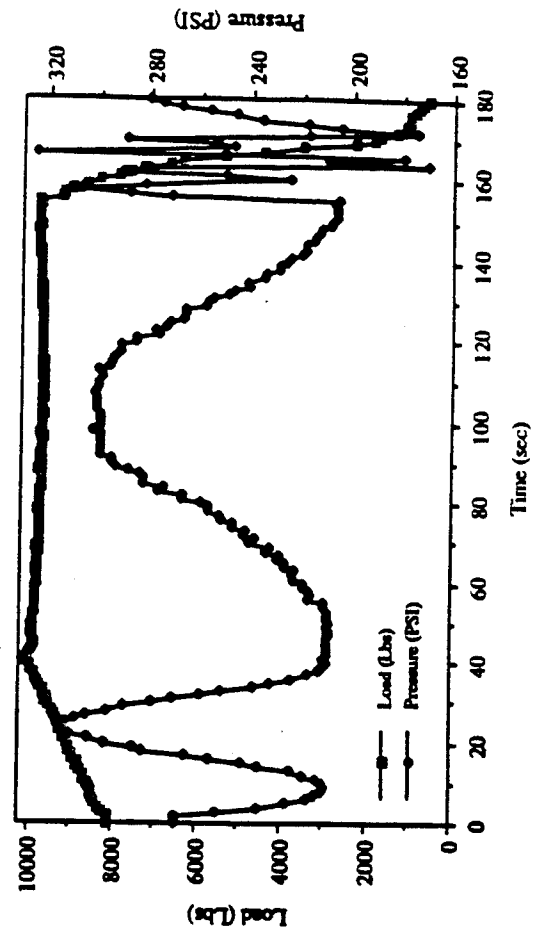


Figure 3.1-23. Test #69 Load/Pressure vs. Time, Side Loading.

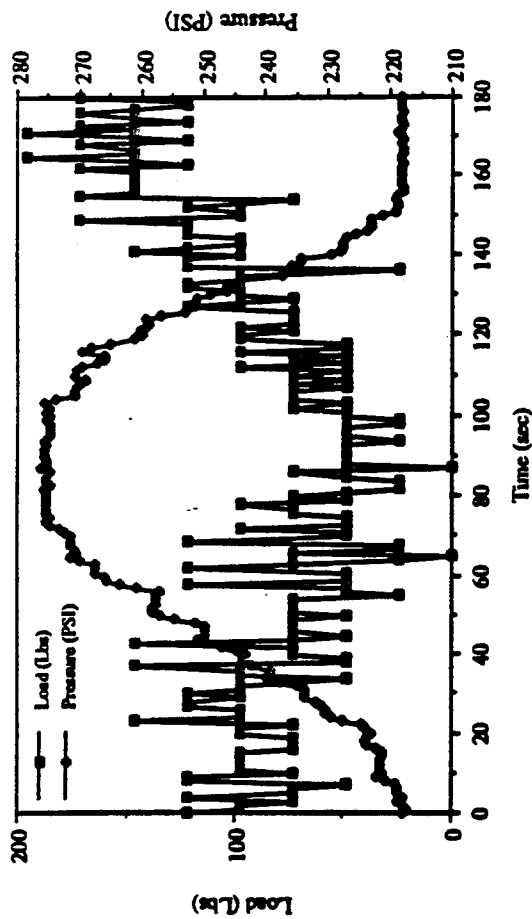


Figure 3.1-24. Test #63 Load/Pressure vs. Time.

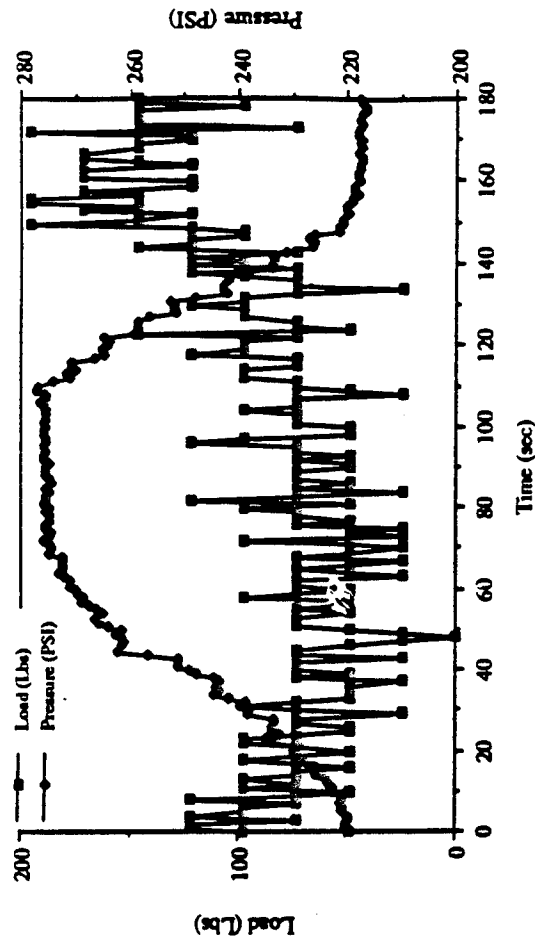


Figure 3.1-25. Test #67 Load/Pressure vs. Time.

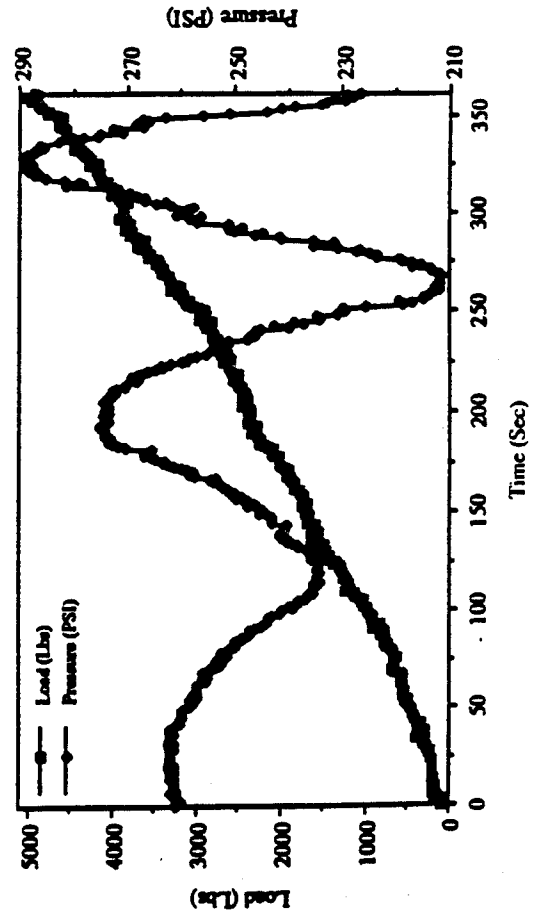


Figure 3.1-26. Test #'s 56, 57 Load/Pressure vs. Time.

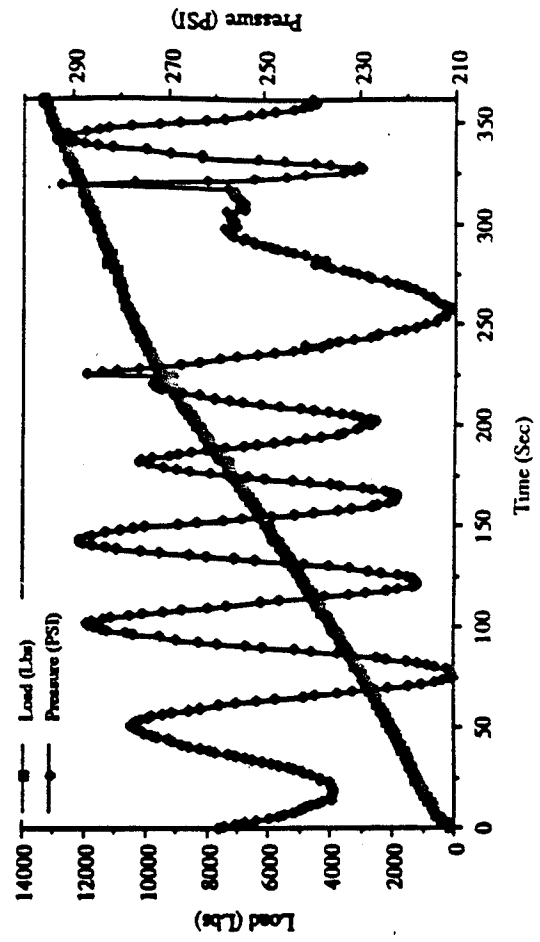


Figure 3.1-27. Test #'s 59, 60 Load/Pressure vs. Time.

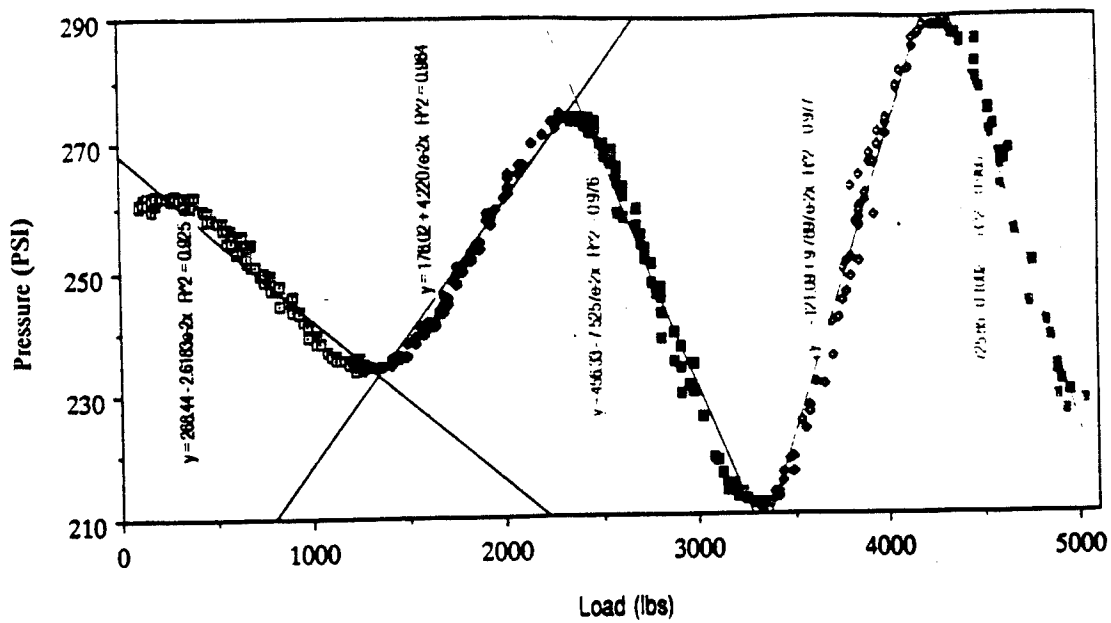


Figure 3.1-28. Test #'s 56, 57 Load vs. Pressure, Cycles and Slopes.

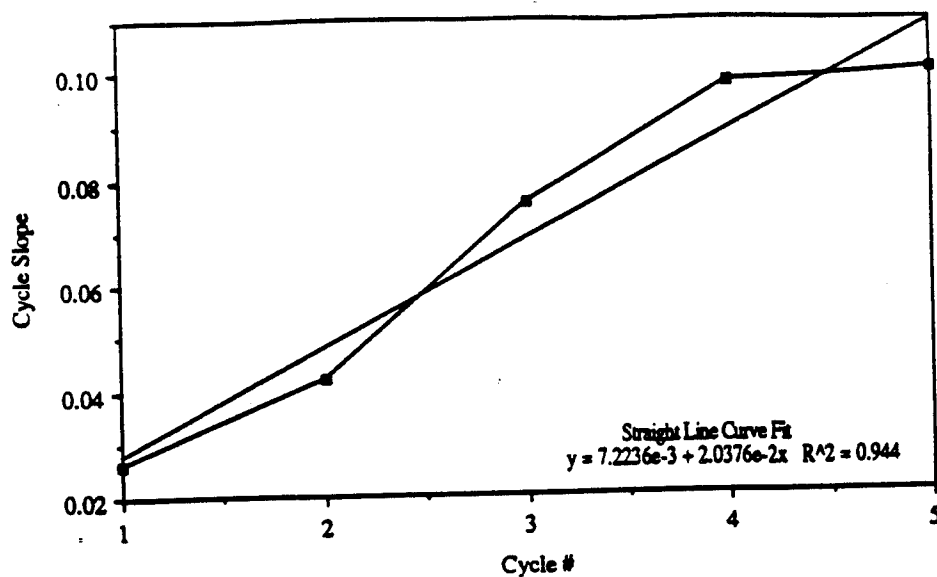


Figure 3.1-29a. Test #'s 56, 57 Cycle Slope Correlation.

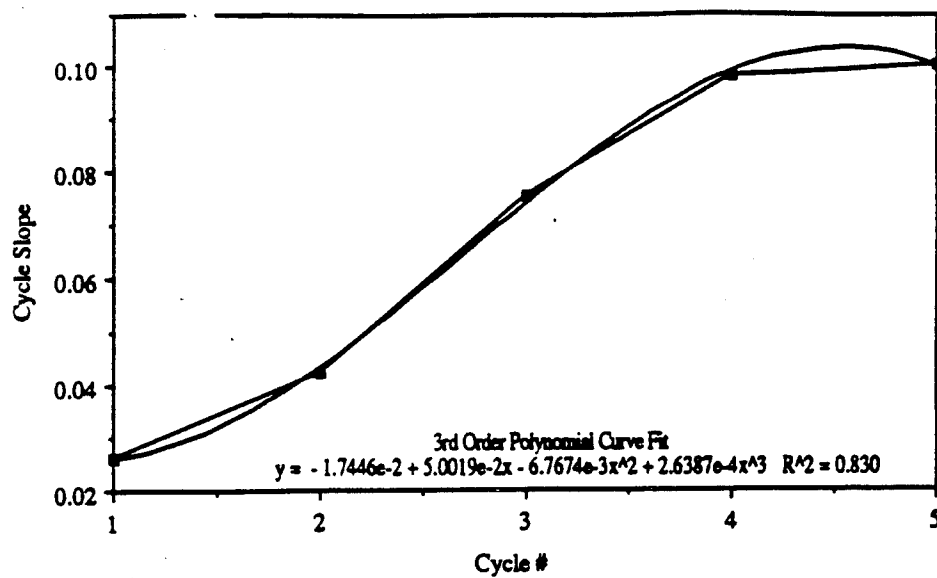


Figure 3.1-29b. Test #'s 56,57 Cycle Slope Correlation.

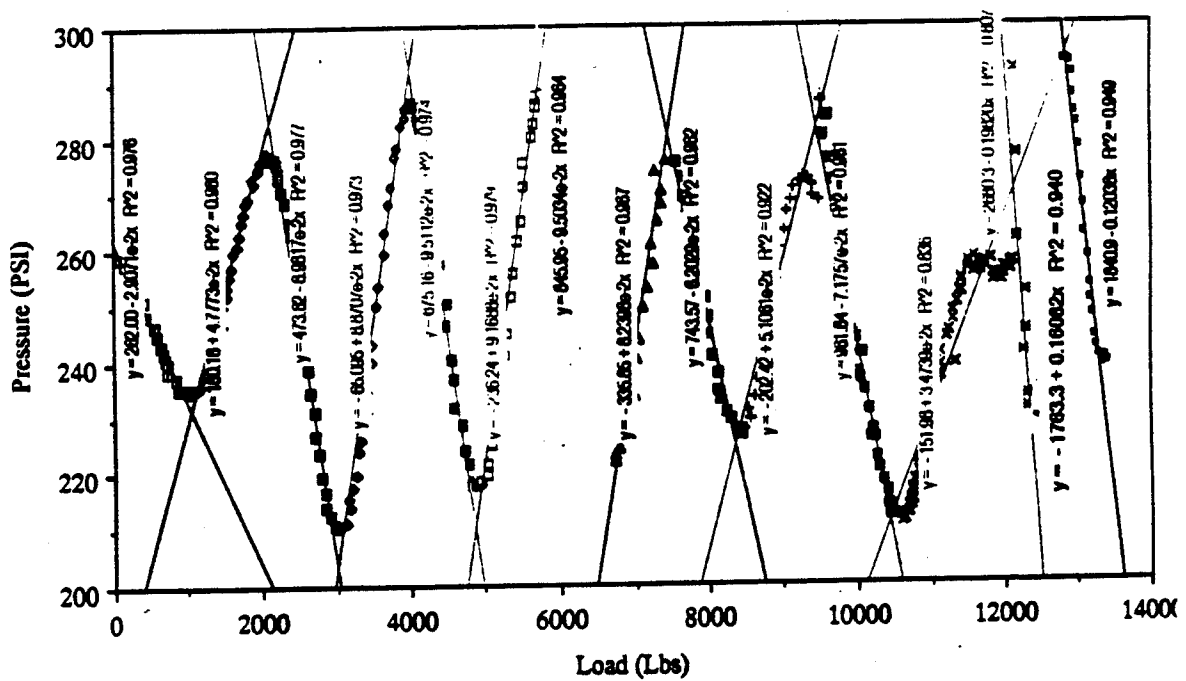


Figure 3.1-30. Test #'s 59, 60 Load vs. Pressure, Cycles and Slopes.

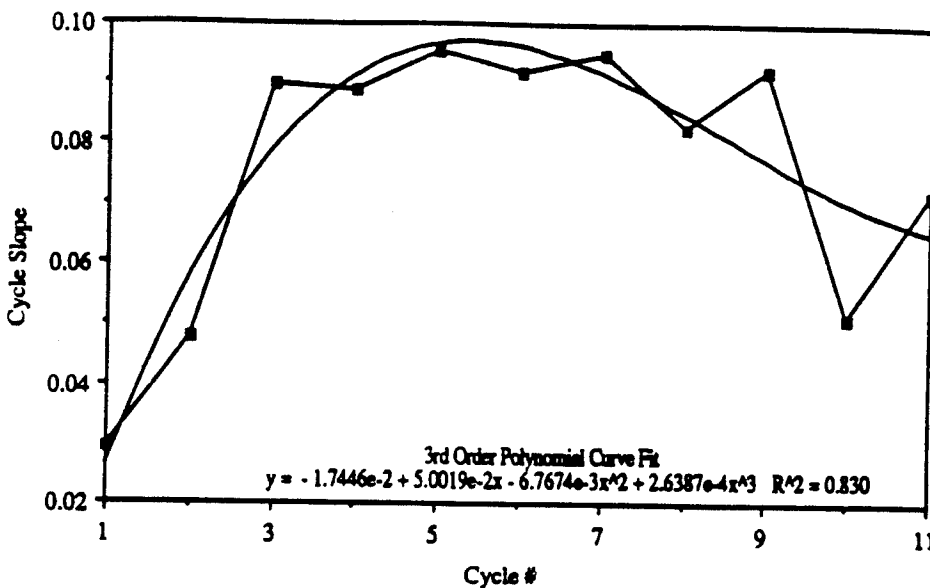


Figure 3.1-31. Test #'s 59, 60 Cycle Slope Correlation.

This was suspected to be caused by the reduced amount of material cushioning imposed by the small panel thickness and by the difficulty of encapsulating the lead wires. Successful foil strain gage encapsulation techniques used custom gages which had extended, right angle, factory encapsulated leads and a custom circuit board for hook-up were not available within the schedule of these tests.

The unreliability of the embedded foil gages lead to the decision not to use them for the ABC Man Program. This decision, along with the limited resources, precluded completing the mechanical tests for the embedded foil gages.

3.1.1.4 PEG Development

The third option for the long bone load sensor was the Post Embedded Gage (PEG). The PEG concept used foil gages which were bonded to a cured substrate which was then overwrapped with several composite layers. The PEG foil gages and lead wires were covered with a foam protective layer to prevent damage during handling and testing. This layer was then overwrapped with the final composite layer consisting of several graphite cloth/epoxy plies.

In order to validate the PEG approach, both panel and tube (to simulate the long bone geometry) specimens were fabricated and tested. As can be seen in the data below, both specimen configurations provided very good data and validated the selection of the PEG concept for the ABC Man long bone instrumentation.

Panel Data

Because surface mounted strain gages are straightforward and well characterized, a set of graphite/epoxy panels were fabricated with foil strain gages mounted on the surface. These panels were used as controls for the tube with true PEG gages. The data for these tests are given below and demonstrate the linear and highly repeatable nature of surface mounted foil gages on simulated ABC Man material. A variety of uniaxial and off-axis layups were used for the panel specimens.

The data from these tests are shown in the following plots. Figures 3.1-32 through 3.1-42 present the raw data from these tests. Figures 3.1-32 through 3.1-39 are plots of the axial loading tests. Figures 3.1-41 through 3.1-42 show the transverse loading tests. Figures 3.1-44 and 3.1-45 are plots of sensor calibration. Figures 3.1-45 through 3.1-54 show load versus strain percent for each strain gage. The slope of these lines, divided by the panel cross-sectional area, gives us the modulus of elasticity (E) for the material in that axis. We used the modulus calculation as a rough confirmation of the accuracy of the gages. A summary of these are provided in Table 3.1-4. Figures 3.1-55a through 3.1-57c plot axial load versus strain for the side loading tests. Figures 3.1-58 through 3.1-63 are plots of transverse versus axial strain. These plots provide Poisson's ratio (μ). The Poisson's ratio is higher than 1.0 which reflects the differential movement of the fibers or scissoring. Isotropic elasticity theory requires Poisson's ratio be less than 0.5, however orthotropic plane stress elasticity theory does not have this constraint. For plane stress theory, the elasticity terms are divided by $1 - \gamma_{12} \gamma_{12}$ (where $\gamma_{21} = \frac{E_2}{E_1} \gamma_{12}$). To be well behaved this quantity should not equal zero. Thus for $E_2 < E_1$ we can have $\gamma_{12} = 1$ and not violate this constraint. Also, for a large percentage of $\pm 45^\circ$ plies (as is the case here) it is common for γ_{12} to approach 1. Thus these ranges of γ_{12} are reasonable. We also used this calculation to check the performance of the gages. A summary of these values is given in Table 3.1-4. The results of the axial versus transverse strain for the side loading tests are shown in Figures 3.1-64 through 3.1-67. Finally, plots of axial versus transverse strain for the two calibration runs are shown in Figure 3.1-68. The data in Table 3.1-4 demonstrates the measurement consistency of PEG foil strain gages. There is little variation from test to test in the measured modulus.

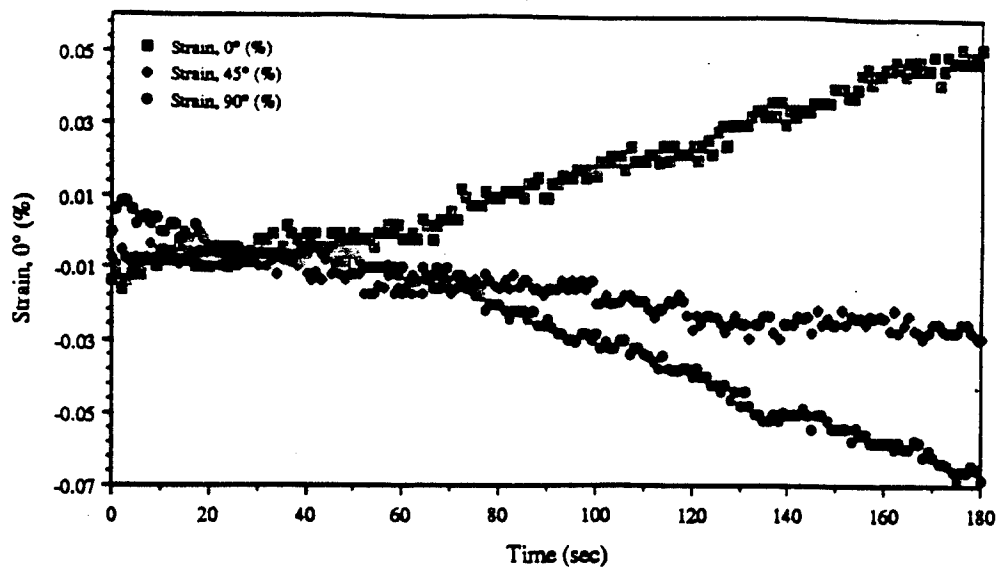


Figure 3.1-32. Test #56 Strain vs. Time.

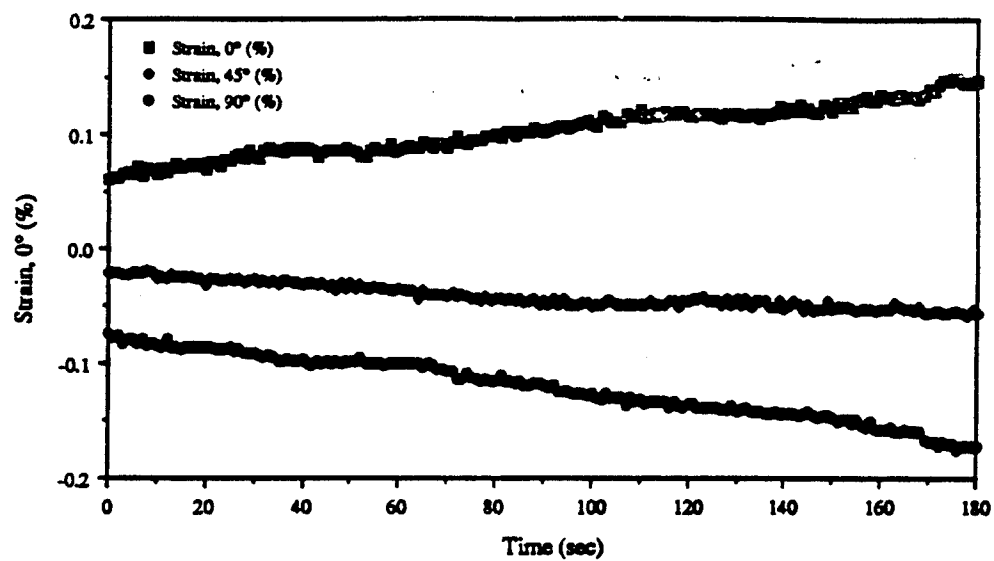


Figure 3.1-33. Test #57 Strain vs. Time.

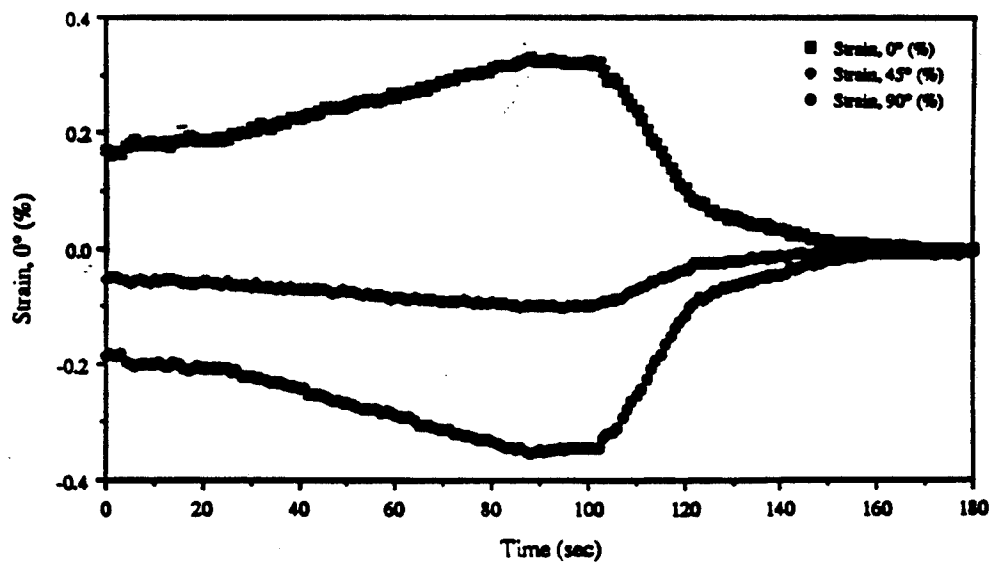


Figure 3.1-34. Test #58 Strain vs. Time.

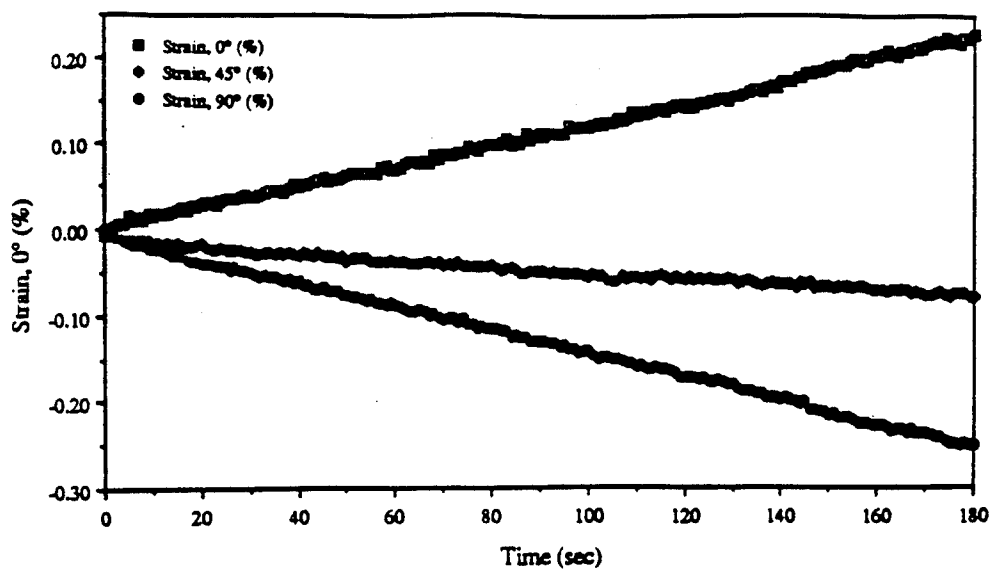


Figure 3.1-35. Test #59 Strain vs. Time.

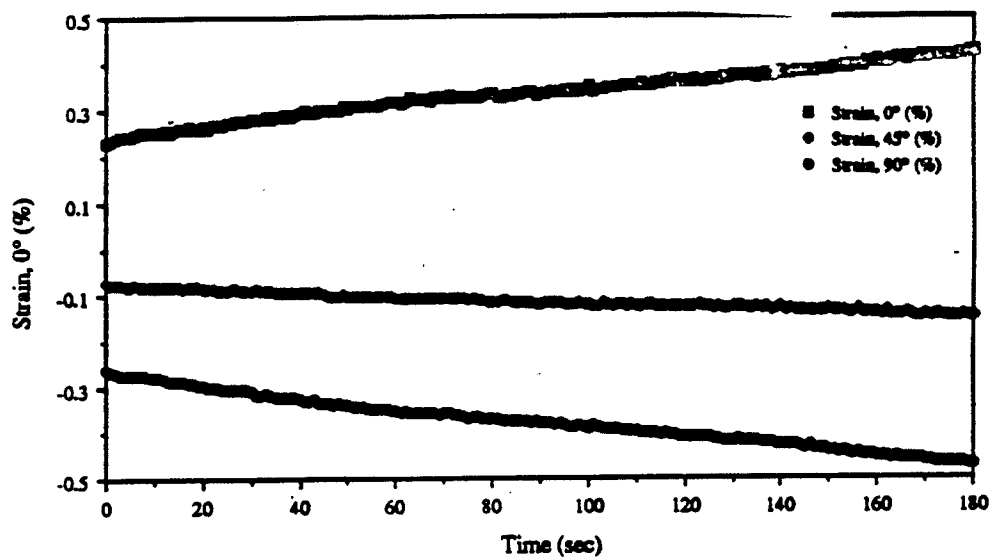


Figure 3.1-36. Test #60 Strain vs. Time.

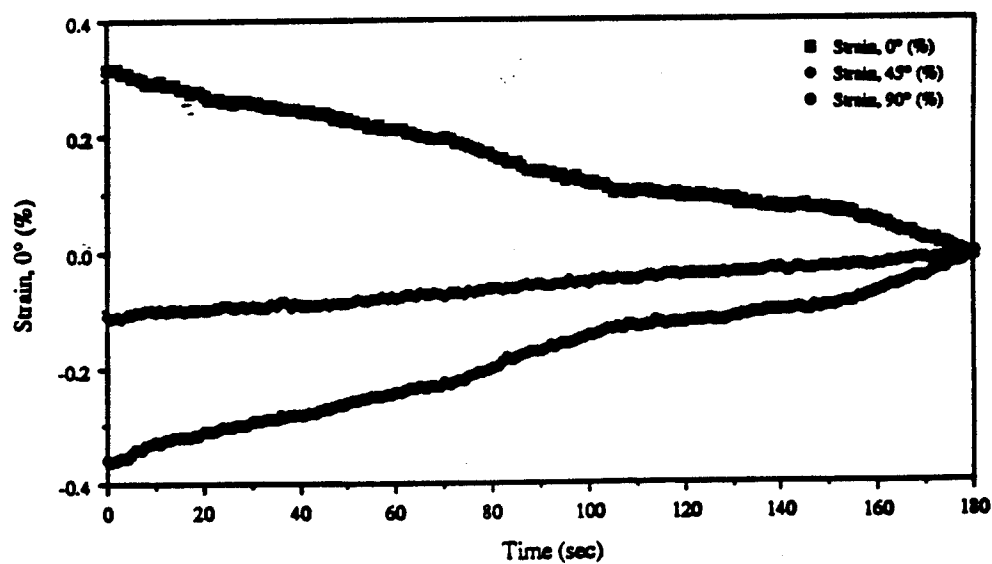


Figure 3.1-37. Test #62 Strain vs. Time.

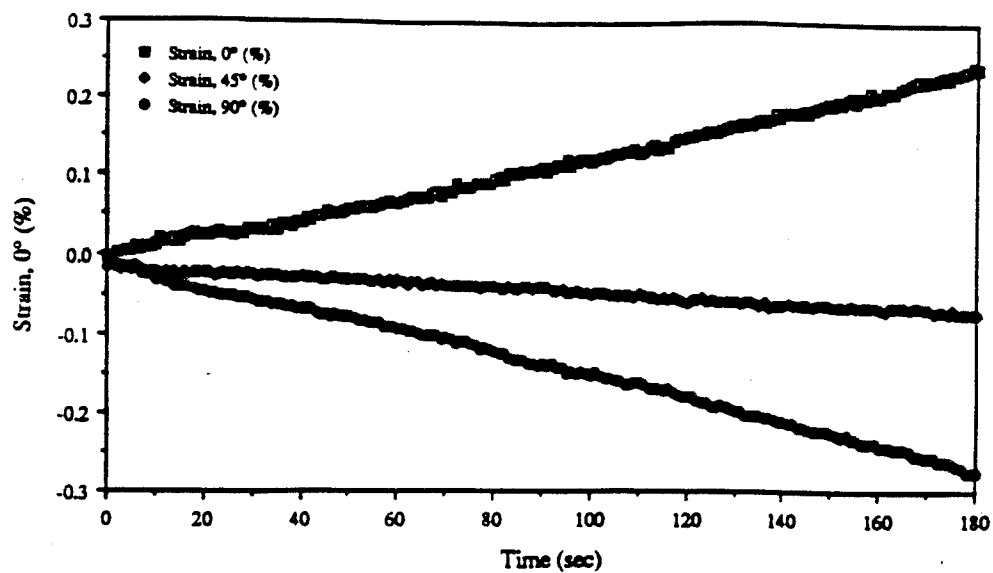


Figure 3.1-38. Test #64 Strain vs. Time.

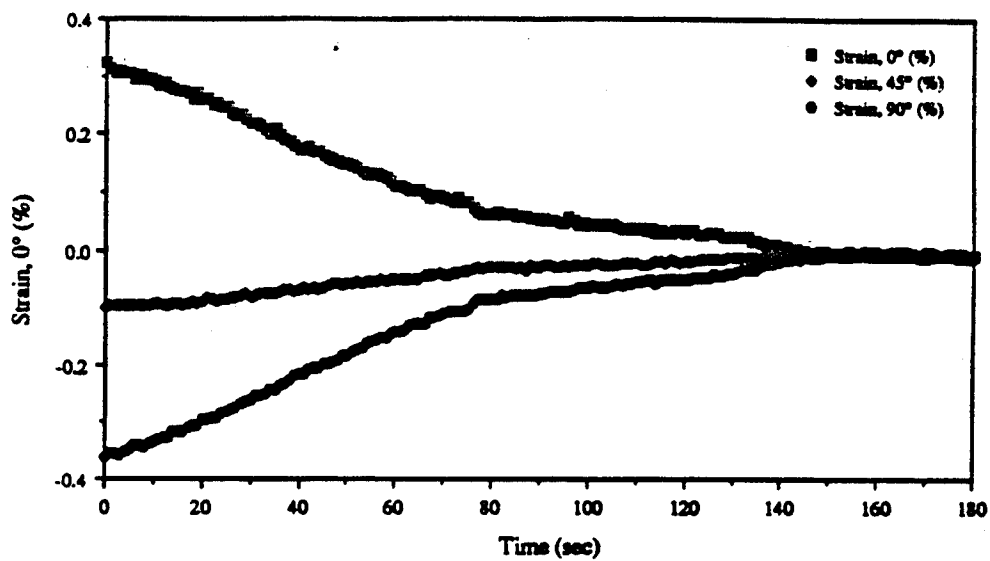


Figure 3.1-39. Test #66 Strain vs. Time.

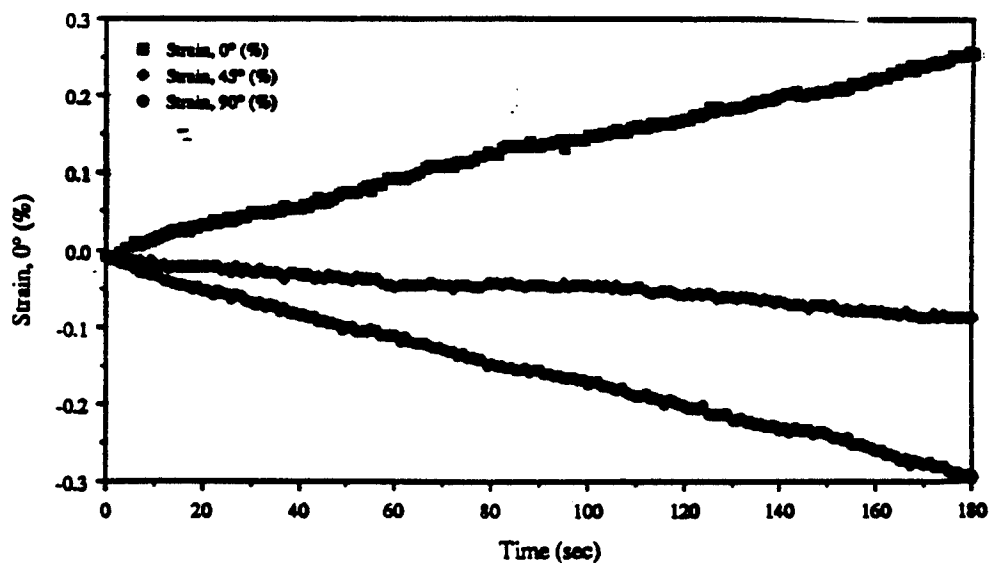


Figure 3.1-40. Test #68 Strain vs. Time.

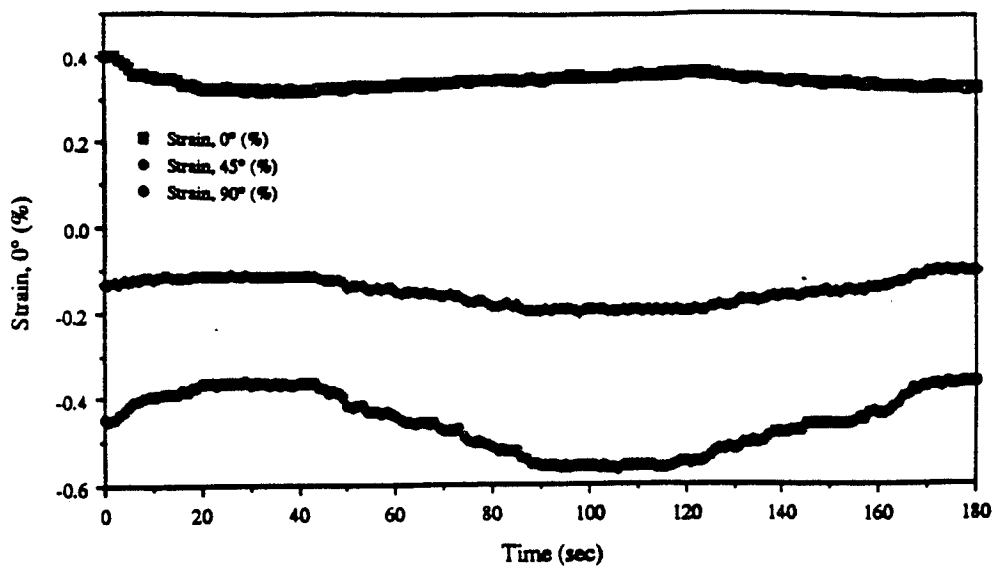


Figure 3.1-41. Test #61 Strain vs. Time.

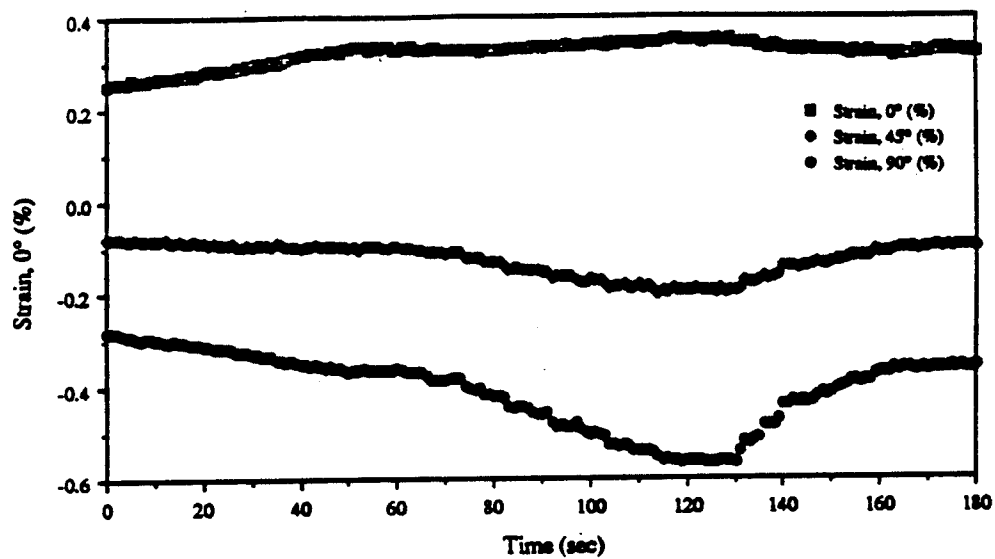


Figure 3.1-42. Test #65 Strain vs. Time.

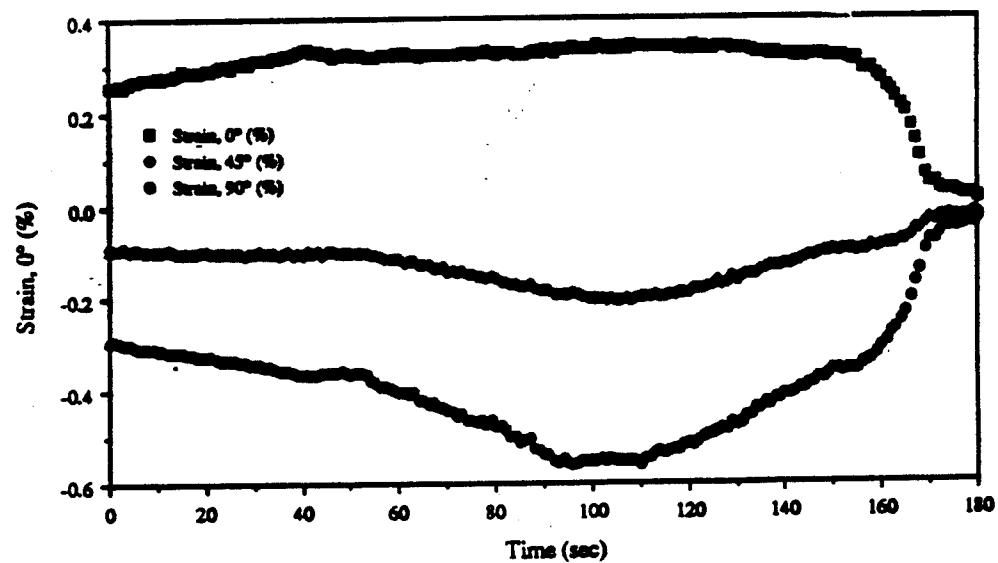


Figure 3.1-43. Test #69 Strain vs. Time.

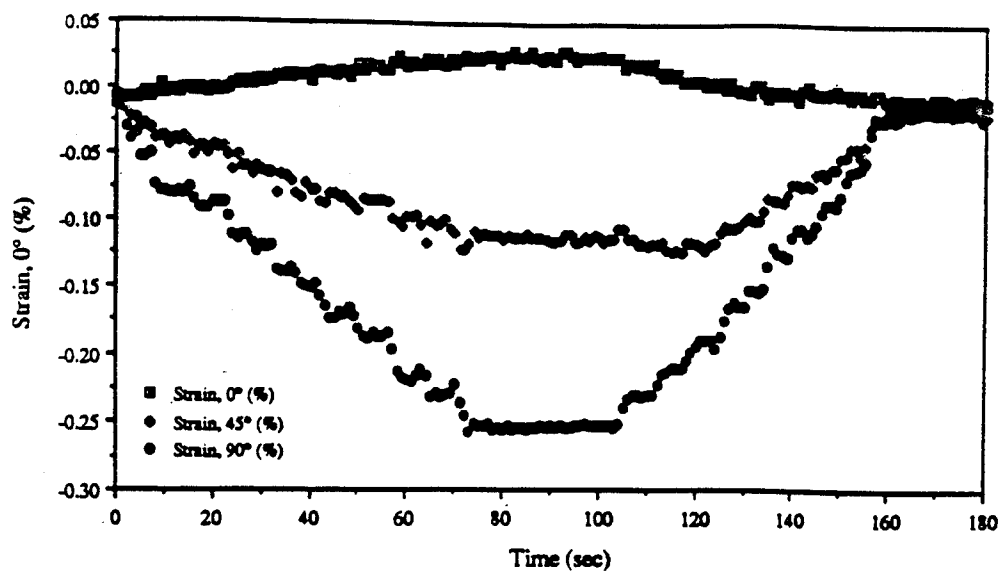


Figure 3.1-44. Test #63 Strain vs. Time.

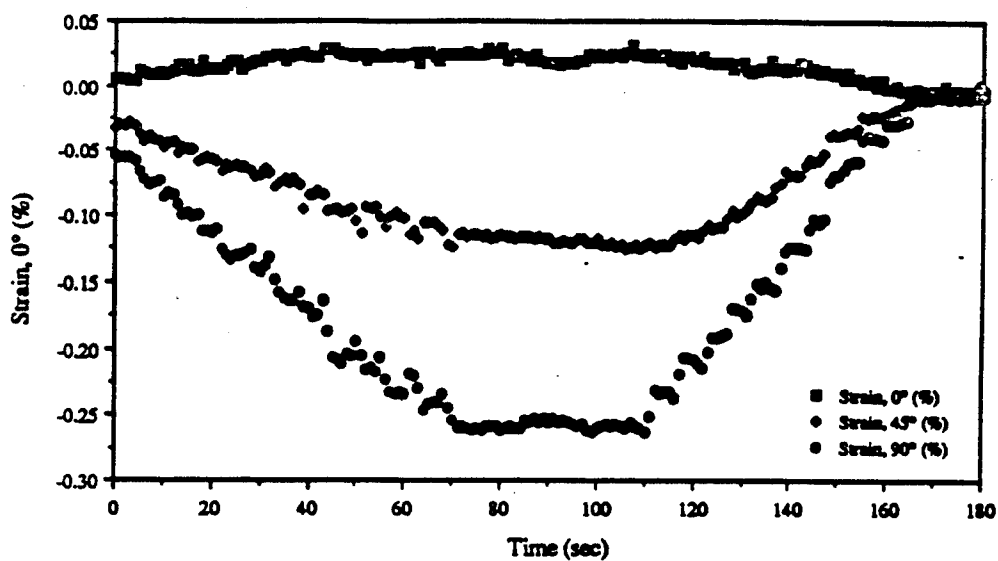


Figure 3.1-45. Test #67 Strain vs. Time.

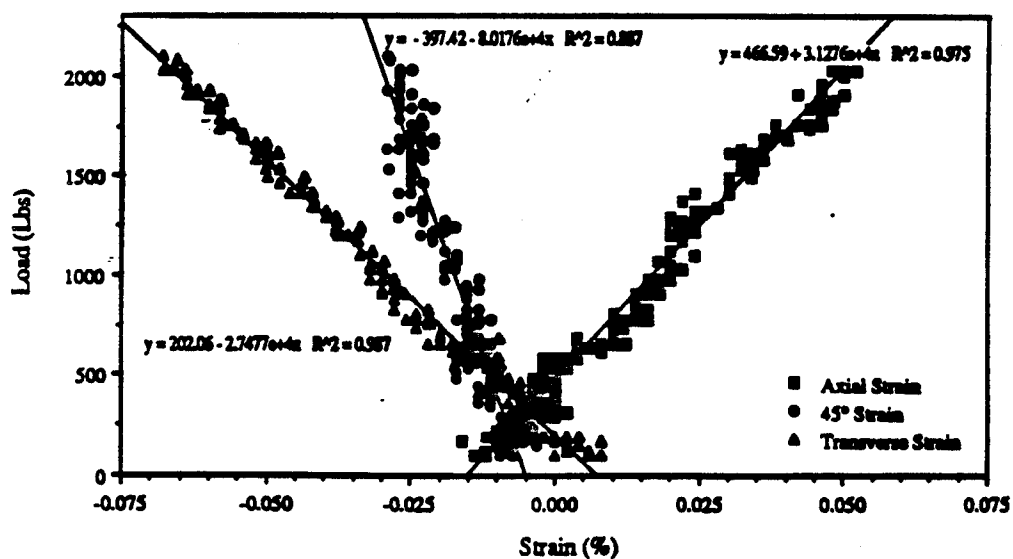


Figure 3.1-46. Test #56 Strain vs. Time.

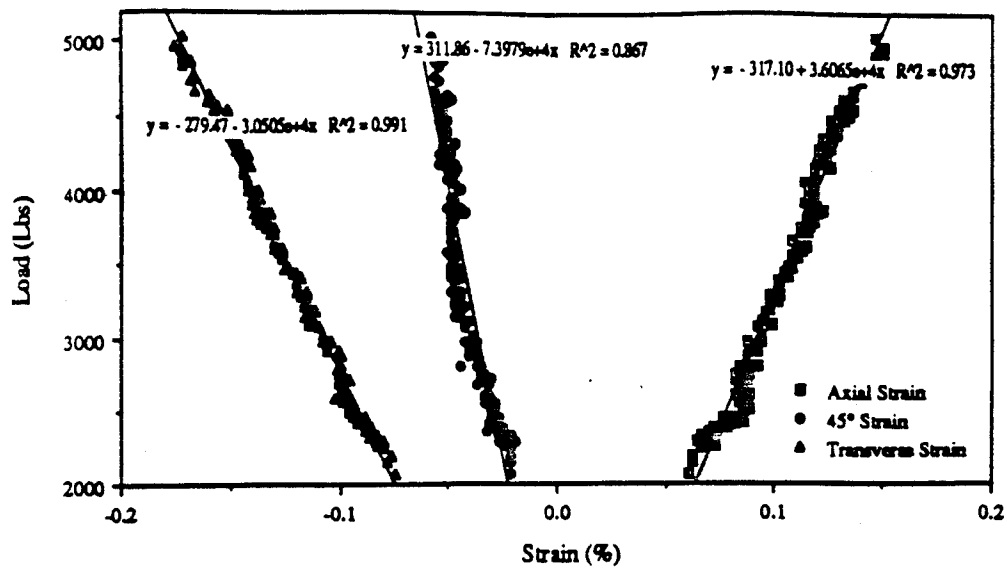


Figure 3.1-47. Test #57 Strain vs. Load.

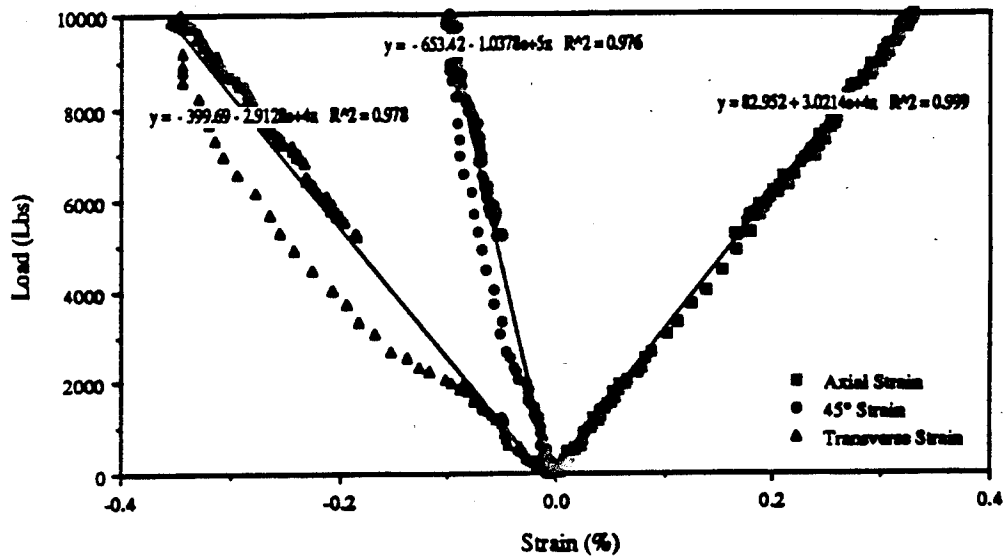


Figure 3.1-48. Test #58 Strain vs. Load.

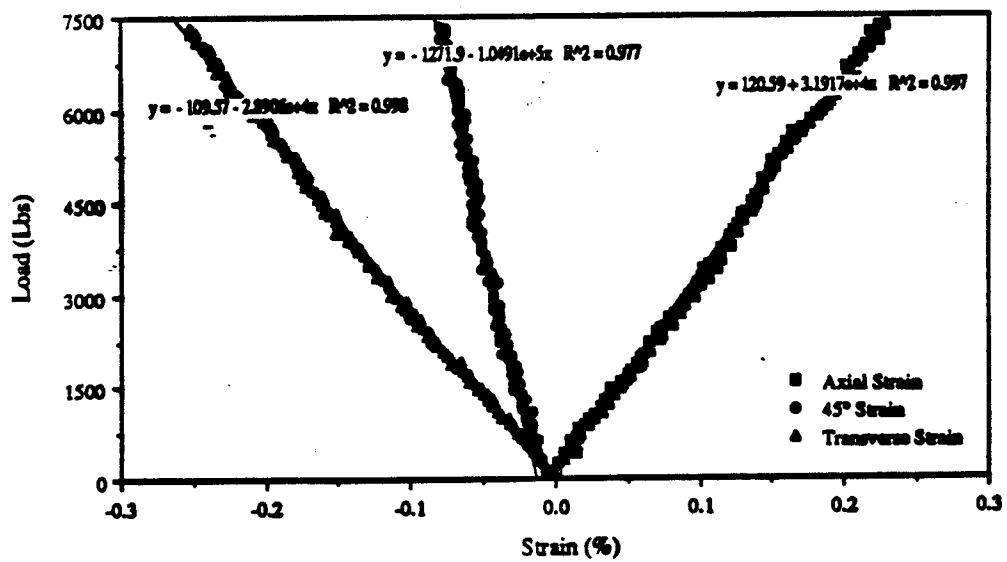


Figure 3.1-49. Test #59 Strain vs. Load.

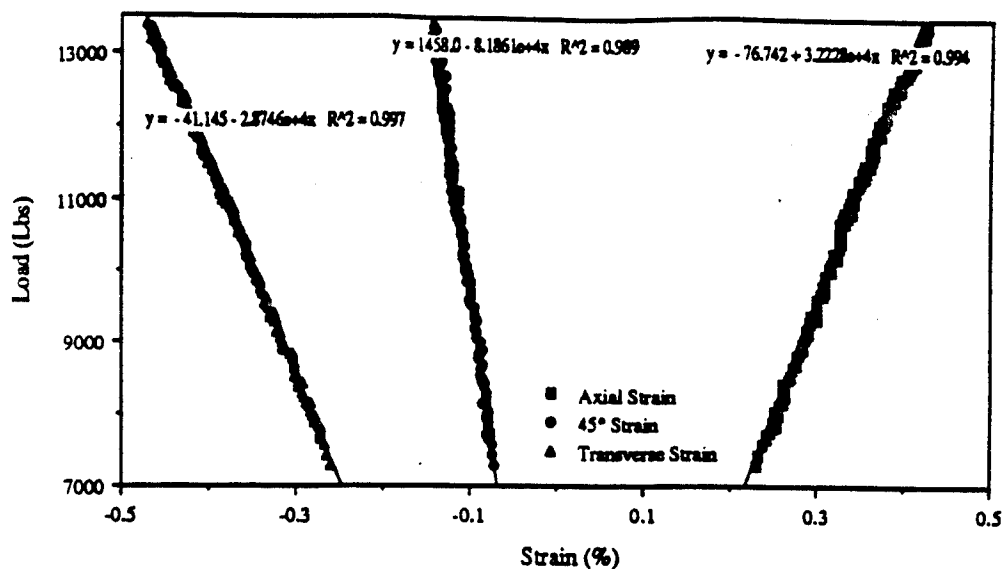


Figure 3.1-50. Test #60 Strain vs. Load.

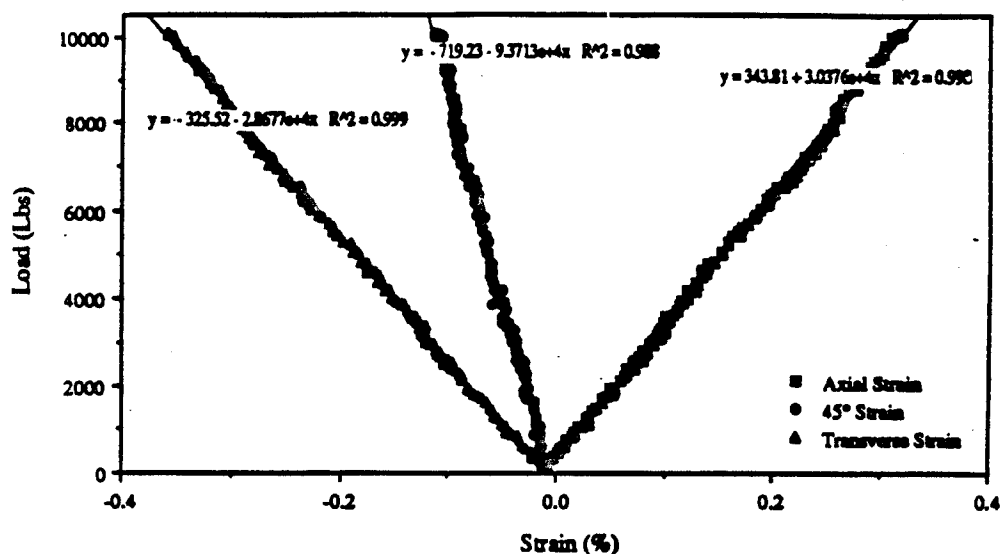


Figure 3.1-51. Test #62 Strain vs. Load.

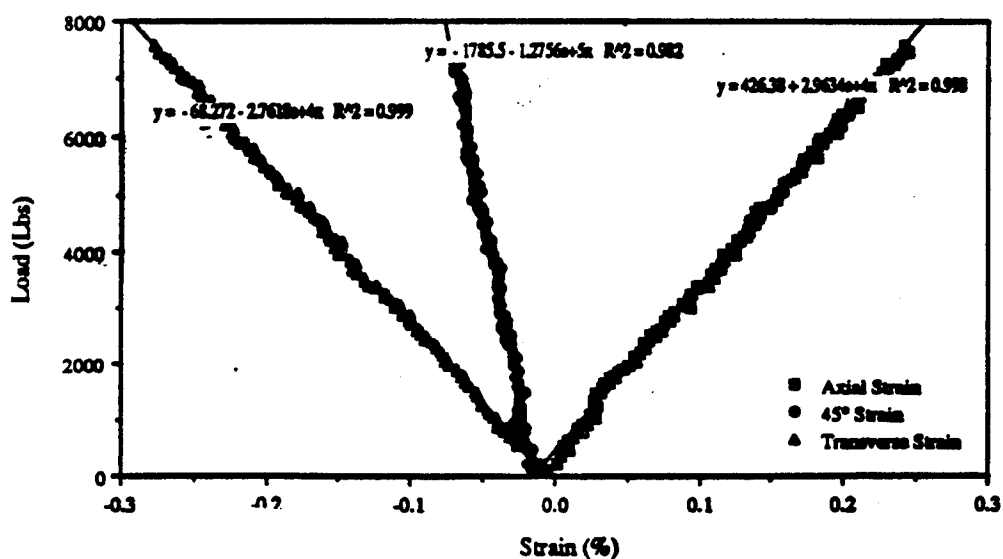


Figure 3.1-52. Test #64 Strain vs. Load.

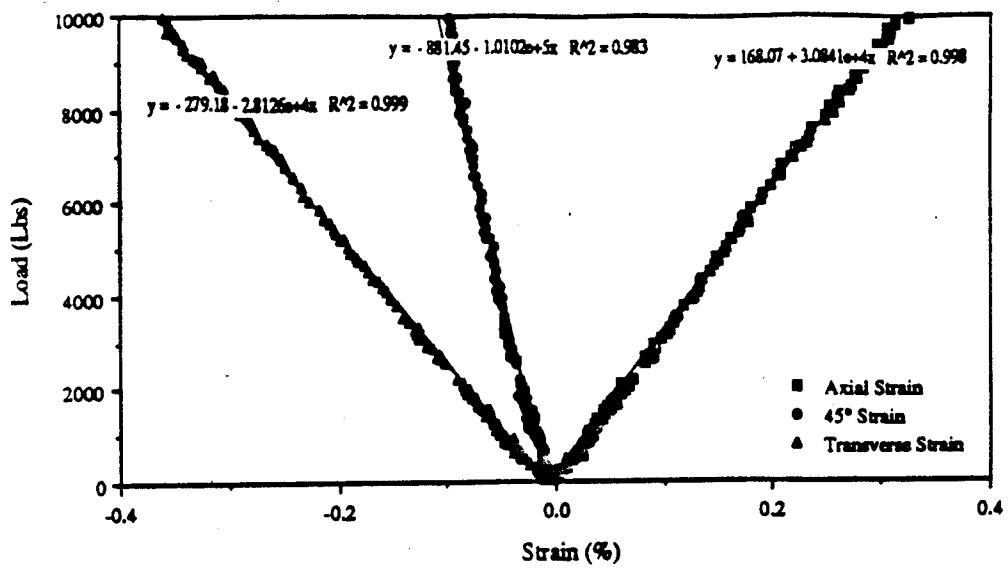


Figure 3.1-53. Test #66 Strain vs. Load.

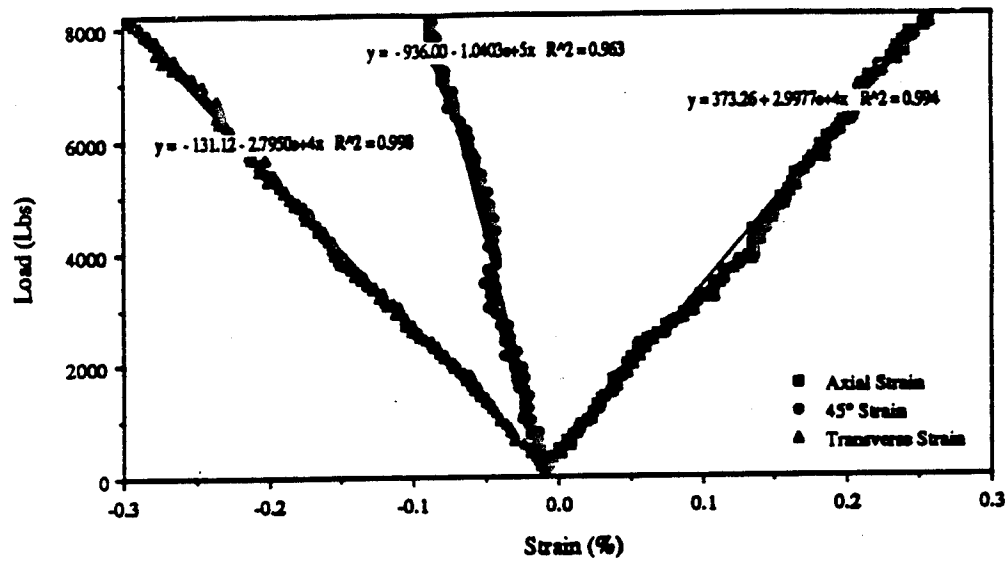


Figure 3.1-54. Test #68 Strain vs. Load.

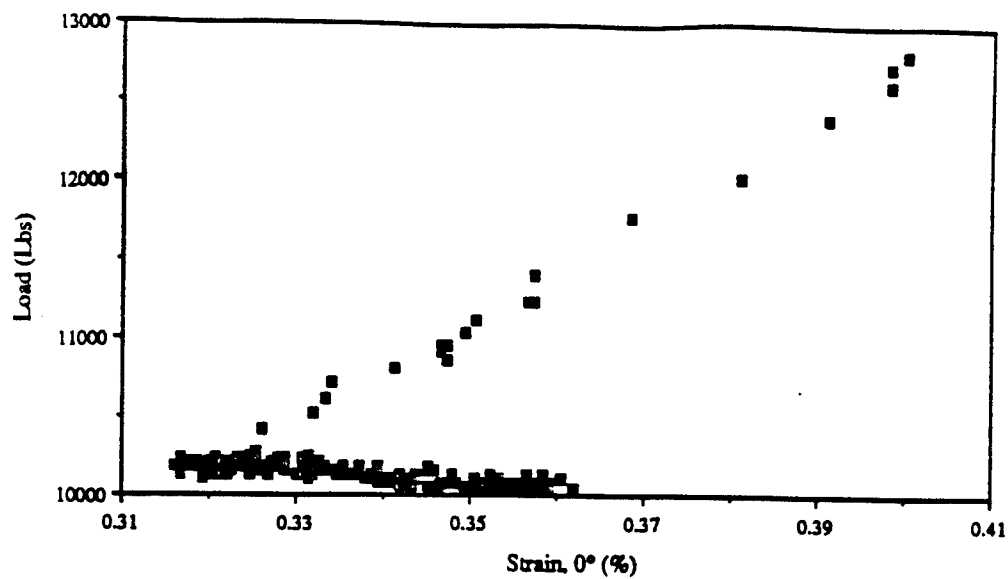


Figure 3.1-55a. Test #61 0° Strain vs. Load, Side Loading.

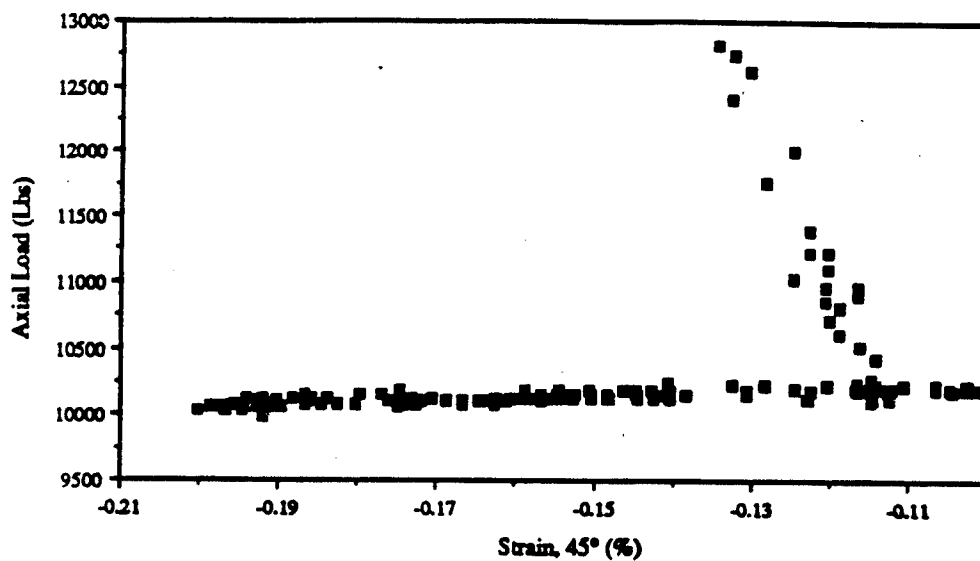


Figure 3.1-55b. Test #61 45° Strain vs. Load, Side Loading.

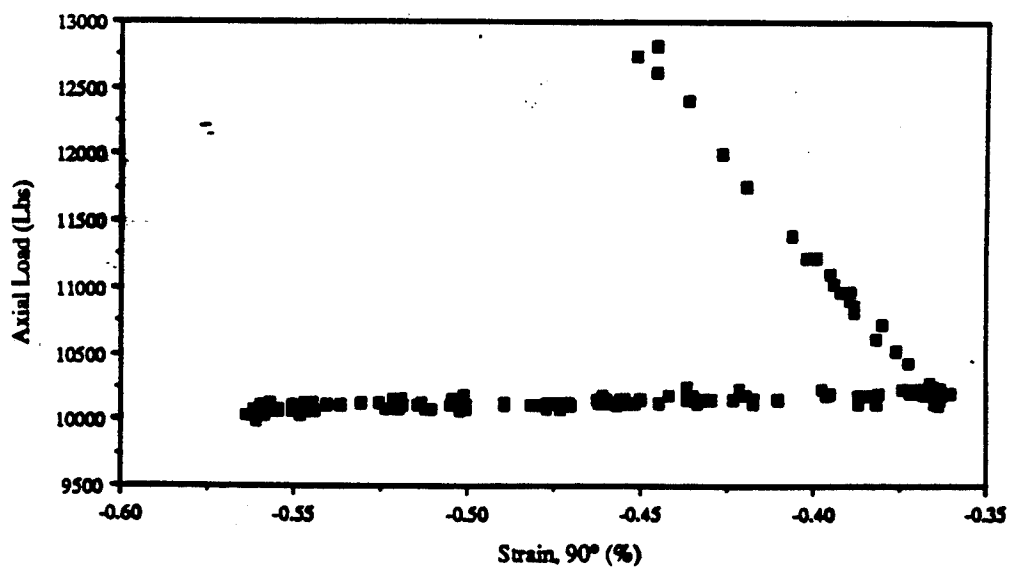


Figure 3.1-55c. Test #61 90° Strain vs. Load, Side Loading.

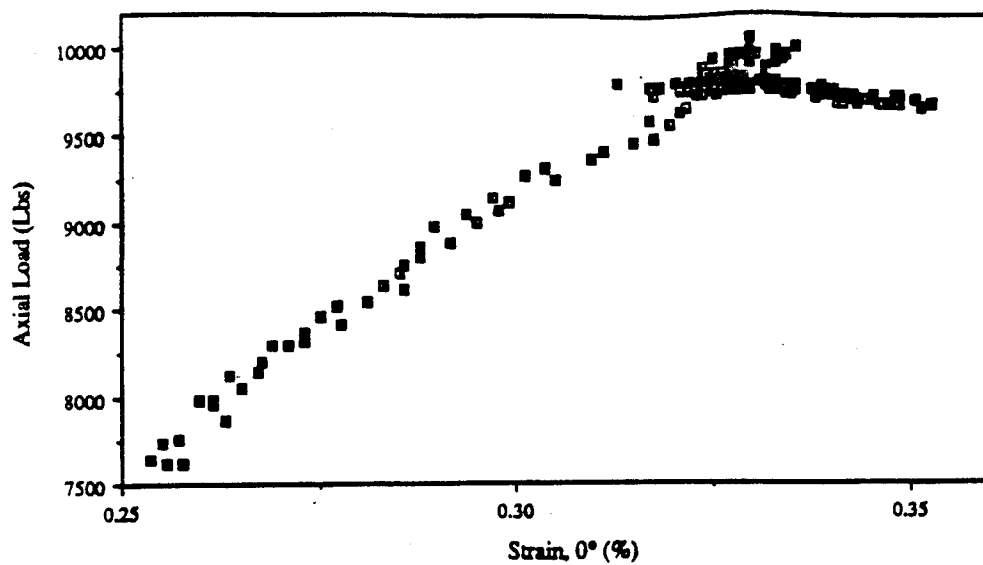


Figure 3.1-56a. Test #65 0° Strain vs. Load, Side Loading.

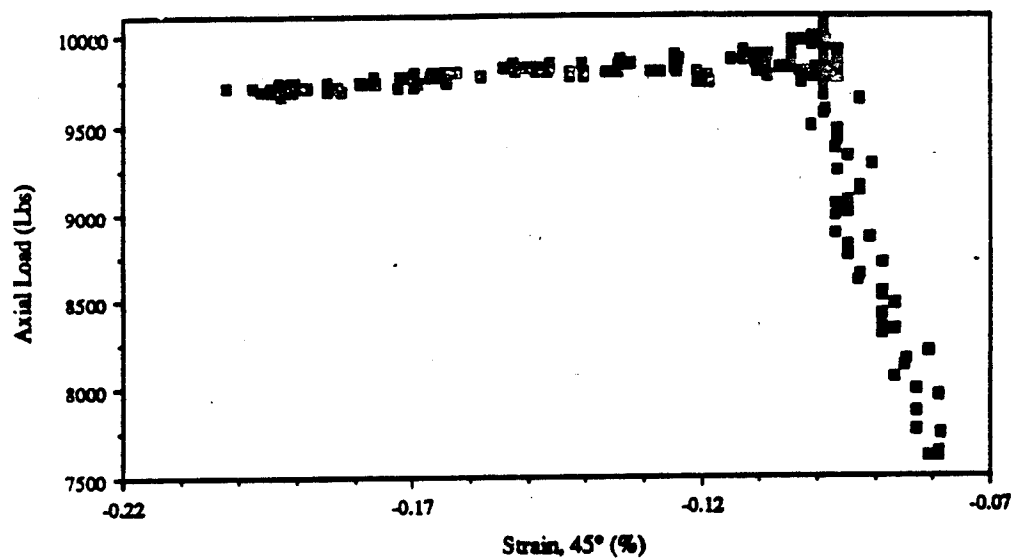


Figure 3.1-56b. Test #65 45° Strain vs. Load, Side Loading.

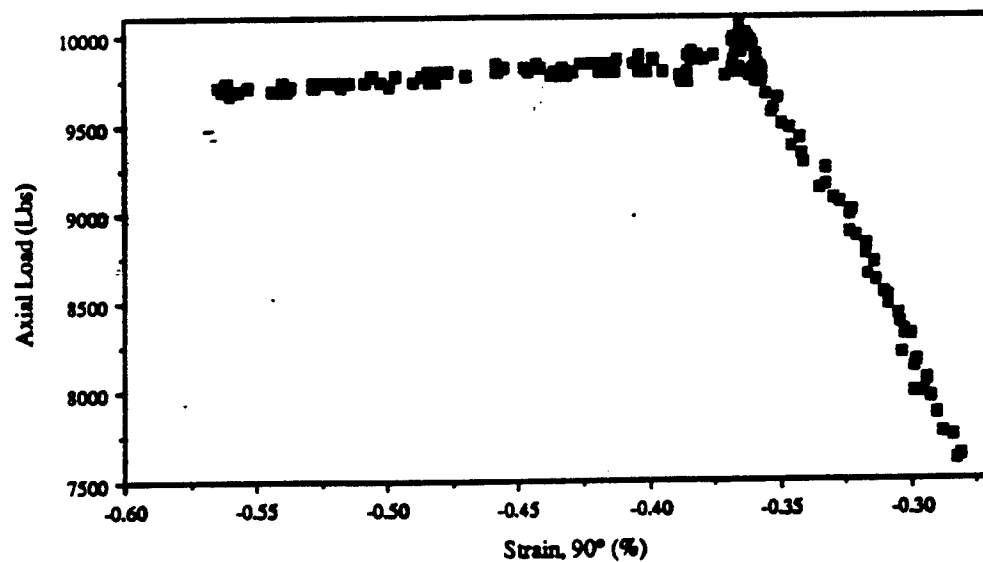


Figure 3.1-56c. Test #65 90° Strain vs. Load, Side Loading.

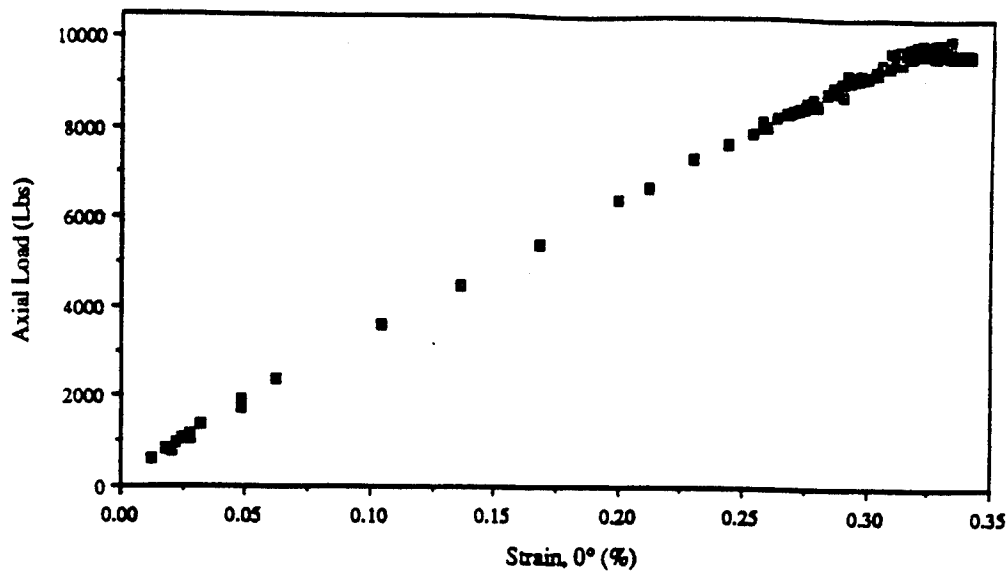


Figure 3.1-57a. Test #69 0° Strain vs. Load, Side Loading.

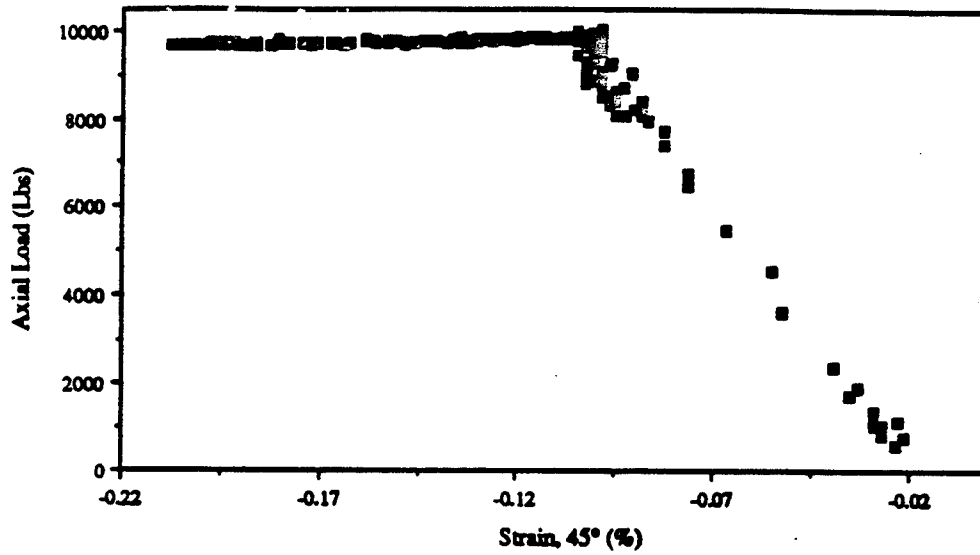


Figure 3.1-57b. Test #69 45° Strain vs. Load, Side Loading.

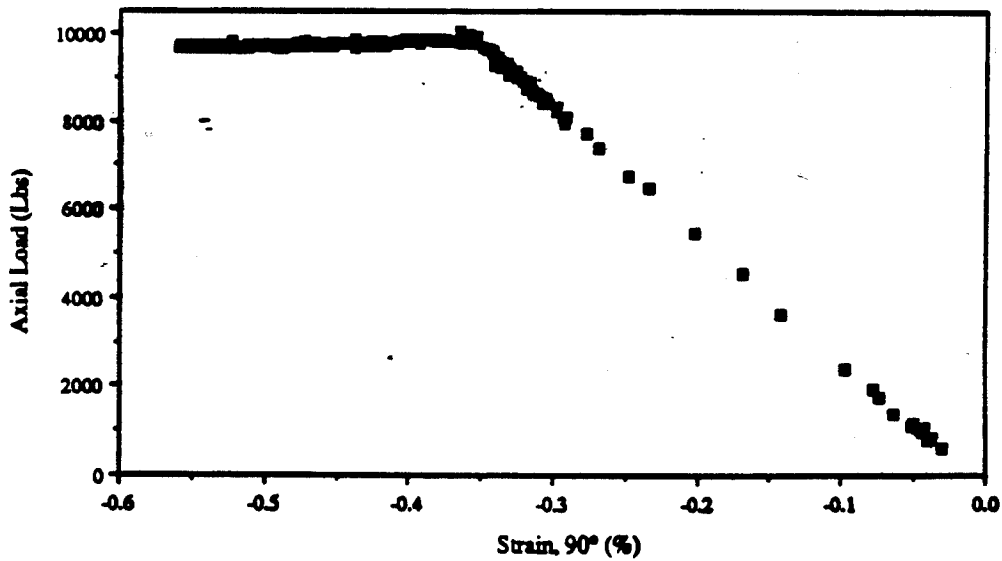


Figure 3.1-57c. Test #69 90° Strain vs. Load, Side Loading.

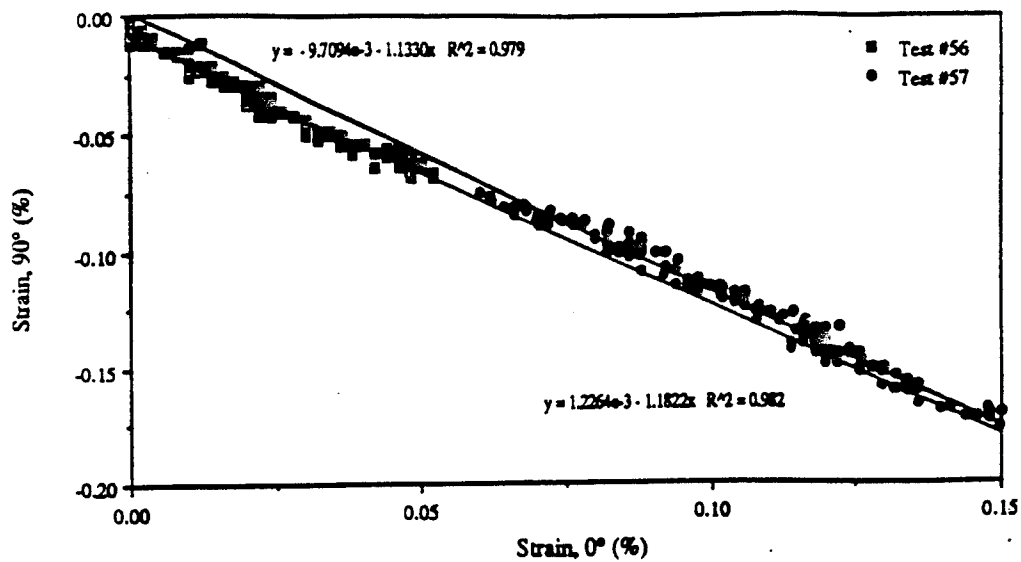


Figure 3.1-58a. Test #'s 56, 57 Axial vs. Transverse Strain.

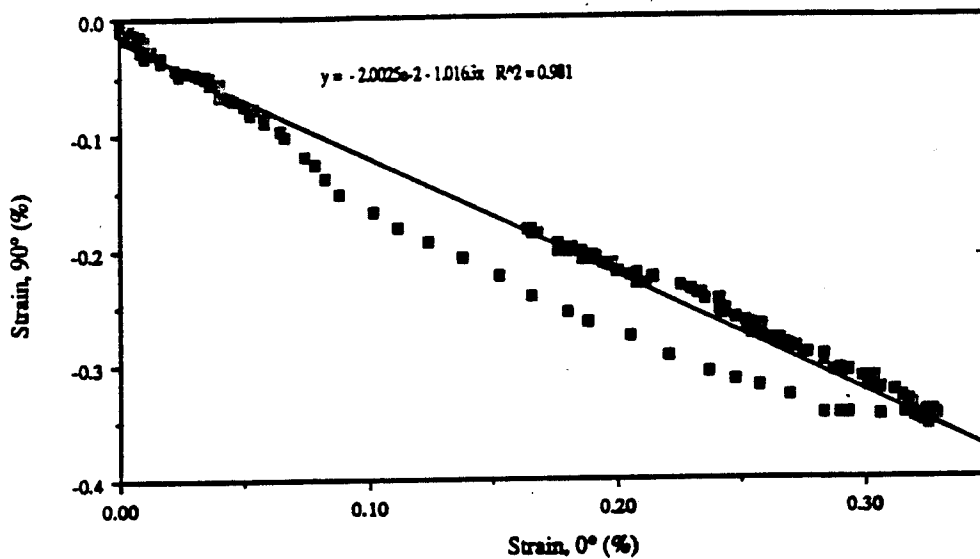


Figure 3.1-59. Test #58 Axial vs. Transver.

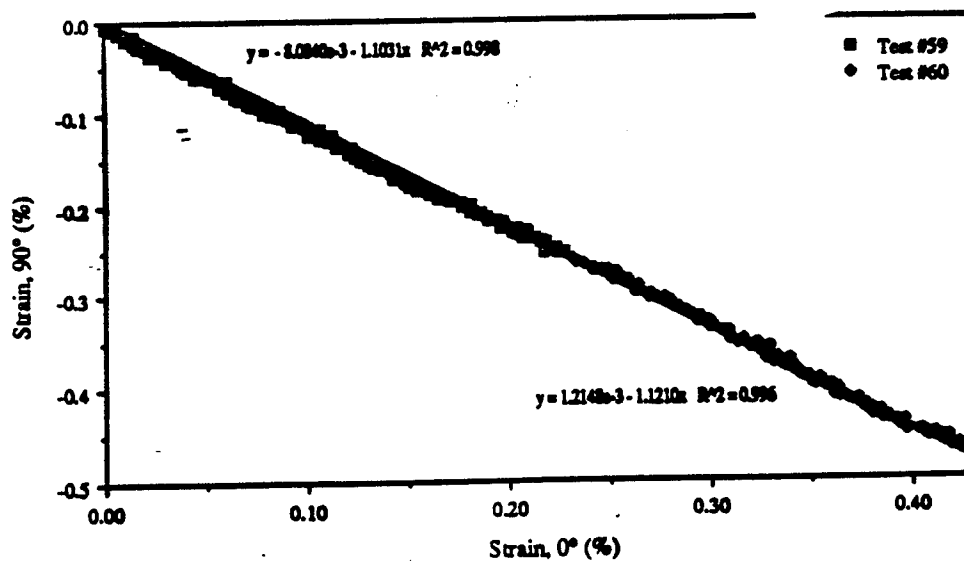


Figure 3.1-60. Test #'s 59, 60 Axial vs. Transverse Strain.

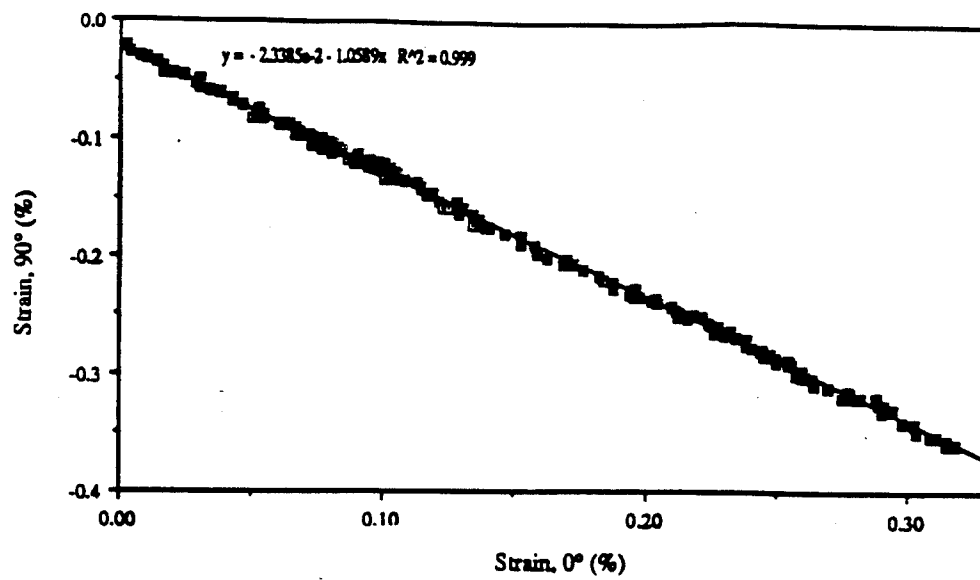


Figure 3.1-61. Test #62 Axial vs. Transverse Strain.

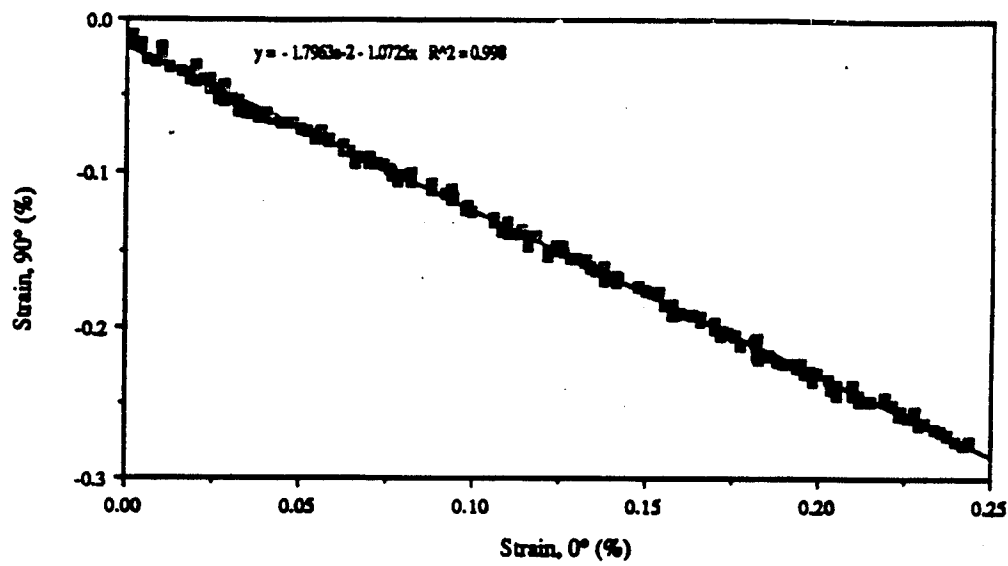


Figure 3.1-62. Test #64 Axial vs. Transverse Strain.

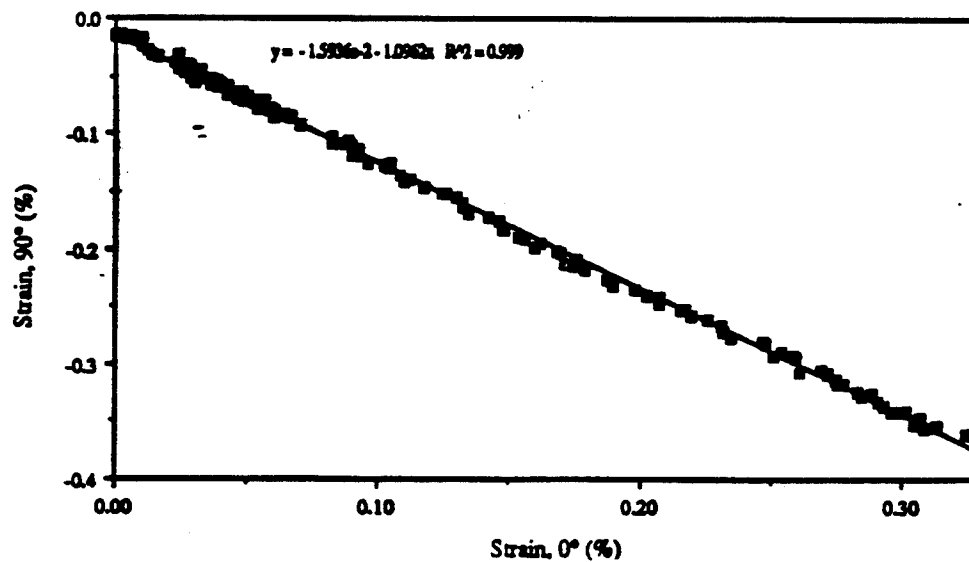


Figure 3.1-63. Test #66 Axial vs. Transverse Strain.

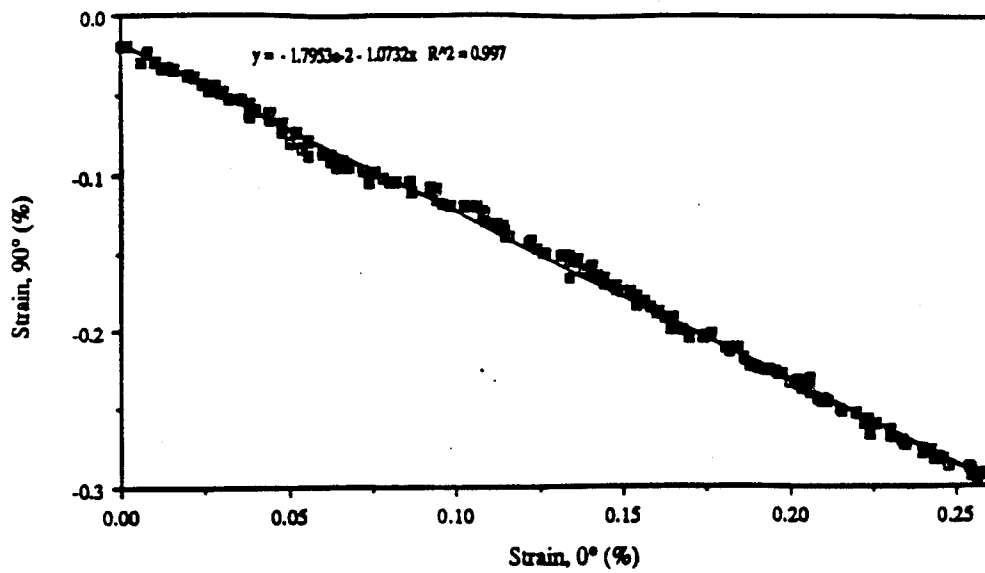


Figure 3.1-64. Test #68 Axial vs. Transverse Strain.

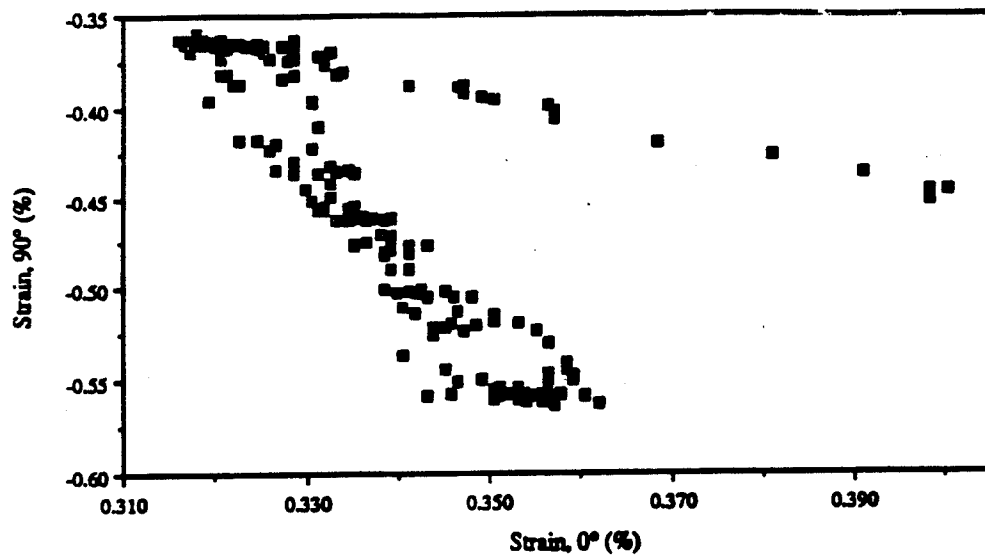


Figure 3.1-65. Test #61 Axial vs. Transverse Strain, Side Loading.

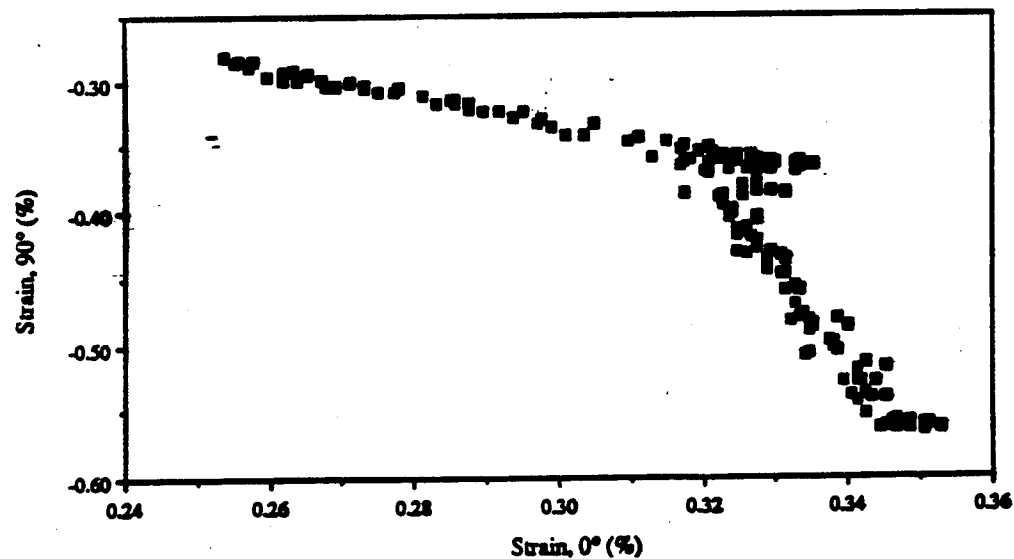


Figure 3.1-66. Test #65 Axial vs. Transverse Strain, Side Loading.

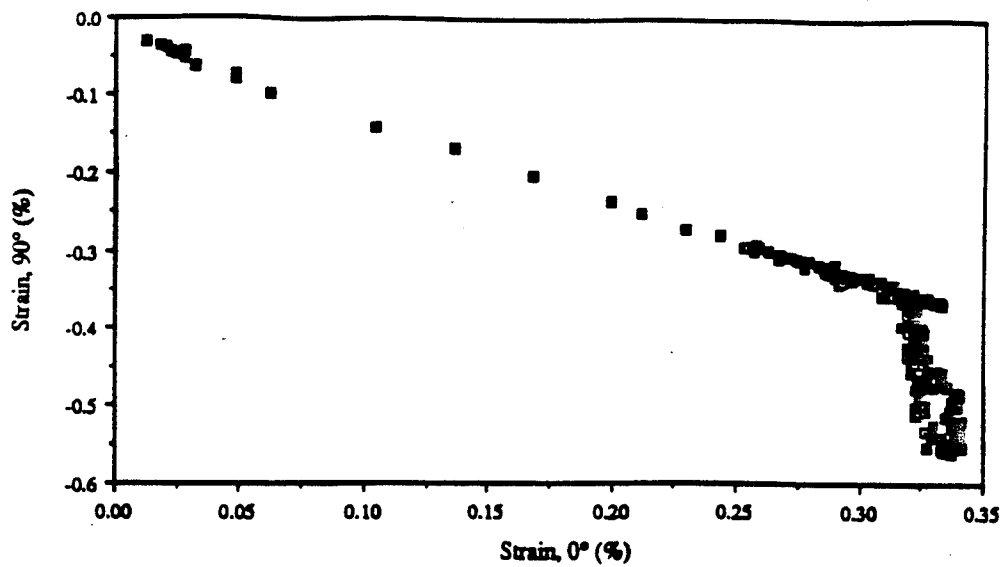


Figure 3.1-67. Test #69 Axial vs. Transverse Strain, Side Loading.

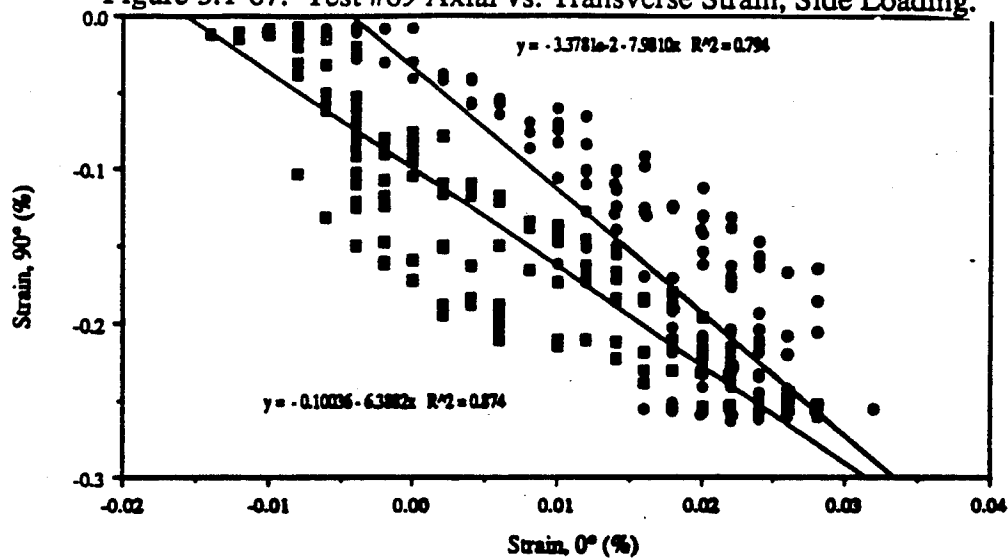


Figure 3.1-68. Test #'s 63, 67 Axial vs. Transverse Strain.

Table 3.1-4. Panel Tensile Modulus of Elasticity and Poissons Ratio Summary.

Test #	E 0° (PSI)	E 90° (PSI)	V ₁₂
56	20.80E+06	18.27E+06	1.133
57	23.98E+06	20.28E+06	1.182
58	21.09E+06	18.27E+06	1.017
59	21.22E+06	18.68E+06	1.103
60	21.43E+06	19.11E+06	1.121
62	20.20E+06	19.07E+06	1.059
64	19.70E+06	18.36E+06	1.073
66	20.51E+06	18.70E+06	1.096
68	19.93E+06	18.58E+06	1.073
Ave	20.98E+06	18.81E+06	1.095

V - Determined using Slope of E0° v E90° Plot

Post Embedded Gage (PEG) Overwrap Cylindrical Test Specimens

Test specimens for validating the embedding of the strain gages and strain gage wires were fabricated as shown in Figure 3.1-69. The test specimens consisted of a 1.2 inch diameter graphite/epoxy tube. The tubes shown in Figure 3.1-69a were fabricated using matched metal mold net shape fabrication methods similar to the fabrication process for the actual long bone segments. Eight (8) foil strain gage rosettes (type EA-06-125RA-120) were bonded to each 10" tube using MBOND 200 adhesive (post cured at 90°F for 1 hour). Mylar tape (1/2" wide) was applied to the inner tube directly adjacent to the gages, underneath the leads, to reduce the chance of electrically shorting the leads to graphite composite. The four (4) gages were located 90° apart at two (2) locations along the length. Two 16-pin connectors were mounted directly to the tube and the wires were routed and bonded to the tube. The gages were locally protected by neoprene synthetic rubber (0.1" thick, 1" wide) to prevent damage due to local shock during handling or operation. The gages and wires were over-wrapped with foam tape. The foam tape provides shock absorption and shock dissipation during impact. Two plies of graphite/epoxy prepreg were laid over the foam and cured at room temperature. The result was a 1.4 inch diameter over-wrapped tube in which the gages and wires are completely protected and the connectors approximately 50% embedded.

Only one problem was identified during the over-wrap process--during layup the liquid epoxy resin leaked into the connector conductors. Subsequent drilling of the connector re-established the electrical path. This problem was addressed during fabrication of the full scale femur and tibia parts by "masking" off the attached connectors.

Table 3.1-5 was the test matrix for the tube compression and torque tests. The primary conclusion from the tube compression and torque tests is that the tube PEG foil strain gages provided useful data under compressive and torsion loading for this geometry and could be used for ABC Man.

The test setup for the compression and torsion tests are shown in Figures 3.1-70 and 3.1-71 respectively. The torque test fixture design is shown in Figure 3.1-72. The loads and measured strains for these tests, plotted versus time, are shown in Figures 3.1-73 through 3.1-90. Figures 3.1-91 and 92 show load versus strain for the compression tests. The slopes of these curves were used to calculate the composite compressive modulus of elasticity. Figures 3.1-93 through 3.1-96 show torque versus shear strain for the torsion tests. The slopes of these curves were used to determine the material modulus of rigidity. The tube's compressive modulus and

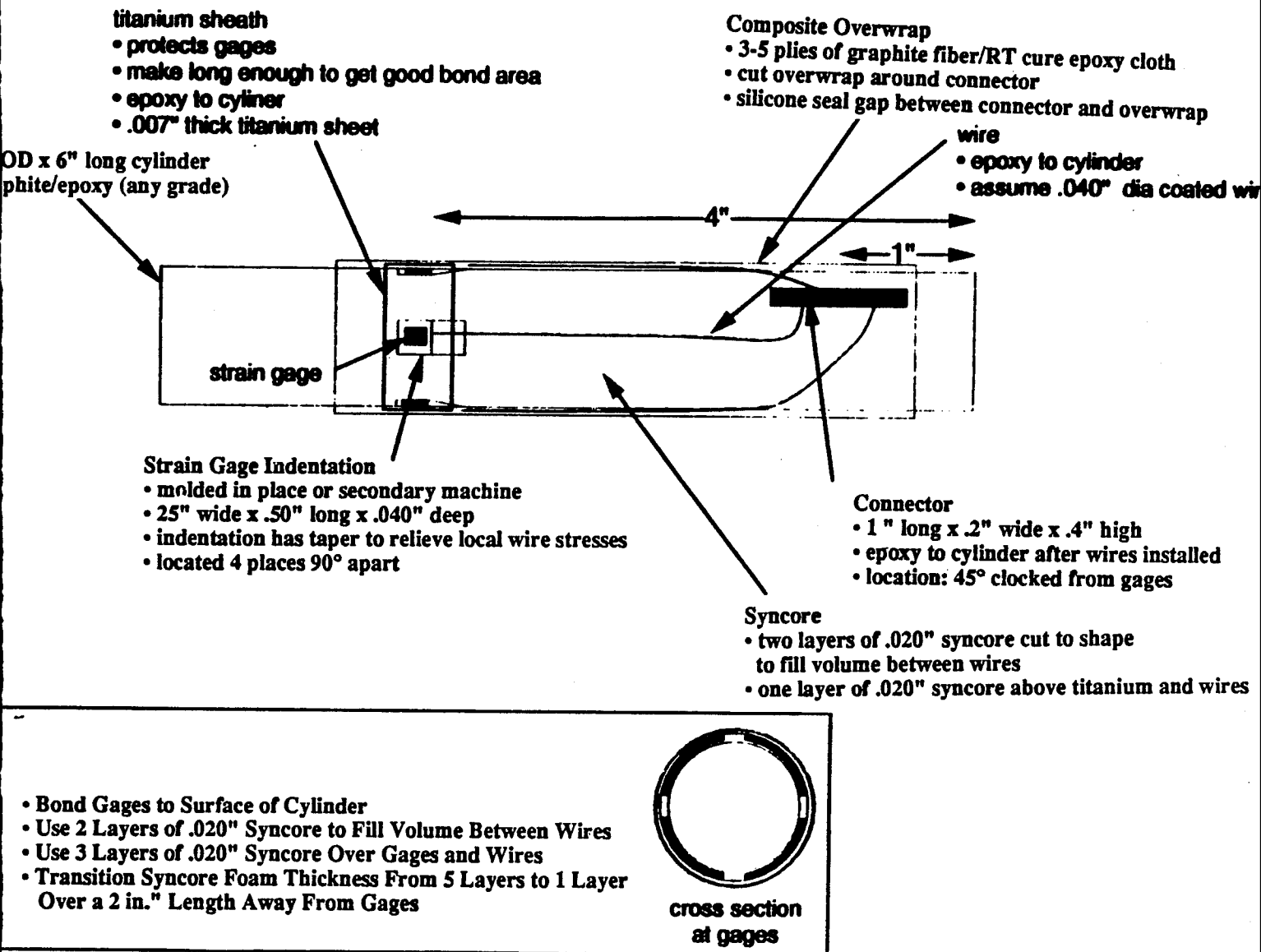


Figure 3.1-69. Test Fabrication Coupon Schematic.

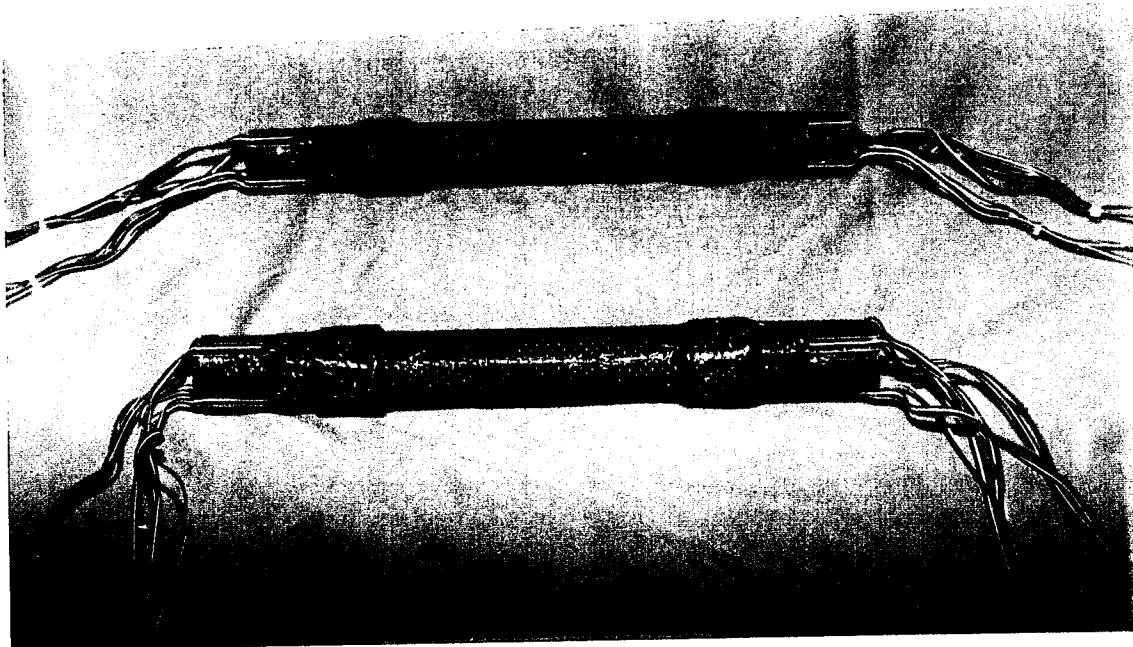


Figure 3.1-69a. Post Embedded Gage (PEG) Tubes Test Specimens.

Table 3.1-5. Tube Test Matrix

Tube #	Specimen #	Length & Diameter (in)	Wall Thickness	Test #	# of Tests	Test Type	Surface Mounted Instrument Description			Composite/ Material Lay-up
							Type	#	Orientation	
1	1a	5.0 in 1.0 OD	0.175	4	1	Compression	Foil - Rosette EA-06-125RA-120	2	0,45,90	IM7/Ep 0° ± 45°
1	1b	5.0 in 1.0 OD	0.175	Bad gauge	1	Compression	Foil - Rosette EA-06-125RA-120	2	0,45,90	IM7/Ep 0° ± 45°
2	2a	5.0 in 1.0 OD	0.175	Bad gauge	1	Compression	Foil - Rosette EA-06-125RA-120	2	0,45,90	IM7/Ep 0° ± 45°
2	2b	5.0 in 1.0 OD	0.175	21	1	Compression	Foil - Rosette EA-06-125RA-120	2	0,45,90	IM7/Ep 0° ± 45°
1	1a	5.0 in 1.0 OD	0.175	7	1	Torque	Foil - Rosette EA-06-125RA-120	2	0,45,90	IM7/Ep 0° ± 45°
1	1b	5.0 in 1.0 OD	0.175	10	1	Torque	Foil - Rosette EA-06-125RA-120	2	0,45,90	IM7/Ep 0° ± 45°
2	2a	5.0 in 1.0 OD	0.175	13	1	Torque	Foil - Rosette EA-06-125RA-120	2	0,45,90	IM7/Ep 0° ± 45°
2	2b	5.0 in 1.0 OD	0.175	16	1	Torque	Foil - Rosette EA-06-125RA-120	2	0,45,90	IM7/Ep 0° ± 45°

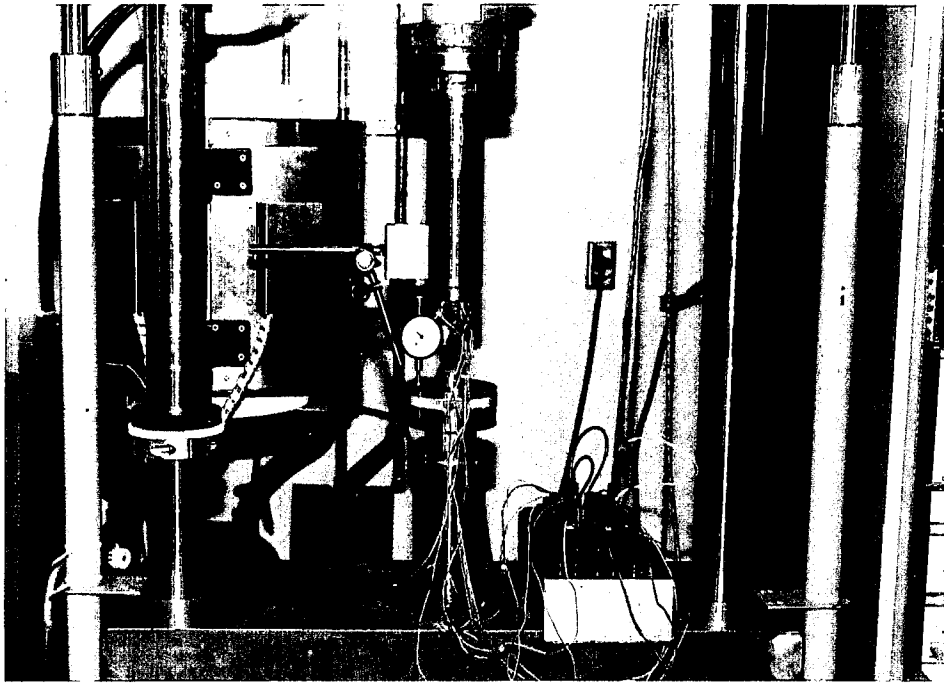


Figure 3.1-70. Tube Specimen in Compression Test Fixture.

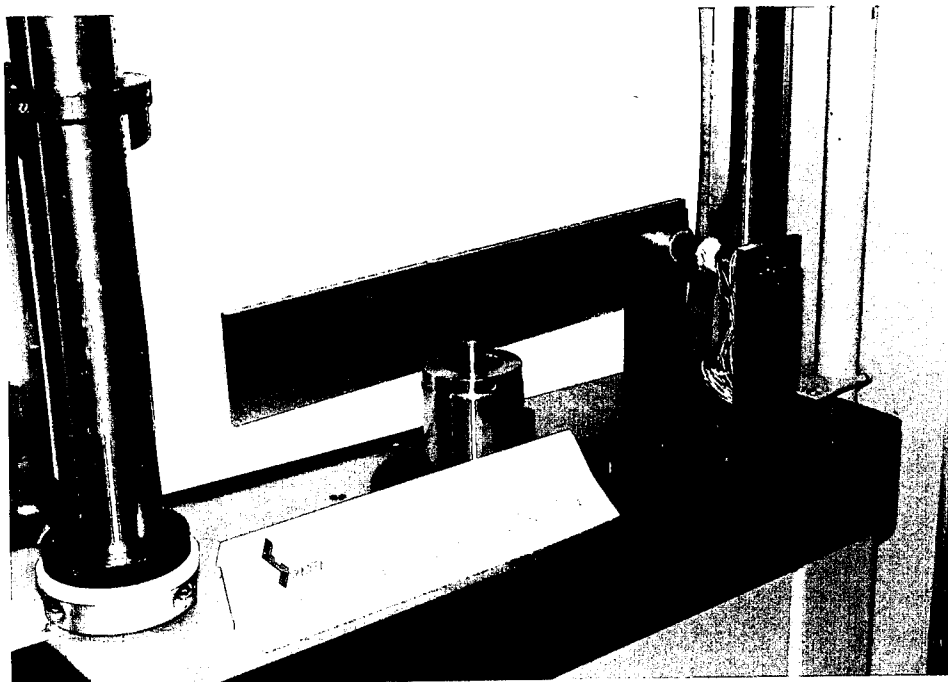
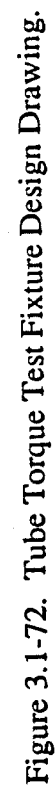


Figure 3.1-71. Tube Specimen in Torque Test Fixture.



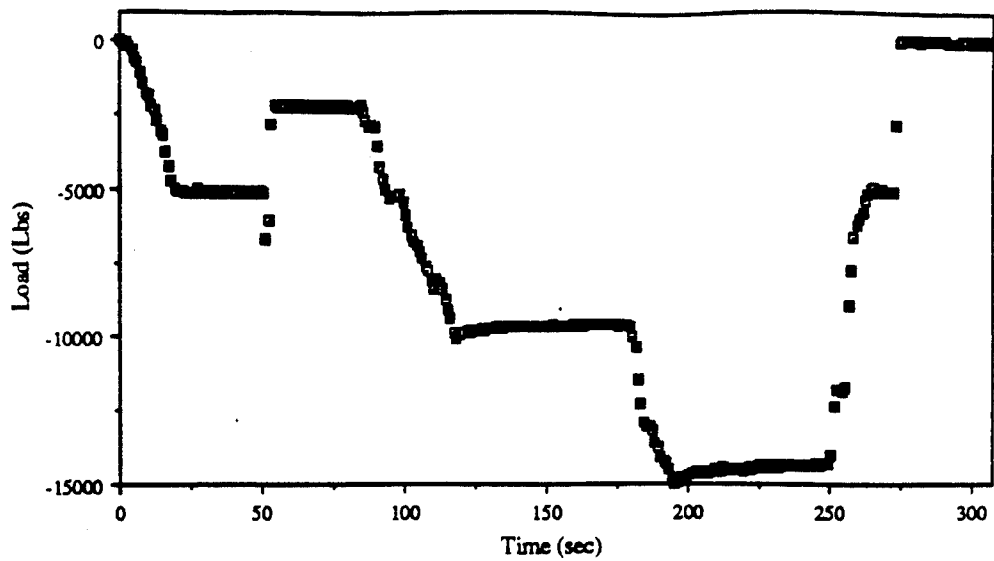


Figure 3.1-73. Test #4 Load vs. Time.

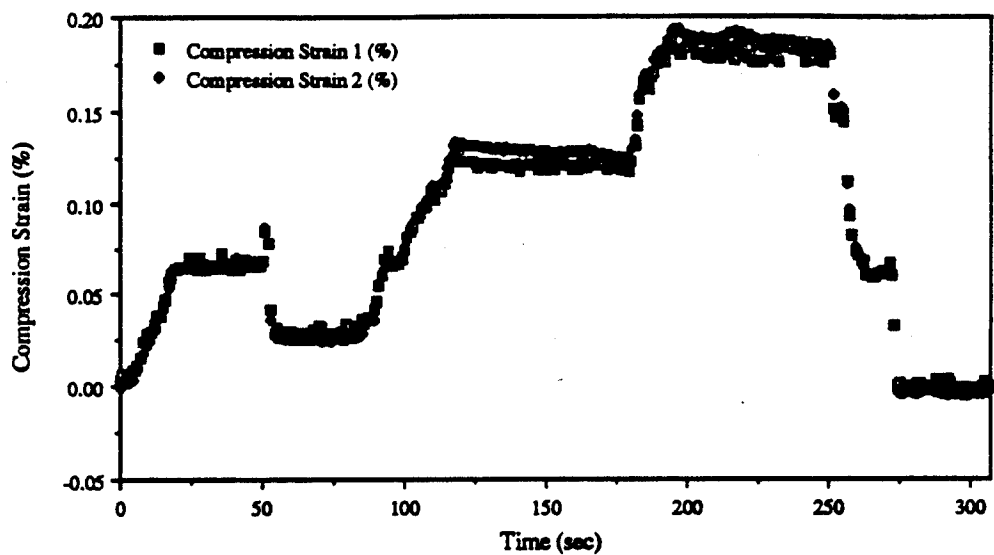


Figure 3.1-74. Test #4 Compressive Strain vs. Time.

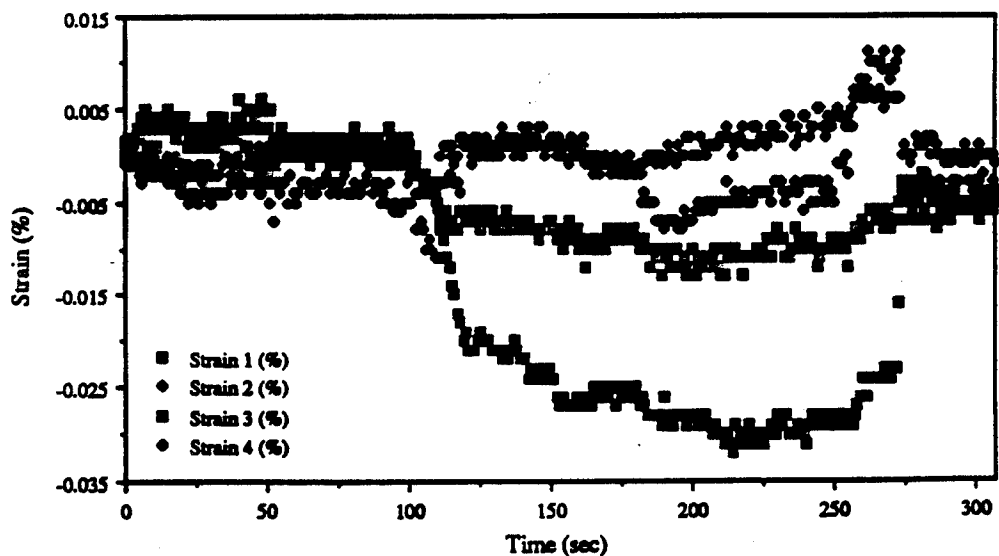


Figure 3.1-75. Test #4 Gauge Strain vs. Time.

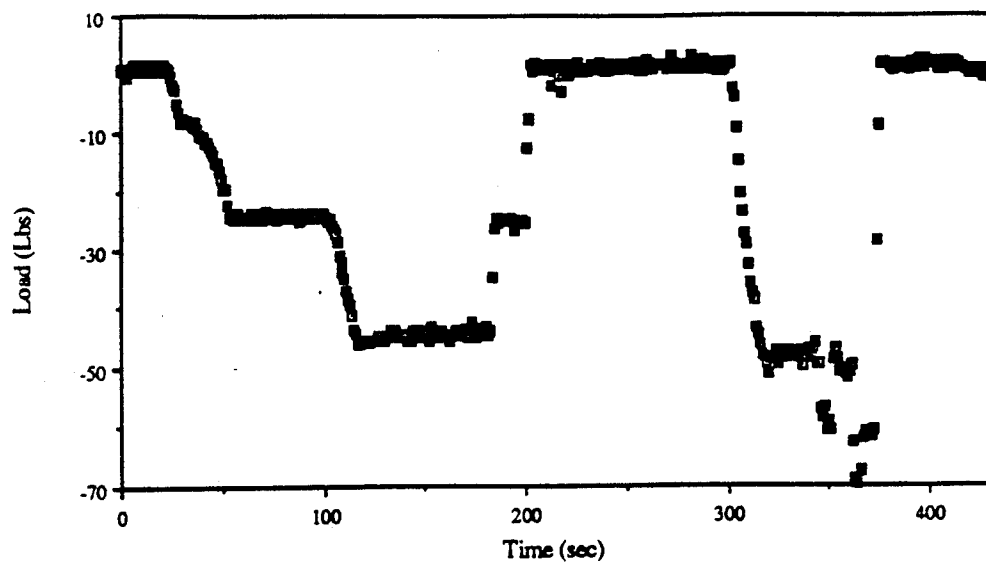


Figure 3.1-76. Test #7 Load vs. Time.

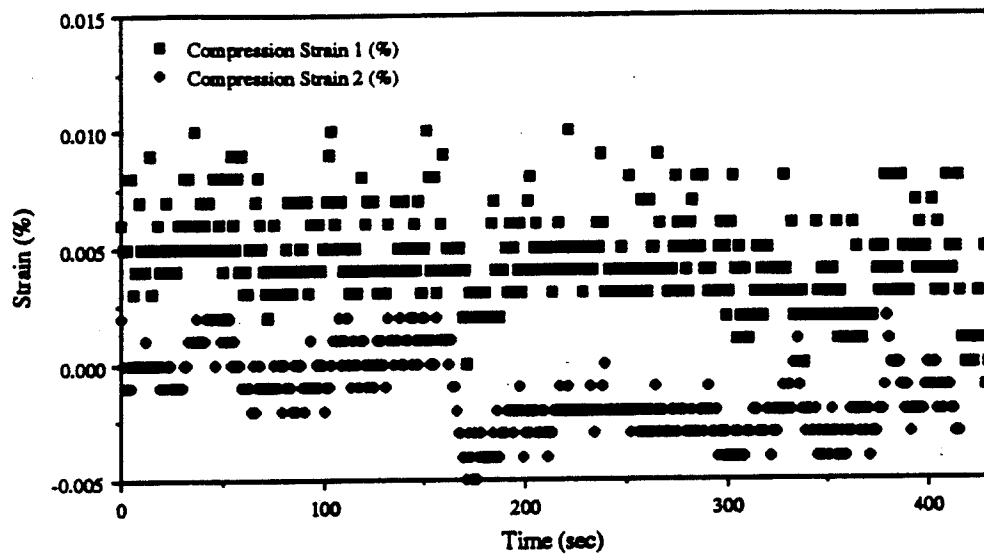


Figure 3.1-77. Test #7 Compressive Strain vs. Time.

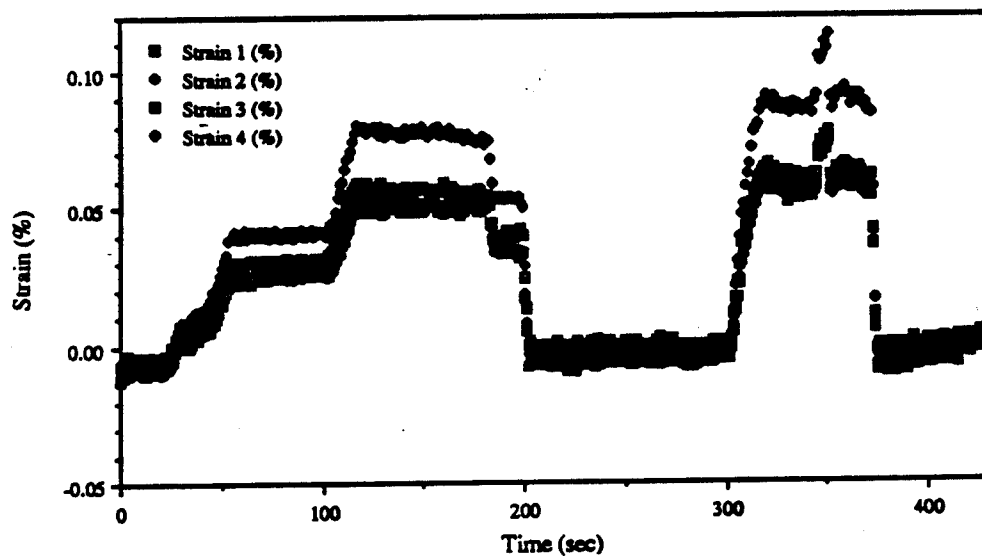


Figure 3.1-78. Test #7 Gauge Strain vs. Time.

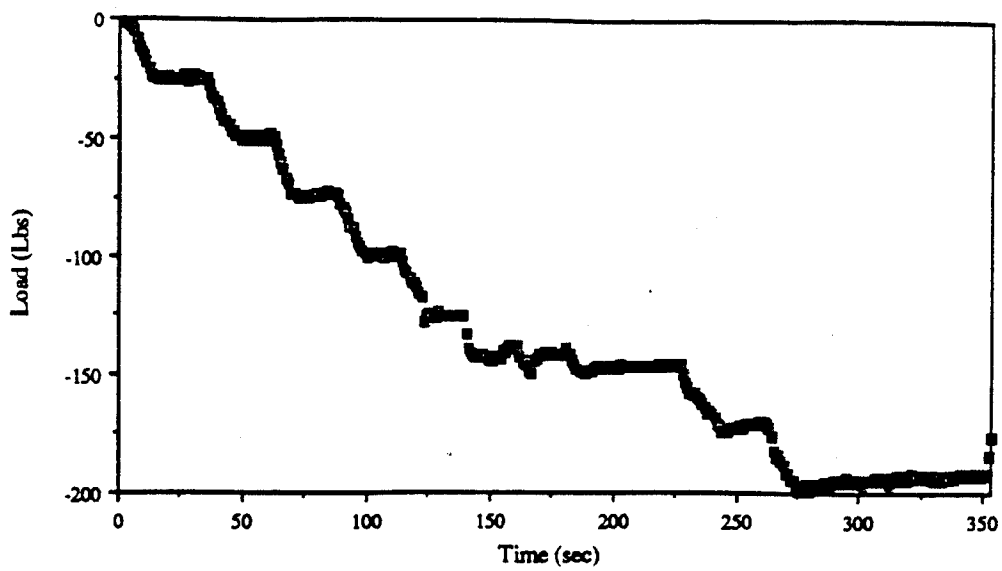


Figure 3.1-79. Test #10 Load vs. Time.

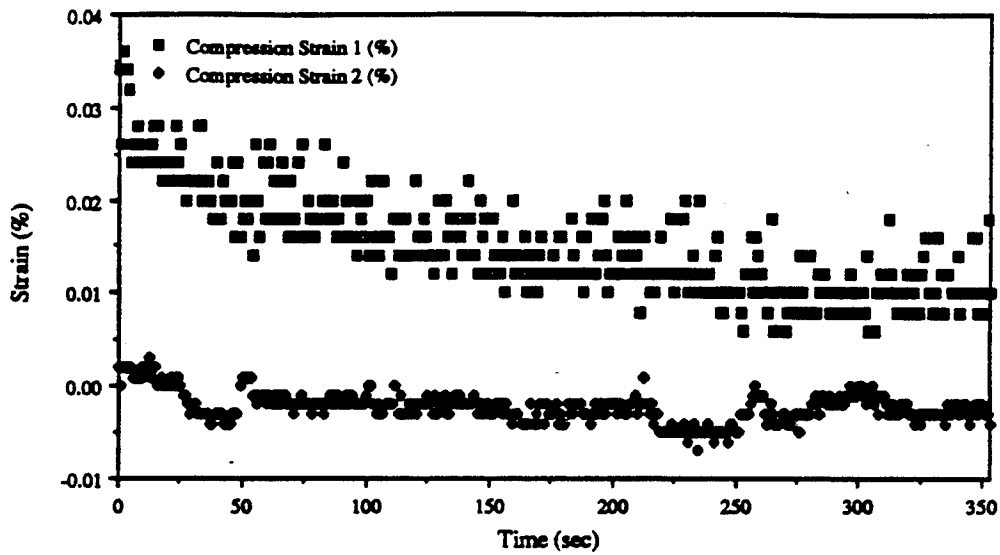


Figure 3.1-80. Test #10 Compressive Strain vs. Time.

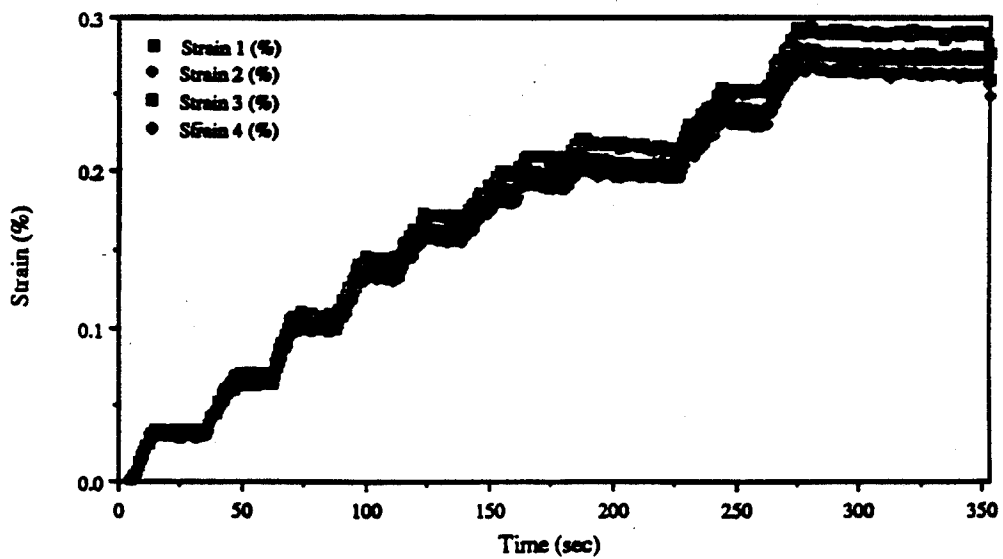


Figure 3.1-81. Test #10 Gauge Strain vs. Time.

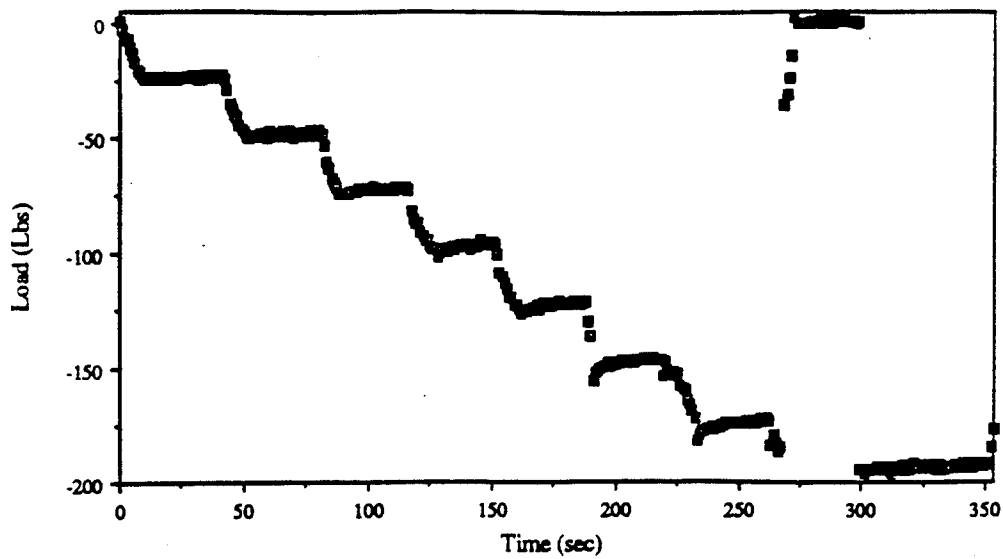


Figure 3.1-82. Test #13 Load vs. Time.

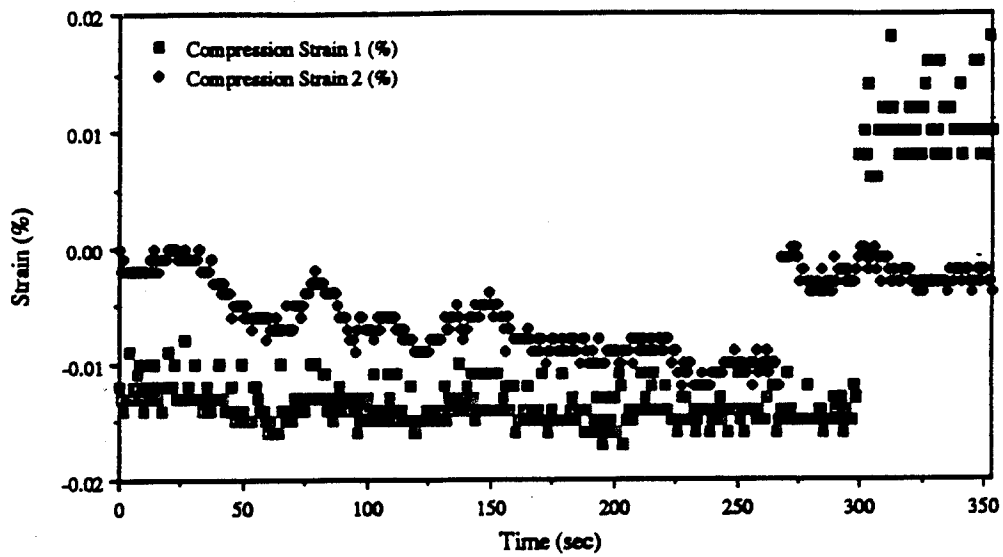


Figure 3.1-83. Test #13 Compressive Strain vs. Time.

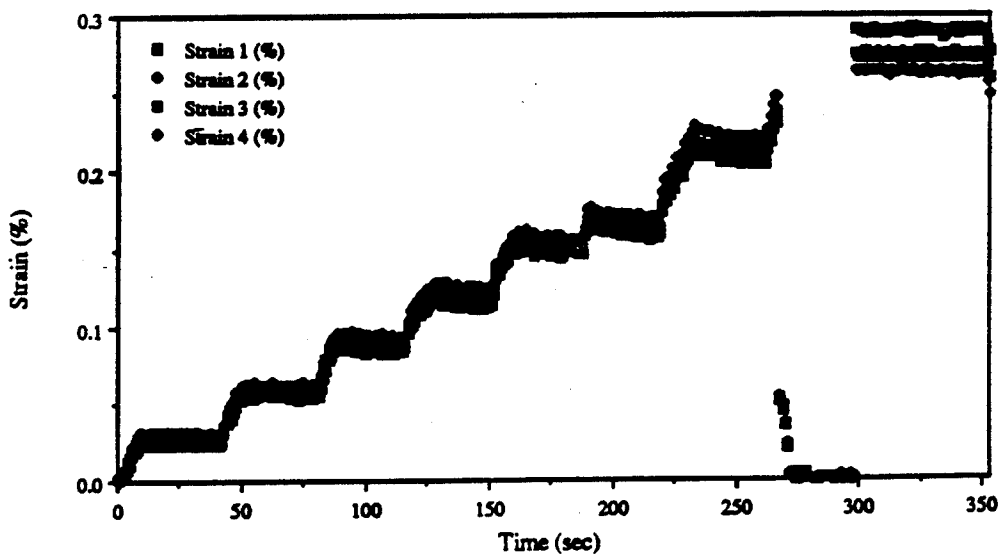


Figure 3.1-84. Test #13 Gauge Strain vs. Time.

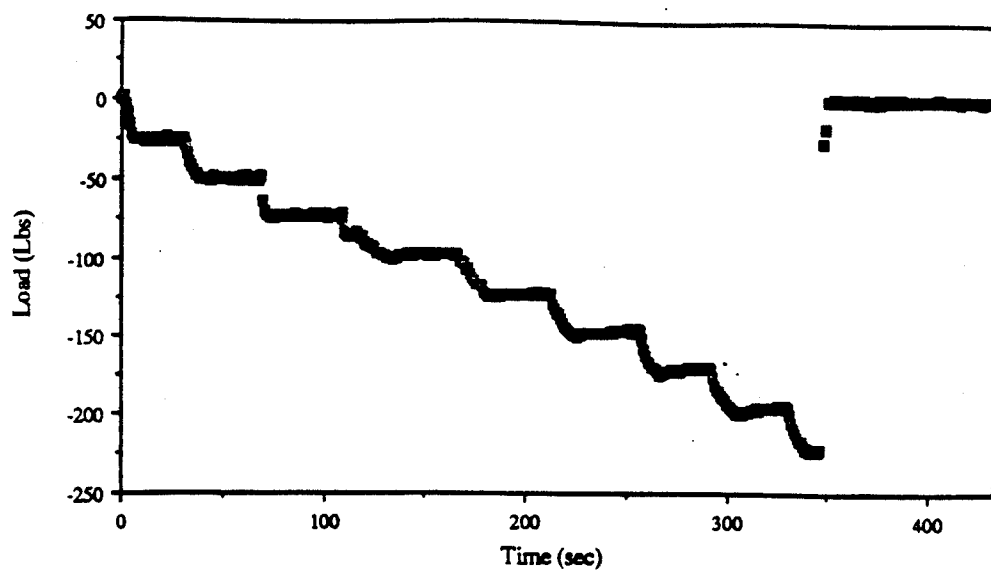


Figure 3.1-85. Test #16 Load vs. Time.

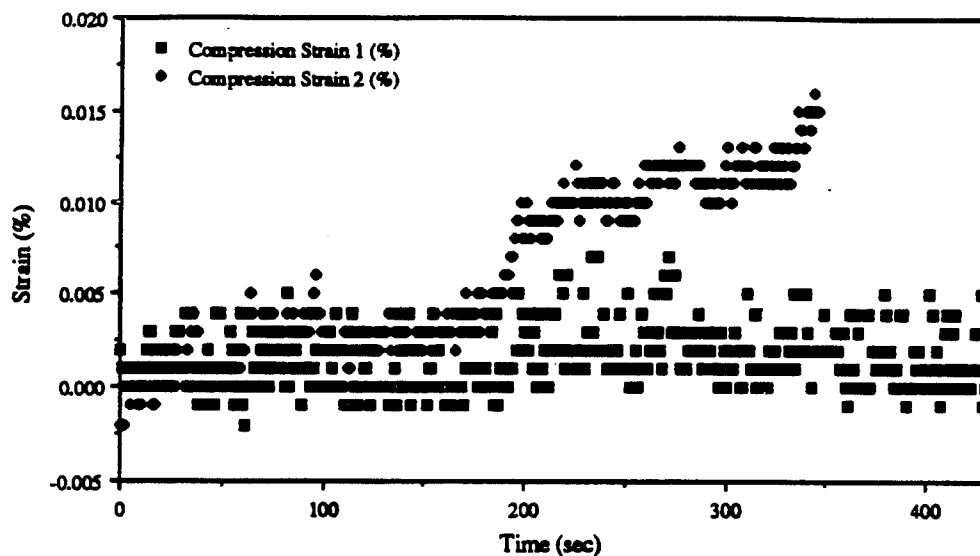


Figure 3.1-86. Test #16 Compressive Strain vs. Time.

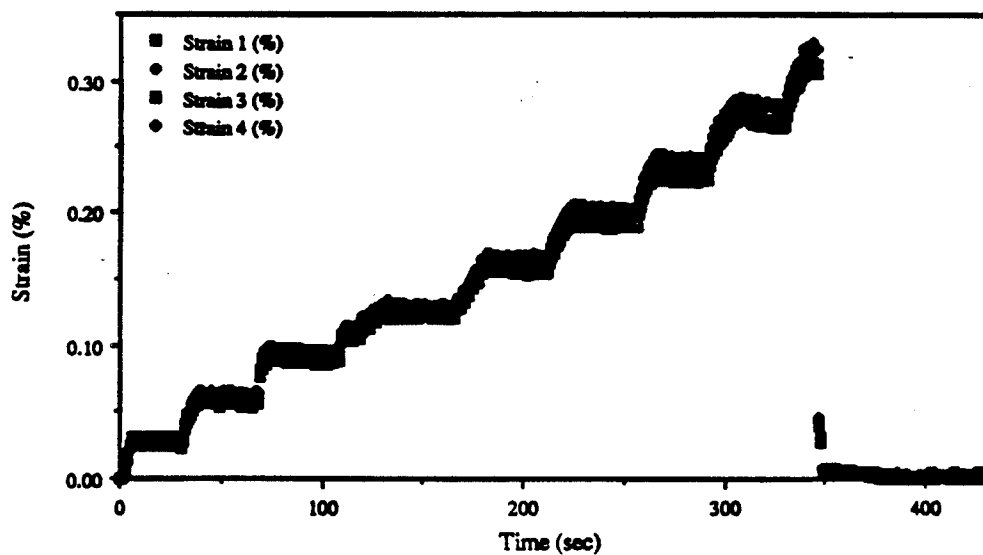


Figure 3.1-87. Test #16 Gauge Strain vs. Time.

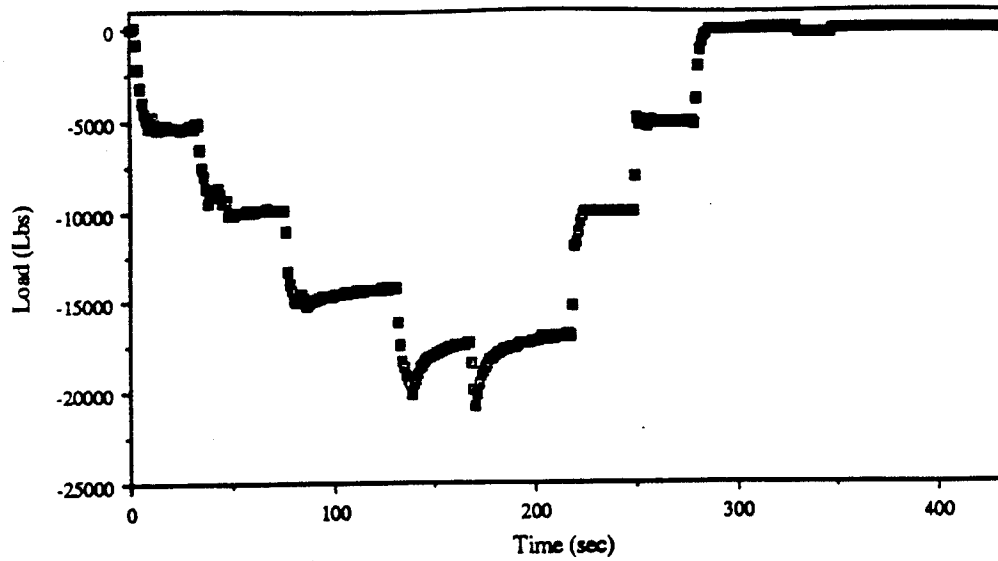


Figure 3.1-88. Test #21 Load vs. Time.

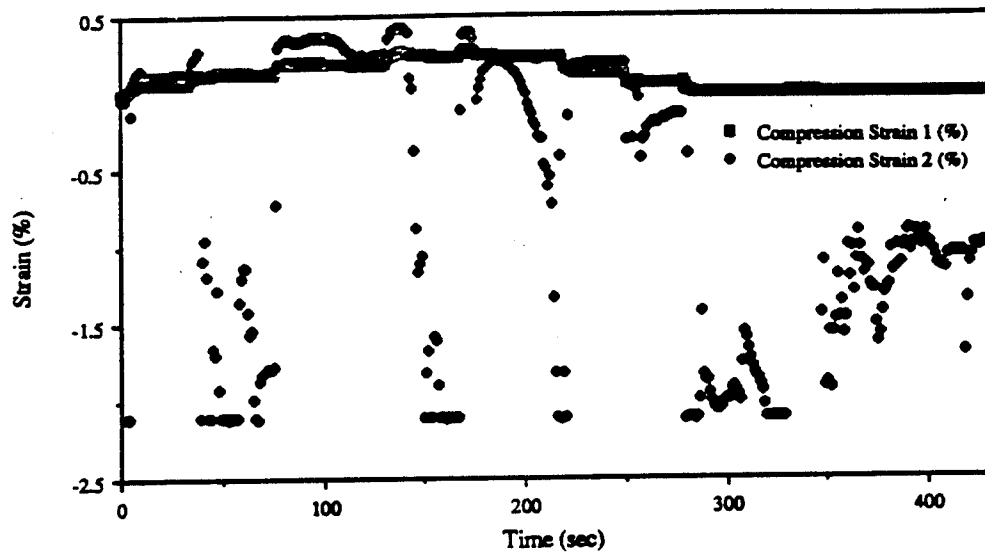


Figure 3.1-89. Test #21 Compressive Strain vs. Time.

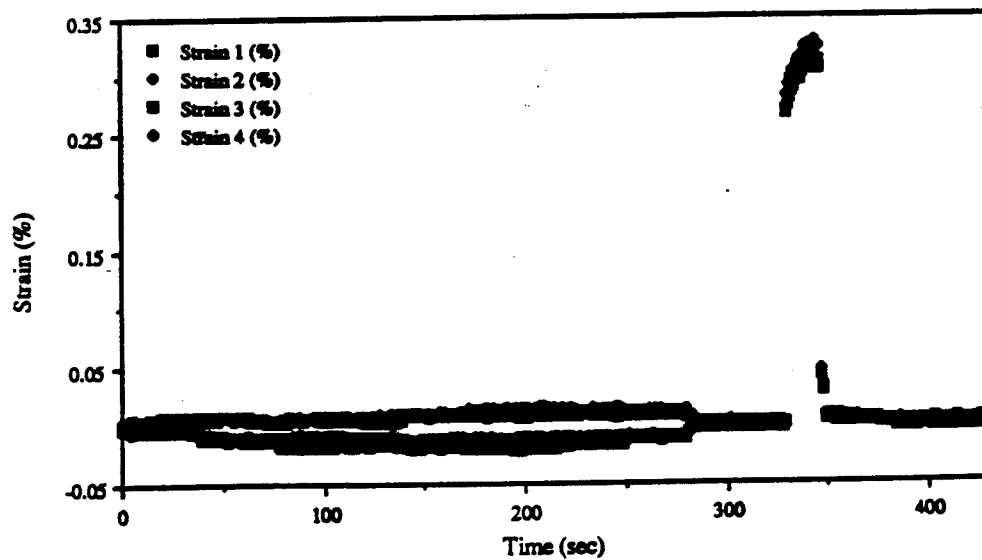


Figure 3.1-90. Test #21 Gauge Strain vs. Time.

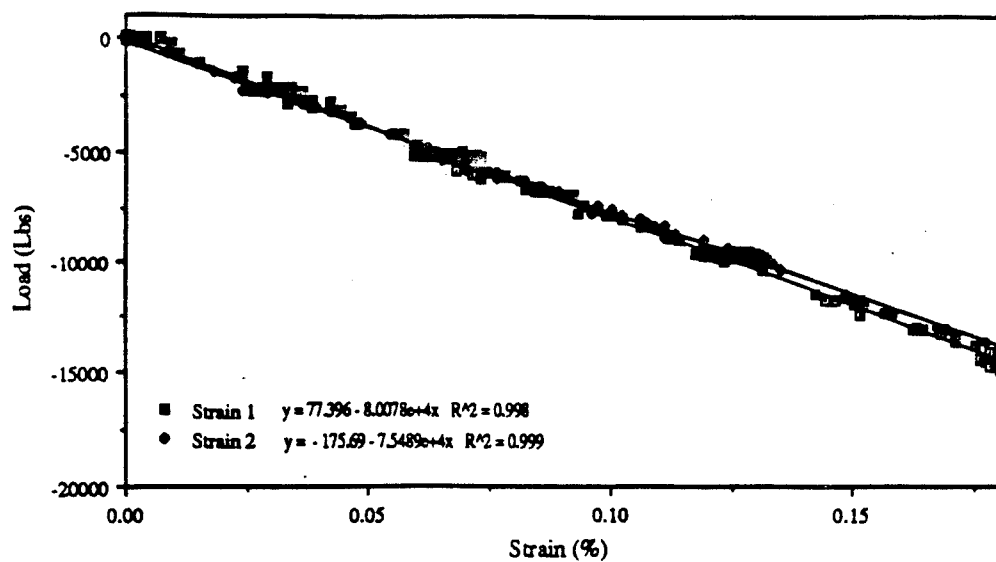


Figure 3.1-91. Test #4 Load vs. Strain.

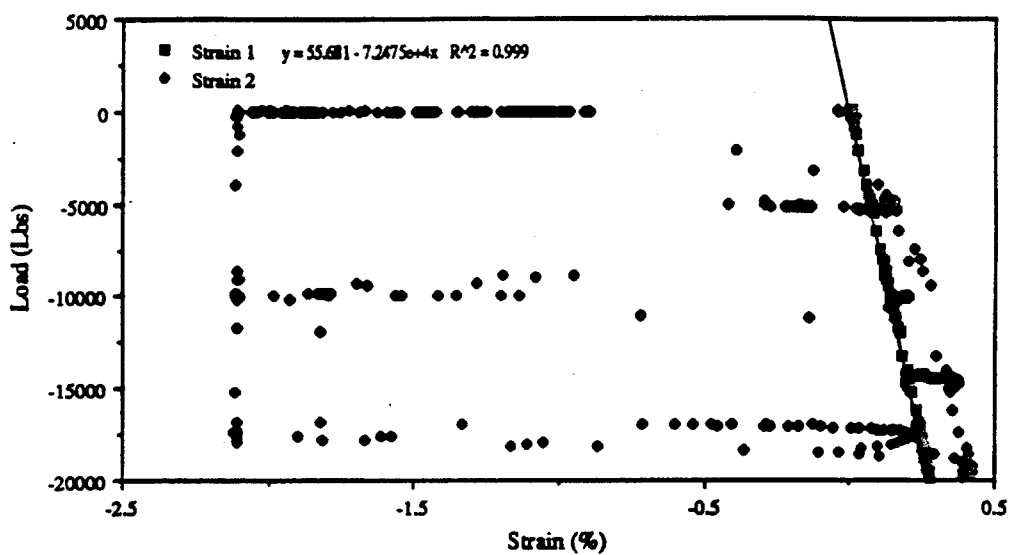


Figure 3.1-92. Test #21 Load vs. Strain.

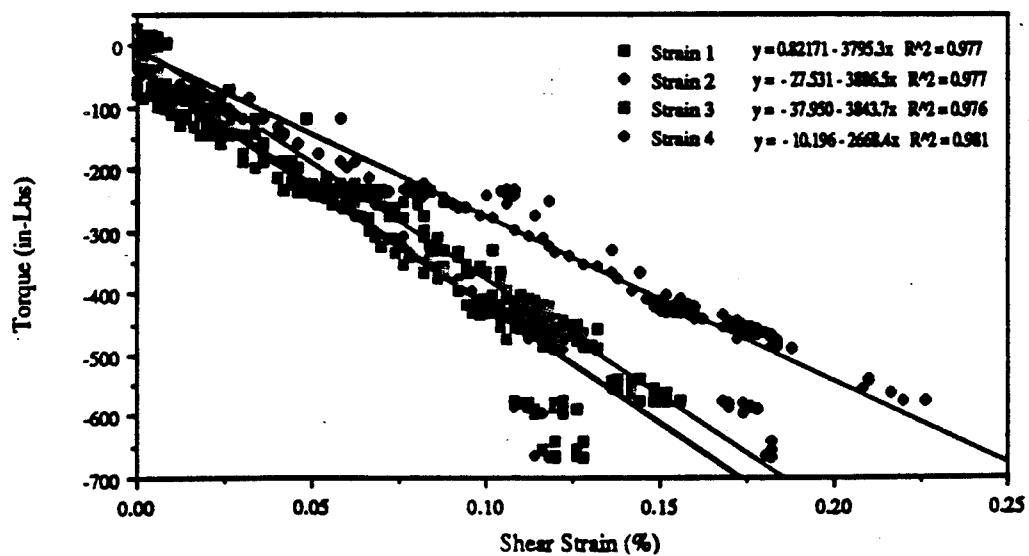


Figure 3.1-93. Test #7 Torque vs. Shear Strain.

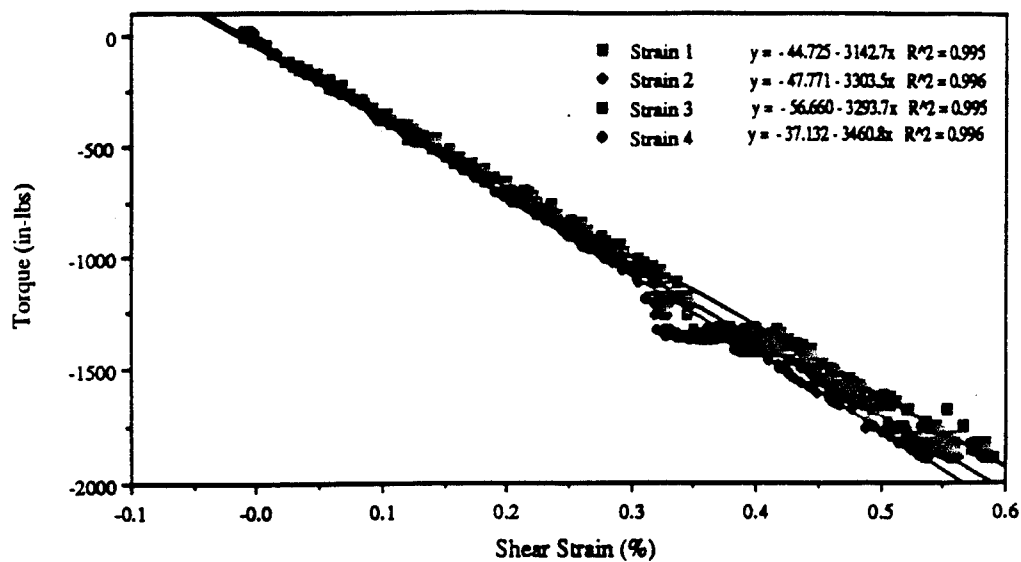


Figure 3.1-94. Test #10 Torque vs. Shear Strain.

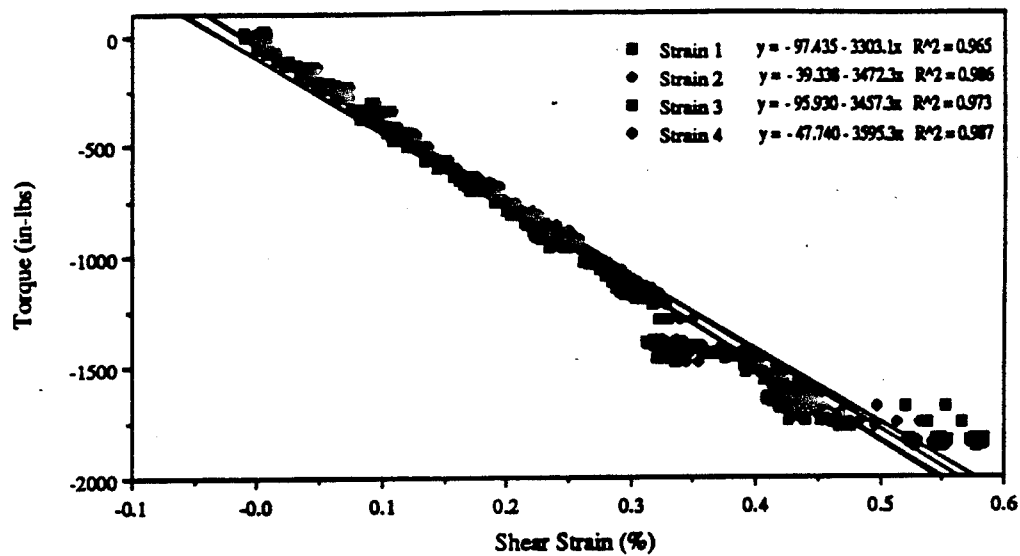


Figure 3.1-95. Test #13 Torque vs. Shear Strain.

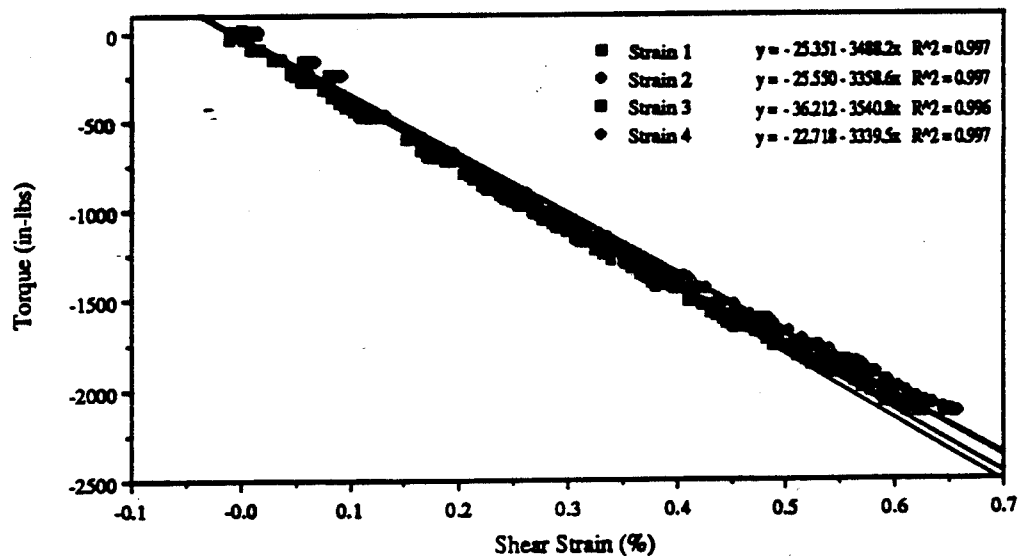


Figure 3.1-96. Test #16 Torque vs. Shear Strain.

modulus of rigidity are summarized in Table 3.1-6. Once again, the measured modulus confirmed the performance of the gages. Figures 3.1-75 and 3.1-90 show torsion gage strain during compression testing. The data from these gages clearly show cross-talk noise. Figures 3.1-77, 80, 83 and 3.1-86 show compression strain during torsion testing. As previously stated, the data from these gages also contain cross-talk noise, as the plots clearly show. Test #21 included one bad compression PEG foil strain gage. Figure 3.1-92, strain 2 shows the unusable data. In all these cases, the data are presented for completeness only.

Table 3.1-6. Tube and Panel Measured Versus Predicted Modulus

	Predicted	Measured
Panel Modulus of Elasticity (PSI)	18.1E+06	21.0E+06
Tube Compressive Modulus (PSI)	18.1E+06	16.8E+06
Panel Modulus of Rigidity (PSI)	na	na
Tube Modulus of Rigidity (PSI)	2.13E+06	2.27E+06

3.1.1.5 Conclusions

The PEG foil gage data had a reproducible, linear response and produced accurate results. Table 3.1-7 shows the predicted and measured mechanical properties of the panel and tube specimens. As can be seen, there is good correlation of the measured and predicted properties. The predicted properties were calculated using an in-house material property analysis code which is used extensively to predict macro properties of composite laminent structures.

Because of the highly consistent results which compared well to predicted data, the PEG concept was selected for the ABC Man long bone strain instrumentation.

Embedded Accelerometers

The long bone segments had single axis accelerometers embedded at the distal ends (knee and ankle). The basic requirements for the accelerometers were:

- Low profile
- Small Foot Print
- Low Mass
- High Impact Resistance

The accelerometers selected for the ABC Man program were ENDEVCCO model 7264-2000 piezo resistive gages. These accelerometers were calibrated at the factory. They had a sensitivity of 0.24969 mv/g with an excitation voltage of 10 Vdc.

As described in Section 3.5, there are two accelerometers perpendicular to each other to measure medial/lateral and anterior/posterior transverse acceleration of each long bone segment.

Long Bone Instrumentation Summary

Table 3.1-7 summarizes the types and models of instrumentation designed for the femur and tibia. Details of the strain gage and accelerometer installation are described in detail in section 3.5.

Table 3.1-7. Types and Models of Instrumentation for the Long Bones

	Model	Quantity Femur	Quantity Tibia
Axial Strain Gages	Measurements Group EA-06-125RA-120	12	6
Rosette Strain Gages	Measurements Group EA-06-125BB-120	4	2
Accelerometers	Endevco Model 7264-2000	2	2

3.1.2 Flesh Embedded Instrumentation Development

One of the objectives of the ABC Man program was to investigate the feasibility of incorporating "tactile foil" in the flesh to measure position and loading histories of blunt trauma impacts. The sensors used for the measurement of impacts applied to the anterior surfaces of the

dummy leg are based on a piezoelectric polymer film called "Kynar®", manufactured by AMP Sensors, Inc. (formerly Elf Atochem). These sensors generate a voltage in response to a change in applied stress. The molecules of this material, known generically as polyvinylidene fluoride, possess a large electrostatic dipole moment. When the material is melted and solidified in the presence of a strong electric field, the molecules will align themselves with this field, and the bulk material will acquire a net polarization. The sensor material is produced in 28 mil thick sheets, polarized through the thickness. To construct the sensors from this film, a conductive coating is applied to each side of the film, and an electrical lead is attached to each. The resulting device is the equivalent of a capacitor, except that the dielectric material separating the electrodes is permanently polarized. The electric field created by this polarization attracts excess electrons to the electrode on the positive side of the film, and expels electrons from the electrode on the negative side. When an applied stress produces a compressive strain in the piezoelectric film, the electric field strength in the polymer increases, because the polarized molecules are brought closer together. If the electrodes are not shorted together so that current can flow to balance this increased field strength, then a potential difference will be created between the two faces of the film, resulting in a measurable voltage.

If the resistance of the voltage-measuring device is high enough, very high voltages can be developed in these films, and they will produce a linear voltage-to-strain response over a very wide range. Unfortunately, however, the current leakage through the voltmeter very quickly diminishes the voltage drop, so there is a complex relationship between the input resistance of the voltage measuring device and the rate sensitivity of the sensor. This means that for a typical oscilloscope with an input resistance of 10 M Ω , a higher instantaneous voltage would be produced by quickly slapping the sensor with a fly swatter than by setting a heavy weight on it.

Previous work in using piezo sensors to instrument crash dummies has been reported in a long-term collaborative effort by groups from Collision Safety Engineering of Orem, Utah, Volvo Automotive Safety Center of Gothenburg, Sweden, and the Mechanical Engineering Department at Brigham Young University.²⁵⁻²⁸ In this work, a Hybrid III dummy head was modified so that the facial region contained 25 piezo sensors, located beneath the rubber skin. The dummy head was calibrated to produce voltage outputs that could be converted to newtons of force. This calibration procedure and signal conditioning algorithm, which includes corrections for current leakage, is described in detail in the article by Warner et al.¹ This work also included testing on human cadaver heads to determine the threshold forces which produce bone fracture in different regions of the face. The calibrated dummy head was then capable of

being used to determine whether a particular car crash condition would result in facial bone fracture.

The piezoelectric sensor manufacturer provided detailed physical and electrical data on the product, and also provided extensive design guidelines. Despite this information, it was still necessary to conduct an extensive experimental investigation to resolve enough unknowns to be able to arrive at a workable design for the sensor array layout, and the placement method and location within the dummy structure. The following list describes some of the questions which were answered empirically.

1. Should the sensor be placed directly on the bone, or embedded within the flesh?
2. How should the sensors be bonded in place?
3. How much mechanical coupling would there be between sensors? How closely must they be spaced to achieve 1/2 inch resolution?
4. Can peak voltage alone be used to characterize the output signal, or is a more complex measure such as area under the curve required?
5. Will there be a linear proportionality between peak voltage and impact energy, velocity, force, or momentum?

In order to investigate these issues, a pendulum impact jig was built which allowed us to deliver well-quantified impacts to a block of synthetic flesh polymer. This impact generating jig was built according to the specifications of the National Highway Traffic Safety Administration regulation "Anthropomorphic Test Dummies" (Code of Federal Regulations, Volume 49, Chapter V, Part 572, Subpart E "Hybrid III Test Dummies"). The condition used was that specified for a knee impact test. This specification calls for an 11 pound pendulum to be traveling at a velocity of 6.9 ft/sec (2.1m/sec) at the moment of impact. The contact face of the pendulum is to be exactly 3.0 inches (76.2 mm) in diameter with an edge radius of 0.02 inches (0.5mm). The setup is shown in Figure 3.1.2-1. It shows a large block of the elastometer which contains several sensors. Wires can be seen coming out of the block on both the top and bottom edges. A cylindrical pendulum is suspended from the ceiling by steel wires which are configured to constrain the pendulum to linear motion, and to prevent rolling and wobbling. The elastometric block is mounted on a heavy steel backing fixture which in turn, is anchored to a sturdy steel table. An oscilloscope is shown next to the test object.

A table was generated which indicated the pendulum velocity, kinetic energy, and collision impulse that would be produced at a variety of horizontal pull-back distances. The 6.9

ft/sec (2.1 m/sec) velocity was used as the standard condition, but a whole range of impact velocities was used to develop a set of load/response curves. A 32 pound (14.51 Kg) pendulum was also fabricated so that a wider range of test conditions could be investigated.

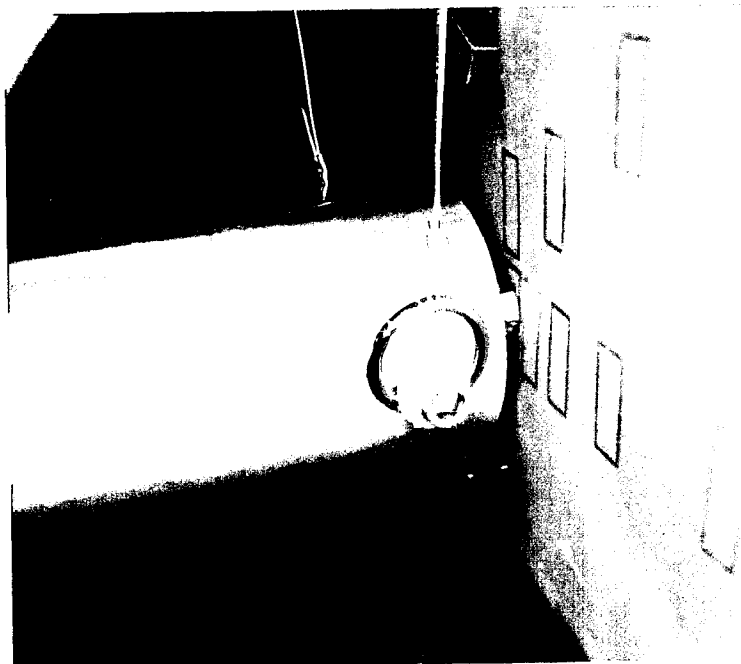


Figure 3.1.2-1. The Pendulum Impact Test Rig used for Testing and Calibrating the Piezo Sensors.

- A. Metal-to-Metal. A brass disc the size of the active portion of the sensor was placed on top of it, and the sensor was mounted directly against the steel backplate.
- B. A 1/4 inch (6.35mm) slab of vinyl elastomer placed over configuration No.1.
- C. The brass disc was removed form configuration No. 2.
- D. A 1 inch (25.4mm) slab of elastomer was substituted for the 1/4 inch (6.35 mm) piece.
- E. A 1 inch (25.4mm) slab of elastomer was placed between the backplate and the sensor, and the sensor was covered with a 1/4 inch (6.35mm) slab of elasatomer.
- F. A 1/4 inch (6.35mm) slab of elastomer was placed behind the sensor, and a 1 inch (25.4mm)slab cover it.

In the first round of experiments, sensor response was studied using the six different sensor placement configurations lists below. The configurations are illustrated in Figure 3.1.2-2.

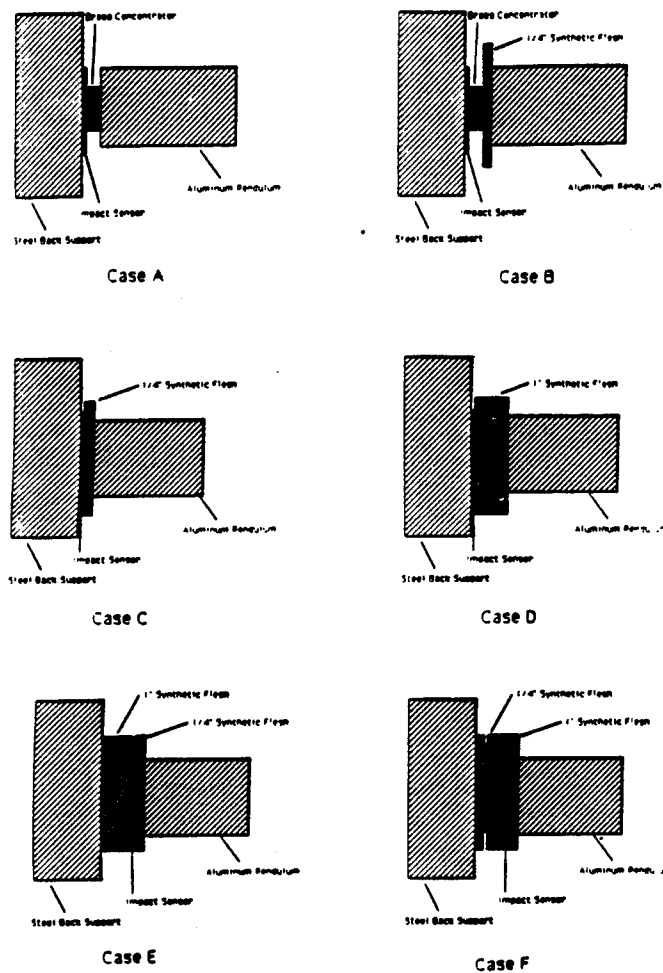


Figure 3.1.2-2. The Six Configurations Employed to Test the Sensor Response.

For each of these test configurations, the pendulum was impacted against the sensor from a range of pull-back distances. A storage oscilloscope acquired the signal and displayed it as a voltage-versus-time plot. One of the main objectives of this set of experiments was to see what type of signal was generated by the sensor, and how it would change from one configuration to another. The first two configurations, in which the sensor was between two pieces of metal, generated signals with a series of large positive and negative spikes, followed by lower frequency components. As more rubber padding was added, first to one and then to both sides of the sensor, these initial spikes were still visible, but became much smaller in relationship to the lower frequency component of the signal, which began to resemble a single cycle of a sine wave. This behavior is illustrated in Figure 3.1.2-3.

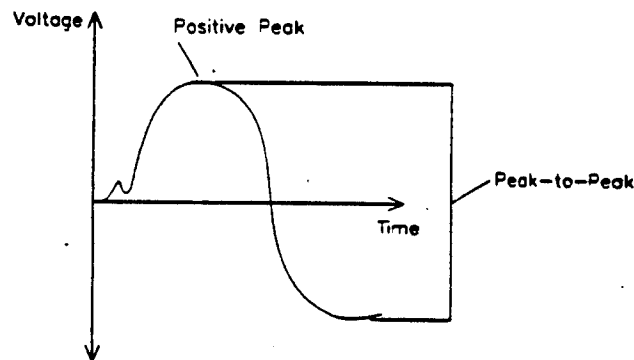
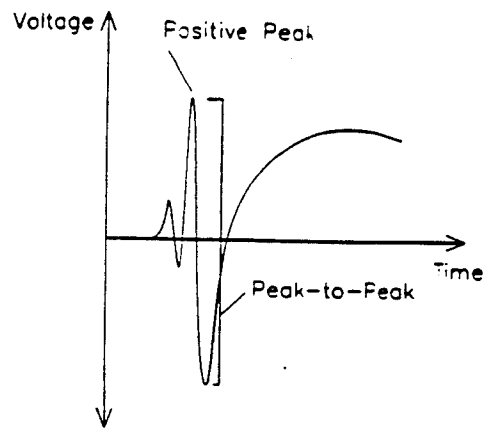


Figure 3.1.2-3. The Behavior of the Piezo Sensor V vs t Output Signal as a Function of Test Configuration.

The data collected from this series of experiments were tabulated and analyzed. The pull-back distance of the pendulum impactor was related to both kinetic energy and impulse (twice the momentum). Both parameters were used as independent variables in the analysis. The sensor response was recorded in terms of both the voltage of the largest single peak, and the peak-to-peak voltage difference between the largest positive and the largest adjacent negative peak. This analysis resulted in four plots of six configurations each, using kinetic energy and impulse as independent variables, and single peak, and peak-to-peak voltage as the dependent variable. These four plots are presented in Figure 3.1.2-4, which follows. Configuration "A" is omitted from the charts because these data were collected over such a low range of impact energies that the points would not be distinguishable given the scale of the graphs.

In the next set of experiments, a range of impact intensities was delivered from two different pendula, one an 11 pound aluminum pendulum, and the other, a 32 pound steel pendulum, both of identical dimensions. The goal of these tests was to determine whether kinetic energy or momentum was more directly related to sensor peak voltage output. The

results of the tests are plotted in Figure 3.1.2-5 a, b & c. These plots illustrate very dramatically that the output signal is not proportional to either kinetic energy or momentum, but instead to pendulum velocity. In the graphs where voltage is plotted as a function of kinetic energy or momentum, the different pendula obtain very different responses in output voltage. This would not occur if the output voltage were truly a function of the input variable. When the same data are replotted using velocity as the input variable, however, all the data falls along a single line.

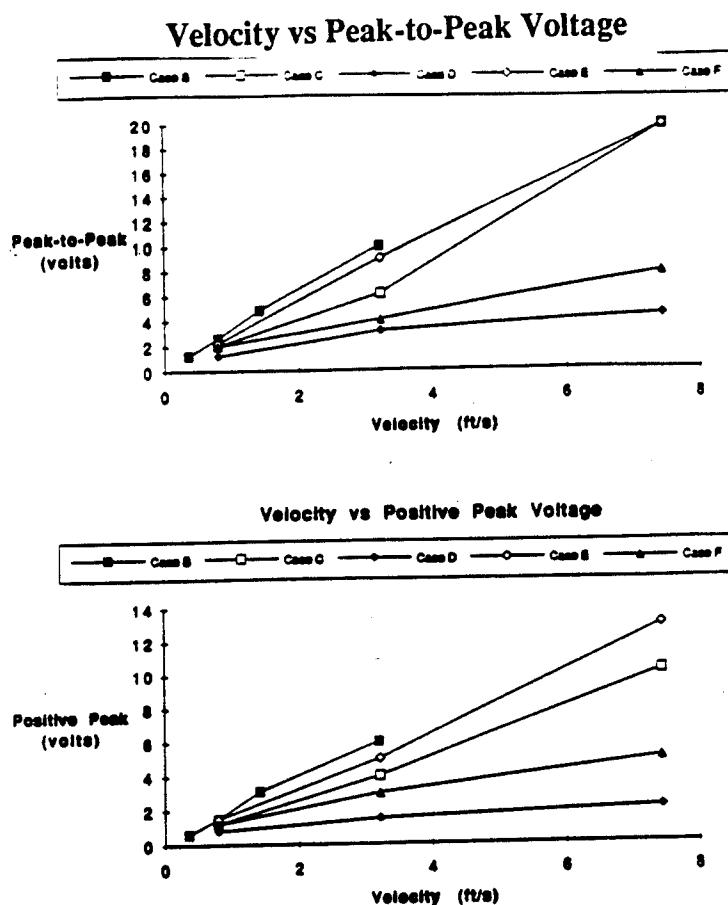


Figure 3.1.2-4. Sensor Voltage Output as a Function of Pendulum Impact Energy and Impulse for Five Sensor Configurations.

This behavior is consistent with some of the information that the sensor manufacturer, AMP Sensors supplied to us. This literature explains that a very high input resistance, on the order of 1 G Ω , is required of the signal measuring instrument in order to get a force-vs-time dependent signal. If the input resistance is too low, the circuit will behave like a high-pass filter, and give the time derivative of a force-vs-time response. This is exactly what has been observed with the velocity-dependent response. This indicates that a resistor of about 1 G Ω must be connected in series with the sensor in order to get an accurate reading from it, otherwise, so much charge leaks through the voltage measuring device that only high frequency components of an impact event can be recorded.

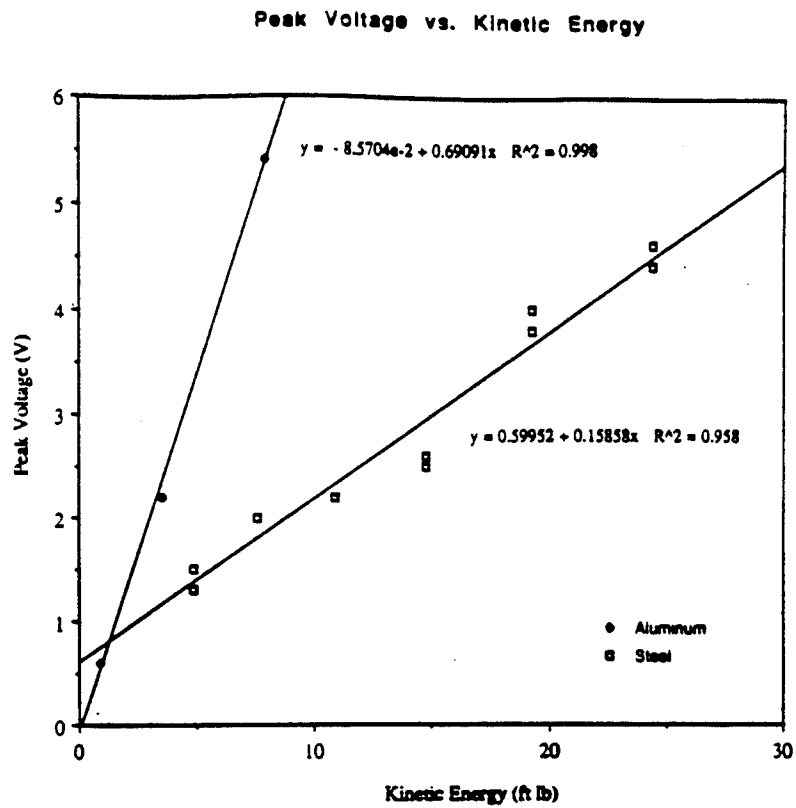


Figure 3.1.2-5a. Sensor Voltage Output as a Function of Kinetic Energy of the Pendulum Impactor for an 11 lb. and a 32 lb. Pendulum.

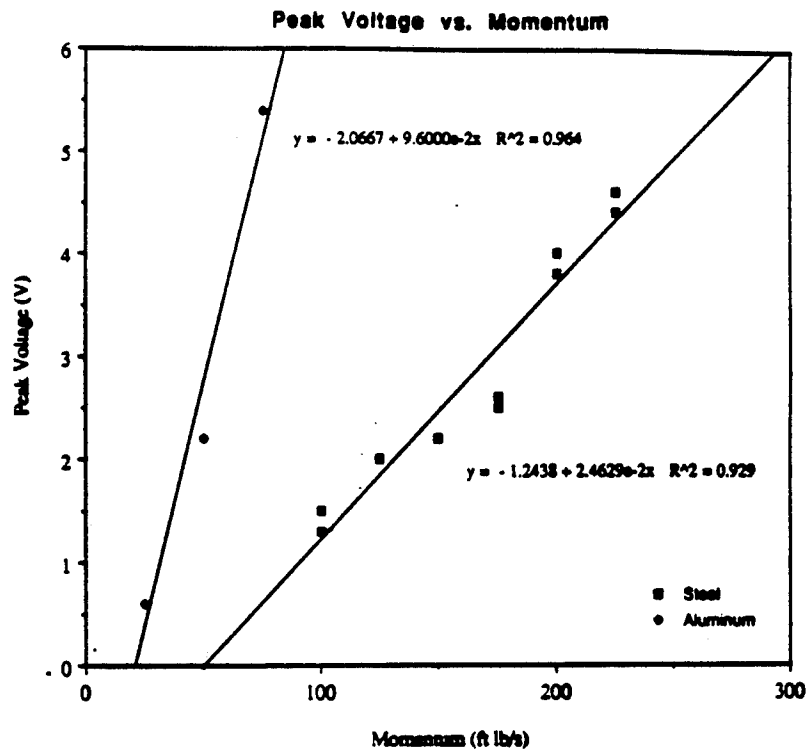


Figure 3.1.2-5b. Sensor Voltage Output as a Function of Momentum of the Pendulum Impactor for an 11 lb. and a 32 lb. Pendulum.

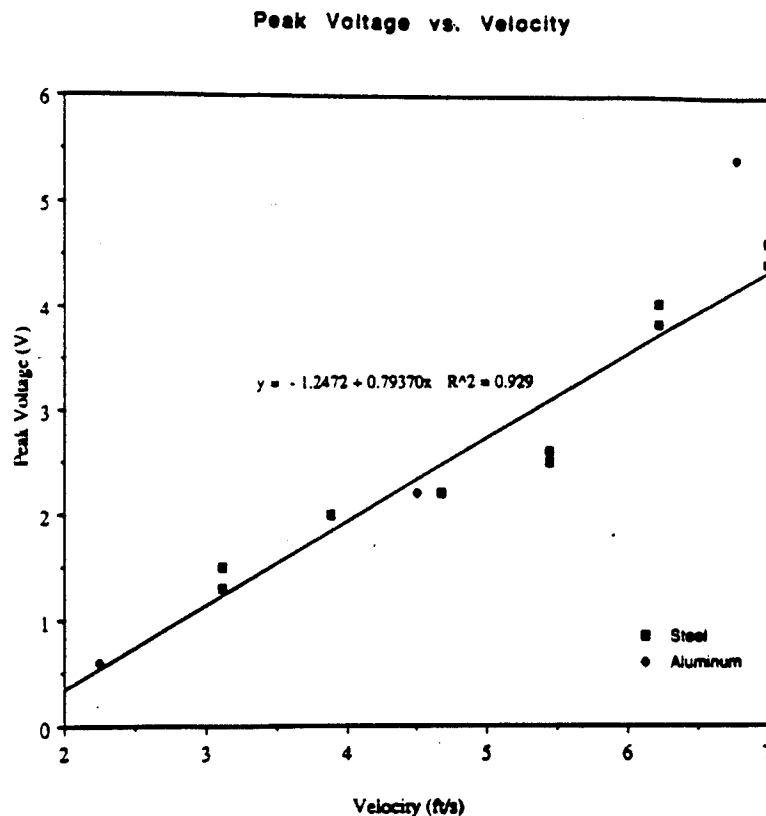


Figure 3.1.2-5c. Sensor Voltage Output as a Function of the Velocity of the Pendulum Impactor for an 11 lb. and a 32 lb. Pendulum.

Another characteristic of the sensor/elastomer system that had to be quantified was the dependence of the output voltage on lateral distance between impact location and sensor location. A major goal of the sensor development was to enable the dummy to differentiate impact locations within one-half inch. In order to determine a suitable inter-sensor spacing and sensor size to satisfy this requirement, it was necessary to measure the attenuation of the sensor output as the impactor-to-sensor distance is increased. The first experiments performed in this regard utilized a strip of six sensors on a single strip of flexible circuit board material. This strip had actually been fabricated from a flexible membrane switch array to which a strip of Kynar had been attached. This sensor array was glued between two slaps of ABC Man flesh and used in all the impact experiments described in preceding paragraphs. If the impactor were aligned to strike the flesh directly over one sensor at one end of this strip, then an output signal could be measured from all the sensors in the array, and thus a plot could be developed showing signal attenuation as increasingly distant sensors are connected to the oscilloscope.

It was found that the sensor location could be up to six inches away from the impact point and still produce approximately the same peak voltage as an equal impact occurring directly over the sensor. This effect was probably influenced by the particular type of sensor array that was used for this testing. It is suspected that the lack of signal attenuation with increasing distance is

a result of a vibrational standing wave which resonated along the sensor strip, owing to the large modulus difference between the stiff plastic sensor strip and the elastomer. The unusual configuration of the particular sensor array, which contained the flexible circuit board backing material, is thought to be the cause of this problem.

A subsequent series of experiments was performed using individual sensor elements (with no backing) bonded between rubber slabs. The layout of these sensors is shown in **Figure 3.1.2-6**. Each sensor is .59 in x 1.57 in. (15 x 40 mm) in size. It is in the form of a single 28 mil thick sheet of polled Kynar with a silver paint applied to each side to form electrodes. Leads are attached to the film with grommets. These sensors were bonded to the synthetic flesh on both surfaces with 3M type 457 film adhesive. A plumbing grade PVC cement was used to bond the slabs of flesh together in areas not covered by the sensors.

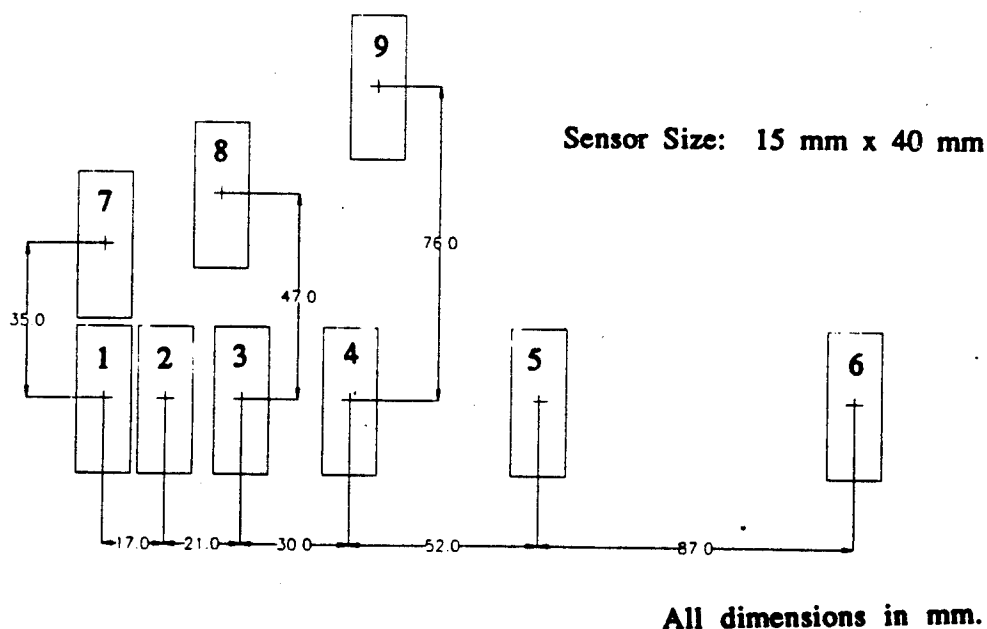


Figure 3.1.2-6. The Placement of Piezo Sensor Within the Block of Synthetic Flesh.

The new sensor test array was assembled using nine individual sensors bonded between two slabs of PVC elastomer. One slab was 1 inch (25.4 mm) thick, and the other was 1/4 inch (6.35 mm) thick. The thinner slab was oriented to face the impact pendulum. A bolt was mounted in the center of the pendulum face to localize the impact to the 1/2 inch (12.5 mm) hex head of the bolt. The face of the rubber slab was marked to indicate the exact locations of the sensors inside. Pendulum impacts were delivered over each sensor location, and the outputs from all the sensors were recorded. All the impacts were generated by pulling back the 11 pound (5 Kg) pendulum 12 inches (304.8 mm).

The sensors were connected one at a time to a storage oscilloscope to display the output signals. The only feature of the output which was recorded was the peak voltage. The shapes, frequencies, and durations of the signals varied widely from one sensor location to another, yet the output from a single sensor for a single impact location was remarkably reproducible. The experiments showed that the signal strength drops off very rapidly with distance away from the impact. A typical peak voltage for an impact delivered a half-inch (12.7mm) away from the sensor would be around 5 volts. This implies that spatial discrimination will be very high for the sensor array mounted in the test dummy, and it should be no problem to achieve the 1/2 inch resolution goal set for the program. The results of these impact experiments are plotted in **Figure 3.1.2-7a** and **3.1.2-7b**. **Figure 3.1.2-7a** shows only those experiments done on the horizontal row of sensors numbered 1 through 6. These results show a standard exponential decay function. The scatter in these data probably results from the "acoustics" within the elastomeric block. The impacts generate subsonic acoustic waves within the elastomer which travel throughout the material, and reflect from the edges. This behavior was evident from the complex waveforms seen from sensors located at larger distances from the site of impact.

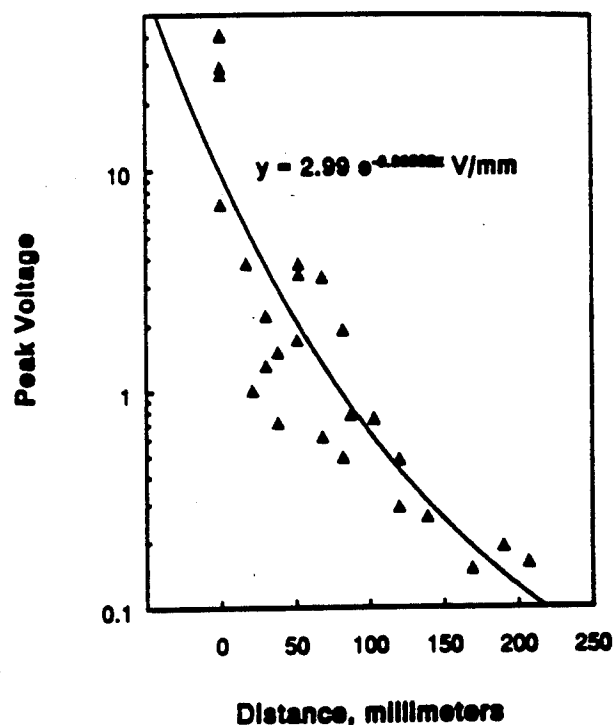


Figure 3.1.2-7a.

The effect of Horizontal Distance Between Impact and Sensor Location on Sensor Output Peak Voltage. The data was Taken from Sensors 1 Through 6 and Impact Locations 1 Through 6 Only. The Impact Resulted from Pulling an 11 Pound Pendulum Back 12 Inches, Which Generates 0.79 ft. lbs. of Energy.

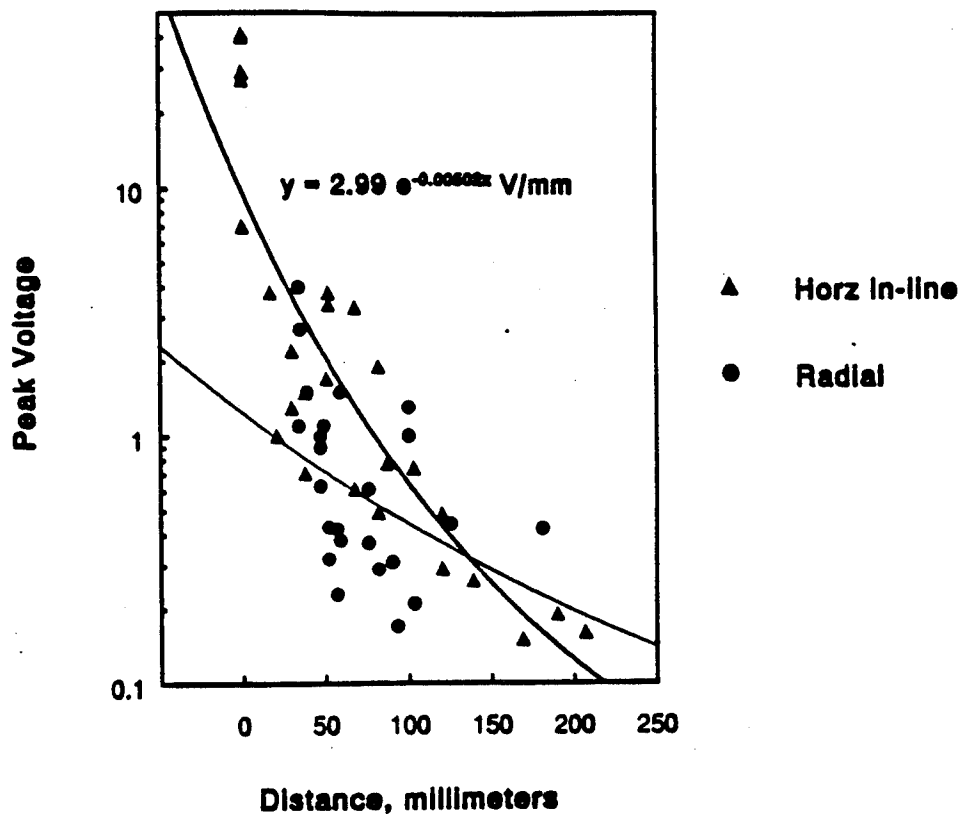


Figure 3.1.2-7b. The Effect of Radial Distance on the Peak Voltage Output of Piezo Sensors Embedded in PVC Elastomer. The Triangles Represent Data Between Horizontal Pairs of Impact and Sensor Locations. The Circles Represent Data from Vertical or Diagonal Pairs.

The data collected from sensors 7 through 9 is somewhat more difficult to interpret. If the peak voltage output is plotted as a function of the radial distance between impact site and sensor location, the nonhorizontal readings show a very large degree of scatter, as shown in Figure 3.1.2-7. This plot seems to indicate that radial distance is not the determining factor in the tests. One complicating factor is that the sensor elements are oblong instead of being square or circular. Since distances were measured from center to center, two sensors that were nearly touching each other in the vertical direction, numbers 1 and 7, still are listed as having a 1.38 in (35mm) separation (center-to-center). Another complicating factor is that the Kynar[®] sensor material has anisotropic piezoelectric coefficients, so it is more sensitive to strains along some axes than along others.

All of this work was conducted with the sensors connected directly to the oscilloscope. As we discussed already, these piezo sensors require an unusually high input resistance to accurately produce static stress and strain readings. Without this high resistance, charge drains out of the sensors before the impact is over, so the signal seen on the oscilloscope is a time derivative of the actual strain vs time event.

This identical series of experiments was then repeated using a 1 GW resistor in series with the sensor. Because this resistor produced a large drop in the voltage of the signal entering the oscilloscope, the steel pendulum was used in place of the aluminum one in order to elicit a larger voltage from the sensor. The addition of the resistor did achieve the desired effect of producing a simpler waveform, however, the data that was recorded from these experiments appeared to be inconsistent. Eventually, it was discovered that several of the sensors had failed during the testing, their voltage output having dropped by an order of magnitude since the beginning of the tests. Some experiments were performed on the remaining functional sensors to determine whether excessively energetic impacts were damaging them. In two instances, sensors were observed to fail after sustaining impacts of 3.6 foot pounds, which corresponds to a 15 inch (381 mm) pull-back distance on the steel (32 pound) (14.5 Kg) pendulum.

The block of synthetic flesh containing the sensors was cut apart to inspect the damage to the sensors. Seven of the nine sensors in the block were found to be torn lengthwise. Individual sensors contained between one and three tears, all perfectly straight and parallel to the edges of the film. All of the tears ran the full length of the sensor. A photograph of one the torn sensors is shown in **Figure 3.1.2-8**. Conversations with the product manufacturers made it clear that this was a common failure mode of the material. The Kynar® film is highly anisotropic in its mechanical properties, with the "2" direction being the weakest. The manufacturers recommended that future sensors be purchased with a mylar film backing for added strength. This recommendation was adopted for the full scale ABC Man flesh sensors.



Figure 3.1.2-8. A View of the Block of Synthetic Flesh After Sectioning and Disbonding to Reveal Three Damaged Sensors.

3.2 STRUCTURAL ANALYSIS

Detailed femur and tibia structural designs were analytically developed to validate the overall long bone segment designs. This effort involved defining the load environment for both long bone segments, conducting preliminary sizing studies, using parametric finite element beam modeling to aid in laminate architecture development, and developing a detailed three-dimensional finite element model.

Loads Development

As part of this effort, SPARTA defined the segment loads for the femur and tibia. Specific loading conditions included maximum axial, lateral, bending, and torsional loads for each component. The baseline femur design load cases from Phase I are shown in Table 3.2-1. These design loads were analytically derived HYBRID III strengths based on steel segments with a factor of safety of 1.5 (i.e., femur design loads = 1.5 x HYBRID III ultimate loads).

Table 3.2-1. Phase I Baseline Femur Design Load Cases

	Load Case	Magnitude
1	Tension	2317 lb
2	Compression	8640 lb
3	Torsion	3488 in. -lb
4	Bending	1623 lb*

* Transverse Cantilever Load (moment arm = 14 inches)

First Technology Safety Systems, Inc. (FTSS) provided the maximum loads envelope for the femur and tibia based on actual test data. The loads data provided by FTSS are maximum values of measured responses from typical automotive industry crash test scenarios. These data are shown in Tables 3.2-2 and 3.2-3. The FTSS data for compression load (7500 lb) and bending load (4500 in-lb) on the femur were replaced as directed by the Air Force with the Phase I magnitudes. Additionally, the Air Force provided a tibia torsion load of 4500 in-lb.

Table 3.2-2. Phase II Baseline Femur Design Load Cases

	Load Case	Magnitude
1	Tension	4500 lb
2	Compression	8640 lb
3	Torsion	4500 in-lb
4	Bending	1623 lb*

* Transverse Cantilever Load (Moment arm = 14 inches)

Table 3.2-3. Phase II Baseline Tibia Design Load Cases

	Load Case	Magnitude
1	Tension	3000 lb
2	Compression	3000 lb
3	Torsion	4500 in-lb
4	Bending	5250 in-lb

3.2.1 Femur Analysis

In the long bone segment design, data from the baseline loads (above) and constitutive material selections were used to develop lightweight, high strength long bone segment designs. This effort focused on parametric analyses of various material layups and geometries. The Phase I femur design was modified to incorporate the design loads as well as more biofidelic joint configurations. The constituent fiber and resin materials selection was based on the Phase I results and the requirements dictated by the structural analysis and tradeoffs between reliability/processing characteristics, weight, cost, availability, and embedded sensors impact.

A long bone segment design spreadsheet was developed for initial sizing of the femur and tibia cross-sections. These analyses used classical beam theory to assess tension/compression, compressive buckling, bending, and torsional loading. The results indicated that the Phase II

femur stem cross-section would be similar to the Phase I design. The parametric spreadsheet analysis was correlated with the Phase I FEM results to insure accurate closed form results. Similar formulae were used for the sizing of the tibia long bone segment which was not assessed in Phase I. The beam sizing for the femur and tibia provided an initial design configuration to be evaluated in more detail using finite element methods. Results from the parametric analysis are shown in Table 3.2.1-1.

Table 3.2.1-1 Preliminary Sizing Geometry for Femur and Tibia

	Femur	Tibia
Length	15.6	14.3
Outer Radius	0.6	0.45
Inner Radius	0.4	0.375

(All values in inches)

Non-Linear Beam Modeling

A non-linear ABAQUS beam model of the femur centerline geometry (Figure 3.2.1-1) developed in Phase I was used for parametric assessment of various material layups and geometries. This study provided data to select the cross-sectional area and moment of inertia of the femur necessary to survive the design loading conditions. The geometry of the femoral stem diaphysis is well represented by this beam model, but the results near the proximal and distal femur ends, the knee portion, as well as the ball joint, are not as well represented, but ensure continuity of the loads and boundary conditions in the diaphysis. These local areas were assessed with solid 3-D finite element models.

In Phase I the maximum laminate stresses in the femur were calculated from the ABAQUS large deformation beam model results. These stresses were compared with calculated laminate strengths for use in designing the composite femur. The laminate strengths were calculated using experimentally and analytically determined unidirectional ply properties. This approach is acceptable for predicting the strength of composites loaded in only one direction, but may not always be conservative for multidirectional loading.

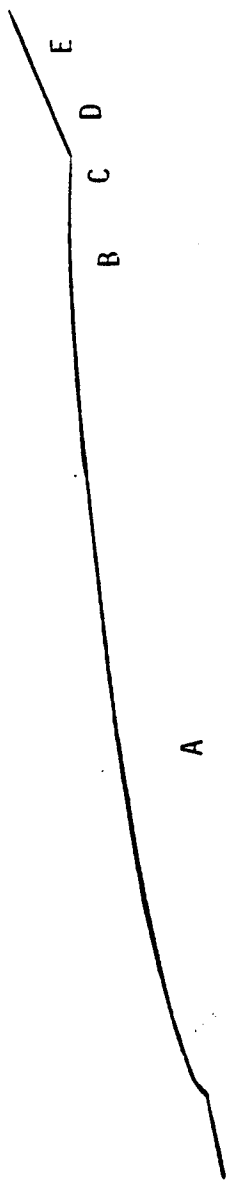


Figure 3.2.1-1. Non-Linear Beam ABAQUS Femur Finite Element Model.

Since the composite long bones are primarily subjected to combined axial and shear stresses, an improved laminate failure criteria was implemented in Phase II to accurately test for the effects of combined loads. The approach takes the laminate strains at a point and transforms them into each of the local ply orientations for comparison with actual lamina (ply) strain allowables. The primary measure of interest using this approach is the lamina strain in the fiber direction for each ply (first ply fiber strain failure criteria).

The Phase II approach used for predicting the strength of the long bone subjected to a given loading condition is outlined below. First, an ABAQUS large deformation finite element beam model is utilized to determine the forces, moments and torques along the beam. These results are read into a post processing computer spreadsheet which is used to calculate the stresses and strains in the beams at each element axial integration point location. A representative curved beam and associated force-displacement relationship used in the analysis are shown in Figure 3.2.1-2. The output from ABAQUS is the axial force, F , transverse shear forces, V_1 and V_2 , bending moments, M_1 and M_2 , and torque about the beam axis, T . From these it is possible to calculate the average stress and strain, σ_0 and ϵ_0 , and bending induced curvature changes, χ_{11} and χ_{22} . These can be used to calculate the axial strain at any location in the cross section defined by coordinates (x_1, x_2) as:

$$\epsilon = \epsilon_0 + \chi_{11} x_2 - \chi_{22} x_1.$$

The torsional strain is obtained from the torque

$$\gamma^T = \frac{-Tr}{GJ}$$

where,

$$r = (x_1^2 + x_2^2)^{1/2}$$

Since the stress and strain at any cross section varies as a function of cross-sectional location (x_1, x_2) it was necessary to pick the maximum locations for comparison with material allowables. This is done as shown in Figure 3.2.1-3. There are four maximum stress locations at each cross section used for strength checks. The first two points are bending stress at extreme locations θ_1^E and θ_2^E , and are found by setting $\frac{\partial \epsilon}{\partial \theta} = 0$. The next two points are maximum transverse shear stress locations, θ_1^V and θ_2^V , which are at $\pm 90^\circ$ from the transverse shear stress resultant, V_{max} . The combined laminate axial and shear stresses/strains are calculated at each of these four points of every beam element axial integration point location.

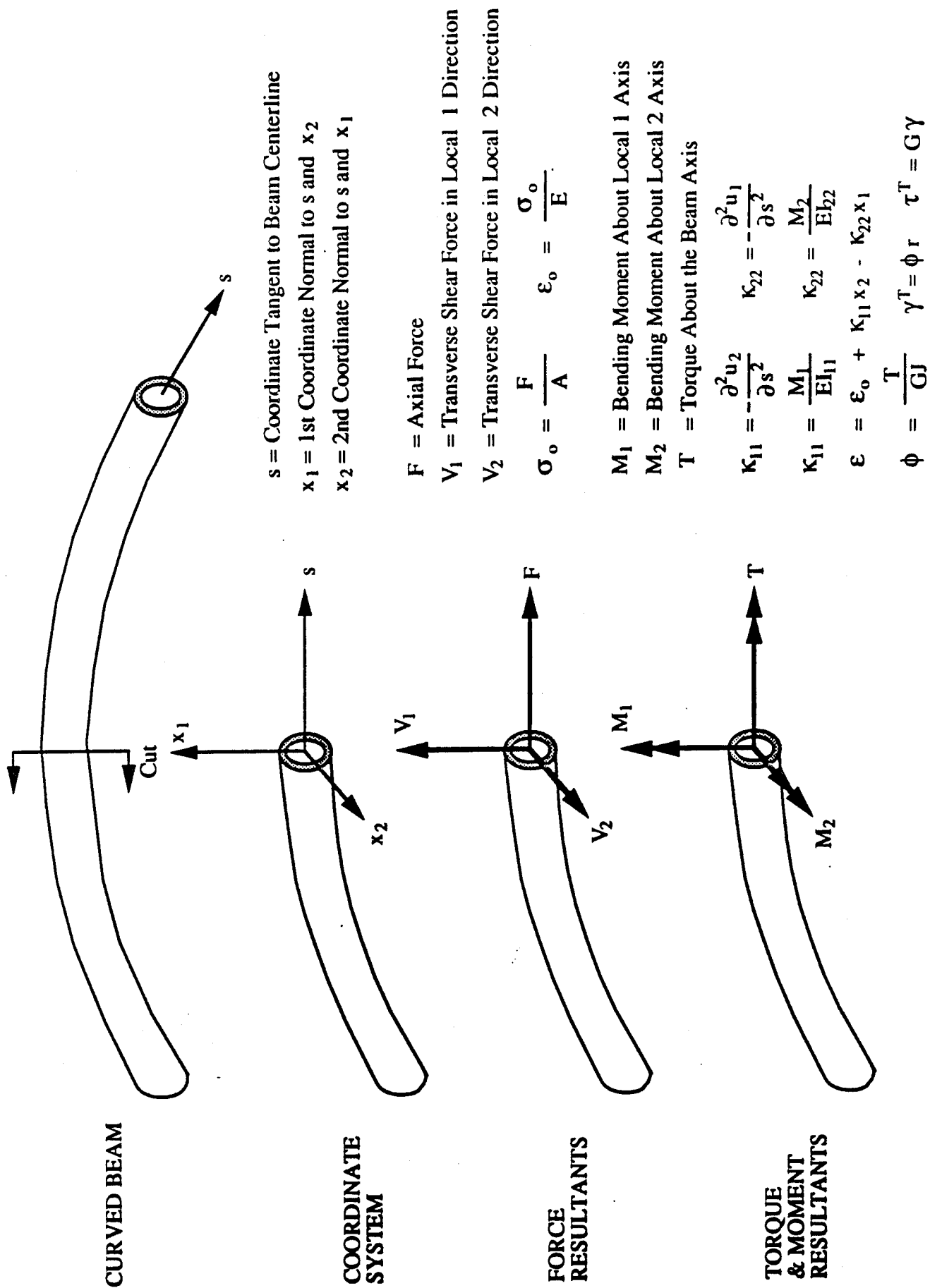


Figure 3.2.1-2. Beam Stress Analysis Force-Displacement Relations and Coordinate System Definition.

$$\begin{aligned}\epsilon &= \epsilon_o + K_{11}x_2 - K_{22}x_1 \\ &= \epsilon_o + r(K_{11} \sin\theta - K_{22} \cos\theta)\end{aligned}$$

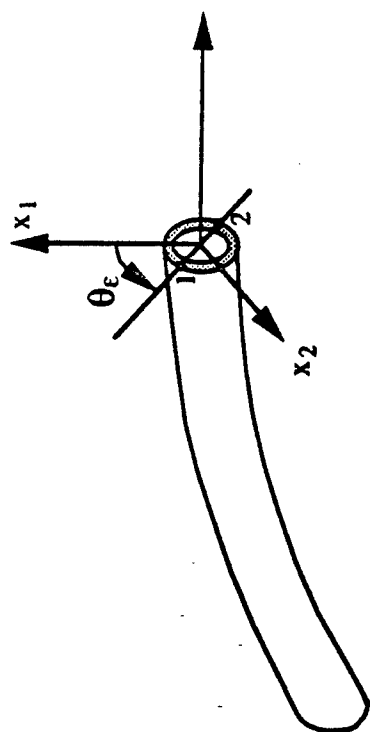
Maximum Bending Strain Location:

$$\frac{\partial \epsilon}{\partial \theta} = 0 \rightarrow \theta^\epsilon = \tan^{-1}\left(\frac{-K_{11}}{K_{22}}\right)$$

$$\theta_1^\epsilon = \theta^\epsilon \quad \theta_2^\epsilon = \theta^\epsilon + \pi$$

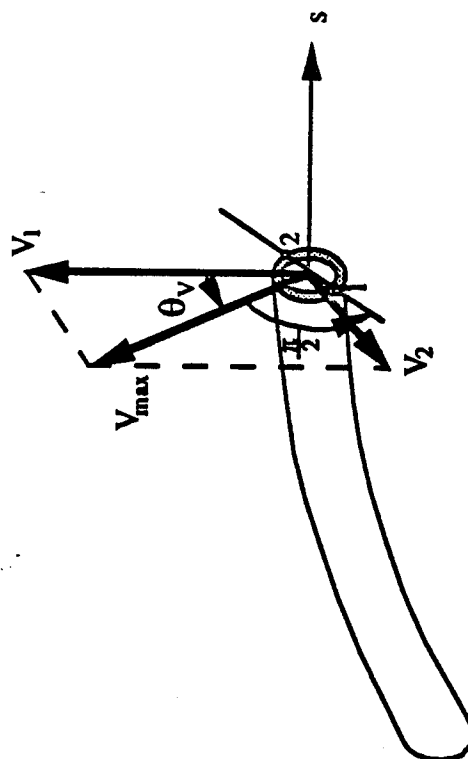
$$\epsilon_1^{\max} = \epsilon_o + r(K_{11} \sin\theta_1^\epsilon - K_{22} \cos\theta_1^\epsilon)$$

$$\epsilon_2^{\max} = \epsilon_o + r(K_{11} \sin\theta_2^\epsilon - K_{22} \cos\theta_2^\epsilon)$$



MAXIMUM
BENDING
STRESS/STRAIN
LOCATION

$$\begin{aligned}V_{\max} &= (V_1 + V_2)^{1/2} & \theta^V &= \tan^{-1}\left(\frac{V_2}{V_1}\right) \\ \theta_1^V &= \theta^V + \frac{\pi}{2} & \theta_2^V &= \theta_1^V + \pi \\ \tau_1^V &= \frac{V_{\max}}{\pi t} & \gamma_1^V &= \frac{\tau_1^V}{G} \\ \tau_2^V &= \frac{-V_{\max}}{\pi t} & \gamma_2^V &= \frac{\tau_2^V}{G} \\ \tau_1^{VT} &= \tau_1^V + \tau^T & \gamma_1^{VT} &= \frac{\tau_1^{VT}}{G} \\ \tau_2^{VT} &= \tau_2^V + \tau^T & \gamma_2^{VT} &= \frac{\tau_2^{VT}}{G}\end{aligned}$$



MAXIMUM
SHEAR
STRESS/STRAIN
LOCATION

Figure 3.2.1-3. Beam Stress Analysis Maximum Bending and Shear Stress/Strain Circumferential Location.

Next, the laminate strains are rotated into the local ply direction as shown in Figure 3.2.1-4. It is assumed that the laminate is composed of 0° , $+\Omega^\circ$ and $-\Omega^\circ$ plies. The algebraic maximum and minimum strains in the fiber direction for each ply orientation at every cross section are calculated based on results at these four locations. These can be compared directly to unidirectional material allowables.

Representative plots for femur compression loading of 7500 lbs (3401 Kg) with an outside radius of 0.6 in. (15.4mm), an inside radius of 0.25 in. (6.35mm), and a (0₃, ± 45 , 0₃)₈ lay-up of T1000-G/Epoxy are shown in Figure 3.2.1-5 through Figure 3.2.1-9. These are based on spreadsheet manipulations of the results from a large deformation beam finite element model of the femur. Force and moment results from ABAQUS are shown in Figure 3.2.1-5. Laminate stresses at the peak bending locations (Ax stress 1 and Ax stress 2), torque induced shear stress, transverse shear stress, and combined torque and transverse shear stress are plotted in Figure 3.2.1-6. Ply fiber direction strains in the 0° , and $\pm\Omega^\circ$ plies at the two extreme bending stress cross-sectional locations are shown in Figure 3.2.1-7. Note that $\Omega = 45^\circ$ in this case. Ply fiber direction strains in the 0° , and $\pm\Omega^\circ$ plies at the two maximum transverse shear stress cross-sectioned locations are shown in Figure 3.2.1-8. Finally, the algebraic maximum and minimum ply fiber direction strains in the 0° , and $\pm\Omega^\circ$ plies are shown in Figure 3.2.1-9. These strains can be compared to the unidirectional allowable tensile and compressive strains for T1000 G/Epoxy of $\epsilon_{1tu} = 0.018$ and $\epsilon_{1cu} = 0.011$. For this case, the fiber direction strains are below the allowables for all plies except at the last element at the ball joint. The results in this region, however, are questionable due to the coarseness of the mesh. The mesh was subsequently refined to better resolve the stresses near the ball joint. Additionally, beam theory assumptions start to break-down near the ends and a detailed three dimensional finite element model as discussed later was used in this region to better resolve the complex stress state.

Various geometries and material layups were assessed for the compression, bending, and torsional load conditions. The tensional load case was not evaluated with the 2-D beam model, because the compressive load case represents a worst case condition in both absolute loading and material strength. However, the tensile load case was evaluated after development of a 3-D finite element model.

An initial sizing of the femur cross section, based upon classical beam theory, gave an outer radius of 0.6 inches (15.24mm) and an inner radius of 0.4 inches (10.16mm). This cross-section was parametrically assessed with the 2-D beam model. The femoral stem has a significant bend at the proximal end as it transitions into the titanium ball joint. The beam model, which had been developed in Phase I, was refined at the proximal end in order to more

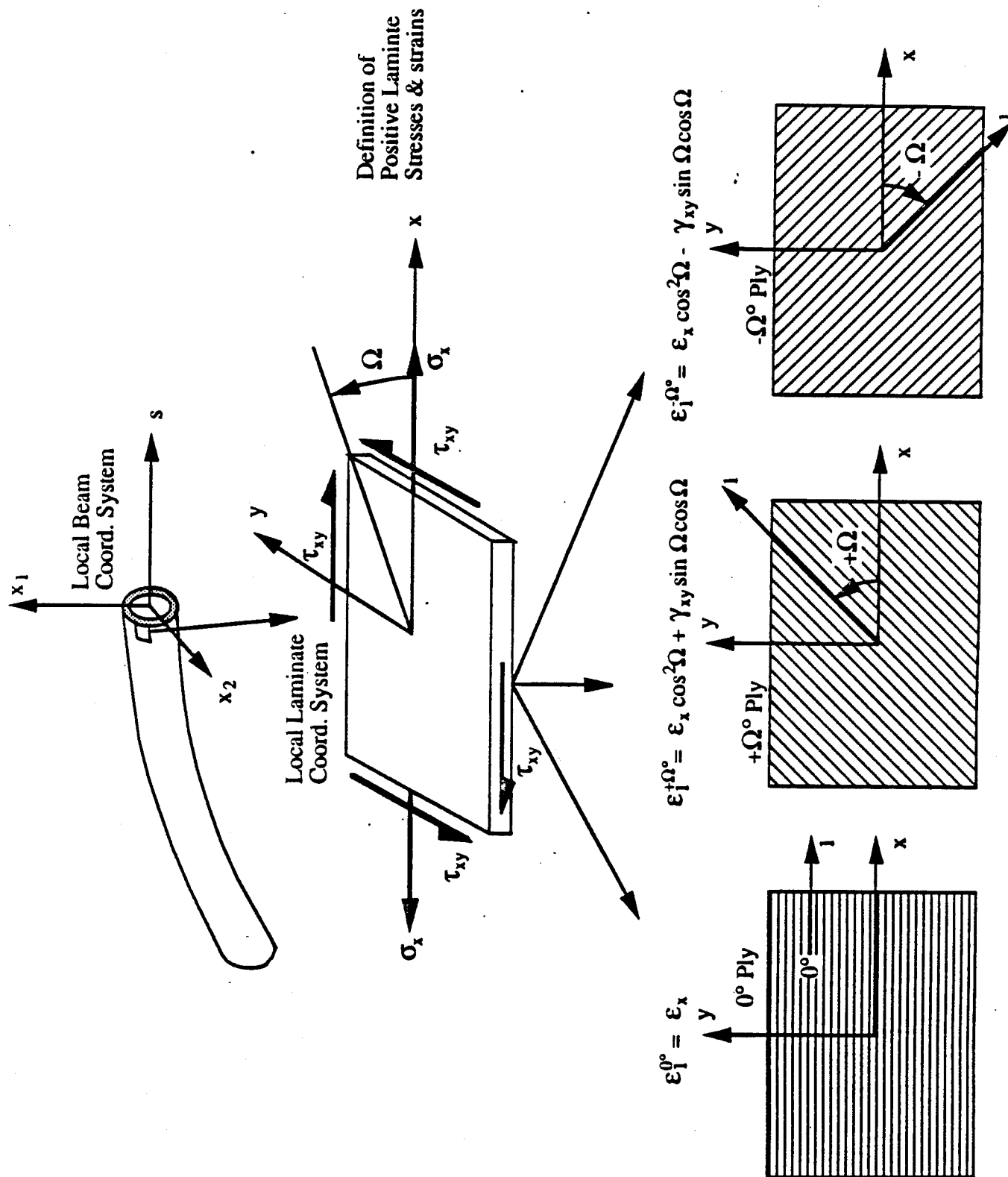


Figure 3.2.1-4. Beam Stress Analysis Local Laminate Coordinate System Used For Composite Stress Analysis.

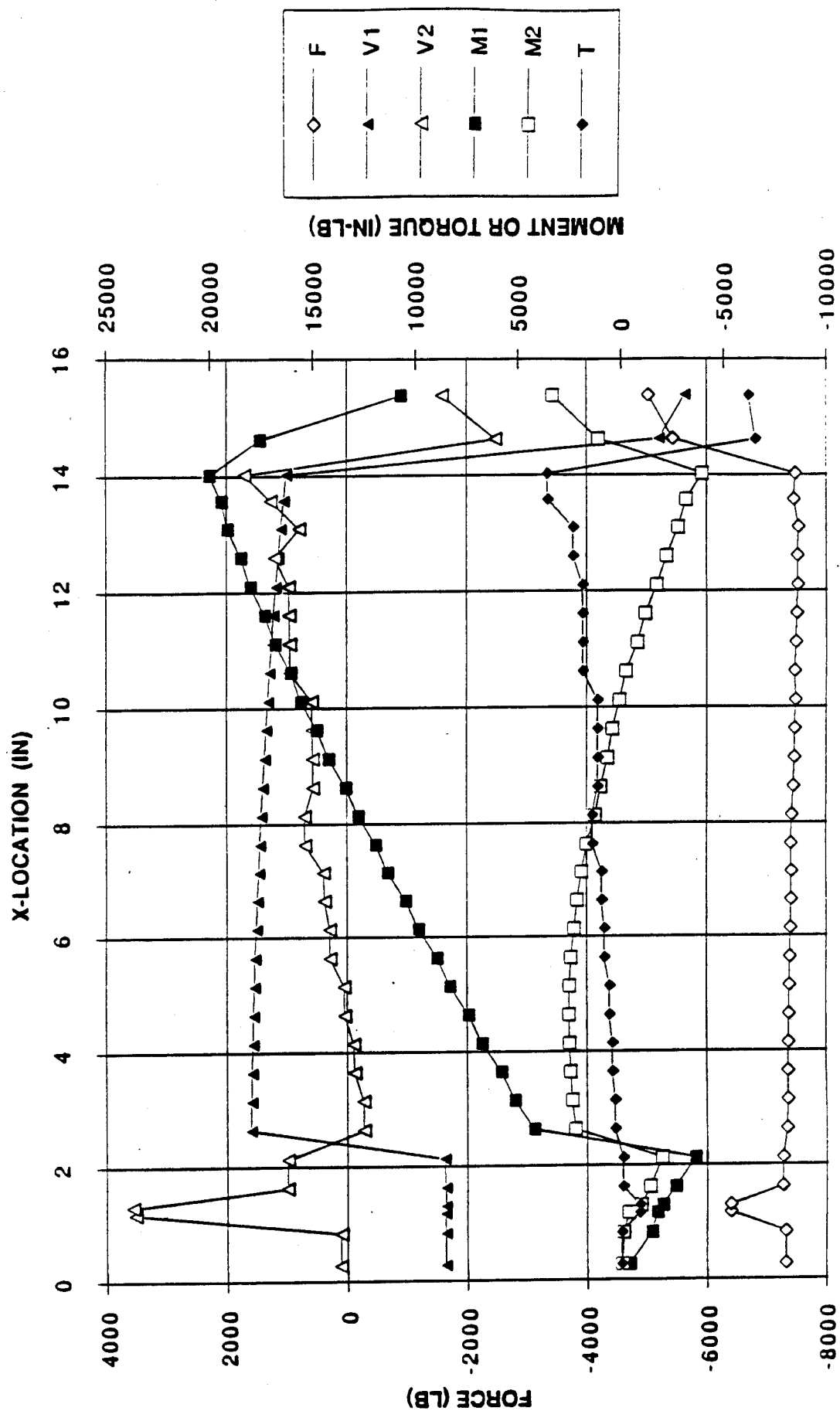


Figure 3.2.1-5. Composite Femur Beam Model Force and Moment Resultants (7500 lbs. Compression, $R_0 = 0.6$ " $R_i = 0.25$ ", 75% $0^\circ/25^\circ \pm 45^\circ$ T1000-G/Epoxy).

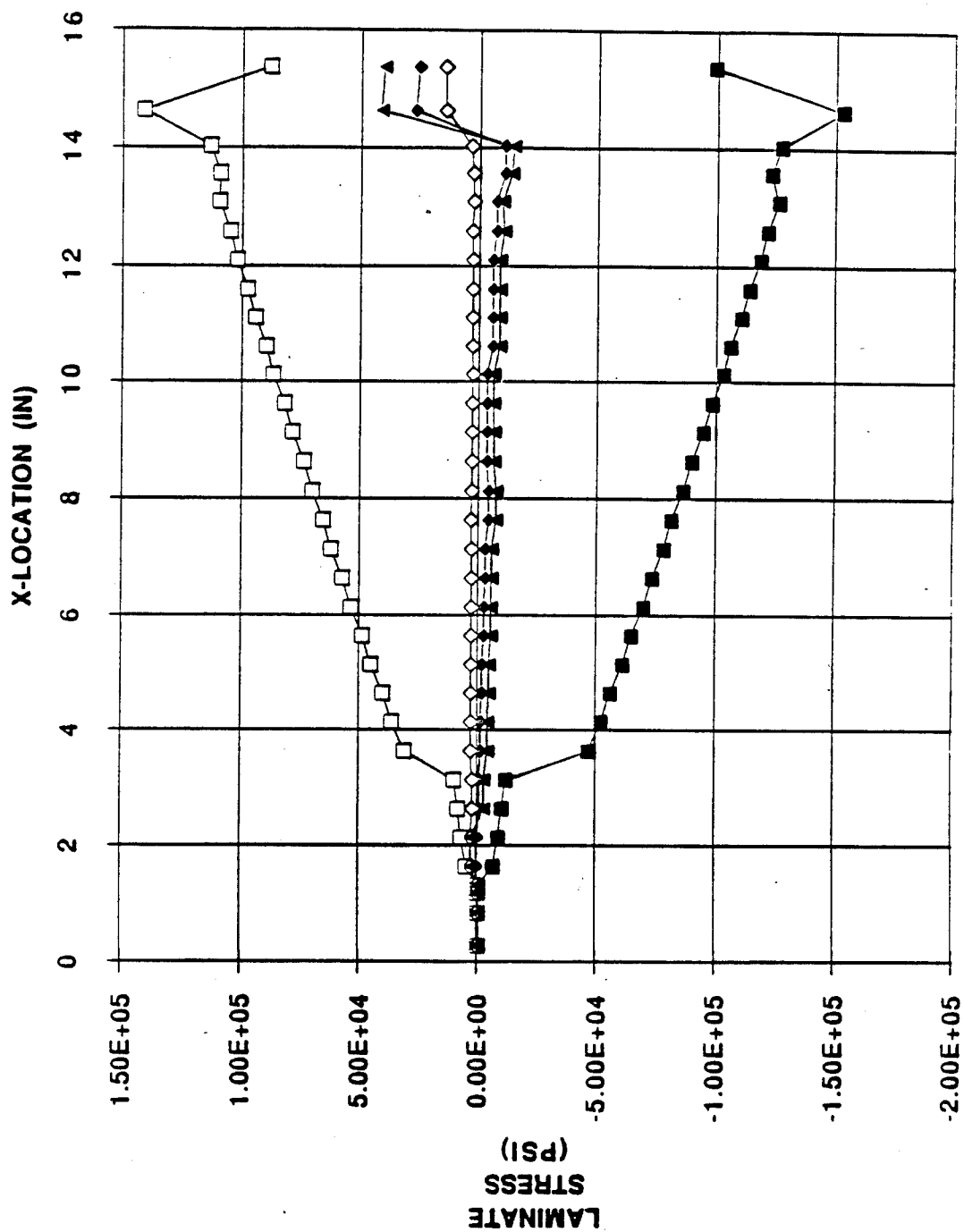


Figure 3.2.1-6. Composite Femur Beam Model Laminate Stress
(7500 lbs. Compression, $R_o = 0.6"$ $R_i = 0.25"$, 75% 0°/25% ±45° T1000-G/Epoxy).

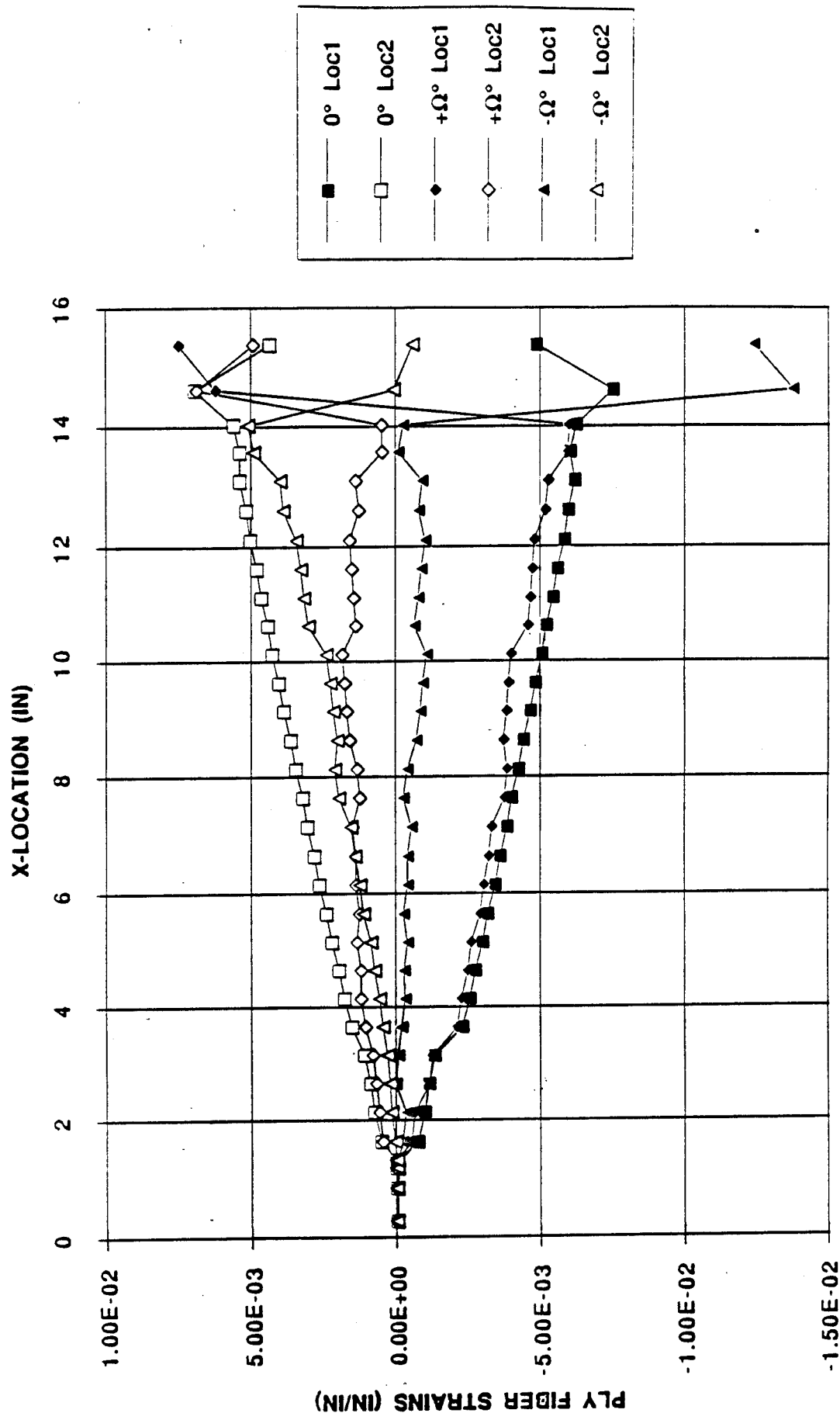


Figure 3.2.1-7. Composite Femur Beam Model Ply Fiber Direction Strains at Extreme Bending Stress Locations (7500 lbs. Compression, $R_o = 0.6"$ $R_i = 0.25"$, 75% 0°/25% $\pm 45^\circ$ T1000-G/Epoxy)

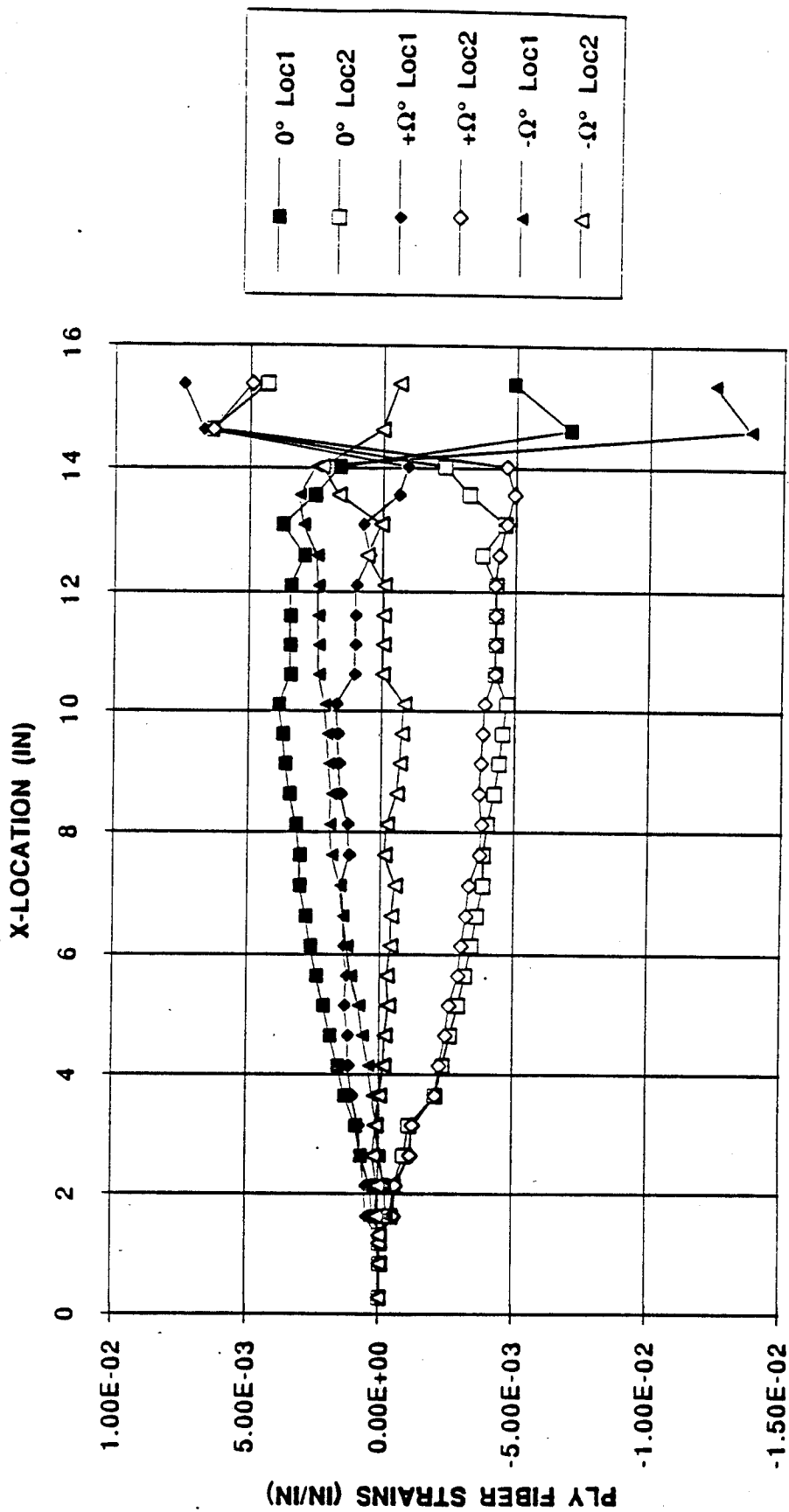


Figure 3.2.1-8. Composite Femur Beam Model Ply Fiber Direction Strains at Maximum Transverse Stress Locations (7500 lbs. Compression, $R_o = 0.6"$ $R_i = 0.25"$, 75% 0°/25% $\pm 45^\circ$ T1000-G/Epoxy)

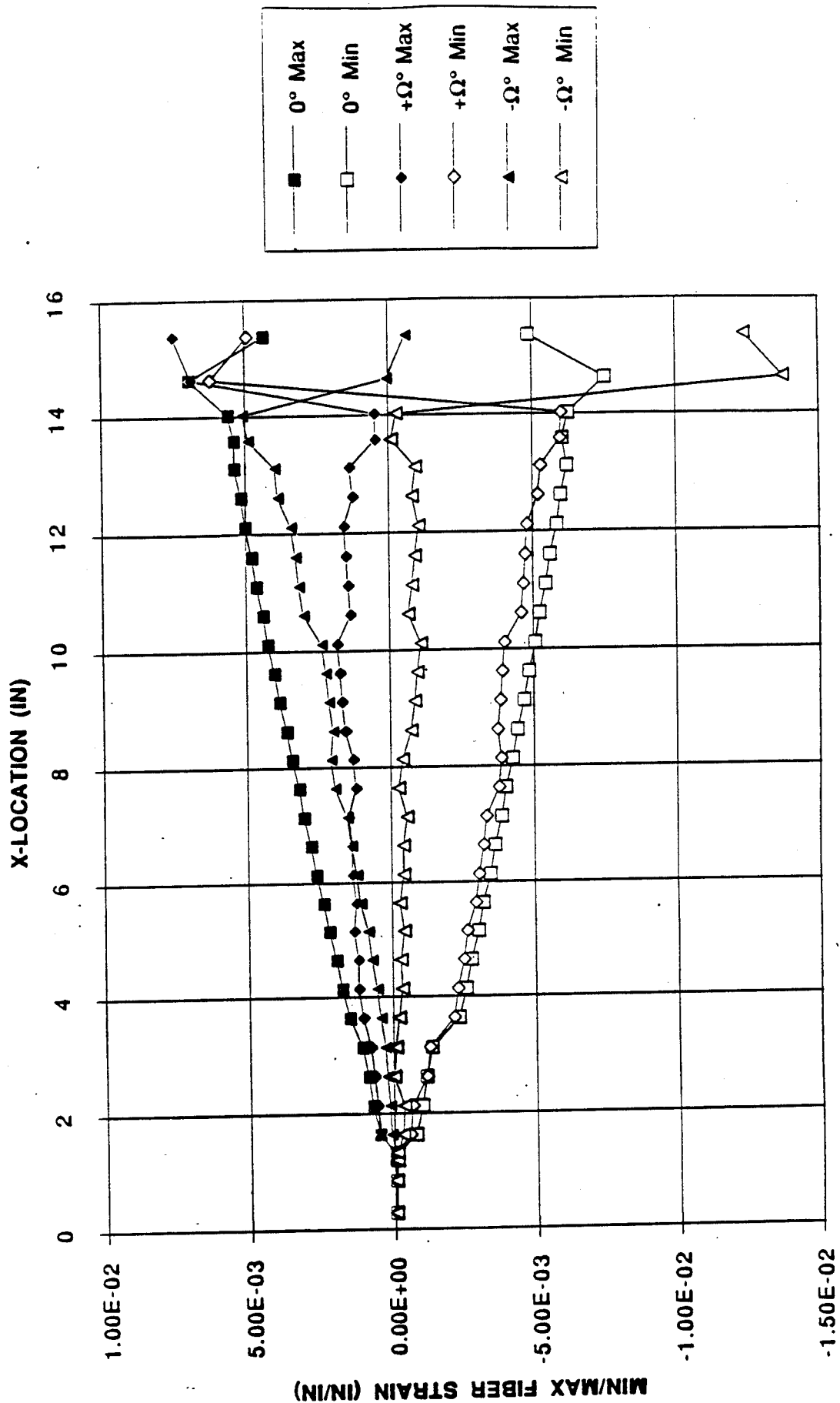


Figure 3.2.1-9. Composite Femur Beam Model Ply Fiber Direction Strains
(7500 lbs. Compression, $R_o = 0.6"$ $R_i = 0.25"$, 75% 0°/25% ±45° T1000-G/Epoxy)

accurately model the cross-section and material combination as the femoral stem tapers into the titanium ball joint.

Elasticities for Toray T1000G/Epoxy were generated using ICAN, and were input to the 2-D beam model. ICAN stands for Integrated Composite Analyzer, and is an industry standard model for predicting composite elasticities. The code allows the user to input the individual fiber and resin (matrix) material properties, and generate composite material elasticities for any specified layup. Table 3.2.1-2 shows the layups schemes, elasticities, and corresponding regions in the model where they were implemented. Again, Figure 3.2.1-1 shows the 2-D beam model, and is used for referencing.

Table 3.2.1-2. ICAN Generated Elasticities for 2-D Beam Model

Region	Layup	E (msi)	G (msi)
A	70% 0°, 20% ±45, 10% 90°	19.36	1.83
B	60% 0°, 30% ±45, 10% 90°	17.14	2.35
C	55% 0°, 35% ±45, 10% 90°	16.08	2.71
D	50% 0°, 40% ±45, 10% 90°	14.98	3.03
E	45% 0°, 45% ±45, 10% 90°	13.84	3.32

Note that the shear modulus (G) increases as the femur stem transitions into the ball joint. This provides additional shear strength in this critical region. Plots for the compression, bending, and torsional load condition are shown in Figures 3.2.1-10 through 3.2.1-24. Results show significant positive margin for each load case, with the exception of the torsional load case at the femur stem/titanium ball interface. However, since beam theory assumptions start to break-down near the ends of the 2-D model, a detailed three-dimensional finite element model was used in this region to better resolve the complex stress state. The strain to failure for Toray T1000G/Epoxy is 1.8% in tension, and 1.1% in compression. The 3-D model (discussed in detail later) shows that the compressive strain at this interface is above the 1.1% strain to failure, and a small increase in outer radius was later accomplished within the allowable geometry to obtain a positive margin of safety.

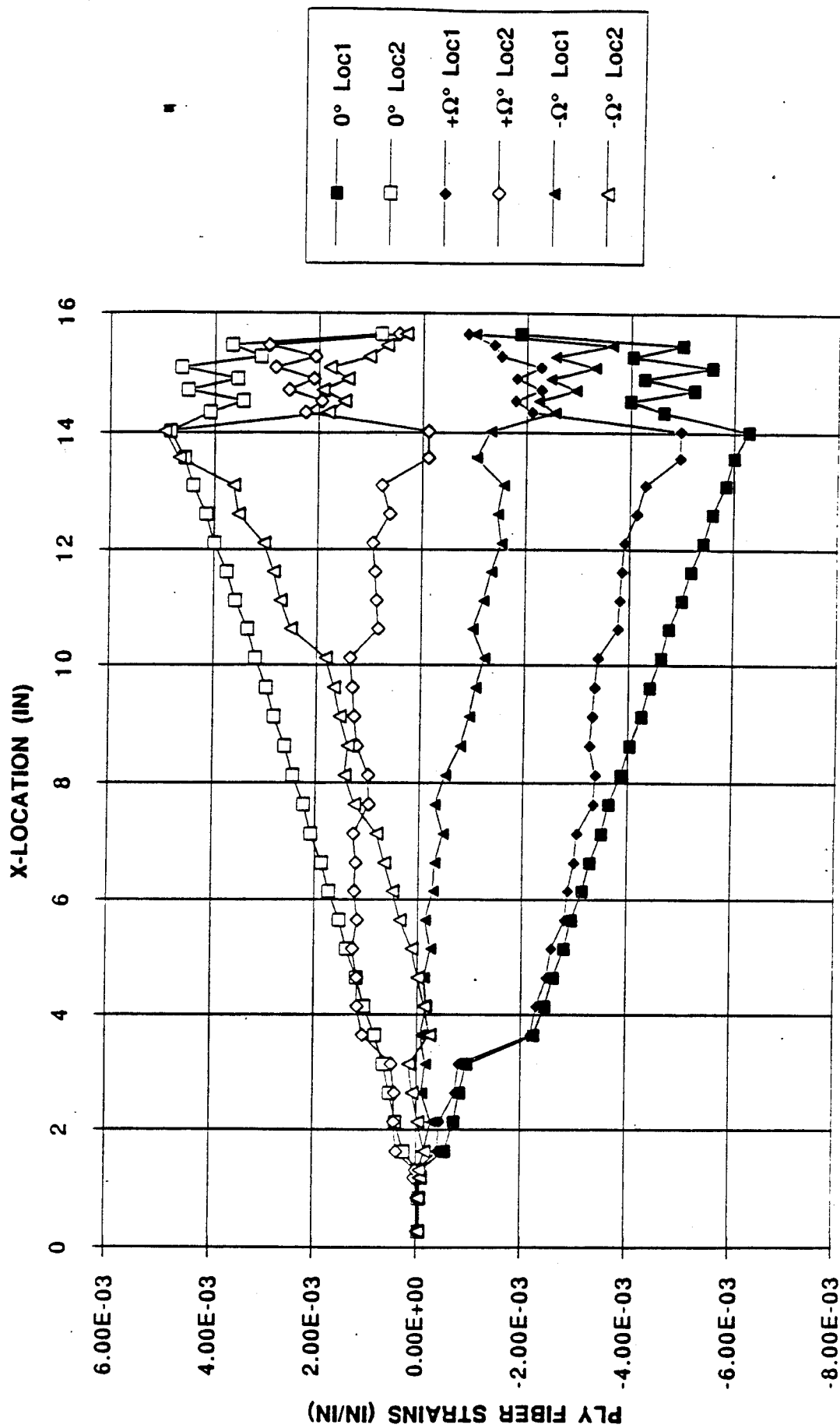


Figure 3.2.1-10. Composite Femur Beam Model Ply Fiber Direction Strains at Extreme Bending Stress Locations (8640 lbs. Compression, $R_o = 0.6"$, $R_i = 0.4"$, T1000G/Epoxy).

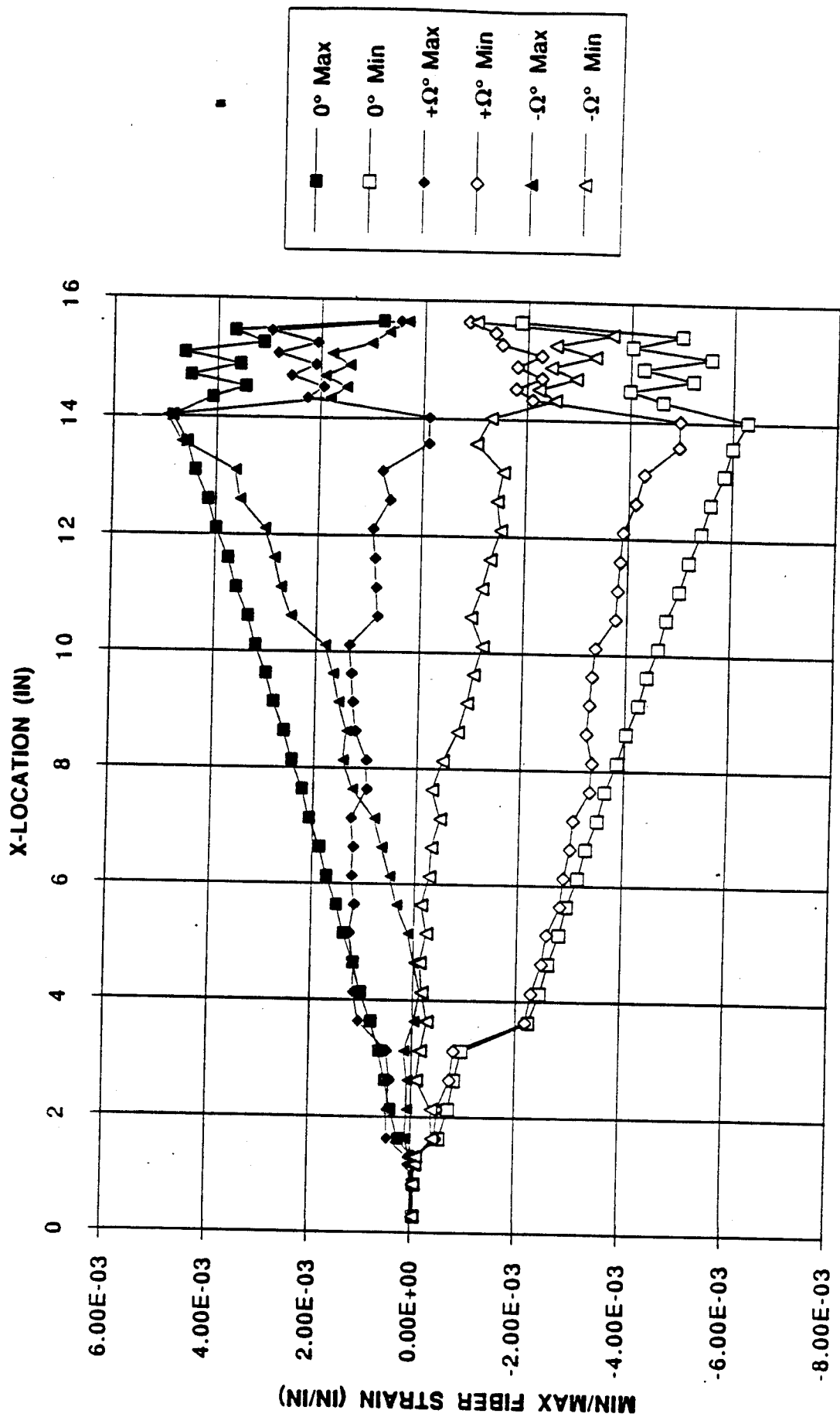


Figure 3.2.1-11. Composite Femur Beam Model Ply Fiber Direction Strains
(8640 lbs. Compression, $R_o = 0.6$ ", $R_i = 0.4$ ", T1000G/Epoxy).

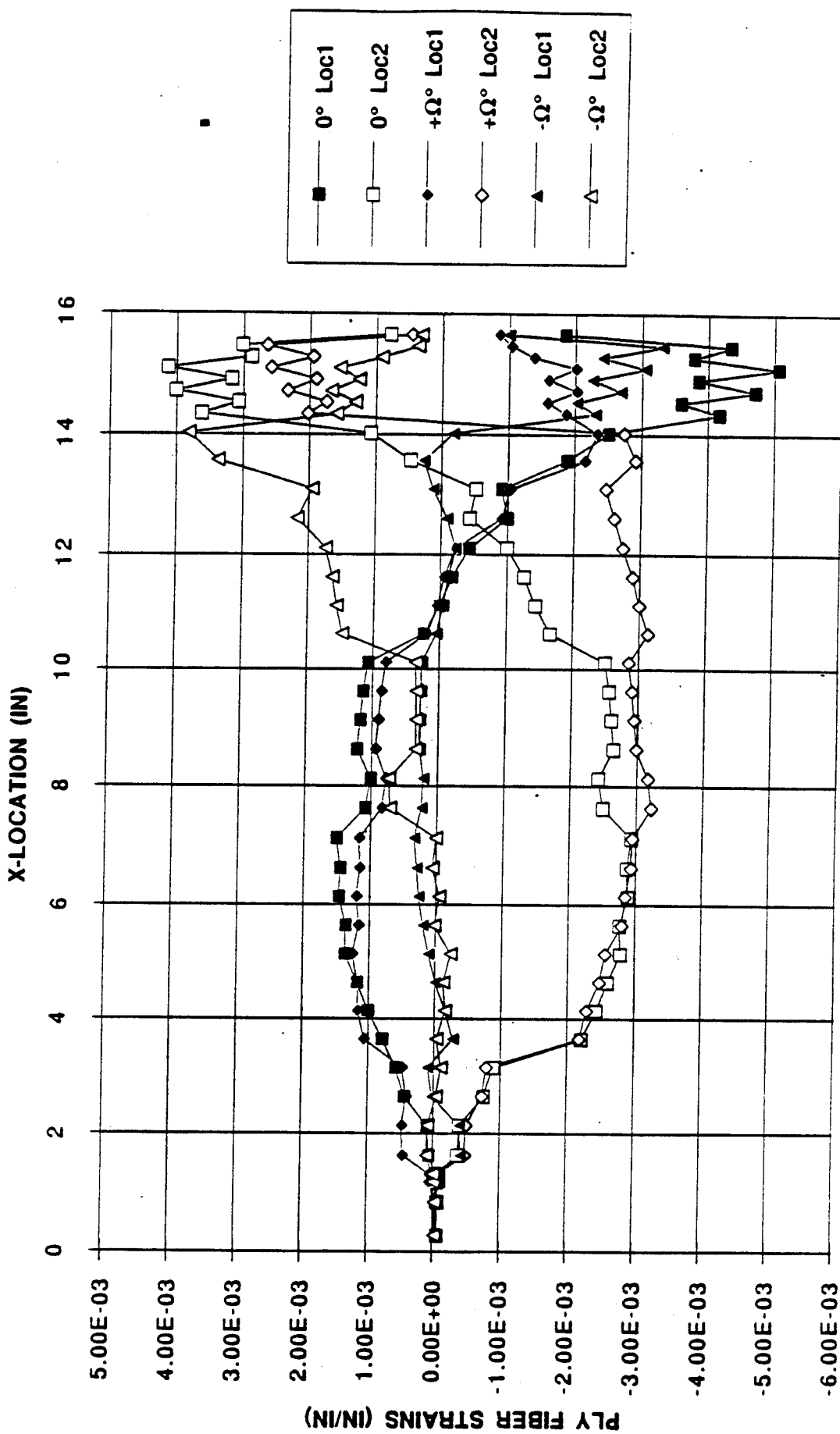


Figure 3.2.1-12. Composite Femur Beam Model Ply Fiber Direction Strains at Maximum Transverse Stress Locations (8640 lbs. Compression, Ro = 0.6", Ri = 0.4", T1000G/Epoxy).

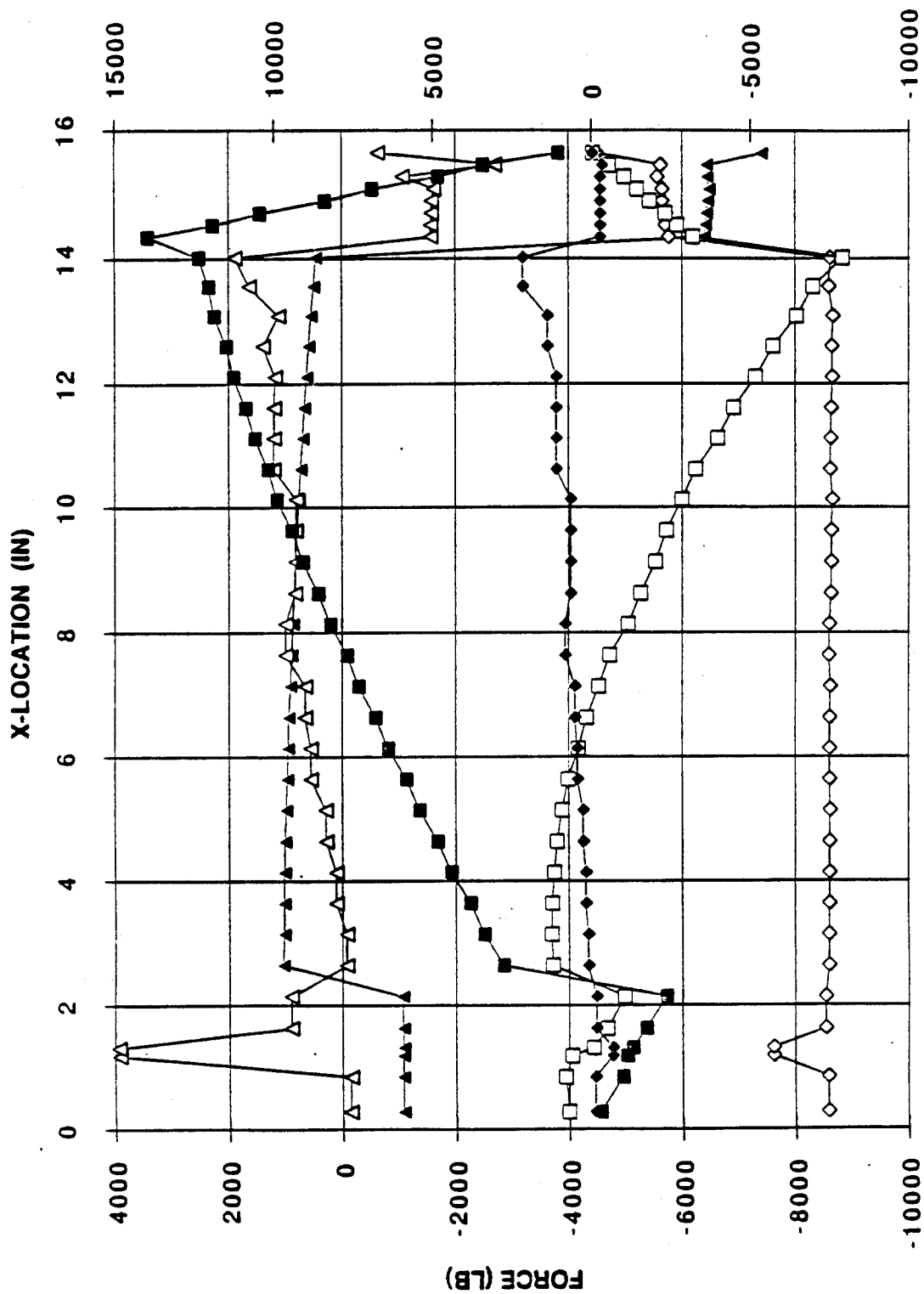


Figure 3.2.1-13. Composite Femur Beam Model Ply Force and Moment Resultants (8640 lbs. Compression, $R_o = 0.6''$, $R_i = 0.4''$, T1000G/Epoxy).

AMR77 ABAQUS FEMUR BEAM MODEL RESULTS

LAMINATE STRESSES

COMPRESSION - OR=.6", IR=.4" (G)

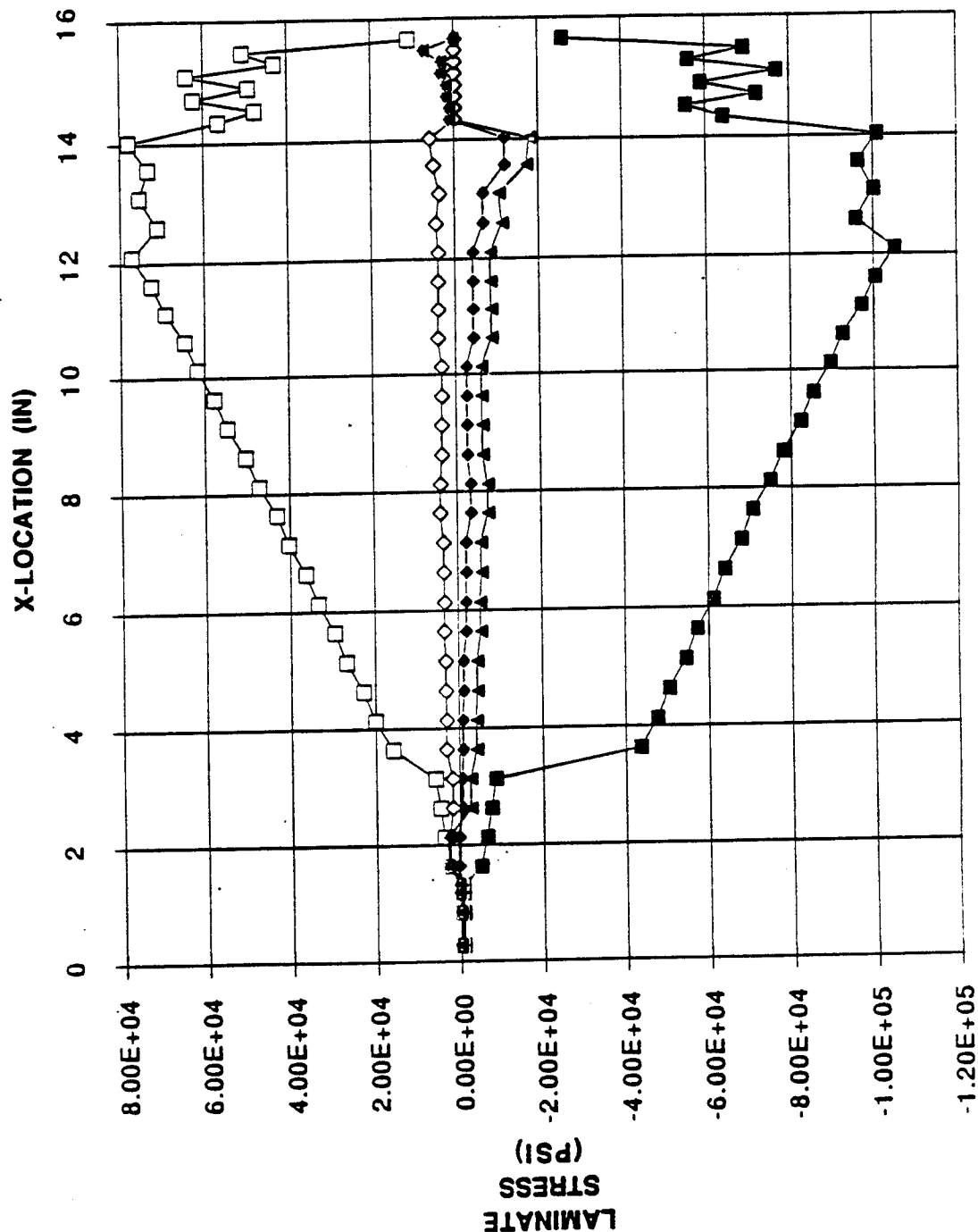


Figure 3.2.1-14. Composite Femur Beam Model Laminate Stress (8640 lbs. Compression, Ro = 0.6", Ri = 0.4", T1000G/Epoxy).

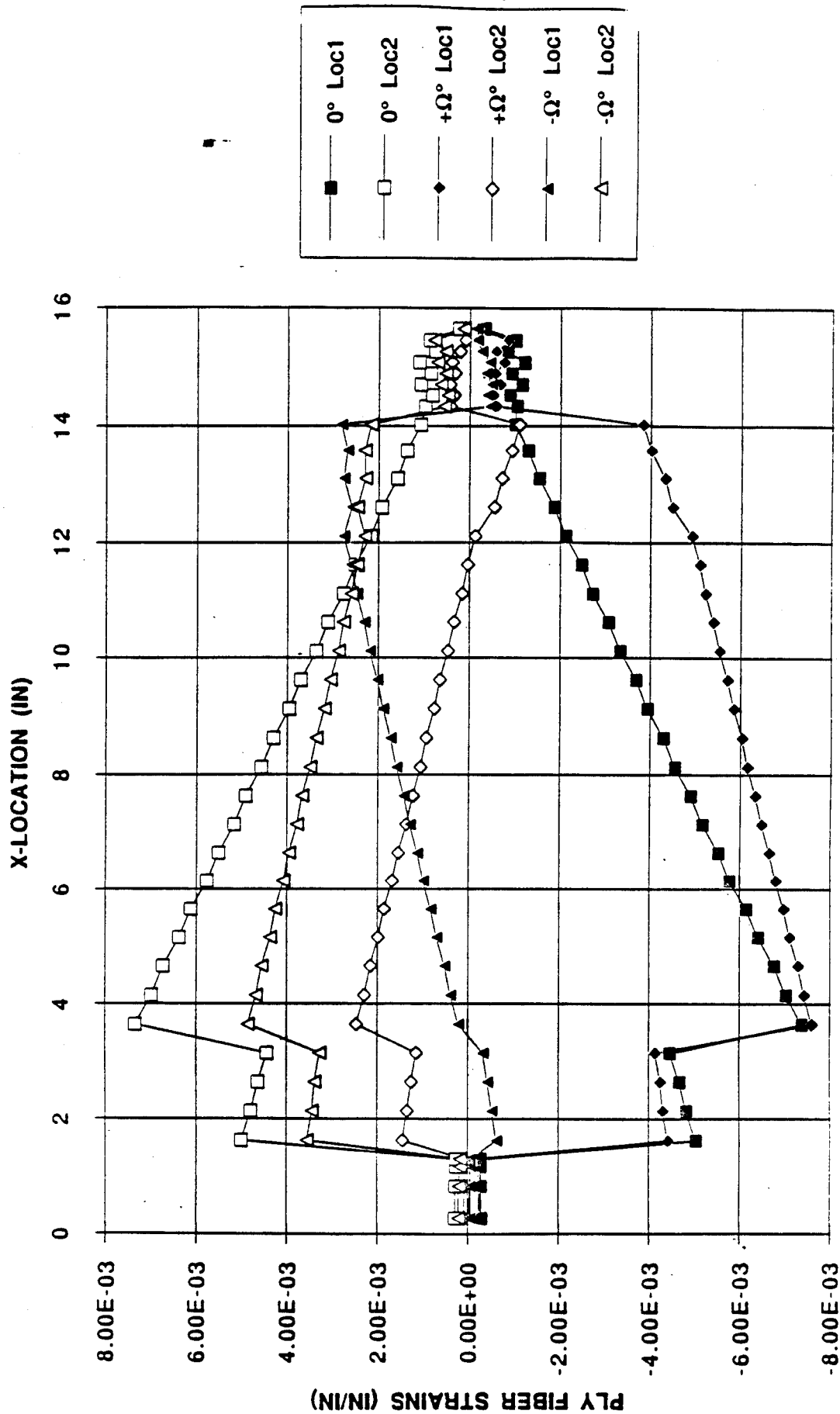


Figure 3.2.1-15. Composite Femur Beam Model Ply Fiber Direction Strains at Extreme Bending Stress Locations (1623 lbs. Cantilever Bending, $R_o = 0.6"$, $R_i = 0.4"$, T1000G/Epoxy).

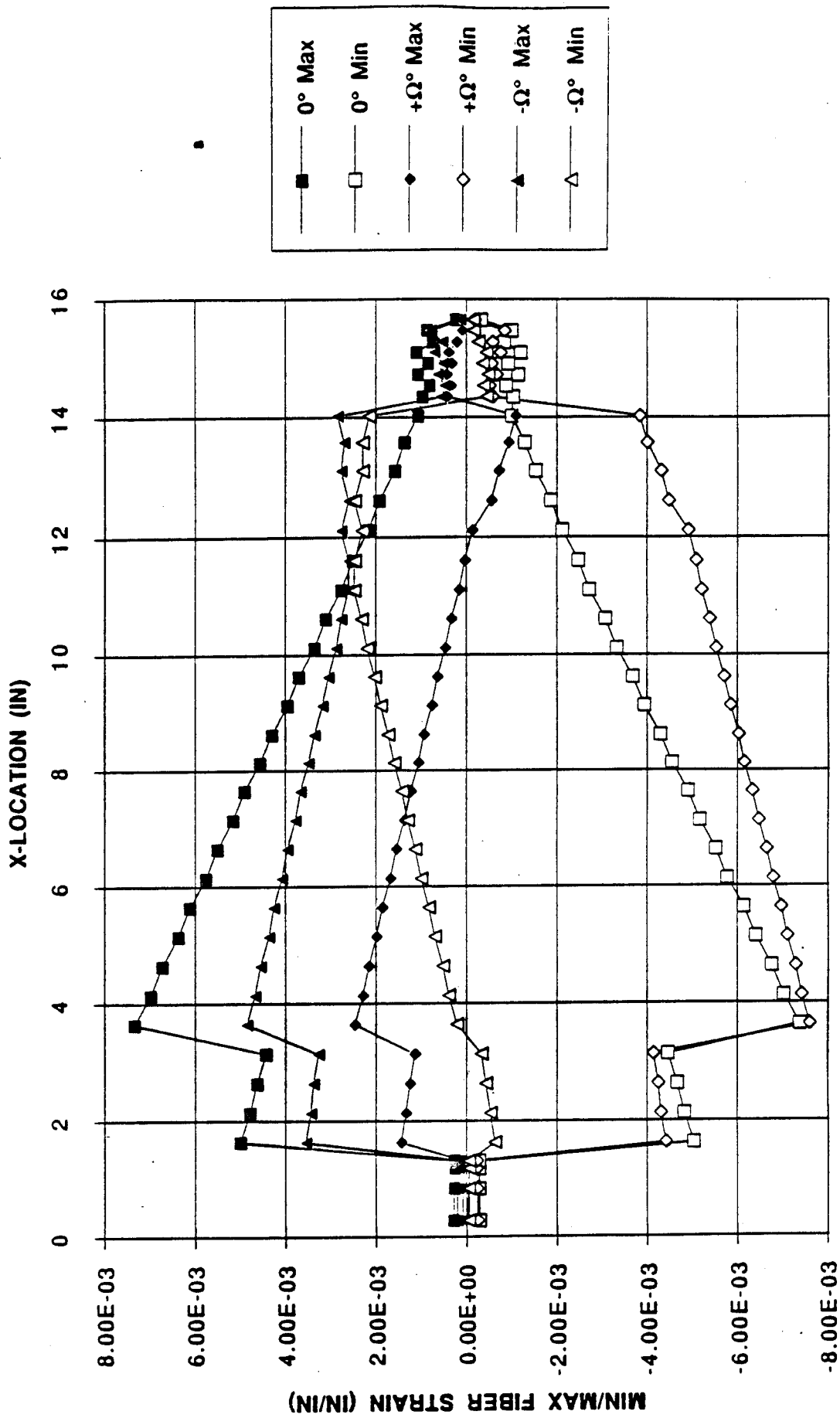


Figure 3.2.1-16. Composite Femur Beam Model Ply Fiber Direction Strains
(1623 lbs. Cantilever Bending, $R_o = 0.6"$, $R_i = 0.4"$, T1000G/Epoxy).

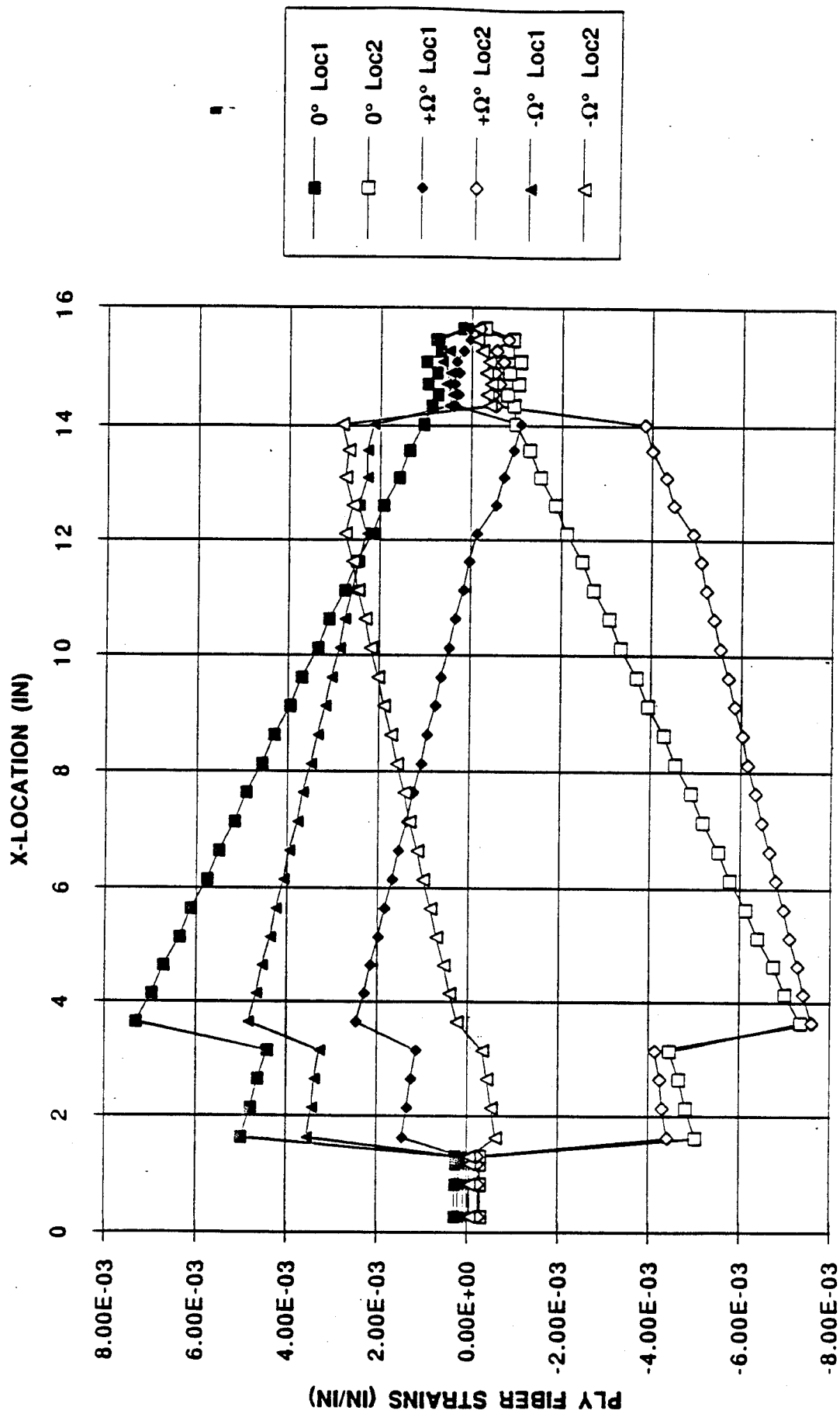


Figure 3.2.1-17. Composite Femur Beam Model Ply Fiber Direction Strains at Maximum Transverse Stress Locations (1623 lbs. Cantilever Bending, $R_o = 0.6"$, $R_i = 0.4"$, T1000G/Epoxy).

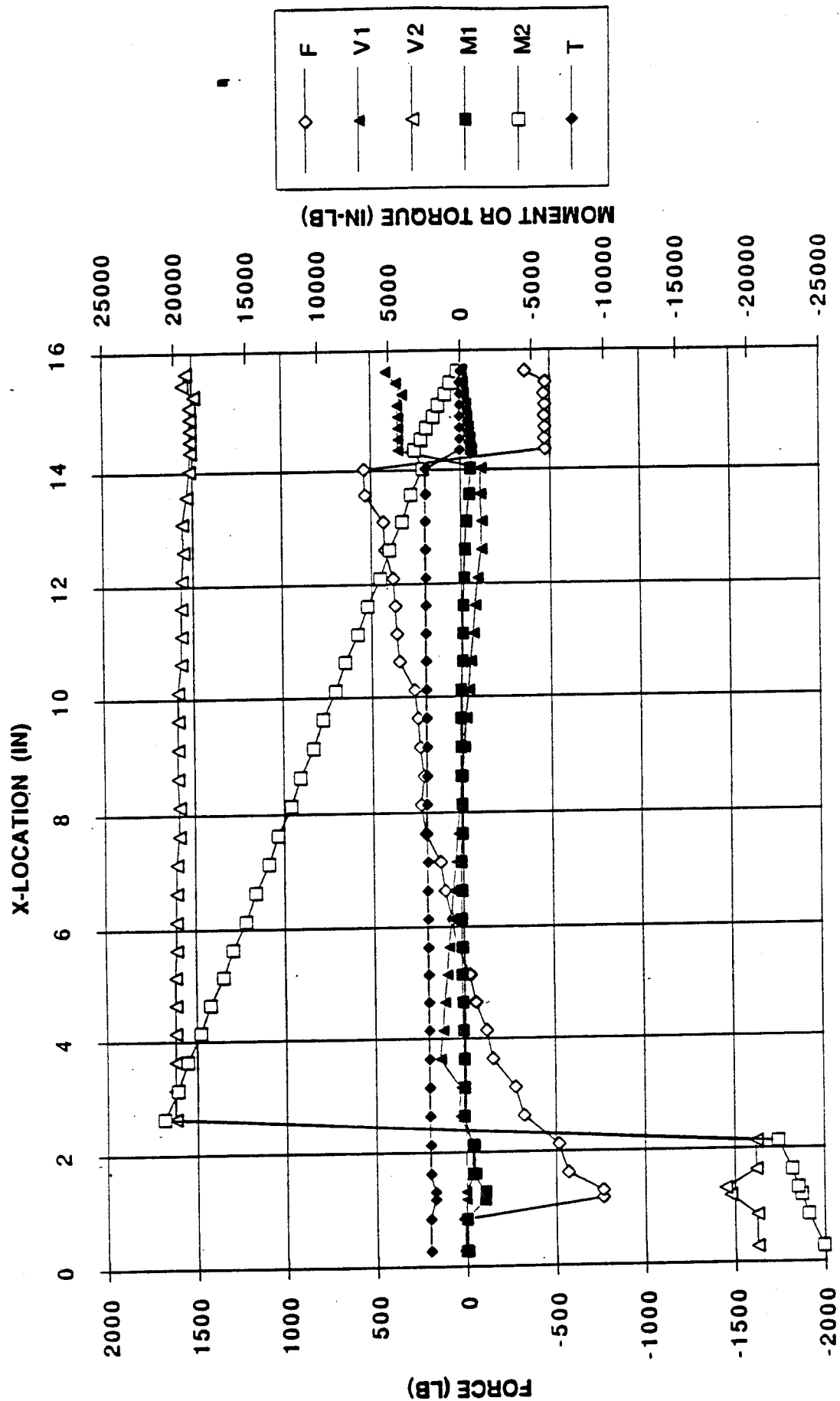


Figure 3.2.1-18. Composite Femur Beam Model Force and Moment Resultants
(1623 lbs. Cantilever Bending, $R_o = 0.6$ ", $R_i = 0.4$ ", T1000G/Epoxy).

AMR77 ABAQUS FEMUR BEAM MODEL RESULTS

BENDING - OR=.6", IR=.4" (G)

LAMINATE STRESSES

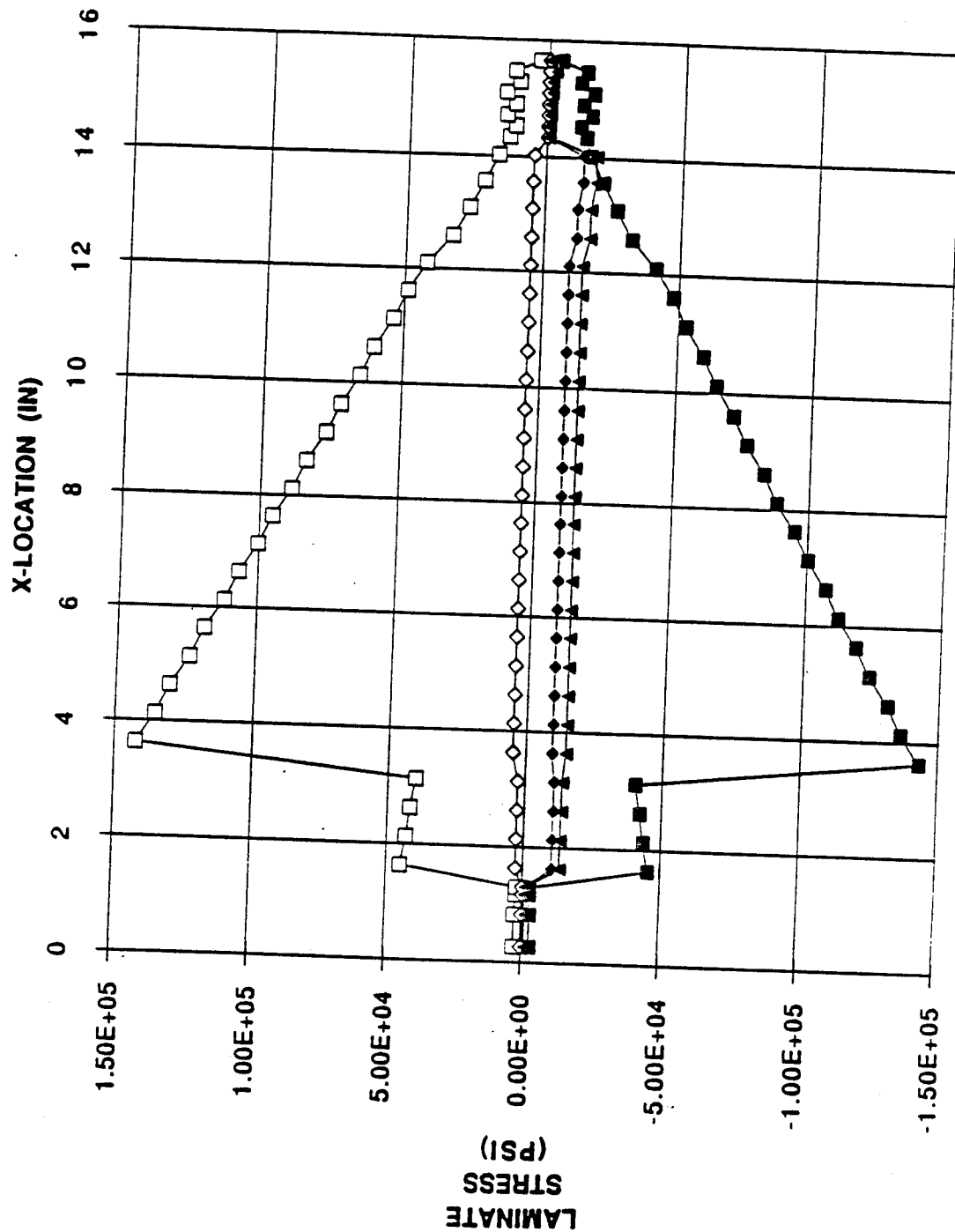


Figure 3.2.1-19. Composite Femur Beam Model Laminate Stress
(1623 lbs. Cantilever Bending, Ro = 0.6", Ri = 0.4", T1000G/Epoxy).

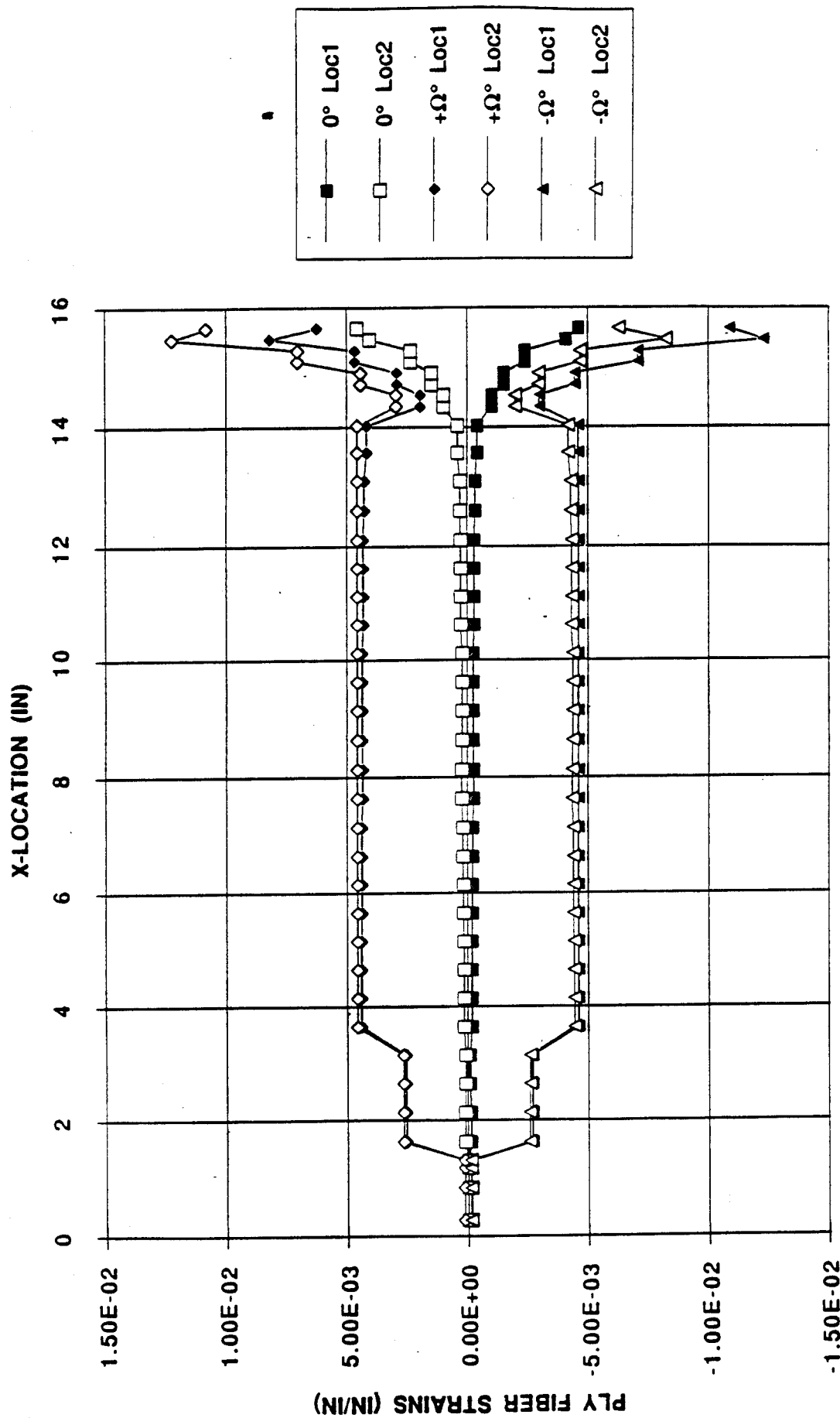


Figure 3.2.1-20. Composite Femur Beam Model Ply Fiber Direction Strains at extreme Bending Stress Locations (4500 in-lbs. Torsion Bending, $R_o = 0.6"$, $R_i = 0.4"$, T1000G/Epoxy).

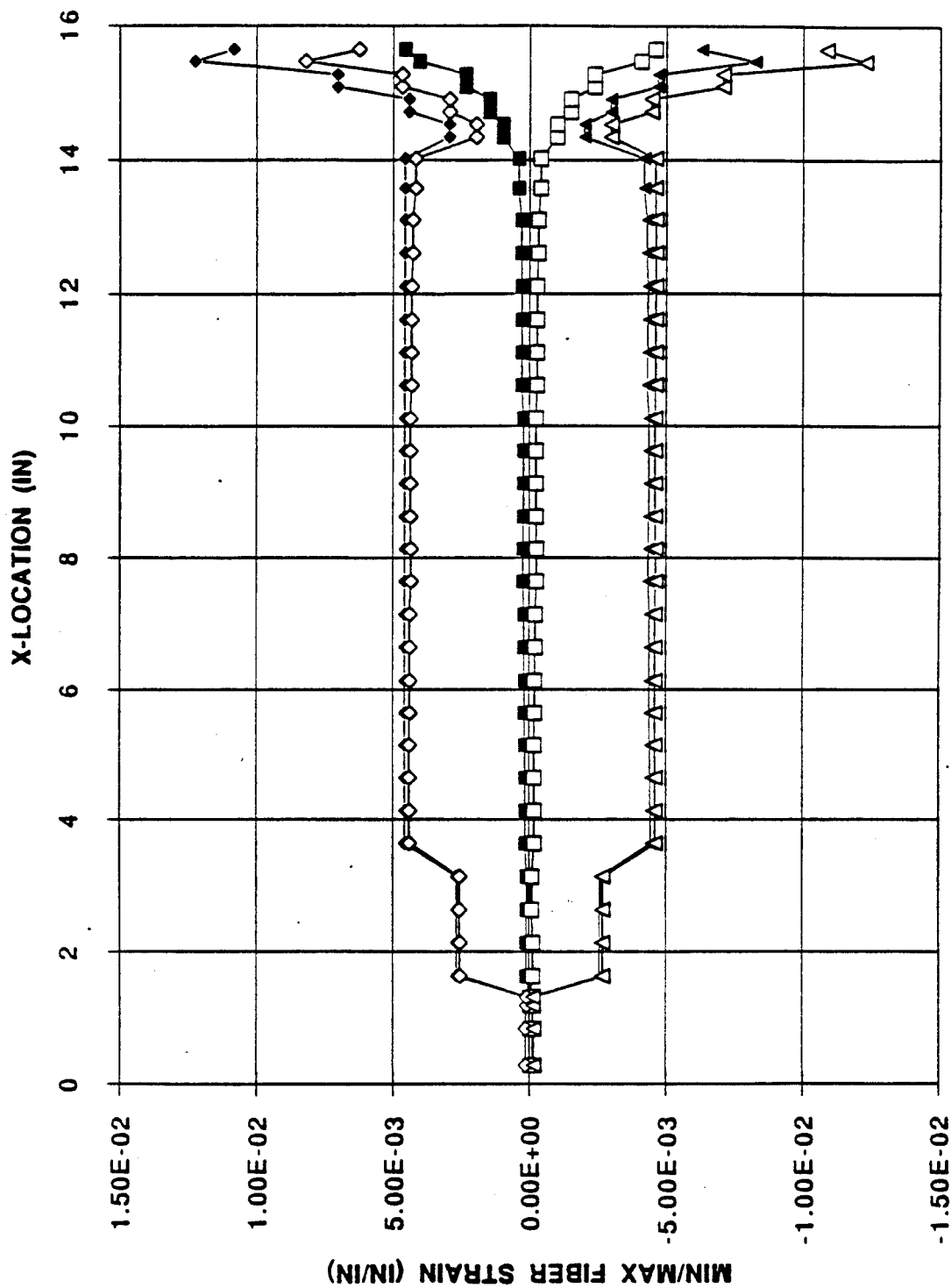


Figure 3.2.1-21. Composite Femur Beam Model Ply Fiber Direction Strains
(4500 in-lbs. Torsion Bending, $R_o = 0.6"$, $R_i = 0.4"$, T1000G/Epoxy).

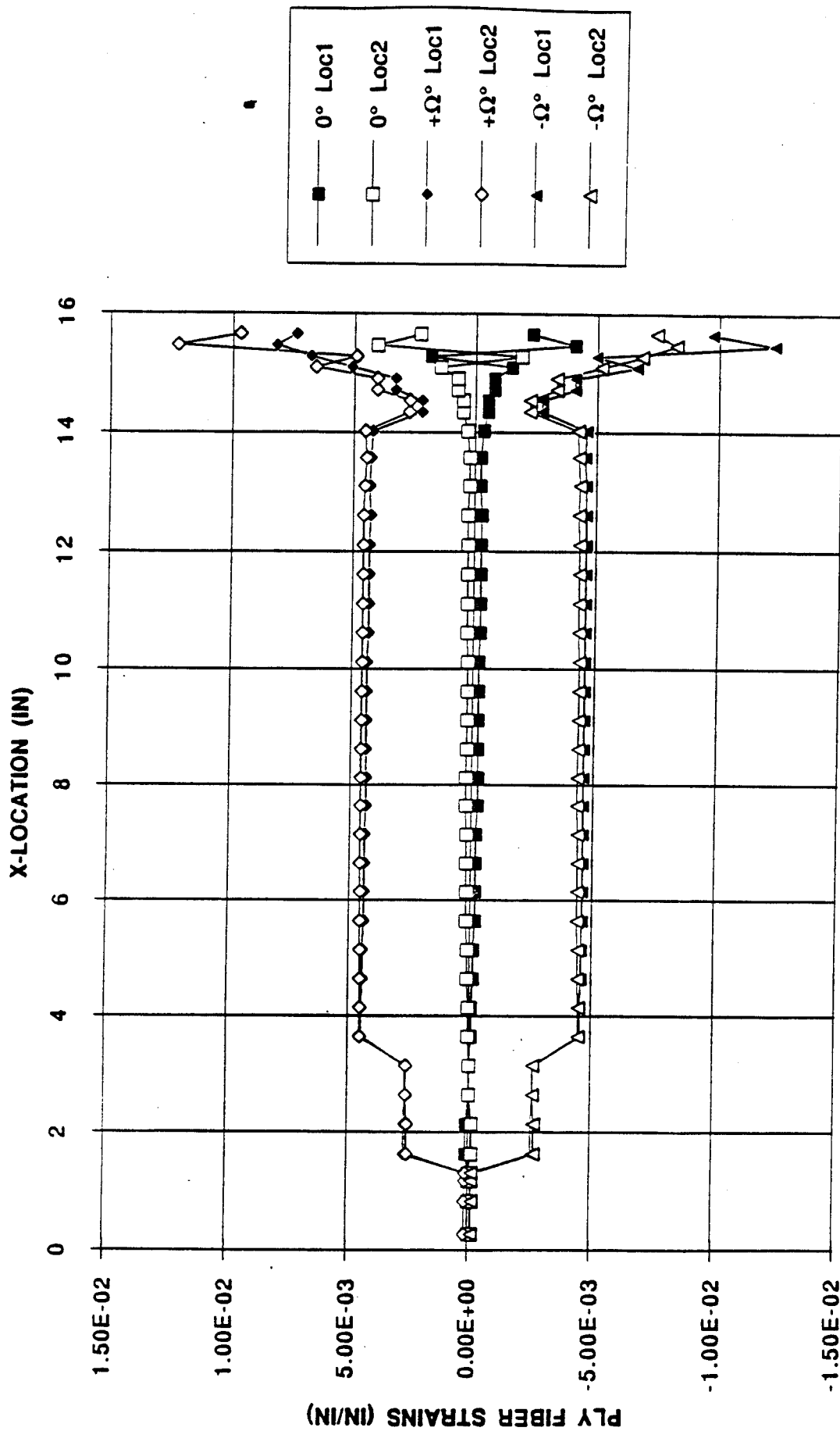


Figure 3.2.1-22. Composite Femur Beam Model Ply Fiber Direction Strains at Maximum Transverse Locations (4500 in-lbs. Torsion, $R_o = 0.6"$, $R_i = 0.4"$, T1000G/Epoxy).

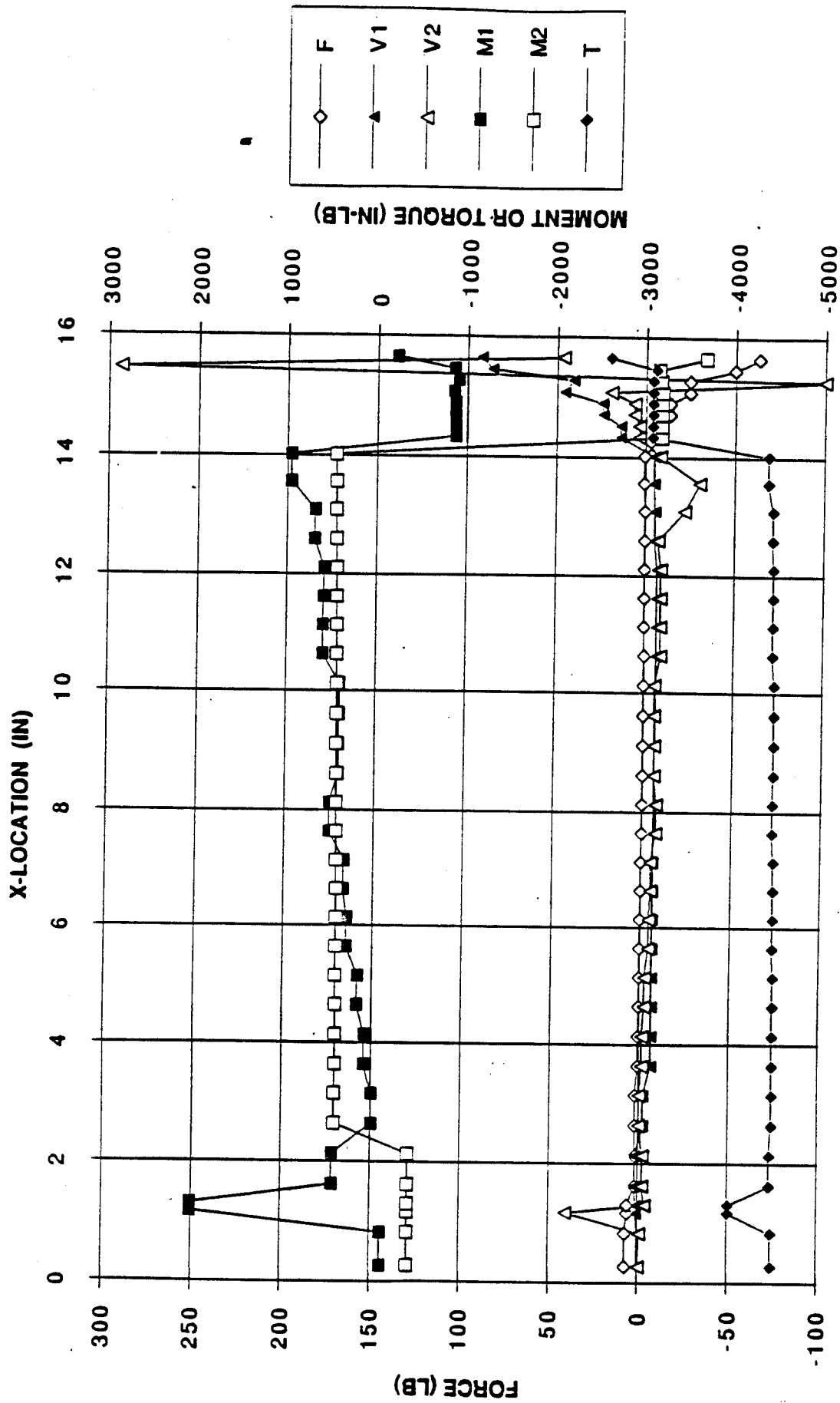


Figure 3.2.1-23. Composite Femur Beam Model Force and Moment Resultants (4500 in-lbs. Torsion, $R_o = 0.6$ ", $R_i = 0.4$ ", T1000G/Epoxy).

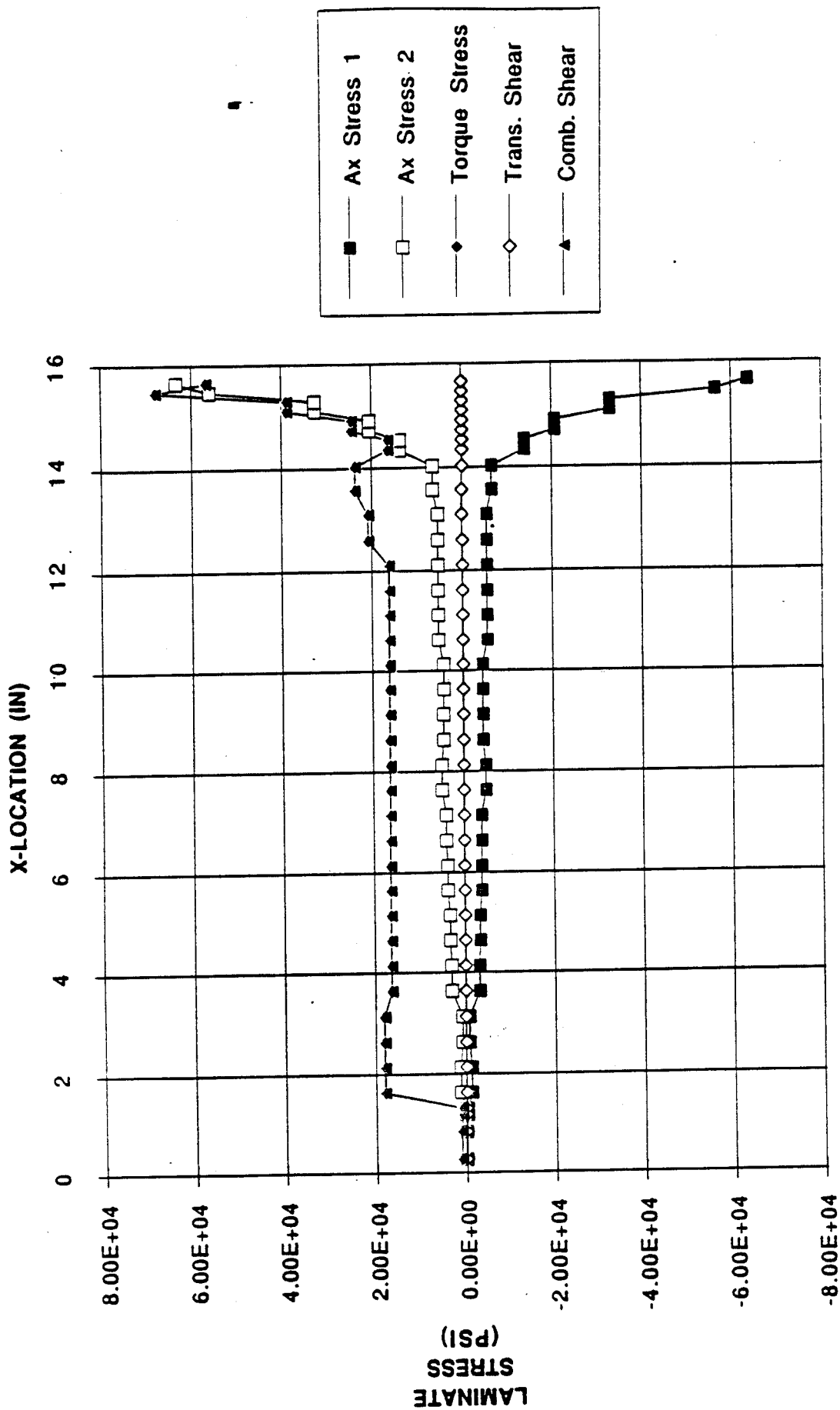


Figure 3.2.1-24. Composite Femur Beam Model Laminar Stress
(4500 in-lbs. Torsion, $R_o = 0.6$ ", $R_i = 0.4$ ", T1000G/Epoxy).

3-D Femur Finite Element Modeling

An AutoCad IGES file of the femur geometry was used as a starting point for development of a 3-D finite element model. The IGES file was imported to PATRAN, and the geometry is shown in Figure 3.2.1-25.

One of the Phase II objectives in the design of the femur, was to reduce weight via modification of the titanium insert. In Phase I, the compression validation test showed the femur could hold up to 83% of the compressive design load. Although there was no catastrophic failure, the test was stopped when the part could not sustain the applied load. "Failure" occurred due to excessive radial stress at the distal end of the titanium insert which reacted to the high compressive load on the ball. Based on the Phase I test results, the Phase II proximal femur was redesigned. Initially, the full 3-D femur F.E. model was developed with the exception of the titanium insert. A local 3-D finite element model of the titanium insert was developed in order to assess whether the re-design (from Phase I) was adequate to overcome the problems (i.e., compressive load condition) seen in the Phase I design.

Titanium Insert Finite Element Modeling

A solid shaded image of this model (cutaway view) is shown in Figure 3.2.1-26. The green shade is the composite material, and the gray shade is the titanium insert. This design attempted to reduce weight by eliminating much of the titanium stem (from the Phase I design). However, the analysis showed this design to be inadequate due to the high bending stresses in the titanium (Figure 3.2.1-27), and excessive compressive strain in the composite material (Figure 3.2.1-28). The strength of titanium is 140 ksi (960 MPa), and the plot in Figure 3.2.1-27 shows a Von Mises stress of 181 ksi (1248 MPa). The compressive strain of -0.0249 in./in. is more than twice the compressive strain to failure of this material. Thus it was concluded that a lower risk approach (similar to that in Phase I) should be investigated.

As previously stated, in Phase I, the compression validation test showed the femur to withstand up to 83% of the compressive design load. The problem was excessive radial stress at the distal end of the titanium insert which reacted the compressive load on the ball. This problem could be overcome by extending the length of the insert further into the composite. A second titanium insert design/analysis iteration was made. The insert geometry is shown in Figure 3.2.1-29, and is very similar to the Phase I design. In order to reduce mass, the titanium insert was hollowed in the femur shaft up to the elbow. Additionally, mass was removed from

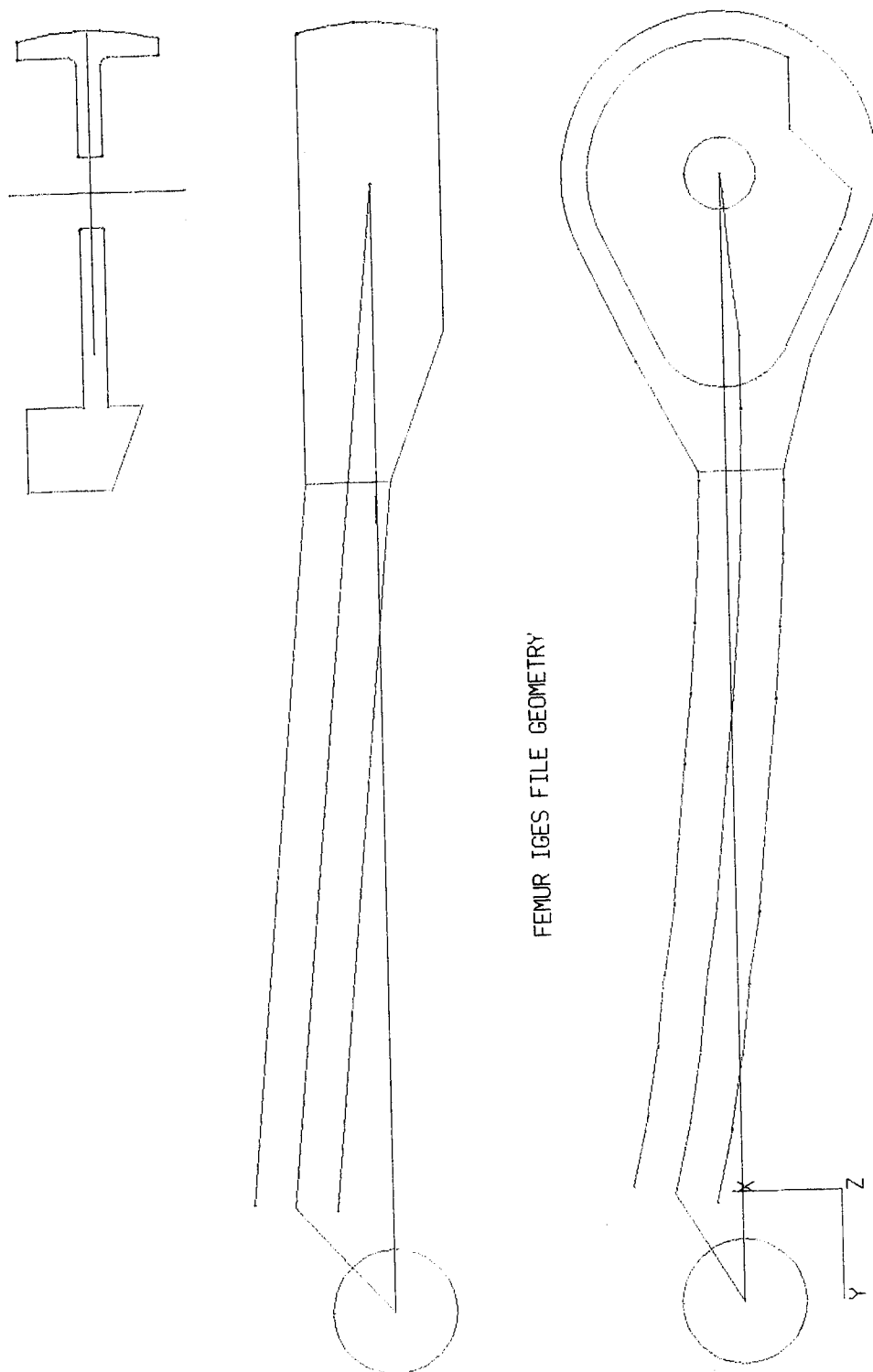


Figure 3.2.1-25. Femur Iges File Geometry.



Figure 3.2.1-26. Solid Shaded Image of Local Titanium Insert Femur F.E. Model.

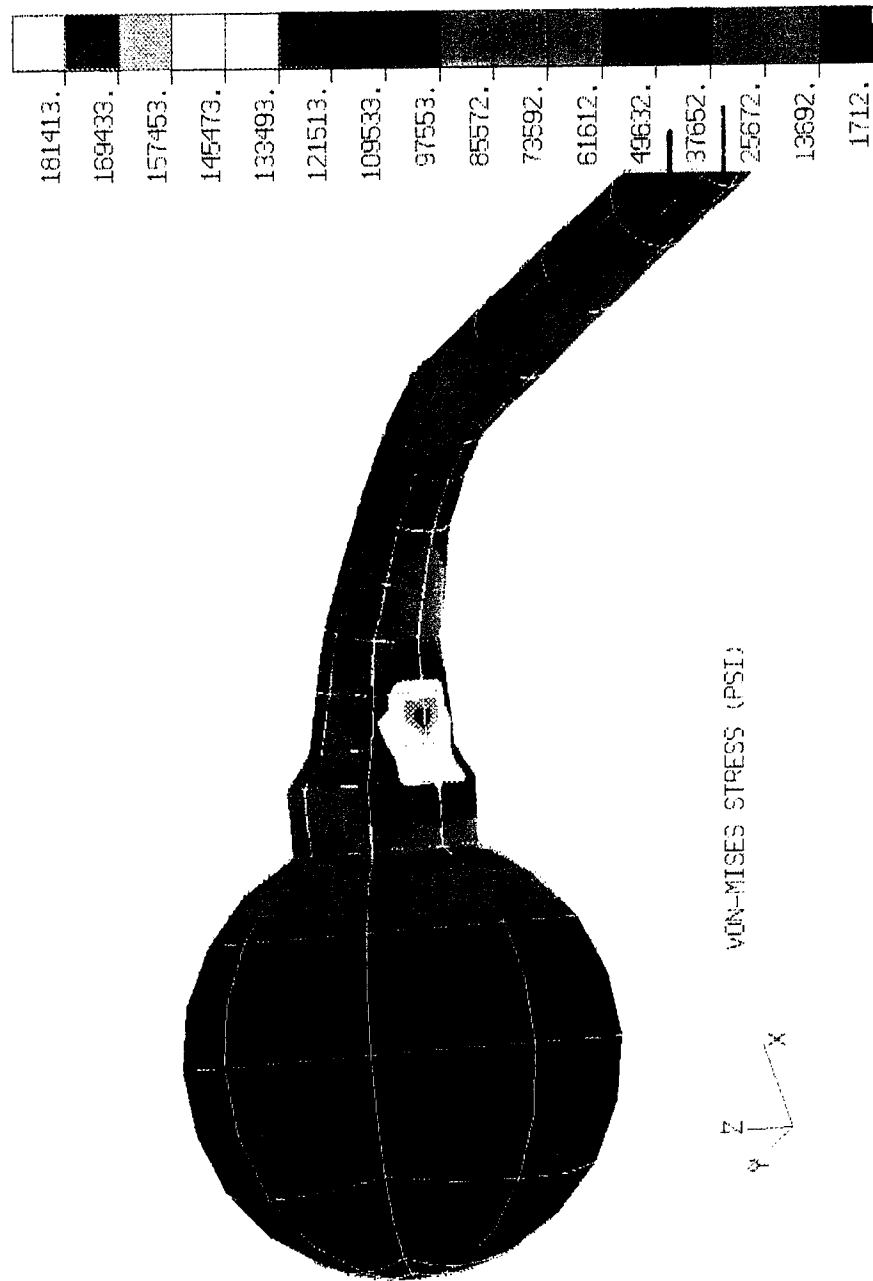


Figure 3.2.1-27. Von-Mises Stress in Titanium Insert under Compressive Load (Design Iteration I).

Design Iteration II

- Stepped-down Ti Stem
- Hollowed Ti Ball
- Tapered Elbow
- Max O.D. = 1.2 in.

Design Iteration III

- Tapered Ti Stem
- Hollowed Ti Ball
- Tapered Elbow
- Max O.D. = 1.3 in.

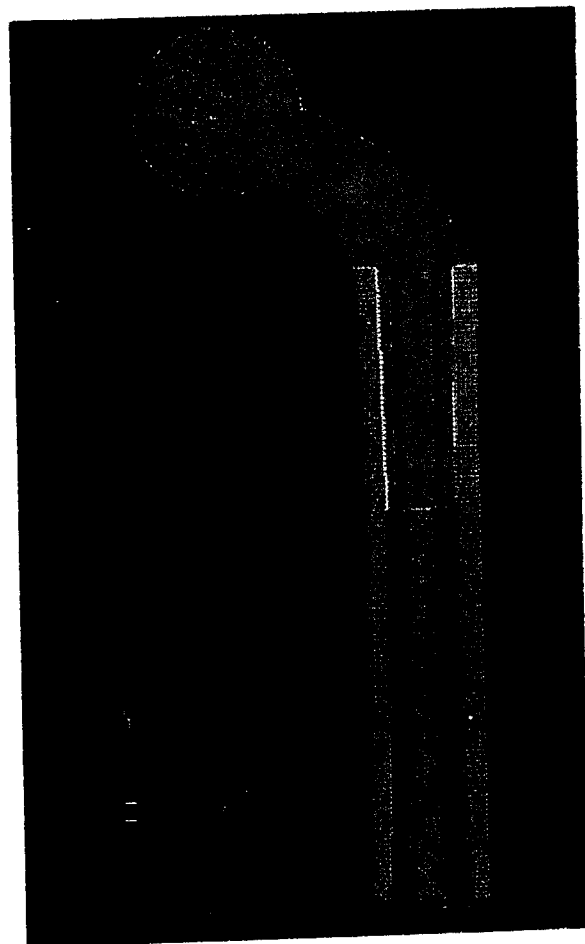
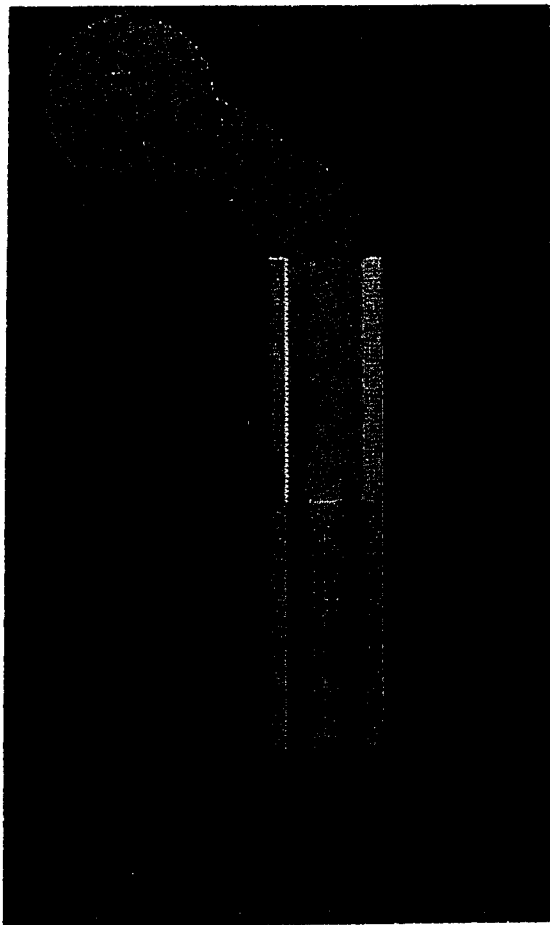


Figure 3.2.1-29. Titanium Insert Geometries (Design Iterations II and III).

the titanium ball. Again, the compressive load condition was assessed. A sensitivity study was conducted to determine the effect of assumed areas of contact. Figure 3.2.1-30 shows where multipoint constraints were put into the model to simulate contact. At the lip where the titanium insert abuts the composite shaft, the 180 degrees of contact are connected axially. Along the shaft, radial multipoint constraints have been included for 180 degrees on the top front surface, and for 180 degrees on the bottom back surface.

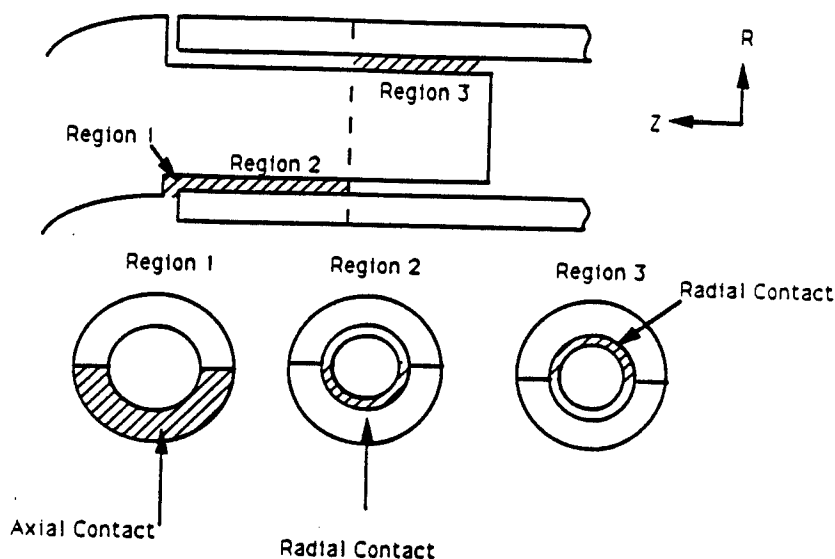


Figure 3.2.1-30. Regions of Contact in Femur Insert Finite Element Model.

Because an initial analytical run had shown the titanium to exceed the yield strength of (140 ksi 965 MPa) a stress-strain curve was added to the model to determine the extent of plastic strain. These results showed that the titanium stem does yield a small amount (equivalent plastic strain of 0.0022 in./in.), the Von Mises stress reached 142.6 ksi (983 MPa), and a maximum residual displacement of 0.0034 inches (.086mm) was present after unloading. This small amount of plasticity should not be alarming, however, the composite stem had a negative strain margin of safety of -0.119 in the 0 degree ply direction at the titanium insert lip. The compressive strain to failure was exceeded at this critical bearing region.

In order to rectify this problem, a third titanium insert design/analysis iteration was made. This geometry is shown along side of Design II in Figure 3.2.1-29. The outer diameter of the lip region was increased from 1.2 inches (30.48mm) to 1.3 inches (33.02mm). Thus, the composite material is thicker in this region with a larger cross sectional area to combat the state of compressive strain. Additionally, the outer diameter of the titanium stem was increased to 1.3 inches (33.02mm) to match up to the composite shaft of the lip. The weight penalty from iteration 2 to iteration 3 was only 0.07 lbs. (0.032 Kg).

Again, the compressive load condition was run. This time, the composite stem showed all positive strain margins of safety. At the critical bearing lip region, the compressive axial strain dropped to -0.0091 in./in. (Figure 3.2.1-31). The Von-Mises stress distribution in the titanium stem is shown in Figure 3.2.1-32 and shows a maximum of 141.5 Ksi (975 MPa). The titanium yields slightly, with a maximum equivalent plastic strain of 0.0012 in./in. The residual displacement (upon unloading) is only 1.27 mils (.032mm) (Figure 3.2.1-33).

Since the baseline femur compressive design load magnitude has a factor of 1.5 over the HYBRID III ultimate loads, the small amount of plasticity predicted in the titanium should not drive the design to a thicker configuration. The goal has been to design this component with a zero margin of safety (considering the factor of 1.5), and while the composite stem has a strain margin of safety of 0.1, the titanium insert margin is very close to zero (albeit slightly negative).

Full 3-D Femur Finite Element Modeling

The geometry in iteration III was added to the full 3-D femur F.E.M., and all load conditions assessed. The baseline load conditions (Figure 3.2.1-34) were applied to the F.E.M. separately. The stress/strain results and corresponding strain margins of safety for all load cases are shown in Table 3.2.1-3. Stresses were expected to be high around the bolt hole since the bolt hole is the only area used to react to the applied load. However, the real boundary condition has a larger surface area than just the bolt hole, thus these series of analyses were conservative.

The material architecture layup for the FEM femur bone is shown in Figure 3.2.1-35. This preliminary layup schematic was used to determine the critical locations of different load cases so subsequent layups could be used to modify, if necessary, any regions of high stress and strain.

Tension

Analysis of the 4500 lb (2041 Kg) tension load shows stresses and strains to be below allowables. The minimum fiber strain margin of safety (MS) in axial (0°) direction is 2.47 . Axial fiber stress and strain color contour plots are shown in Figures 3.2.1-36 and 3.2.1-37. The tension load case is one of the mildest load cases. The deformed shape is shown in Figure 3.2.1-38 with a maximum axial deflection of 0.19 inches (4.83mm).

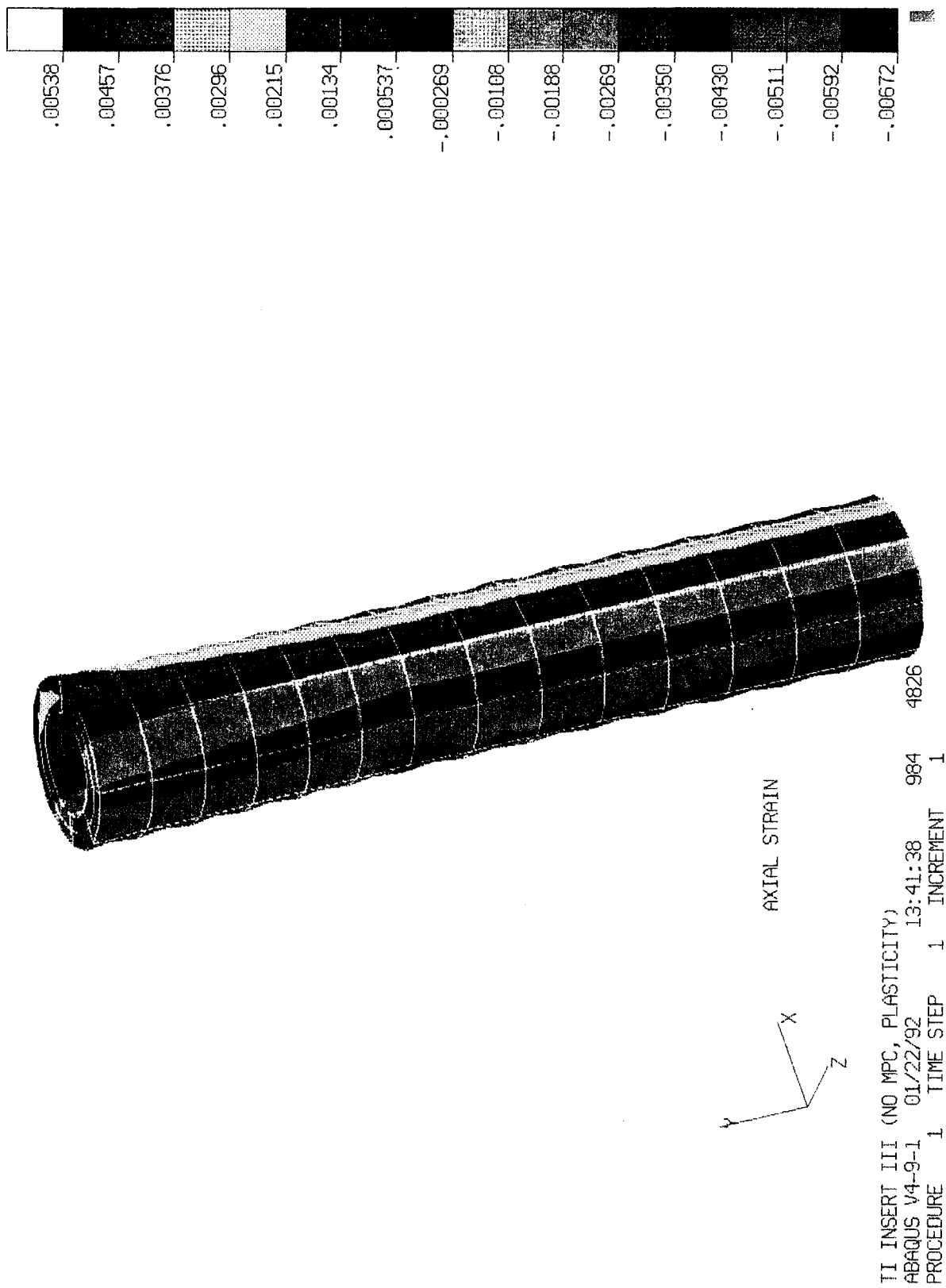
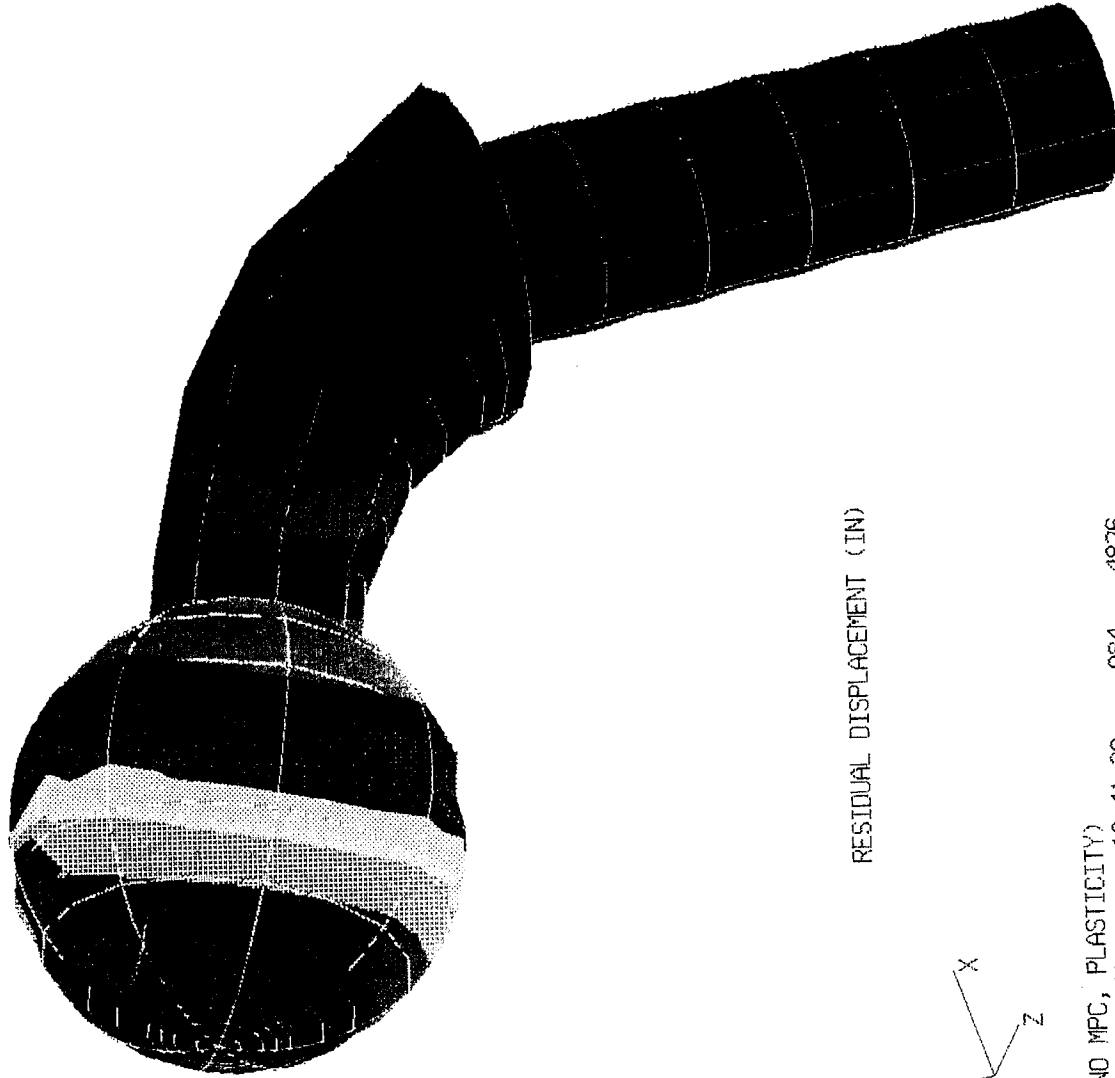
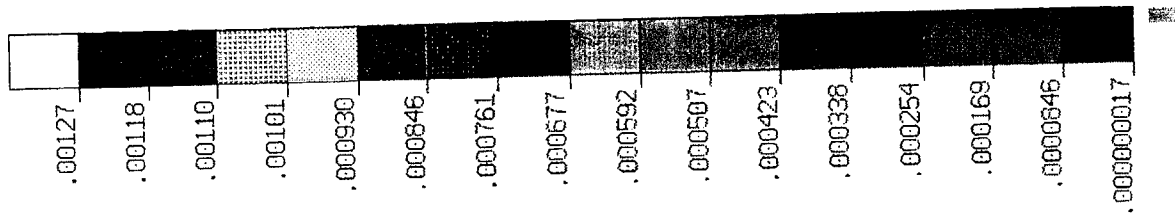


Figure 3.2.1-31. Axial Strain in Composite Stem under Compressive Load (Design Iteration III).



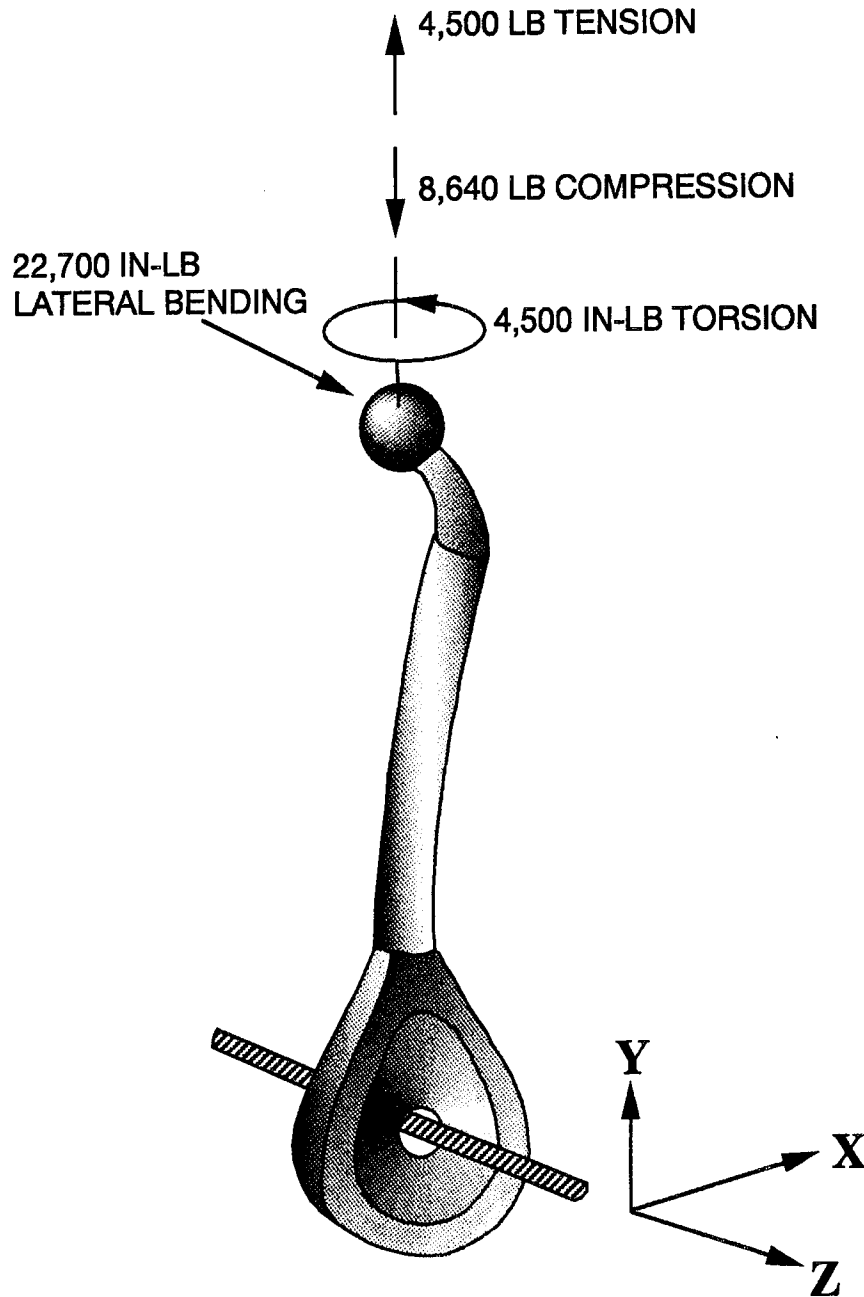
Figure 3.2.1-32. Von-Mises Stress in Titanium Insert under Compressive Load (Design Iteration III).



RESIDUAL DISPLACEMENT (IN)

TI INSERT III (NO MPC, PLASTICITY) 13:41:38 964 4826
 ABAQUS V4-9-1 01/22/92
 PROCEDURE 1 TIME STEP 2 INCREMENT 1

Figure 3.2.1-33. Residual Displacement in Titanium Insert (Design Iteration III).



* EACH LOAD CASE IS APPLIED SEPARATELY

Figure 3.2.1-34. Femur Design Loads and Boundary Condition.

Table 3.2.1-3. Femur Fiber Stress, Strain, and MS and Titanium Insert Von Mises Stress Summary Table

LOAD CASE	FEMUR MAXIMUM STRESS/STRAIN RESULTS							
	0° FIBER STRESS		0° FIBER STRAIN		± 45° FIBER STRESS		± 45° FIBER STRAIN	
	(ksi)		(in/in)		(ksi)		(in/in)	
TENSION	MAX. COMP	26.0	0.0018		14.2		0.0007	
	MAX. TEN	38.0	0.0026		17.4		0.0007	
COMPRESSION	MAX. COMP	74.0	0.0050		33.4		0.0013	
	MAX. TEN	50.0	0.0034		27.3		0.0014	
LATERAL BENDING	MAX. COMP	138.9	0.0078		76.5		0.0041	
	MAX. TEN	174.6	0.0098		92.1		0.0084	
TORSION	MAX. COMP	17.6	0.0018		20.8		0.0033	
	MAX. TEN	6.7	0.0006		7.0		0.0008	
FEMUR FIBER STRAIN MARGIN OF SAFETY				VON MISES STRESS IN THE TITANIUM INSERT				
	0° FIBER	±45° FIBER	90° FIBER					
TENSION	2.47	>5	>5					
COMPRESSION	0.81	>5	0.81					
LATERAL BENDING	0.28	0.48	0.69					
TORSION	4.08	1.70	>5					

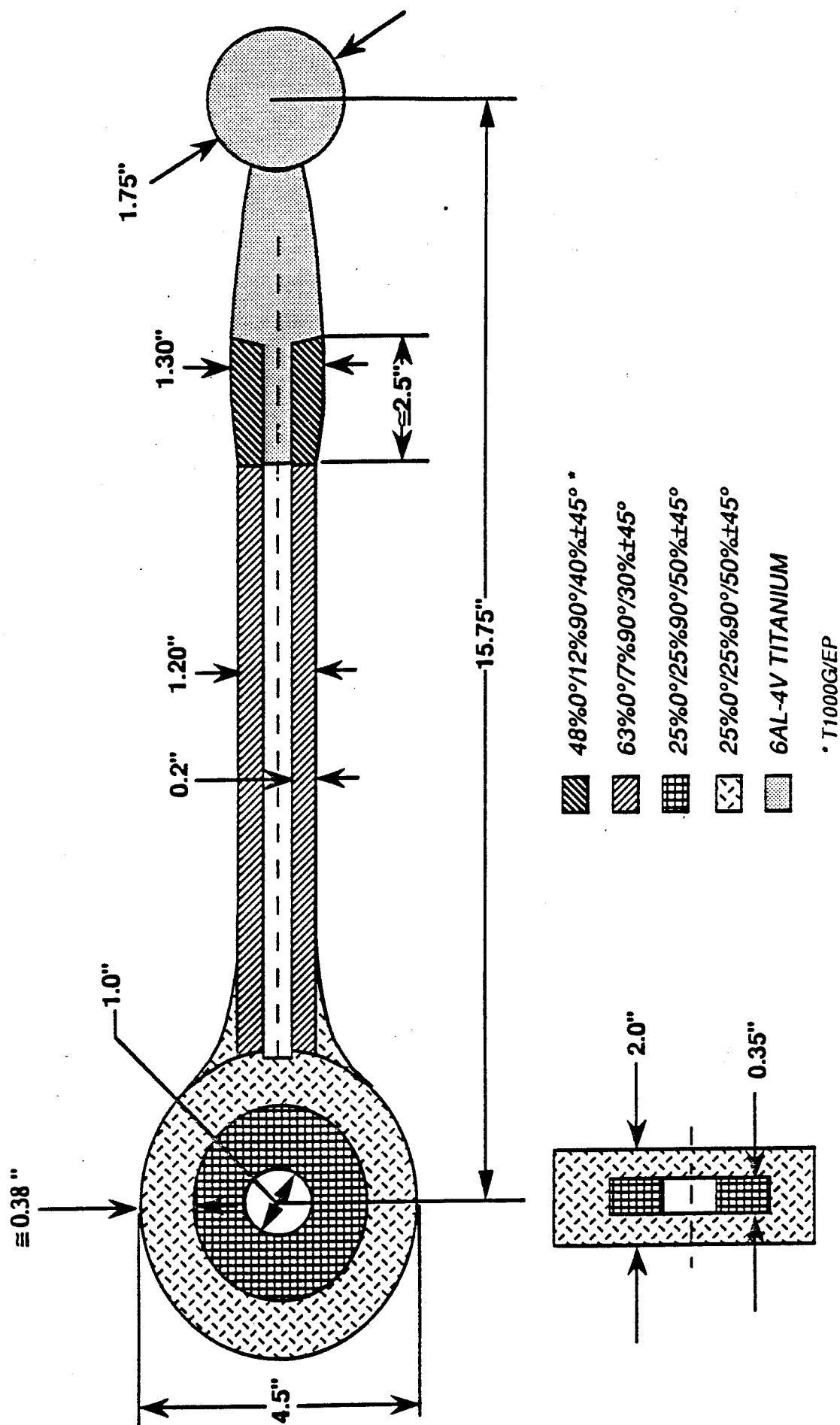


Figure 3.2.1-35. ABAQUS Femur Layout Schematic (not to scale).

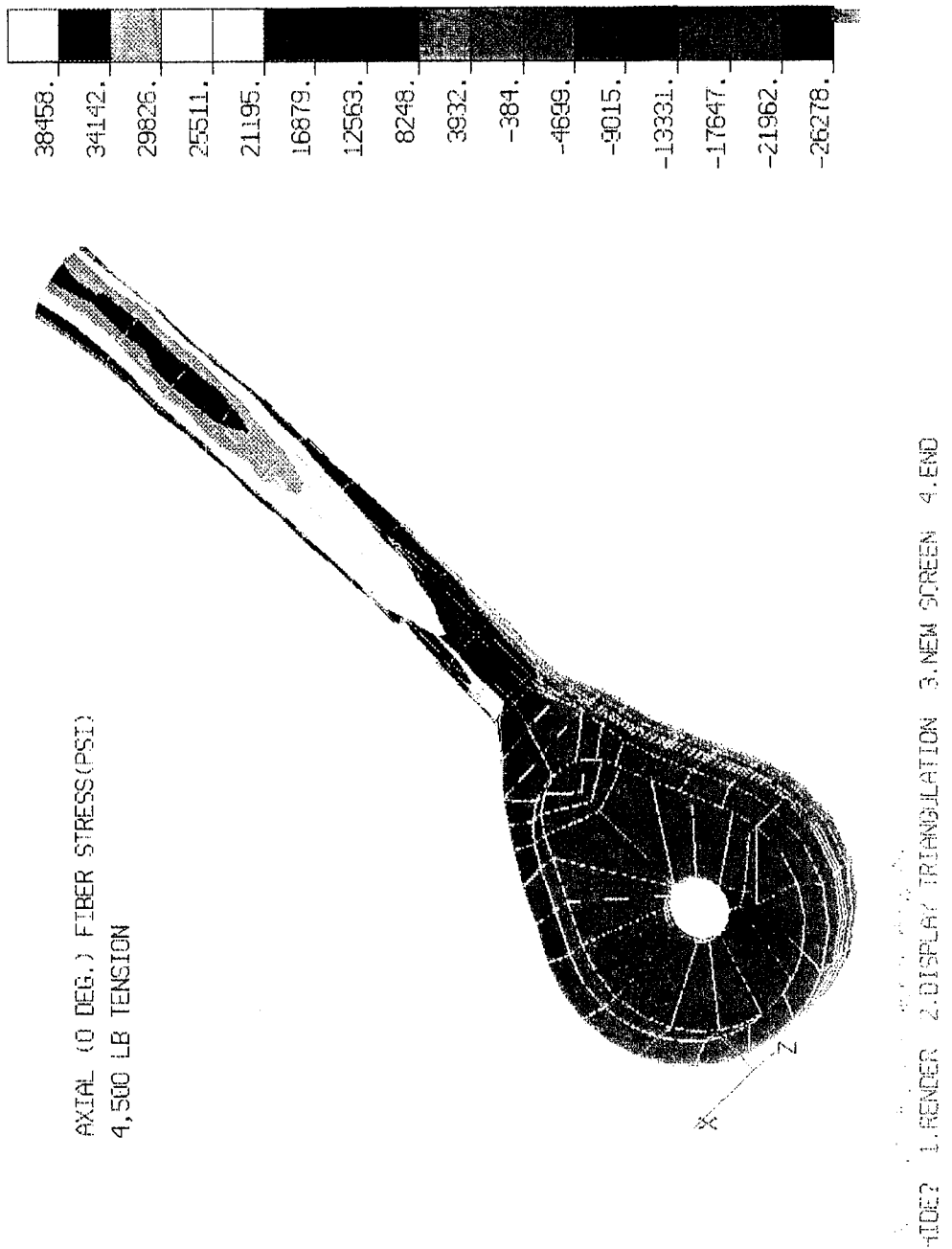


Figure 3.2.1-36. Femur Axial (0 Degree) Fiber Stress (psi) Under 4,500 lb Tension Load.

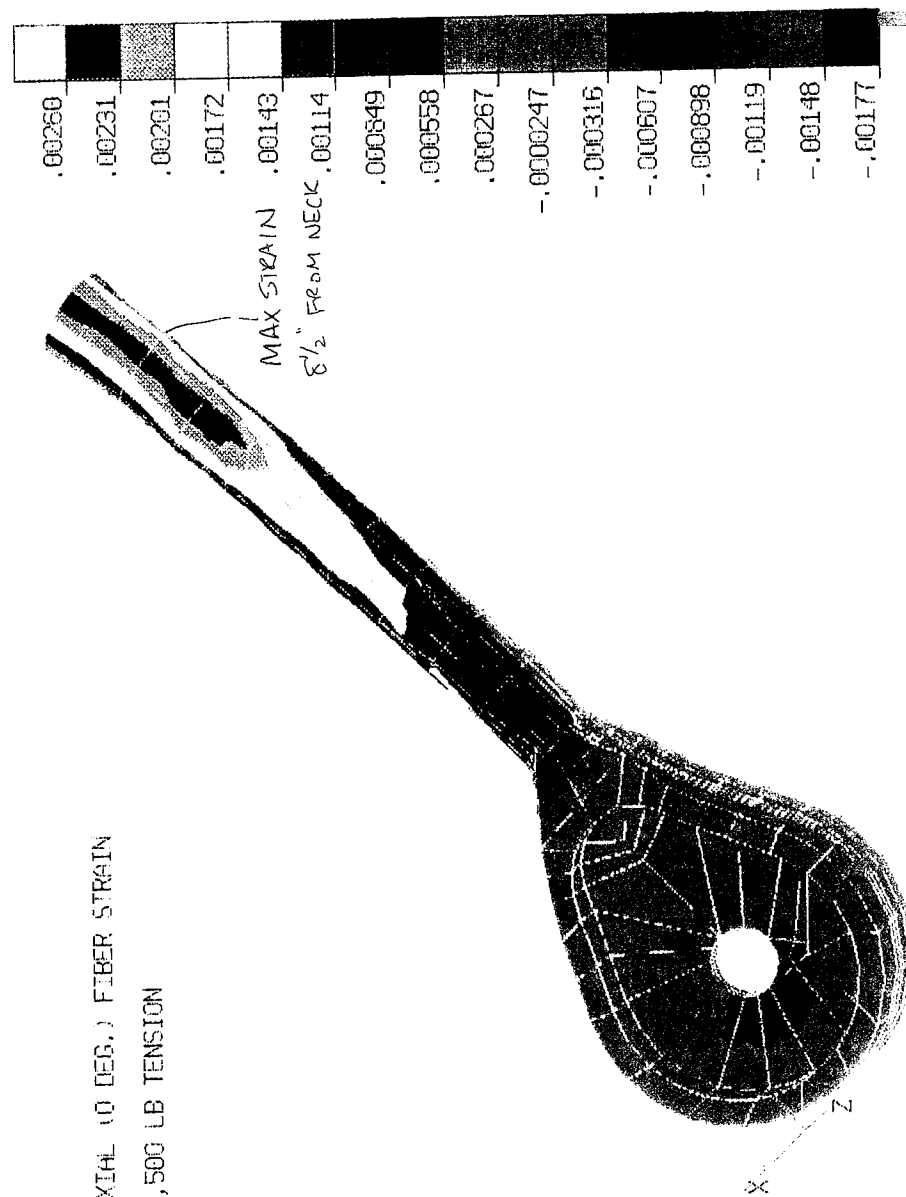
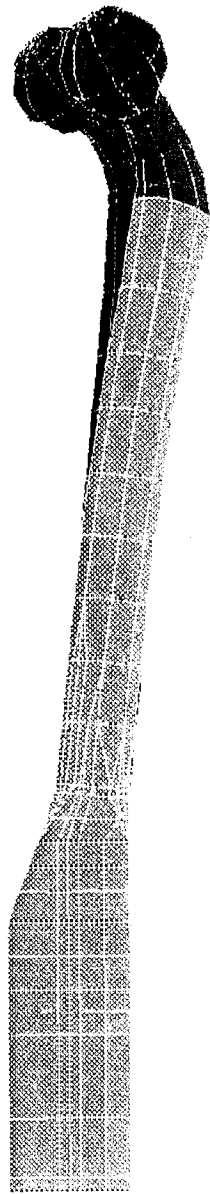


Figure 3.2.1-37. Femur Axial (0 Degree) Fiber Strain (in./in.) Under 4,500 lb Tension Load.



DEFORMED SHAPE (SF=5)

FEMUR LAYUP #1 4500 LB TENSION
 ABAQUS V4-9-1 02/19/92 17:46:10 737 3715
 PROCEDURE 2 TIME STEP 1 INCREMENT 1
 5. INTERFACE 6. STOP 7. PDA_PCL 8. USER_MENU

Figure 3.2.1-38. Femur Deformed Shape (Scale Factor = 5) Under 4,500 lb Tension Load.

Compression

The deformed shape plotted over the undeformed F.E.M. of the femur bone structure under 8640 lb (3918 Kg) compression load is shown in Figure 3.2.1-39. Because of the combined bending and compression loads due to a two inch (50.8mm) offset from the centerline of the femur long bone, high stresses and strains occur around the proximal titanium insert area. However, as discussed previously, the stress and strain magnitudes are acceptable at this location. Stress, strain, and margin of safety plots of the femur structure are shown in Figures 3.2.1-40 to 3.2.1-42. Minimum axial strain fiber margin of safety is 0.8. The maximum axial deflection under the compression load is 0.39 inches (9.9mm).

Lateral Bending

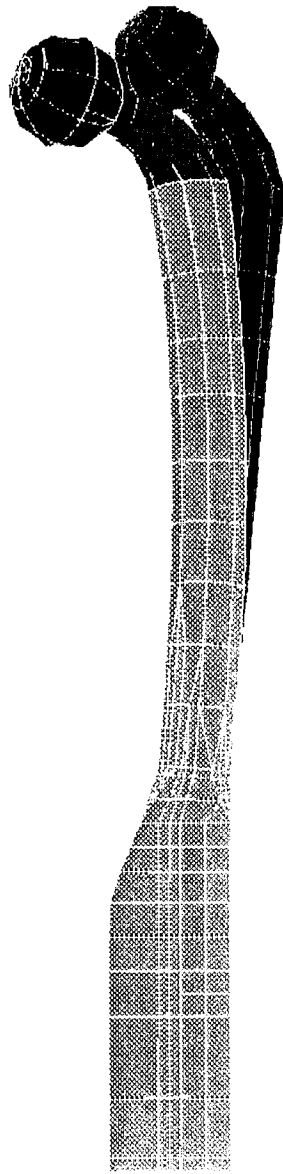
Lateral bending was found to be the most severe load case. Since the load moment arm is the whole length of the femur bone and the reaction is only at the bolt hole, stresses and strains were expected to be high and centralized around the bolt hole and bone-knee transition areas (Figures 3.2.1-43 to 3.2.1-45). Minimum margins of safety in all directions - especially in axial (0°) fiber (0.28) are lower than all other load cases. By using the bolt hole alone to react the whole lateral bending load application, the total lateral deflection is high and may be unrealistic (2.85 inches (72.4mm)) (Figure 3.2.1-46). An additional analysis was conducted for the same load case by adding spacer block constraints on both sides of the bolt hole and the lateral deflection came down to 1.67 inches (42.4mm).

Torsion

Torsional load is applied by applying force at the titanium ball about the axial axis of the femur bone and reacting at the bolt hole. The maximum stresses and strains are localized at the knee-bone transition and bolt hole locations. The computed angle of twist is 0.14 radians (8 degrees). Deformed shape, stress, and strain plots are presented in Figures 3.2.1-47 to 3.2.1-48

Conclusion

Figures 3.2.1-50 to 3.2.1-53 show the Von Mises stress of the titanium insert for all load cases. All load cases have stress levels below the titanium strength (140 Ksi) except for the compression load case which has a maximum stress of 144 Ksi. However, as previously mentioned, this small amount of very localized plasticity in the titanium should not be alarming



DEFORMED SHAPE (SF=5)

K Y
 FEMUR LAYUP #1 8640 LB COMPRESSION 737 3715
 ABAQUS V4-9-1 02/19/92 17:34:40
 PROCEDURE 2 TIME STEP 1 INCREMENT 1
 5. INTERFAC 6.501P 7. FUL FOL 8. OVER PENJ

Figure 3.2.1-39. Femur Deformed Shape (Scale Factor = 5) Under 8,640 lb Compression Load.

AXIAL (0 DEG.) FIBER STRAIN
8,640 LB COMPRESSION

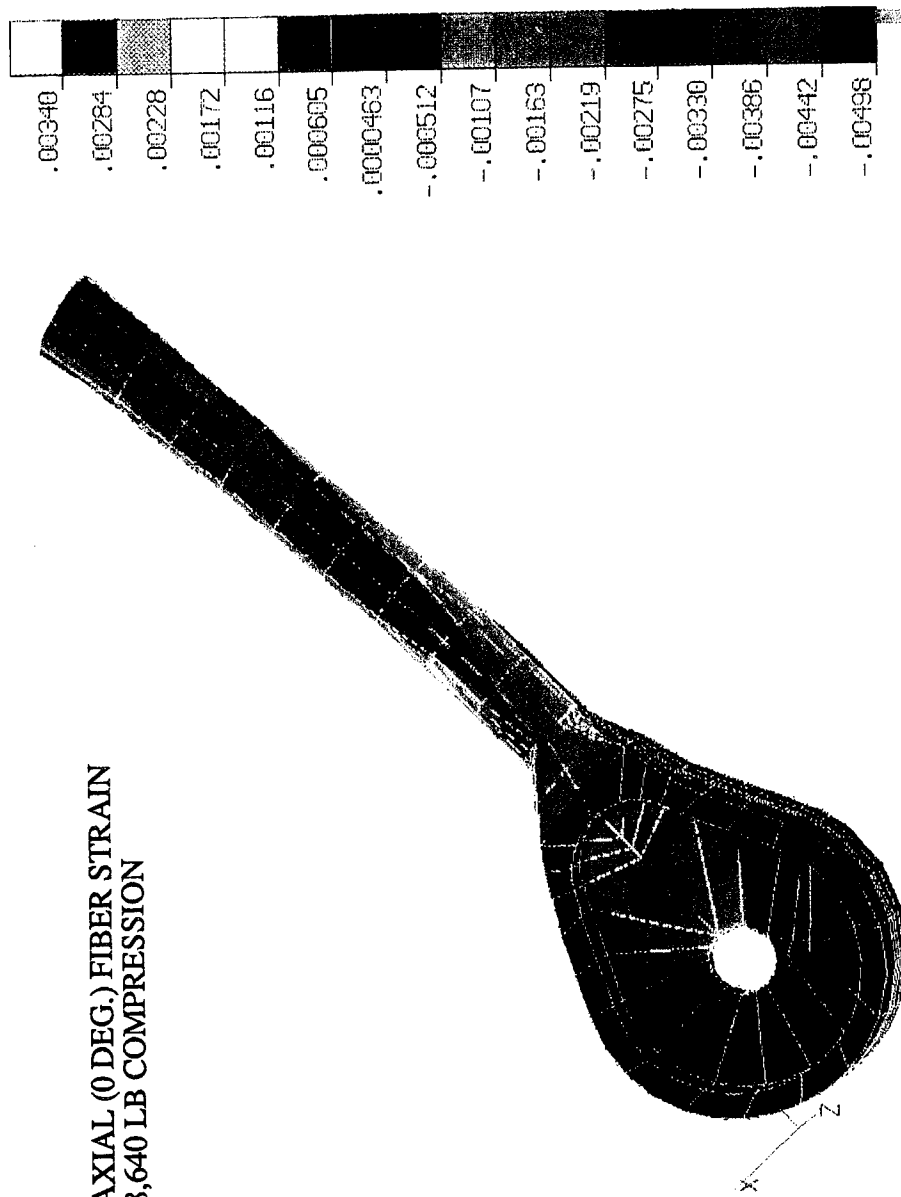
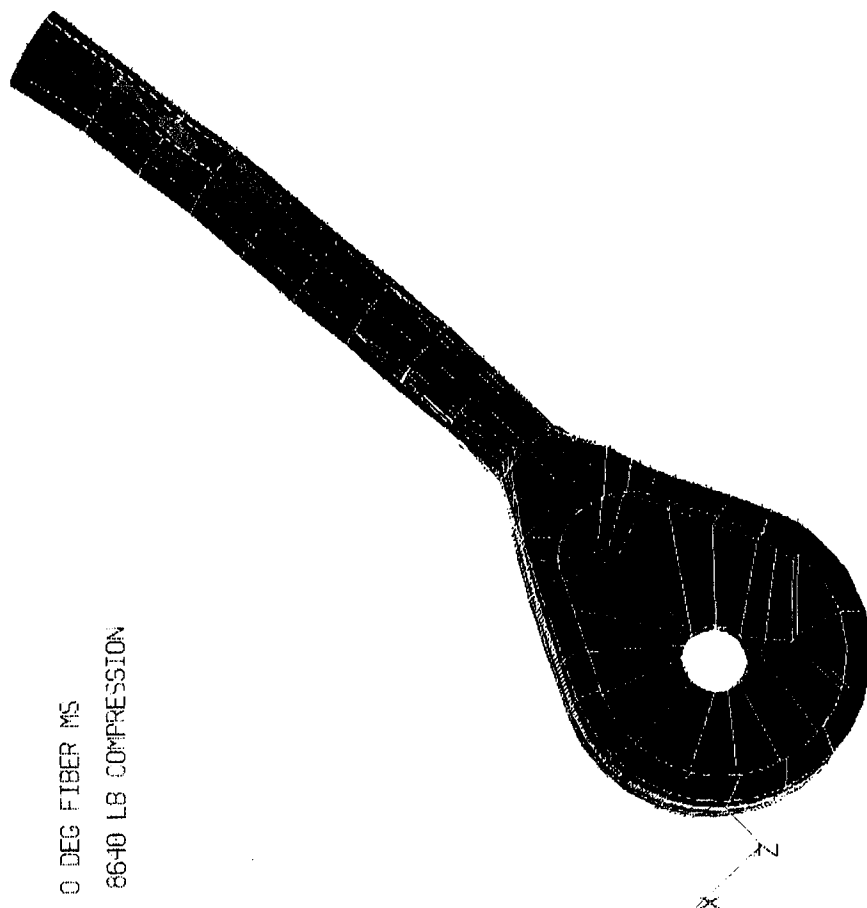
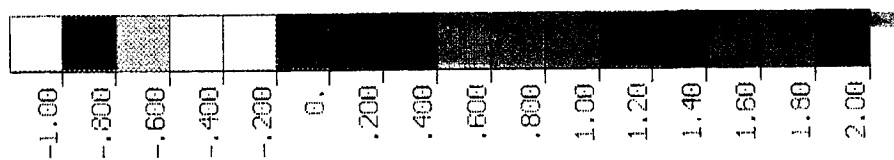


FIGURE 3.2.1-40. FEMUR AXIAL (0 DEGREE) FIBER STRAIN (IN./IN.) UNDER 8,640 LB COMPRESSION LOAD.

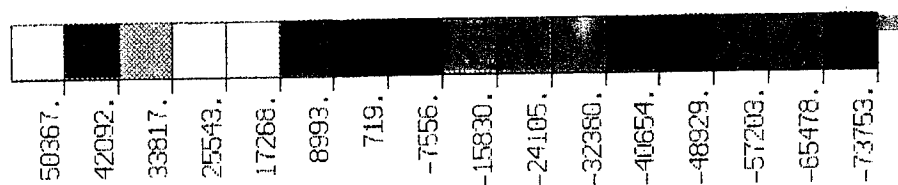
Figure 3.2.1-40. Femur Axial (0 Degree) Fiber Strain (in./in.) Under 8,640 lb Compression Load.



MIN MS = 0.81

5. CURRENT LEVELS STRESS

Figure 3.2.1-41. Femur Axial (0 Degree) Fiber Margin of Safety Under 8,640 lb Compression Load.



AXIAL (0 DEG.) FIBER STRESS(PSI)
8,640 LB COMPRESSION

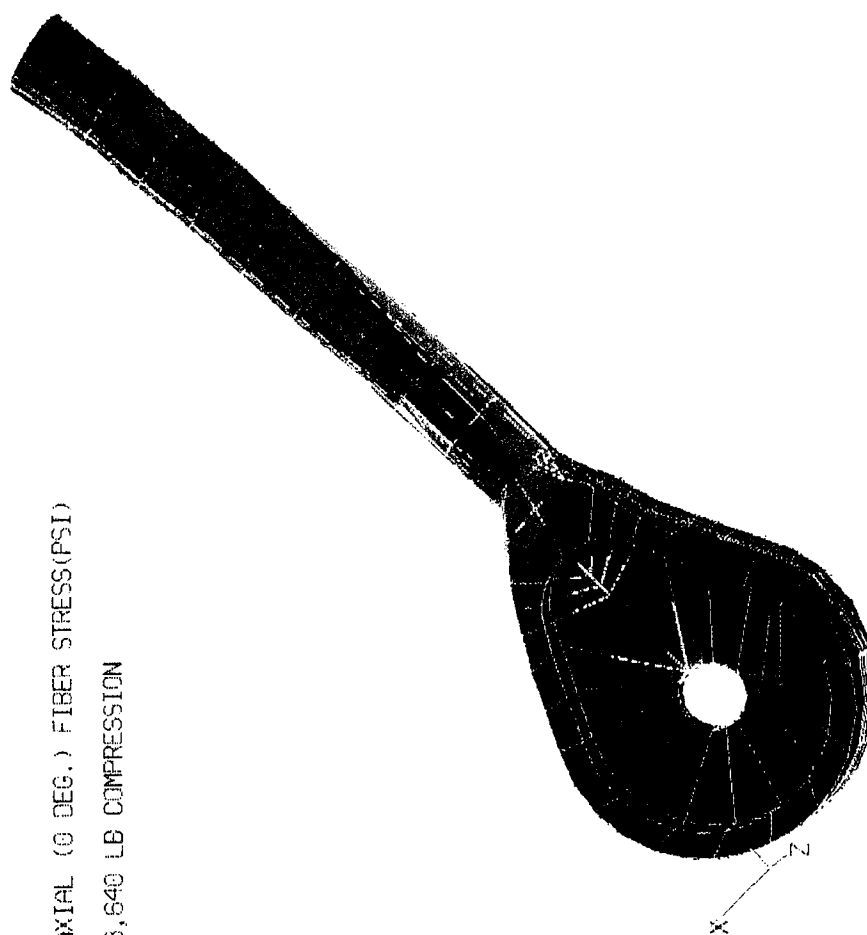


FIGURE 3.2.1-42. 6 FEMUR AXIAL (0 DEGREE) FIBER STRESS (PSI) UNDER 8,640 LB COMPRESSION LOAD.
HIDE? 1.RENDER 2.DISPLAY TRIANGULATION 3.NEW SCREEN 4.END

Figure 3.2.1-42. 6 Femur Axial (0 Degree) Fiber Stress (psi) Under 8,640 lb Compression Load.

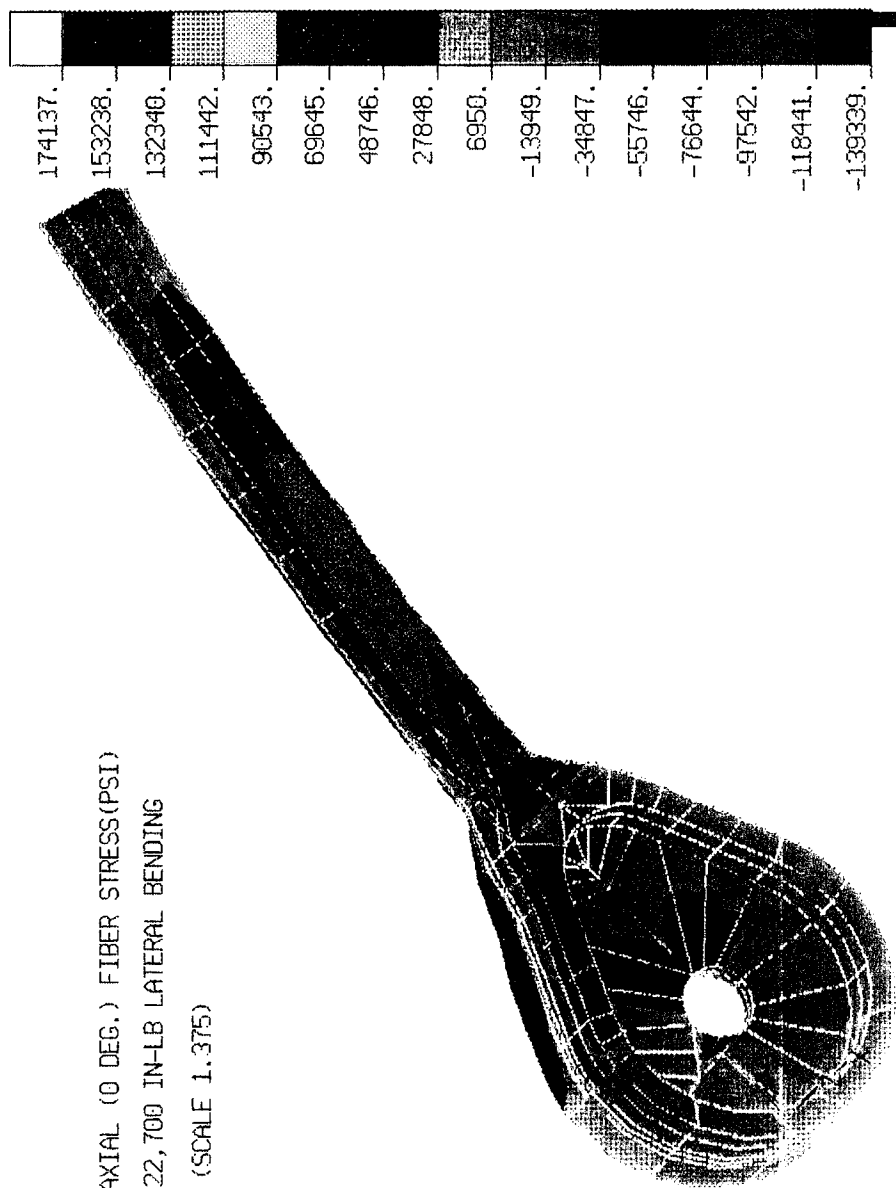


Figure 3.2.1-43. Femur Axial (0 Degree) Fiber Stress (psi) Resulted From 22,700 in.-lb Lateral Bending Load.

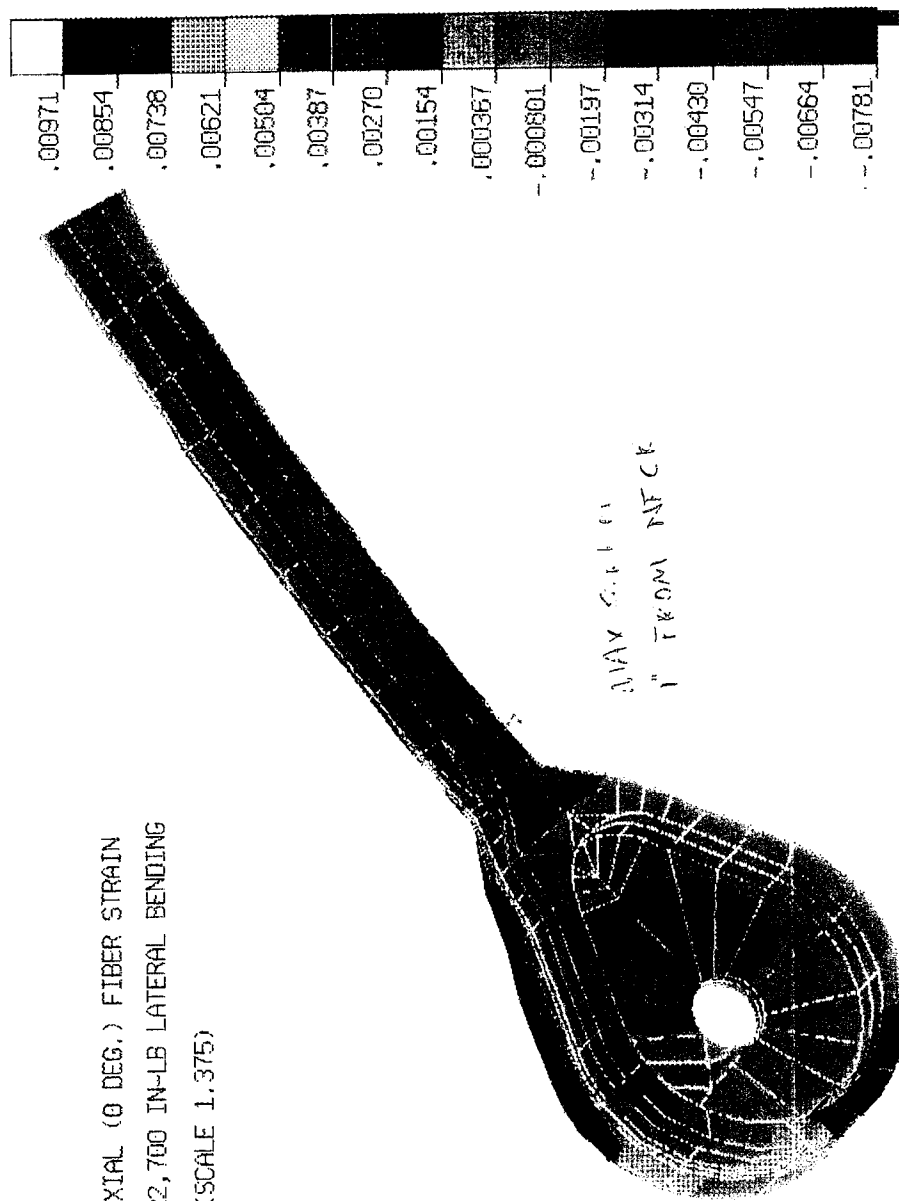
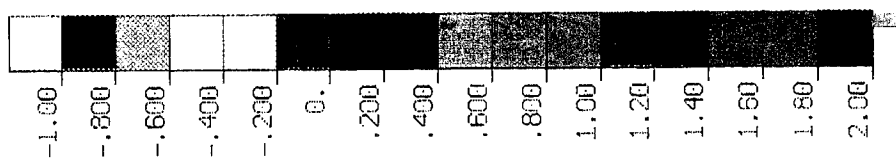
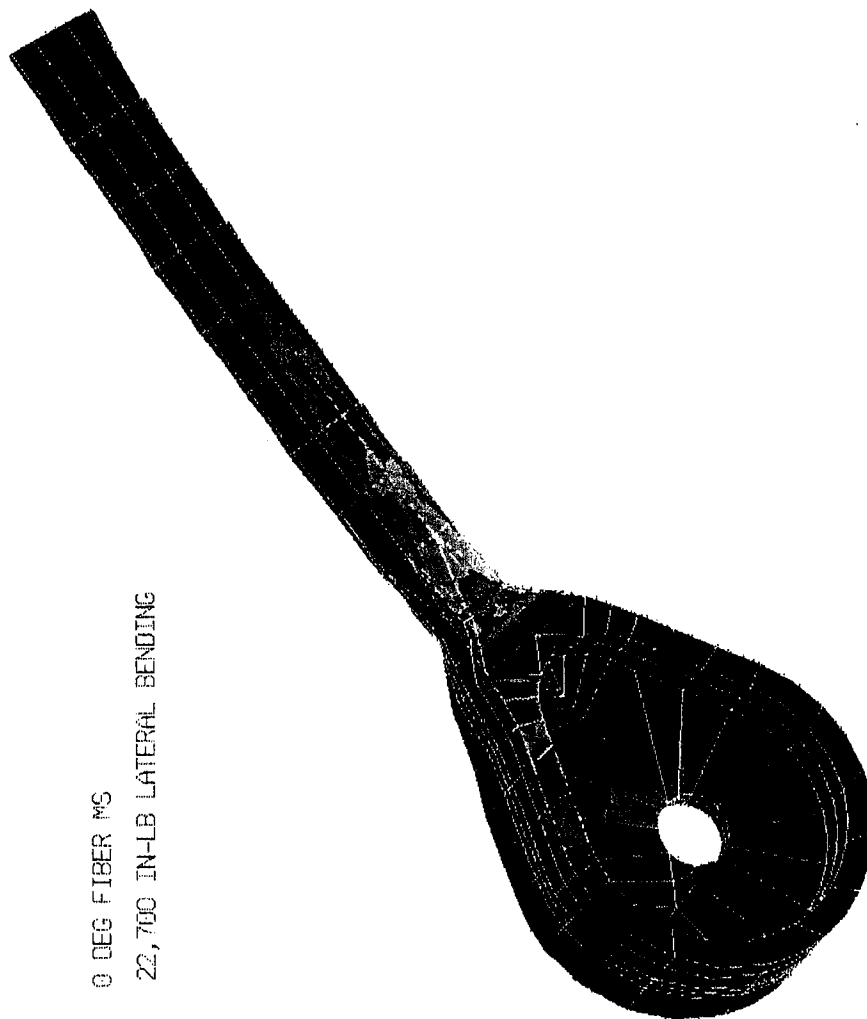


Figure 3.2.1-44. Femur Axial (0 Degree) Fiber Strain (in./in.) Resulted From 22,700 in.-lb Lateral Bending Load.

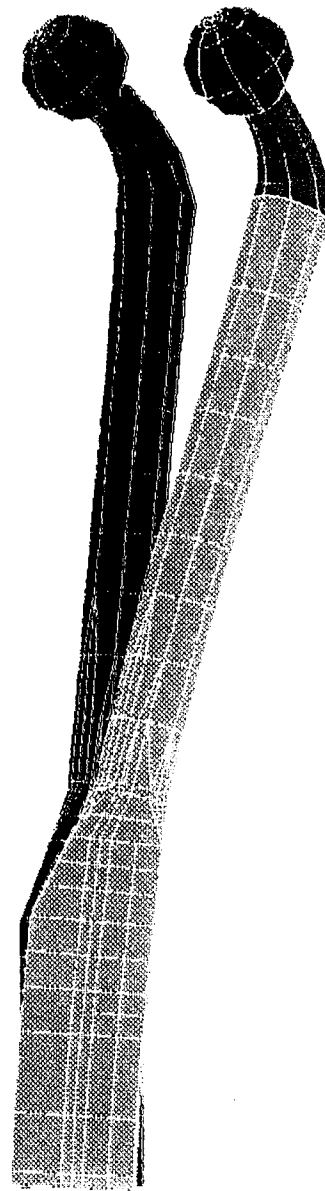


0 DEG FIBER MS
22,700 IN-LB LATERAL BENDING



HIDE? RENDER 2-DISPLAY TRIANGULATION 3-NEW SCREEN 4-FWI

Figure 3.2.1-45. Femur Axial (0 Degree) Fiber Margin of Safety Resulted From 22,700 in.-lb Lateral Bending Load.



DEFORMED SHAPE (SF=1)

K Y

FEMUR LAYUP #1 22,700 IN-LB LATERAL BENDING 3715
 ABAGUS V4-9-1 02/20/92 08:44:58 736
 PROCEDURE 2 TIME STEP 1 INCREMENT 1
 5, INTERFACE 6, STOP 7, PDA, POL 8, USER_MENU

Figure 3.2.1-46. Femur Deformed Shape (Scale Factor = 1) Resulted From 22,700 in.-lb Lateral Bending Load.

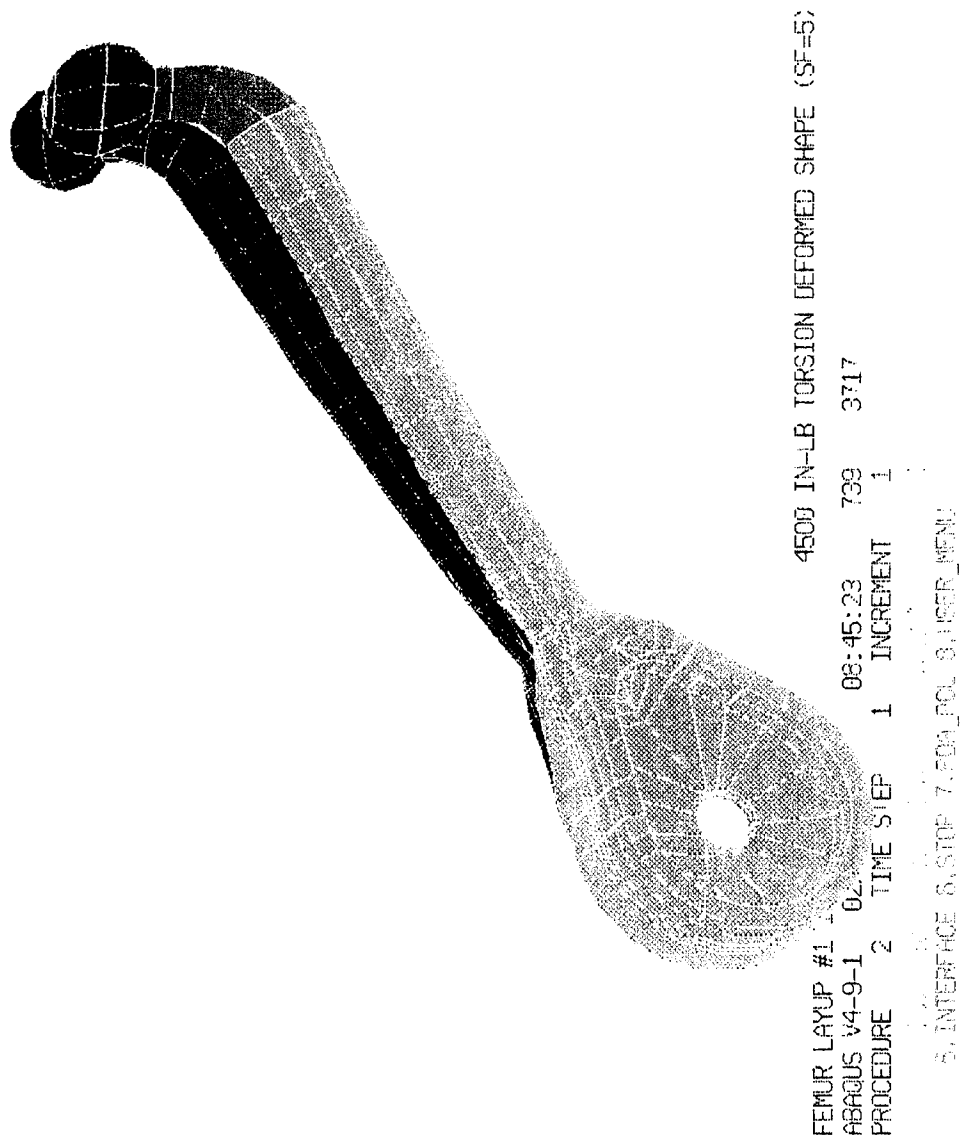
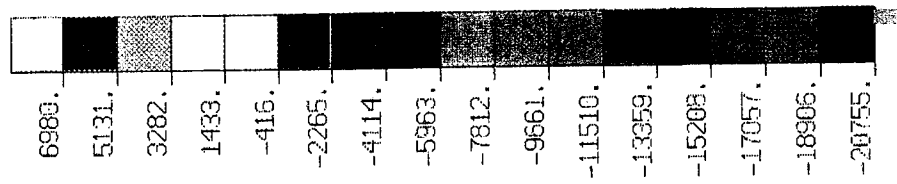
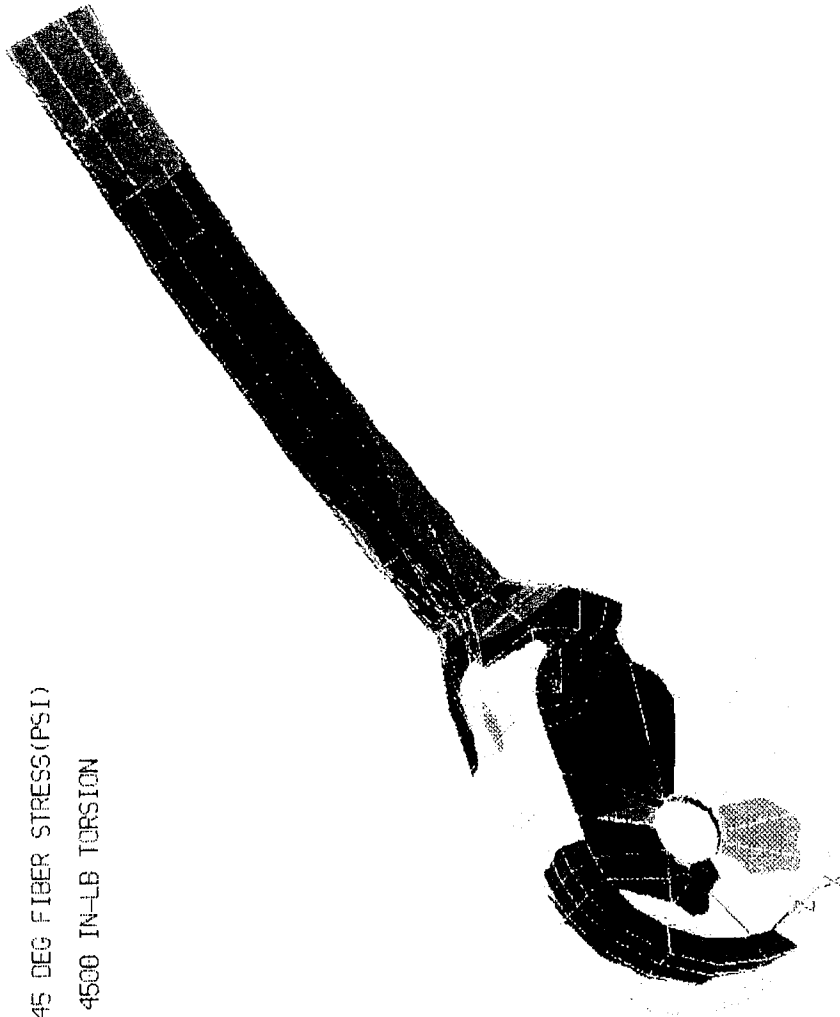


Figure 3.2.1-47. Femur Deformed Shape (Scale Factor = 5) Resulted From 4,500 in.-lb Torsion.



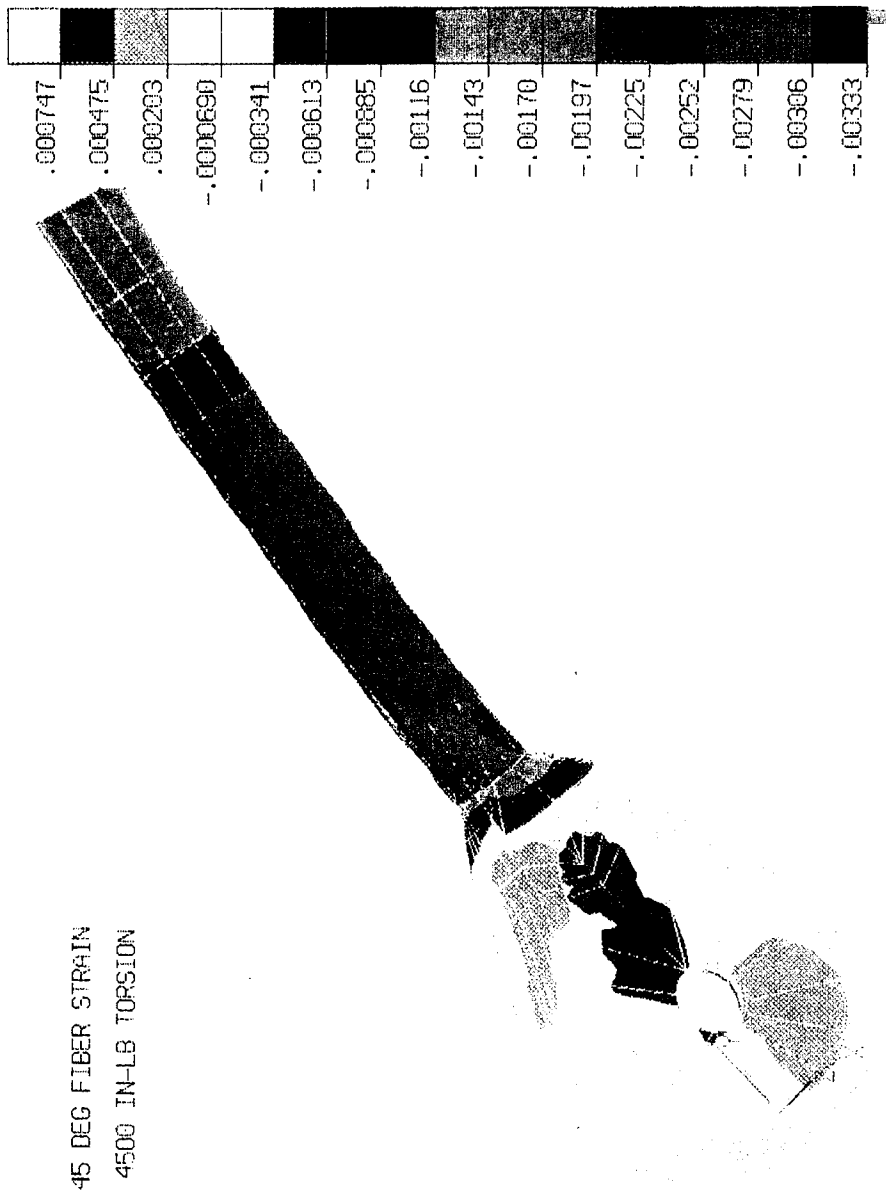
45 DEG FIBER STRESS(PSI)
4500 IN-LB TORSION



3D FEMUR 2-DISPLAY DEFORMATION AND STRESS (PSI)

Figure 3.2.1-48. Femur 45 Degree Fiber Stress (psi) Resulted From 4,500 in.-lb Torsion.

45 DEG FIBER STRAIN
4500 IN-LB TORSION



FILE? 1.FEMUR 2.DISPLAY TRIANGULATION 3.HELP 4.EXIT

Figure 3.2.1-49. Femur 45 Degree Fiber Strain (in./in.) Resulted From 4,500 in.-lb Torsion.

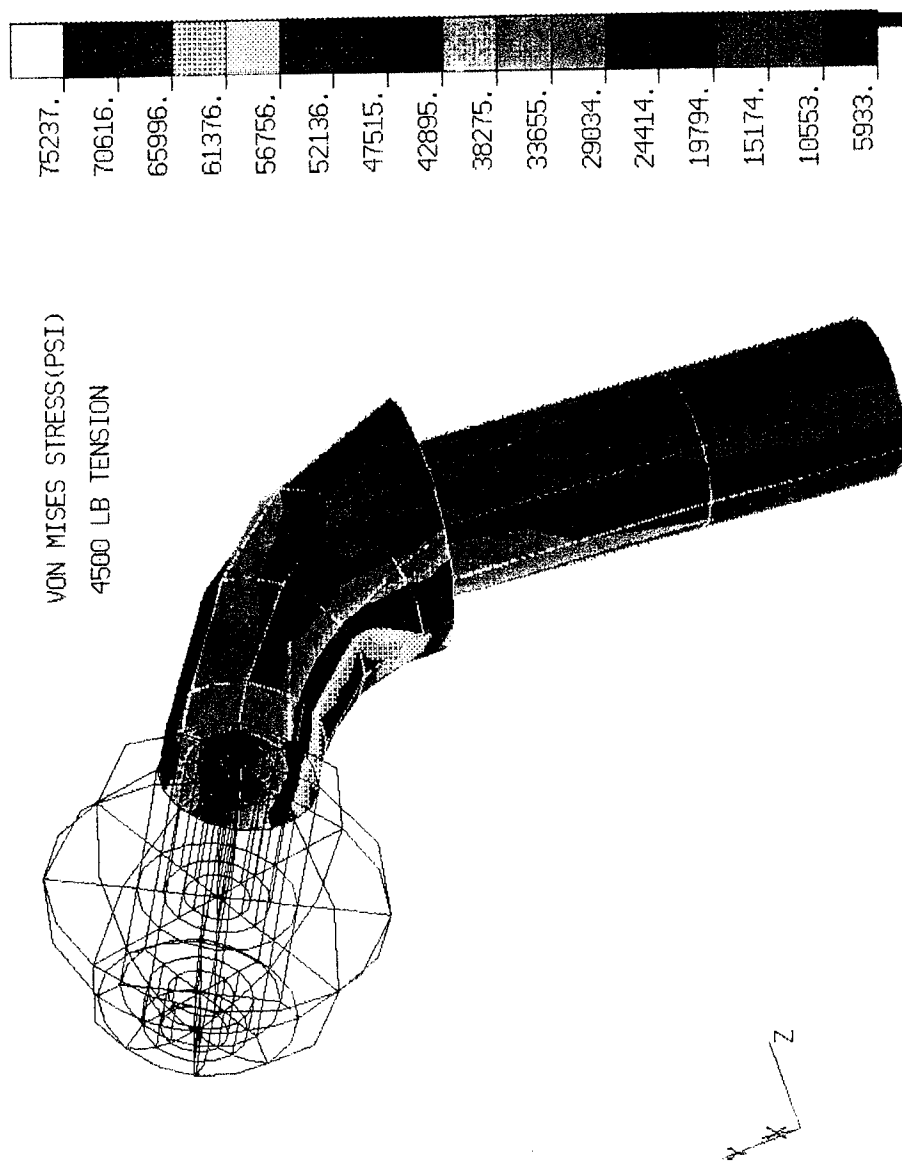
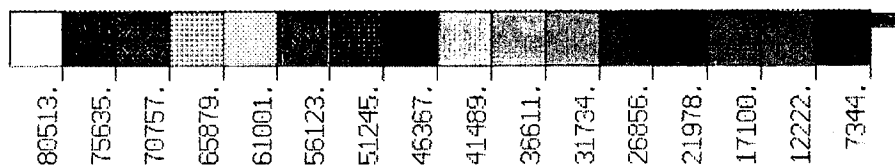


Figure 3.2.1-50. Von Mises Stress (psi) of the Titanium Insert Resulted From 4,500 lb Tension Load.



VON MISES STRESS(PST)
4500 IN-LB TORSION

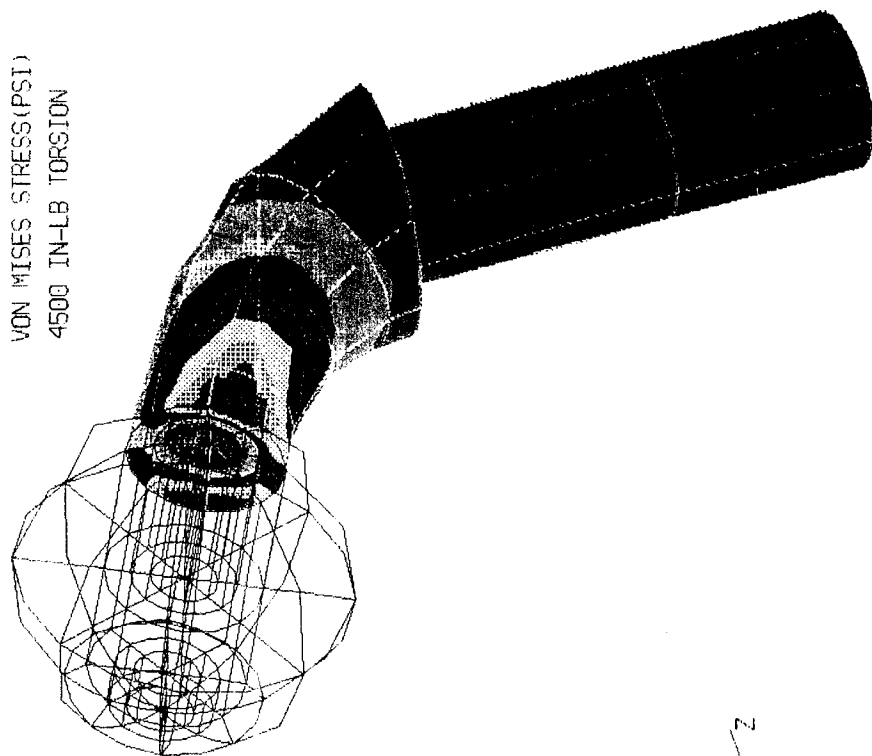


Figure 3.2.1-53

INTERFERENCE FIT STEP 1, PLD, PL 8, 10, 11, 12, 13, 14, 15, 16, 17, 18, 19, 20, 21, 22, 23, 24, 25, 26, 27, 28, 29, 30, 31, 32, 33, 34, 35, 36, 37, 38, 39, 40, 41, 42, 43, 44, 45, 46, 47, 48, 49, 50, 51, 52, 53, 54, 55, 56, 57, 58, 59, 60, 61, 62, 63, 64, 65, 66, 67, 68, 69, 70, 71, 72, 73, 74, 75, 76, 77, 78, 79, 80, 81, 82, 83, 84, 85, 86, 87, 88, 89, 90, 91, 92, 93, 94, 95, 96, 97, 98, 99, 100

Figure 3.2.1-53. Von Mises of the Titanium Insert Resulted From 4,500 in.-lb Torsion.

since the applied compression load magnitude has a factor of 1.5 over the HYBRID III ultimate loads. For all load cases, the carbon graphite fiber stresses and strains are below allowables and margins of safety are positive (Table 3.2.1-4). Thus, a femur long bone segment has been designed that satisfies all structural requirements.

Table 3.2.1-4. Femur Structural Analysis Results Summary

LOAD CASE	FIBER STRAIN MARGIN OF SAFETY			INSERT MARGIN OF SAFETY
	0 ° FIBER	+ - 45 ° FIBER	90 ° FIBER	TITANIUM
TENSION	+ 2.47	> 5	> 5	+ 0.87
COMPRESSION	+ 0.81	> 5	+ 0.81	- 0.01*
BENDING	+ 0.28	+ 0.48	+ 0.69	+ 4.19
TORSION	+ 4.08	+ 1.70	> 5	+ 0.75

* VON-MISES STRESS = 141.6 KSI (STRENGTH OF TITANIUM = 140 KSI)

- ANALYSIS PREDICTS VERY LOCAL PLASTIC STRAIN OF 0.0012 In./In.

- THE RESIDUAL DISPLACEMENT (UPON UNLOADING) IS 1 MIL

REMEMBER: COMPRESSIVE DESIGN LOAD HAS A FACTOR OF SAFETY OF 1.5

3.2.2 Tibia Analysis

The design of the tibia long bone is shown in Figure 3.2.2-1. The initial design cross-section was derived by performing closed form analyses based on classical beam theory. The outer radius of the tibia long bone is 1/2 " (12.7mm) and the inner radius is 3/8" (9.53mm). The clevis knee joint was designed to fit in the existing tibia joint design using high, specific strength graphite fiber/epoxy composite cloth. Similarly, the ankle joint was designed to ensure a correct interface to attach the existing Hybrid III foot/ankle to the new tibia.

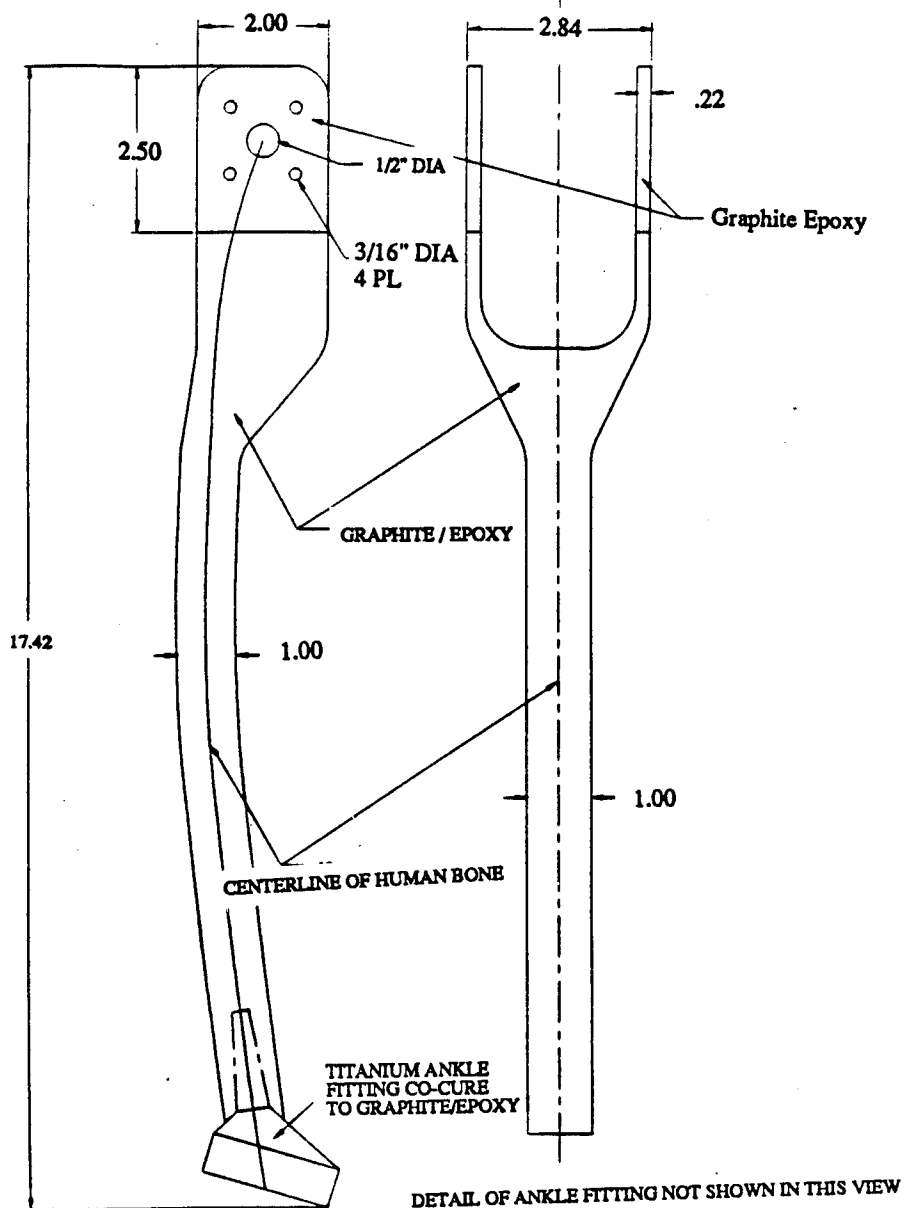


Figure 3.2.2-1. Preliminary Design of the Tibia Long Bone.

Prior to developing a detailed 3-D finite element model of the tibia long bone, preliminary analyses were done by using finite element beam models with appropriate cross-section geometry of the initial design. The beam elements can be modeled for the long bone section of the tibia quite well, however as was the case with the femur, beam theory is not accurate near the ends at the joint sections (i.e. knee and ankle joints). The beam model does accurately represent the diaphysis of the tibia and was used to determine whether the design cross-section would satisfy the design requirements.

Parametric analyses of various material lay-ups of T1000G/Epoxy is shown in **Table 3.2.2-1**. For simplicity, these material properties were modeled as pseudo-isotropic properties based upon ICAN computer code predictions. Two different lay-ups were used in this initial beam model analysis effort with the baseline lay-up being 70% 0°/20% ±45°/10% 90° and the first iteration lay-up being 50% 0°/40% ±45°/10% 90°. The iteration was necessary since the strain margin of safety using the baseline lay-up was low as will be discussed later.

Table 3.2.2-1. Parametric Analyses of Various Material Lay-ups of T1000G/Epoxy. Pseudo-Isotropic Elastic Properties Predicted by ICAN Computer Code

LAY-UP				
% 0°	% ±45°	% 90°	E (MSI)	G (MSI)
70	20	10	19.40	1.83
50	40	10	15.00	3.00
45	45	10	14.00	3.30
60	30	10	17.10	2.35
55	35	10	16.10	2.71
65	25	10	18.30	2.11

The baseline load conditions are shown in **Figure 3.2.2-2**. These load cases were based upon measured response from typical automotive industry crash test scenarios as well as input from the Air Force with a factor of safety of 1.5. Each load case was evaluated separately.

	LOAD CASE	MAGNITUDE
1	TENSION	3000 lb
2	COMPRESSION	3000 lb
3	TORSION	4500 IN-LB
4	BENDING	5250 in-lb

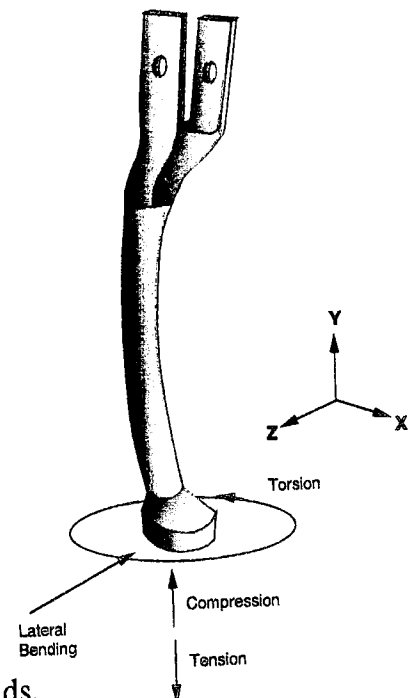


Figure 3.2.2-2. Baseline Tibia Design Loads.

Initially, each of the four load cases were assessed for the baseline material lay-up. The maximum bending, shear induced strains and maximum/minimum fiber strains vs location plots for each of these cases are shown in Figures 3.2.2-3 to 3.2.2-14. The laminate stress vs location plots are also shown in Figures 3.2.2-15 to 3.2.2-18. Location zero (or the origin) is referenced at the large bolt of the knee joint, while the maximum location ≈ 14.5 " (368.3mm) is at the ankle joint.

As mentioned earlier, the analyses were based upon beam theory, thus only the results in the diaphysis (middle segment) or away from the joints are reliable. From the strain result plots, it can be seen that the strains for tensile, compressive, and bending load cases are quite small (less than 0.3%). For the torsional load case the maximum strains are approximately 1% and approach the 1.1% allowable unidirectional compressive strain of T1000G/Epoxy. Margin of safety vs location plots for the torsional load case are shown in Figures 3.2.2-19 to 3.2.2-21.

The baseline material lay-up was modified in order increase the strain margin of safety for the torsion load condition. For this iteration, a material architecture lay-up of 50% 90°/40% $\pm 45^\circ$ /10% 90° was chosen and the torsion load condition was analyzed. The strain results plots are shown in Figures 3.2.2-22 to 3.2.2-24. The addition of $\pm 45^\circ$ plies reduced the strain to approximately 0.6% and increased the margin of safety substantially, as shown in Figures 3.2.2-25 to 3.2.2-27. Based on these finite element beam analyses, it was determined that the diaphysis region of the tibia design had all positive strain margins of safety.

3-D Tibia Finite Element Modeling

A detailed 3-D ABAQUS finite element model of the tibia (Figure 3.2.2-28) was constructed in order to verify the structural design of the complex geometry at the distal and proximal ends. The material architecture for tibia regions A, B, and C, are shown in Figure 3.2.2-29. An initial evaluation of the detailed 3-D FEM analysis results showed good correlation with the simple beam analysis at the diaphysis. Detailed stress, strain, and fiber strain margin of safety results are reported below for each load condition.

AMR77 ABAQUS TIBIA BEAM MODEL RESULTS
TENSION - OR=5", IR=375"

MAX BENDING INDUCED STRAINS

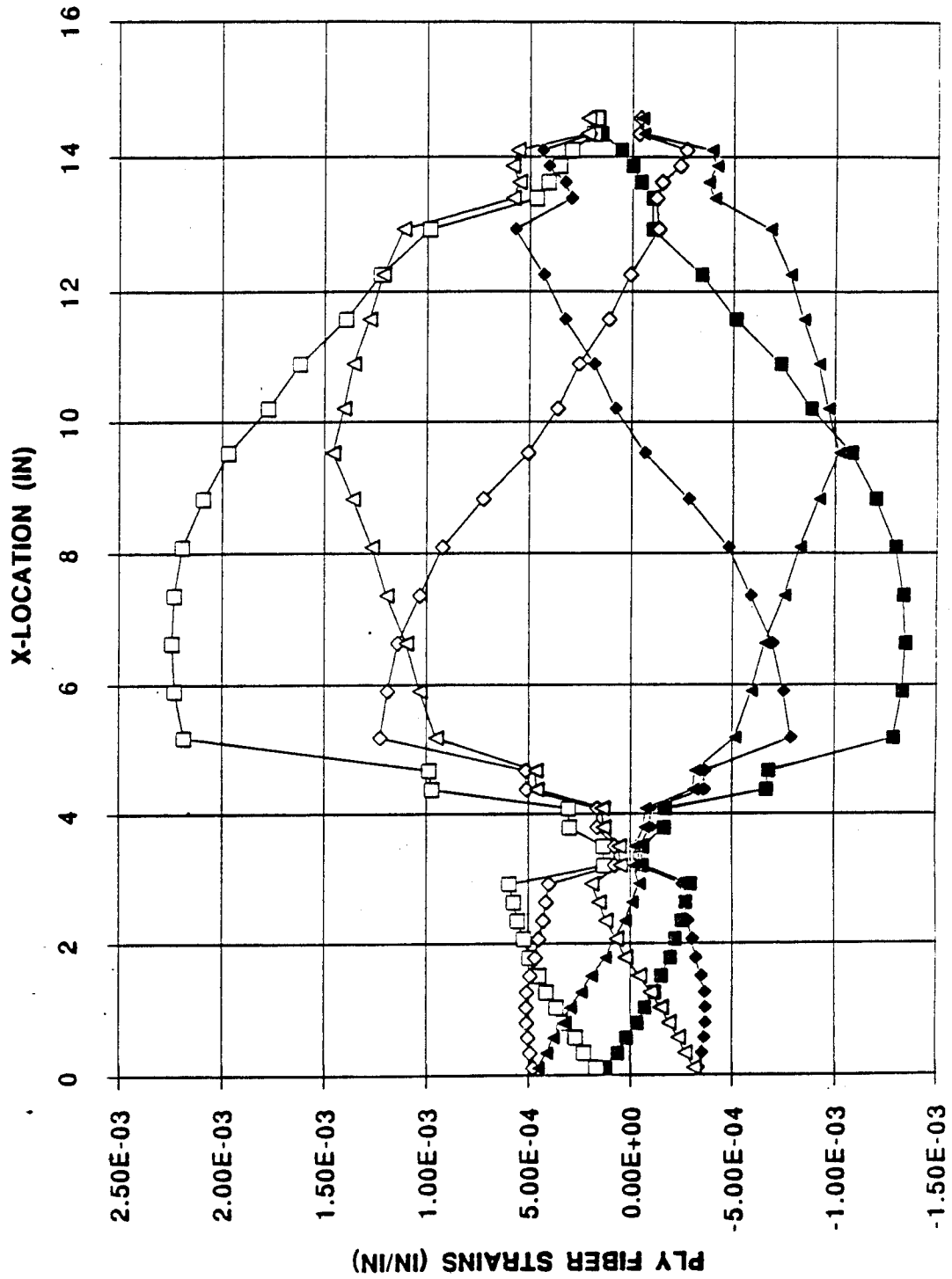


Figure 3.2.2-3. Maximum Bending Induced Strains - Tension Load Case

AMR77 ABAQUS TIBIA BEAM MODEL RESULTS
COMPRESSION - OR=5", IR=375"

MAX BENDING INDUCED STRAINS

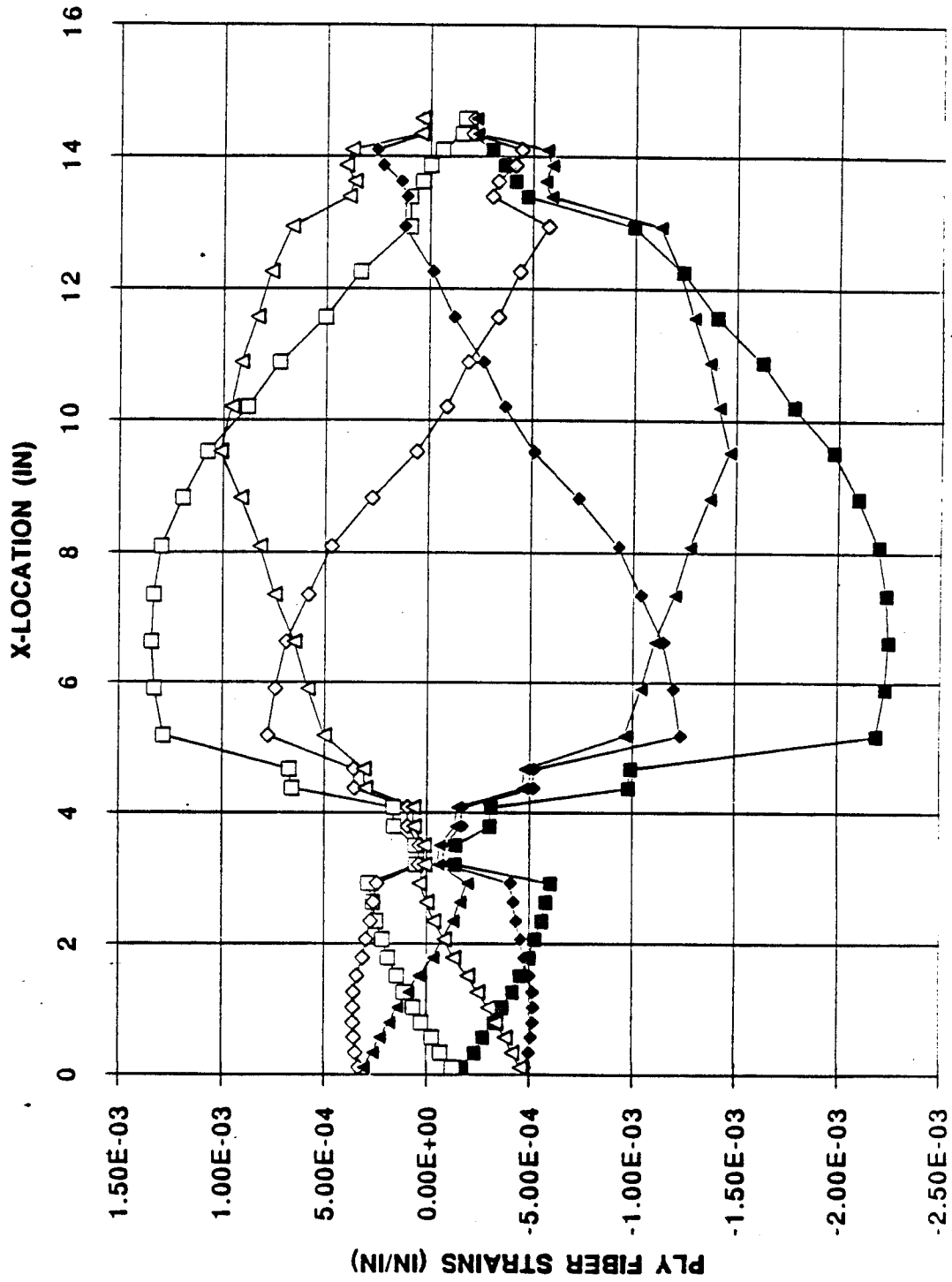


Figure 3.2.2-4. Maximum Bending Induced Strains - Compression Load Case (T1000G/EPOXY 70%/20% $\pm 45^\circ$ /10% 90°).

MAX BENDING INDUCED STRAINS

AMR77 ABAQUS TIBIA BEAM MODEL RESULTS

TORSION - OR=5", IR=375"

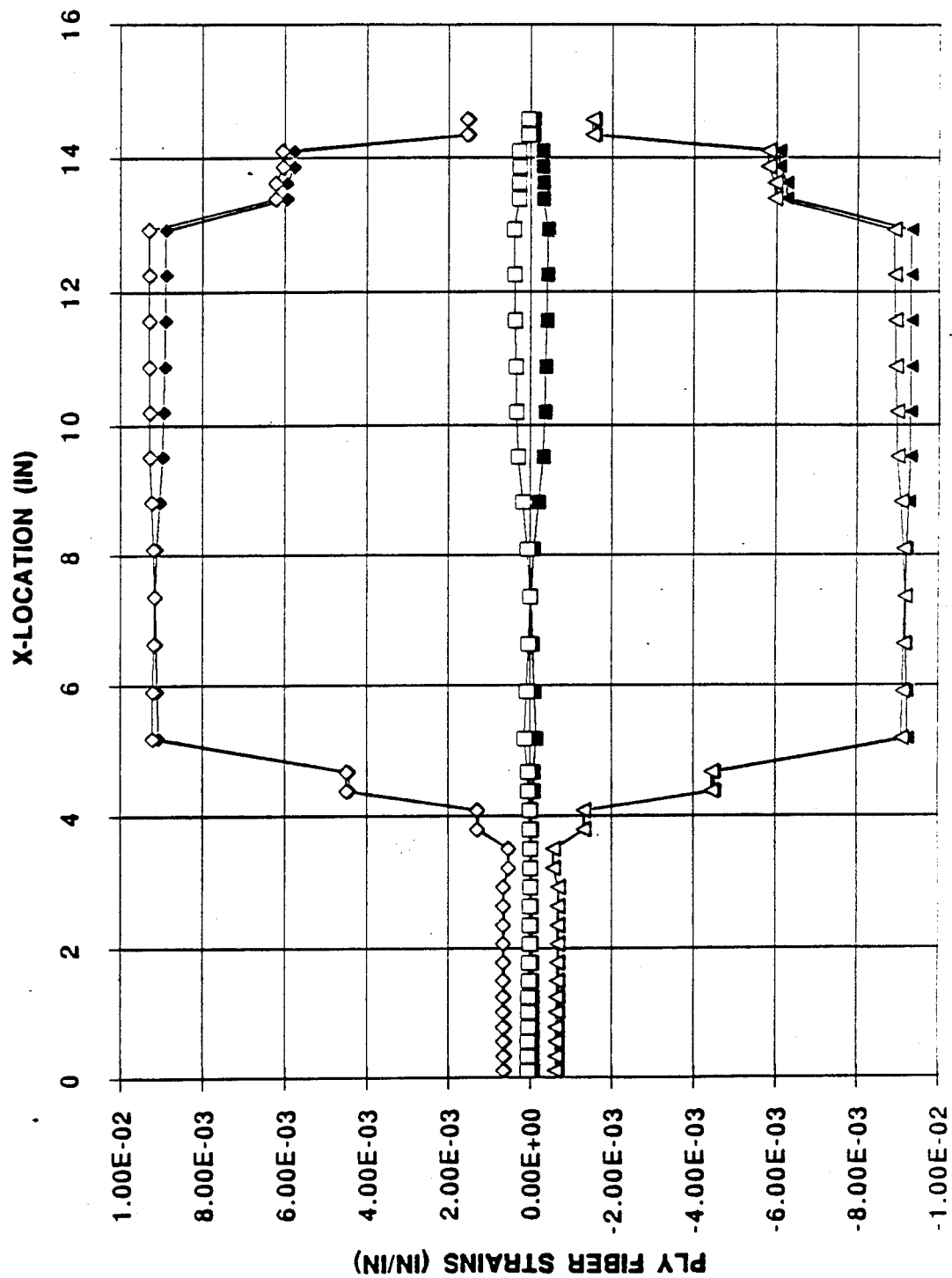


Figure 3.2.2-5. Maximum Bending Induced Strains - Torsion Load Case

AMR77 ABAQUS TIBIA BEAM MODEL RESULTS

BENDING - OR=5", IR=375"

MAX BENDING INDUCED STRAINS

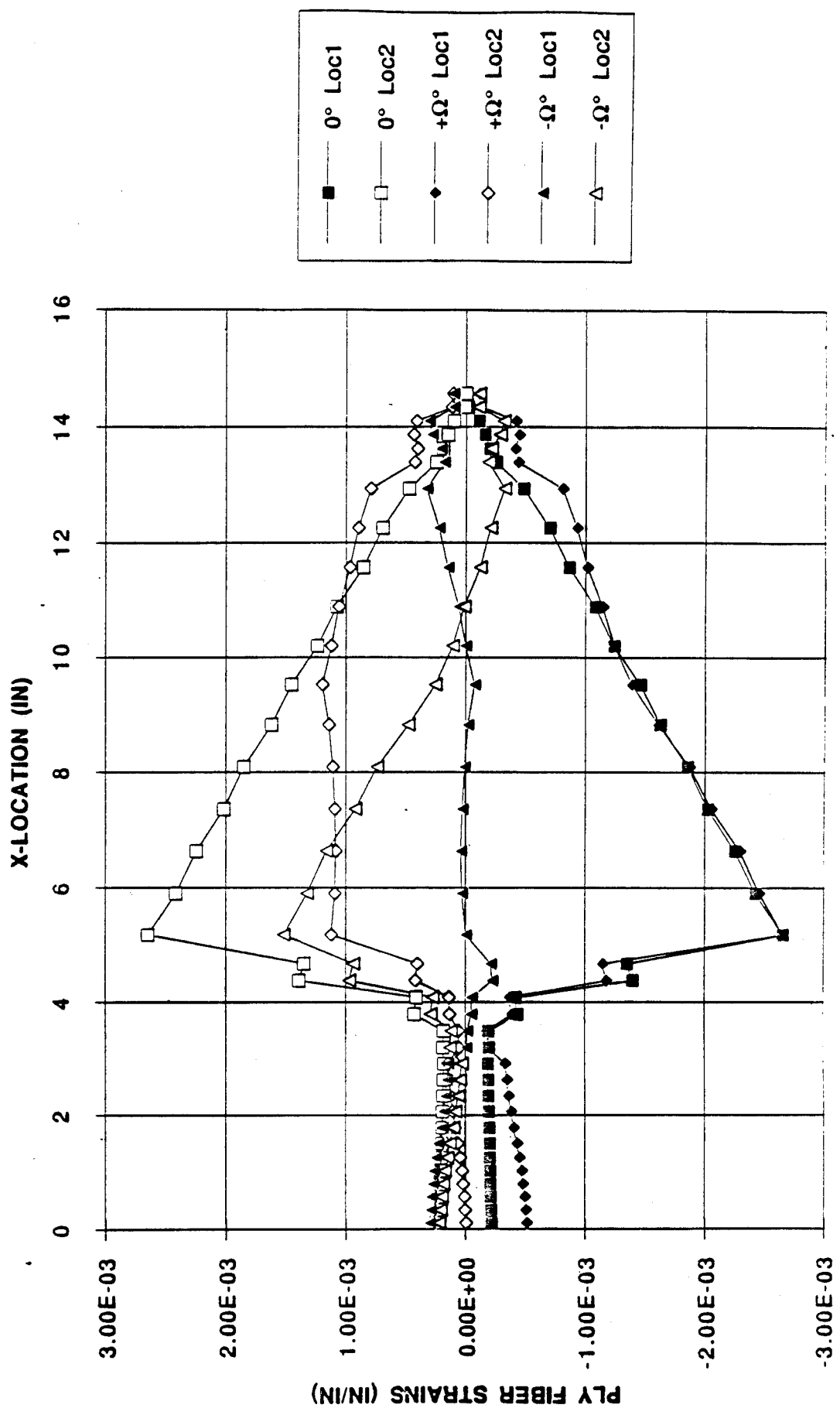


Figure 3.2.2-6. Maximum Bending Induced Strains - Bending Load Case (T1000G/EPOXY 70%/20% $\pm 45^\circ$ / 10% 90°).

AMR77 ABAQUS TIBIA BEAM MODEL RESULTS

TENSION - OR=.5", IR=.375"

MAX SHEAR INDUCED STRAINS

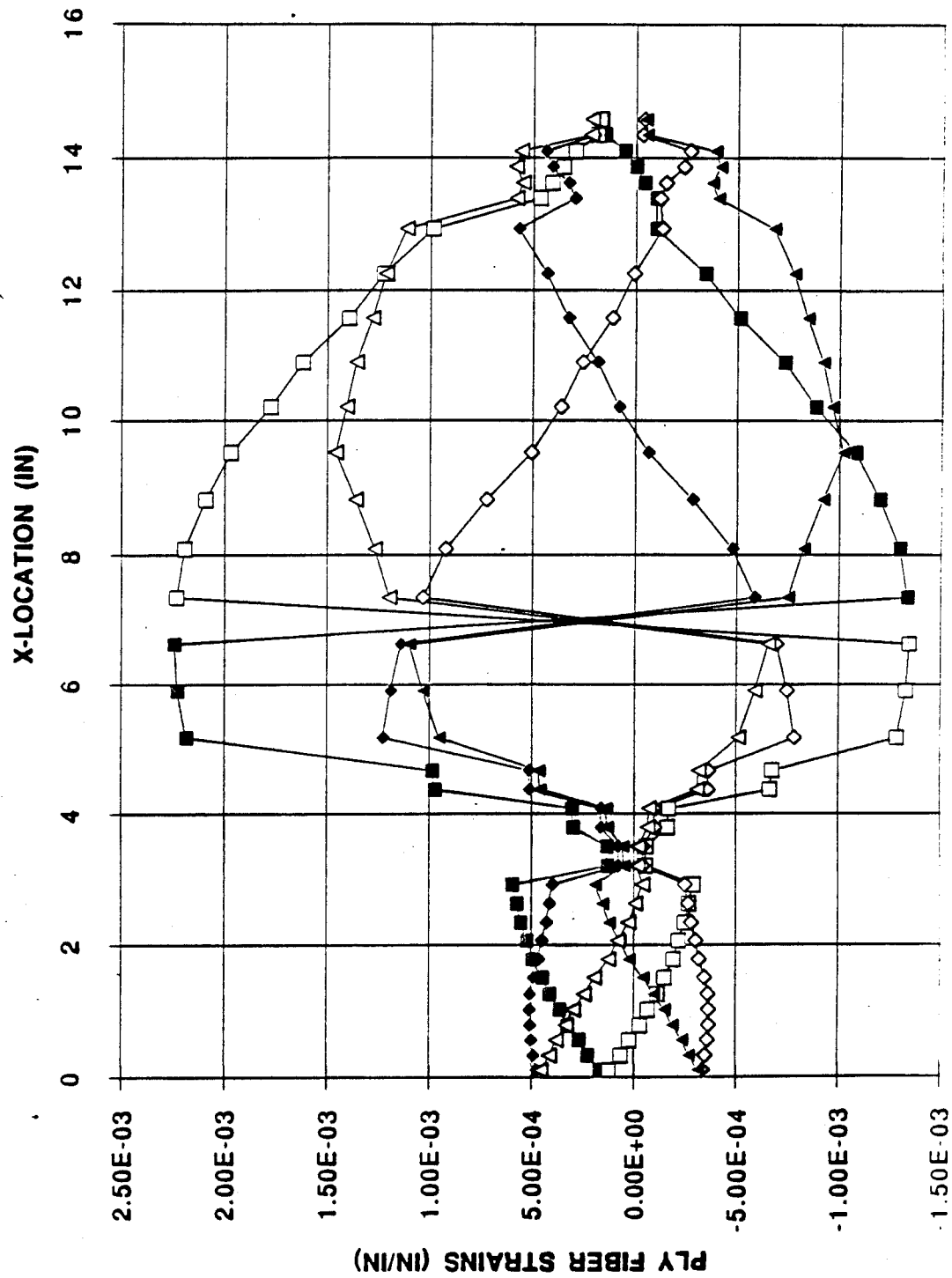


Figure 3.2.2-7. Shear Induced Strains - Tension Load Case
(T1000G/EPOXY 70% 0°/20% ±45°/ 10% 90°)

AMR77 ABAQUS TIBIA BEAM MODEL RESULTS
COMPRESSION - OR=5", IR=.375"

MAX SHEAR INDUCED STRAINS

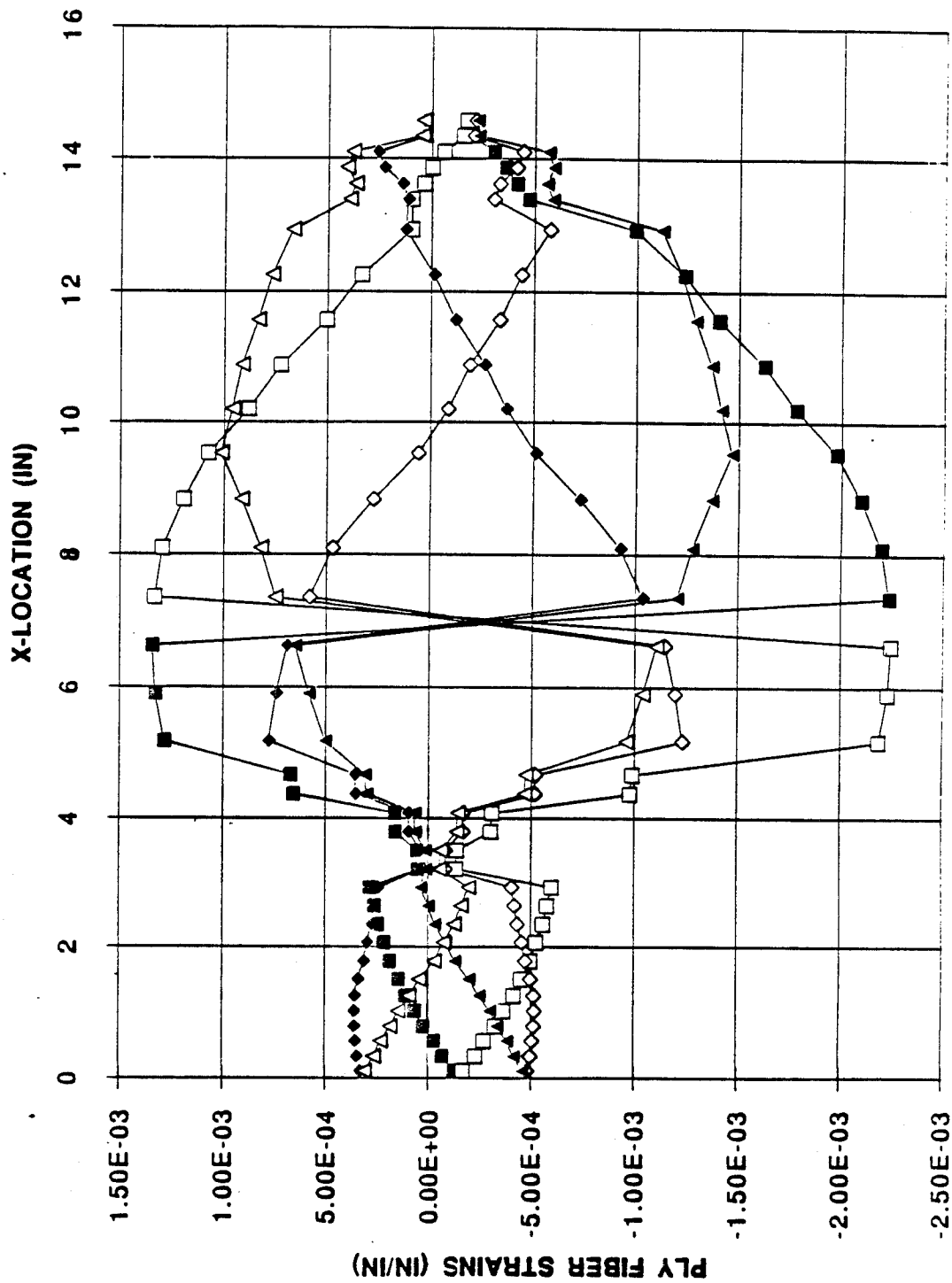


Figure 3.2.2-8. Shear Induced Strains - Compression Load Case.
(T1000G/EPOXY 70%/20% 0°/20% ±45°/10% 90°).

MAX SHEAR INDUCED STRAINS

AMR77 ABAQUS TIBIA BEAM MODEL RESULTS

TORSION - OR=.5", IR=.375"

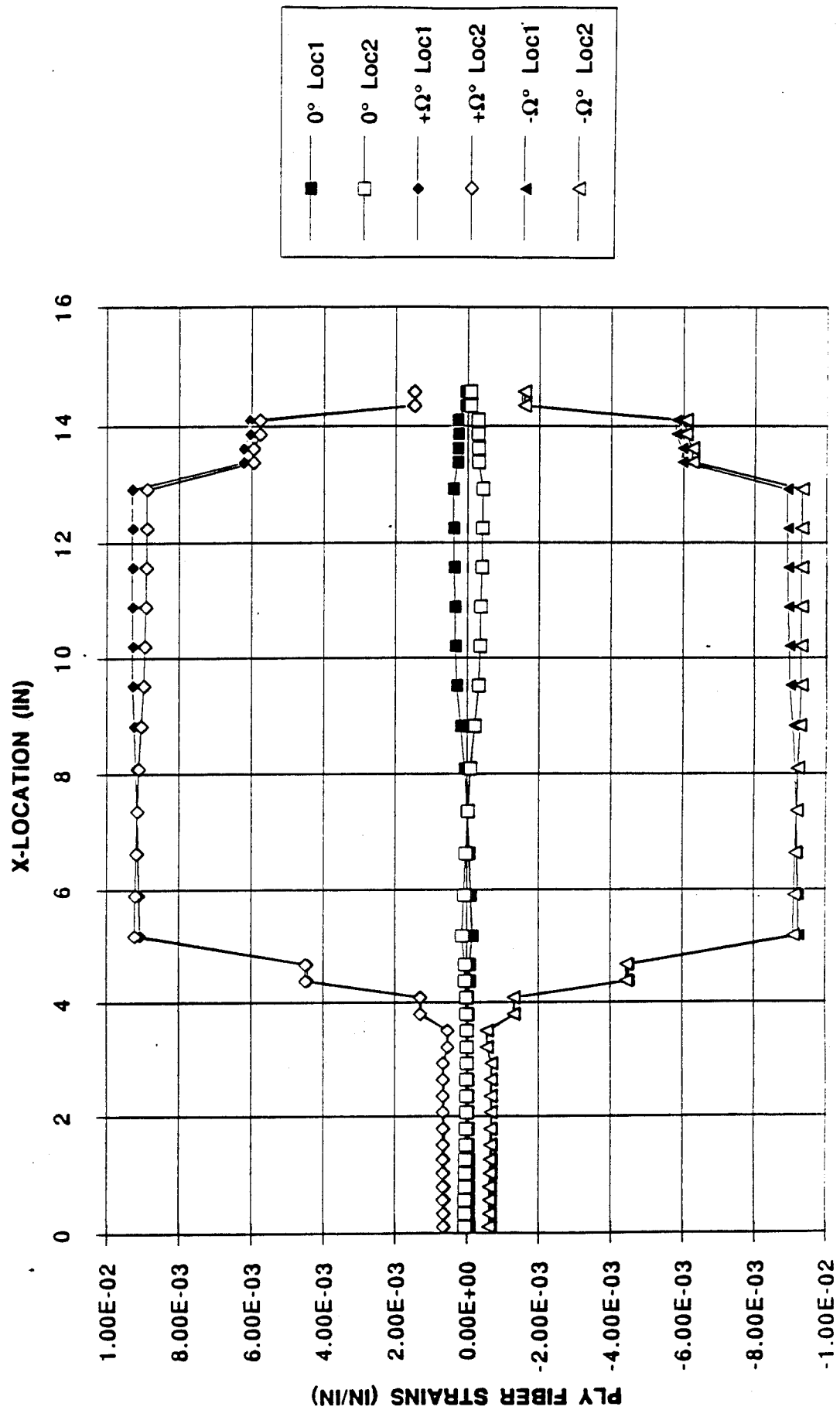


Figure 3.2.2-9. Shear Induced Strains - Torsion Load Case
(T1000G/EPOXY 70%/20% ±45°/10% 90°).

AMR77 ABAQUS TIBIA BEAM MODEL RESULTS

MAX SHEAR INDUCED STRAINS

BENDING - OR=5", IR=375"

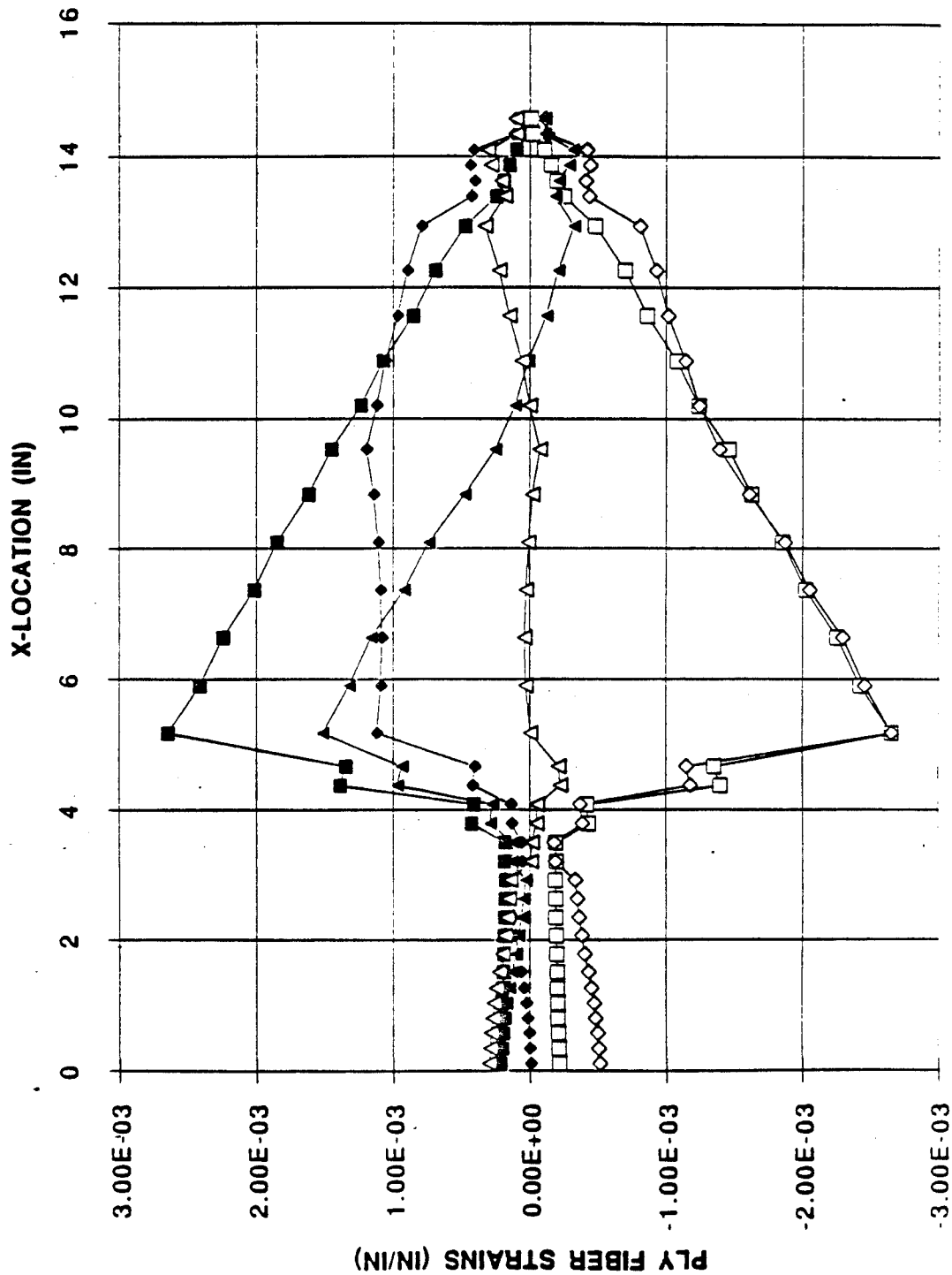


Figure 3.2.2-10. Shear Induced Strains - Bending Load Case. (T1000G/EPOXY 70% 0°/20% ±45°/ 10% 90°).

MIN/MAX FIBER STRAINS

AMR77 ABAQUS TIBIA BEAM MODEL RESULTS
TENSION - OR=5", IR=375"

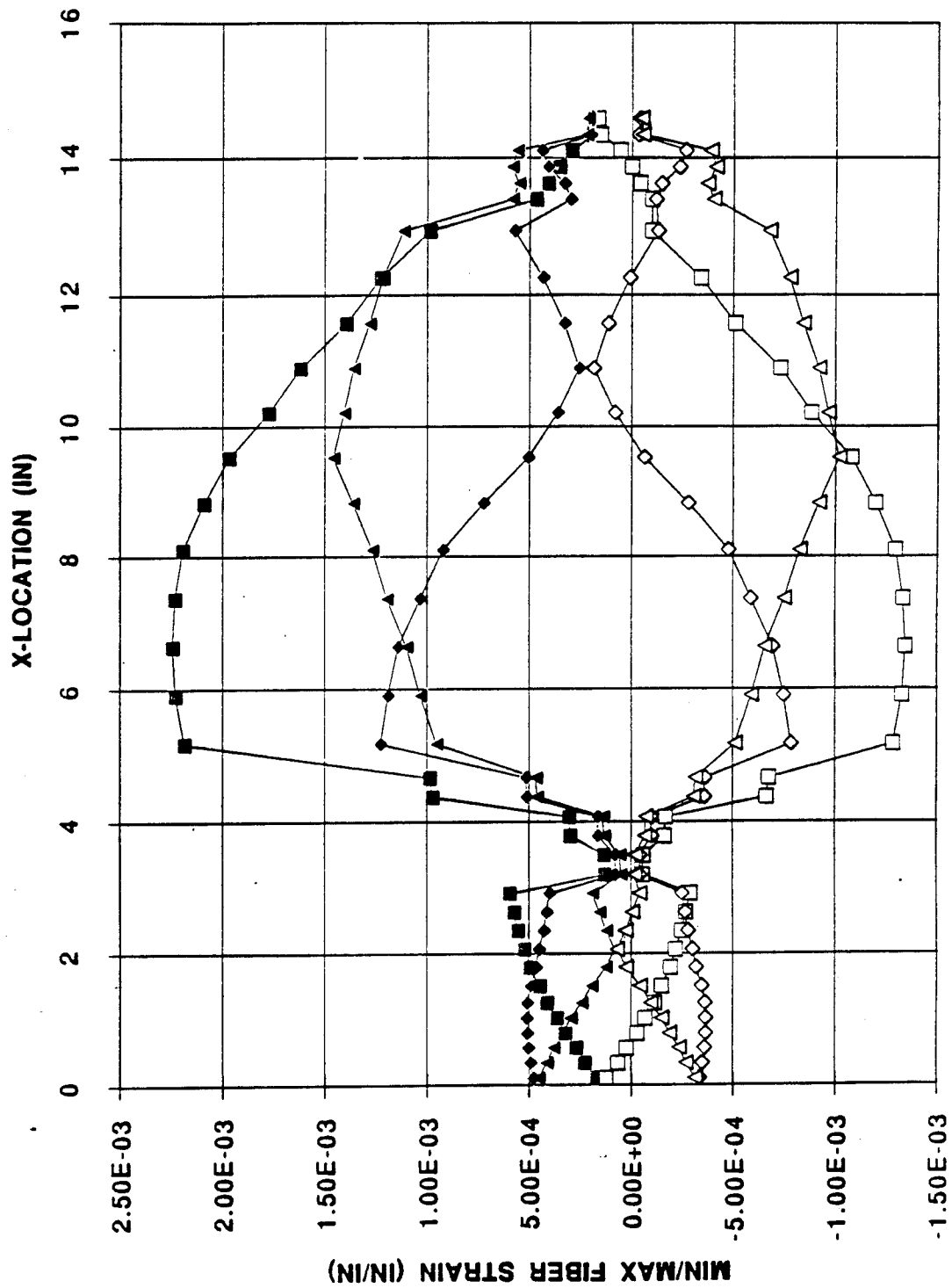


Figure 3.2.2-11. Maximum/Minimum Fiber Strains - Tension Load Case
(T1000G/EPOXY 70%/20% ±45°/ 10% 90°).

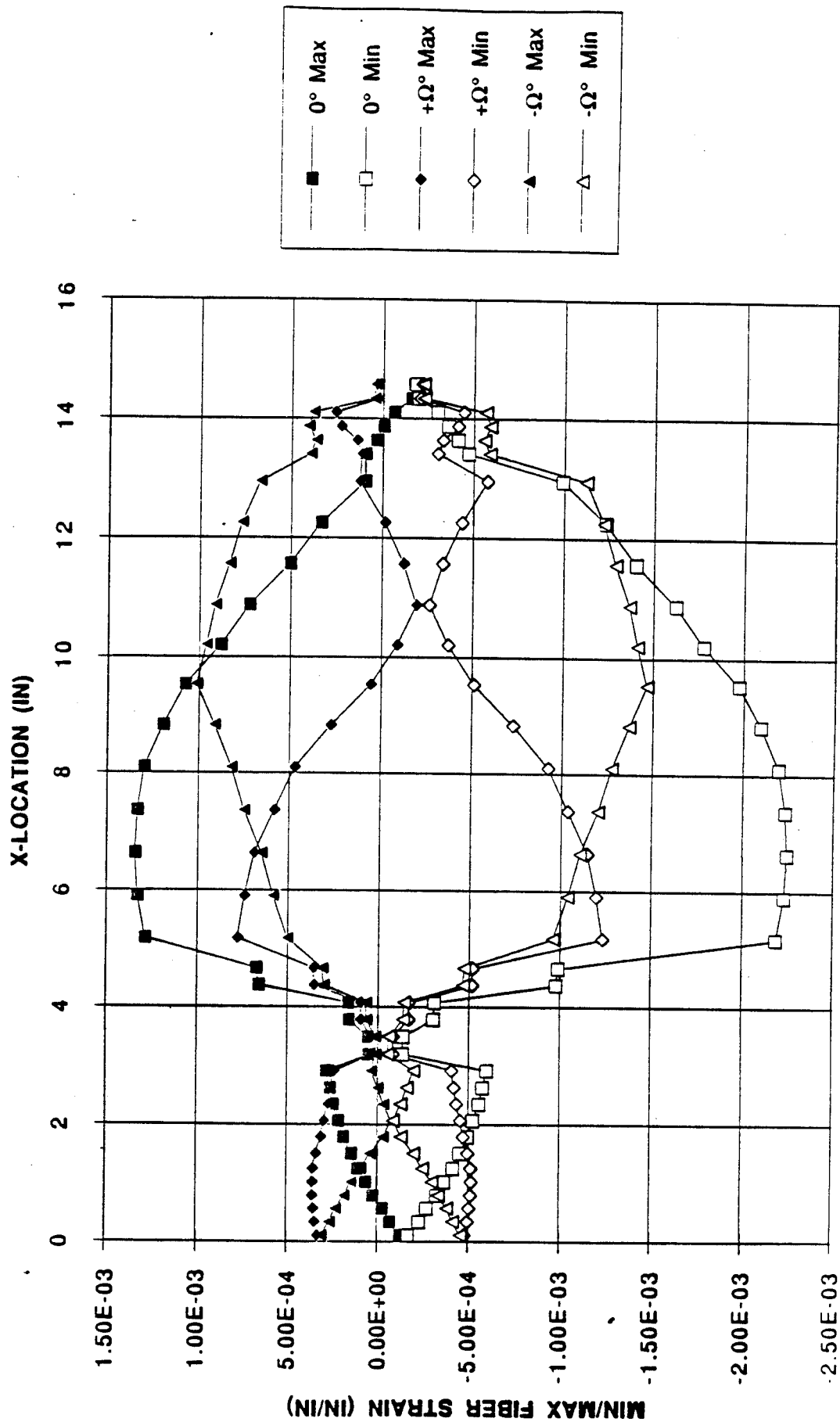


Figure 3.2.2-12. Maximum/Minimum Fiber Strains - Compression Load Case (T1000G/EPOXY 70%/20% 0°/45°/ 10% 90°).

MIN/MAX FIBER STRAINS

AMR77 ABAQUS TIBIA BEAM MODEL RESULTS
TORSION - OR=5", IR=375"

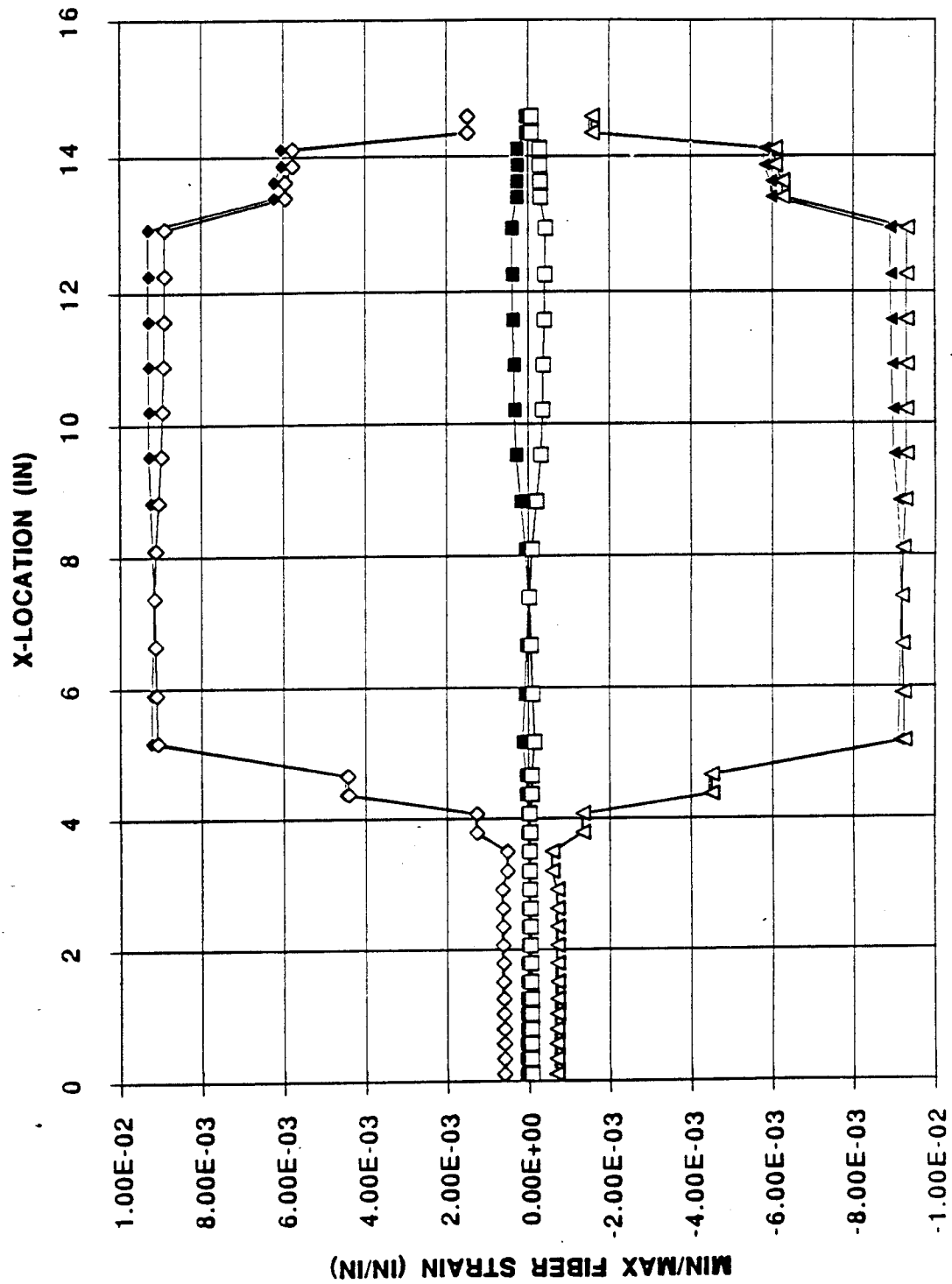


Figure 3.2.2-13. Maximum/Minimum Fiber Strains - Torsion Load Case
(TI100KG/EPOXY 70%/20% 0°/20% ±45°/10% 90°).

**MIN/MAX FIBER STRAINS AMR77 ABAQUS TIBIA BEAM MODEL RESULTS
BENDING - OR=5", IR=3.75"**

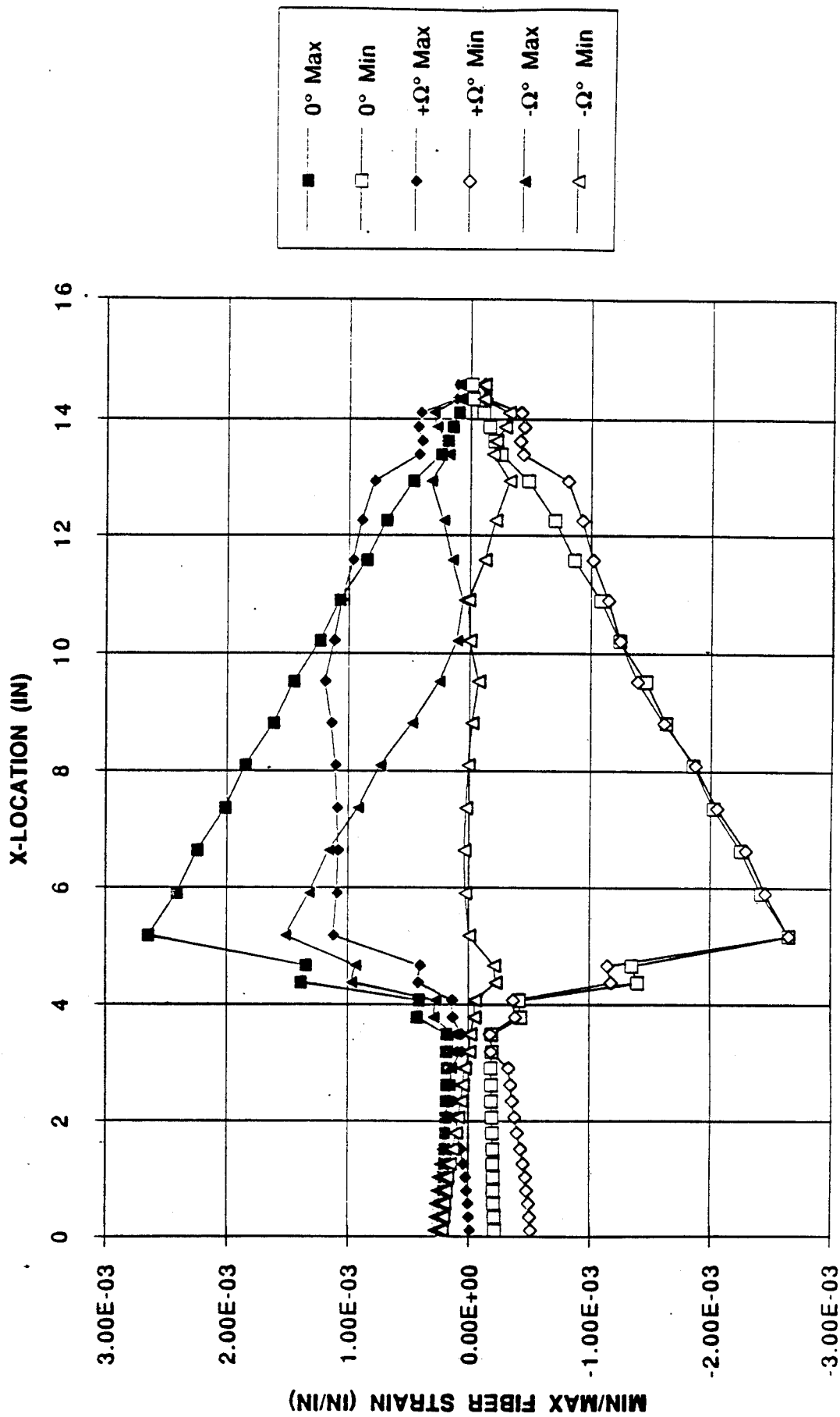


Figure 3.2.2-14. Maximum/Minimum Fiber Strains - Bending Load Case (T1000G/EPOXY 70%/20% 0°/20% ±45°/ 10% 90°).

AMR77 ABAQUS TIBIA BEAM MODEL RESULTS

LAMINATE STRESSES

TENSION - OR=.5", IR=.375"

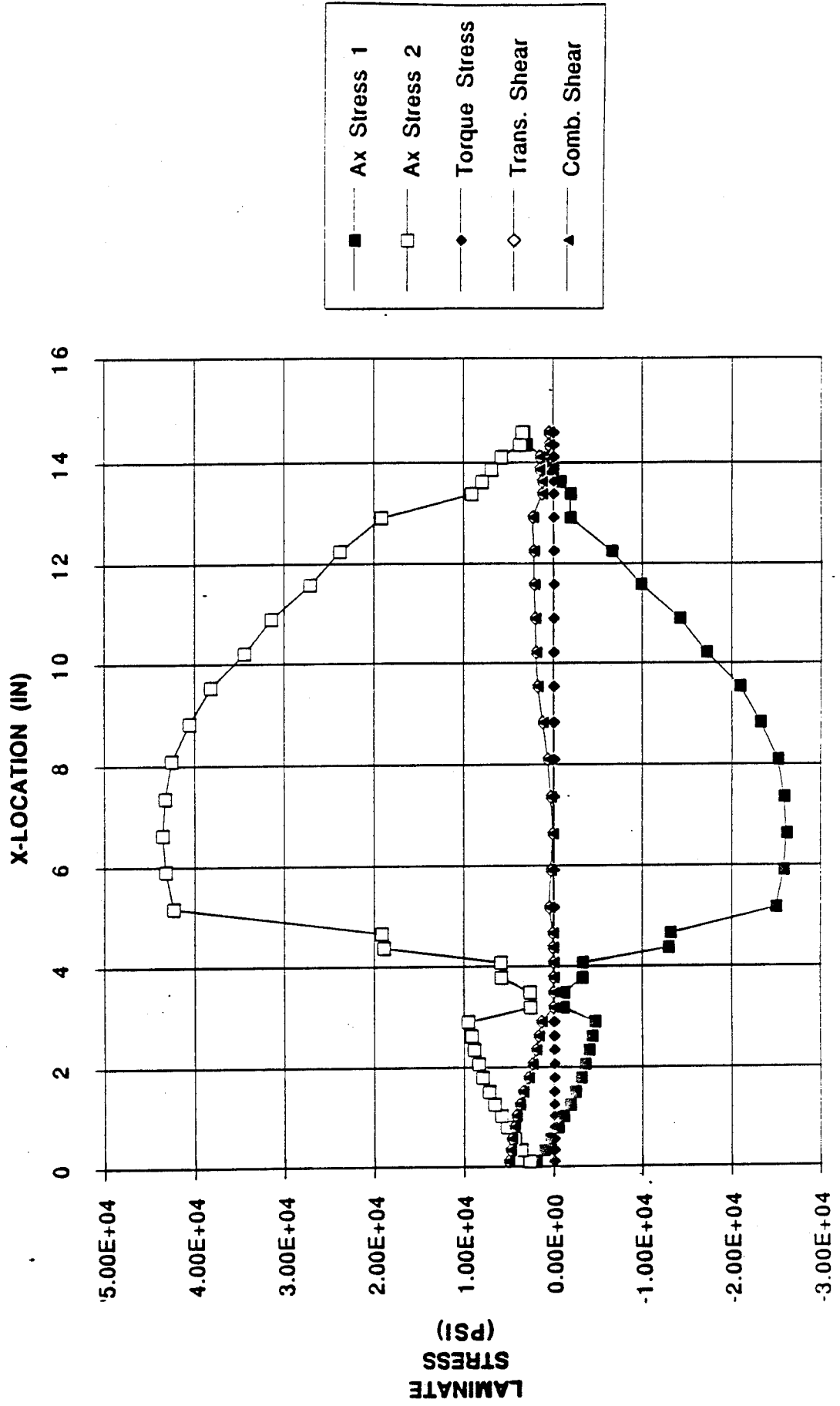


Figure 3.2.2-15. Laminate Stress - Tension Load Case
(T100KG/EPOXY 70% 0°/20% ±45°/10% 90°).

AMR77 ABAQUS TIBIA BEAM MODEL RESULTS

LAMINATE STRESSES

COMPRESSION - OR=.5", IR=.375"

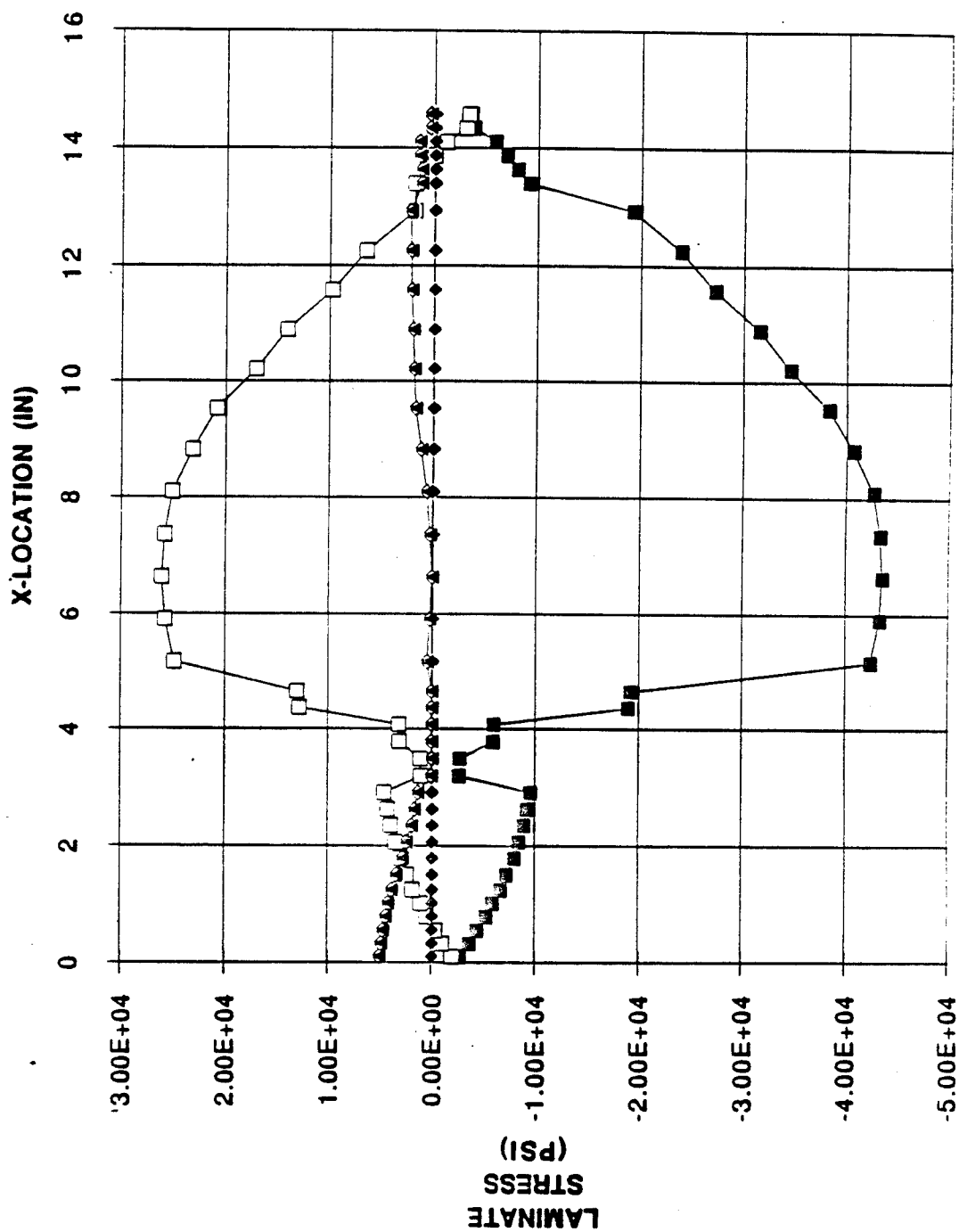


Figure 3.2.2-16. Laminate Stress - Compression Load Case (T1000G/EPOXY 70% 0°/20% ±45°/ 10% 90°).

AMR77 ABAQUS TIBIA BEAM MODEL RESULTS

TORSION - OR=.5", IR=.375"

LAMINATE STRESSES

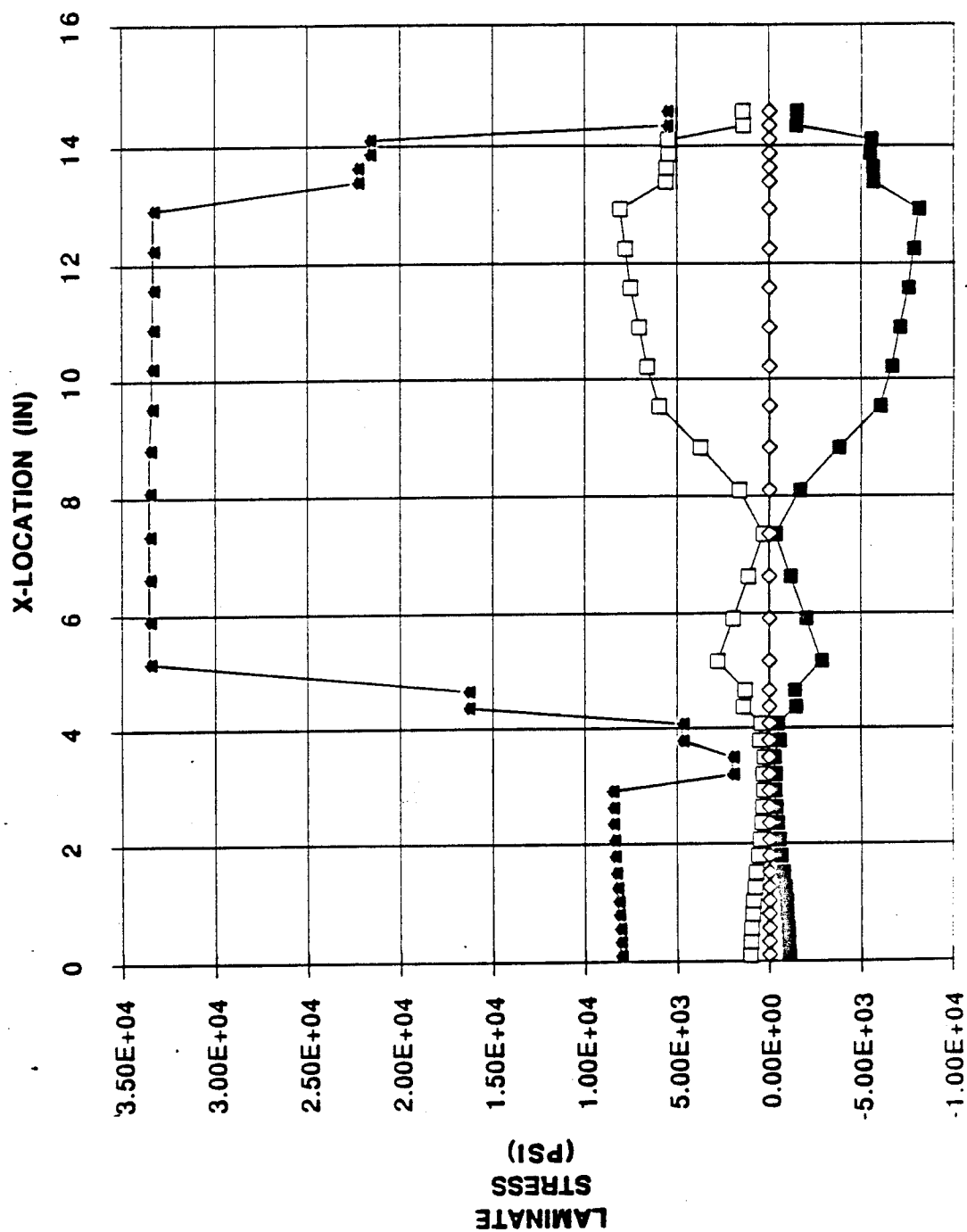


Figure 3.2.2-17. Laminate Stress - Torsion Load Case

AMR77 ABAQUS TIBIA BEAM MODEL RESULTS

BENDING - OR=.5", IR=.375"

LAMINATE STRESSES

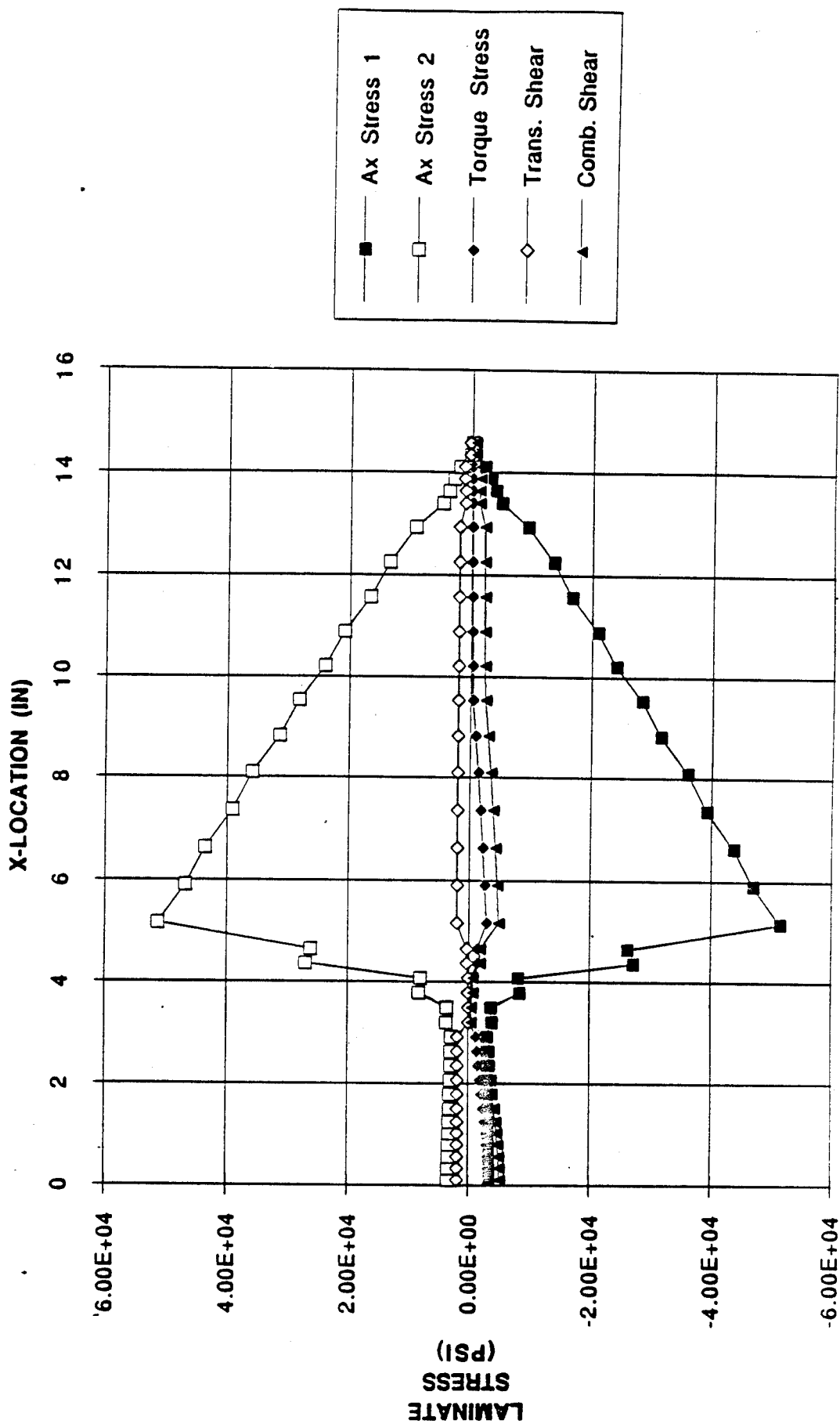


Figure 3.2.2-18. Laminate Stress - Bending Load Case
(T1000G/EPOXY 70% 0°/20% ±45°/ 10% 90°).

**MAX BENDING INDUCED STRAIN
MARGIN OF SAFETY**

AMR77 ABAQUS TIBIA BEAM MODEL RESULTS

TORSION - OR=.5", IR=.375"
T1000G 70% 0°/20% ±45°/10% 90°

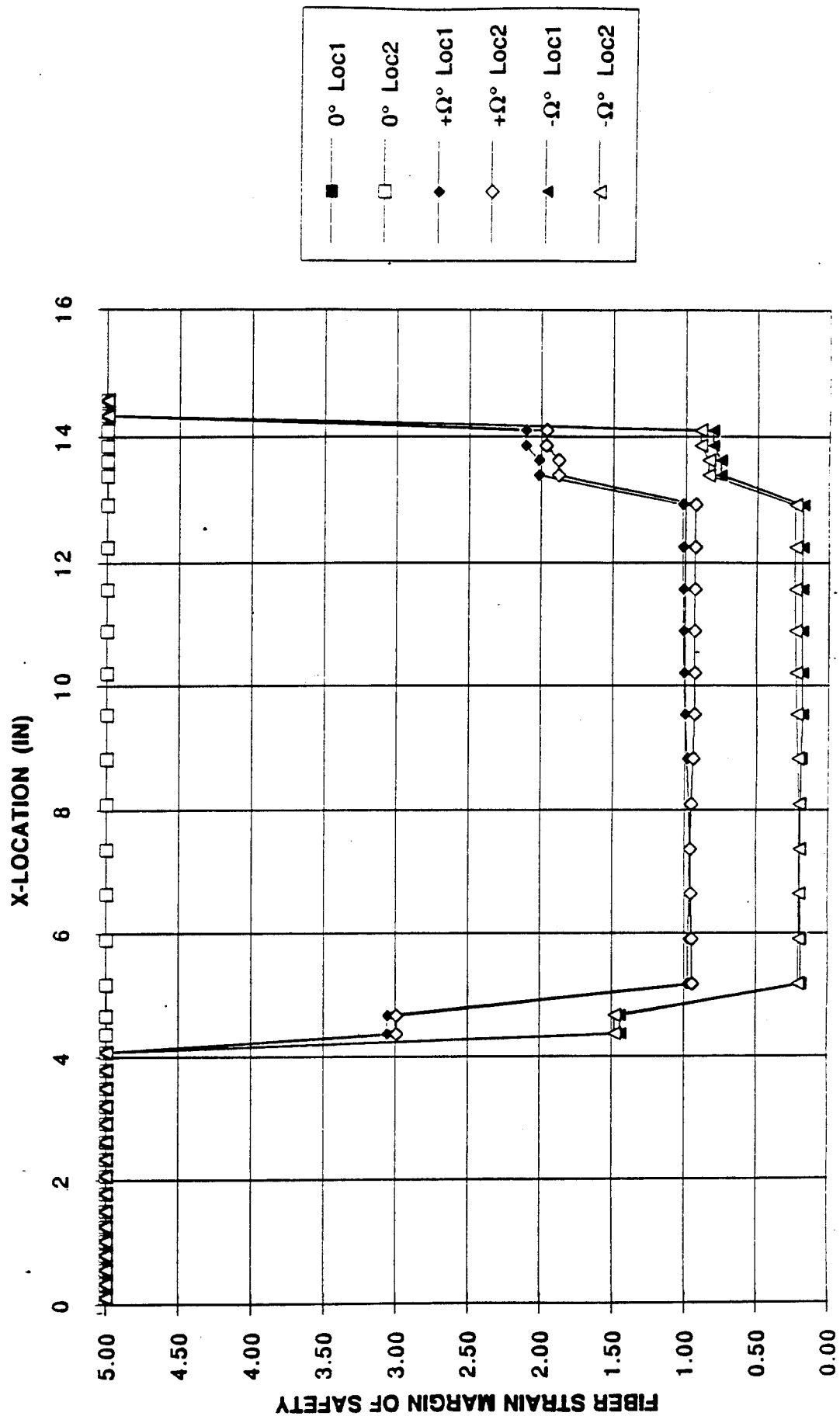


Figure 3.2.2-19. Max Bending Induced Strain Margin of Safety - Torsion
 (T1000G/EPOXY 70% 0°/20% ±45°/10% 90°)

**MAX SHEAR INDUCED STRAIN
MARGIN OF SAFETY**

AMR77 ABAQUS TIBIA BEAM MODEL RESULTS

TORSION - OR=.5", IR=.375"
T1000G 70% 0°/20% ±45°/10% 90°

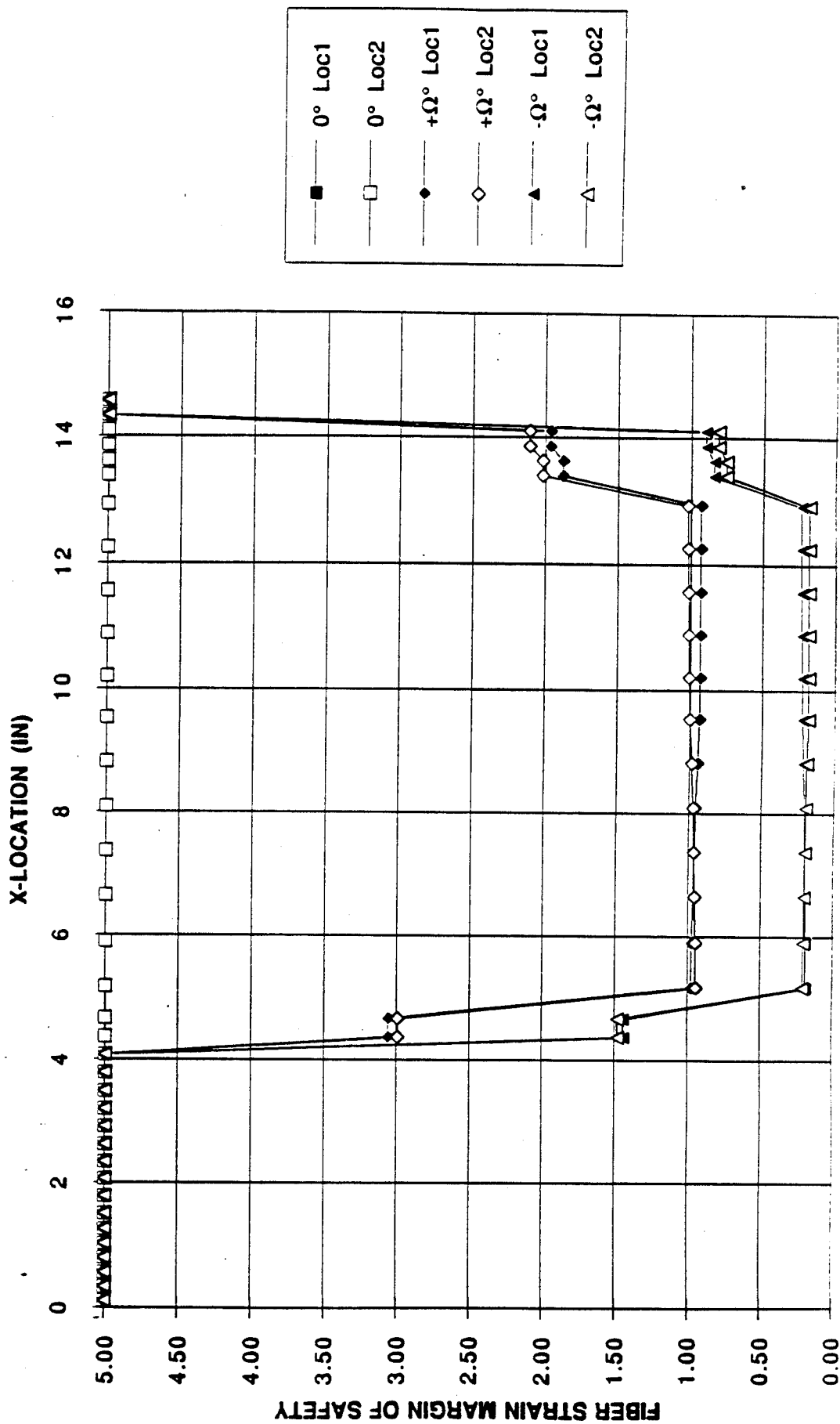


Figure 3.2.2-20. Max Shear Induced Strain Margin of Safety - Torsion
(T1000G/EPOXY 70% 0°/20% ±45°/10% 90°).

MIN/MAX FIBER STRAIN
MARGIN OF SAFETY

AMR77 ABAQUS TIBIA BEAM MODEL RESULTS

TORSION - OR=.5", IR=.375"
T1000G 70%0°/20%±45°/10%90°

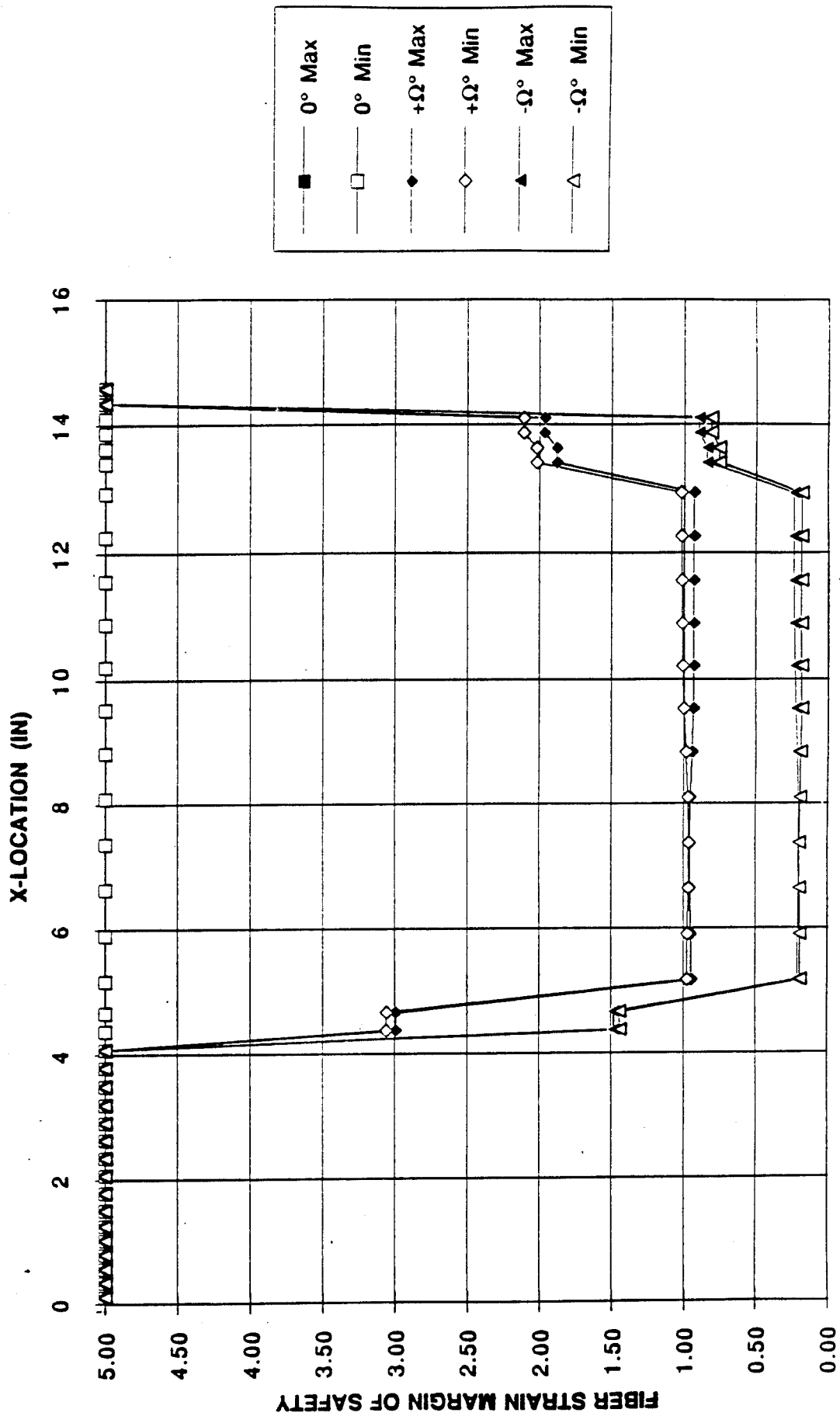


Figure 3.2.2-21. Max/min Fiber Strain Margin of Safety - Torsion Case
(T1000G/EPXY 70%/20%±45°/10% 90°)

AMR77 ABAQUS TIBIA BEAM MODEL RESULTS

TORSION - OR=.5", IR=.375"

T1000G 50%0°/40%±45°/10%90°

MAX BENDING INDUCED STRAINS

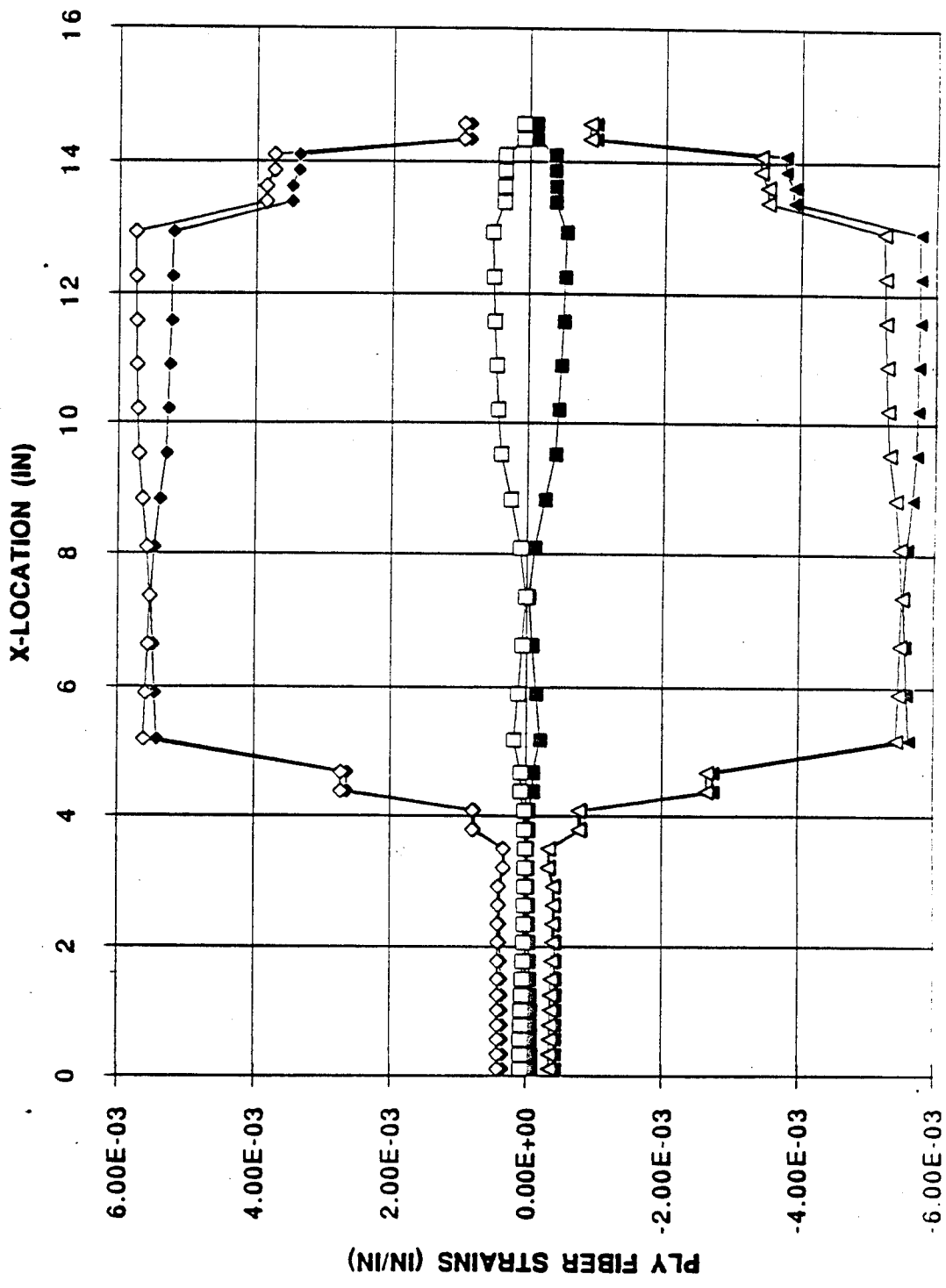


Figure 3.2.2-22. Maximum Bending Induced Strains - Torsion Load Case (T1000G/EPOXY 50%0°/40%±45°/10%90°).

AMR77 ABAQUS TIBIA BEAM MODEL RESULTS

TORSION - OR=.5", IR=.375"
T1000G 50%0°/40%±45°/10%90°

MAX SHEAR INDUCED STRAINS

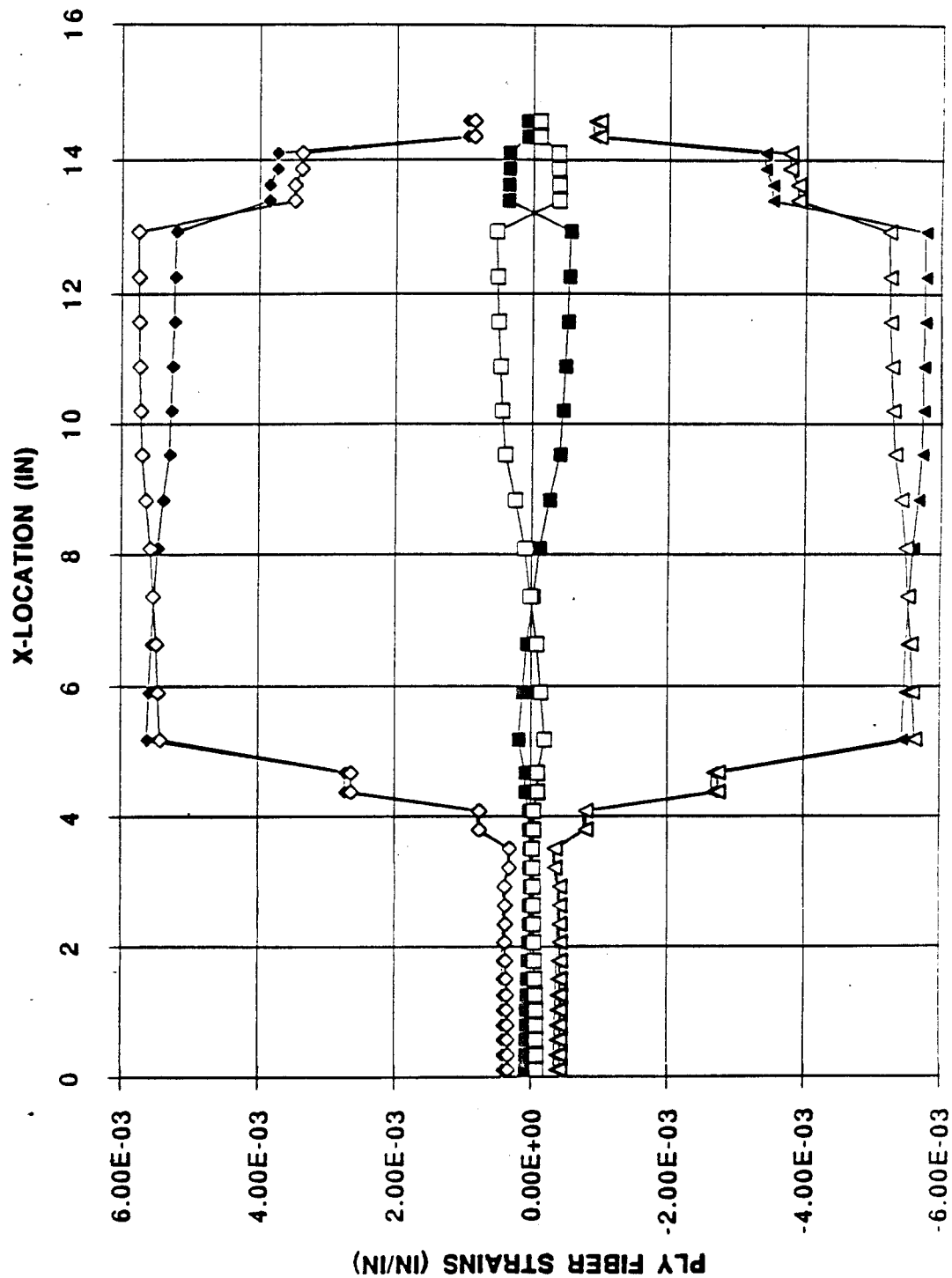


Figure 3.2.2-23. Shear Induced Strains - Torsion Load Case

MIN/MAX FIBER STRAINS

AMR77 ABAQUS TIBIA BEAM MODEL RESULTS

TORSION - OR=5", IR=375"
T1000G 50%0°/40%±45°/10%90°

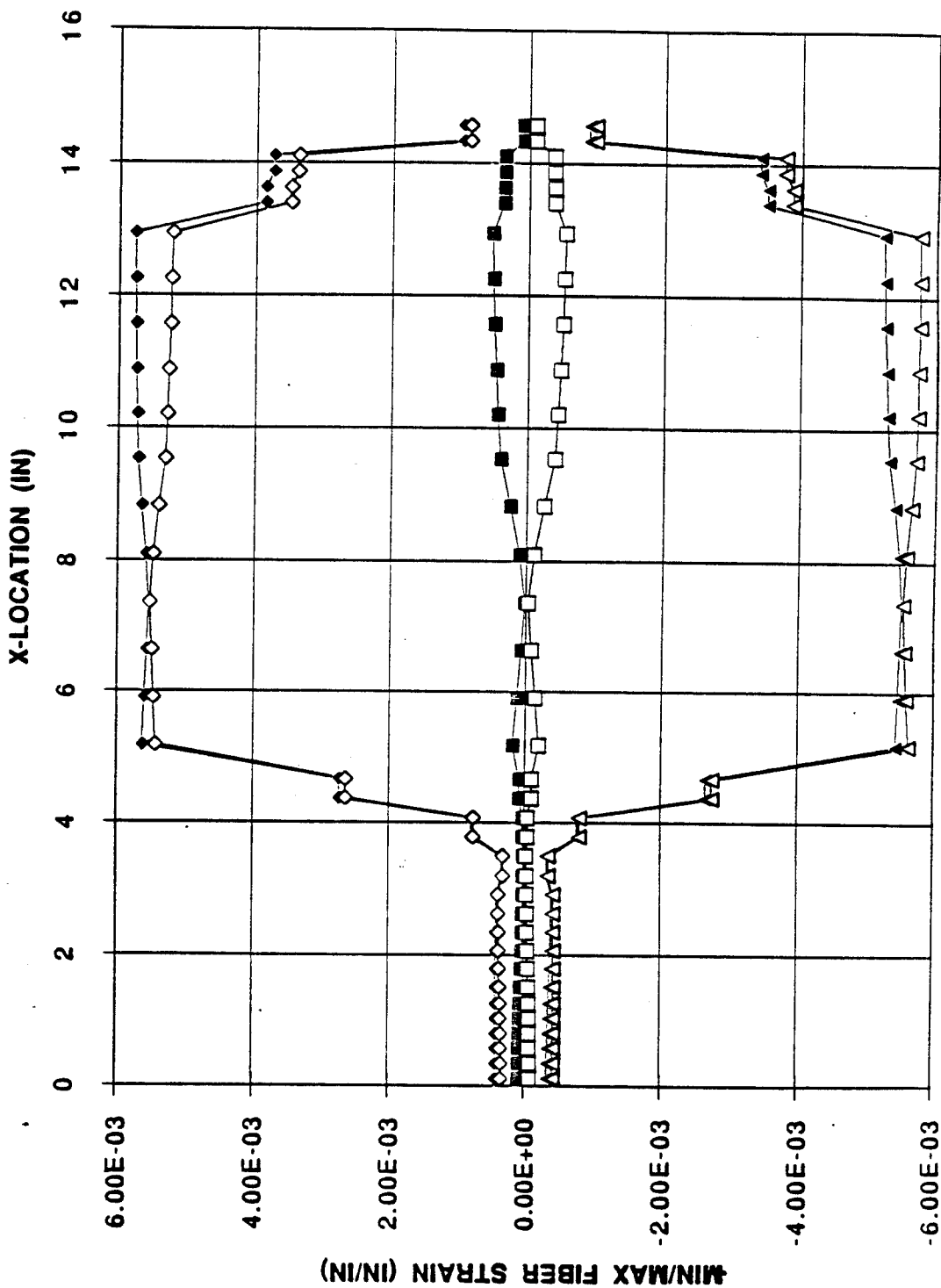


Figure 3.2.2-24. Maximum/Minimum Fiber Strains - Torsion Load Case (T1000G/EPOXY 50% 0°/40% ±45°/10% 90°).

MAX BENDING INDUCED STRAIN
MARGIN OF SAFETY

AMR77 ABAQUS TIBIA BEAM MODEL RESULTS

TORSION - OR=.5", IR=.375"
T1000G 50%0°/40%±45°/10%90°

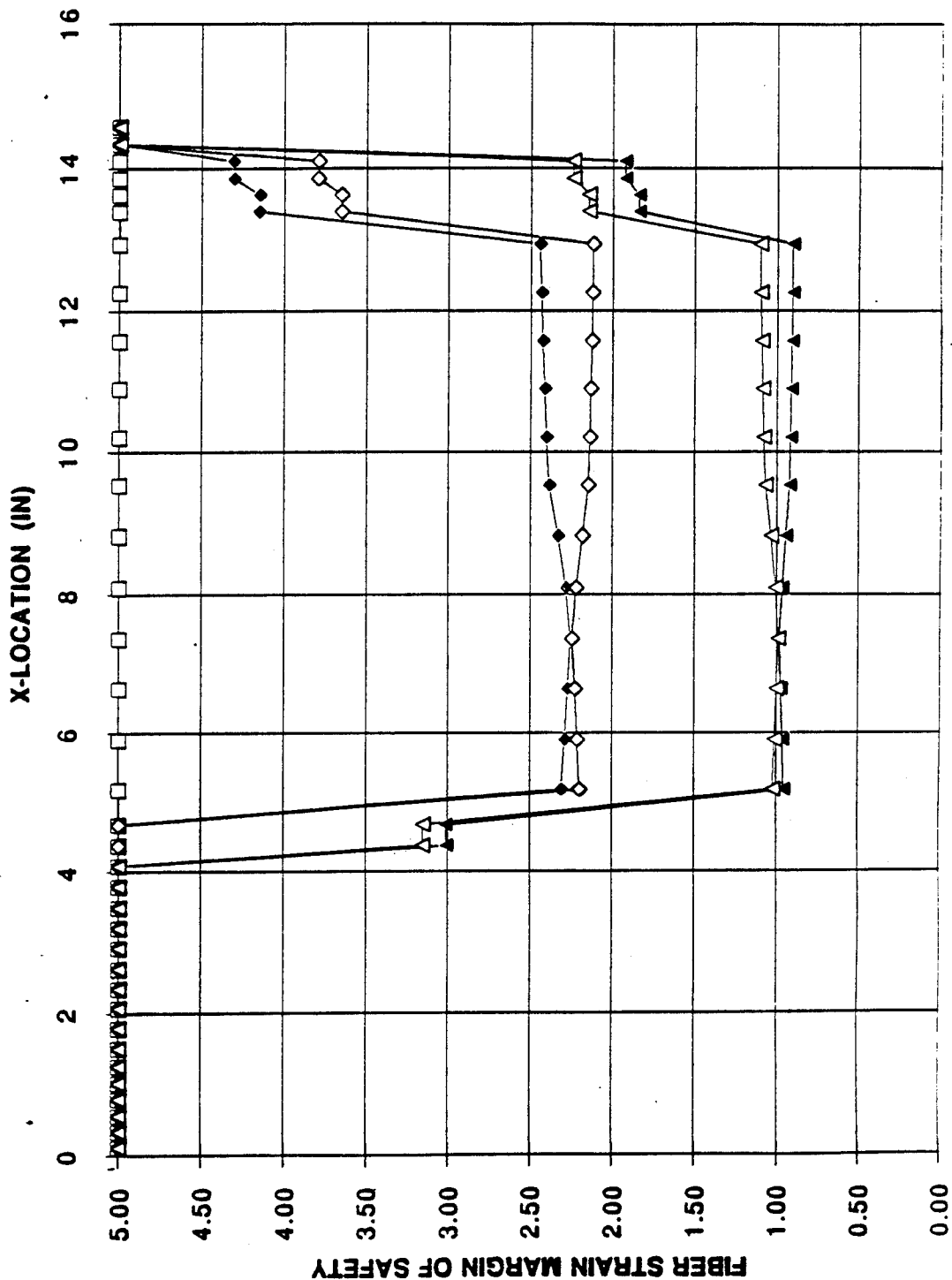


Figure 3.2.2-25. Maximum Bending Induced Strains - Torsion Load Case

CT1000G/EDOV V 50% 0°/40% ±45°/10% 90°

**MAX SHEAR INDUCED STRAIN
MARGIN OF SAFETY**

AMR77 ABAQUS TIBIA BEAM MODEL RESULTS

TORSION - OR=.5", IR=.375"
T1000G 50%0°/40%±45°/10%90°

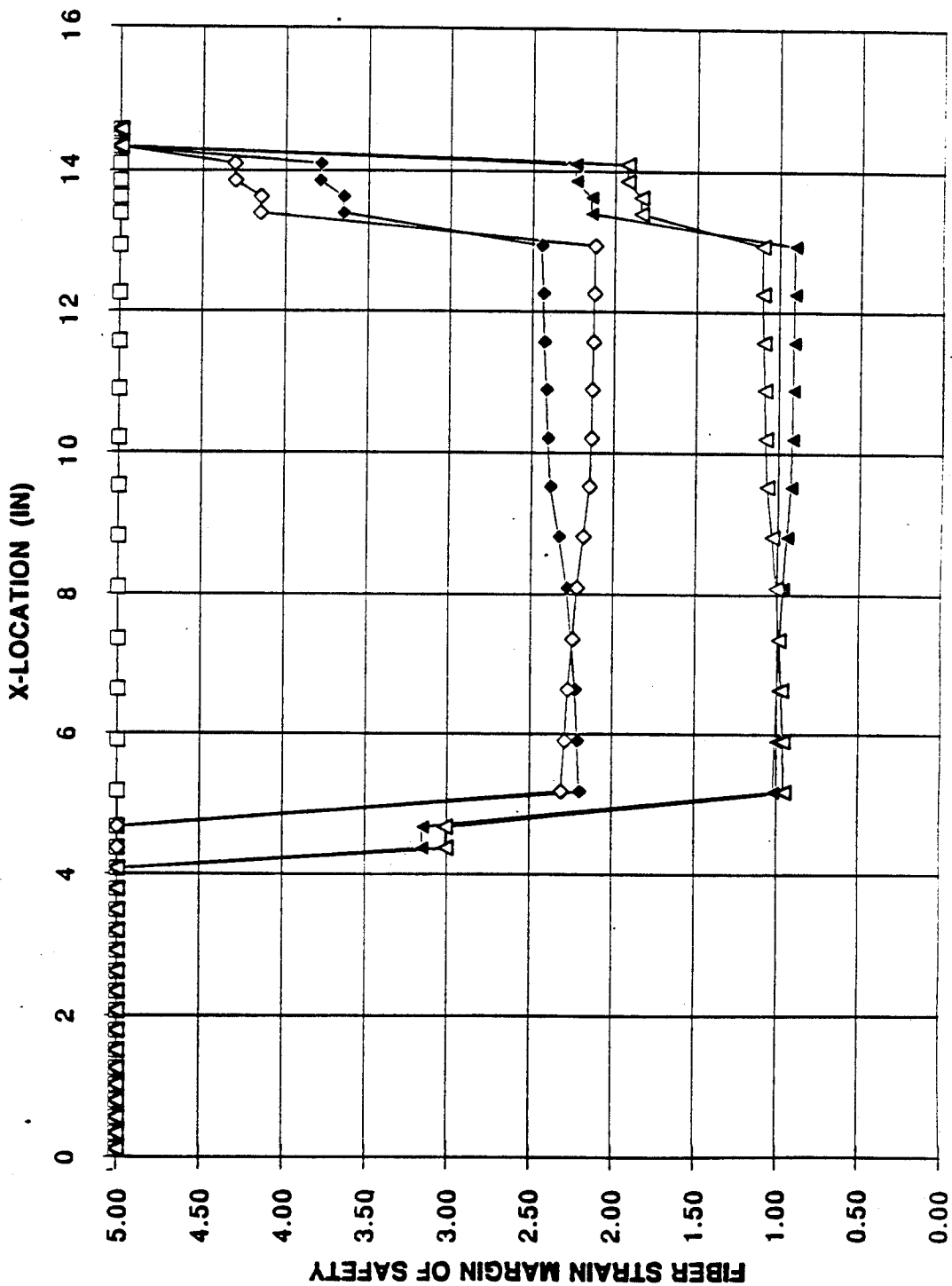


Figure 3.2.2-26. Maximum Shear Induced Strains - Torsion Load Case (T1000G/EPOXY 50% 0°/40% ±45°/10% 90°).

**MIN/MAX FIBER STRAIN
MARGIN OF SAFETY**

AMR77 ABAQUS TIBIA BEAM MODEL RESULTS

TORSION - OR=.5", IR=.375"
T1000G 50%0°/40%±45°/10%90°

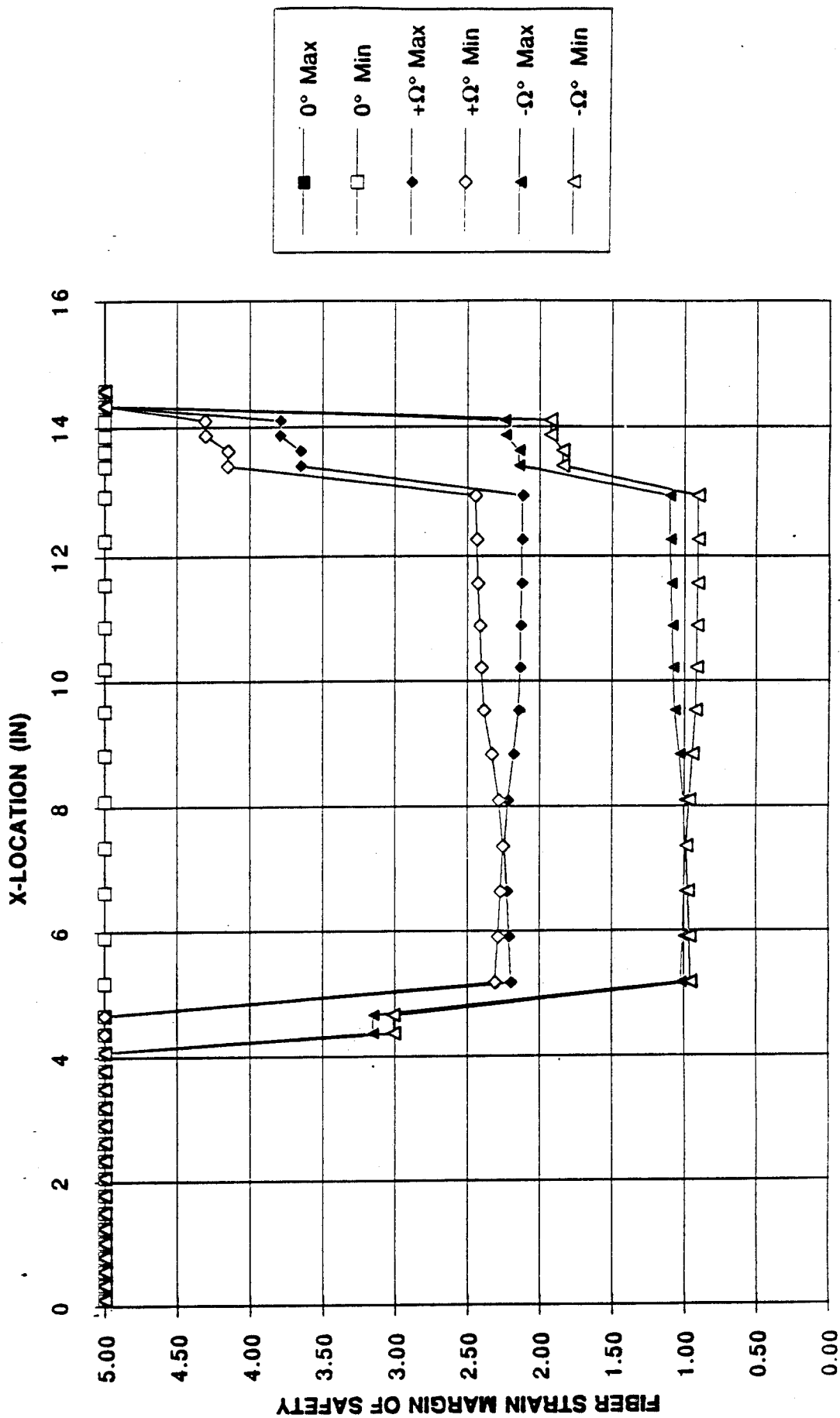


Figure 3.2.2-27. Maximum/Minimum Fiber Strains - Torsion Load Case
 (T1000G/EPOXY 50% 0°/40% ±45°/10% 90°)

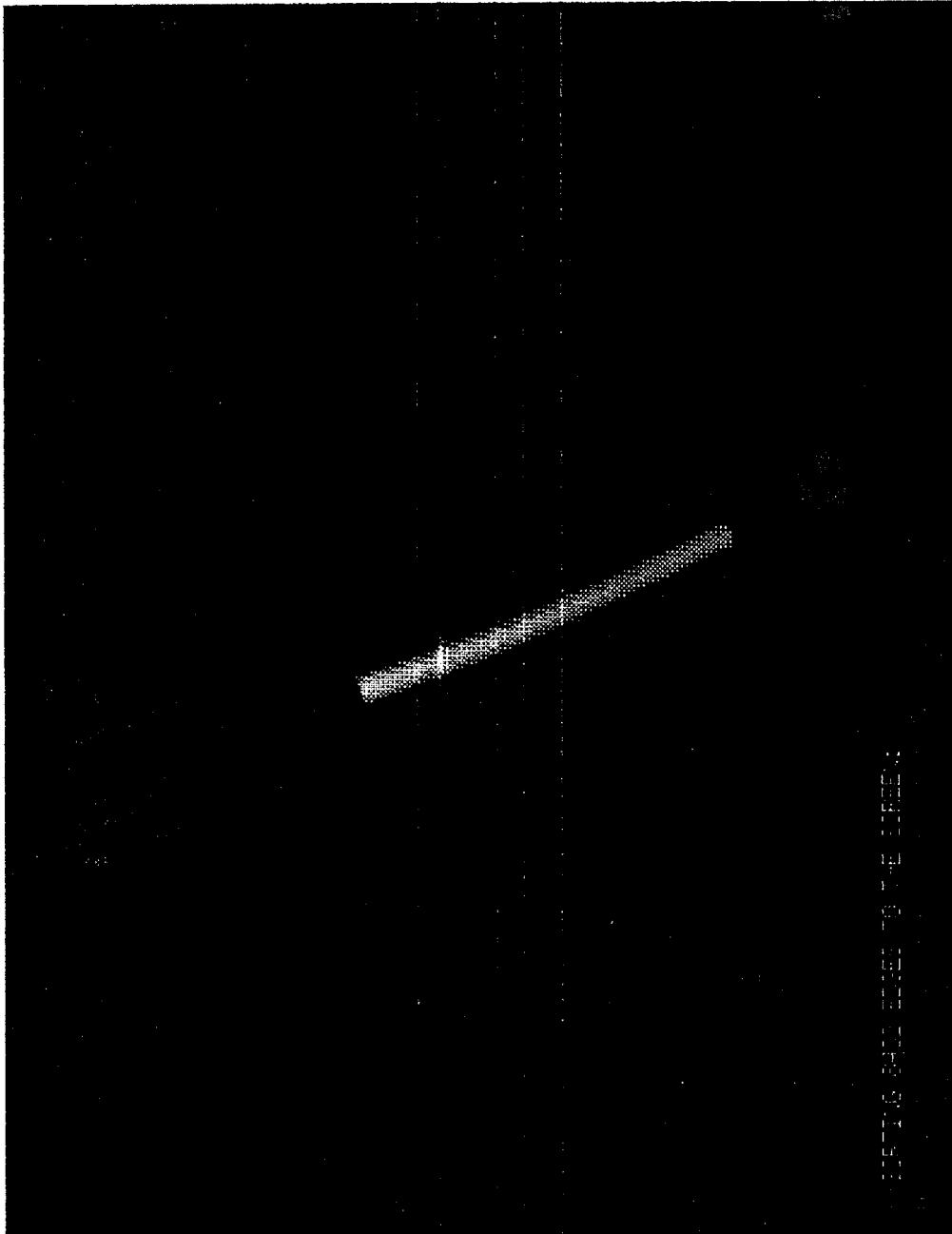
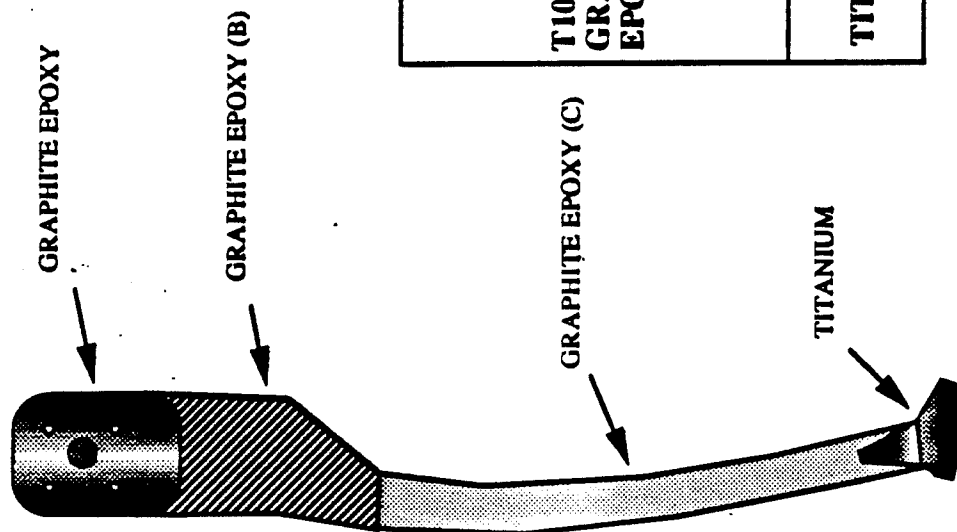


Figure 3.2.2-28. Detailed 3-D ABAQUS Finite Element Model.



T1000G GRAPHITE EPOXY	LAYER	A	B	C
	0°	15%	39%	50%
	±45°	22%	44%	40%
	90°	15%	17%	10%
TITANIUM		48%		

Figure 3.2.2-29. Material Architecture Layup for the Tibia Long Bone.

Tension/Compression Analysis

The load magnitudes for the tibia in compression and tension are identical (3000 lb), and by small displacement theory, the results are the same with opposite signs for all stress and strain components. Figures 3.2.2-30 through 3.2.2-39 present color contour plots of the axial stress, axial strain, 45° stress, 45° strain, shear stress and shear strain under the 3000 lb tension and compression loads. A summary of the stress, strain, and margin of safety results is shown in Table 3.2.2-2. Deformed shape contour plots for the compression and tension load cases plotted over the undeformed shape are shown in Figures 3.2.2-40 and 3.2.2-41. The main contribution to the deflections for both load cases are the in-plane lateral (forward/backward) movement at the diaphysis of the tibia long bone. Finite element analyses predicted the maximum in-plane lateral deflection to be about 0.12 inches and maximum compression/extension displacement to be 0.04 inches. All stresses and strains are below allowables, and thus margins of safety are all positive as shown in Figures 3.2.2-42 and 3.2.2-43.

Lateral Bending and Torsion Analysis

Stress and strain components and strain margins of safety for the lateral bending and pure torsion load cases are shown in Table 3.2.2-2. Color contour plots of the results are shown in Figures 3.2.2-44 to 3.2.2-57. As seen in these plots, most high stresses and strains are localized at the tibia "neck" where the transition between the long bone and the knee joint is located. However, all resulting stresses and strains are below material allowables (Table 3.2.2-3) resulting in adequate margins of safety for both load cases (Figures 3.2.2-58 to 3.2.2-62). Total displacement contour plots for both load cases are shown in Figures 3.2.2-63 and 3.2.2-64. The maximum angle of twist caused by torsion is about 12 degrees (0.21 radians), and the maximum lateral bending deflection is about 0.12 inches.

Conclusions

Based on the results from the tibia finite element analyses, it is concluded that the structural design is adequate. As shown in Table 3.2.2-4 margins of safety are positive in all loading cases for the final tibia design. The lowest margins are in the "neck" region. The estimated weight of the tibia, including the titanium ankle, was 1.20 lb (0.46Kg).

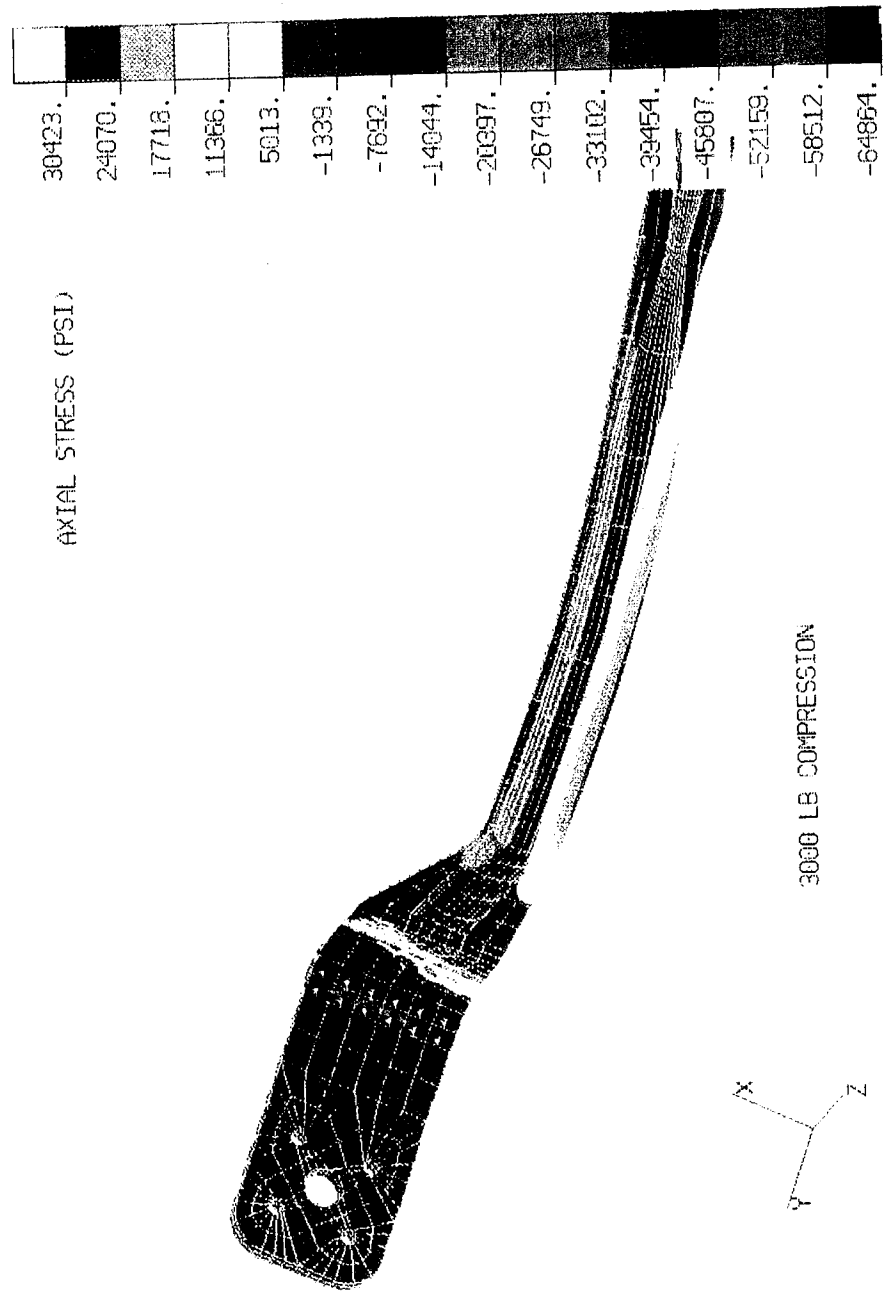


Figure 3.2.2-30. Tibia Axial Stress Resulting from 3000 lb Compression.

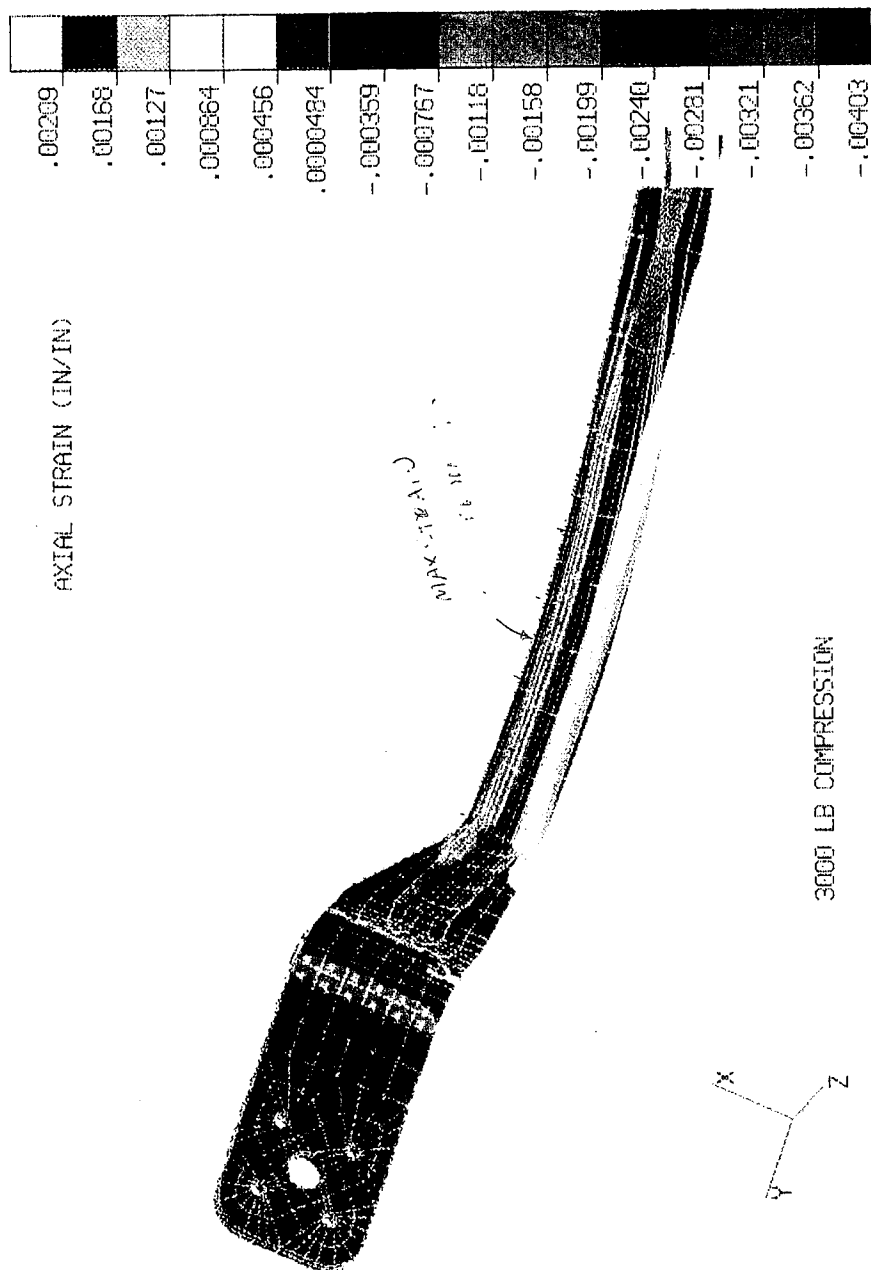


Figure 3.2.2-31. Tibia Axial Fiber Strain Resulting From 3000 lb. Compression.

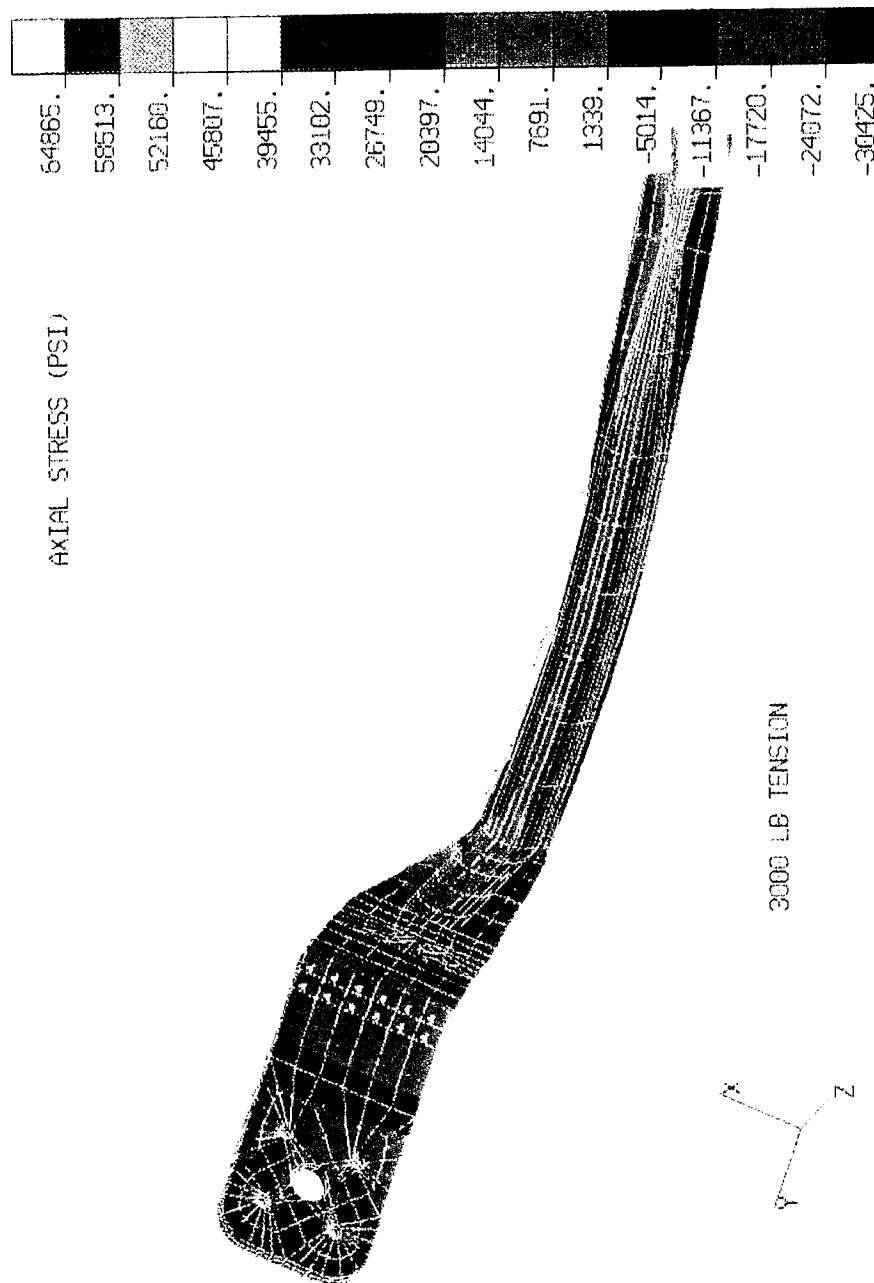


Figure 3.2.2-32. Tibia Axial Stress Resulting From 3000 lb. Compression.

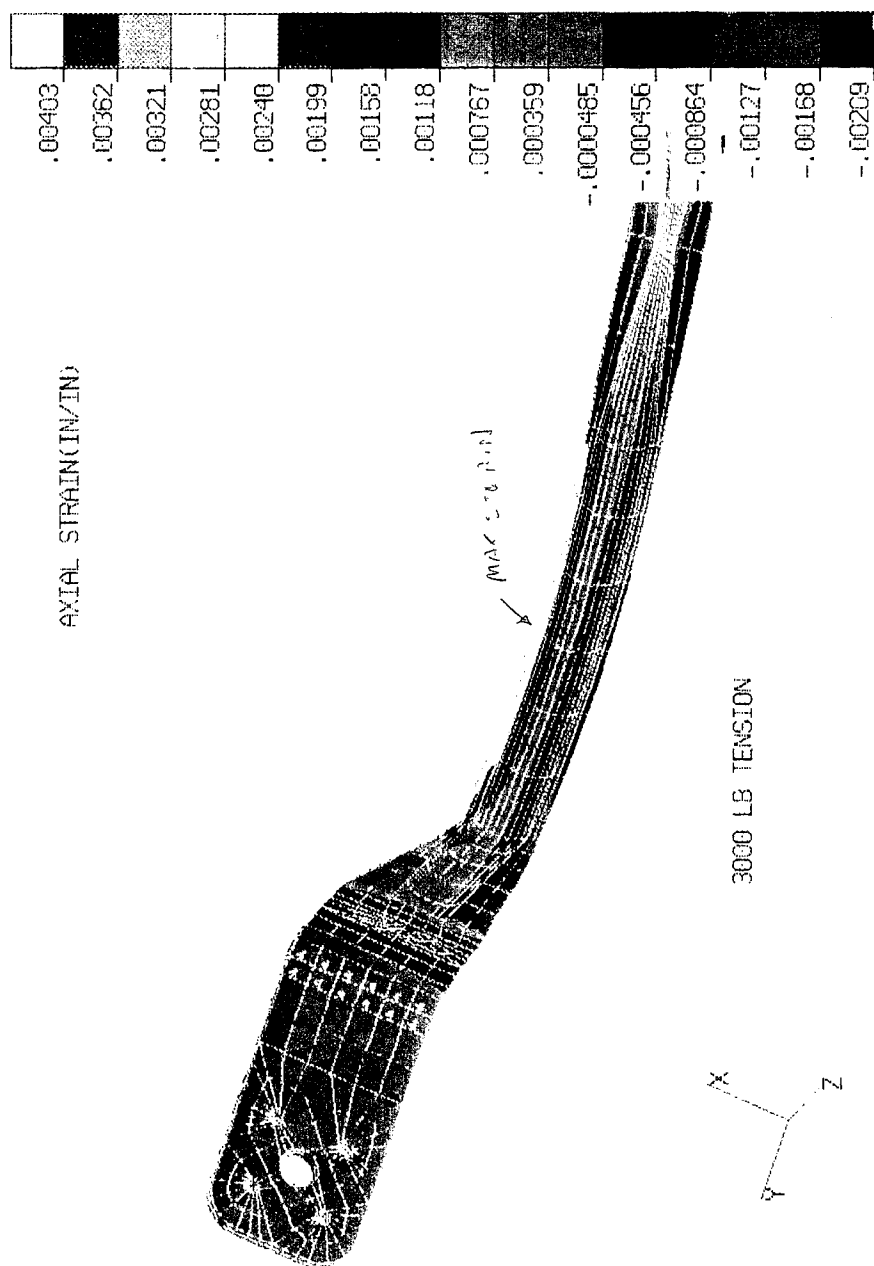


Figure 3.2.2-33. Tibia Axial Fiber Strain Resulting From 3000 lb. Compression.

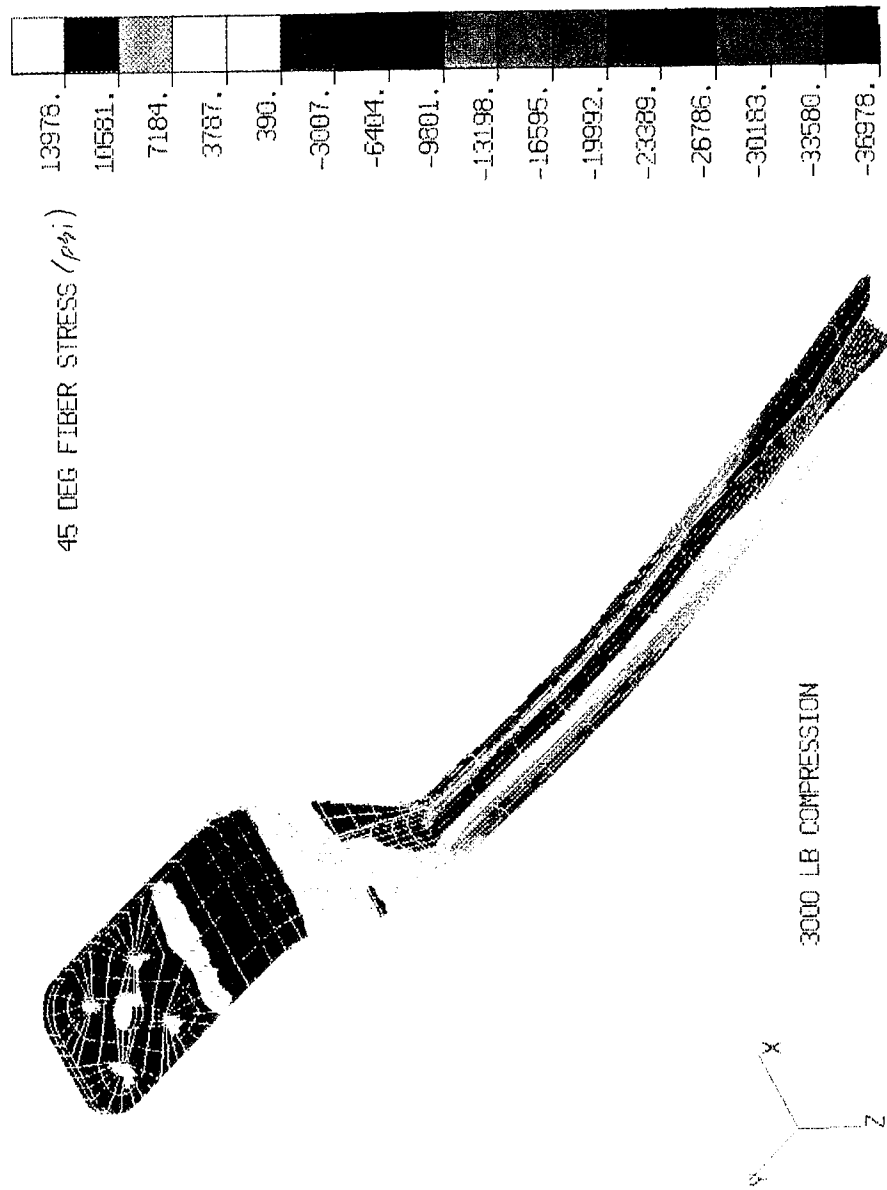


Figure 3.2.2-34. Tibia 45° Fiber Strain Resulting From 3000 lb. Compression.

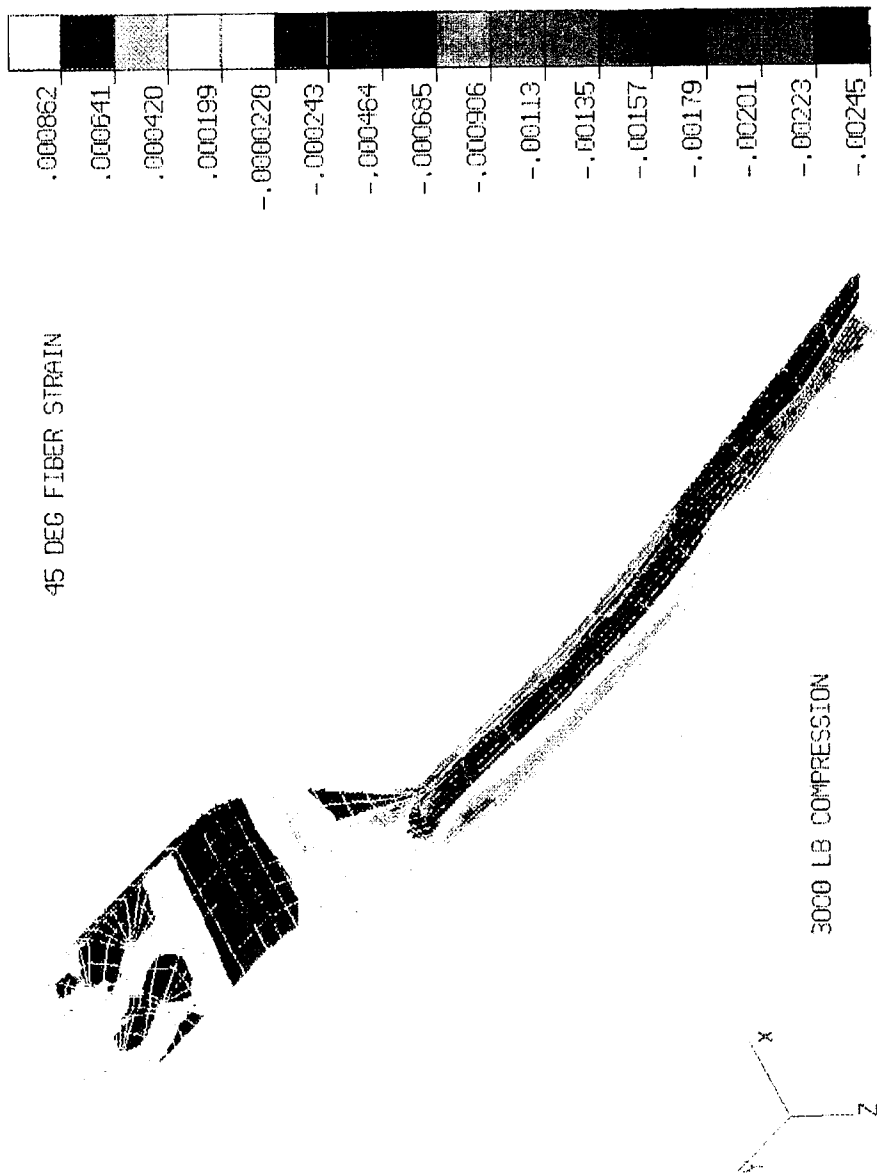


Figure 3.2.2-35. Tibia 45° Fiber Strain Resulting From 3000 lb. Compression.

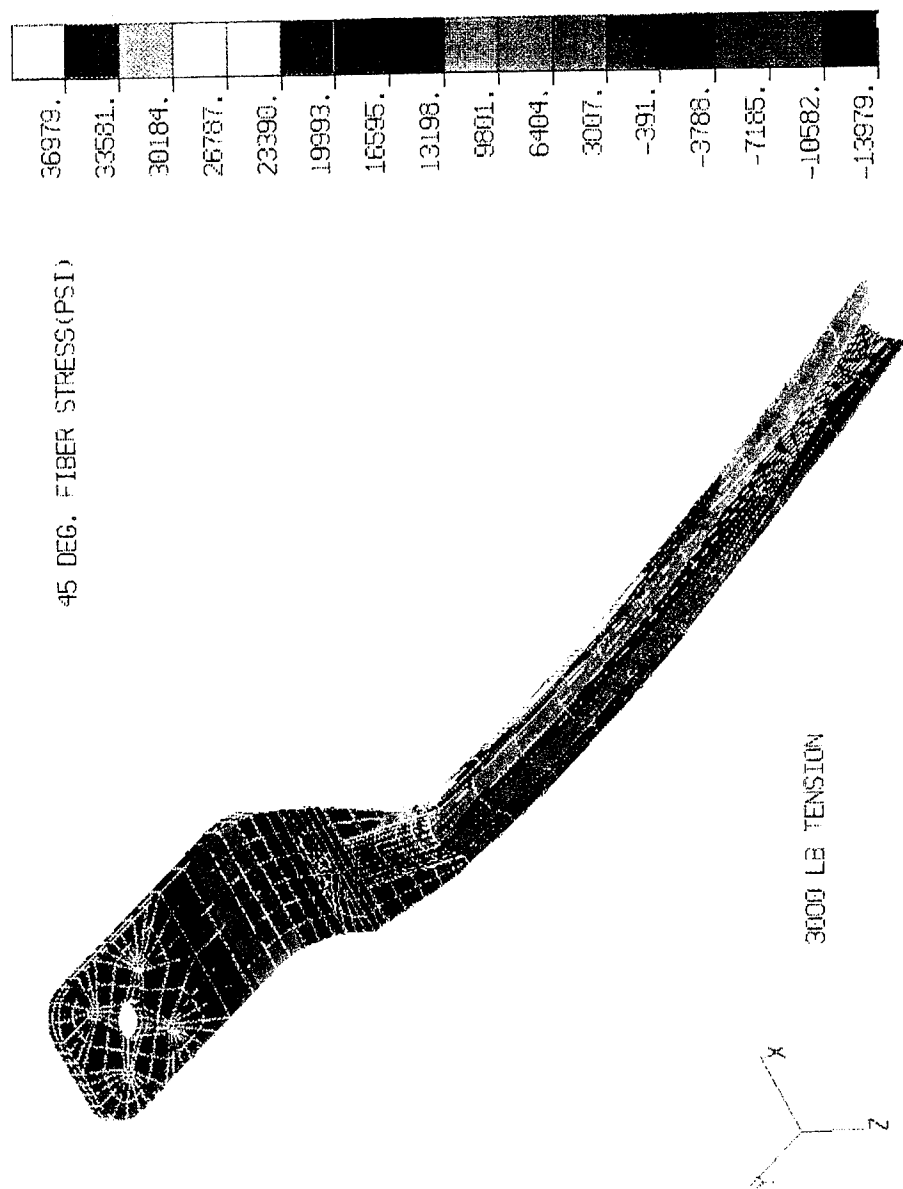


Figure 3.2.2-36. Tibia 45° Fiber Stress Resulting From 3000 lb. Compression.

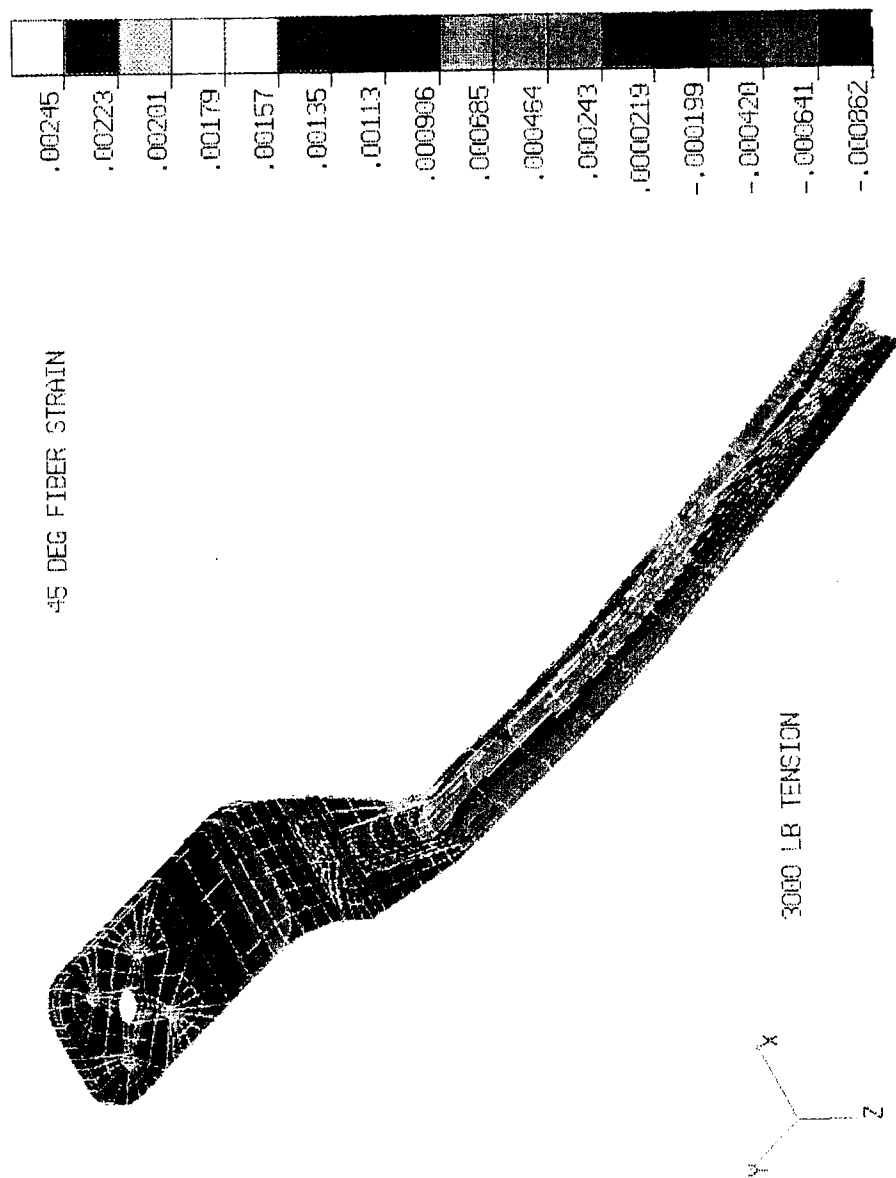


Figure 3.2.2-37. Tibia 45° Fiber Strain Resulting From 3000 lb. Compression.

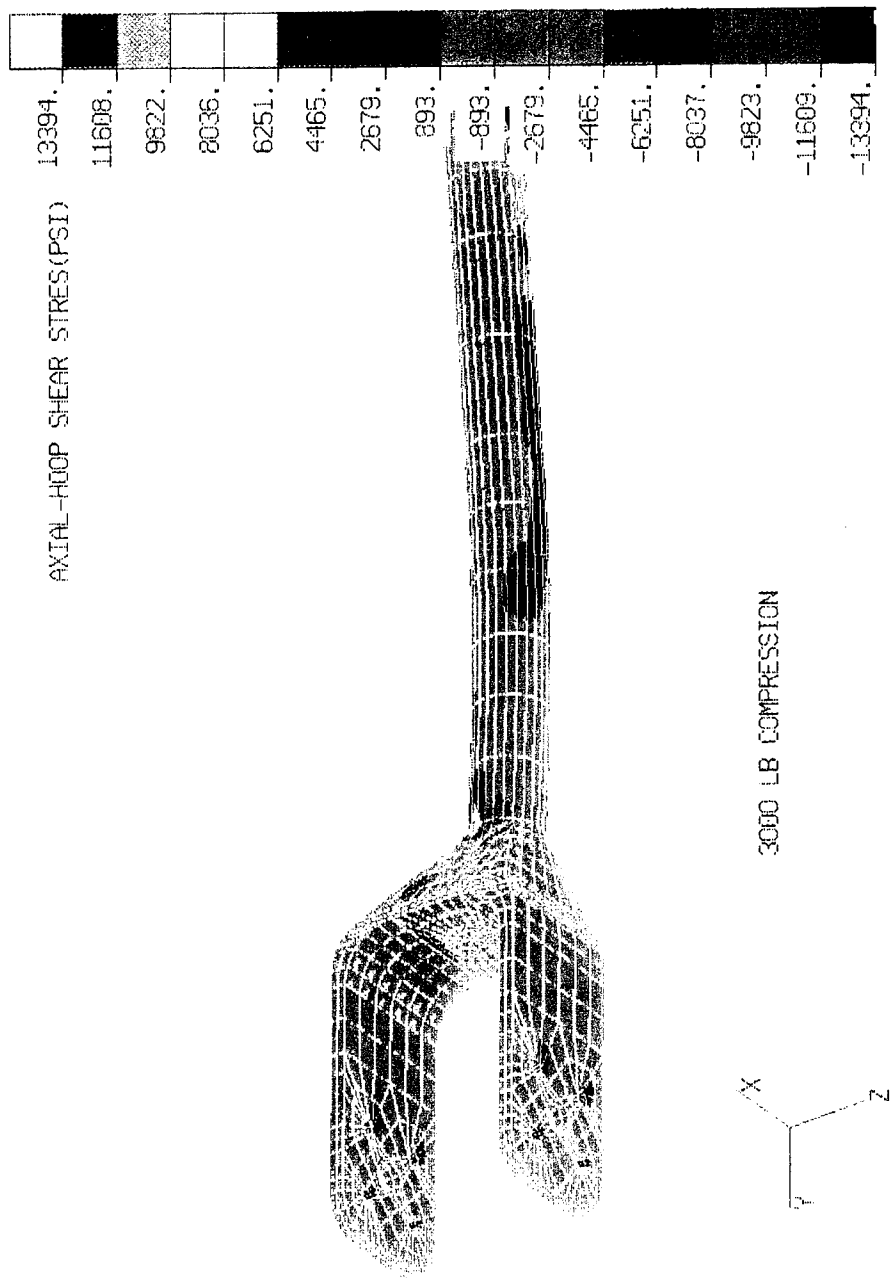


Figure 3.2.2-38. Axial Hoop Shear Stress Resulting From 3000 lb. Compression/Tension.

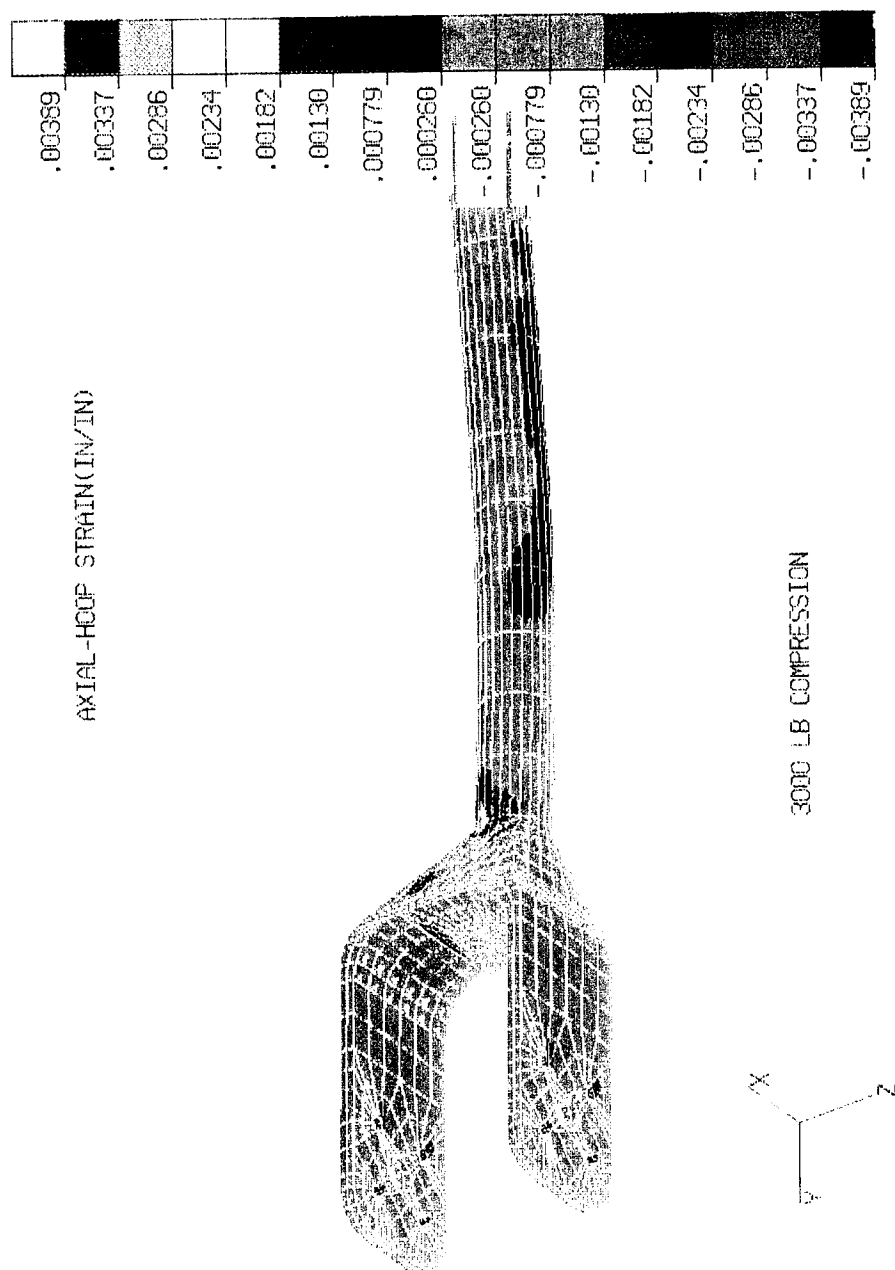


Figure 3.2.2-39. Axial Hoop Shear Strain Resulting From 3000 lb. Compression/Tension.

This page left intentionally blank

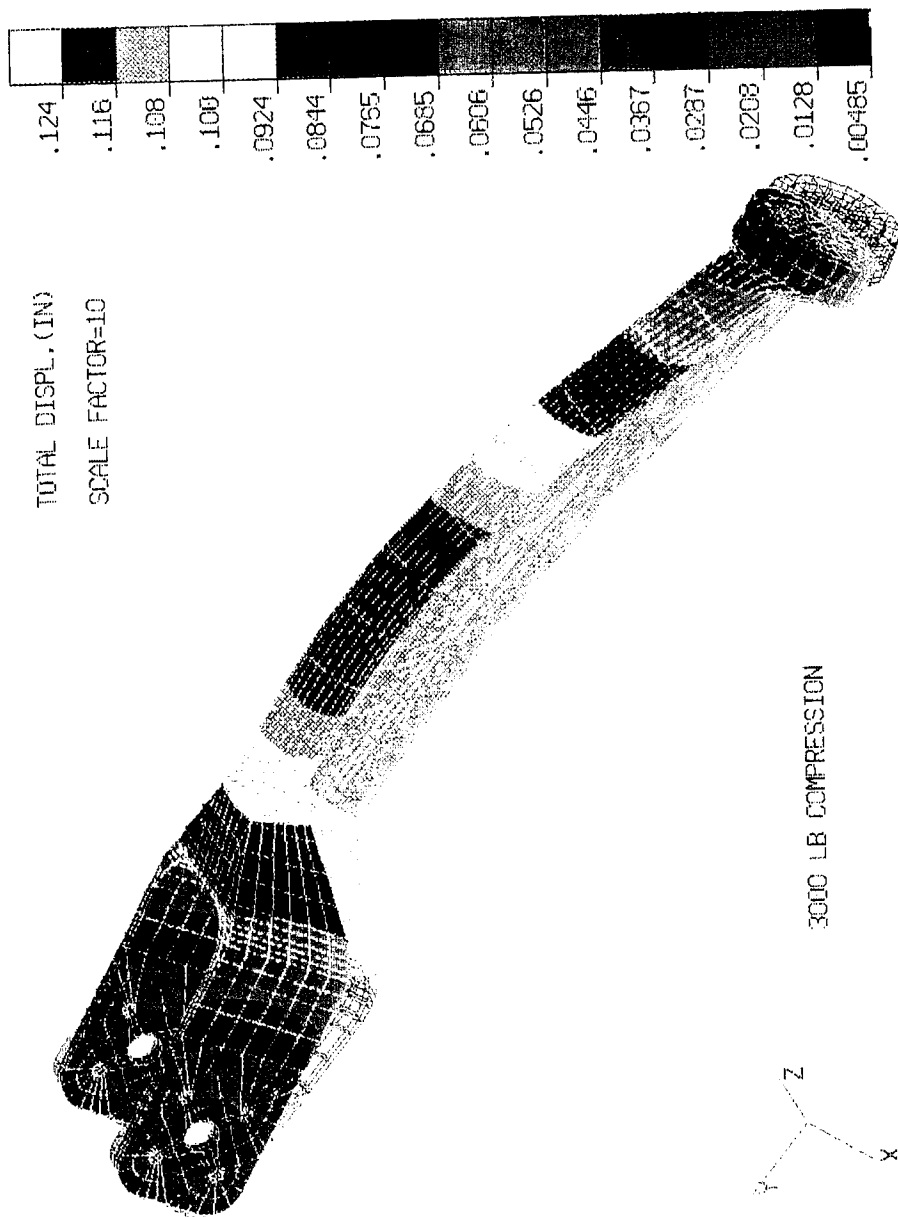


Figure 3.2.2-40. Tibia Total Displacement Resulting From 3000 lb. Compression.

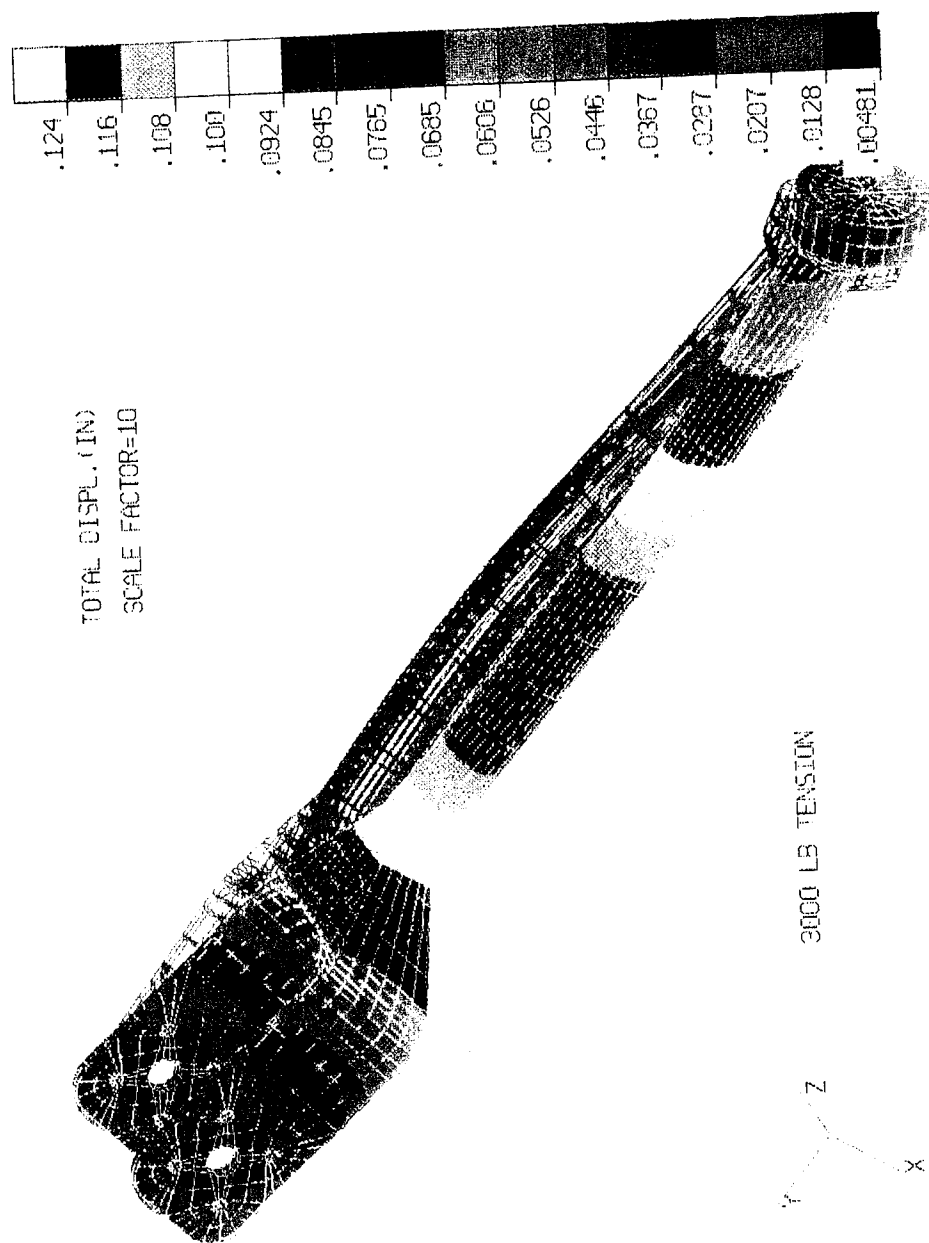


Figure 3.2.2-41. Tibia Total Displacement Resulting From 3000 lb. Tension.

AXIAL FIBER STRAIN M.S.

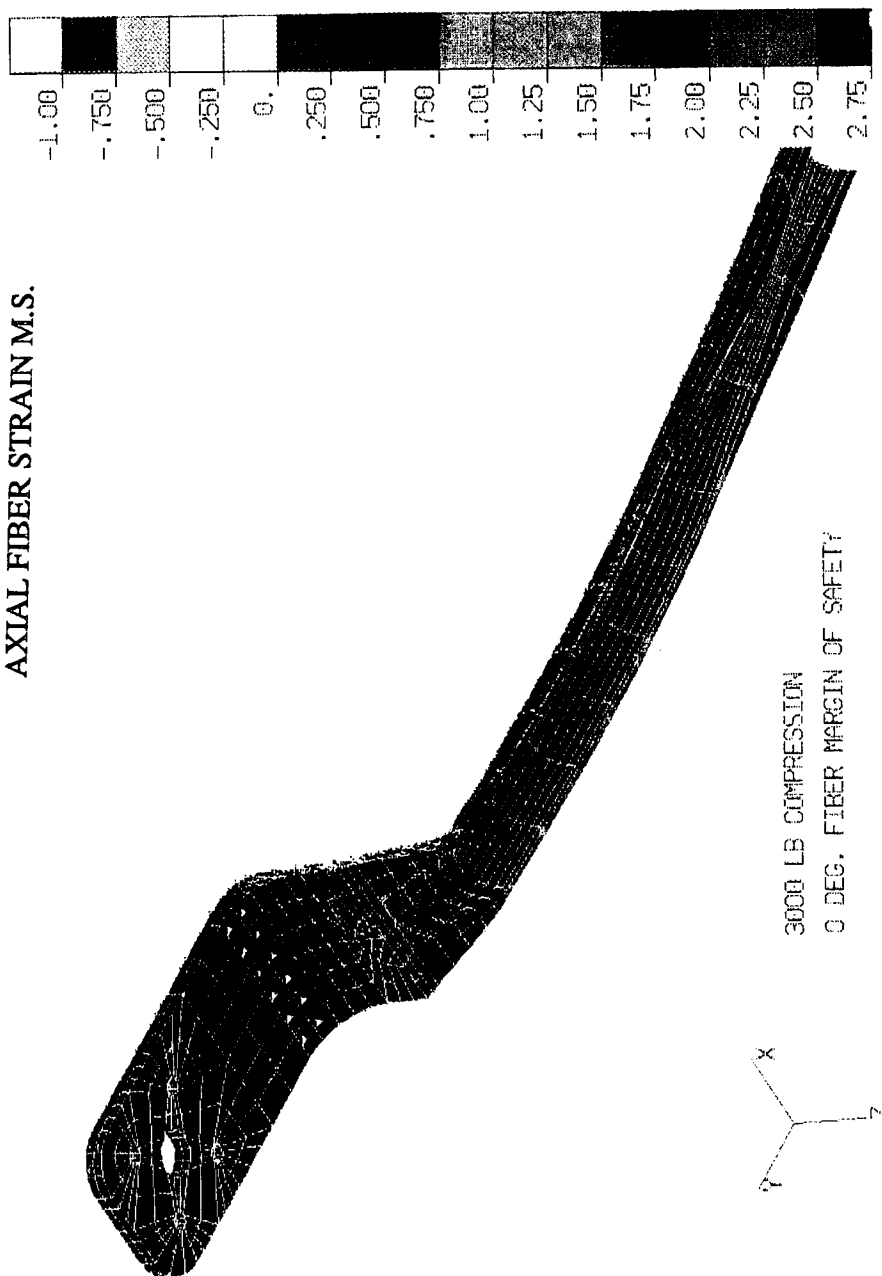


Figure 3.2.2-42. Tibia 3000 lb Compression or Tension has High Axial Fiber Strain Margin of Safety.

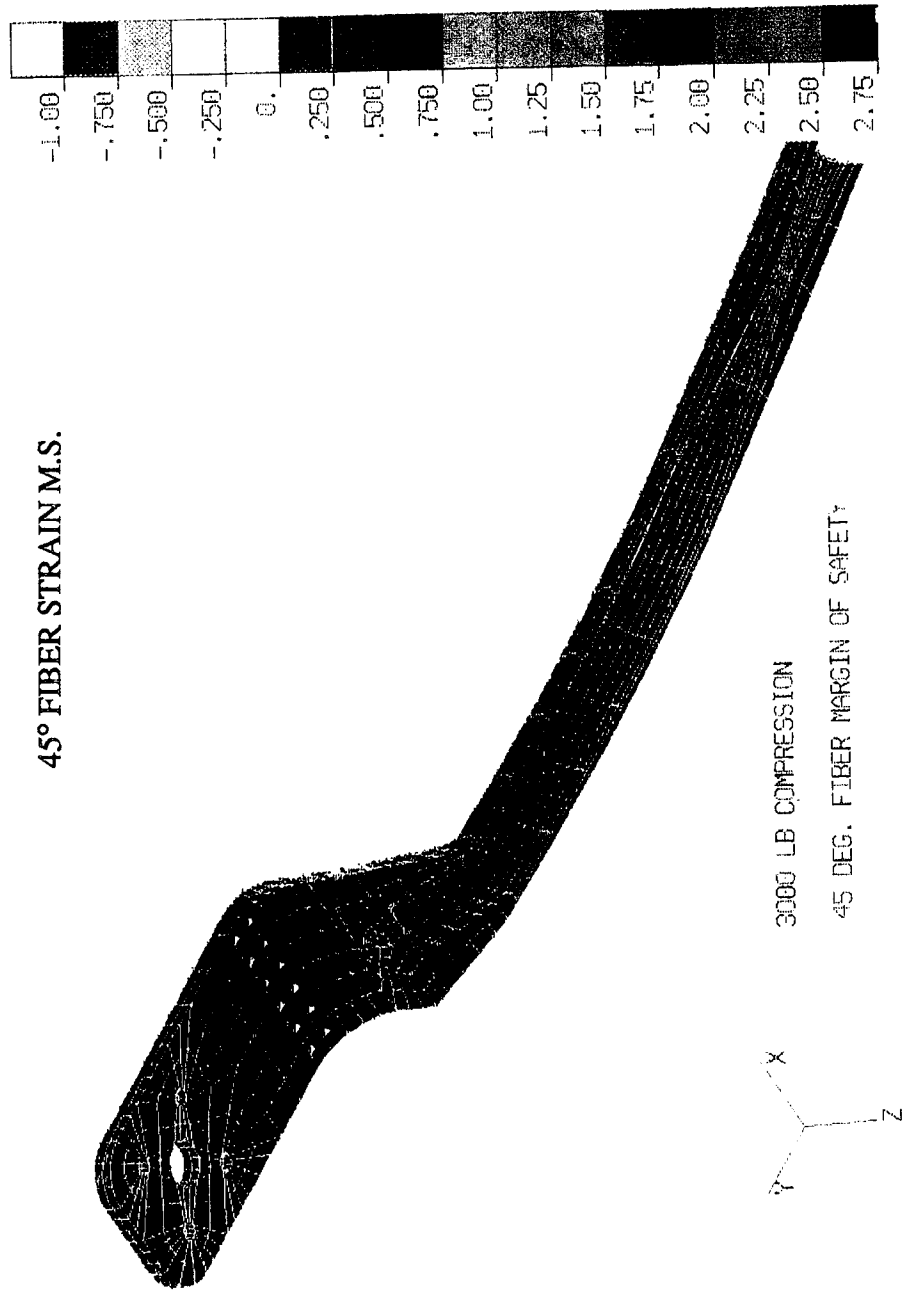


Figure 3.2.2-43. Tibia 3000 lb Compression or Tension has 45° Fiber Strain Margin of Safety.

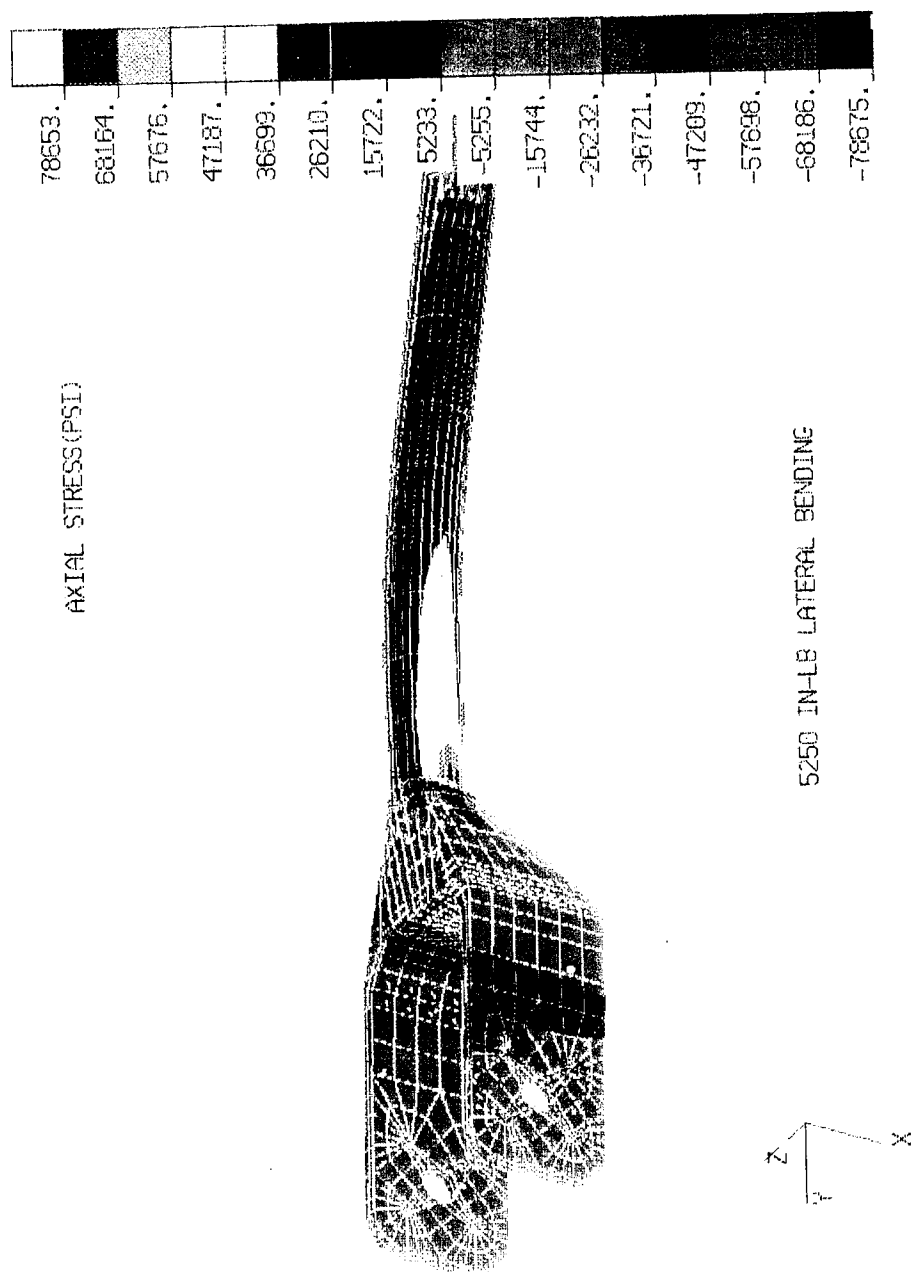


Figure 3.2.2-44. Tibia Axial Stress Resulting from 5250 in-lb. Lateral Bending.

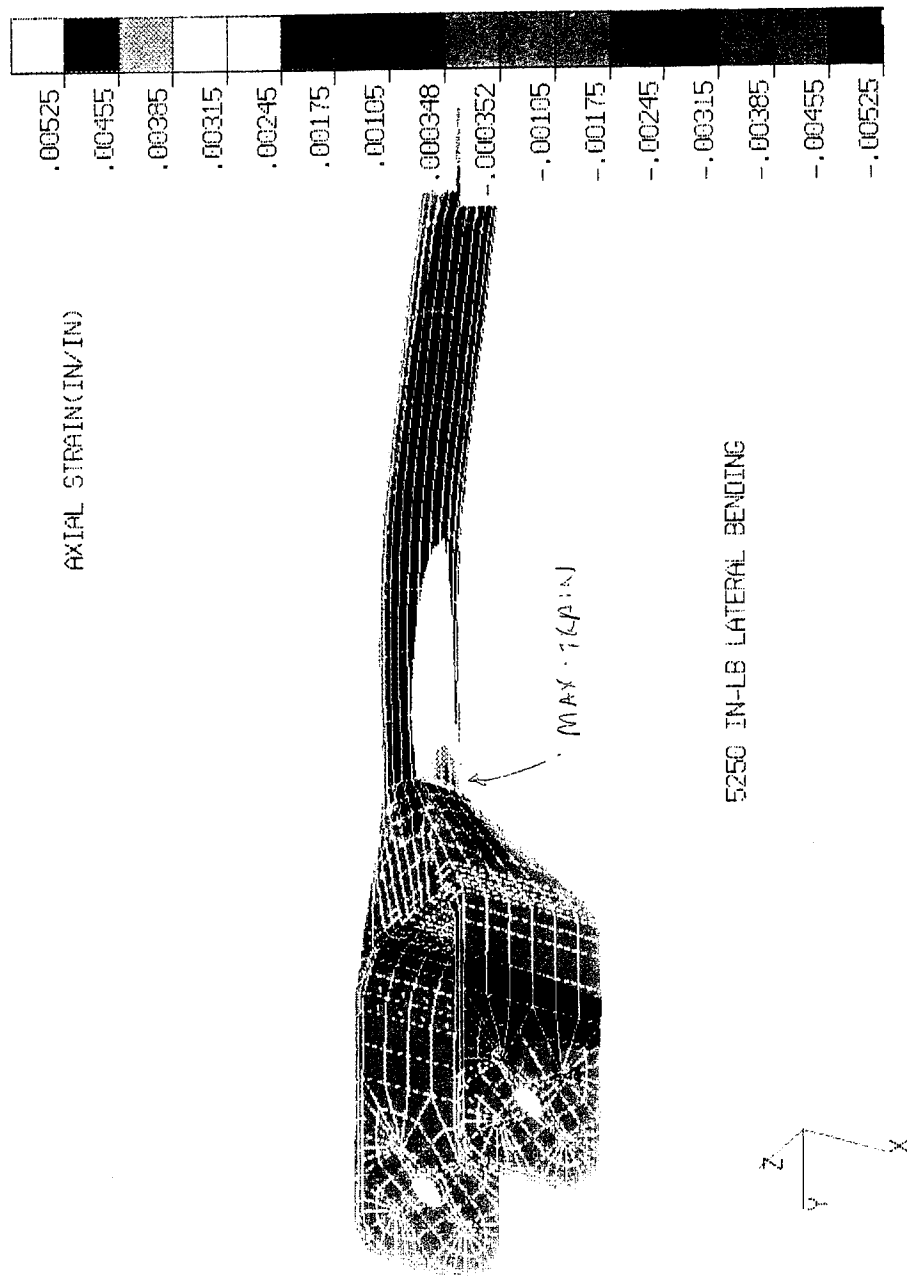


Figure 3.2.2-45. Tibia Axial Fiber Strain Resulting from 5250 in-lb. Lateral Bending.

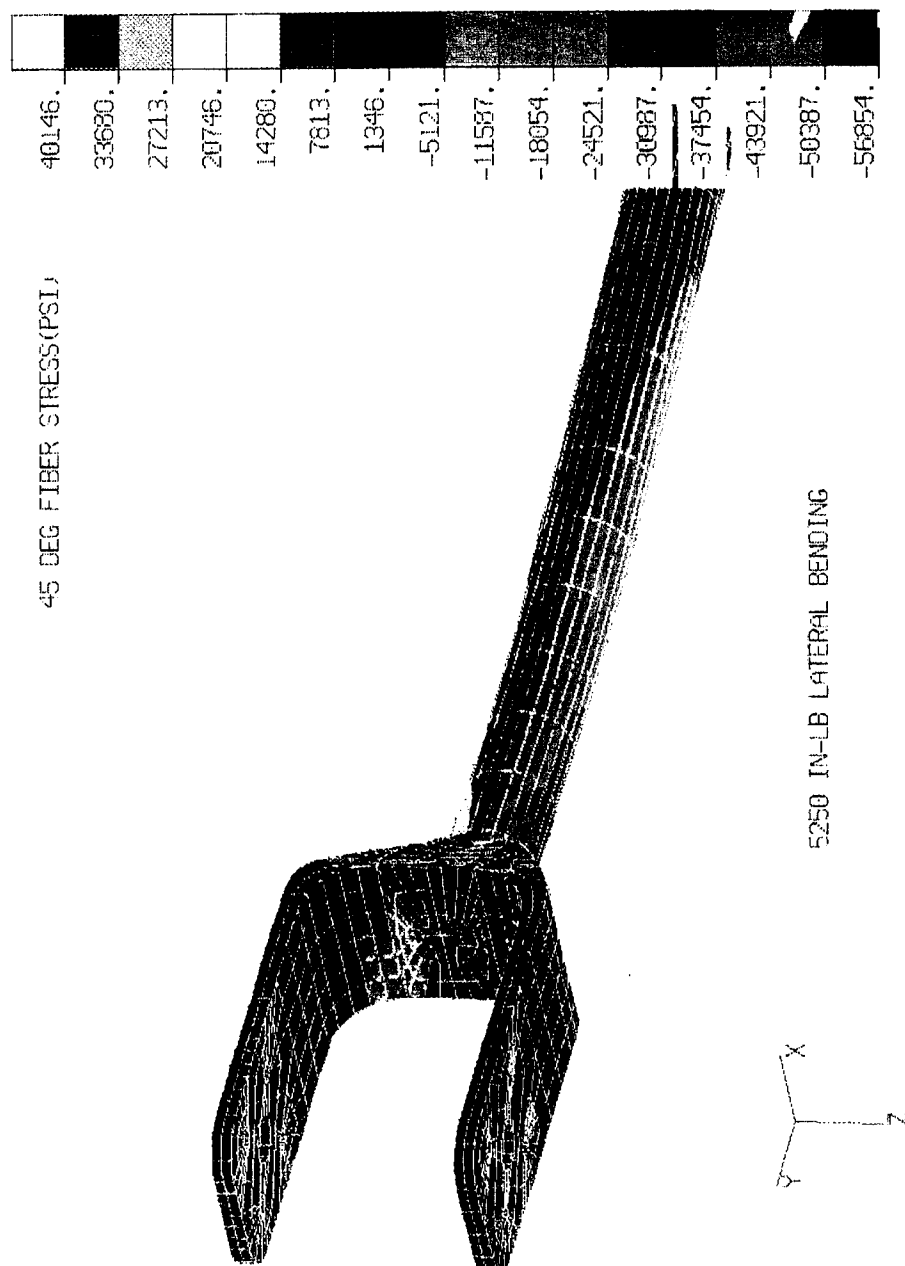


Figure 3.2.2-46. Tibia 45° Fiber Stress Resulting from 5250 in-lb. Lateral Bending.

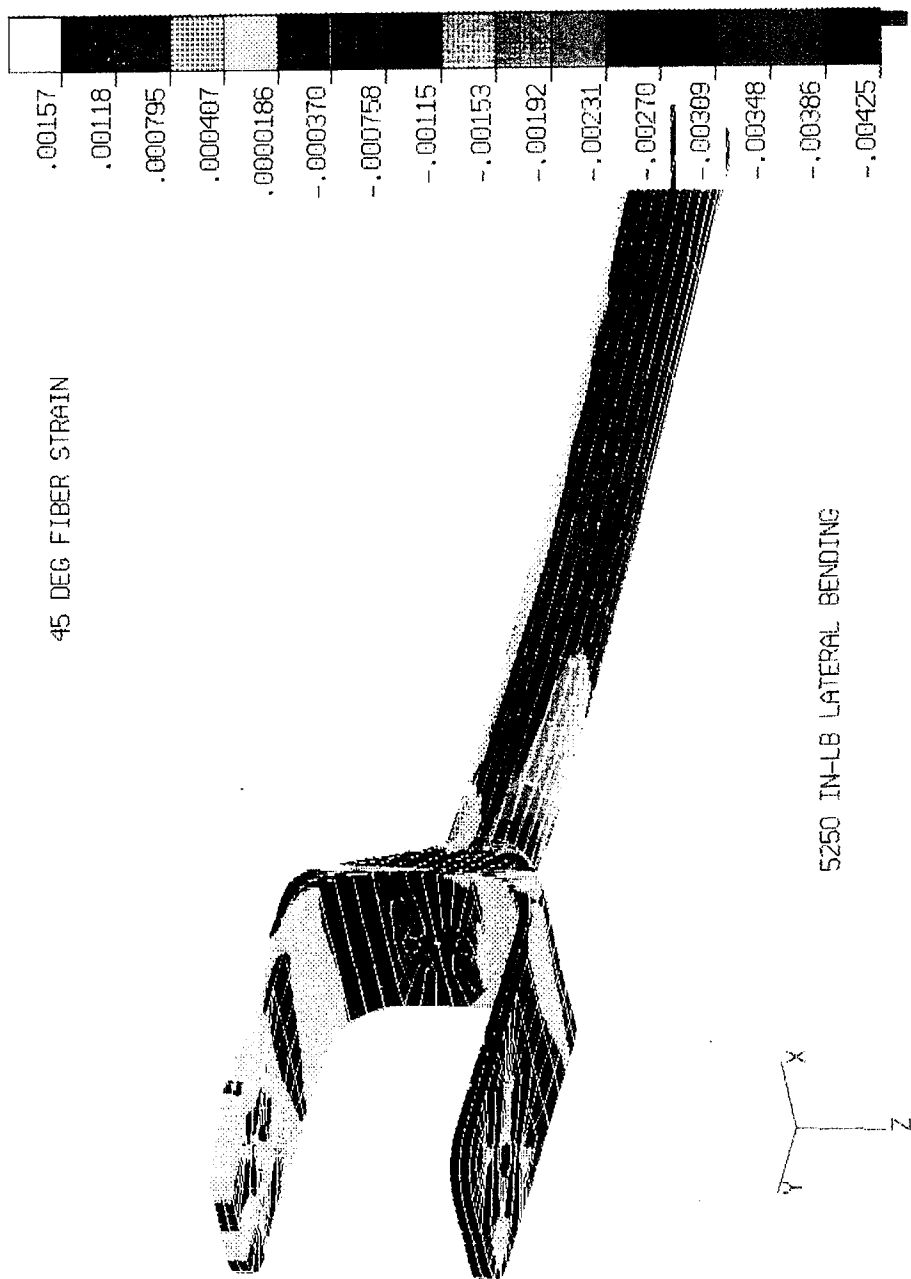


Figure 3.2.2-47. Tibia 45° Fiber Strain Resulting from 5250 in-lb. Lateral Bending.

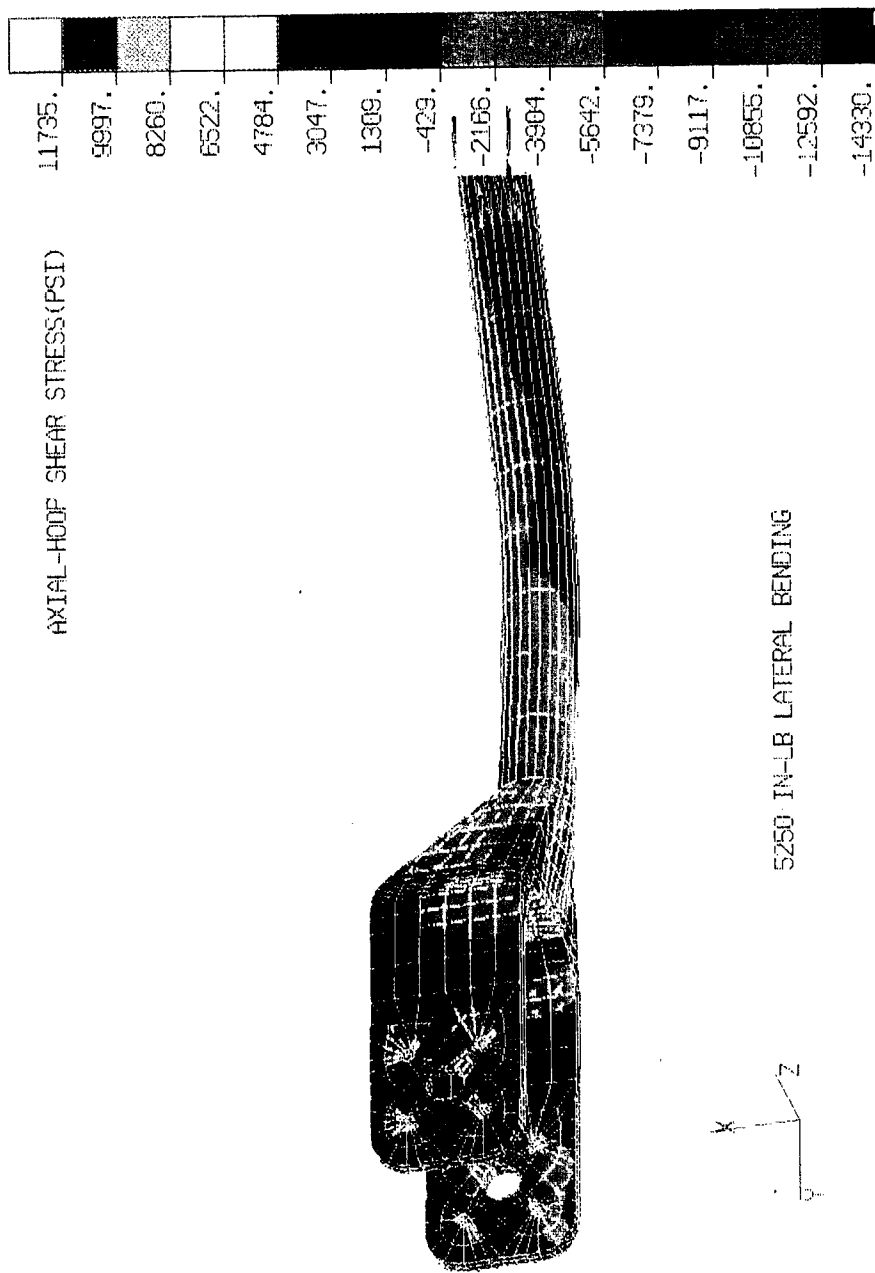


Figure 3.2.2-48. Tibia Axial Hoop Shear Stress Resulting from 5250 in-lb. Lateral Bending.

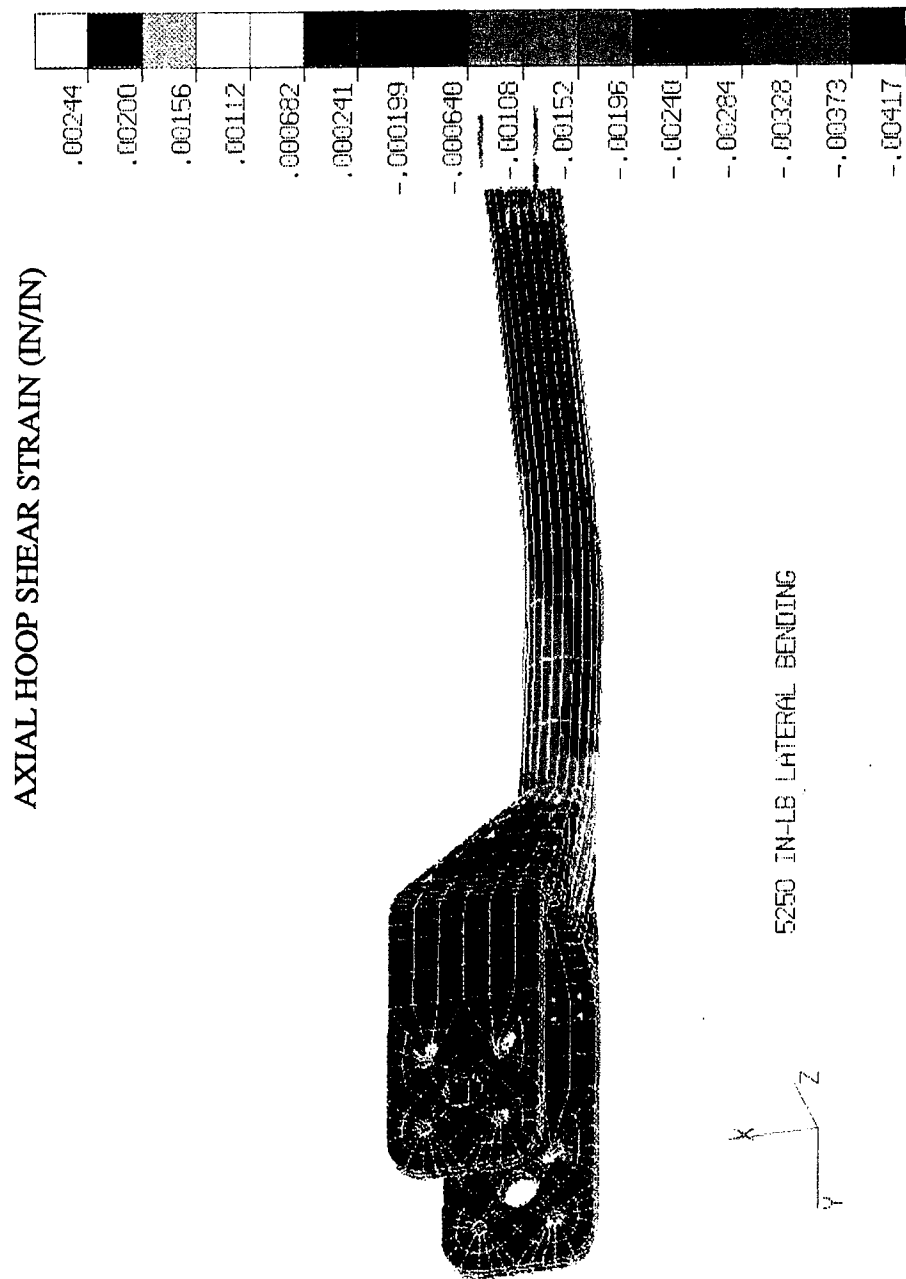


Figure 3.2.2-49. Tibia Axial Hoop Shear Strain Resulting from 5250 in-lb. Lateral Bending.

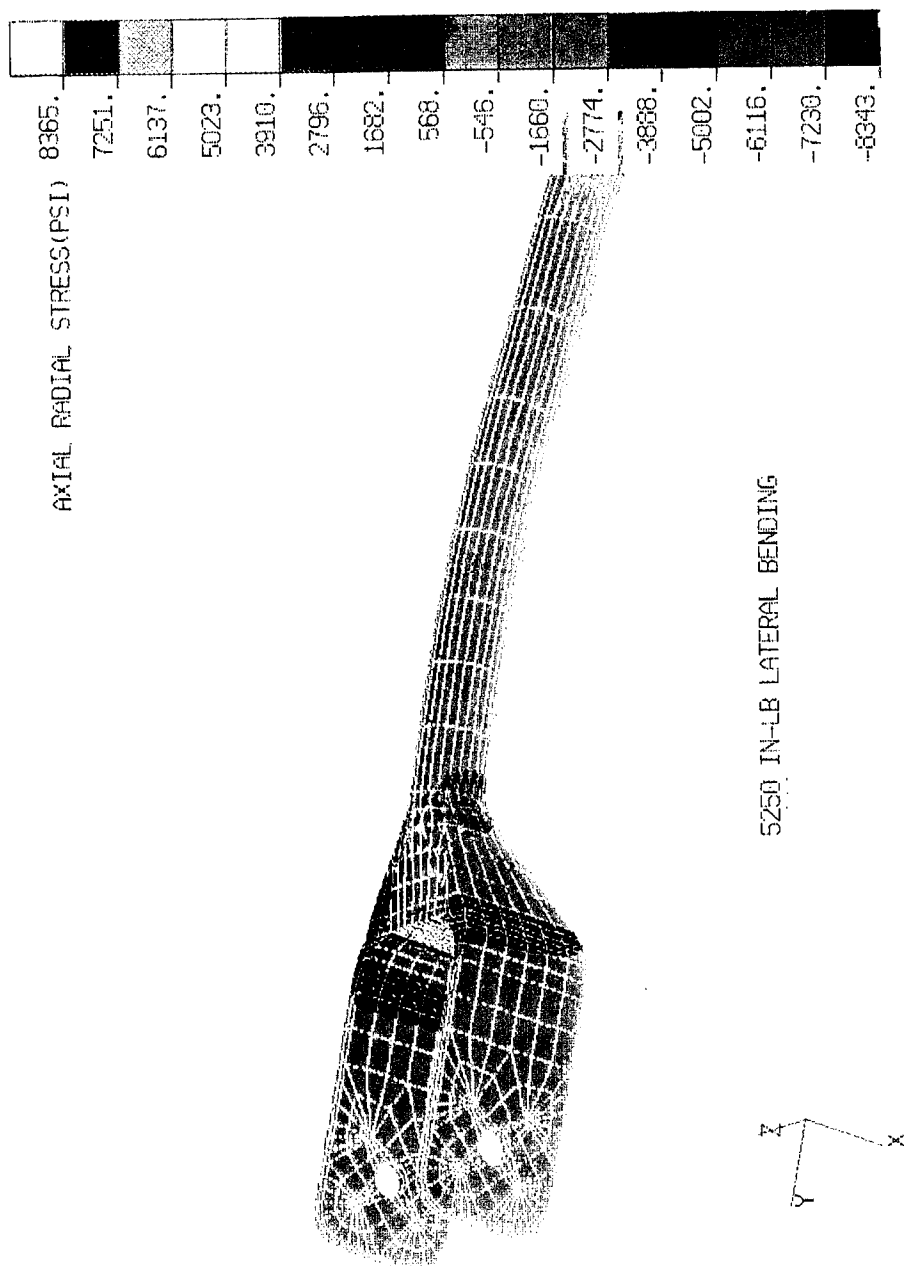


Figure 3.2.2-50. Tibia Axial Radial Shear Stress Resulting from 5250 in-lb. Lateral Bending.

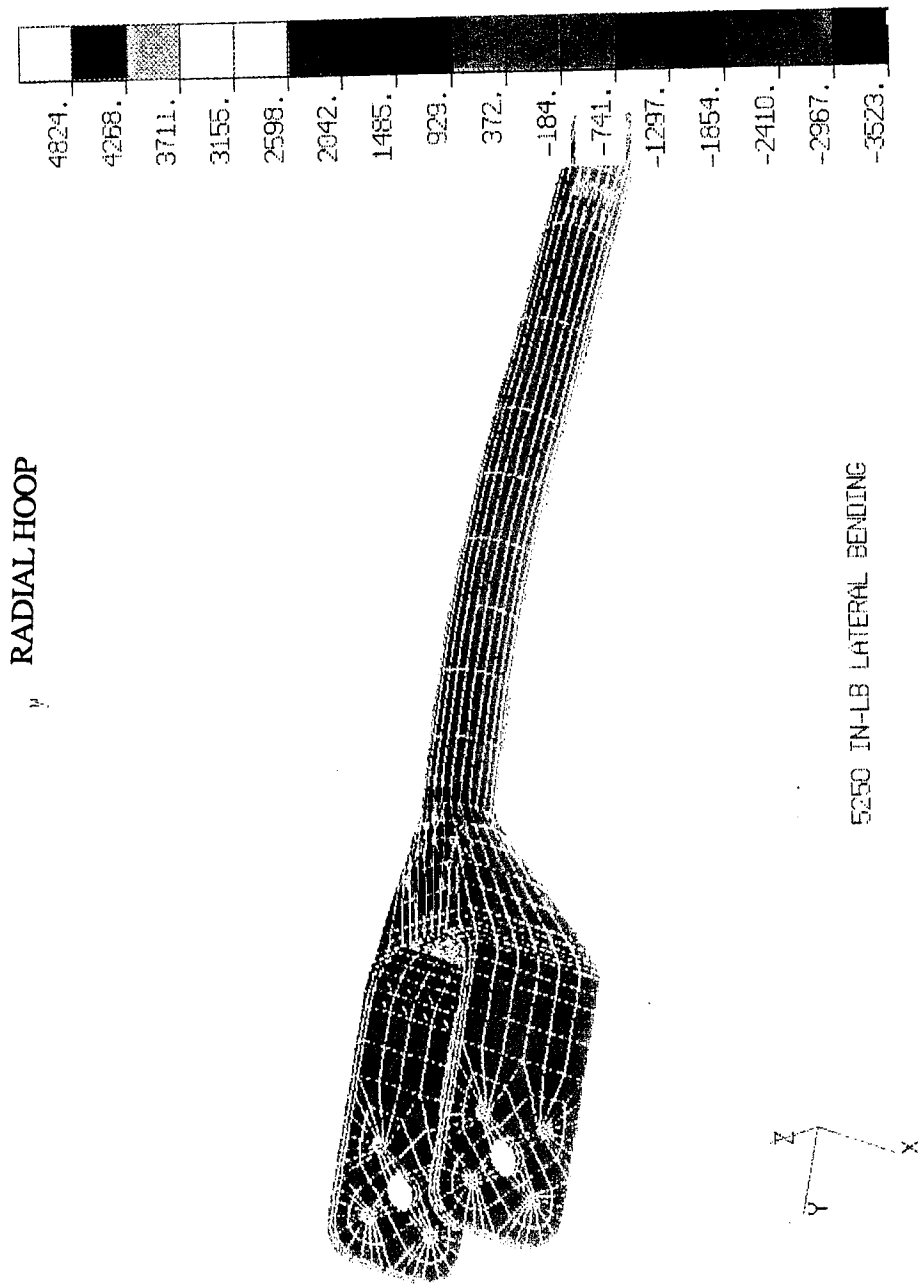


Figure 3.2.2-51. Tibia Radial Hoop Shear Stress Resulting from 5250 in-lb. Lateral Bending.

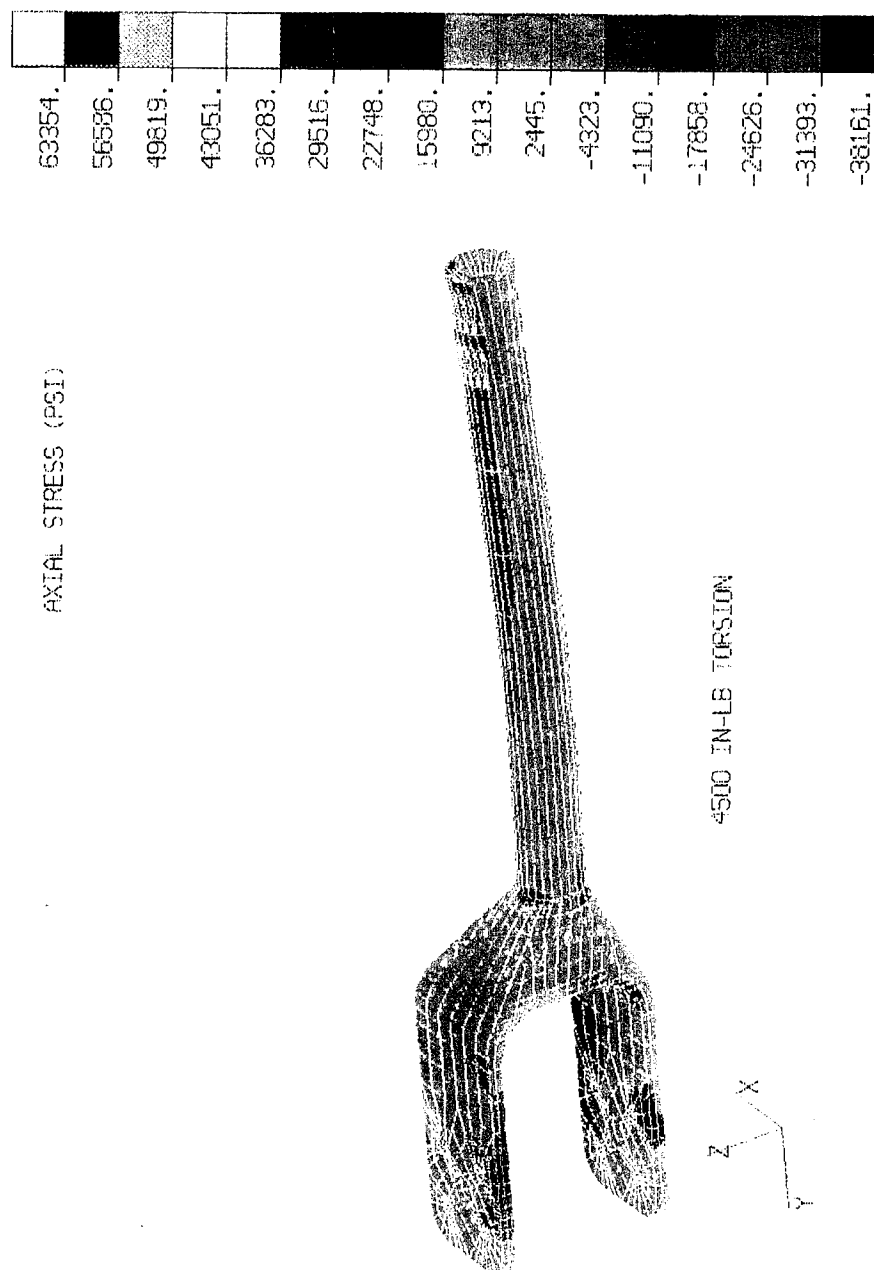


Figure 3.2.2-52. Tibia Axial Stress Resulting from 4500 in-lb. Lateral Bending.

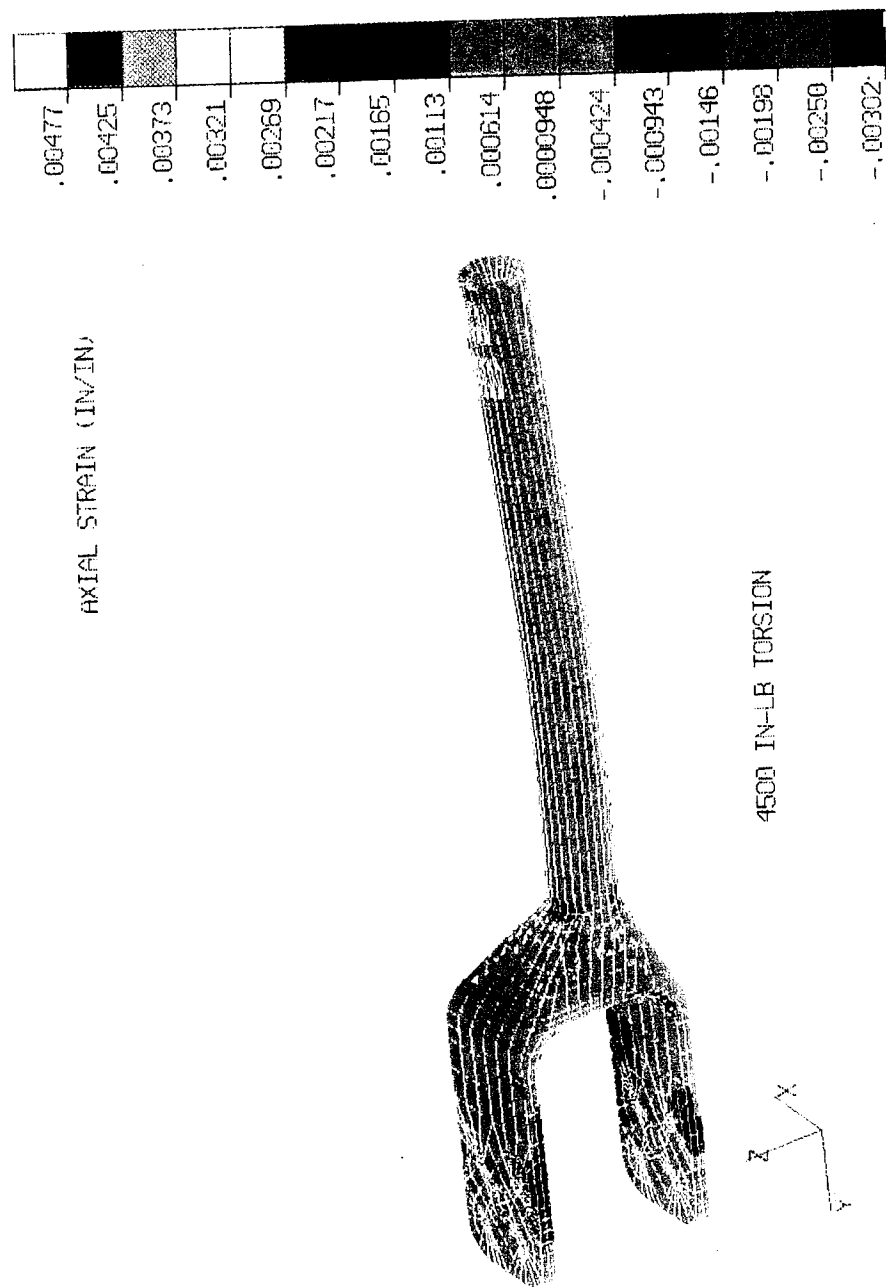


Figure 3.2.2-53. Tibia Axial Strain Resulting from 4500 in-lb Torsion.

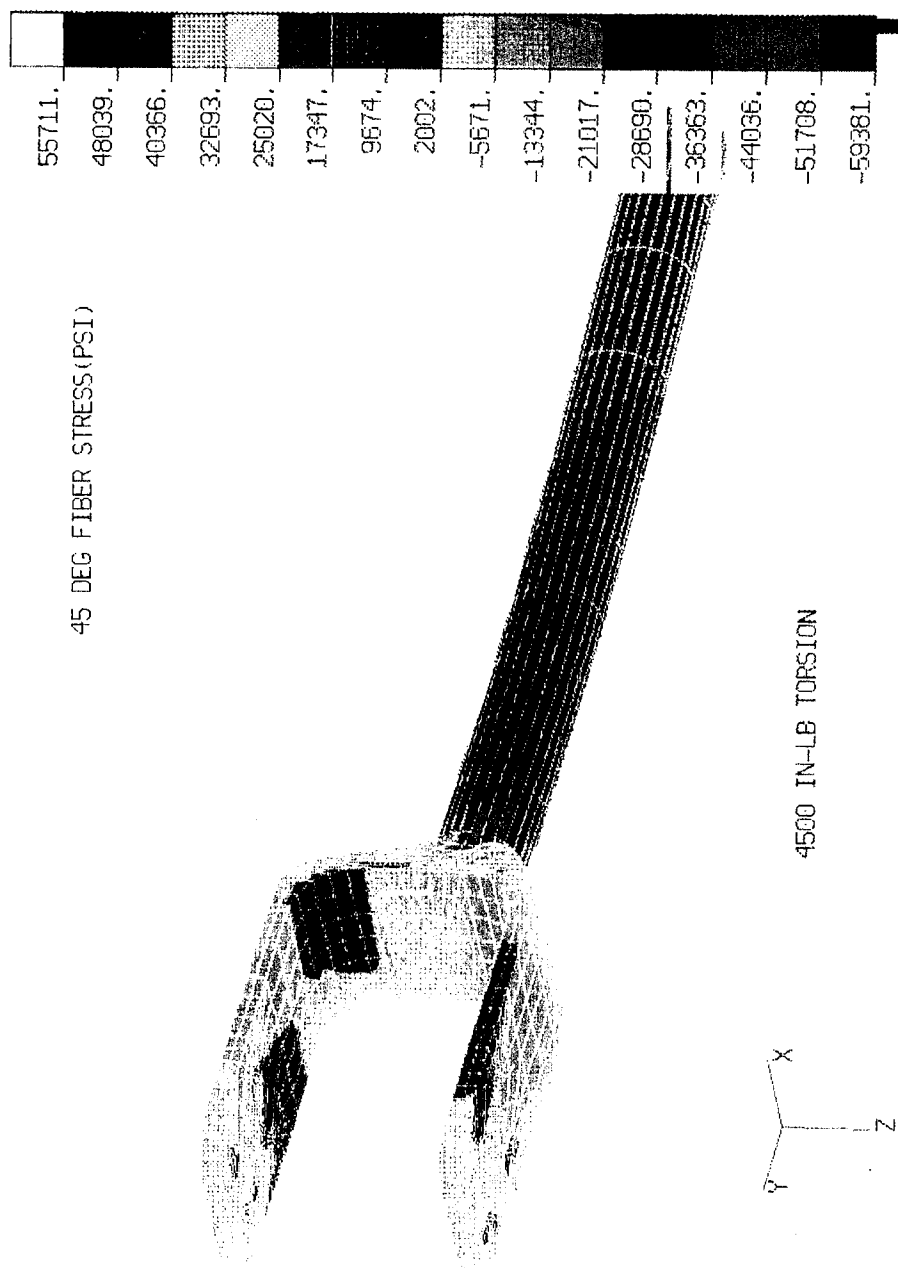


Figure 3.2.2-54. Tibia 45° Fiber Stress Resulting from 4500 in-lb Torsion.

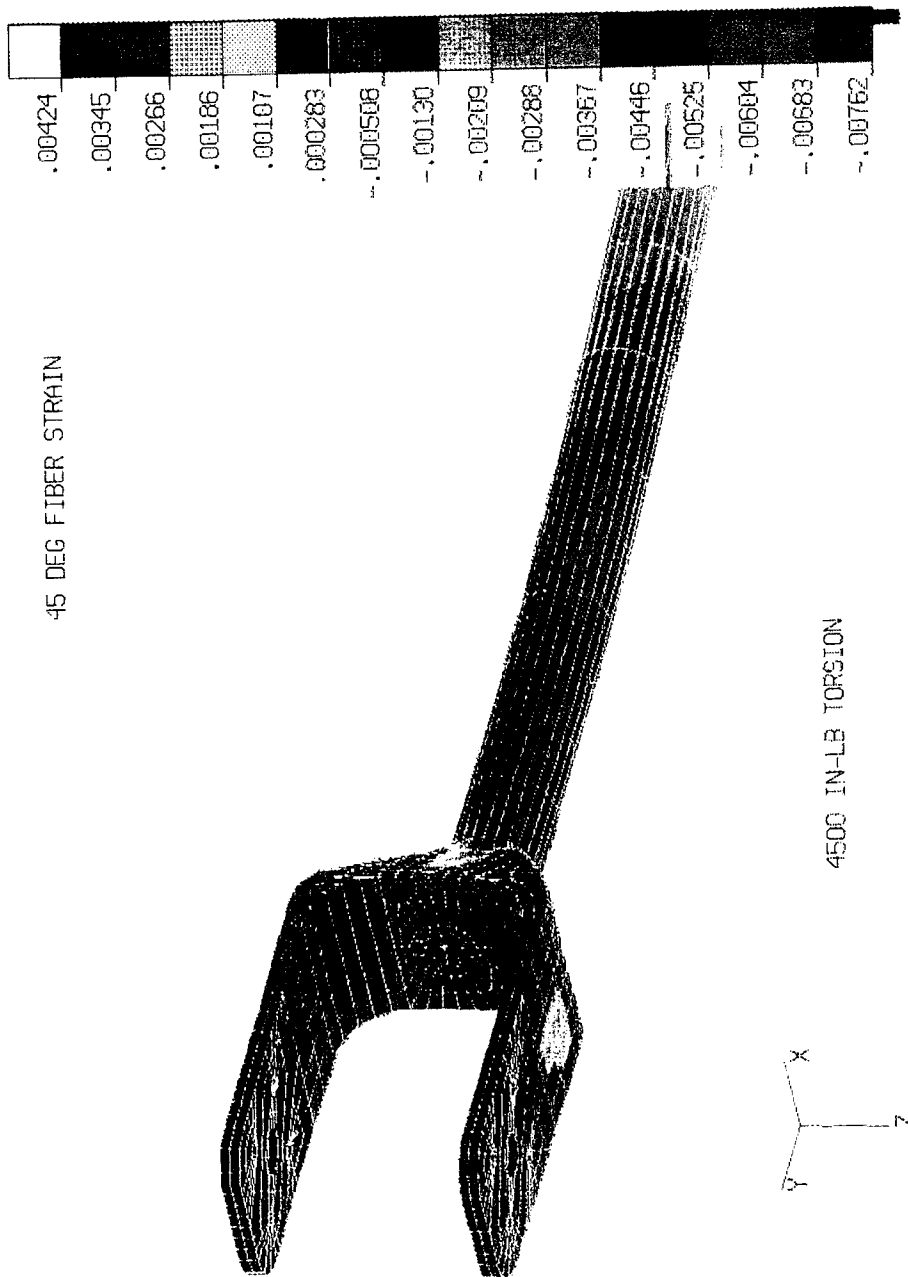


Figure 3.2.2-55. Tibia 45° Fiber Strain Resulting from 4500 in-lb Torsion.

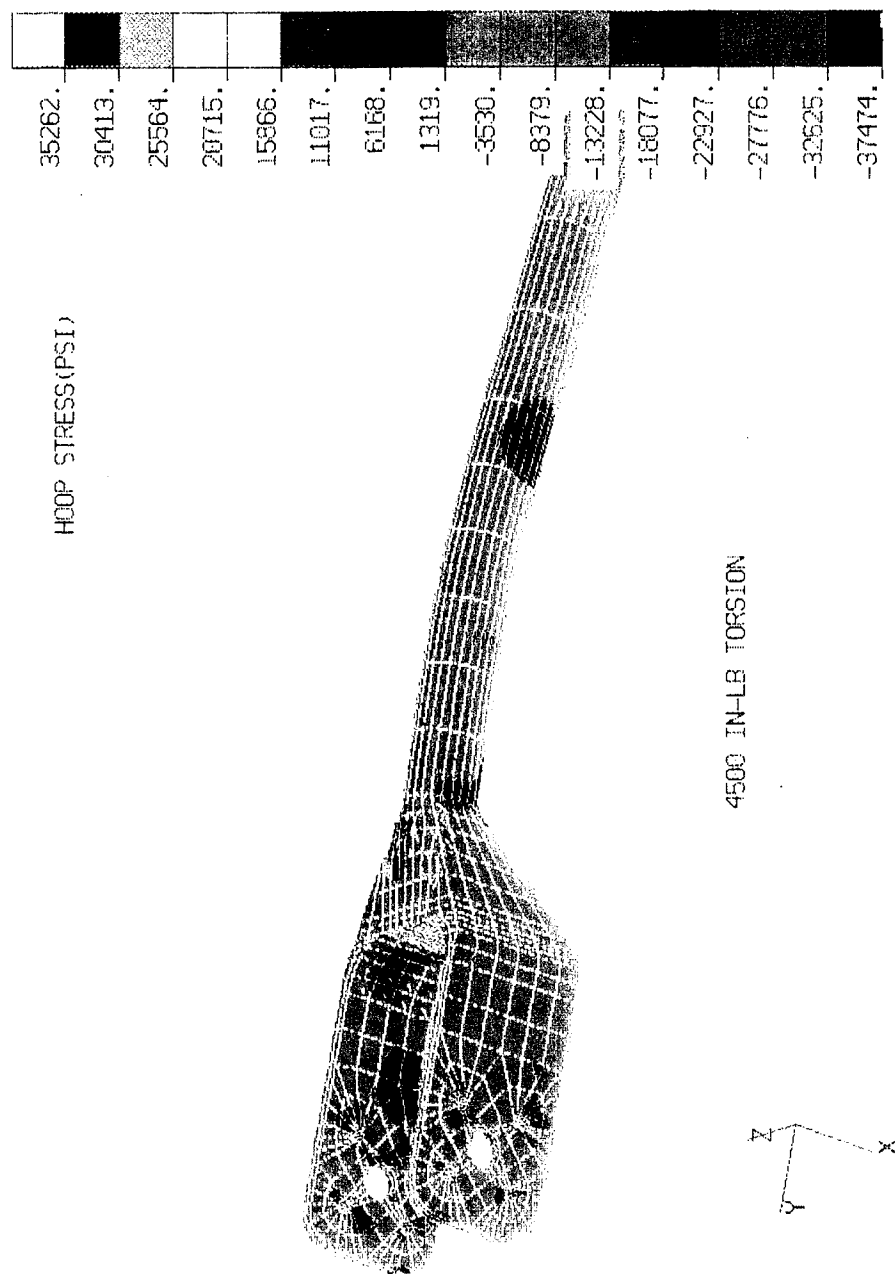


Figure 3.2.2-56. Tibia Hoop Stress Resulting from 4500 in-lb Torsion.

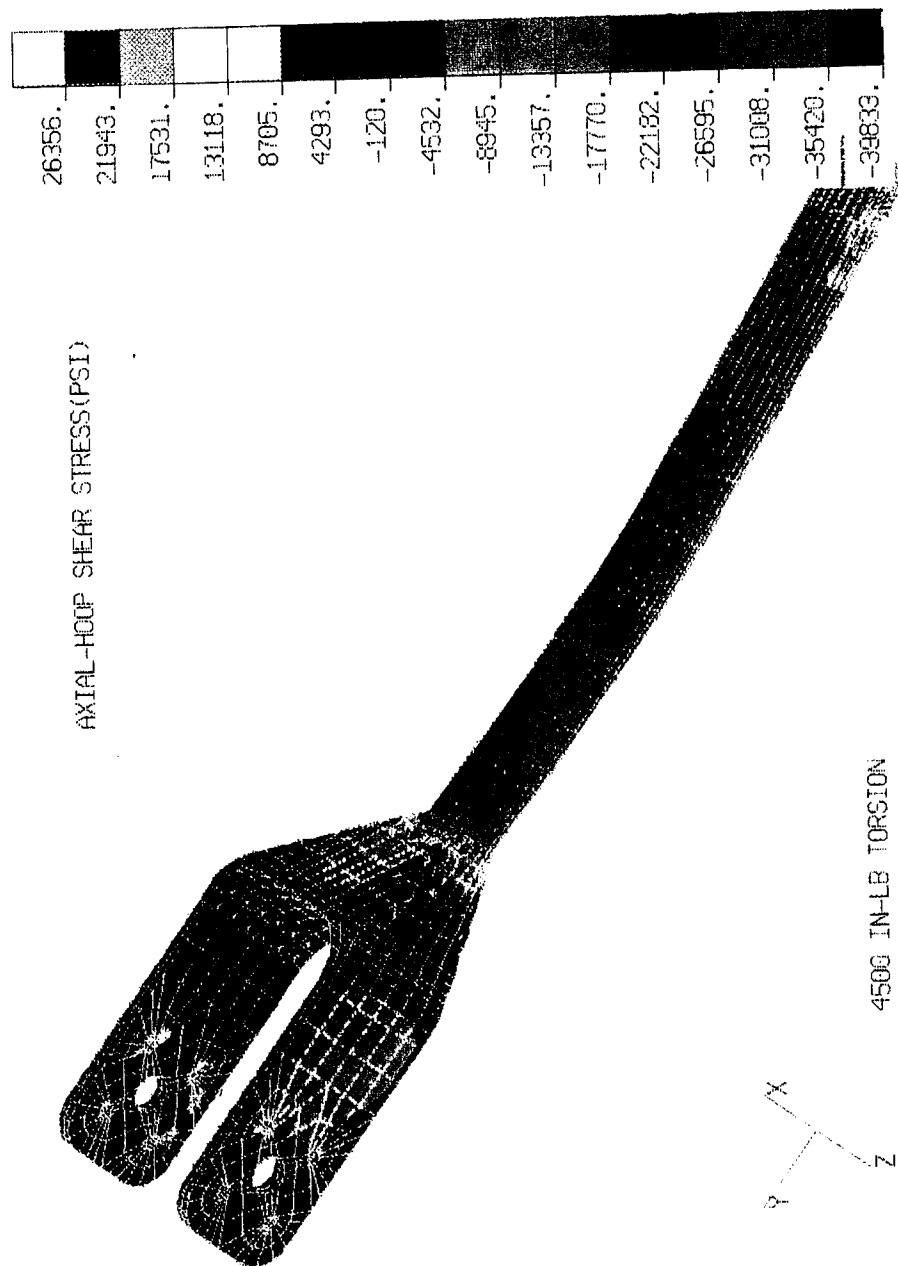


Figure 3.2.2-57. Tibia Axial Hoop Shear Stress Resulting from 4500 in-lb Torsion.

Table 3.2.2-3. Material Properties of T1000G/Epoxy and 6AL-4V Titanium

PROPERTY (UNITS)	6AL-4V TITANIUM	UNIDIRECTION T1000G/EPOXY
STIFFNESS		
E11 (MSI)	16	25.5
E22 (MSI)	16	1.3
G12 (MSI)	6.4	1
NU12	0.25	0.3
STRENGTH		
EPS11TU	0.009	0.018
EPS22TU	0.009	0.008
GAM12SU	0.014	0.007
EPS11CU	0.009	0.01
EPS22CU	0.009	0.03
F11TU (KSI)	140	450
F22TU (KSI)	140	7
F12SU (KSI)	90	13
F11CU (KSI)	140	250
F22CU (KSI)	140	15
F11BRU(KSI)	140	39
DENSITY (LB/CU.IN.)	0.16	0.058

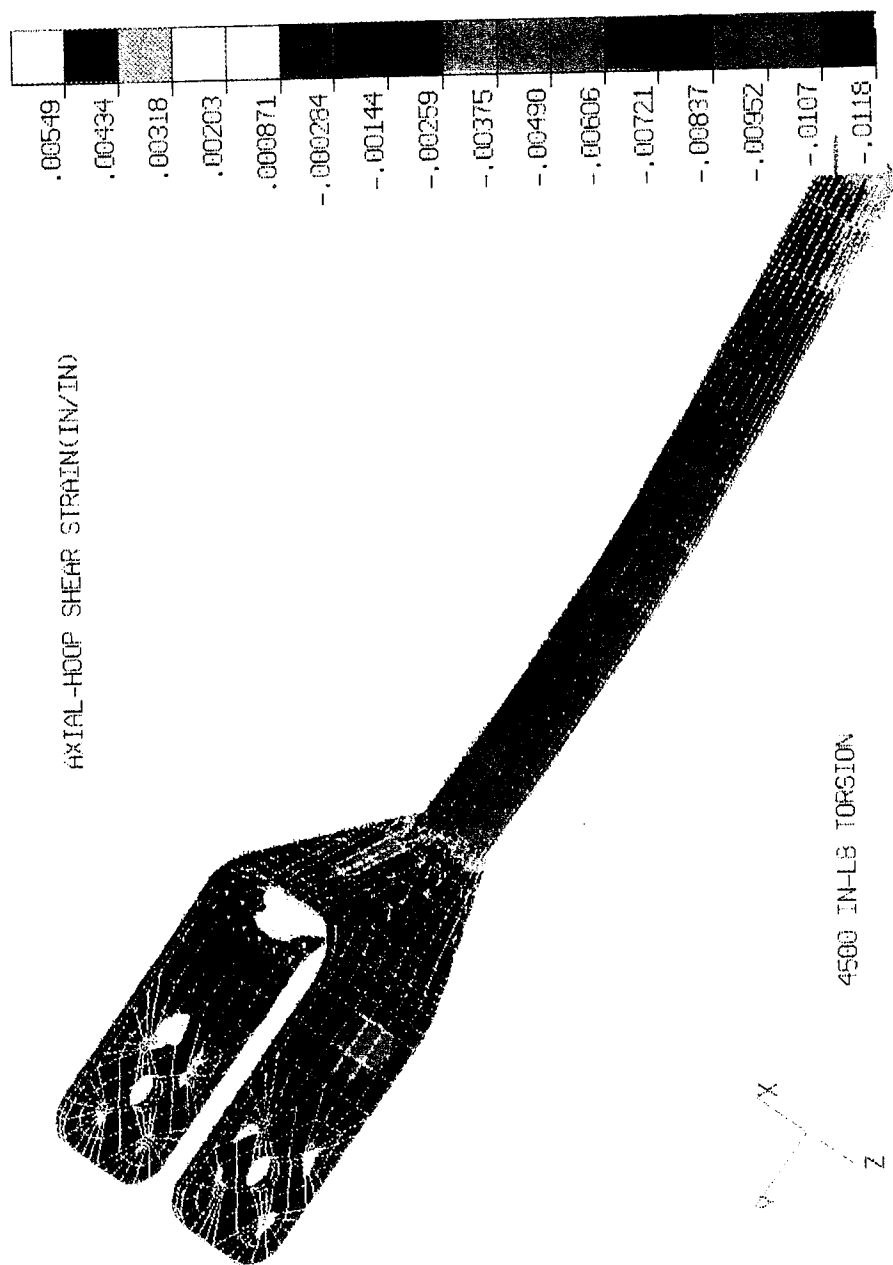


Figure 3.2.2-58. Tibia Axial Hoop Shear Strain Resulting from 4500 in-lb Torsion.



Figure 3.2.2-59. Tibia 5250 in-lb Lateral Bending has High Axial Fiber Strain Margin of Safety.



Figure 3.2.2-60. Tibia 5250 in-lb Lateral Bending has High 45° Axial Fiber Strain Margin of Safety.

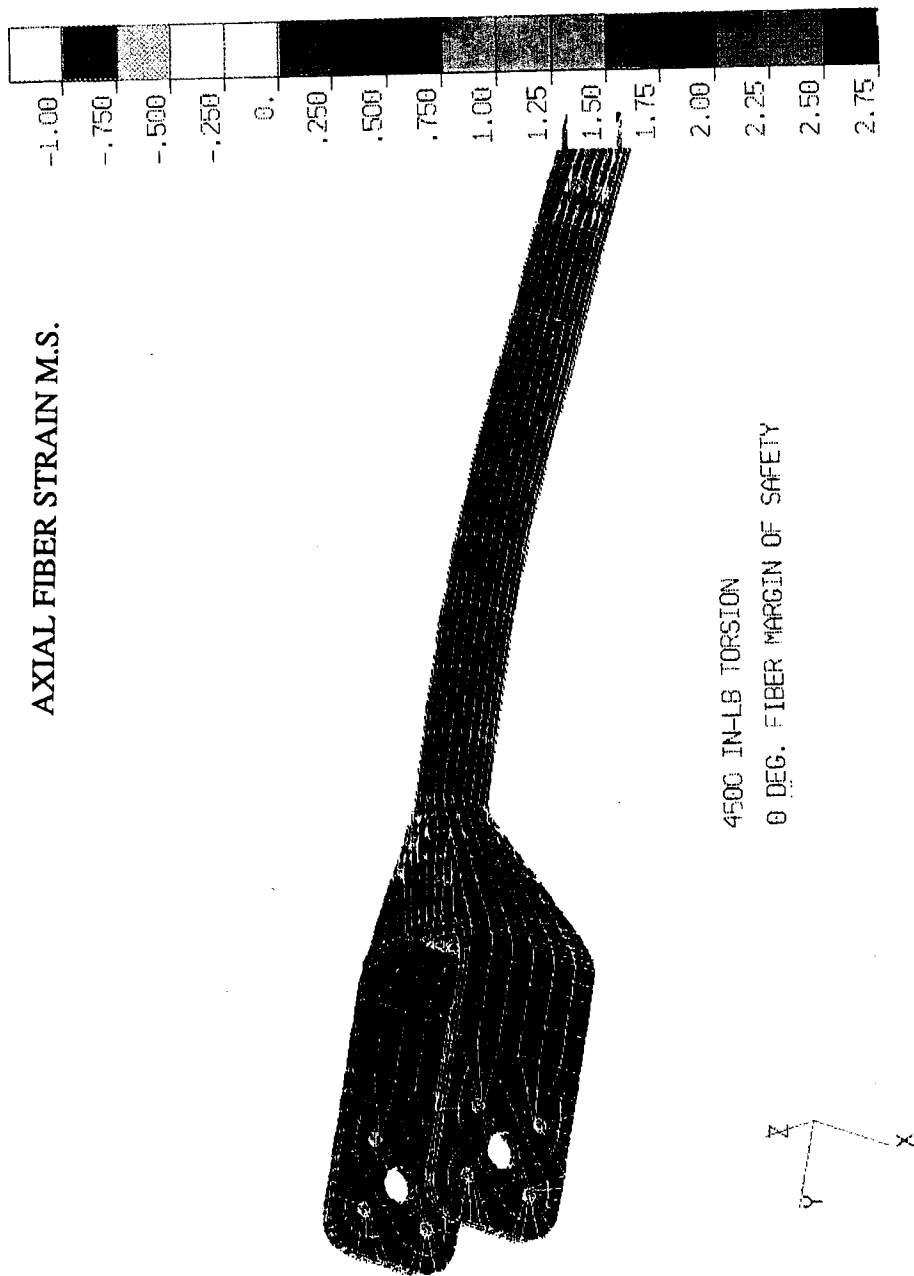


Figure 3.2.2-61. Tibia 4500 in-lb Torsion has High Axial Fiber Strain Margin of Safety.

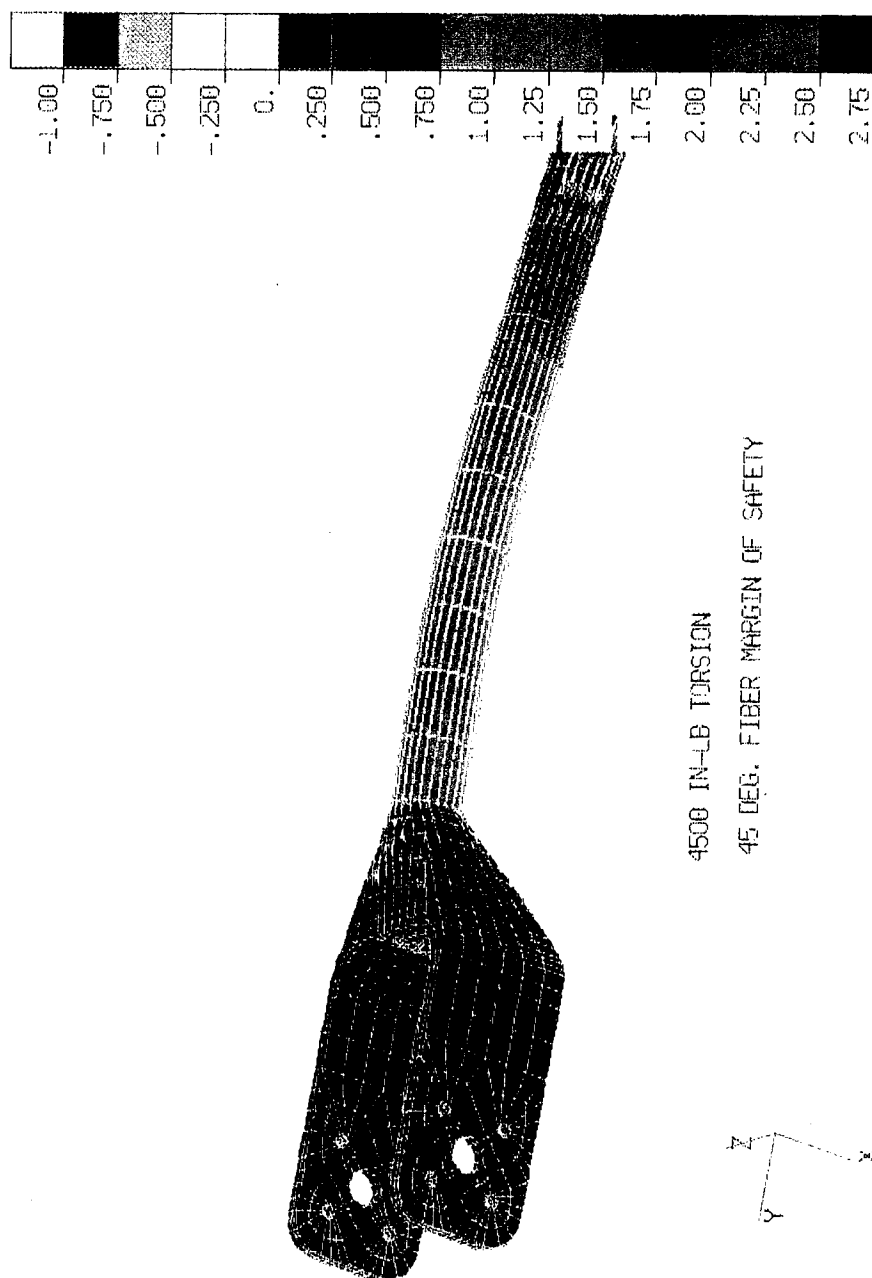


Figure 3.2.2-62. Tibia 4500 in-lb Torsion has Moderately High 45° Fiber Strain Margin of Safety.

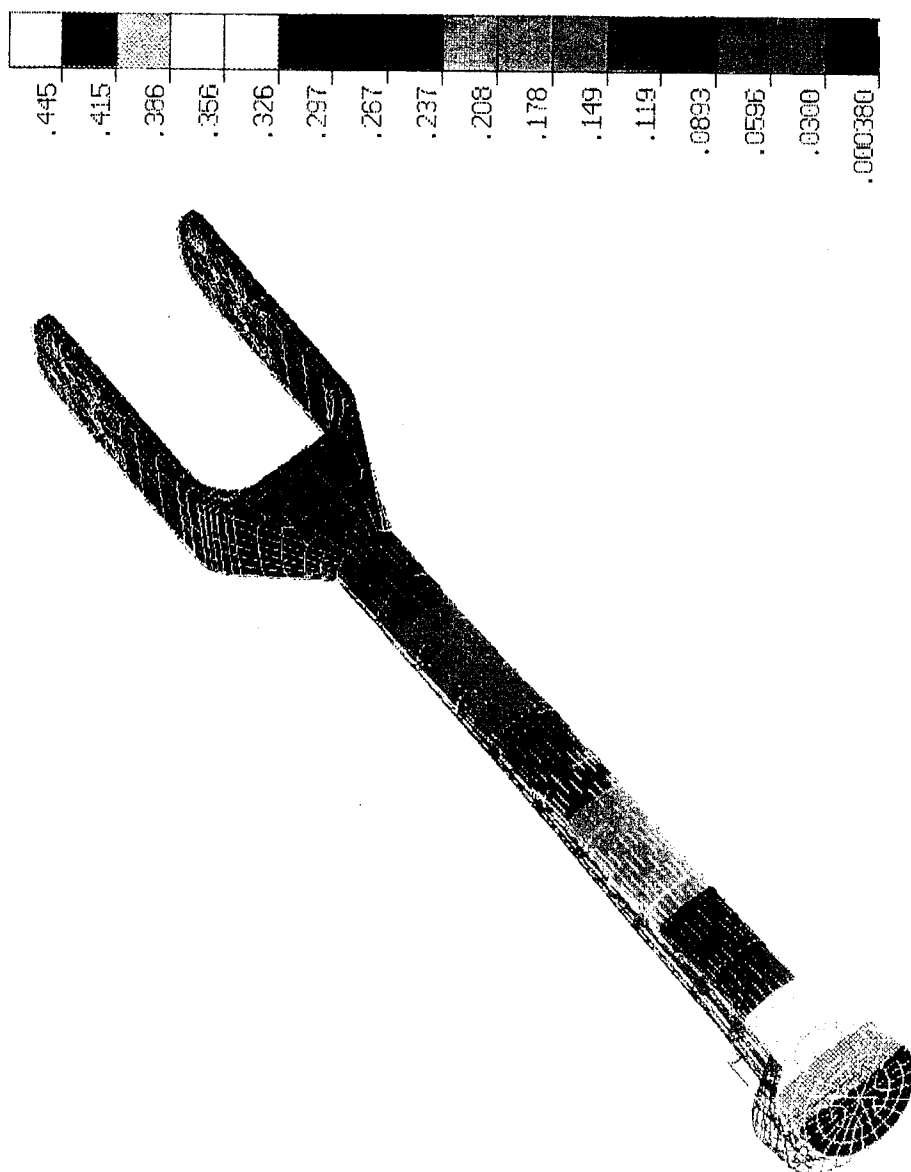


Figure 3.2.2-63. Tibia Total Displacement Resulting from 5250 in-lb Lateral Bending.

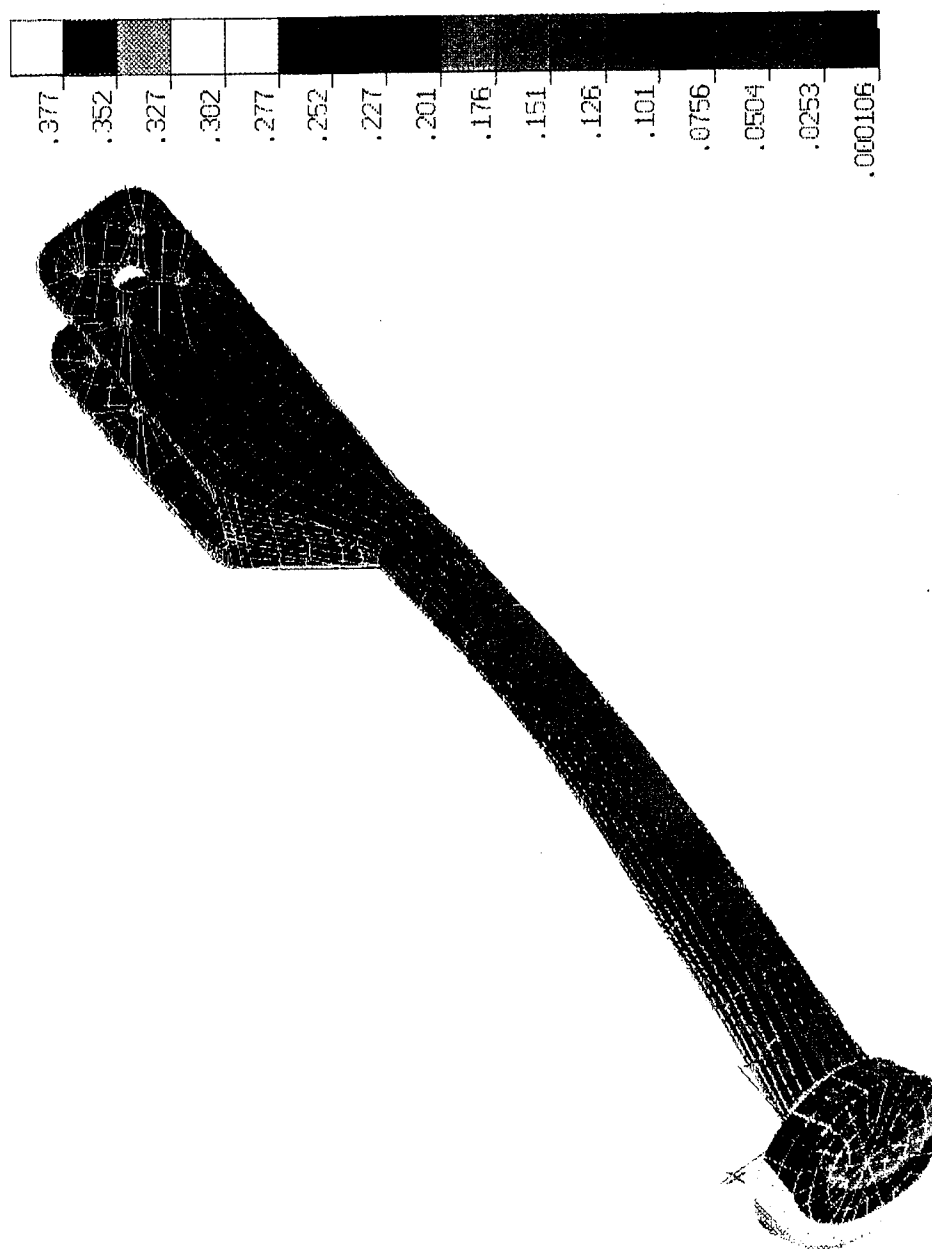


Figure 3.2.2-64. Tibia Total Displacement Resulting from 4500 in-lb Torsion.

Table 3.2.2-4. Tibia Structural Analysis Results Summary

LOAD CASE	FIBER STRAIN MARGIN OF SAFETY			INSERT MARGIN OF SAFETY
	0 ° FIBER	+ - 45 ° FIBER	90 ° FIBER	TITANIUM
TENSION	+ 2.68	+ 3.02	> 5	+ 1.33
COMPRESSION	+ 2.68	+ 3.02	> 5	+ 1.33
BENDING	+ 0.89	+ 1.28	+ 1.59	+ 0.78
TORSION	+ 0.91	+ 0.29	+ 0.71	+ 3.32

- HIGHEST STRESSES AND STRAINS ARE IN TIBIA 'NECK' REGION (LATERAL BENDING AND TORSION LOAD CASES)
- ALL STRESSES AND STRAINS HAVE POSITIVE MARGINS OF SAFETY

3.3 LONG BONE COMPOSITE DESIGN

The overall objective of the composite design task is to develop lightweight, high strength, biofidelic femur and tibia long bones. The specific design goals were to: 1) match weight of the human femur and tibia, 2) provide an interface with standing pelvis, 3) provide an interface with the ankle, 4) provide space in the knee joint for sliding knee hardware, and 5) withstand design loads. Discussion of the long bone composite design has been divided into five sections, material selection, weight summary, femur design, tibia design and knee joint design.

Section 3.2, Structural Analysis, discusses the development of the structural loading on the femur and the tibia. Initial sizing of the long bone cross-section geometries was performed through the use of a design spreadsheet which incorporated closed form analyses based on classical beam theory. The approach in developing this design spreadsheet was to correlate results with the Phase I femur finite element analysis (and Phase I loads) to insure accuracy, and then use Phase II loads to determine an initial design configuration. Details of the classical beam theory were presented in Section 3.2 Structural Analysis.

3.3.1 Material Selection

The femur and tibia were made of high strength graphite fiber/epoxy resin composite material. Figure 3.3-1 shows a plot of the fiber reinforcements available in industry. Because weight reduction was a critical design parameter, the fiber selected for the femur and tibia is the highest specific strength fiber available, called T1000G manufactured by Toray. The epoxy resin is 1908 manufactured by AMOCO and is a standard toughened resin system that is easy to fabricate, inexpensive and has extensive material property data.

Material layups are described in detail in Section 3.2 Structural Analysis. The femur and tibia were fabricated by a composite process called matched metal net molding, which will be discussed in detail in Section 3.5.

3.3.2 Weight Summary

Table 3.3-1 summarizes the Phase II composite weight goals, the Phase II composite actual weights, and actual weight of the human femur and tibia, respectively. During the initial phase of the project, the weight of the instrumentation overwrap was estimated at only 5% of the total weight. However, as seen by the table, the instrumentation overwrap accounts for 20% of

the total weight. The additional weight is considered necessary to provide protection of the strain gages and accelerometers during a direct impact of the leg segment with the cockpit frame. The knee joint hardware has not been included in the weight of either segment. The total segment weights (bone and flesh) show the segment mass totals are very close to the design goals ($\approx 2.7\%$).

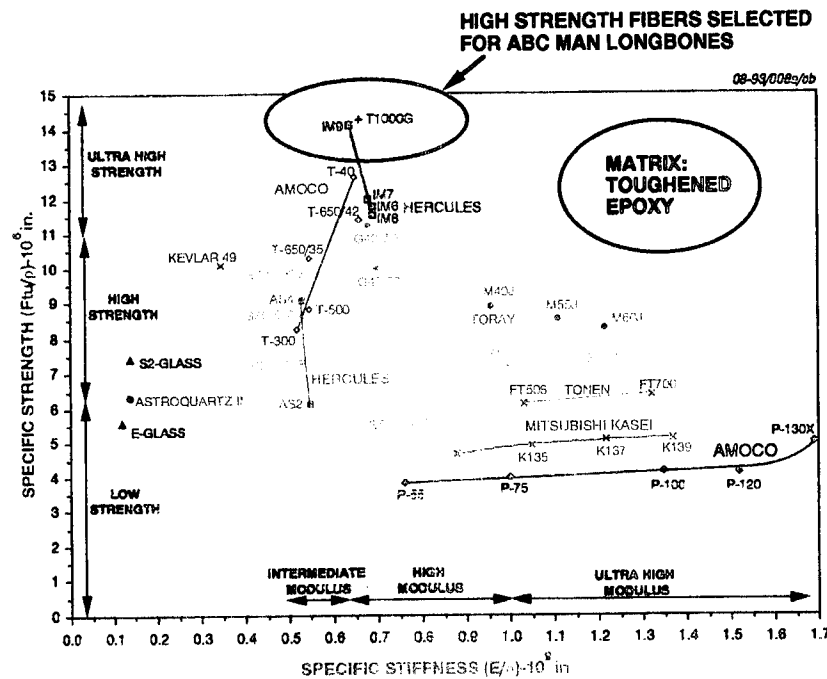


Figure 3.3.1-1. Plot of Fiber Reinforcement Physical Properties Shows the High Strength Fiber Selected for the Longbones.

Table 3.3.1-1. Summary of Phase II Composite Weight Goals.

08-93/ABC Final/Wt

		FEMUR	TIBIA	TOTAL
GOAL	COMPOSITE BONE + INSTRUMENTATION/OVERWRAP	952 g	544 g	1,496 g
	TOTAL SEGMENT (Basis Hybrid III)	8890 g	4354 g	13,244 g
ACTUAL	COMPOSITE BONE	898 g	519 g	1,417 g
	INSTRUMENTATION/OVERWRAP	171 g	165 g	336 g
	FLESH	8139 g	3716 g	11,855 g
	TOTAL SEGMENT	9208 g	4400 g	13,608 g
	HUMAN BONE	652 g	724 g	1,376 g

3.3.3 Femur Structural Design

One of the Phase II objectives in the design of the femur was to reduce weight via modification of the titanium insert. In Phase I, the compression validation test showed the femur could withstand up to 83% of the compressive design load. Although there was no catastrophic failure, the test was stopped when the part could not sustain the applied load. "Failure" occurred due to excessive radial stress at the distal end of the titanium insert which reacted to the high compressive load on the ball. Based on the Phase I test results, the proximal end of the femur was redesigned. A finite element model of the femur was developed and is discussed in Section 3.2 Structural Analysis.

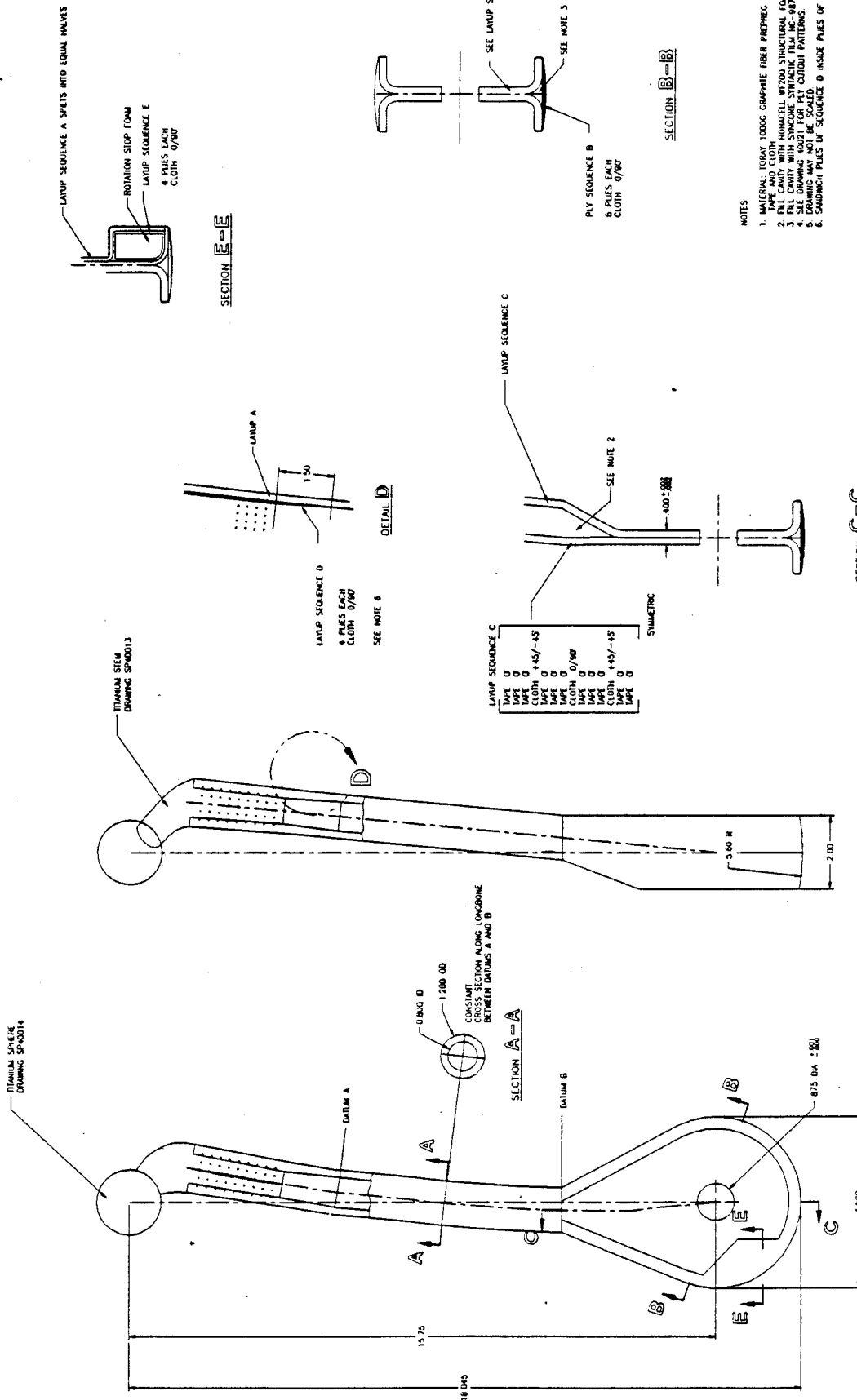
Composites offer a high degree of flexibility in design by taking advantage of the inherent anisotropy of the material. Well established composite material architecture and laminating technologies permit the designer to tailor the inherently anisotropic properties of composite materials to achieve an optimal weight/performance structure that satisfies the directionally sensitive stiffness and strength requirements of both the femur and tibia long bones. The material architecture of the femur, the bone geometry and placement of the titanium stem is shown in Figure 3.3.3-2. This architecture was developed based on the detailed finite element structural analysis. Specific layups shown in the figure reflect the multiple load paths in the femur which must be reacted during tension, compression, bending and torsional loads developed during testing. In addition, the femur layup accounts for secondary loads such as induced shear and local bearing at the titanium stem and knee articulation hole. Detail drawings of the titanium stem and the titanium ball joint are shown in Figures 3.3.3-3 and 3.3.3-4, respectively.

3.3.3.1 Femur Instrumentation

The installation of the femur instrumentation is depicted in Figure 3.3.3-5. The color contour plots of Figures 3.3.3-6 through Figures 3.3.3-9 show the fiber strains under the four loading conditions for the femur. Reviewing the contours show that the location of the femur strain gages will be 3 inches (76.2mm) from the titanium stem/composite interface. Placing the gages closer to the knee reduces the tension load strain to less than 2 $\mu\text{in/in}$. Placing the gages closer to the hip puts the gages too close to the connector to transition the wires.

There are a total of four sets of gages, a set being defined as one rosette strain gage and 3 axial strain gages. The rosette strain gage measures the torsional and axial strain due to bending

NOTICE
 THE DRAWING IS THE PROPERTY OF SPARTA, INC. AND IS NOT TO BE REPRODUCED OR TRANSMITTED IN ANY FORM OR BY ANY MEANS, ELECTRONIC OR MECHANICAL, WITHOUT WRITTEN AUTHORIZATION FROM SPARTA, INC.
 NOTES: UNLESS OTHERWISE SPECIFIED



- NOTES
1. MATERIAL: TORAY 1000G GRAPHITE FIBER PREPREG WITH 3507 CURE EPOXY.
 2. TAPES AND CLOTH.
 3. FILL CAVITY WITH HONEYCELL W7200 STRUCTURAL FOAM.
 4. SEE DRAWING 30021 FOR FAY CLOTH PATTERNS.
 5. DRAWING MAY NOT BE SCALED.
 6. SANDWICH PILES OF SEQUENCE D INSIDE PILES OF SEQUENCE C.

SPARTA		12-40012	1
ABC MANIKIN FEMUR ASSEMBLY		E 91129	12-40012
REV		DATE	BY
1		12-1-88	1
2		12-1-88	1
3		12-1-88	1
4		12-1-88	1
5		12-1-88	1
6		12-1-88	1
7		12-1-88	1
8		12-1-88	1
9		12-1-88	1
10		12-1-88	1
11		12-1-88	1
12		12-1-88	1
13		12-1-88	1
14		12-1-88	1
15		12-1-88	1
16		12-1-88	1
17		12-1-88	1
18		12-1-88	1
19		12-1-88	1
20		12-1-88	1
21		12-1-88	1
22		12-1-88	1
23		12-1-88	1
24		12-1-88	1
25		12-1-88	1
26		12-1-88	1
27		12-1-88	1
28		12-1-88	1
29		12-1-88	1
30		12-1-88	1
31		12-1-88	1
32		12-1-88	1
33		12-1-88	1
34		12-1-88	1
35		12-1-88	1
36		12-1-88	1
37		12-1-88	1
38		12-1-88	1
39		12-1-88	1
40		12-1-88	1
41		12-1-88	1
42		12-1-88	1
43		12-1-88	1
44		12-1-88	1
45		12-1-88	1
46		12-1-88	1
47		12-1-88	1
48		12-1-88	1
49		12-1-88	1
50		12-1-88	1
51		12-1-88	1
52		12-1-88	1
53		12-1-88	1
54		12-1-88	1
55		12-1-88	1
56		12-1-88	1
57		12-1-88	1
58		12-1-88	1
59		12-1-88	1
60		12-1-88	1
61		12-1-88	1
62		12-1-88	1
63		12-1-88	1
64		12-1-88	1
65		12-1-88	1
66		12-1-88	1
67		12-1-88	1
68		12-1-88	1
69		12-1-88	1
70		12-1-88	1
71		12-1-88	1
72		12-1-88	1
73		12-1-88	1
74		12-1-88	1
75		12-1-88	1
76		12-1-88	1
77		12-1-88	1
78		12-1-88	1
79		12-1-88	1
80		12-1-88	1
81		12-1-88	1
82		12-1-88	1
83		12-1-88	1
84		12-1-88	1
85		12-1-88	1
86		12-1-88	1
87		12-1-88	1
88		12-1-88	1
89		12-1-88	1
90		12-1-88	1
91		12-1-88	1
92		12-1-88	1
93		12-1-88	1
94		12-1-88	1
95		12-1-88	1
96		12-1-88	1
97		12-1-88	1
98		12-1-88	1
99		12-1-88	1
100		12-1-88	1

Figure 3.3.3-2. Detail Drawing of Femur Longbone.

4

3

2

1

NOTICE
THIS DOCUMENT MAY CONTAIN INFORMATION PROPRIETARY TO SPARTA, INC. NEITHER RECEIPT NOR POSSESSION THEREOF CONFERS ANY RIGHTS TO REPRODUCE, OR USE OR DISCLOSE, IN WHOLE OR IN PART, ANY SUCH INFORMATION WITHOUT WRITTEN AUTHORIZATION FROM SPARTA, INC.

NOTES: UNLESS OTHERWISE SPECIFIED

1. SUPPLIER TO SUPPLY PINS AND DRILL HOLES
SPARTA WILL PREPARE SURFACE AND INSTALL PINS
2. BREAK ALL EDGES .015
3. PREPARE SURFACE WITH AMERICAN CYANAMIDE
BRI27 BEFORE INSTALLING PINS.
4. TO MINIMIZE FABRICATION COST, SQUARING OF CROSS SECTION IS ALLOWED.
5. MAINTAINING RADIUS CONTOUR NOT CRITICAL.

13/16-16 UNF EXTERIOR THREAD

2. BREAK ALL EDGES .015

3. PREPARE SURFACE WITH AMERICAN CYANAMIDE

BRI27 BEFORE INSTALLING PINS.

4. TO MINIMIZE FABRICATION COST, SQUARING OF CROSS SECTION IS ALLOWED.

5. MAINTAINING RADIUS CONTOUR NOT CRITICAL.

1/4" DIA WEIGHT REDUCTION HOLE

SECTION A-A

1/4" DIA WEIGHT REDUCTION HOLE

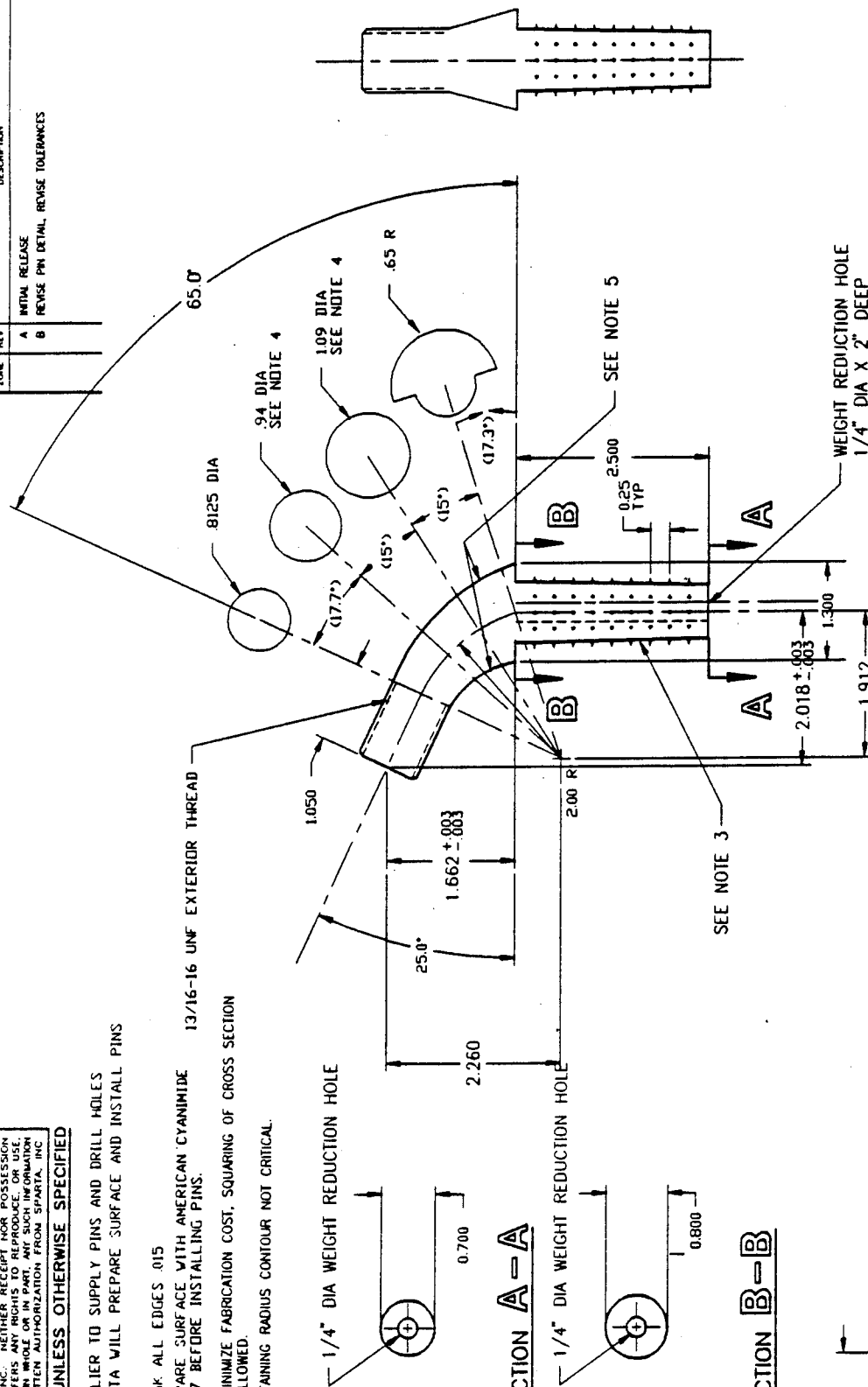
SECTION B-B

PIN
MAKE FROM 0060" DIA STAINLESS STEEL
BOND WITH LOCTITE ADHESIVE
8 COLUMNS 45° APART
9 DRILL 1/16 DIA TO .18 DEPTH


0.080 TYP

PIN DETAIL
SCALE: NONE

ZONE	REV	DESCRIPTION	DATE	APPROVED
A	INITIAL RELEASE		04-23-92	
B	REVISE PM DETAIL REVISE TOLERANCES		07-20-92	



UNLESS OTHERWISE SPECIFIED DIMENSIONS ARE IN INCHES TOLERANCES ARE:	UTR	CL BARKER	07/20/92
FRACTIONS	DECIMALS	ANGLES	
X ± 1	± 1	± 1/2 DEG.	
XX ± .03	XX ± .03		
XXX ± .010	XXX ± .010		
DO NOT SCALE DRAWING	QUALITY		
	PROD. MGR.		
	MATERIAL		
	FINISH		
	CONTRACT NO.		
	AMR77		
	SP40012		
	NO. REQD.		
	5		
	6AL-4V TITANIUM		
	UNLESS OTHERWISE NOTED		

 SPARTA		9455 Torrey Centre Drive San Diego, CA 92121	
Drawing TITLE			
ABC MANIKIN FEMUR STEM			
SIZE	CAGE	DRAWING NO.	REV.
C	9T129	SP40013	B
SCALE	1/1	TOTAL WT.	SHEET 1 OF 1

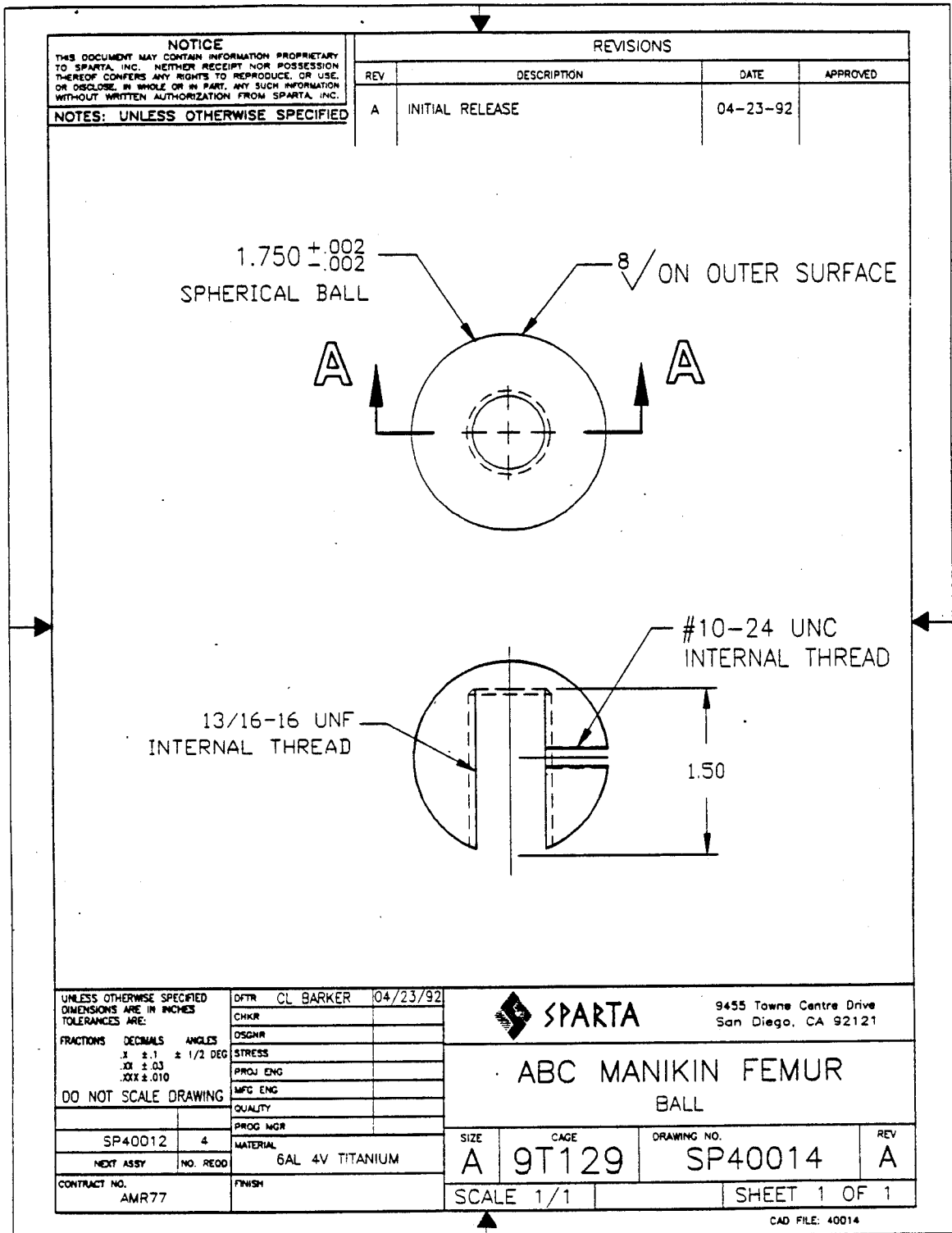


Figure 3.3.3-4. Detail Drawing of Titanium Ball.

RIGHT LEG

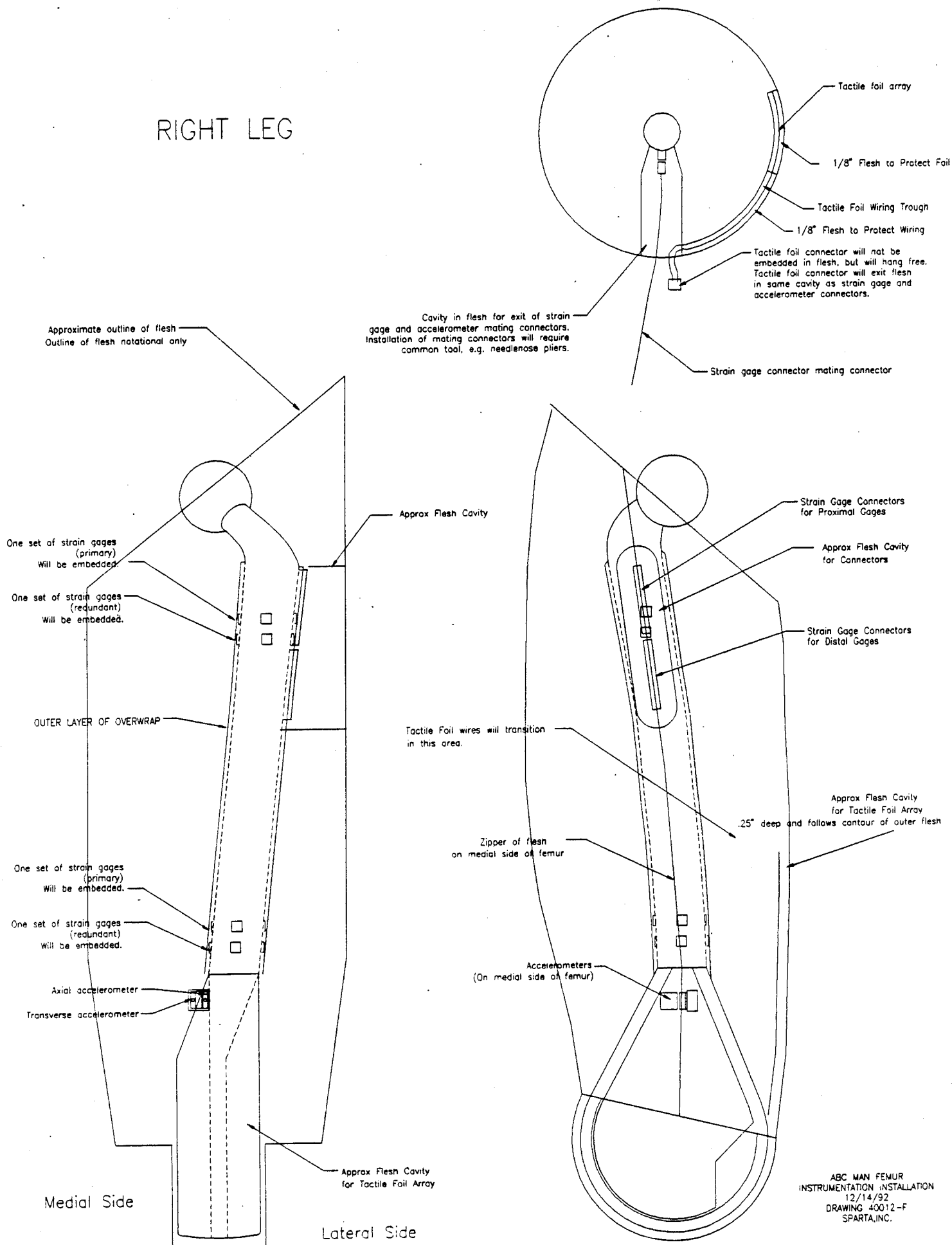


Figure 3.3.3-5. Instrumentation Installation for the Femur.

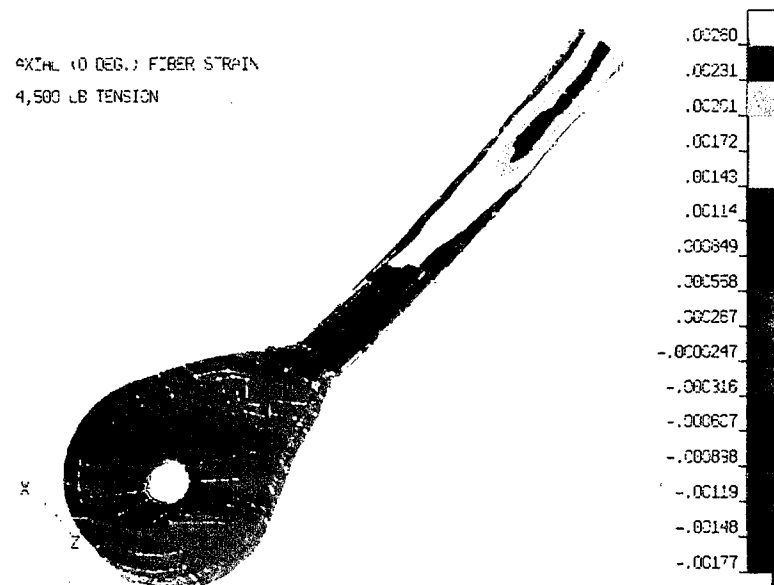


Figure 3.2.3-6. Femur Axial (0 Degree) Fiber Strain (in./in.) under 4,500 lb. Tension Load.

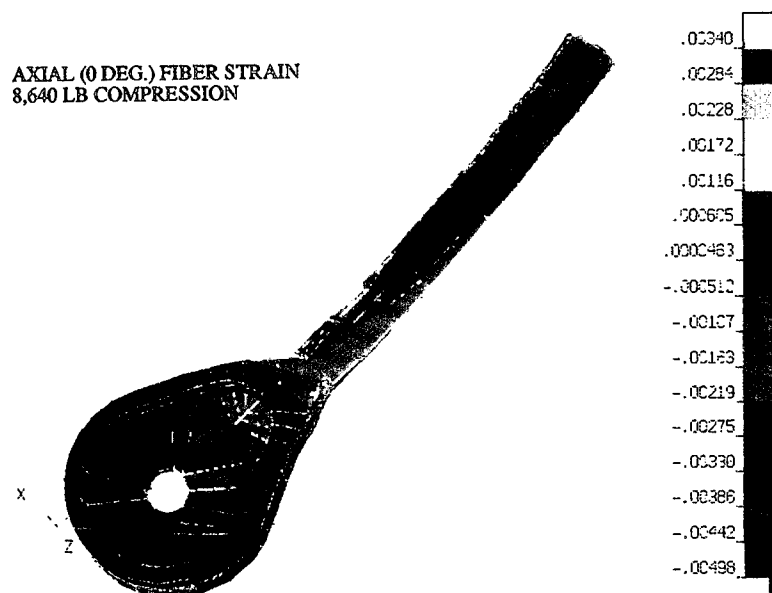


Figure 3.2.3-7. Femur Axial (0 Degree) Fiber Strain (in./in.) under 8,640 lb. Compression Load.

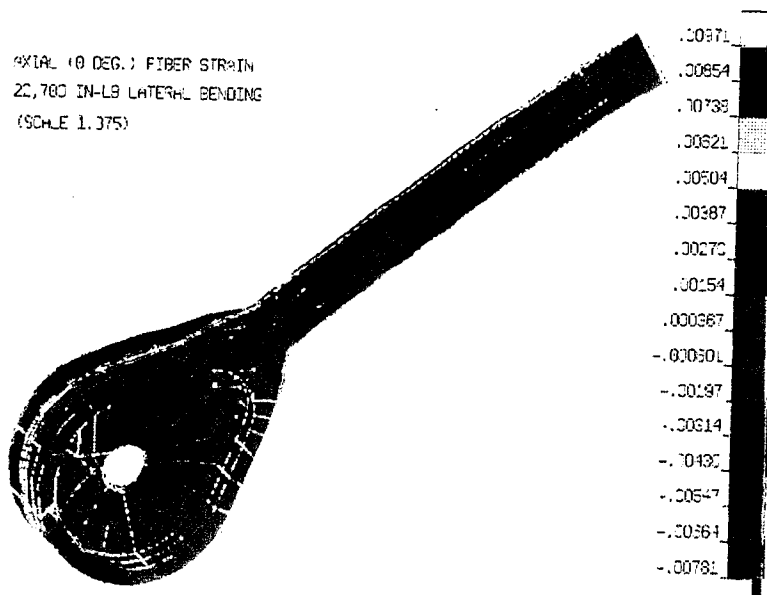


Figure 3.2.3-8. Femur Axial (0 Degree) Fiber Strain (in./in.) Resulted from 22,700 in.-lb Lateral Bending Load.

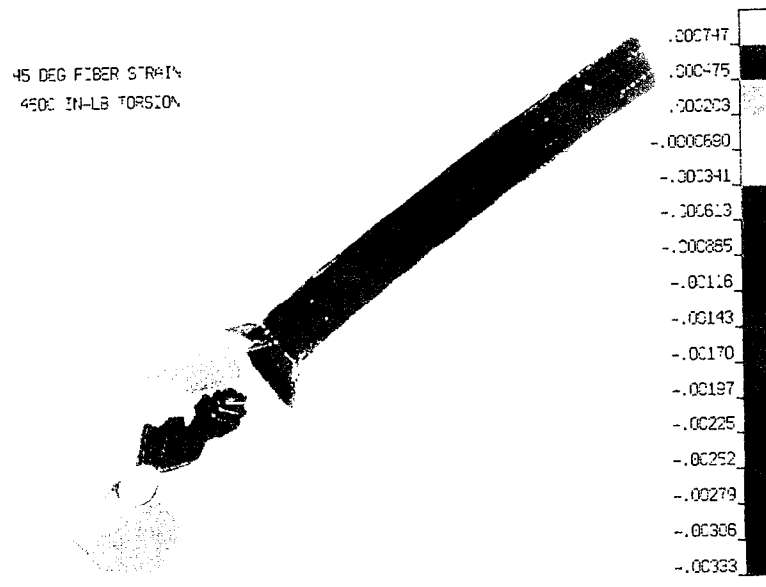


Figure 3.2.3-9. Femur 45 Degree Fiber Strain (in./in.) Resulted from 4,500 in.-lb. Torsion.

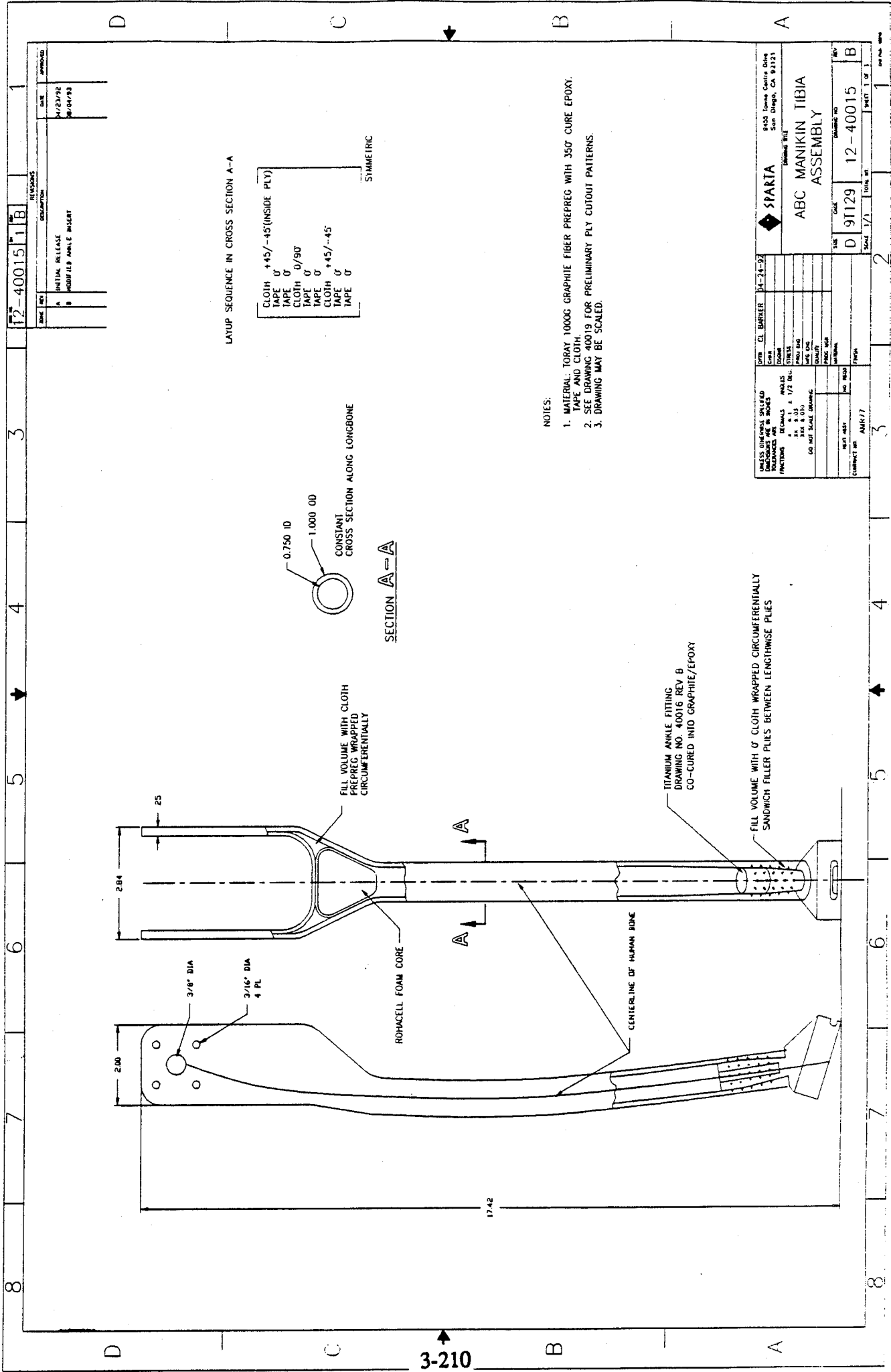
and torsion and the axial gages will measure the pure axial strain. The rosette strain gage has 6 wires and the axial strain gages each have 2 wires. Two sets are primary, one at each end of the long bone and two sets are redundant, one set located adjacent to each primary set. All wires for the strain gages will be embedded inside the graphite/epoxy overwrap. There are two connectors, one for each strain gage set for redundancy, that will all terminate at the proximal end of the femur. The strain gage connectors are 34 position AMP-LATCH, 2.0 mm ribbon cable connectors manufactured by AMP. In order to minimize the amount of flesh cut away to give access to the connectors, a 20° cavity was molded into the flesh. The 20° cavity will likely necessitate the use of a tool (e.g. needle nose pliers) to install the mating connectors. A larger cut could be made into the flesh, however, the larger access hole means a potentially more adverse influence on the response of the tactile foil sensor.

3.3.4 Tibia Structural Design

The design of the tibia long bone was developed based on the structural analysis and the detail design drawing shown in Figure 3.3.4-1. The drawing shows the composite material layup, bone geometry and placement of the titanium ankle. As with the femur, the material architecture reflects the complex tri-axial stress state of the tibia determined by the finite element structural analysis described in Section 3.2.2. The design cross-section was derived by performing closed form analyses based on classical beam theory and verified by finite element analysis. The outer radius of the tibia long bone is 1/2" (12.7mm) and the inner radius is 3/8" (9.53mm). The tibia has a clevis joint that attaches the tibia to the femur. The clevis knee joint design was based on the Hybrid III clevis design. The ankle joint interface was designed to ensure attachment to the existing Hybrid III foot/ankle. A drawing of the titanium ankle is shown in Figure 3.3.4-2. Aluminum, steel and titanium were considered for the ankle joint material, but titanium was selected for the ankle joint for two reasons. First, the density of titanium is 0.16 lb/cu in. and steel has a density of 0.286 lb/cu in. When aluminum is in contact with graphite, a galvanic reaction will corrode the aluminum. Titanium is not corrosive when used in the vicinity of graphite material.

3.3.4.1 Tibia Instrumentation

The installation of the tibia instrumentation is depicted in Figure 3.3.4-3. The installation procedure of the strain gages, wires, connector and protection cover for the tibia are identical to that for the femur. The color contour plots shown in Figure 3.3.4-4 through Figures 3.3.4-7 show the fiber strains for the four loading conditions for the tibia. Review of the plots



8 7 6 5 4 3 2 1

REV	DATE	DESCRIPTION	APPROVED
1	12-23-92	INITIAL RELEASE	
2	01-04-93	MODIFIED ANKLE INSERT	

LAYUP SEQUENCE IN CROSS SECTION A-A

CLOTH	++5/-45 (INSIDE PLY)
TAPE	0°
TAPE	0°
CLOTH	0/90°
TAPE	0°
TAPE	0°
CLOTH	++5/-45°
TAPE	0°
TAPE	0°

SYMMETRIC

SECTION A-A

NOTES:

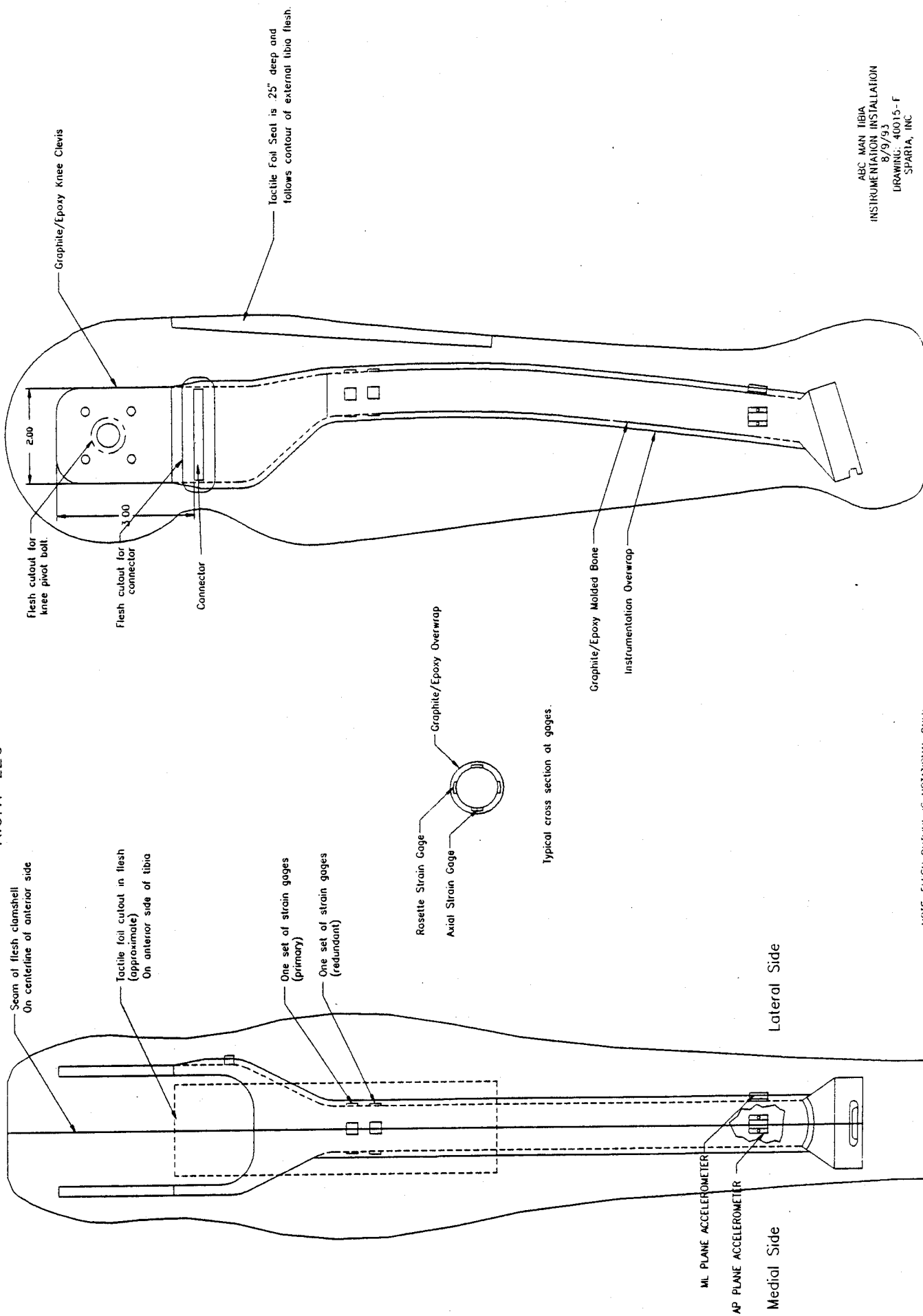
1. MATERIAL: TUBAY 1000G GRAPHITE FIBER PREPREG WITH 350° CURE EPOXY. TAPE AND CLOTH.
2. SEE DRAWING 40019 FOR PRELIMINARY PLY CUTOUT PATTERNS.
3. DRAWING MAY BE SCALED.

FILL VOLUME WITH 0° CLOTH WRAPPED CIRCUMFERENTIALLY SANDWICH FILLER PILES BETWEEN LENGTHWISE PILES

TITANIUM ANKLE FITTING
DRAWING NO. 40016 REV B
CO-CURED INTO GRAPHITE/EPOXY

SPARTA 9450 Town Centre Drive San Diego, CA 92123	
DATE: 12-24-92 DRAWN BY: [blank] CHECKED BY: [blank] DESIGNED BY: [blank] APPROVED BY: [blank]	PROJECT NO: 91129 REV: 12-40015 SHEET: 1 OF 1

RIGHT LEG



ABC MAN TIBIA
INSTRUMENTATION INSTALLATION
8/9/93
DRAWING: 40015-F
SPARIA, INC

NOTE: FLESH OUTLINE IS NOTATIONAL ONLY.

Figure 3.3.4.2 Instrumentation Installation - Right Leg

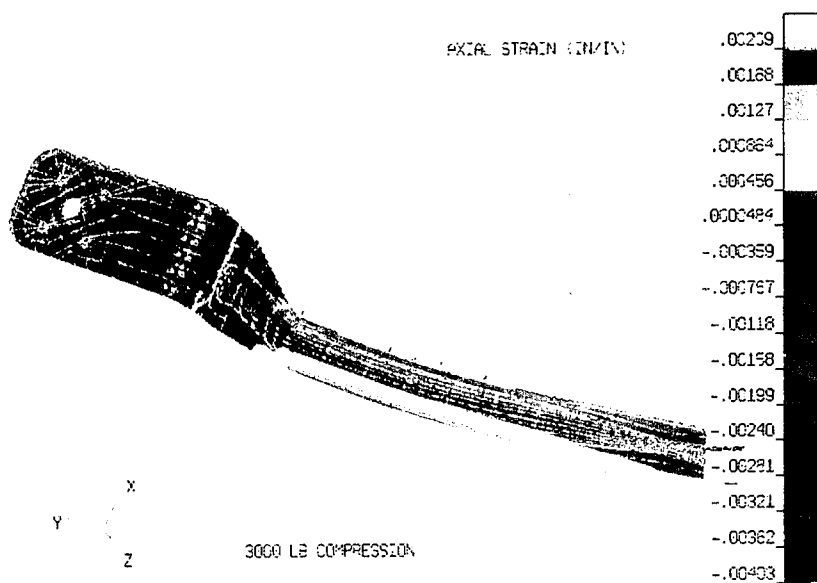


Figure 3.3.4-4. Tibia Axial Fiber Strain Resulting from 3000 lb. Compression.

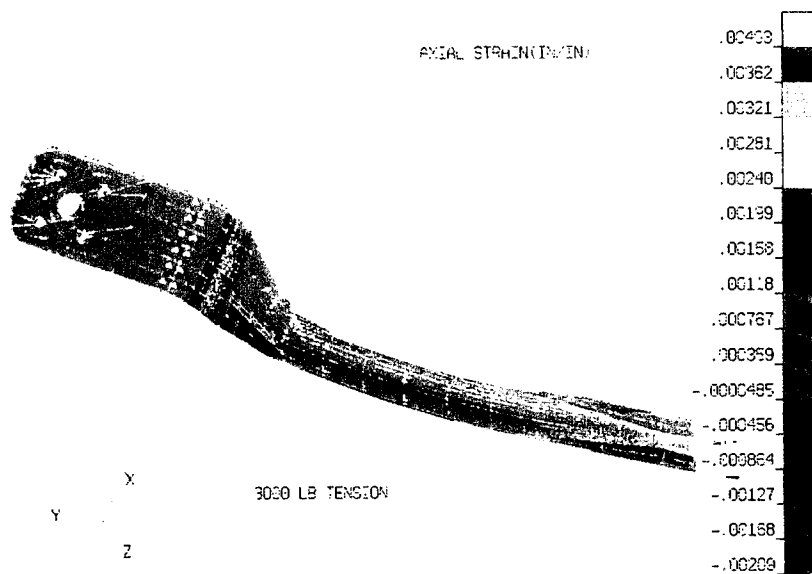


Figure 3.3.4-5. Tibia Axial Fiber Strain Resulting from 3000 lb. Compression.

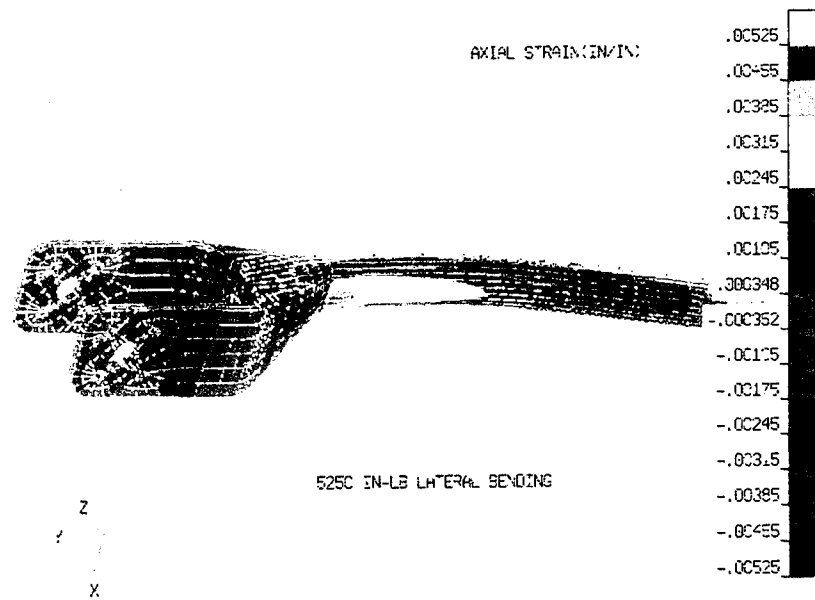


Figure 3.3.4-6. Tibia Axial Fiber Strain Resulting from 5250 in-lb. Lateral Bending.

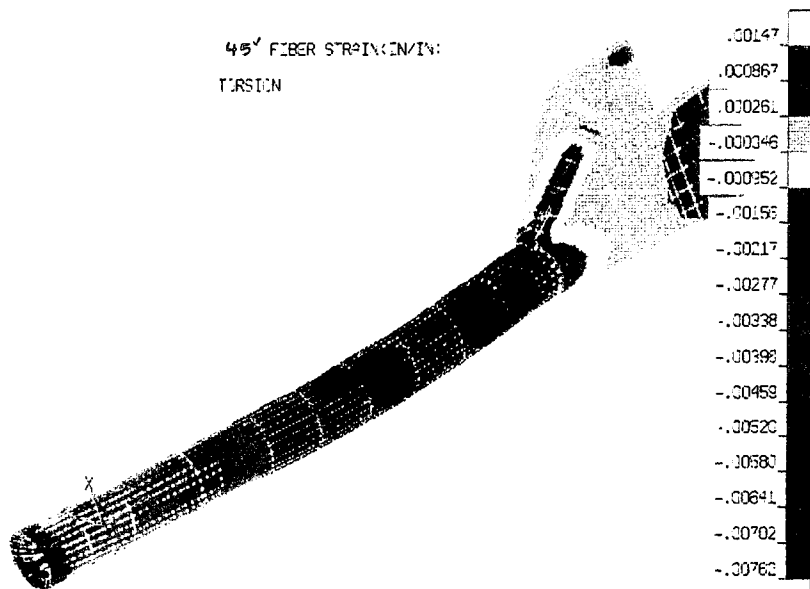


Figure 3.3.4-7. Tibia 45° Fiber Strain Resulting from 4500 in-lb Torsion.

shows the location of the tibia strain gages will be 1 inch from the neck. Placing the gages closer to the knee causes interference with the stem to knee joint transition. Placing the gages closer to the ankle reduces the strain due to lateral bending to less than 2 $\mu\text{in/in}$.

There are a total of two sets of gages, a set being defined as two rosette and 2 axial strain gages. One set is primary, located at the proximal end of the long bone and one set is redundant, located adjacent to the primary set. All wires for the strain gages will be embedded inside the graphite/epoxy overwrap. There are two connectors, one for each strain gage set, that will all terminate at the proximal end of the tibia near the knee joint. The strain gage connectors are 34 position AMP-LATCH, 2.0 mm ribbon cable connectors manufactured by AMP.

3.3.5 Accelerometers

It is assumed that the femur rotates about the hip joint and the hip joint is fixed from translating relative to the manikin pelvis. Therefore, the location of the femur pivot point and the moment arm between the pivot and the knee are fixed and the angular acceleration can be measured by a single axis linear accelerometer mounted at the knee. Although originally considered, the use of an angular accelerometer sensor would be redundant. An accelerometer mounted along the axis of the long bone will measure anterior-posterior (AP) plane acceleration. An accelerometer mounted perpendicular to the axis of the long bone will measure medial-lateral (ML) plane acceleration. The two accelerometers are mounted on the femur near the knee. The wires are terminated in the primary instrumentation connector at the proximal end of the femur. The accelerometer wires were embedded inside the graphite/epoxy overwrap.

Like the femur, there are two accelerometers on the tibia, one to measure the axial acceleration and one to measure the transverse acceleration, both relative to the axis of the tibia. The accelerometers are located at the distal end of the long bone. The wires are terminated in the connector located at the proximal end of the tibia. The accelerometer wires were embedded inside the graphite/epoxy overwrap. The accelerometer on the tibia is redundant for the reasons as explained for the femur. All accelerometers were calibrated at the factory.

3.3.6 Instrumentation Installation

The strain gages, accelerometers and associated wiring were installed on the femur and the tibia long bone segment. The installation procedure for both the femur and the tibia is as follows:

1. The bare long bone segment is cleaned to remove any mold release left on the surface.
2. The strain gages and accelerometers are bonded to the bone with epoxy.
3. The wires are soldered to the strain gages leads. The accelerometers come from the manufacturer with the wiring already attached.
4. The connectors are bonded to the bone with epoxy.
5. The wires are routed from the gages and accelerometers to the connectors and bonded to the bone with epoxy.
6. The wires are fed into the connectors and the connectors closed. Figure 3.3.6-1 shows the instrumented femur and tibia long bone segments.

Figures 3.3.6-2 and 3.3.6-3 identify the femur and tibia strain gages and accelerometers, respectively. Table 3.3.6-1 summarizes which pins correspond to the gage identified by Figures 3.3.6-2 and 3.3.6-3.

After the instrumentation is installed, the graphite/epoxy overwrap layer is installed. The procedure for installing the overwrap layer of both the femur and tibia is as follows:

1. The strain gages are protected by an 1/8" thick of cellular urethane as shown by the arrow in Figure 3.3.6-4.
2. Foam tape is cut to shape and placed between the wires, as shown in Figure 3.3.6-5, to provide a flush surface to wrap the graphite epoxy prepreg material.
3. The graphite epoxy prepreg is wrapped around the long bone and cured with a heat gun. Pressure for the cure is achieved with shrink tape. The completed femur and tibia overwrapped long bone segments are shown in Figure 3.3.6-6.

3.3.7 Knee Joint Design

The objective of the knee joint design was to lower the weight and improve the biofidelity of the Hybrid III clevis knee joint. Criteria for the design effort were:

- 1) To better simulate mass distribution of an in-vivo joint,
- 2) Accommodate embedded strain gages and/or accelerometers on the femur or tibia,
- 3) Withstand the worst case design load of compression plus bending in femur, and
- 4) Allow for use of sliding knee mechanism (although mechanism was not included in this design).



Figure 3.3.6-1. Instrumented Femur and Tibia Long Bone Segments.

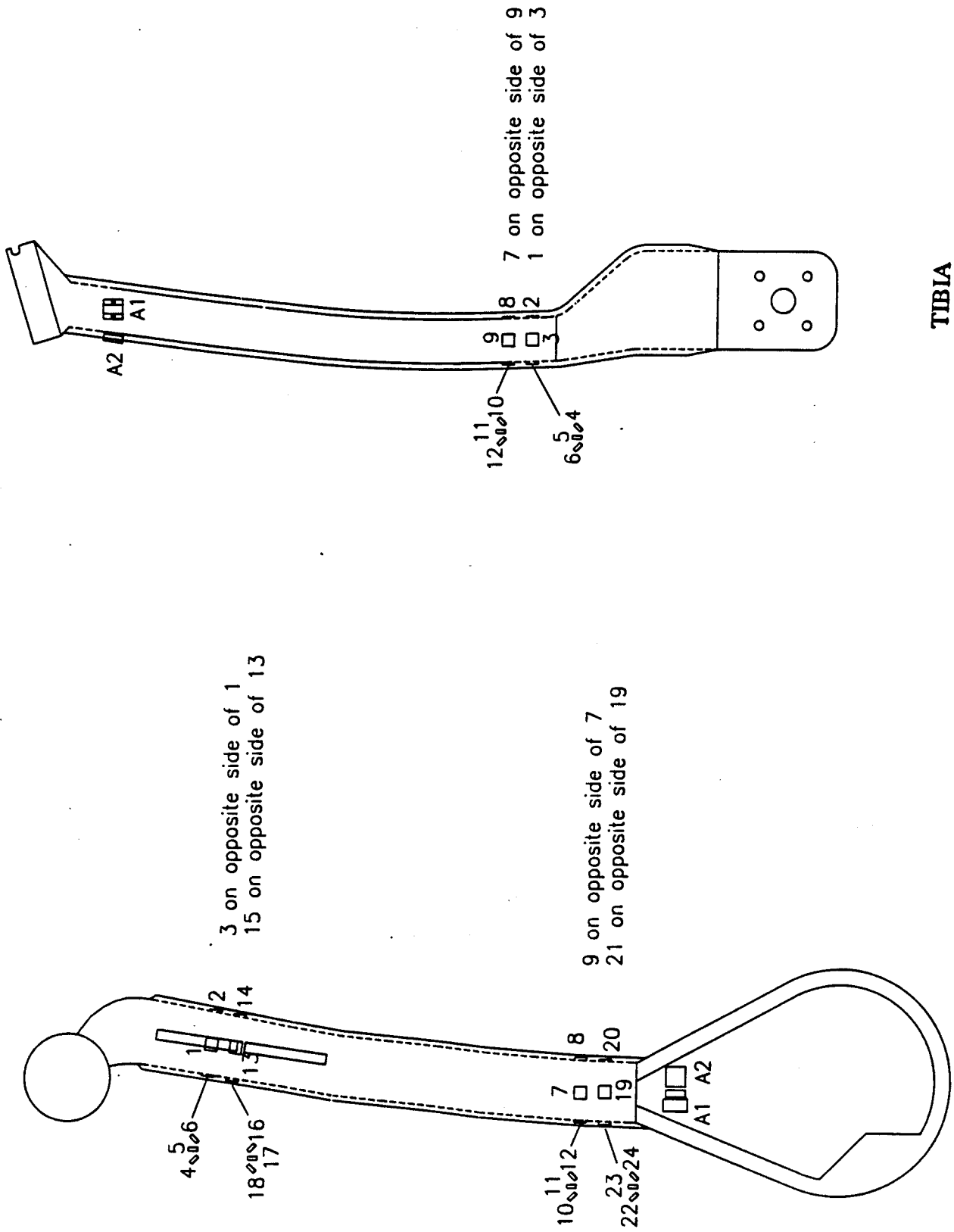
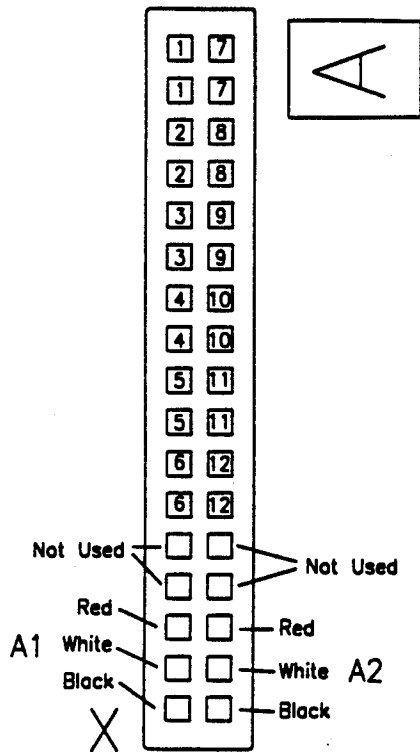


Figure 3.3.6-2. Femur Showing Strain Gage

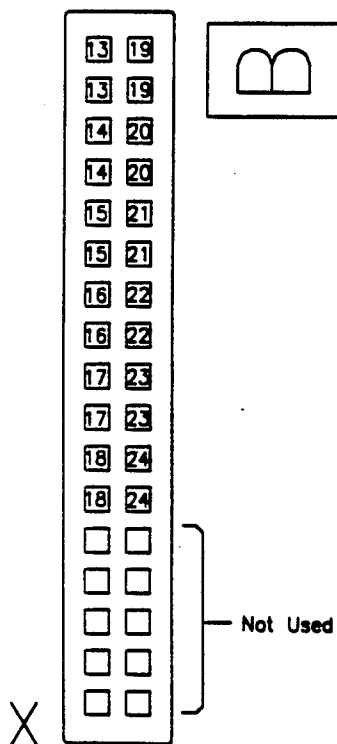
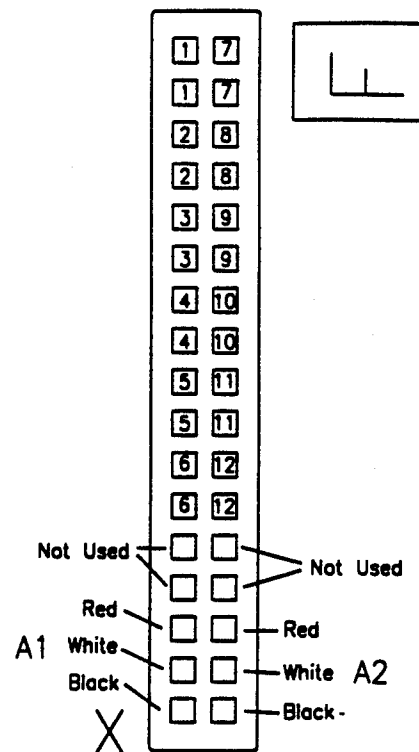
Figure 3.3.6-3. Tibia Showing Strain Gage

Table 3.3.6-1. Femur and Tibia Pin Allocations

Femur Pin Allocations



Tibia Pin Allocations



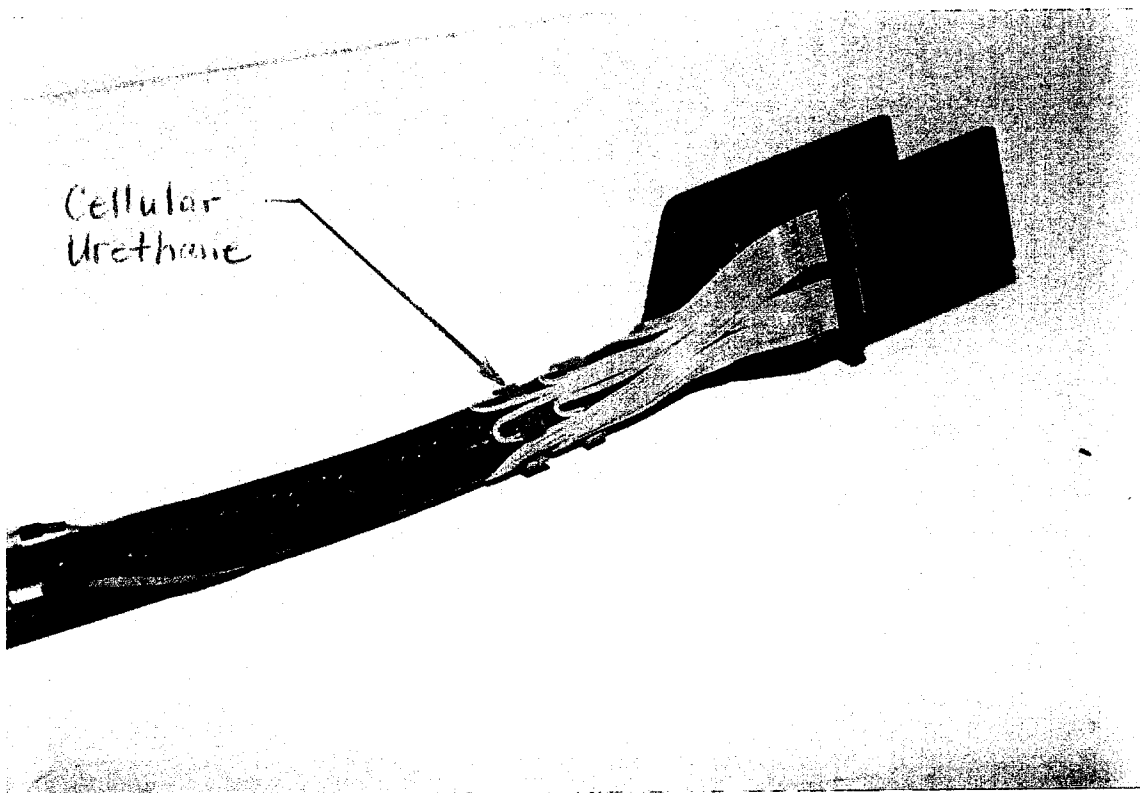


Figure 3.3.6-4. Strain Gages are Protected by an 1/8" Thick Piece of Cellular Urethane.

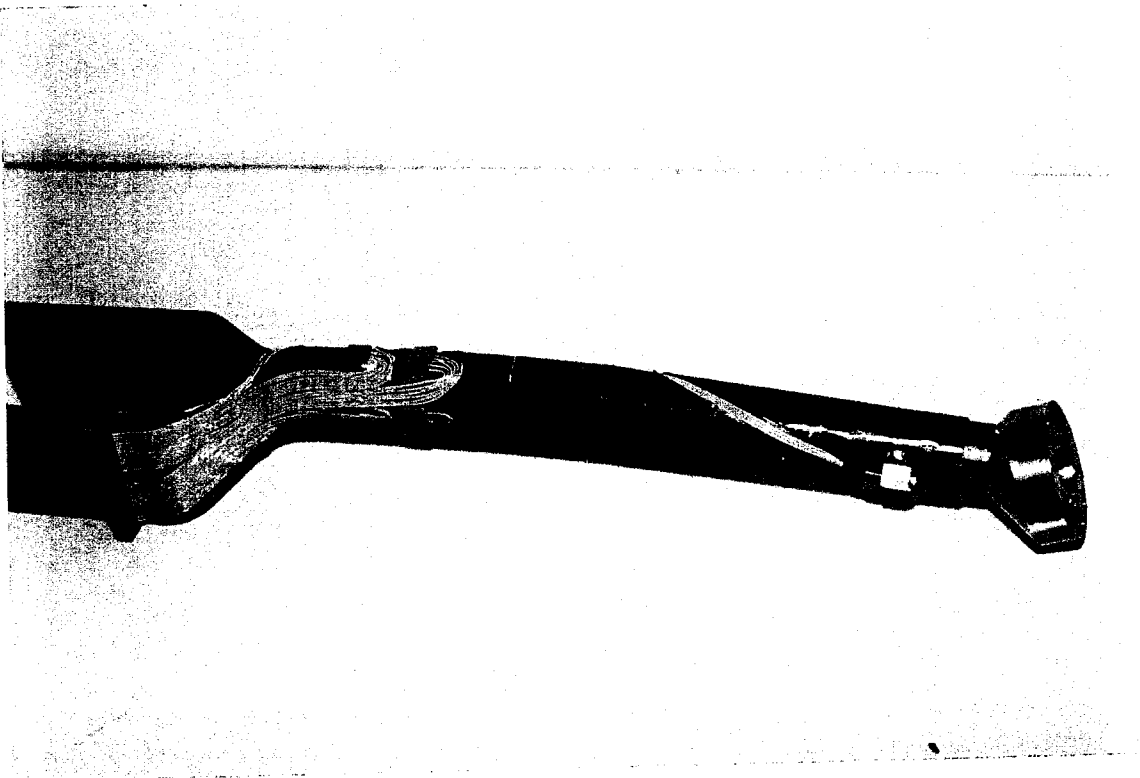


Figure 3.3.6-5. Foam Tape is Placed Between the Wire to Provide a Flush Surface for the Overwrap.

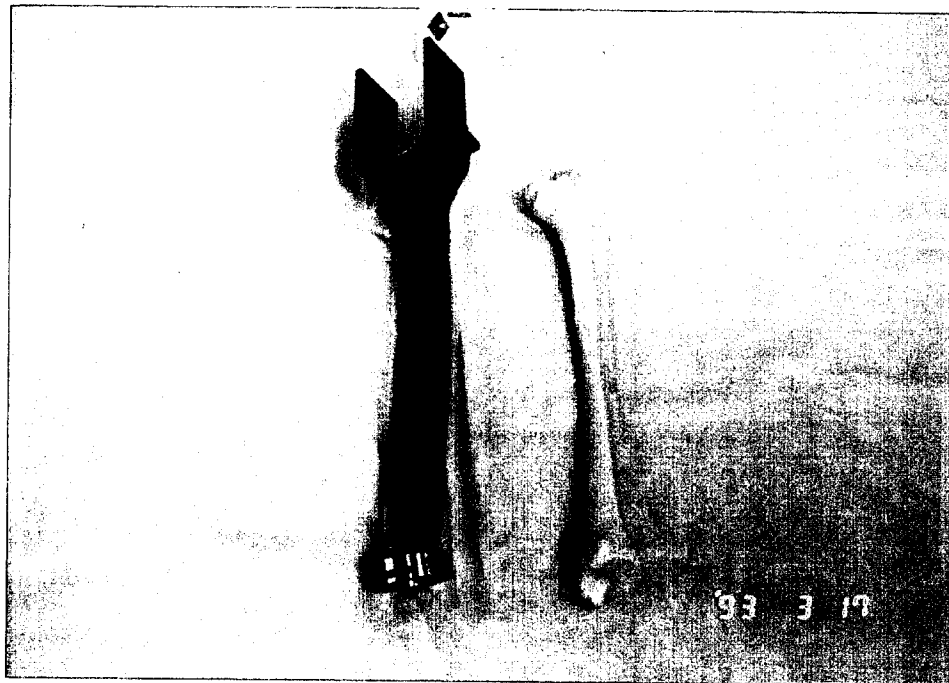
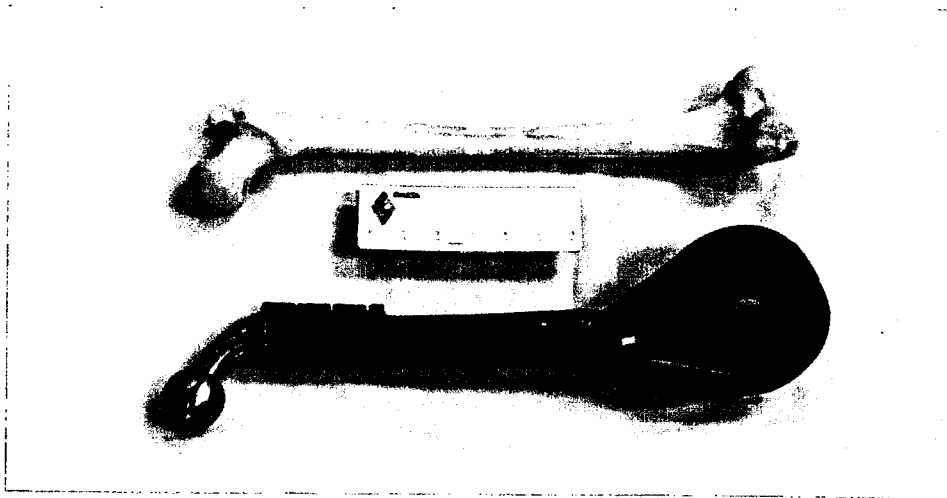
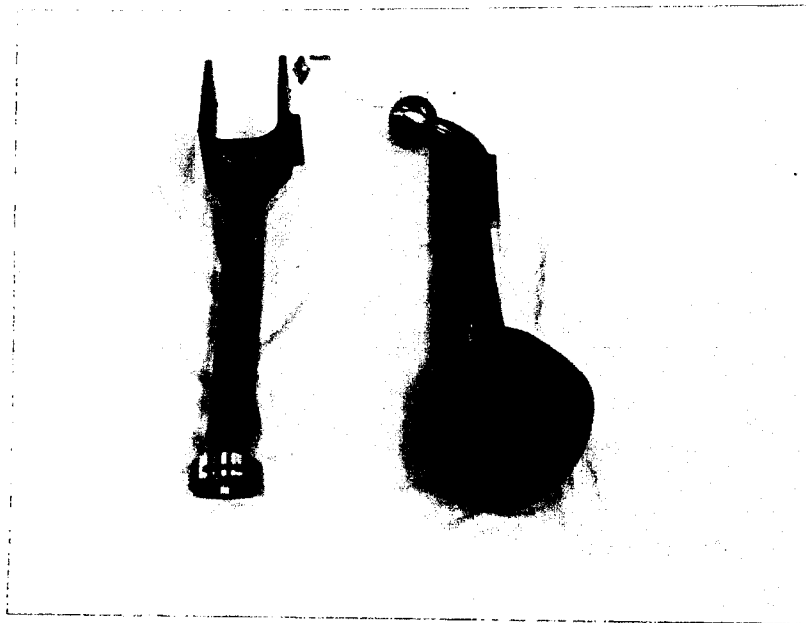


Figure 3.3.6-6. Instrumented and Overwrapped Femur and Tibia Long Bone Segments.

The design approach to meet the requirements was a knee joint configuration similar to Hybrid III, but instead of metal, uses high performance composite materials. Use of the composite materials was necessary to achieve the weight and inertia of the human femur and tibia segments. Preliminary analysis shows the need for high strength composite material such as T1000G/Epoxy which was used for the femur and tibia long bone segments.

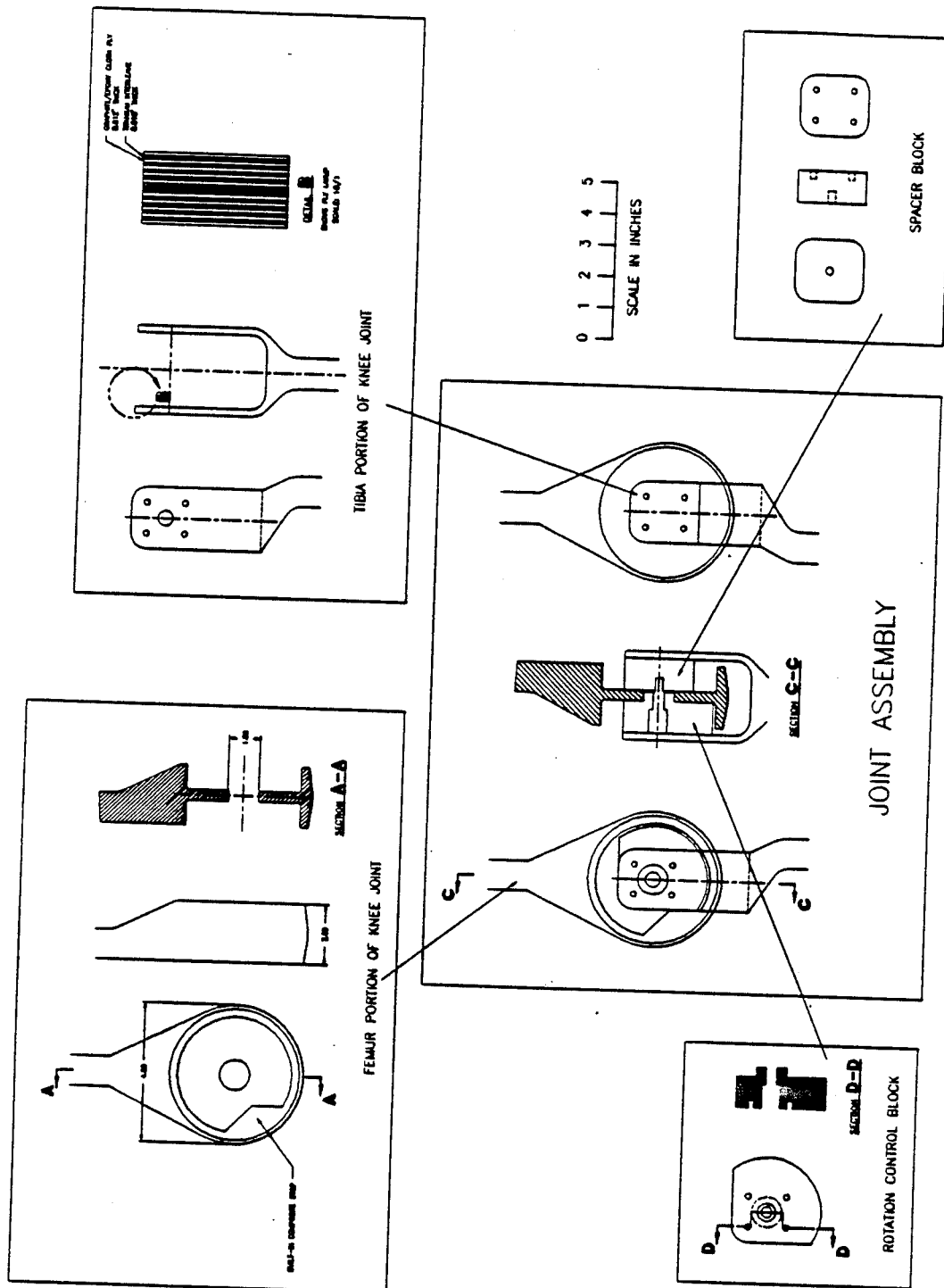
The knee joint design was developed using AutoCAD, a computer aided design drafting software package. The wire frame geometry was transferred from AutoCAD to the finite element model program called PATRAN. PATRAN generated a finite element mesh on the wire frame that was used in the analysis. The knee joint design consists of the femur, the tibia, and two pieces of hardware that simulate the sliding knee hardware, specifically called the rotational control block and the spacer block, drawings of which are shown in Figure 3.3.7-1.

The rotational control block is used to control rotation of the tibia with respect to the femur. Figure 3.3.7-2 shows how the block stops on the composite stop that is built into knee on the femur side. The stop allows motion through 135°. The stop stops the rotation when the leg is fully extended and fully bent. The block is made of titanium and is Teflon coated on the sliding surfaces to reduce friction in the joint.

The purpose of the spacer block is to provide material for the bolting of the tibia to the femur. The block has been sized to simulate a sliding knee mechanism such that the spacer block can be replaced by the sliding knee components. Like the rotational control block, the spacer block is made of titanium and will be Teflon coated on the sliding surfaces.

3.4 Flesh Development

From the start of the Advanced Biofidelic Composite Manikin (ABC-Man) Development Program it was agreed upon between the customer (AL/CFBV-WPAFB), the contractor (SPARTA, Inc.) and SPARTA subcontractors (such as First Technology Safety Systems, Inc. [FTSS]), that the existing manikin flesh materials would not meet the requirements of the ABC Man Program. The primary goal of the ABC MAN program was to redistribute segment mass to achieve an inertial biofidelic response. This involved greatly reducing the long bone mass while maintaining the strength. In order to maintain the correct total segment mass and geometry a large increase in flesh density (mass) was required. Thus a project to develop synthetic flesh for the ABC Man was begun. This small flesh development project consisted of six tasks:



3.3.7-1. Knee Joint Design Consists of Four Pieces.

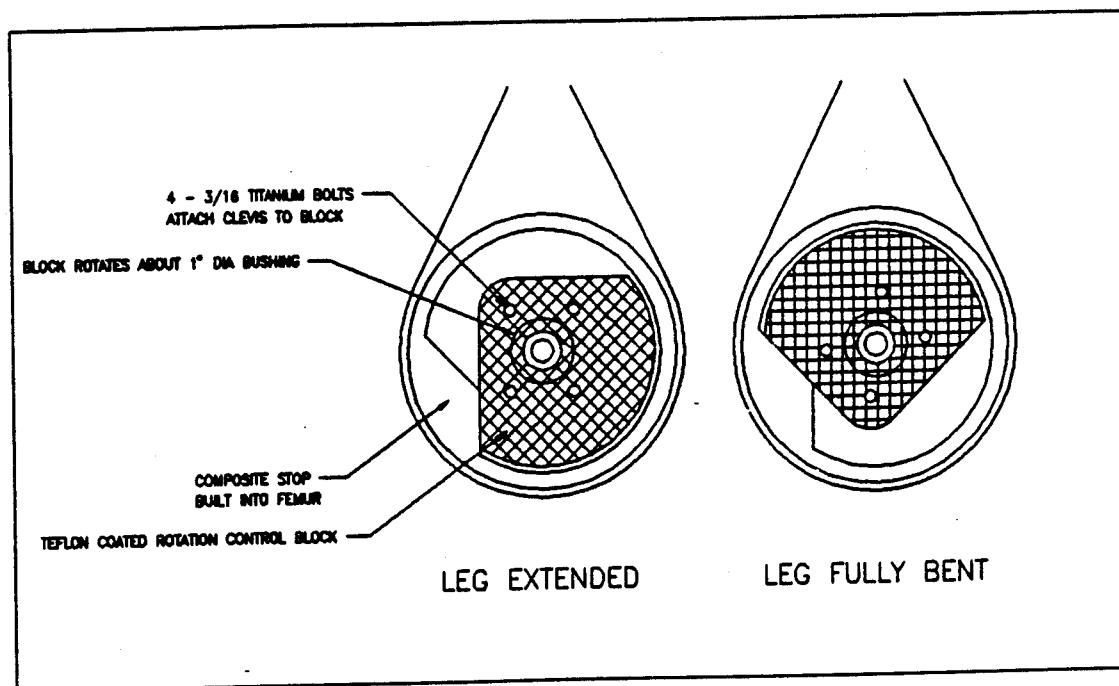


Figure 3.3.7-2. Rotation Control Block Controls Rotations of the Tibia with Respect to the Femur.

- 1) Identification of manikin flesh requirements
- 2) Survey of existing manikin flesh materials and potential flesh materials
- 3) Initial selection of candidate materials
- 4) Preliminary testing
- 5) Further selection of candidate materials
- 6) Final testing

Each of these tasks are discussed in greater detail below.

3.4.1 Identification of Manikin Flesh Requirements

After conversations with the then program monitor Lt. Eric K. Spittle (of AL/CFBV-WPAFB) and various employees of SPARTA subcontractor FTSS, the definition of the synthetic flesh requirements for the ABC manikin were agreed upon. These requirements are included in Table 3.4-1 in comparison with the properties of the synthetic flesh material utilized by FTSS in their existing crash test manikins. Included with the properties are weighting factors, which were utilized in the comparison of the different candidate synthetic flesh materials, in order to determine the most suitable material. These factors were in, SPARTA's judgment, the most accurate descriptions of the flesh material requirements. Input and concurrence from the Air Force was solicited.

3.4.2 Survey of Existing Materials

It was recognized that a wide variety of materials have been used for test manikins during recent times, with many of the materials being proprietary or not very well defined. It was recognized that the SPARTA subcontractor FTSS had a good knowledge of the types of synthetic flesh utilized by the commercial manikin companies (such as themselves) for use for civilian (mainly auto crash testing) purposes. Thus a survey of the material recommendations from various government laboratories was conducted, along with additional commercial companies. The following locations and personnel were contacted:

Government Sources:

- Colonel Martin Fackler, Retired, formerly with the Letterman Army Research Institute in San Francisco, soon to be with the International Wound Ballistics Association in Pinole Valley, California; they generally used the Ordinance Gelatine for their testing, a material that is not suitable for our needs.

- Mr. Larry Sturdivan with the Edgewood Arsenal, Aberdeen, Maryland; he referred me to Dave Neades at Army-BRL.
- Mr. Dave Neades of the Army Ballistic Research Laboratory at Aberdeen Proving Grounds, Aberdeen, Maryland. Included in his experience base was information on European manikins developed under various NATO contracts.
- Dr. Richard Frote, with the Division of Forensic Pathology, Armed Forces Institute of Pathology in Washington, D.C. He sent information from his files on the subject.
- Army Applied Technology Laboratory, at Fort Eustis, Virginia; SPARTA spoke with several staff members at this laboratory, but did not find any information of interest to the program.

Table 3.4-1. Required Materials Properties for Improved Synthetic Flesh

PROPERTY	CURRENT FTSS PROPERTIES	GOAL PROPERTIES	WEIGHTING FACTOR
Density	1.16 g/cm ³	1.00	0.20
Processability	-	Can be utilized in existing First Technology molds	0.15
Resilience	???	Mimics flesh, value to be determined	0.10
Tear Strength	0.41 MPa (60 lb/in ²)	As high as possible, 60 psi minimum	0.10
Cost	???	As low as possible	0.075
Aging Behavior (in sunlight for example)	???	No yellowing, cracking, or deterioration in properties	0.075
Tensile Elongation	325%	100% (minimum)	0.05
Durometer (Shore A)	45 ± 5	40 ± 5	0.05
Cure Temperature	177°C (350°F)	As close to room temperature as possible, below 205°C (400°F) ¹	0.05
Operating Temperature	-	0 to 71°C (32 to 160°F)	0.05
Maximum Storage Temperature	-	54°C (130°F)	0.05
Organic Solvent Resistance	???	Moderate	0.025
Reaction to Burning	???	Produces minimum harmful fumes	0.025
TOTAL:			1.000

Notes:

1) 205°C (400°F) is the upper temperature limit for the embedded sensors.

Commercial Sources:

- Kind and Knox Division of Knox Gelatine, Inc. in Englewood Cliffs, New Jersey
- Mr. Gene Reeck and Ms. Carolyn Van Ingen-Dunn with Simula, Inc. in Phoenix, Arizona. They produce and test crash resistant seats for the U.S. Air Force and also have done work in manikins. However, they consider all of their materials and designs proprietary.
- Shell Chemical Company, Houston, Texas; potential resins for synthetic flesh.
- Huls America Inc., Piscataway, New Jersey; potential resins for synthetic flesh.
- FMC Corporation, Chemical Products Group, Philadelphia, Pennsylvania; potential resins for synthetic flesh.
- Crowley Chemical Company, New York, New York; potential resins for synthetic flesh.
- Argus Division, Witco Corporation, New York, New York; potential resins for synthetic flesh.
- Portland Plastics, Portland, Michigan; potential resins for synthetic flesh.

3.4.3 Initial Selection of Candidate Flesh Materials

Replies were received and correlated from all of the polymer processing and producing companies identified in Section 3.4.2, as to their recommendations for synthetic flesh based on the required properties (Table 3.4-1) sent them. A total of eight material combinations were identified as potential candidate materials. Seven of the materials were conventional PVC materials with plasticizers added. The last of the materials had chopped glass added to modify the load-displacement characteristics of the material.

Portland Plastics of Portland, Michigan shipped to SPARTA two 30.5 x 21.6 x 5.1 cm (12 x 8.5 x 2 inch) blocks of candidate improved synthetic flesh, shown in Figures 3.4-1 and 3.4-2. They also sent SPARTA one gallon of each resin so that SPARTA could cast their own shapes

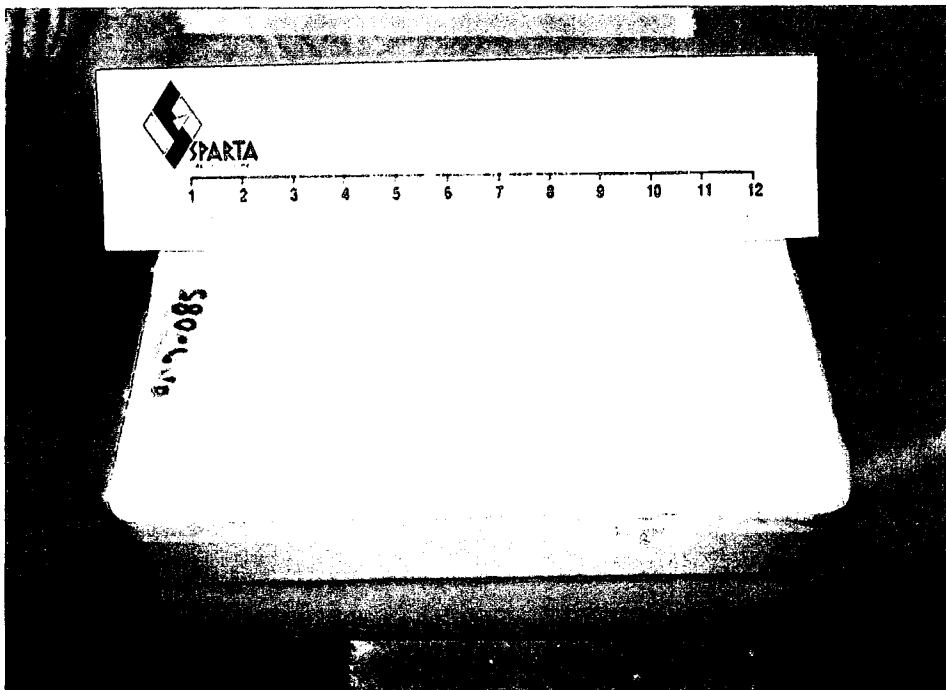


Figure 3.4-1. Block of Cured Candidate Synthetic Flesh Material PRD-085.

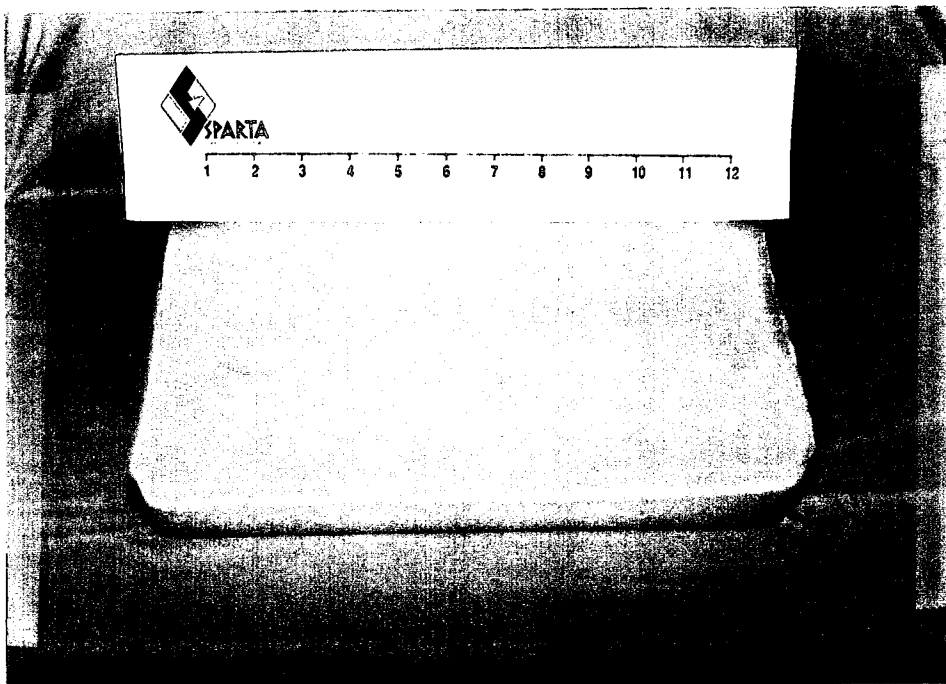


Figure 3.4-2. Block of Cured Candidate Synthetic Flesh Material PRD-086.

from the candidate materials. These two materials are modifications of the existing manikin formulation that Portland makes for First Technology Safety Systems (FTSS), Inc. of Plymouth, Michigan. As mentioned earlier, FTSS was a subcontractor to SPARTA on this program. The formulation consisted of conventional PVC (poly-vinyl chloride) with plasticizer's added (about 40% by volume) in order to make the PVC material less stiff (i.e. more rubber like). However, the plasticizers all tend to be more dense than water (greater than 1.00 g/cm³) and when the plasticizers they use for their current manikins are added to the PVC (which has an uncompounded density of 0.098 to 1.01 g/cm³) a material with a density of 1.16 g/cm³ was obtained.

Portland recommended a series of plasticizers which have decreased density, while still retaining (they believed) the following desirable manikin synthetic flesh properties:

- Processability in existing manikin molds
- Resilience
- Moderate to high tear strength
- Low to moderate cost
- Good aging behavior (in sunlight for example)
- High tensile elongation
- Hardness near Durometer 40 (Shore A)
- Cure temperature less than 177°C (350°F)
- Operating temperature capability of 0 to 71°C (32 to 160°F)
- Storage capability at 54°C (130°F) with no degradation of properties
- Organic solvent resistance
- Non-harmful products upon burning

The two materials that were sent from Portland Plastics to SPARTA were:

MATERIAL	UN-PIGMENTED COLOR	DENSITY (gm/cm ³)
PRD-085	White	1.121
PRD-086	Brown	1.118

The densities of these two candidate materials were disappointingly high as the goal densities were in the 1.00 to 1.06 gm/cm³ range. In order to reduce the density of these two materials it was realized that the addition of micro-balloons into the resins would have to be accomplished without compromising their ductility or hardness of the cured resin. It was calculated that a loading of 12% would be needed in order to sufficiently reduce the density to

the goal value of 1.00 gm/cm³. It was necessary to start with a polymer that was softer than that needed, so that when the glass micro-balloons are added the hardness would be at the level desired.

Approximately 20 different manufacturers of micro-balloons (used to reduce density, alter viscosity, or reduce cost) were contacted. Three different samples of glass and thermoplastic micro-balloons were received. These included:

- Q-Cel 2106 from The PQ Corporation, Valley Forge, PA; this is a sodium borosilicate glass microballoon product; density 0.20 g/cm³
- Scotchlite grade 70-0703-7720-8, from the 3-M Corporation, St. Paul, MN; this is a soda lime borosilicate glass (amorphous silicate); density 0.125 g/cm³
- Expancel 091-DE, from Expancel Nobel Industries, Marietta, GA; this is an organic thermoplastic microballoon material; density 0.025 g/cm³

Included in Table 3.4-2 is a listing of the required volume and weight fraction of each microballoon material to bring the two resins (PRD 105 and PRD 106) down to the goal density.

Table 3.4-2 Amounts of Microballoons Required To Bring Synthetic Flesh Resins To Goal Density of 1.0 g/cm³

RESIN	UNIT	EXPANCEL $\rho = 0.025$	SCOTCHLITE $\rho = 0.125$	Q-CEL $\rho = 0.20$
PRD 105 $\rho = 1.12$	V_f	11.0%	12.1%	13.0%
	W_f	0.27%	1.51%	2.61%
PRD 106 $\rho = 1.08$	V_f	7.6%	8.4%	9.1%
	W_f	0.19%	1.05%	1.82%

3.4.4 Preliminary Testing

Each of these three grades of microballoons identified during the Initial Selection of Candidate Flesh Materials task were mixed into each of the two synthetic flesh compositions in order to bring their densities down to goal value of 1.0 gm/cm³. A series of 2.5 cm (1.0 in.) diameter x 2.5 cm (1 in.) tall blocks were cast from the six materials (two resins x three fillers).

Density and compressive modulus determination tests were performed on each, with the data presented in Table 3.4-3.

Table 3.4-3. Summary of Density and Compressive Modulus Measurements

COD E	MATRIX	FILLER	MEASURED DENSITY (g/cm ³)	COMPRESSIVE MODULUS GPa (kpsi)
A	PRD 105	Expancel	1.010	1.682 (244)
B	PRD 106	Expancel	0.990	1.420 (206)
C	PRD 105	Scotchlite	1.000	2.530 (367)
D	PRD 106	Scotchlite	0.991	1.724 (250)
E	PRD 105	Q-Cel	0.979	2.392 (347)
F	PRD 106	Q-Cel	0.990	1.765 (256)
PRD 105-1	PRD 105	-	1.12	1.993 (289)
PRD 106-1	PRD 106	-	1.08	1.758 (255)
PRD 105-2	PRD 105	-	1.12	-
PRD 106-2	PRD 106	-	1.09	-

As can be seen the goal density was reached relatively closely. In addition, it is seen that the density measurements of the two castings of unfilled PRD 105 and PRD 106 were very similar, indicating the repeatability of the density measuring procedure. In all cases the PRD 105 resin was stiffer than the PRD 106 resin, filled or unfilled. The addition of the organic (thermoplastic) microballoons (Expancel) resulted in a drop in modulus (15.6 and 19.2 respectively for the PRD 105 and 106 resins). The addition of the glass Scotchlite microballoons resulted in a 27% increase in stiffness for the PRD 105 resin and in a 2% drop in the PRD 106 resin. The addition of the glass Q-Cel microballoons resulted in a 20% increase in stiffness for the PRD 105 resin and basically no change in the PRD 106 resin. It seems evident that the PRD 105 resin bonded to the glass microballoons better than did the PRD 106 resin. In addition the higher modulus glass resulted in an increase in the stiffness of the filled material, despite their hollow construction.

Three instrumented specimens were fabricated. The purpose of these specimens was to investigate the effect of different curing temperatures on the performance of the tactile foil sensors. Three different curing times/temperatures were investigated. The recommended cure cycle for the PRD-106 resin is thirty minutes at 400°F (204°C). However, it is known that this temperature would irreparably damage the tactile sensors. Thus temperatures ranging from 107 to 163°C (225 to 325°F) were tried at much longer cure times (up to forty eight hours). It was

found that the lower temperature cycles did not fully cure the resin and the higher temperature cycles destroyed the sensors.

Based on these results it was decided to investigate a different method to install the tactile sensors in the synthetic flesh. In this method the body part would be cast with a void cured in place. The sensor would be bonded into the void and a piece of synthetic flesh bonded over the top utilizing a solvent adhesive to join the vinyl PRD-106 to itself. This method involves the forming (during casting of the synthetic flesh) of a "hollow". The tactile sensor is adhesively bonded into the hollow utilizing a low temperature cure laminating (pressure sensitive) adhesive. Afterwards a "close-out" of synthetic flesh is bonded into the "hollow" utilizing a combination of laminating adhesive (to join the top of the sensor to the bottom of the "close-out" piece) and solvent adhesive (to bond the PVC to the PVC).

The acrylic based adhesive grade 467 (produced by the 3-M Corporation) was chosen as the laminating adhesive because of the high strength bond it forms to polyester (from which the bottom of the sensor is made from). In addition the adhesive also displays good adhesion to vinyl and polyurethane (synthetic flesh candidate materials). These solvent adhesives will not join the polyester coating of the tactile sensors to vinyl or polyurethane, necessitating the need for the second adhesive to join the urethane to the sensor. A number of adhesives were ordered for these bonding investigations.

A quantity of the grade 467 adhesive was obtained and successfully test bonded to the polyester backing of the sensor gage and to blocks of the synthetic flesh. The bond was further strengthened by a cure-cycle of 80°C (176°F) for 30 minutes. This cycle did not harm the tactile sensor foil. Additional demonstration of the solvent based adhesive to join polyurethane to itself was demonstrated.

Much effort was put into identifying and obtaining an adhesive to join the piezo-electric sensor to the flexible circuit board substrate. The desired properties of the adhesive include:

- electrically conductive in the through-the-thickness direction
- curing temperature less than 100°C
- ability to bond well to the sensor and the substrate materials
- availability as a commercial product and conformity to existing specifications
- compatibility with the other adhesives used to join the tactile sensor package into the synthetic flesh

- flexible to allow sensor to deform when flesh is loaded
- moderate shear and tensile strength to prevent failure of bond between sensor element and substrate

The material found that best suited these requirements was 3-M Corporation's Scotch Brand 9703 conductive adhesive transfer tape. This is a "Z-Axis" tape, meaning that it has properties (in this case, electrical conductivity) that are strongest in the Z-Axis (that is out of the plane of the tape). The tape is not electrically conductive in the plane of the tape.

The tape is room temperature curing (reaching full strength in about 24 hours) and is available in a wide variety of lengths. It has a very uniform thickness (75 microns [0.003 in.]) which is ideal for the sensor application. The 3-M Corporation sent SPARTA samples of the material for evaluation.

SPARTA shipped to Portland Plastics approximately one pound of grade K-1 glass micro-balloons made by the 3-M Company (tradename Scotchlite). The micro-balloons were mixed into the resin (grade PRD-106) at the following percentages (either measurement could be used, whichever was easier to measure at the time of preparation):

by weight: 1.05%

by volume: 8.4%

As described previously, the purposed of the micro-balloons was to reduce the density of the synthetic flesh resin to approximately 1.00 gm/cm³.

Three attempts (conducted on November 19, 1992) were made using the experimental PVC thermosetting (i.e., a material which is permanently shaped at an elevated temperature) material in the ADAM thigh mold. The goal in each attempt was to find the optimum cure cycle for the experimental material, which began as a liquid with the consistency of water, but cured into a solid, rubber-like material. This cycle is a function of the cure temperature of the material, which was known in advance, and the geometry and material of the mold, which had never been used with this material.

Based on preliminary experiments conducted at SPARTA, the first attempt at molding the material involved a cure cycle with several steps:

1. preheat the mold in a convection oven for 30 minutes at 205°C (400°F)
2. remove the mold and pour in the uncured material
3. replace the mold in the oven and heat for 40 minutes at 205°C (400°F)
4. remove the mold, allow sufficient cooling and open.

Two major problems occurred during the first trial casting. First, while pouring the material into the mold in step 2, it was found that a major leak existed in the mold, resulting in a significant spillage of the liquid material (this did not create a safety hazard). This required sealing the leak, and resulted in significant cooling of the preheated mold before it could be re-filled. Second, possibly due in part to the first problem, it was found upon opening the mold that only a partial cure had been achieved.

The second attempt at molding the part was similar to the first with two exceptions. First, the leaky section of the mold was sealed before preheating. Second, the material cure time was doubled to eighty (80) minutes to insure a complete cure. In this attempt, cooling of the mold was accelerated with a slow water quench after about 15 minutes of outdoor cooling. The results were much better for this trial, although there were indications that the material was cured for too long a period of time. These indications included discoloration of the final product, which does not necessarily indicate a degradation of the material, but might indicate a slight hardening of the material, which would be undesirable from a synthetic flesh standpoint. Two photographs of the thigh section from Trial #2 are included as Figure 3.4-3.

To adjust for the over-curing in the second trial, a third trial was performed identical to the second, except for a reduced cure time of sixty (60) minutes. The results of the third trial indicated that complete cure was achieved, with little indication of overcure, except at the most outer part of the flesh component. Thus, the last cure cycle tested appeared to be relatively close to optimal for the type of mold and oven utilized. Minor formulation adjustments would solve any other problems. In addition, small changes to the mold design which were suggested by the results of these tests would greatly improve the cure cycle, including making a mold insert which heats as rapidly as the mold exterior surface.

The second of the three thigh specimens that were produced at Portland on November 19, 1992 was shipped to SPARTA where density and micro-balloon uniformity specimens were cut from it as shown in Figure 3.4-4. Density measurements were conducted according to ASTM D1895 (so called Archimedes method) and the results are included in Table 3.4-4. As can be seen very uniform values were measured over the entire thigh. Figure 3.4-5 shows the interior of the thigh flesh where differences in cure temperature produce color variations, but the color variation does not cause a density variation. Specimen number 6 was cut into three pieces to show the uniformity from the outer surface (6A) to the inner surface (6C) of the thigh.

variation does not cause a density variation. Specimen number 6 was cut into three pieces to show the uniformity from the outer surface (6A) to the inner surface (6C) of the thigh.

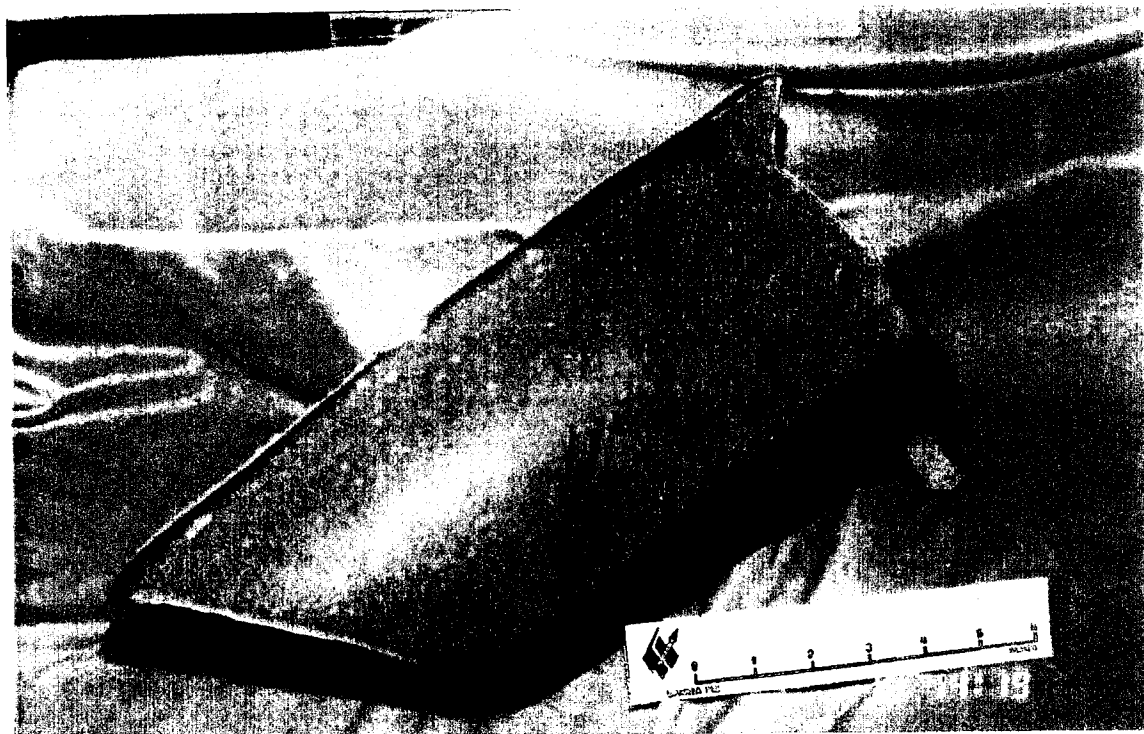
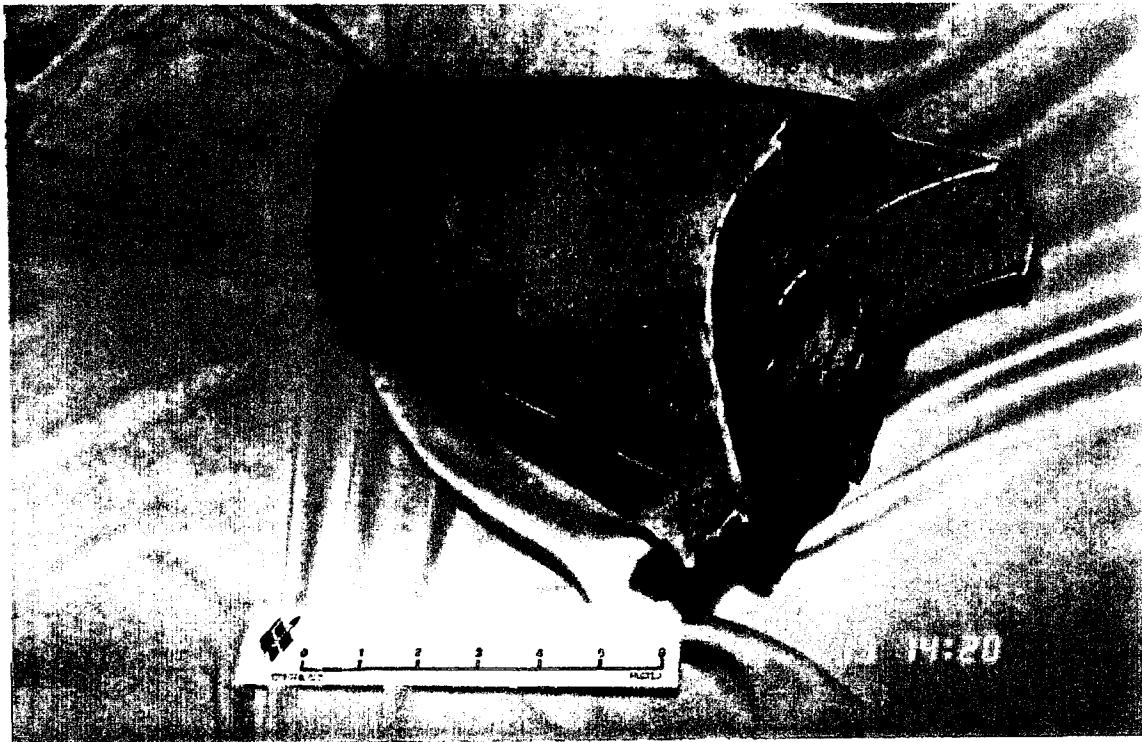


Figure 3.4-3. Representative Photographs of ADAM Thigh Produced from SPARTA Synthetic Flesh.

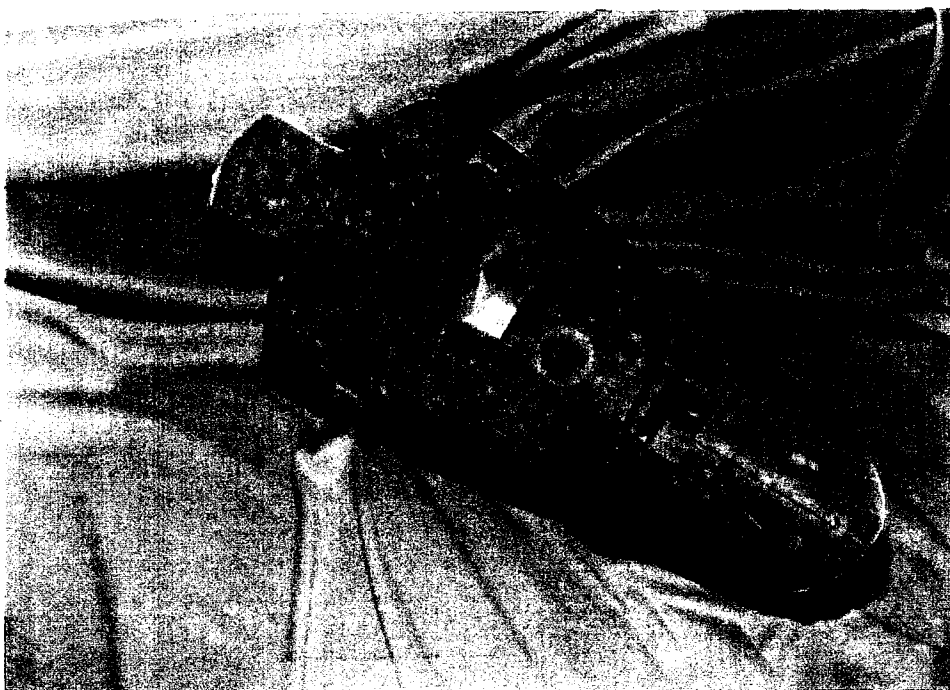


Figure 3.4-4. Representative Photograph of ADAM Thigh Produced from SPARTA Synthetic Flesh Indicating Areas Where Density/Uniformity Specimens Were Cut Out.

Table 3.4-4. Density Measurements Taken From Thigh Produced From SPARTA Synthetic Flesh Material

SAMPLE NUMBER	DENSITY (g/cm ³)
1	1.009
2	0.997
3	1.007
4	1.004
5	0.990
6a	1.017
6b	1.007
6c	0.980
7	1.045
8	0.999
9	0.991

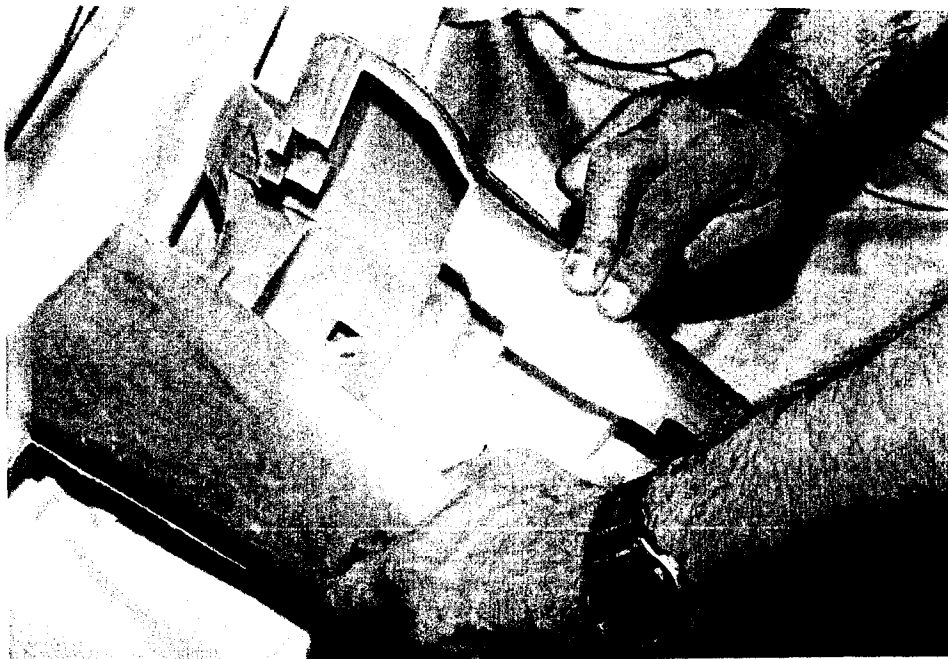


Figure 3.4-5. Representative Photograph of ADAM Thigh Produced from SPARTA Synthetic Flesh Indicating Area Where Difference in Cure Temperature Produce Color Variations.

Included as **Figure 3.4-6** are representative micrographs (30X magnification) revealing the microstructure of the synthetic flesh material at areas distant from one another. The uniformity of the microballoon spacing and density is seen.

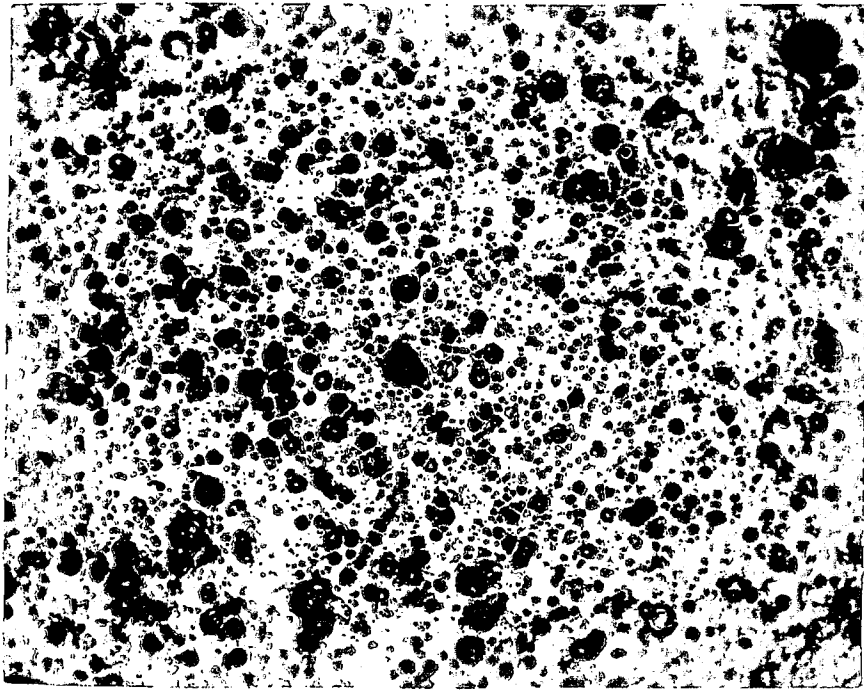
3.4.5 Further Selection of Candidate Materials

Samples of the previously manufactured glass micro-balloon loaded vinyl synthetic flesh material were shown to the following people:

- Mr. Mike Bebe of the VRTC (Vehicle Research and Test Center, a Department of Transportation Research Center) in East Liberty, Ohio
- Personnel of Vehicle Research Center, a SETA contractor to VRTC
- Mr. Mike Salloum of First Technology Safety Systems, Inc. in Plymouth, Michigan

All were of the subjective opinion that the material was too rigid for a manikin and that a "softer" material was needed. In addition, First Technology, who made the mold for the casting of the body components, much prefers a room temperature curing resin system as this permits the use of fiberglass tooling which is far quicker and lower cost to manufacture than the aluminum tooling that would be needed for the higher temperature curing vinyl based system. Although the initial candidate PVC flesh material met the technical specifications of the U.S. Air Force, it was decided after conferring with AL/CFBV personnel, that a more "biofidelic" tactile flesh should be used, based on the subjective evaluation of current workers in the field.

a)



b)

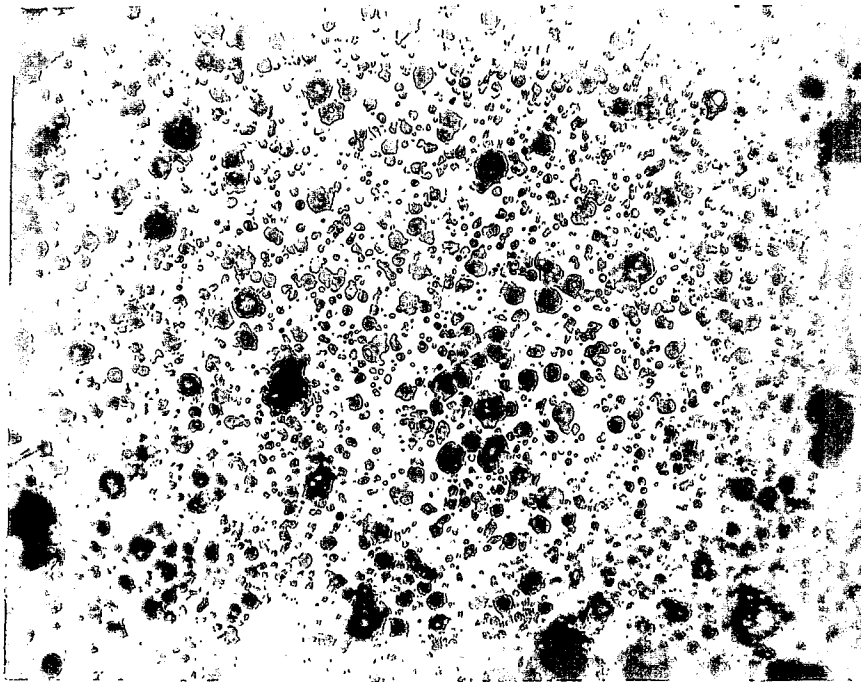


Figure 3.4-6. Representative Micrographs of Specimens Cut From ADAM Thigh Produced from SPARTA Synthetic Flesh (30X magnification).

Alternate Flesh Material

After an investigation into various commercially available resin compounds, urethane (a room temperature curing polymer) was selected. A large number of companies market urethane system (for example Hexcel, BASF, DuPont, PSI Urethanes, BJB, Uniroyal, and many others). Urethane is a shortened form of the more correct usage, "polyurethane elastomers." These materials can be formulated to range in hardness from 10 Shore A (durometer) which is about the hardness of a gum eraser to 90 Shore D (durometer) which is harder than a golf-ball casing. Chemically, polyurethane elastomers are polymers containing urethane groups (-NH-CO-O-), created by reacting isocyanates with polyols and chain extenders. By varying the nature of these three components, a processor can create thousands of different combinations of properties. Because of this versatility polyurethanes can be custom tailored to suit a wide variety of applications.

Urethanes have many advantages, including (also comparisons with vinyl included, where known):

- High strain to failure (better than vinyls in general)
- room temperature cure (compared to the 205°C (400°F) cure of the vinyl)
- moderate to good un-notched tear strength (approximately same as vinyl)
- flexible at low temperatures (slightly better than vinyl)
- stable up to 90°C (194°F)
- stability (i.e. no swelling or deterioration) in water (same as vinyl)
- impact resistant (but not as good as vinyl)
- paintable (better than vinyl)
- low-pressure, liquid casting with room temperature cure leads to low-cost tooling (vinyl needs elevated temperature cure, but can be liquid cast)
- virtually immune to ozone and oxygen attack (not as true for vinyl)
- wide resistance to oil, grease and chemical attack (about the same as vinyl)
- will not support mold, mildew or fungus growth (also true for vinyl)

In general the disadvantages of urethanes include:

- only fair weathering capability (due to UV interaction), but can be painted with flexible polyurethane paints to greatly increase weatherability, vinyl tends to be far more weatherable

- poor notched tear strength; although the materials' un-notched tear strength is high, in the presence of a notch it is greatly reduced. Thus it is important to have smoothly blended edges and corners of polyurethane elastomer parts. Some people cast scrim cloth (glass cloth) in the edges of a part to improve notched tear strength. Vinyl has much better notched tear strength than urethane.

The comparison of PVC and Urethane systems is shown in Table 3.4-5. The exact system chosen for the manikin is polymer system called "Skin Flex III", which is a castable urethane made by BJB Enterprises, Inc. in Garden, Grove, California. This material was originally developed for manikins and BJB markets the plasticizers (to change the hardness), necessary paints, colorants and mold releases for use with the material. When used in the standard mix ratio (50 parts of A to 100 parts of B by weight) it gives a hardness of approximately 25 Shore A (durometer). When 10% of the part C plasticizer is added (in order to bring the density down to 1.00) the hardness drops to approximately 20 Shore A, which is an excellent match to that of untensed (i.e., unflexed) human flesh. The vinyl material has a hardness of approximately 40 to 45 Shore A (durometer). The properties of this polyurethane material is included in Table 3.4-6.

Table 3.4-5 Comparison of PVC and Urethane Systems

PROPERTY	VINYL (PVC)	POLYURETHANE
Strain To Failure	Good	Good - Very Good
Cure Temperature	205°C (400°F)	Room Temperature
Tear Strength	Moderate - Good	Moderate - Good
Notched Tear Strength	Good	Poor - Fair (Can be Reinforced)
Flexibility (At Low Temperatures)	Fair - Good	Good
Temperature Stability	Good	Good
Water Stability	Excellent	Excellent
Impact Resistance	Excellent	Good
Paintable	Good	Very Good
Tooling	Compatible With 205°C (400°F) Cure	Simple
Ozone/Oxygen Attack	Good	Excellent
Oil, Grease, Chemical Resistance	Very Good	Very Good
Mold, Mildew, Fungus Resistance	Very Good	Very Good
Weathering Capability	Excellent	Fair (Can be Painted)
Repairability	Heat Sealable	Adhesive Bonded

Table 3.4-6 Summary of Polyurethane Properties

PROPERTY	REQUIREMENT	URETHANE
Density	1.0 g/cm ³ (0.036 lb/in ³)	1.0 g/cm ³ (0.036 lb/in ³)
Tear Strength	> 0.414 MPa (60 lb/in ²)	65 to 70
Tensile Elongation	> 100%	> 200%
Durometer	25 ± 5 Shore A Hardness	20 to 25
Cure Temperature	As Close To Room Temperature As Possible	Room Temperature (Can Be Accelerated At 49°C [(120°F)])
Operating Temperature Range	0 to 71°C (32 to 160°F)	-18 to 77°C (0 to 170°F)
Resistant to Environment Aging	No Yellowing, Cracking or Deterioration In Properties	Only Fair Without Painting or Pigmentation
Processability	Can Be Processed in Existing First Technology Molds	Demonstrated
Burning	Produces Minimal Harmful Fumes	Minimal

Based on the above discussion, the decision was made to substitute the polyurethane elastomer system "Skinflex III" for the micro-balloon loaded vinyl material previously developed during the program. However the loaded vinyl material was still kept in consideration, and kept as a back-up material.

The new flesh, a modified "Skin-Flex III", material manufactured by BJB Enterprises, Inc. of Garden Grove, California was procured. The flesh is composed of a three part urethane mixture with each constituent having a different density (A-1.060 g/cm³, B-1.000 g/cm³, C-0.985 g/cm³). The recommended mix ratio is 50 parts of A to 100 parts of B by weight. Part C may be added to lower the density of the overall mixture, but with a slight reduction in tear strength of the cured flesh. However, because glass microspheres are not required to adjust the effective density and the cure cycle is at room temperature, the "Skin-Flex III" is considerably easier to manufacture.

Several flesh specimens were cast, each with varying proportions of parts A, B, and C, to yield specimen densities between 0.985 g/cm³ and 1.030 g/cm³. The specimen stiffness and tear strength was then subjectively compared between the differing densities. Tear tests indicated that tear strength increased with increasingly heavier densities. Flesh with a density of 1.005 g/cm³ was selected as the final density with which to make a new impact test sample.

3.4.6 Final Testing

Tests were performed to determine effective ways of bonding the synthetic flesh. The best flesh-to-flesh bond was achieved by applying uncured (parts A+B) "Skin-Flex III" material to both bonding surfaces and allowing the part to cure under light pressure.

Mike Salloum of FTSS did a touch-and stretch test of the Skin-Flex III flesh samples varying in density from 1.000 to 1.030 g/cm³. He indicated that the 1.03 density flesh is more representative of a muscle in a tense condition, as would be seen in a crash. However, the 1.005 density flesh is not much different tactile-wise and its tear strength not significantly lower than the 1.03 density flesh. It was decided that the 1.005 density flesh will be used as the flesh for both the femur and tibia due to its minimum density.

FTSS has completed the molds of the femur and tibia. A photograph of the open femur mold is shown in Figure 3.4-7. The molds are constructed of a wood frame and fiberglass mold surface. As seen in the photograph, the composite femur is an insert in the mold and forms the cavity for the bone. The aluminum plate creates a 0.10" wide seam in the flesh so that the flesh can be removed from the bone. Cavity inserts, shown in Figures 3.4-8a and b, mold the cavity for the femur connectors and the accelerometers, respectively. Figure 3.4-9 depicts the raised area on the surface of the femur which will create the cavity in the femur flesh for the tactile foil sensor array. Figure 3.4-10 shows the open molds that will create the flesh cover for the tactile foil sensor cavity for both the femur and the tibia. A photograph of the open tibia mold is shown in Figures 3.4-11. Figures 3.4-12 and 3.4-13 show the closed molds for the femur and tibia, respectively.

3.4.7 Conclusions

Two separate flesh materials, one PVC based and one polyurethane based were developed (including methods to bond the sensors to the flesh material), made into test samples, and tested. The polyurethane based material was selected for the demonstration parts because of its perceived "biofidelic" response to human touch.

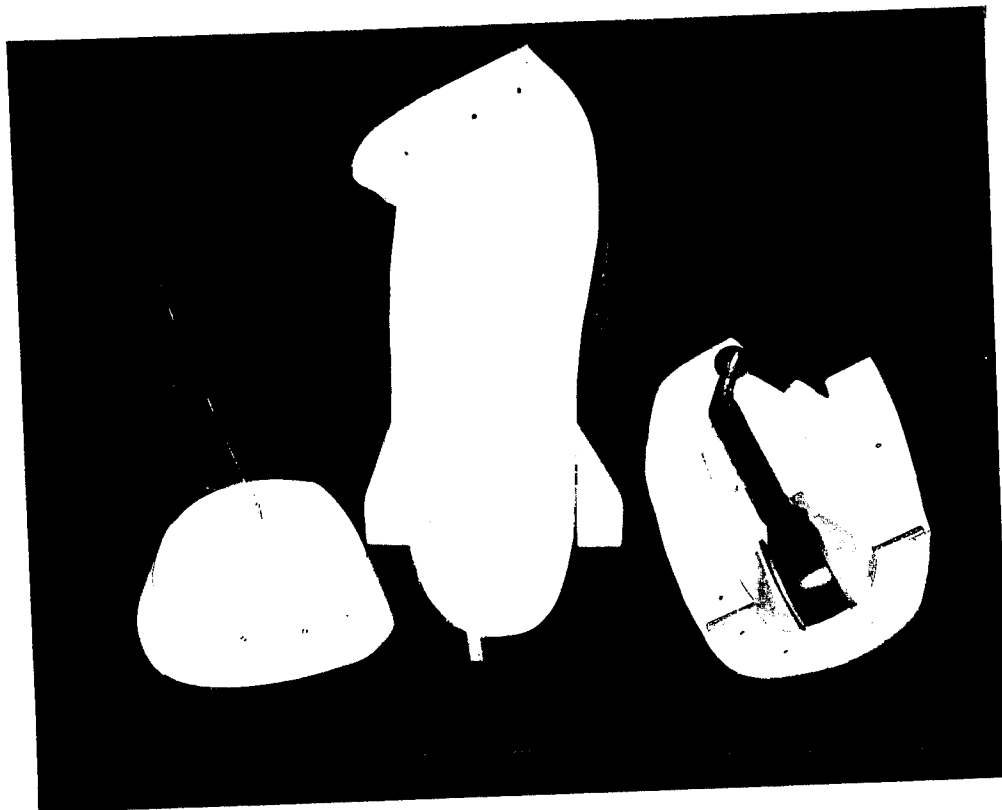


Figure 3.4-7. Open Mold for the Femur Flesh.

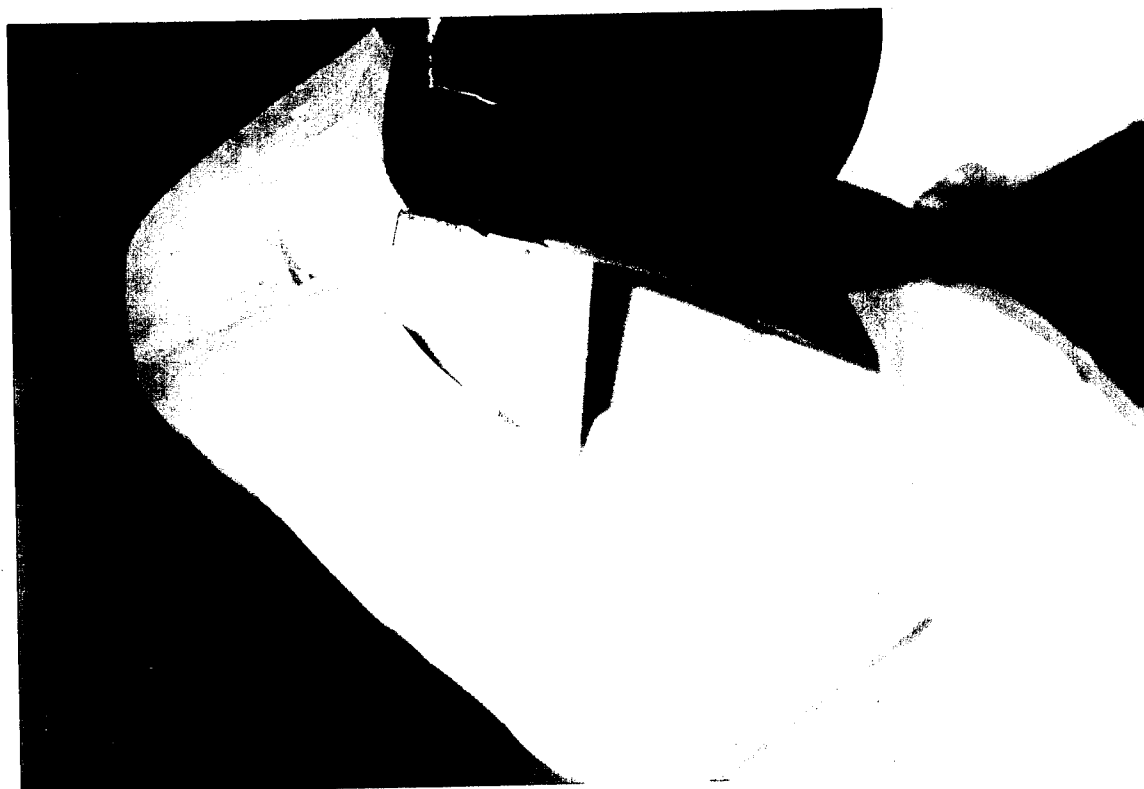


Figure 3.4-8a. Close Up of Insert to Form Cavity for Femur Connector Access.

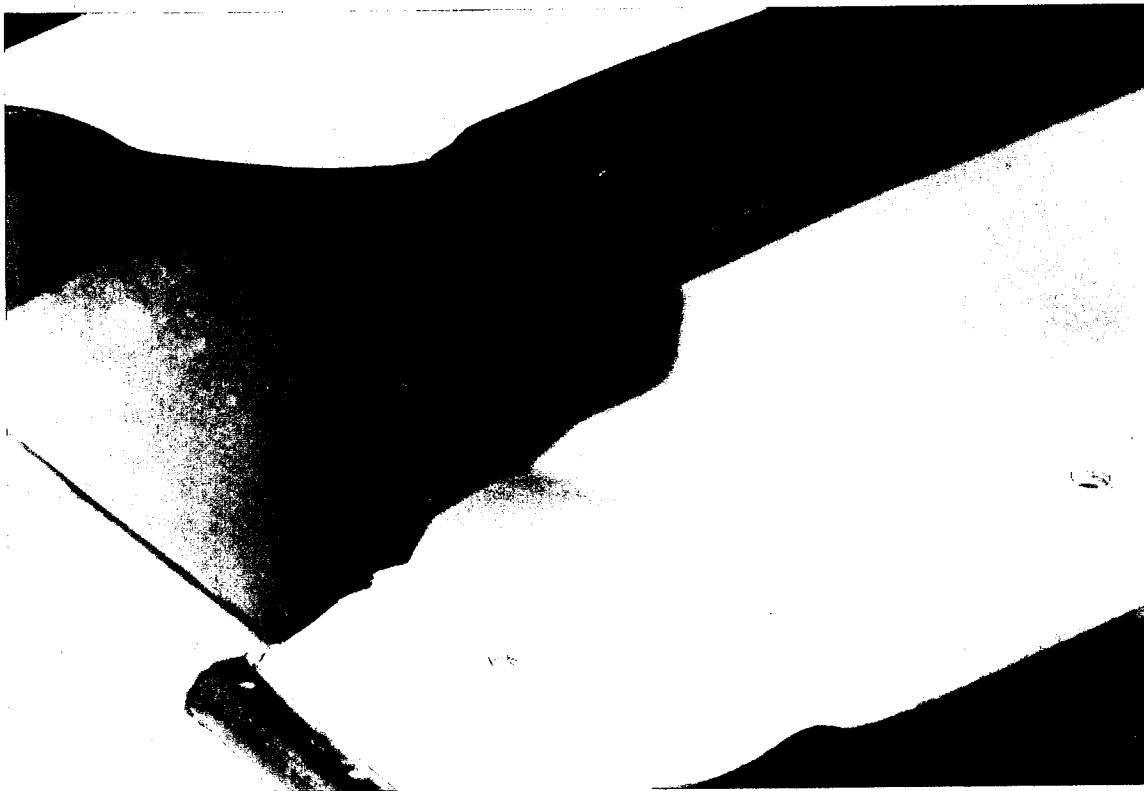


Figure 3.4-8b. Close Up of Insert to Form Cavity for Femur Accelerometer.



Figure 3.4-9. Raised Area in Femur Mold That will Form Cavity for Tactile Foil Array Sensor.

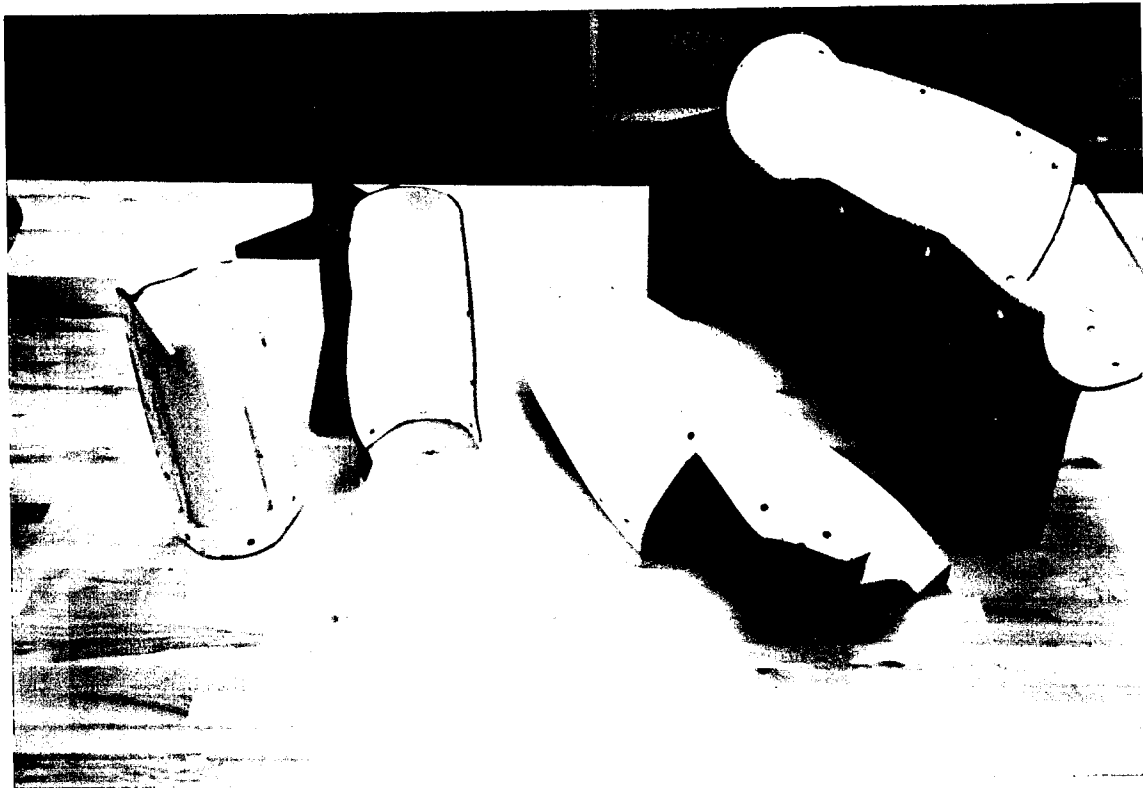


Figure 3.4-10. Open Molds to From Covers for Femur and Tibia Tactile Foil Array Sensor Cavities.

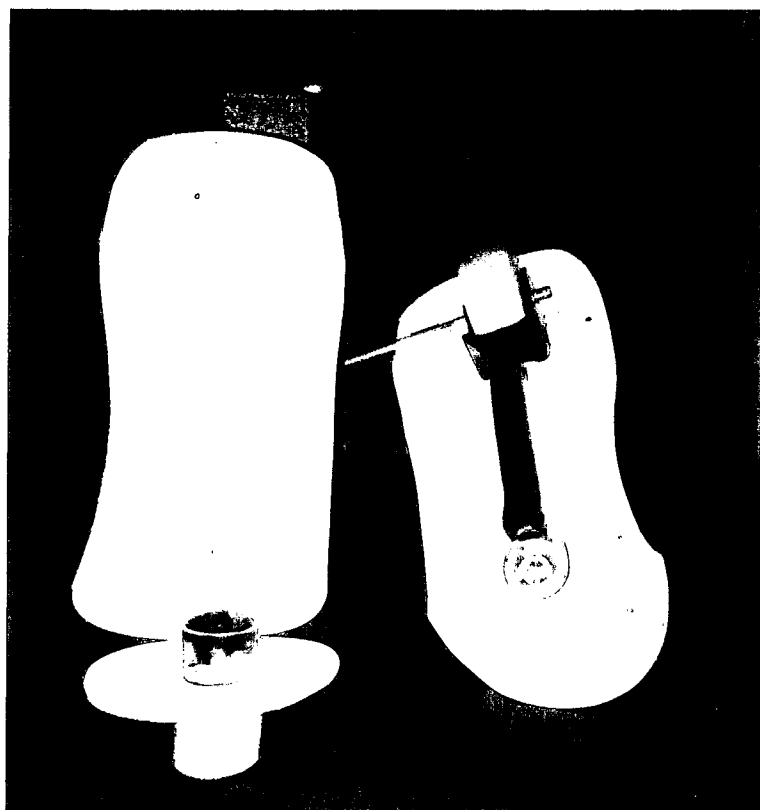


Figure 3.4-11. Photograph of the Open Flesh Mold.

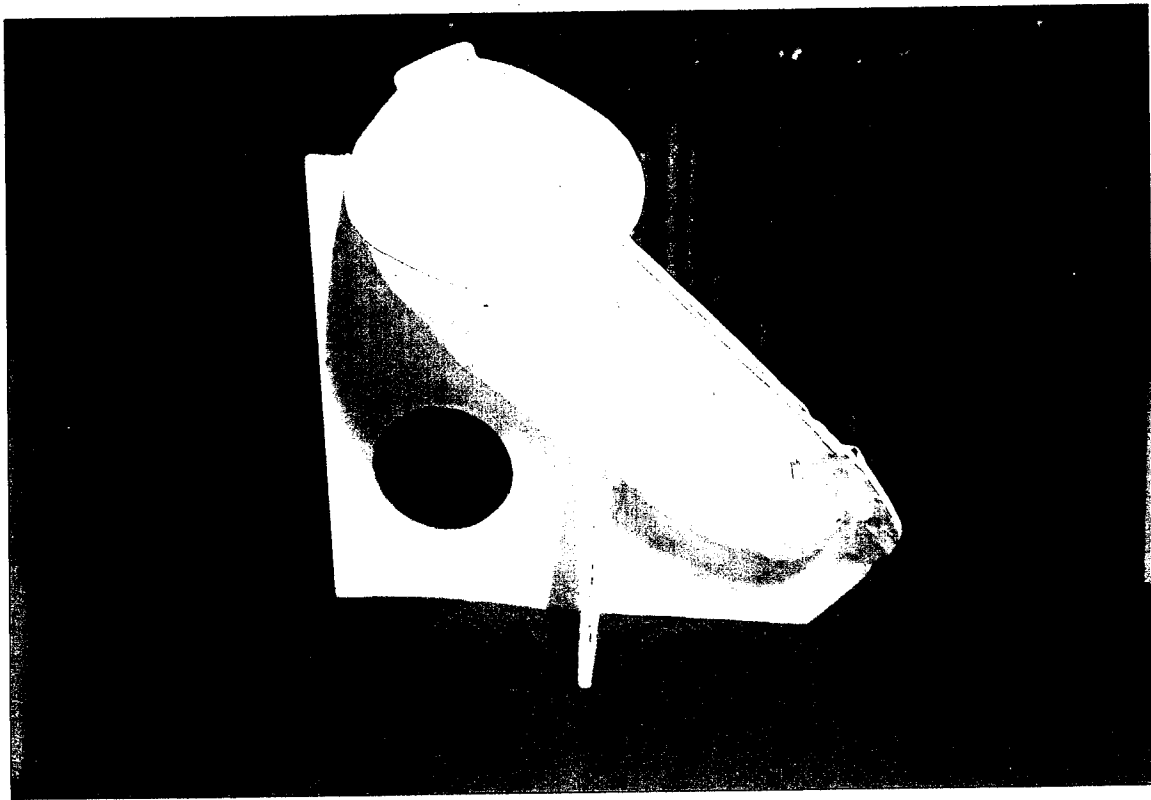


Figure 3.4-12. Closed Mold for Femur Flesh.

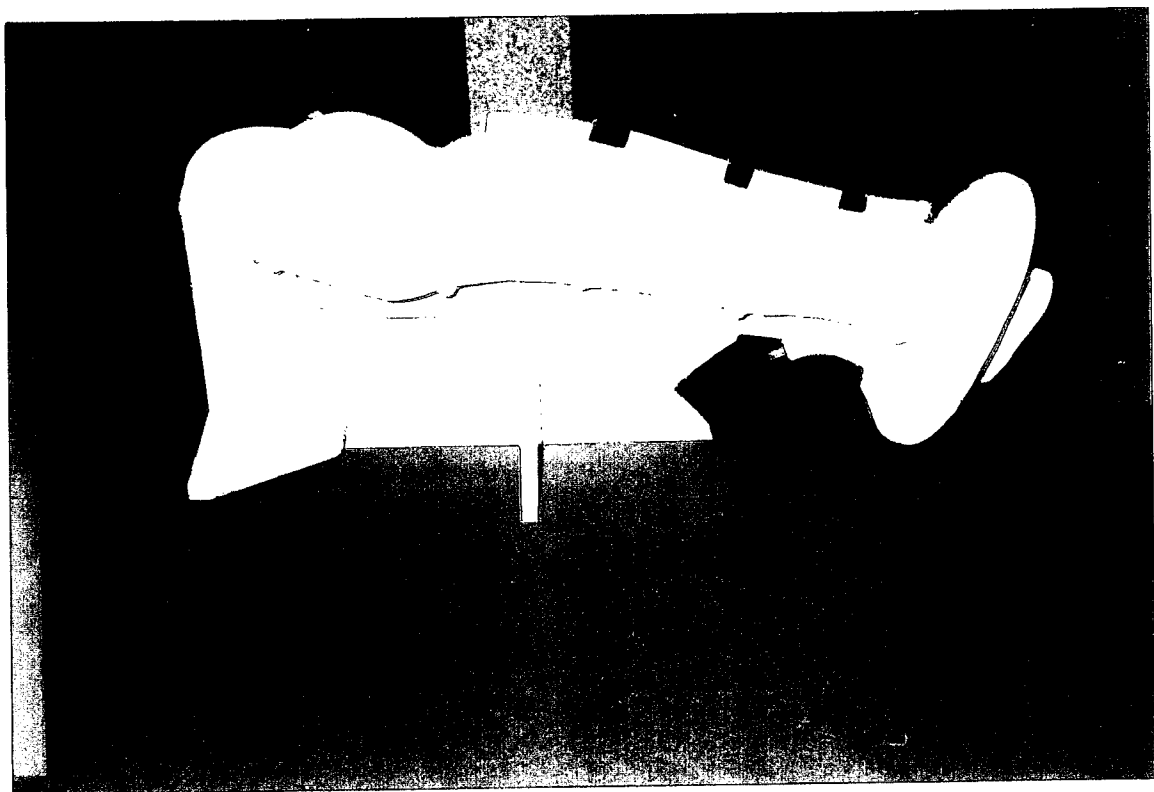


Figure 3.4-13. Closed Mold for the Tibia Flesh.

3.5 FABRICATION

3.5.1 Titanium Component Fabrication

Three titanium components were manufactured for the composite leg segment:

- 1) femur hip stem,
- 2) femur hip stem ball, and
- 3) tibia ankle

The components were machined of 6Al-4V titanium by Cycam, Inc. of Houston, PA. Drawings of the components were shown in Section 3.3 Long bone Composite Design. Photographs of the femur titanium components are shown in Figure 3.5-1. The titanium ankle joints for the tibia are shown in Figure 3.5-2.

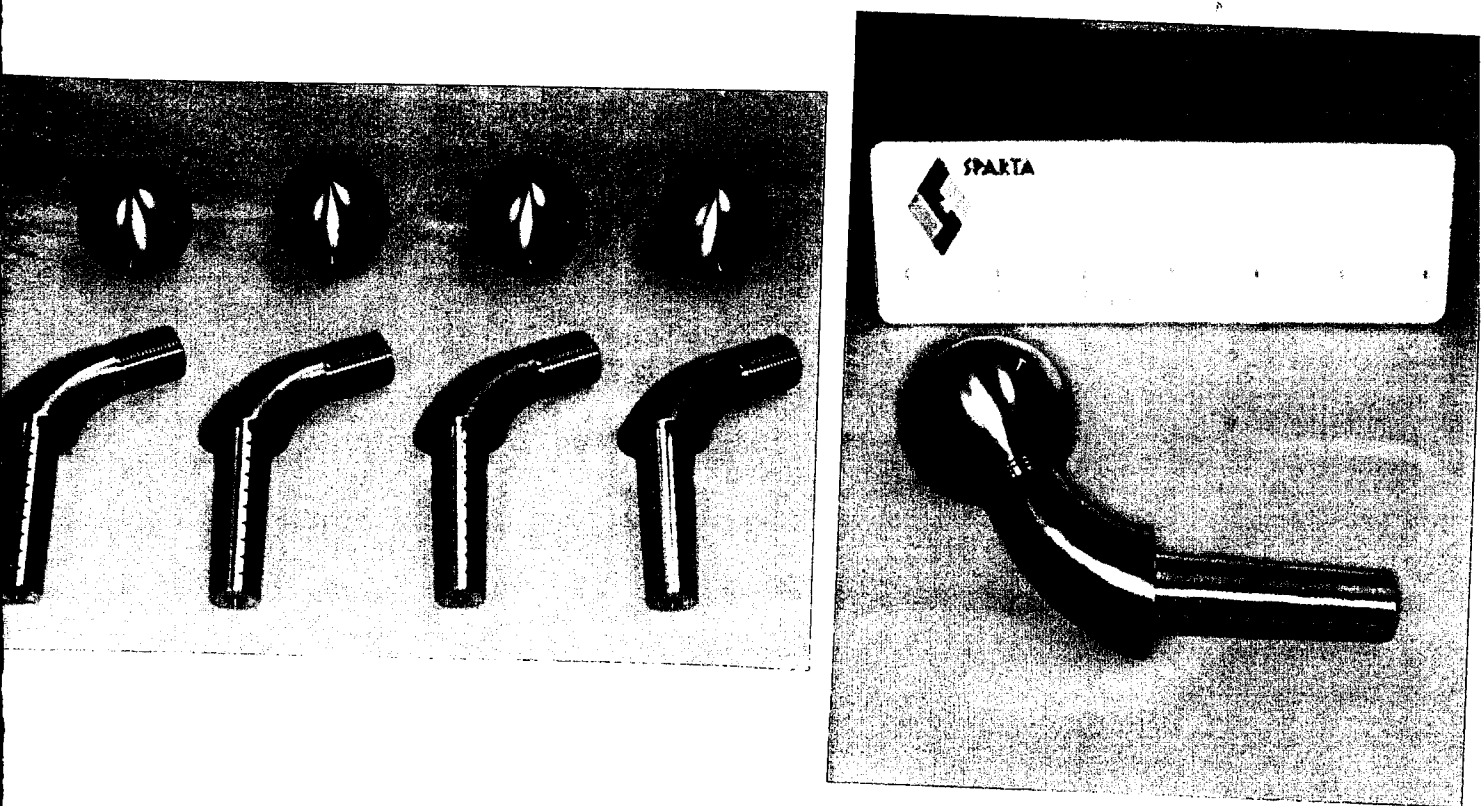


Figure 3.5-1. Femur Titanium Stems and Titanium Balls.

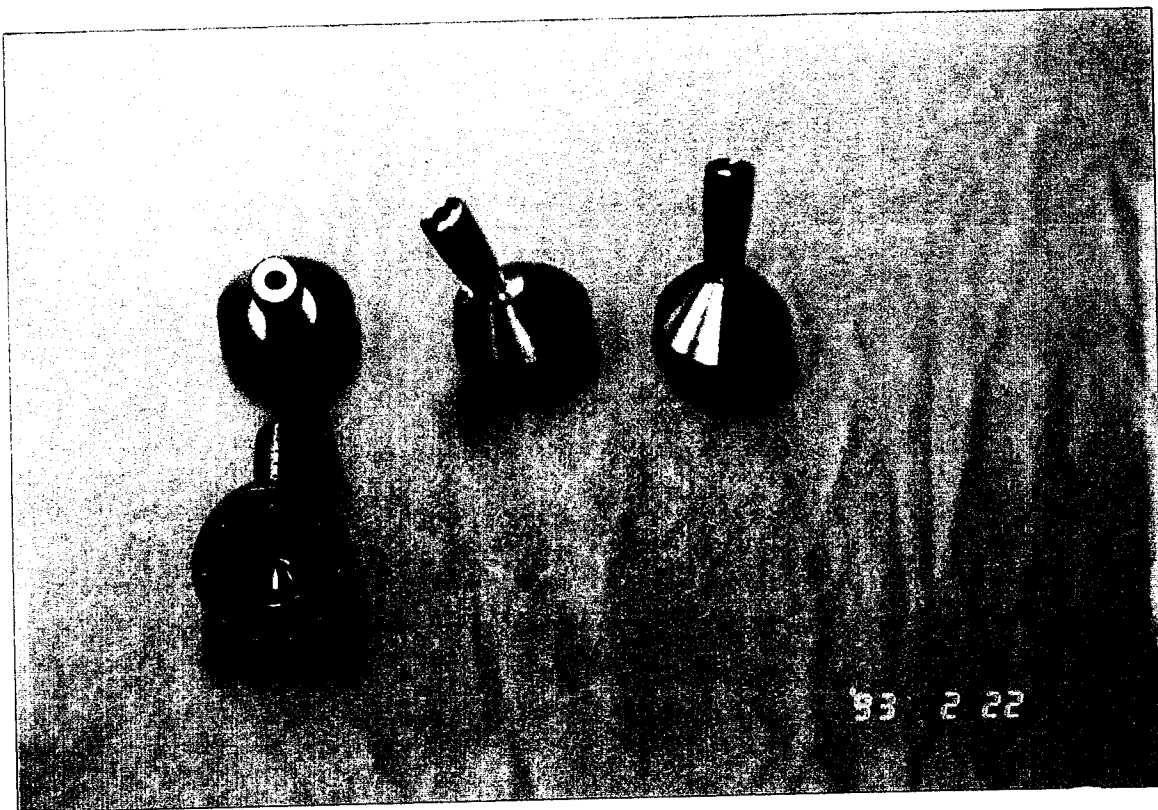
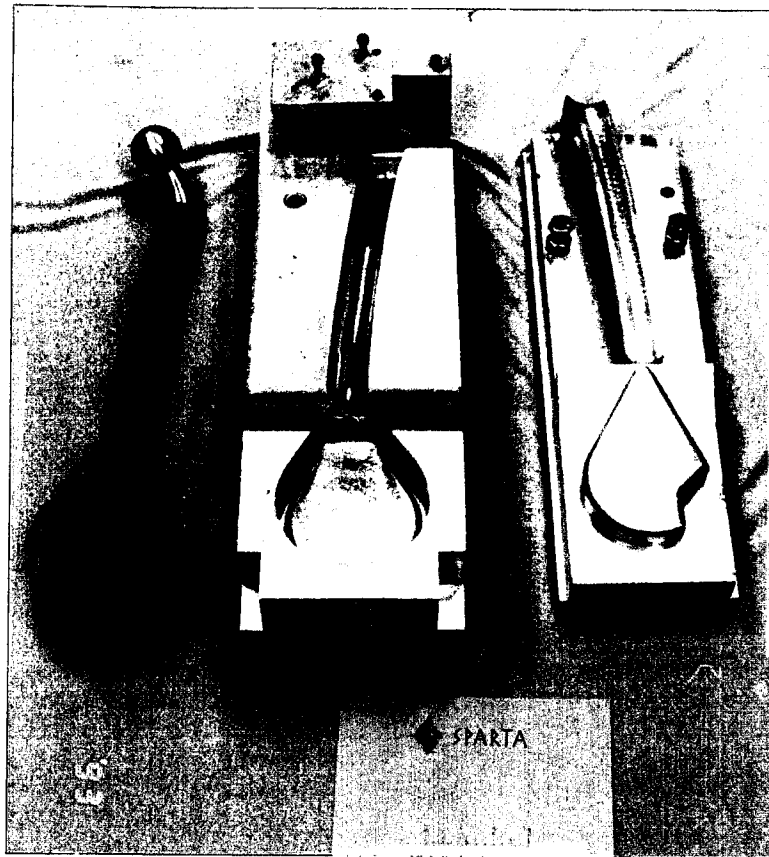


Figure 3.5-2. Tibia Titanium Ankle Insert Show 4 Different Views.

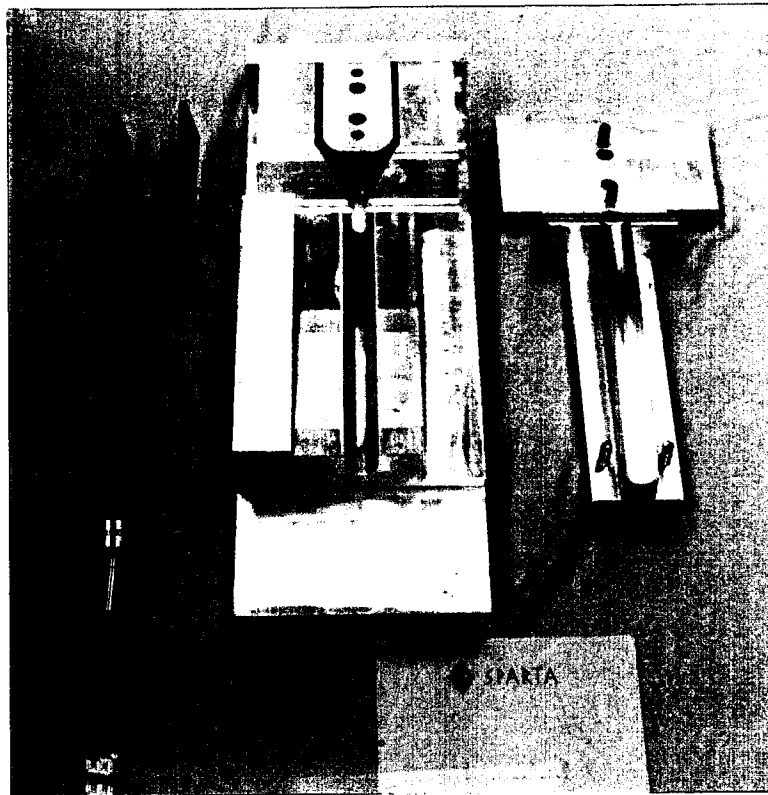
3.5.2 Composite Component Fabrication

The femur and tibia long bone segments were manufactured by a composite process called net compression molding (NCM). NCM uses a resin impregnated fiber preform, or prepreg. Prepreg patterns are cut using steel rule dies or Gerber NC cutters. The prepreg plies are laid into the mold. Mold-in-place hardware (e.g., the titanium stem and ankle) is installed and the mold is closed. Consolidation pressures are created by closing the mold to positive mechanical stops. Heat is applied during the processing cycle with external heat sources such as heated press platens, blanket heats, or cartridge heaters embedded in the tool. Thermocouples can also be embedded in the tool to continuously measure the tool temperatures. Microprocessors, can also be used to continuously measure the tool temperatures and regulate the heating element rates. The molding process is "smart" because the pressure/temperature cycle is controlled, process repeatability is guaranteed and part to part variations are minimized. The closed mold process ensures high dimensional tolerances and minimizes post-cure inspection.

The tooling for the femur and tibia are shown in Figure 3.5-3. A "tool proof" component for both the femur and tibia were fabricated. These tool proofs were instrumented with mock-up wiring and connectors and were sent to First Technology Safety Systems for use in making the flesh molds. The deliverable femur and tibia parts are shown in Figure 3.5-4.



FEMUR

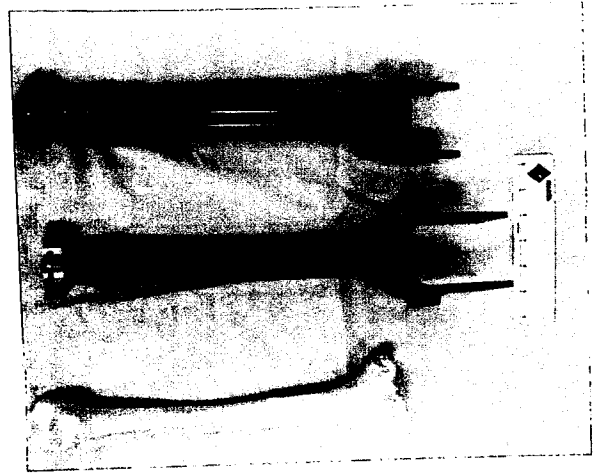


TIBIA

Figure 3.5-3. Photographs of Partially Assembled Femur and Tibia Net Compression Molding Tools.



FEMUR



TIBIA



Comparison of Assembled Human Femur and Tibia
with Assembled ABC Man Femur and Tibia

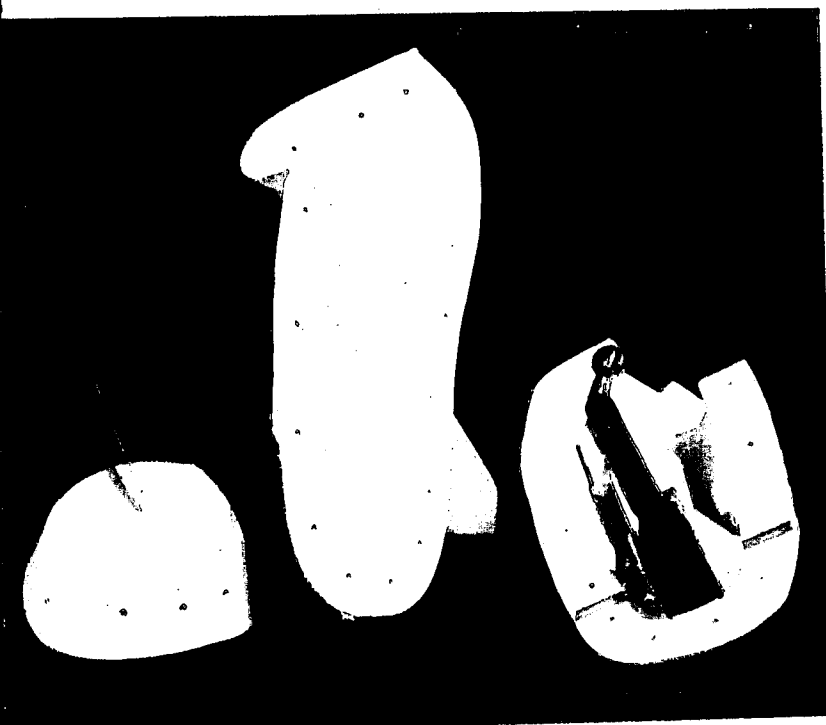
Figure 3.5-4. Full Scale ABC Man Femur and Tibia Compared to Hybrid III and Human Femur and Tibia.

3.5.3 Flesh Fabrication

First Technology Safety Systems (FTSS) is a company in Michigan that specializes in the design and manufacture of human manikin skeleton and flesh components for the automotive industry. SPARTA subcontracted FTSS to design and manufacture the flesh for the femur and tibia.

A photograph of the femur and tibia flesh molds is shown in Figure 3.5-5. The molds are made out of fiberglass with a plywood frame support. The molds are designed to form the flesh in one operation, there are no secondary finishing operations required. A cavity for the tactile foil sensor was also molded in place. The sensor is bonded into the cavity and a flesh "plug" bonded onto the sensor which forms a flush flesh surface. The adhesive used was the A and B parts of the urethane resin for the flesh itself. The composite long bone segments are used as inserts in the molds when making the flesh. All features of the flesh are formed by the molds, including the zipper cavity and the tactile foil cavity. The deliverable molded femur and tibia flesh segments are shown in Figure 3.5-6.

FEMUR



TIBIA

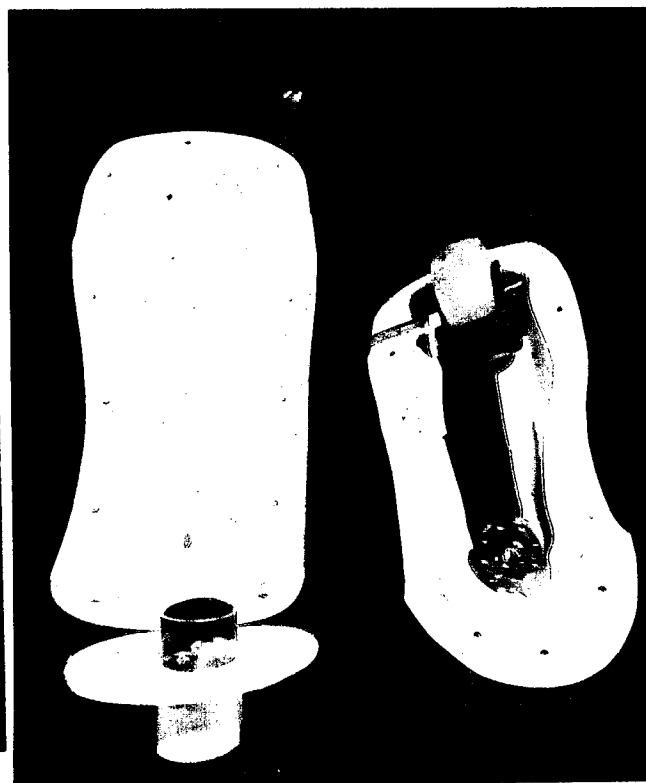
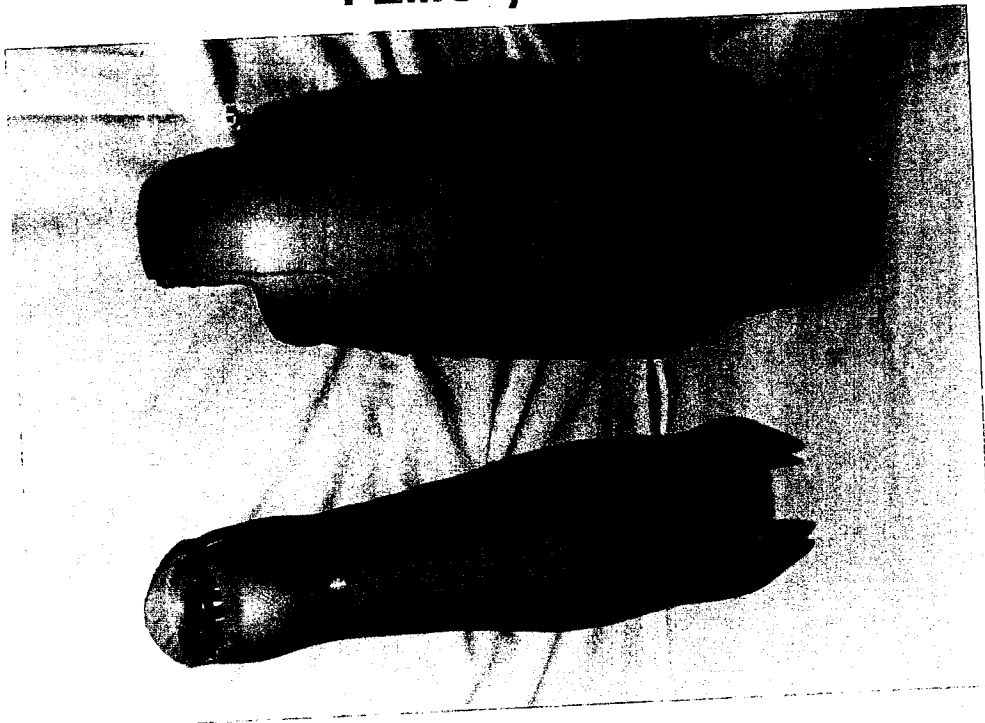
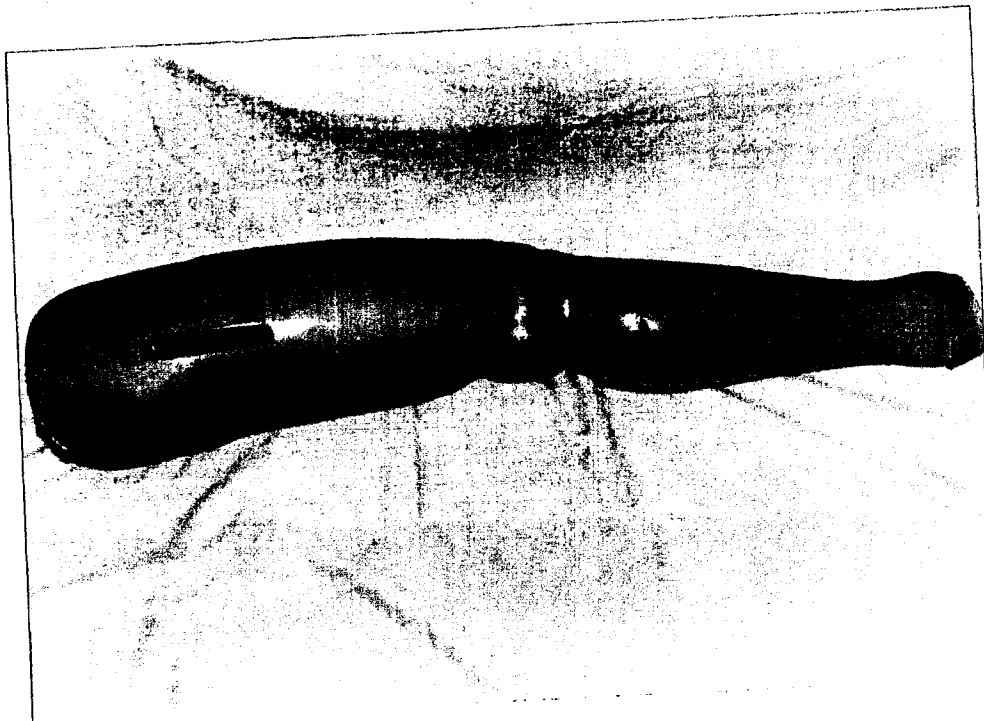


Figure 3.5-5. Photograph of Fiberglass Femur and Tibia Flesh Molds Notice Bone In-Place; Flesh was Molded Around Actual Long Bone Segments to Insure Conformal Fit.

FEMUR/TIBIA



ANTERIOR VIEW OF FLESH



LATERAL VIEW OF FLESH WITH LONG
BONE CONNECTIONS SHOWING

Figure 3.5-6. Full Scale Molded ABC Man Deliverable Flesh Segments.

3.6 Validation Testing

Validation Testing included mechanical testing of the femur and tibia composite bones, flesh instrumentation testing, and the sled test of the fully assembled dummy.

3.6.1 Long Bone Segment Mechanical Testing

Mechanical testing was conducted on both the femur and tibia composite bones. The objective of the testing was to verify the static analytical design load cases, as well as provide calibration data for the embedded strain gages. The following sequence of testing was performed:

1. Femur Bending
2. Femur Compression
3. Tibia Bending
4. Tibia Compression

Figure 3.6.1-1 shows the long bone sensor hookup schematic which was used for both the static test and dynamic sled tests.

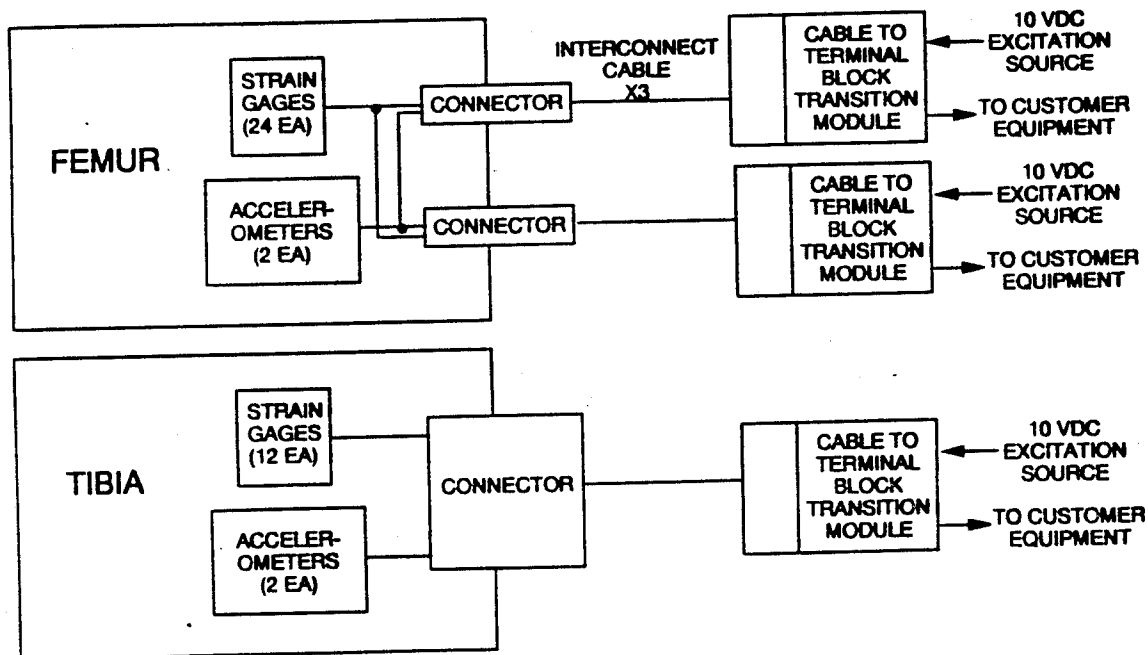


Figure 3.6.1-1. Long Bone Sensor Interface Schematic.

3.6.1.1 Femur Static Bending

The femur bending test is shown schematically in Figure 3.6.1.1-1, where the knee is rigidly fixed horizontally, using the actual knee joint hardware, and the ball joint is loaded in the transverse direction 15.0" (381mm) from the center of the rigid support. The test, shown in progress in Figure 3.6.1.1-2, was conducted twice to calibrate both sets of internal strain gages. Figure 3.6.1.1-3 and Figure 3.6.1.1-4 show load versus displacement data for the respective bending tests. Dial gage locations are indicated in Figure 3.6.1.1-1. The maximum load achieved was 350 lbs (152.7Kg), which corresponds to a root moment of 5250 in-lbs (350 lbs x 15.0") [60,476 Kg/mm]. The design load was specified to be 22,722 in-lbs (1515 lbs x 15.0") [261776 Kg/mm]. The reason the article was taken to only 350 lbs (152.7Kg) is explained below.

An initial femur bending test was performed on the first femur specimen which identified a femur fabrication problem. During the test a crack developed at the shaft/knee interface where the maximum load was predicted. The load was increased to 650 lbs (295 Kg) at which point the femur was no longer able to sustain load, and the test was halted. During the post test evaluation of the femur, the damaged area was sectioned as shown in Figure 3.6.1.1-5. Visual inspection of the damaged cross-section revealed excessive internal fiber waviness, as shown in Figure 3.6.1.1-6. This misalignment caused a significant reduction in the strength and stiffness in the crack area. These misaligned fibers were located in the complex geometry of the knee/shaft interface. The complexity of the femur tool geometry and tool closing sequence at this location geometry caused buckling of the local fibers to be introduced during tool closure and processing. Modification of the femur tooling in the knee/shaft interface area would maintain the correct fiber alignment. Because of the program schedule, both the test femur and delivered femur were fabricated before the calibration test was conducted. When additional femurs are fabricated, the tool will incorporate the required modification. In order to obtain the femur calibration loads, the backup femur was calibrated. Because the calibration data was linear, extrapolation to the design load is straight forward.

The results reported here are those obtained by testing the second femur test article. As noted above, the load levels achieved were conservative to avoid damaging the femur, so that the calibrated test article could be used during the sled test.

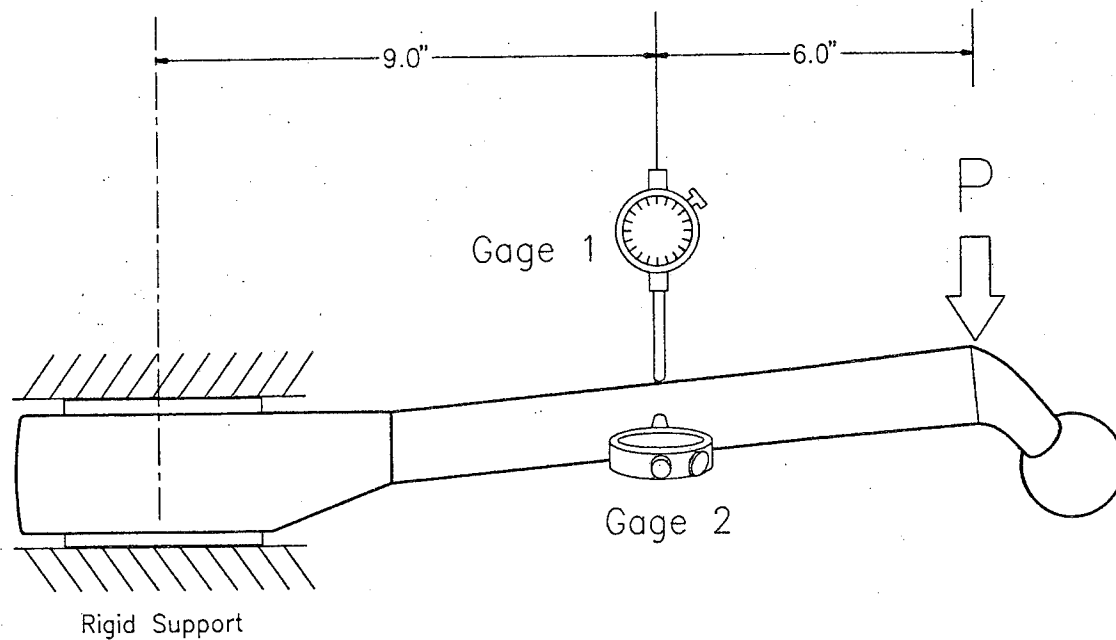


Figure 3.6.1.1-1 Schematic of Static Femur Bending Test.

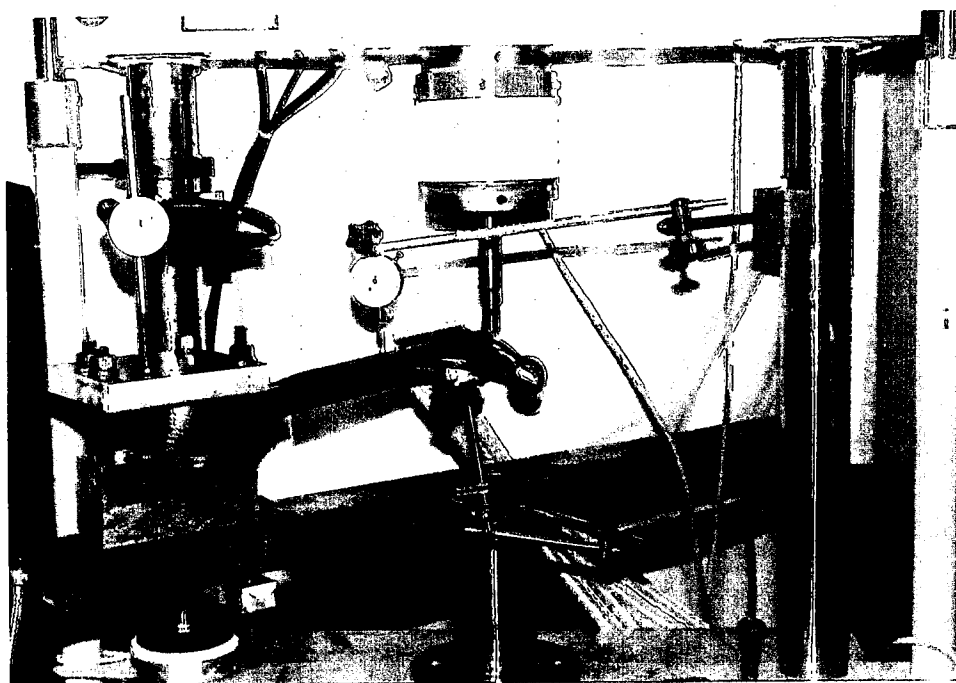


Figure 3.6.1.1-2 Picture of Static Femur Bending Test In-Progress.

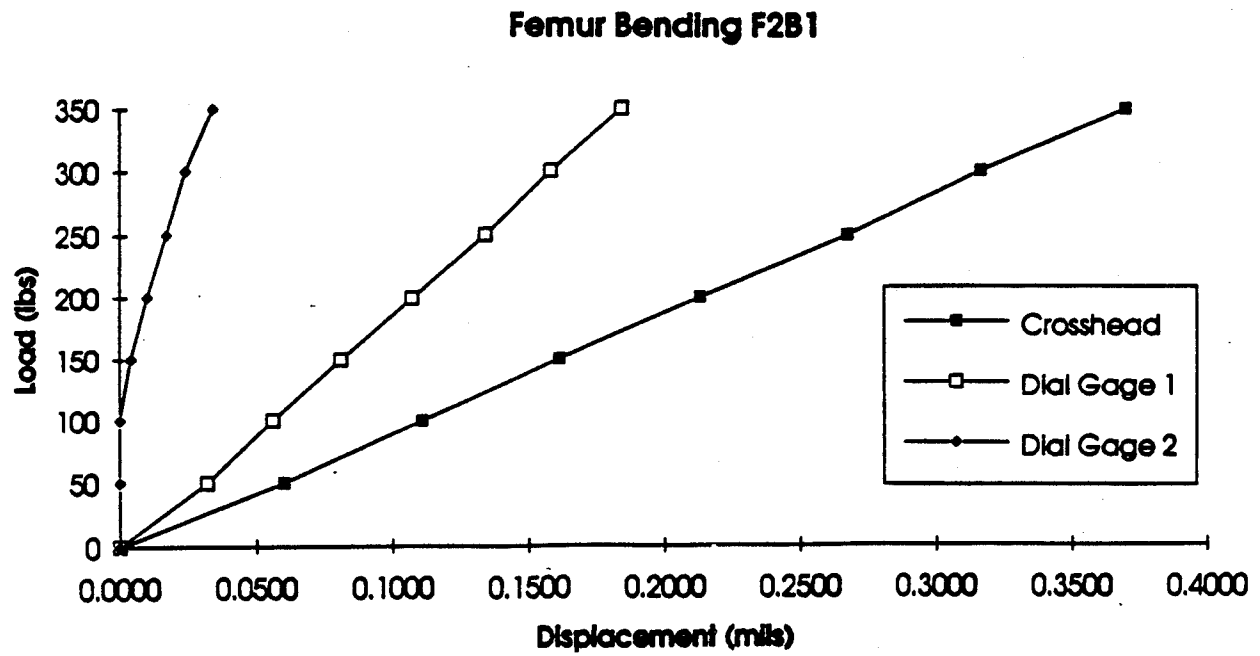


Figure 3.6.1.1-3 Plot of Load versus Displacement for Static Femur Bending (Test 1).

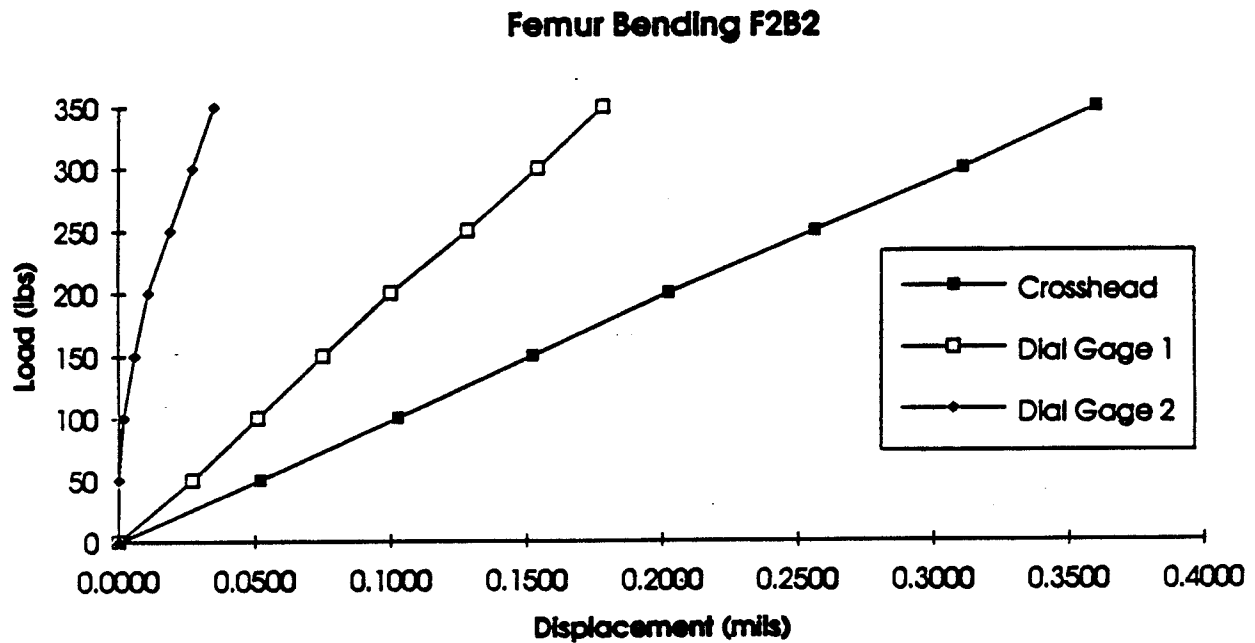


Figure 3.6.1.1-4 Plot of Load versus Displacement for Static Femur Bending (Test 2).

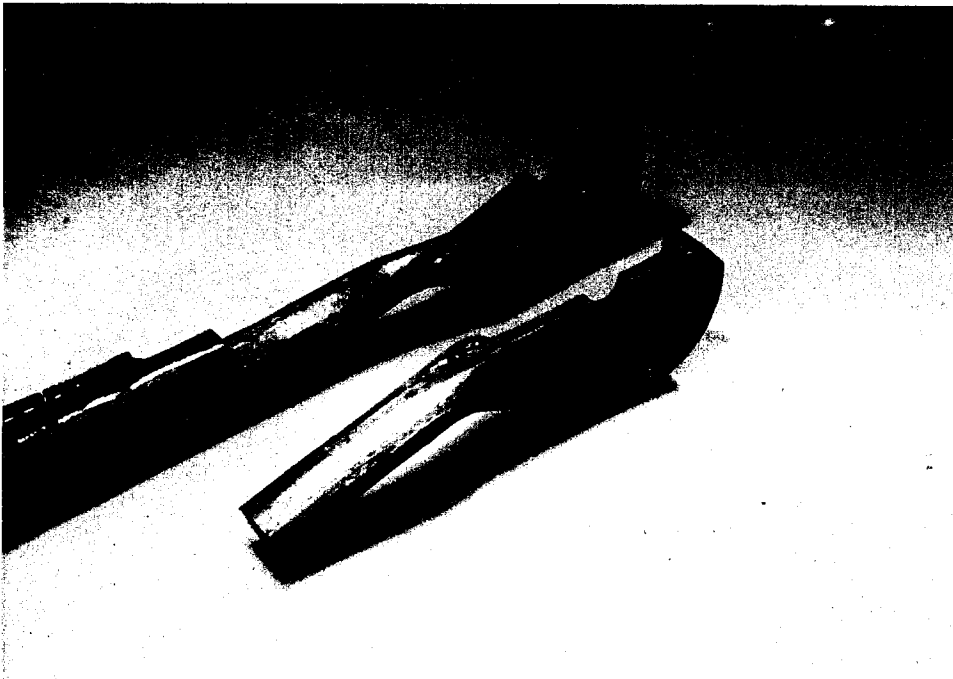


Figure 3.6.1-5. Picture of Sectioned Femur.

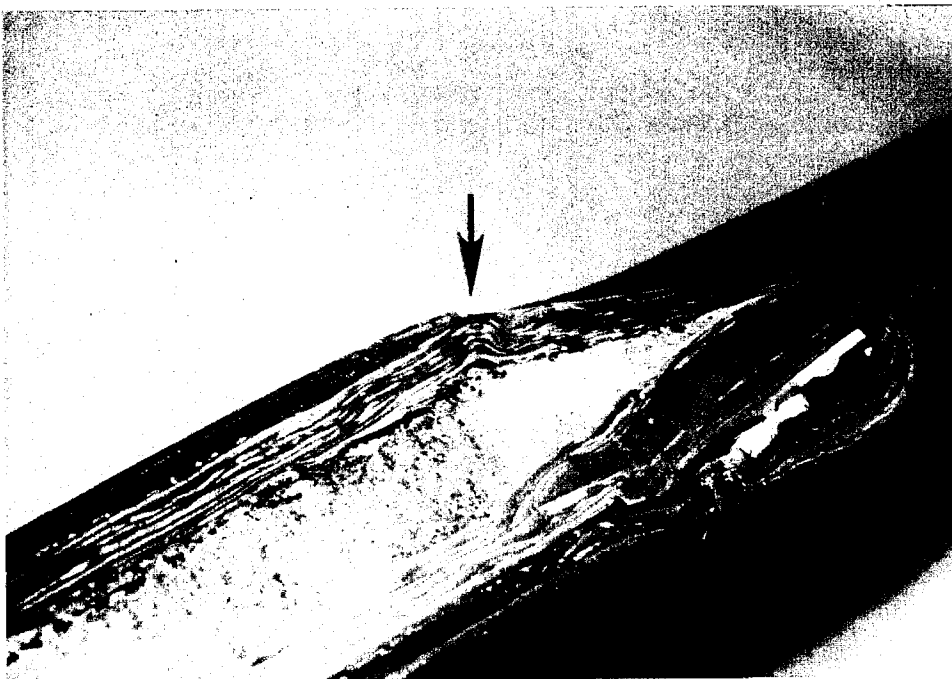


Figure 3.6.1-6. Picture of Knee/Shaft Region with Wavy Fibers Indicated.

3.6.1.2 Femur Static Compression

Figure 3.6.1.2-1 shows a schematic of the femur compression test, where the knee is rigidly fixed in a vertical configuration, using the actual knee joint hardware, and the ball joint is loaded in the axial direction by a compression platen with a hemispherical indentation. The test, shown in progress in Figure 3.6.1.2-2, was conducted twice to calibrate both sets of internal strain gages. Figure 3.6.1.2-3 and Figure 3.6.1.2-4 show load versus displacement data for the respective compression tests. Dial gage locations were indicated in Figure 3.6.1.2-1. The maximum load achieved was 4400 lbs (1995 Kg), which is approximately half of the design load (8640 lbs [3918 Kg]), as explained in section 3.6.1.1.

3.6.1.3 Tibia Static Bending

The tibia bending test is shown schematically in Figure 3.6.1.3-1, where the knee is rigidly fixed horizontally, using the actual knee joint hardware, and the ankle is loaded in the transverse direction 16.0" (406.4mm) from the center of the rigid support. The test is shown in-progress in Figure 3.6.1.3-2. Figure 3.6.1.3-3 shows load versus displacement data for the bending test. Dial gage locations were indicated in Figure 3.6.1.3-1.

3.6.1.4 Tibia Static Compression

The tibia compression test is shown schematically in Figure 3.6.1.4-1, where the ankle is rigidly fixed in a vertical position. Using the actual knee joint hardware, a compression platen was used to apply an axial compressive load. Figure 3.6.1.4-2 shows the test in-progress. Figure 3.6.1.4-3 shows load versus displacement data for the respective compression tests. Dial gage locations are indicated in Figure 3.6.1.4-1. The maximum design load of 3000 lbs (1361 Kg) was exceeded by 25 lbs. (11.3 Kg) At 3025 lbs (3372 Kg), the test article showed no sign of weakness or degradation in strength.

3.6.1.5 Summary of Experimental versus Design Loads

Table 3.6.1.5-1 shows a matrix of the various load cases tested, and the corresponding design and test loads. The tibia passed both bending and compression tests without difficulty. The femur was tested to lower load levels to eliminate any risk of damage due to the anticipated weakness caused by waviness in the knee/shaft transition fibers.

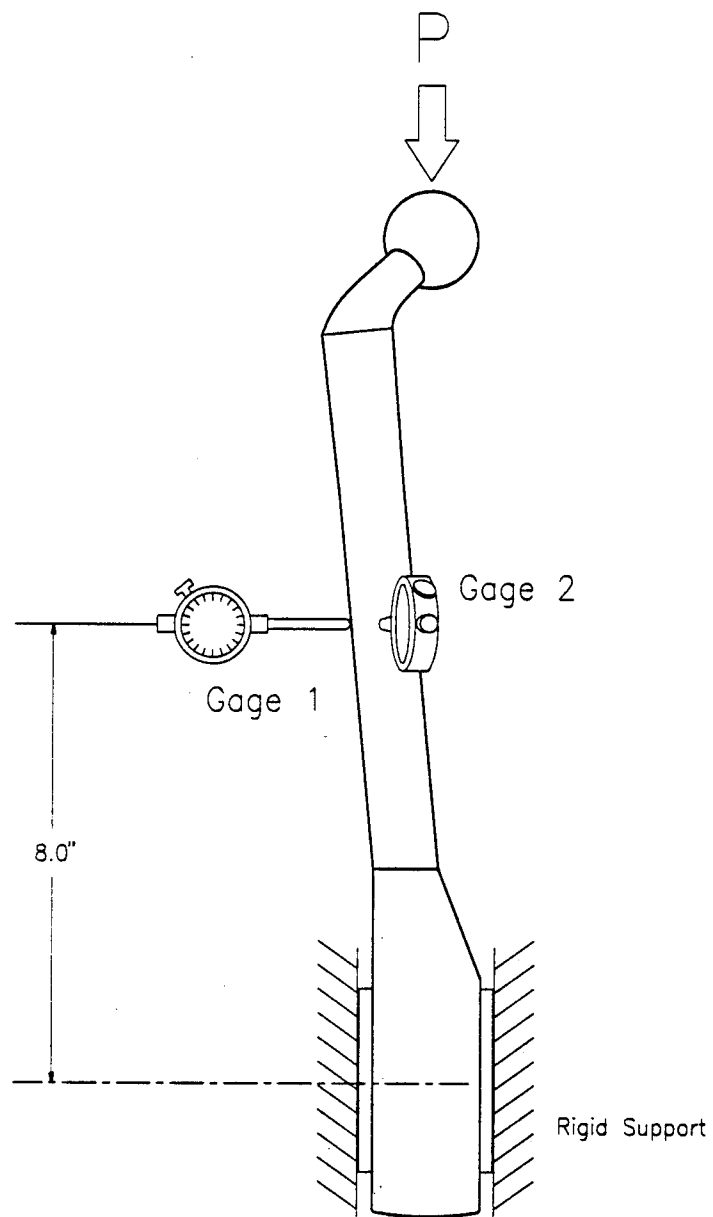


Figure 3.6.1.2-1 Schematic of Static Femur Compression Test.

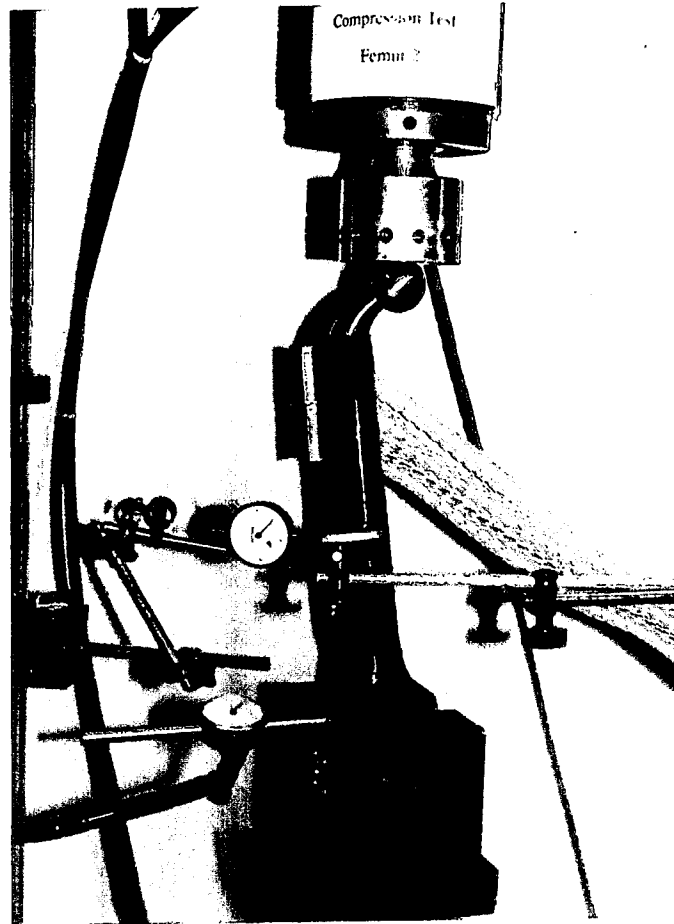


Figure 3.6.1.2-2 Picture of Static Femur Compression Test In-Progress.

Femur Compression 2C1

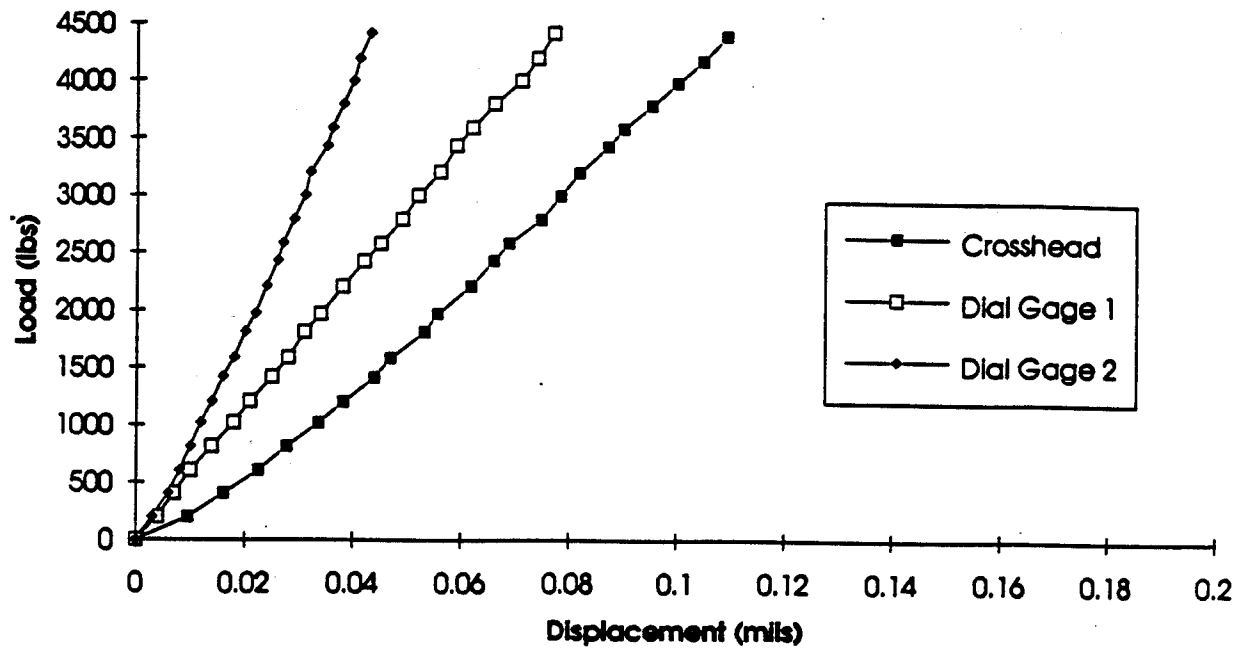


Figure 3.6.1.2-3 Plot of Load versus Displacement for Static Femur Compression (Test 1).

Femur Compression 2C2

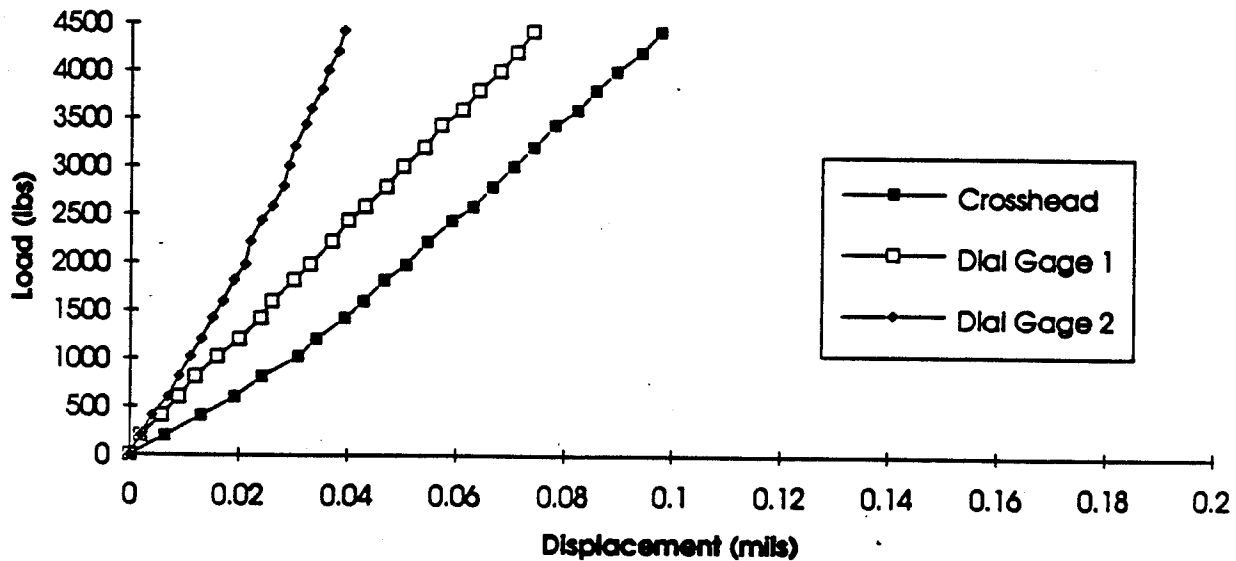


Figure 3.6.1.2-4 Plot of Load versus Displacement for Static Femur Compression (Test 2).

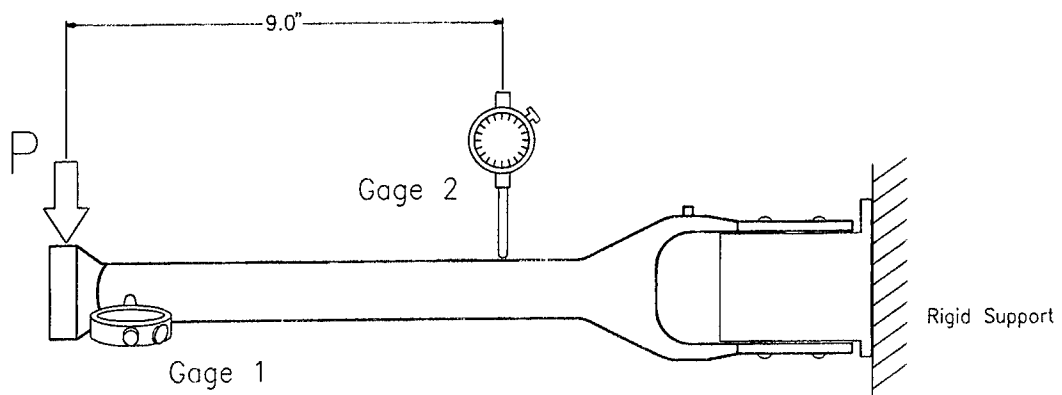


Figure 3.6.1.3-1 Schematic of Static Tibia Bending Test.

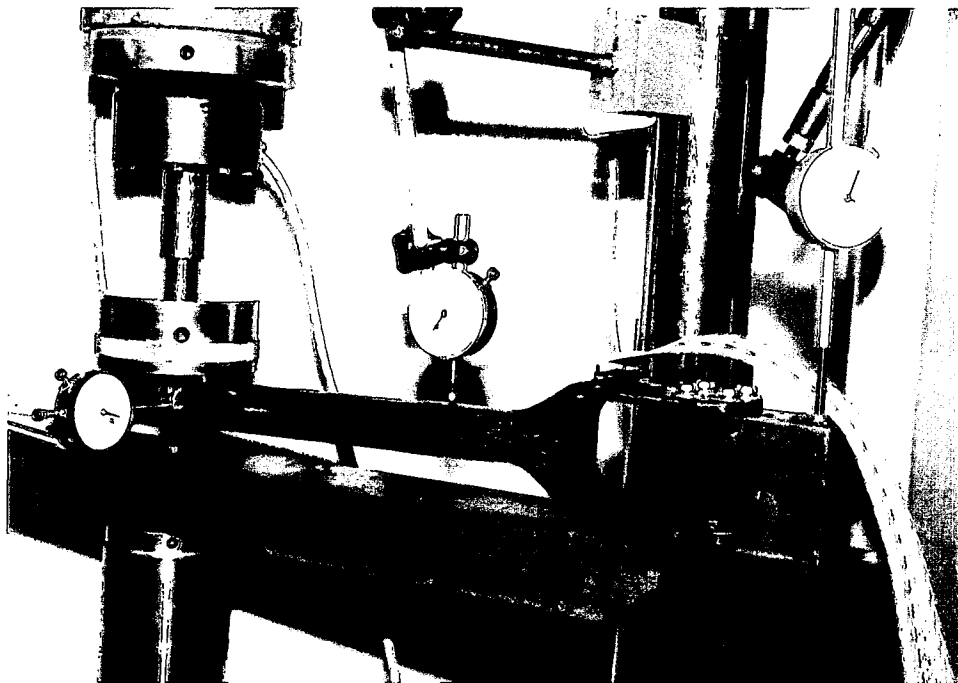


Figure 3.6.1.3-2 Picture of Static Tibia Bending Test In-Progress.

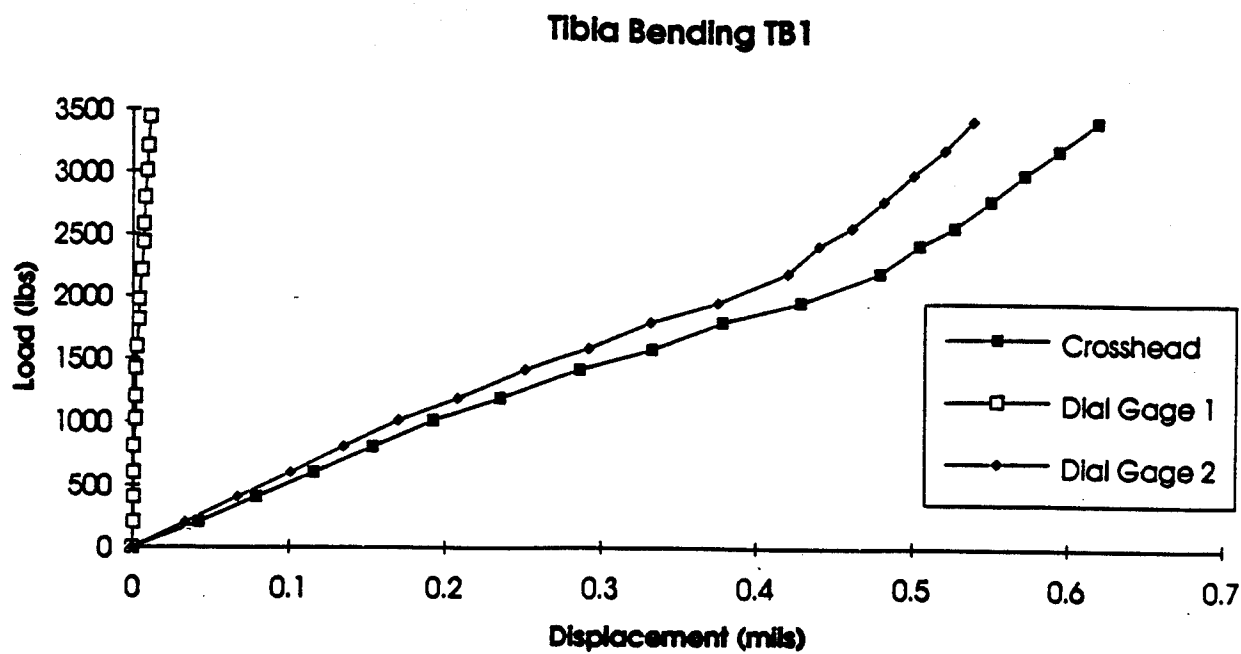


Figure 3.6.1.3-3 Plot of Load versus Displacement for Static Tibia Bending.

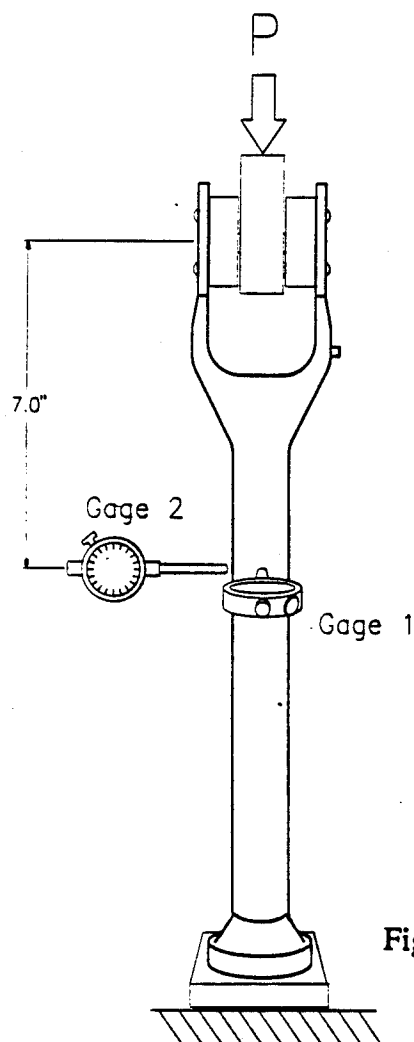


Figure 3.6.1.4-1 Schematic of Static Tibia Compression Test.

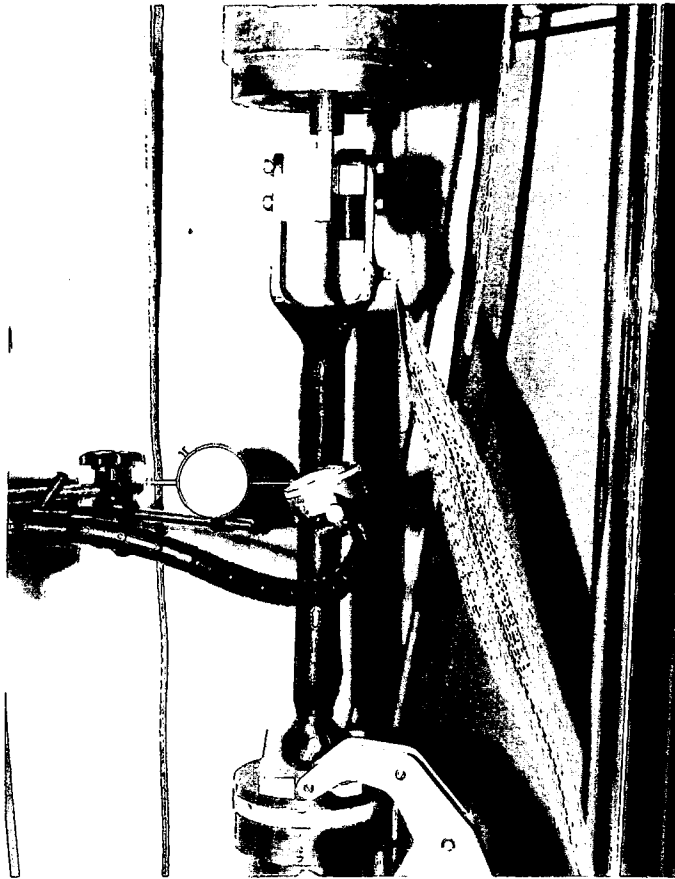


Figure 3.6.1.4-2. Picture of Static Tibia Compression Test In-Progress.

Tibia Compression TC1

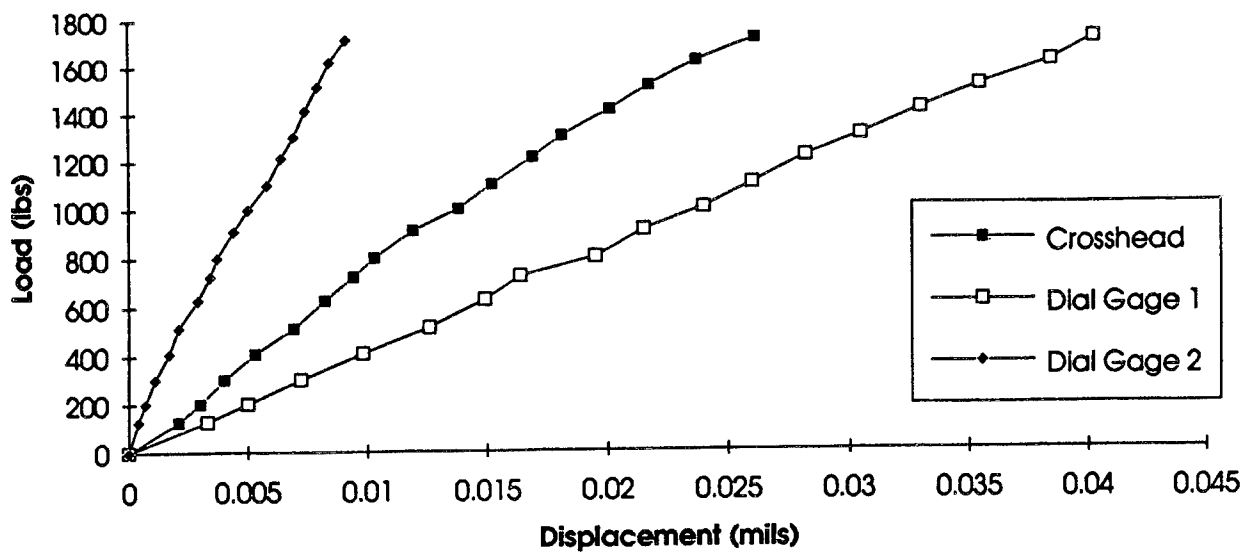


Figure 3.6.1.4-3 Plot of Load versus Displacement for Static Tibia Compression.

Table 3.6.1.5-1. Matrix of Various Load Cases Tested and the Corresponding Design and Load Test

ARTICLE	LOAD CASE	DESIGN LOAD	TEST LOAD
Femur	Bending	(15" x 1515 lb) 22.722 in lb	(15" x 350 lb) 5250 in lb
Femur	Compression	8640 lb	4400 lb
Tibia	Bending	(16" x 328 lb) 5250 in lb	(16" x 328 lb) 5250 in lb
Tibia	Compression	3000 lb	3025 lb

The strain load and moment coefficients were obtained from the static load tests reported above. In these tests a strain profile was measured as a function of load. The finite element model results were used to determine the load/moment at the gage location. This allowed a high degree of confidence in determining the following calibration factors.

Femur Strain Gage Calibration Factors

The femur strain gage calibration factors were calculated according to the following equations where moment and load at strain gage locations are a function of strain.

$$\begin{aligned}
 M_x^{(3)} &= C_{M_x}^{(3)}(\epsilon_1 - \epsilon_3) & M_y^{(3)} &= C_{M_y}^{(3)}(\epsilon_1 - \epsilon_3) & F_z^{(3)} &= C_{F_z}^{(3)}(\epsilon_1 + \epsilon_3) \\
 M_x^{(9)} &= C_{M_x}^{(9)}(\epsilon_7 - \epsilon_9) & M_y^{(9)} &= C_{M_y}^{(9)}(\epsilon_7 - \epsilon_9) & F_z^{(9)} &= C_{F_z}^{(9)}(\epsilon_7 + \epsilon_8 + \epsilon_9 + \epsilon_{11}) \\
 M_x^{(15)} &= C_{M_x}^{(15)}(\epsilon_{13} - \epsilon_{15}) & M_y^{(15)} &= C_{M_y}^{(15)}(\epsilon_{17} - \epsilon_{14}) & F_z^{(15)} &= C_{F_z}^{(15)}(\epsilon_{13} + \epsilon_{15}) \\
 M_x^{(21)} &= C_{M_x}^{(21)}(\epsilon_{19} - \epsilon_{21}) & M_y^{(21)} &= C_{M_y}^{(21)}(\epsilon_{22} - \epsilon_{20}) & F_z^{(21)} &= C_{F_z}^{(21)}(\epsilon_{19} + \epsilon_{20} + \epsilon_{21} + \epsilon_{23})
 \end{aligned}$$

$$\begin{aligned}
 C_{M_x}^{(3)} &= 0.102\text{E}6\text{in.lb.} & C_{M_y}^{(3)} &= 0.102\text{E}6\text{in.lb.} & C_{F_z}^{(3)} &= -2.814\text{E}6\text{lb.} \\
 C_{M_x}^{(9)} &= 2.367\text{E}6\text{in.lb.} & C_{M_y}^{(9)} &= 2.637\text{E}6\text{in.lb.} & C_{F_z}^{(9)} &= -1.149\text{E}6\text{lb.} \\
 C_{M_x}^{(15)} &= 0.209\text{E}6\text{in.lb.} & C_{M_y}^{(15)} &= 0.209\text{E}6\text{in.lb.} & C_{F_z}^{(15)} &= -2.398\text{E}6\text{lb.} \\
 C_{M_x}^{(21)} &= 2.556\text{E}6\text{in.lb.} & C_{M_y}^{(21)} &= 2.556\text{E}6\text{in.lb.} & C_{F_z}^{(21)} &= -1.191\text{E}6\text{lb.}
 \end{aligned}$$

The femur moment and load notation is shown in Figure 3.6.1.6-1a, along with the femur primary and redundant strain gage locations.

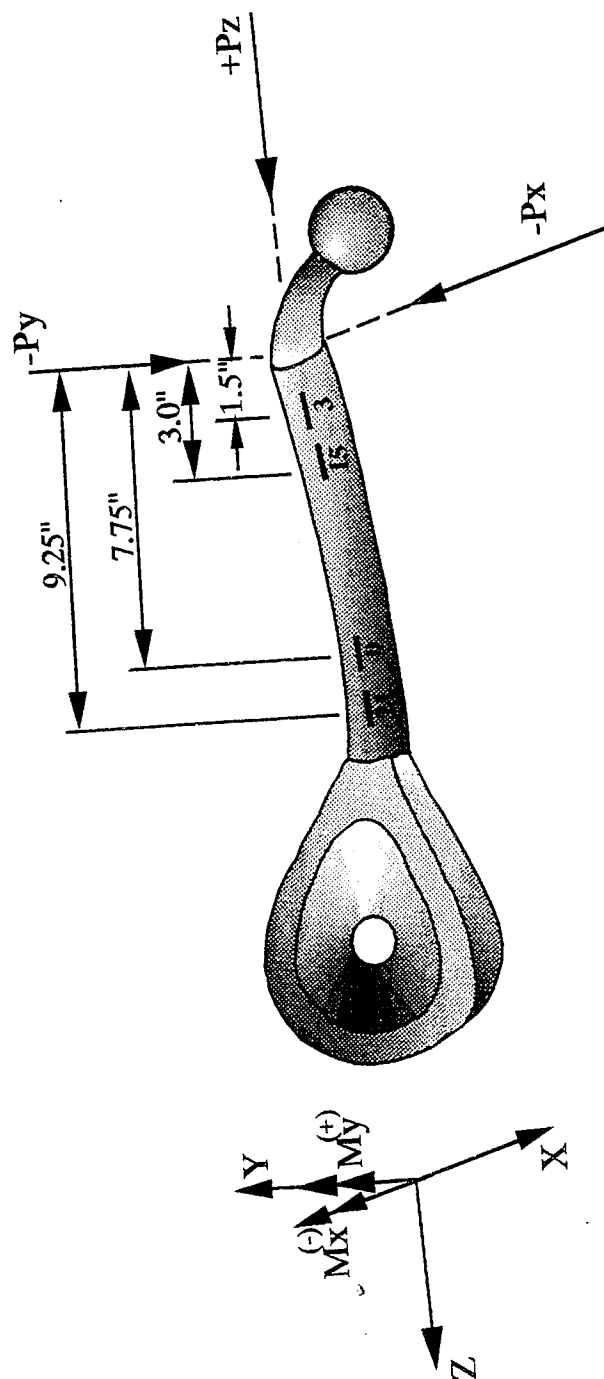


Figure 3.6.1.6-1a Femur Strain Gage Locations and Moment and Load Notations

Tibia Strain Gage Calibration Factors

The tibia strain gage calibration factors were calculated according to the following equations where moment and load at strain gage locations are a function of strain.

$$\begin{aligned} M_x^{(3)} &= C_{M_x}^{(3)}(\epsilon_1 - \epsilon_3) & M_y^{(3)} &= C_{M_y}^{(3)}(\epsilon_1 - \epsilon_3) & F_z^{(3)} &= C_{F_z}^{(3)}(\epsilon_1 + \epsilon_3) \\ M_x^{(9)} &= C_{M_x}^{(9)}(\epsilon_7 - \epsilon_9) & M_y^{(9)} &= C_{M_y}^{(9)}(\epsilon_7 - \epsilon_9) & F_z^{(9)} &= C_{F_z}^{(9)}(\epsilon_7 + \epsilon_8 + \epsilon_9 + \epsilon_{11}) \\ C_{M_x}^{(3)} &= 0.255\text{E}6\text{in.}\cdot\text{lb.} & C_{M_y}^{(3)} &= 0.255\text{E}6\text{in.}\cdot\text{lb.} & C_{F_z}^{(3)} &= -0.828\text{E}6\text{lb.} \\ C_{M_x}^{(9)} &= 0.173\text{E}6\text{in.}\cdot\text{lb.} & C_{M_y}^{(9)} &= 0.173\text{E}6\text{in.}\cdot\text{lb.} & C_{F_z}^{(9)} &= -0.367\text{E}6\text{lb.} \end{aligned}$$

The tibia moment and load notation is shown in Figure 3.6.1.6-1b, along with the strain gage locations for the primary and backup gages.

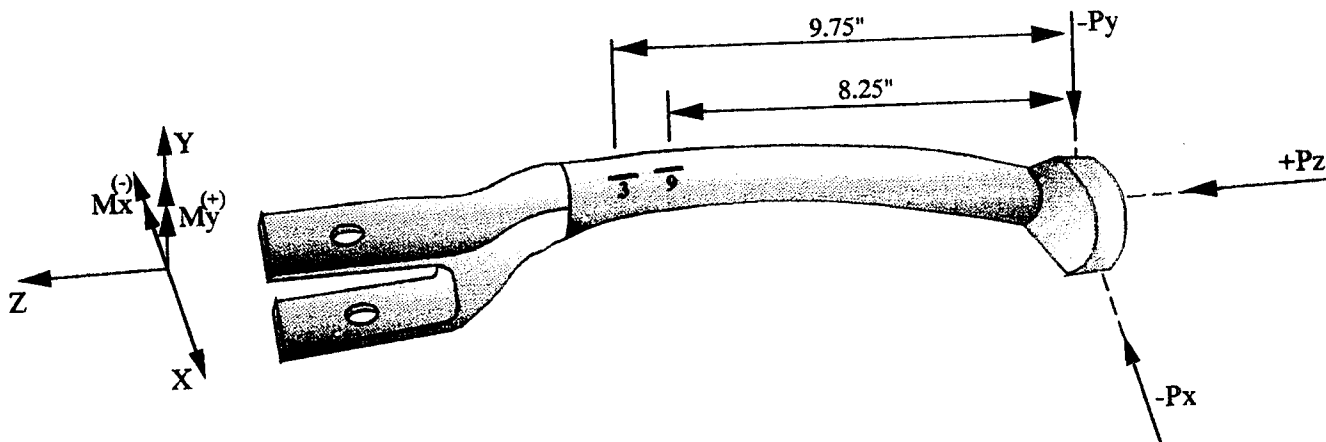


Figure 3.6.1.6-1b. Tibia Strain Gage Locations and Moment and Load Notations.

Femur and Tibia Strain Gage Calibration and Data

The calibration data for the strain gages in the Rosette positions on the femur and tibia is shown in Figure 3.6.1.6-2, while the calibration data for the strain gages in the Axial positions is shown in Figure 3.6.1.6-3.



Micro-measurements
Division
Made in USA

MEASUREMENTS GROUP, INC.
RALPH, NORTH CAROLINA

PRECISION STRAIN GAGES

F007

011414-1652
CODE

(+0.7 ± 0.2)%
K1

2.060 ± 0.5%
GAGE FACTOR AT 24°C

120.0 ± 0.15%
RESISTANCE IN OHMS AT 24°C

R-A56AD16
LOT NUMBER

QUANTITY

5

OPTION

ACAL

TYPE

EA-06-125BB-120

EA-06-125BB-120

GENERAL INFORMATION: EA-SERIES STRAIN GAGES

GENERAL DESCRIPTION: EA-Series gages are a general purpose family of constantan strain gages widely used in experimental stress analysis. These gages are of open-faced construction with a 1 mil (0.001 in. (0.03 mm)) tough, flexible polyimide film backing.

TEMPERATURE RANGE: -100° to +350° F (-75° to +175° C) for continuous use in static measurements; -320° to +400° F (-195° to +205° C) for special or short-term exposure.

SELF-TEMPERATURE COMPENSATION: See data curve below.

STRAIN LIMITS: Approximately 5% for gage lengths 1/8 in. (3.2 mm) and larger and approximately 3% for gage lengths under 1/8 in. (3.2 mm).

FATIGUE LIFE: 10⁶ cycles at ±2000µin/in (µm/m); 10⁶ cycles at ±1500µin/in (µm/m); 10⁶ cycles at ±1500µin/in (µm/m); 10⁶ cycles at ±2500µin/in (µm/m) for unidirectional tension or compression loading. Longer gage lengths and lower resistances result in greater endurance and less scatter in fatigue life.

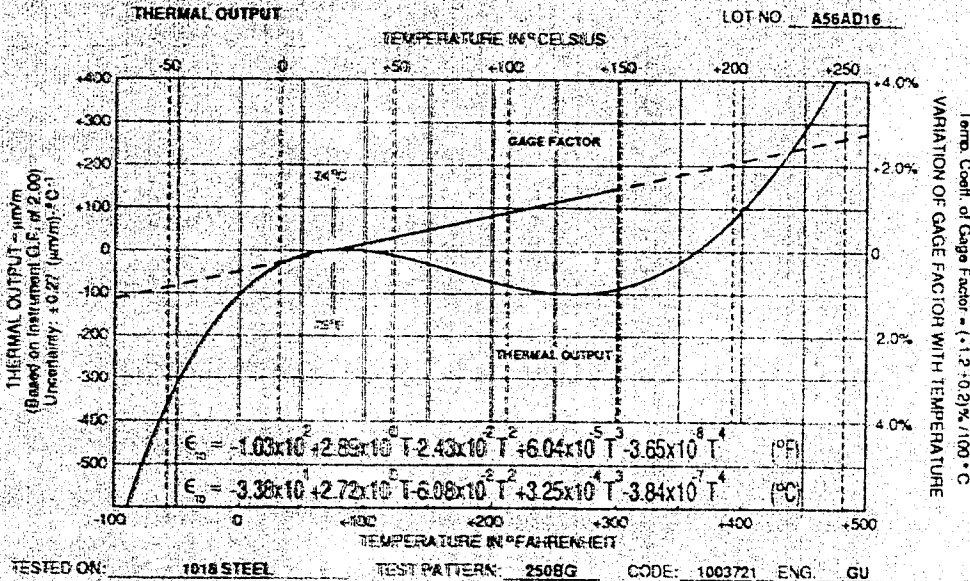
CEMENTS: Compatible with M-M Cement M-Bond 200 but it will normally not provide the greatest fatigue life. Micro-Measurements M-Bond AE-1075, M-Bond GA-2, M-Bond 510, and M-Bond 610 are excellent. M-Bond 510 is the best choice over the entire operating range. Refer to M-M Catalog A-110 for information on bonding agents, and Bulletins B-127, B-130, and B-137 for installation procedures.

SOLDER: Operating temperature will not exceed +300° F (+150° C). M-Line 361 (63/37) tin-lead solder may be used for lead attachment. M-Line 450 (95/5) tin-antimony is satisfactory to +400° F (+205° C). When solder turrets (Option S) are supplied on these gages, they are formed with +572° F (+300° C) lead-free silver solder alloy. Refer to M-M Catalog A-110 for further information on solder, and Tech Tip TT-602 for lead attachment techniques.

PROTECTIVE COATINGS: These EA open-faced gages should always be protected with a suitable coating that is applied as soon as possible after gage installation. Refer to M-M Catalog A-110 for information on Strain Gage Protective Coatings.

NOTE: The backing of EA-Series gages has been specially treated for optimum bond formation with all appropriate strain gage adhesives. No further cleaning is necessary if contamination of the prepared surface is avoided during handling.

G023



TEST PROCEDURES USED BY MICRO-MEASUREMENTS

OPTICAL DEFECT ANALYSIS	M-M Procedure and Standards
GAGE RESISTANCE AT 24°C AND 50% RH	M-M Procedure, Direct NBS Traceability on Resistance Standards
GAGE FACTOR AT 24°C & 50% RH (UNIDIRECTIONAL STRESS FIELD - POISSON RATIO = 0.285)	ASTM E-251 (Constant Stress Cantilever Method)
TEMPERATURE COEFFICIENT OF GAGE FACTOR	ASTM E-251 (Step Deflection Method)
THERMAL OUTPUT	ASTM E-251 (Slow Heating Rate, Continuously Recorded)
TRANSVERSE SENSITIVITY AT 24°C AND 50% RH	ASTM E-251
FATIGUE LIFE	NAS 942 (Modified)
STRAIN LIMITS	NAS 942 (Modified)
GAGE THICKNESS	M-M Procedure
CREEP AND DRIFT	M-M Procedure (Similar to NAS 942 Method)

NOTE: Gage resistance, gage factor, temperature coefficient of gage factor, thermal output, and transverse sensitivity testing and information presentation are in compliance with OMI International Performance Standard A2. The term "gage factor" is defined as the ratio of resistance change to strain. Creep tests are not included in ILS NO. 82.

T001

Figure 3.6.1.6-3. Femur and Tibia Calibration Data for the Strain Gages in the Axial Positions.

Table 3.6.1.6-1 shows the femur strain gages and the corresponding resistance for each strain gage. Table 3.6.1.6-2 shows the tibia strain gages and the corresponding resistance for each strain gage.

Femur Accelerometer Data

The locations of the accelerometers (A1, A2) on the femur were shown in Figure 3.3.3-5 in the Instrumentation Section. The calibration data for the femur accelerometers (A1, A2) are shown in Figures 3.6.1.6-4 and -5 respectively.

Table 3.6.1.6-1. Femur Strain Gage Resistance

Strain Gage	Resistance (Ohms)
1	120.07
2	120.16
3	120.04
4	119.86
5	119.01
6	119.90
7	119.90
8	119.64
9	119.40
10	120.16
11	119.98
12	120.13
13	120.20
14	120.12
15	120.14
16	120.18
17	119.68
18	120.03
19	119.26
20	120.11
21	119.24
22	120.04
23	120.20
24	119.91

Table 3.6.1.6-2. Tibia Strain Gage Resistance

Strain Gage	Resistance (Ohms)
1	120.11
2	119.21
3	119.91
4	121.19
5	120.03
6	120.31
7	120.05
8	119.05
9	119.94
10	120.16
11	120.21
12	120.14

: 4HF-91-13470

Calibration Data

Transverse Sensitivity 0.3 %

ACCELEROMETER MODEL 7264-2000TZ SERIAL NO. AC971

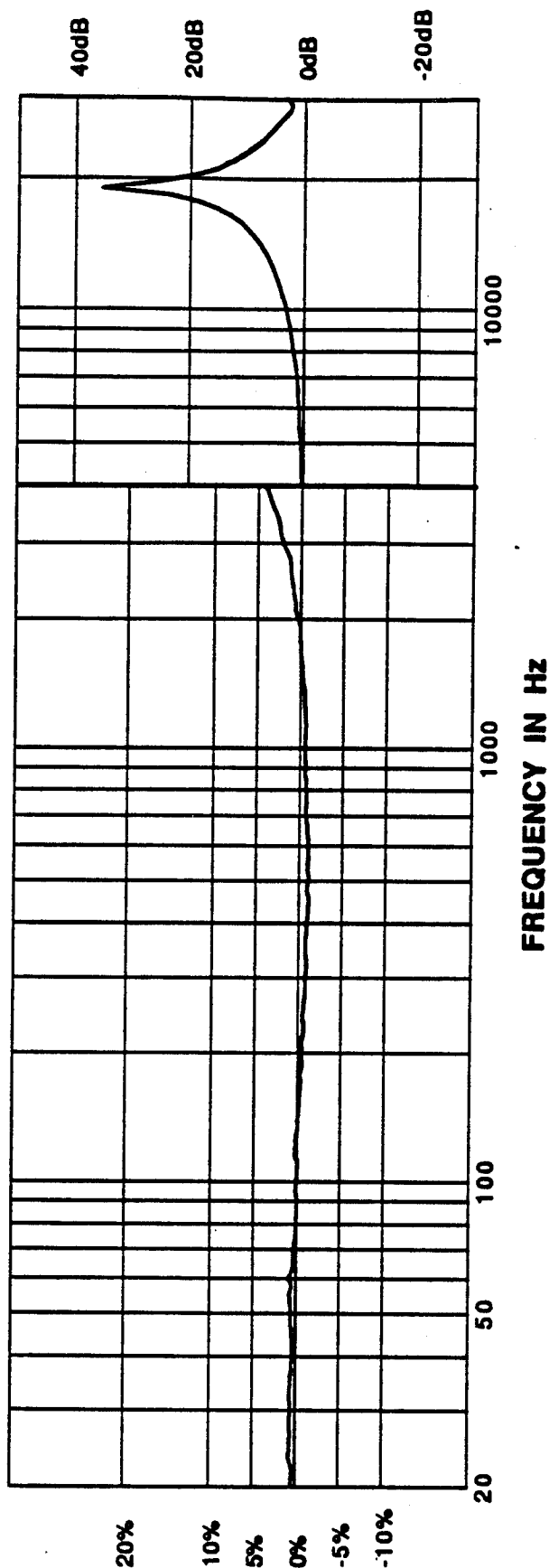
Input resistance : 2526 Ω

Sensitivity 0.2516 mV/g @ 100 Hz, 10 g pk

ZMO : -7.4 mV

Excitation : 10.00 V

FREQUENCY RESPONSE



MEGGITT
AEROSPACE

Date 1/22/93 8:19:07 AM

By 

ENDEVCO

All calibrations are traceable to the National Institute of Standards and Technology and in accordance with MIL-STD-45662.

Figure 3.6.1.6-4. Calibration Data for the Femur Accelerometer A1.

: 4HF-91-13467

Calibration Data

Transverse Sensitivity 0.5 %

ACCELEROMETER MODEL 7264-2000TZ SERIAL NO. (AC942)

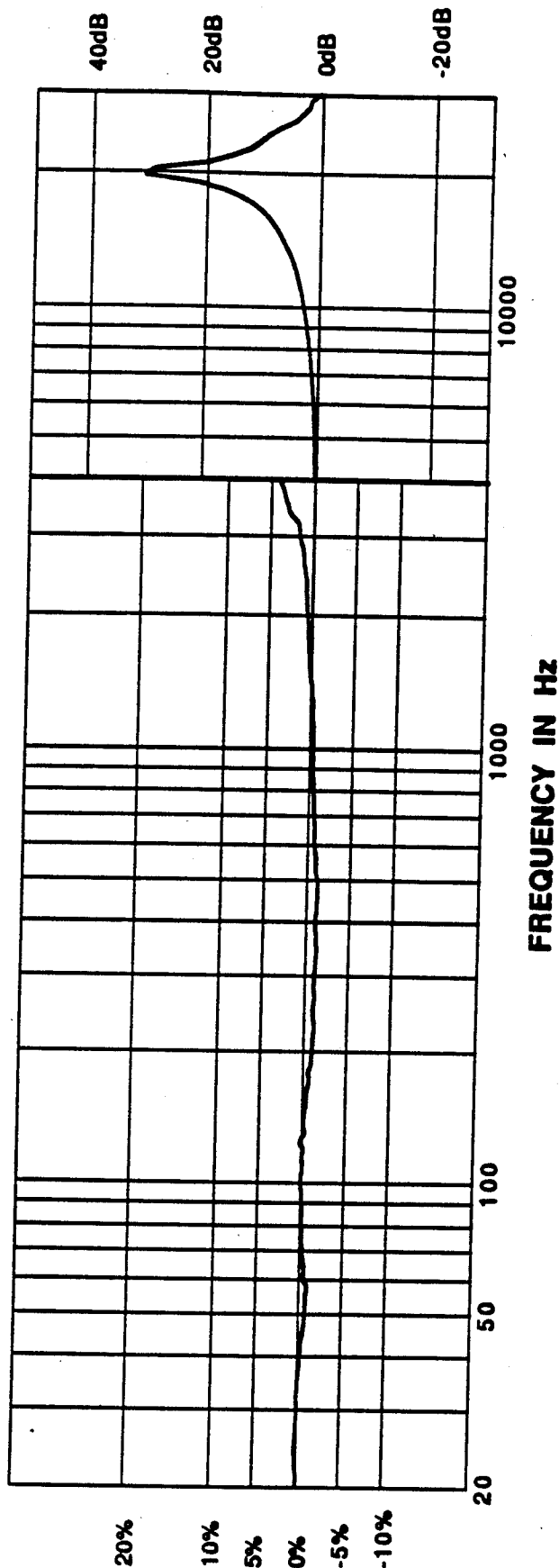
Sensitivity 0.2454 mV/g @ 100 Hz, 10 g pk

Input resistance : 2478 Ω

ZMO : 2.0 mV

Excitation : 10.00 V

FREQUENCY RESPONSE



MEGGITT
AEROSPACE

Date 1/22/93 8:03:53 AM

By 

ENDEVCO

All calibrations are traceable to the National Institute of Standards and Technology and in accordance with MIL-STD-45662.

Figure 3.6.1.6-5. Calibration Data for the Femur Accelerometer A2.

Tibia Accelerometer Data

The locations of the accelerometers (A1, A2) on the tibia were shown in Figures 3.3.4-3 and 3.3.6-3 in the Instrumentation Section. The calibration data for the tibia accelerometers (A1, A2) are shown in Figures 3.6.1.6-6 and -7 respectively. Two accelerometers were used for each long bone segment; one orientated in the medial-lateral plane, the other in the anterior-posterior plane. It was assumed that the femur and tibia were essentially rigid rods and that the relative axial accelerations were known at the hip.

3.6.2 Flesh Sensor Calibration Test

Tests were performed to investigate the response of the tactile foil pressure sensor embedded within the density-adjusted synthetic flesh. The objective of these tests were to characterize the dependence of the output signal on the sensor location and energy input levels.

Tactile Foil Sensor Array Calibration

Calibration tests were performed on the tactile foil sensor arrays embedded within the flesh sections of the tibia and femur to determine an impact energy/peak output voltage relationship. The existing pendulum impact test apparatus was used to deliver the required energy level as shown in Figure 3.6.2-1. To simulate actual test conditions the foil arrays were calibrated with the composite long bones in-place within the flesh. The segment being tested was attached to the back support and impacted at different energy levels, shown in close-up in Figure 3.6.2-2. The tactile foil layout information for both the femur and tibia are included in Figure 3.6.2-3. Figure 3.6.2-4 shows the flesh sensor interface to DAS schematic.

The orange junction boxes K-M (see terminal block in Figure 3.6.2-4) are provided with 1 gigaohm resistors in place to impedance match the tactile foil arrays when connected to a low input impedance measuring device. Tables 3.6.2-1 and 3.6.2-2 contain terminal numbers and corresponding sensor numbers in the foil array.

The calibration curves are shown for the femur and tibia foil arrays in Figures 3.6.2-5 and 3.6.2-6, respectively. The equations are given below as a function of peak output voltage for any arbitrary sensor. The femur array is described by two equations, one cubic equation for low energy levels (below 0.039 Volts peak), and a linear equation for voltage levels above 0.039 Volts peak. V in the following equation is in absolute volts.

:4HF-91-13480

Calibration Data

ACCELEROMETER MODEL 7264-2000TZ SERIAL NO AC935

Sensitivity 0.2284 mV/g @ 100 Hz, 10 g pk

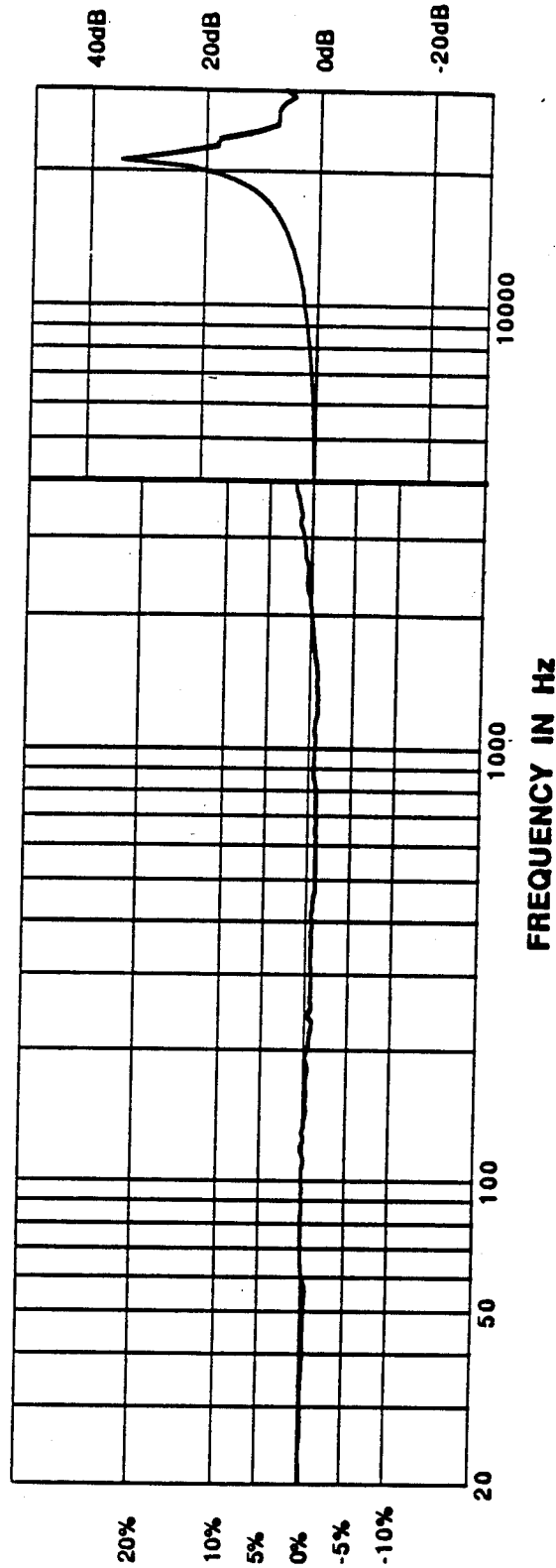
Transverse Sensitivity 0.4 %

Input resistance : 2467 Ω

ZMO : 2.6 mV

Excitation : 10.00 V

FREQUENCY RESPONSE



MEGGITT
AEROSPACE

Date 1/22/93 9:21:29 AM
By 

ENDEVCO

All calibrations are traceable to the National Institute of Standards and Technology and in accordance with MIL-STD-4542

Figure 3.6.1.6-6. Calibration Data for the Tibia Accelerometer A1.

:4HF-91-13478

Calibration Data

Transverse Sensitivity 0.4 %

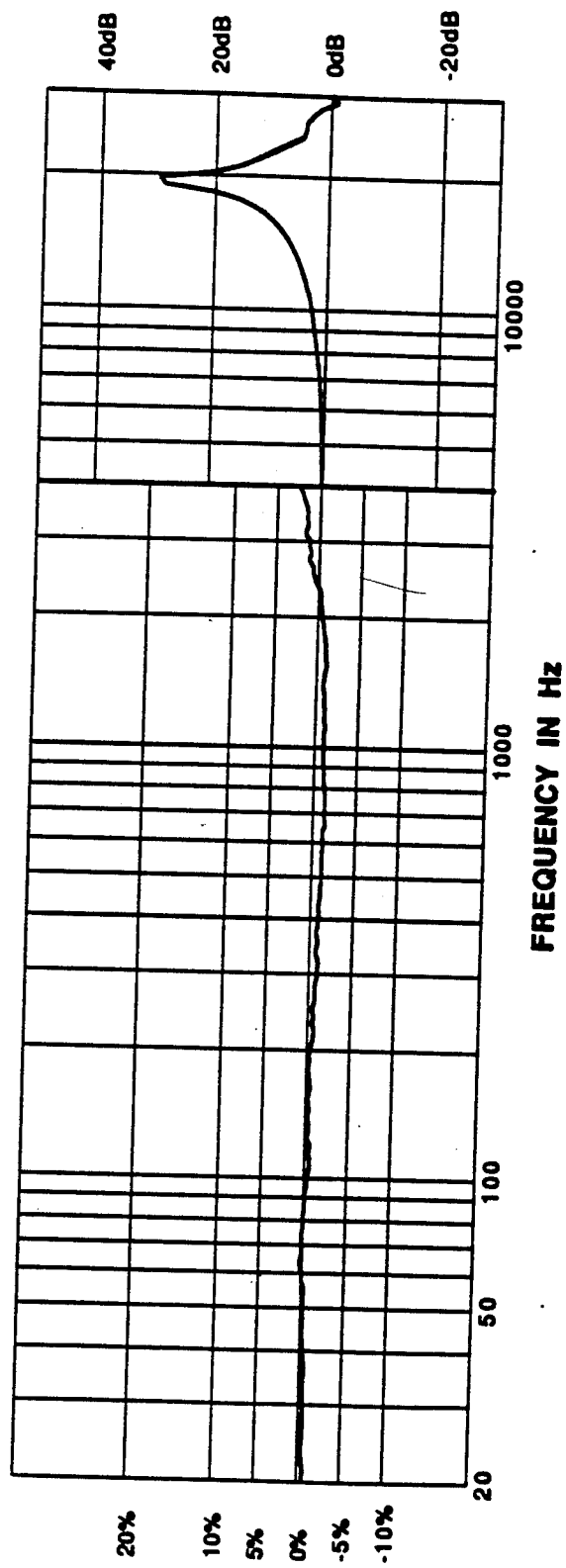
ACCELEROMETER MODEL 7264-2000TZ SERIAL NO. AC974

Sensitivity 0.2923 mV/g @ 100 Hz, 10 g pk


Input resistance : 2443 Ω

ZMO : 0.6 mV
Excitation : 10.00 V

FREQUENCY RESPONSE



MEGGITT
AEROSPACE

Date 1/22/93 9:12:19 AM
By 

ENDEVCO 

All calibrations are traceable to the National Institute of Standards and Technology and in accordance with MIL-STD-45642.

Figure 3.6.1.6-7. Calibration Data for the Tibia Accelerometer A2.

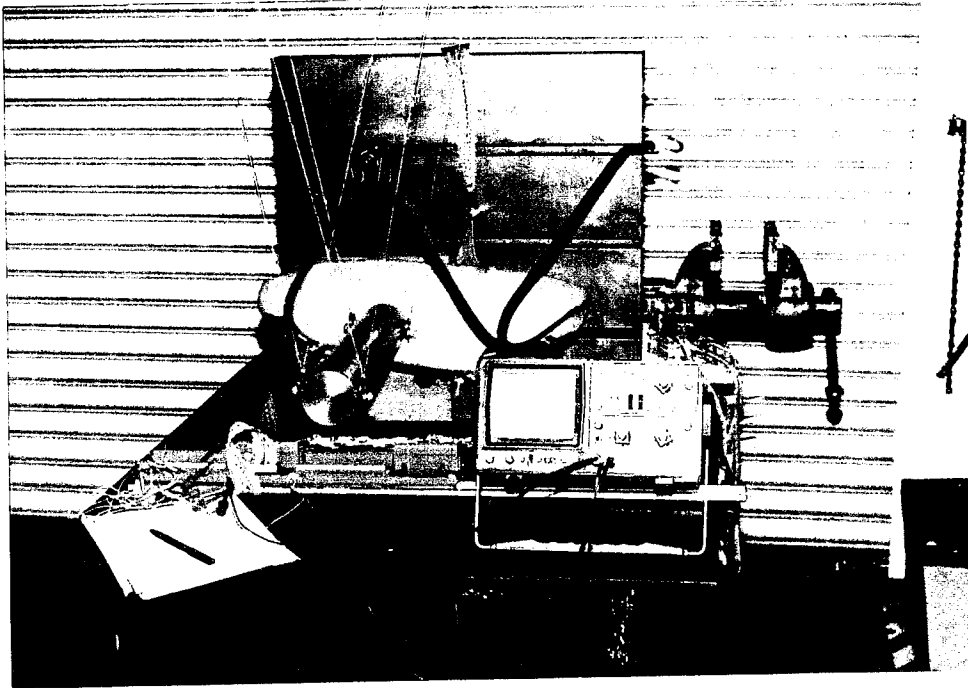


Figure 3.6.2-1. Photo of Tactile Foil Array Calibration Test Apparatus.

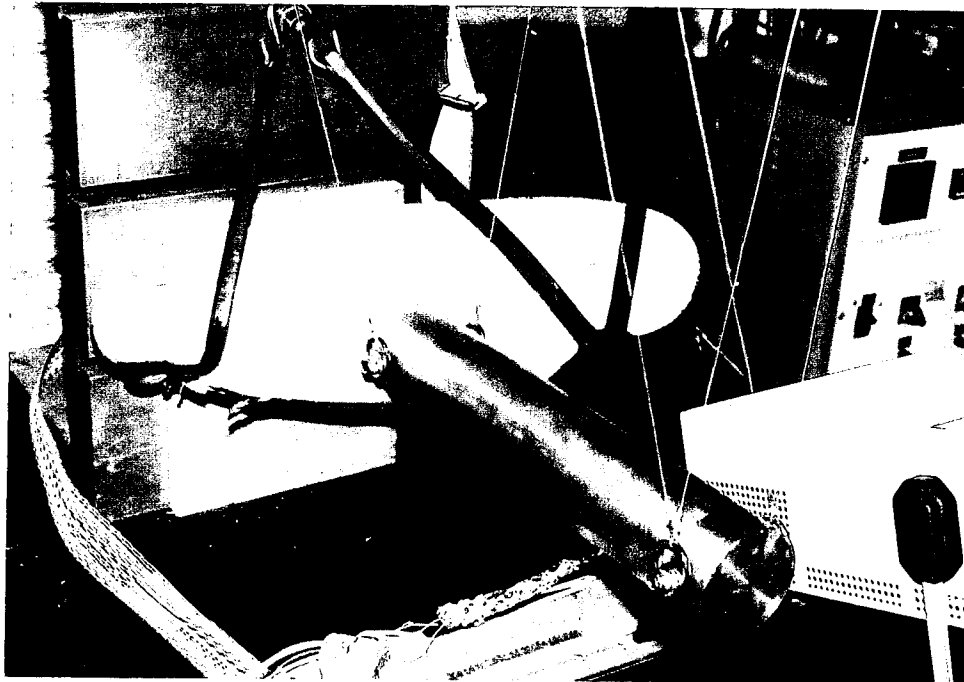


Figure 3.6.2-2. Close-Up of Segment Being Tested.

ABC Man Tactile Foil Layout

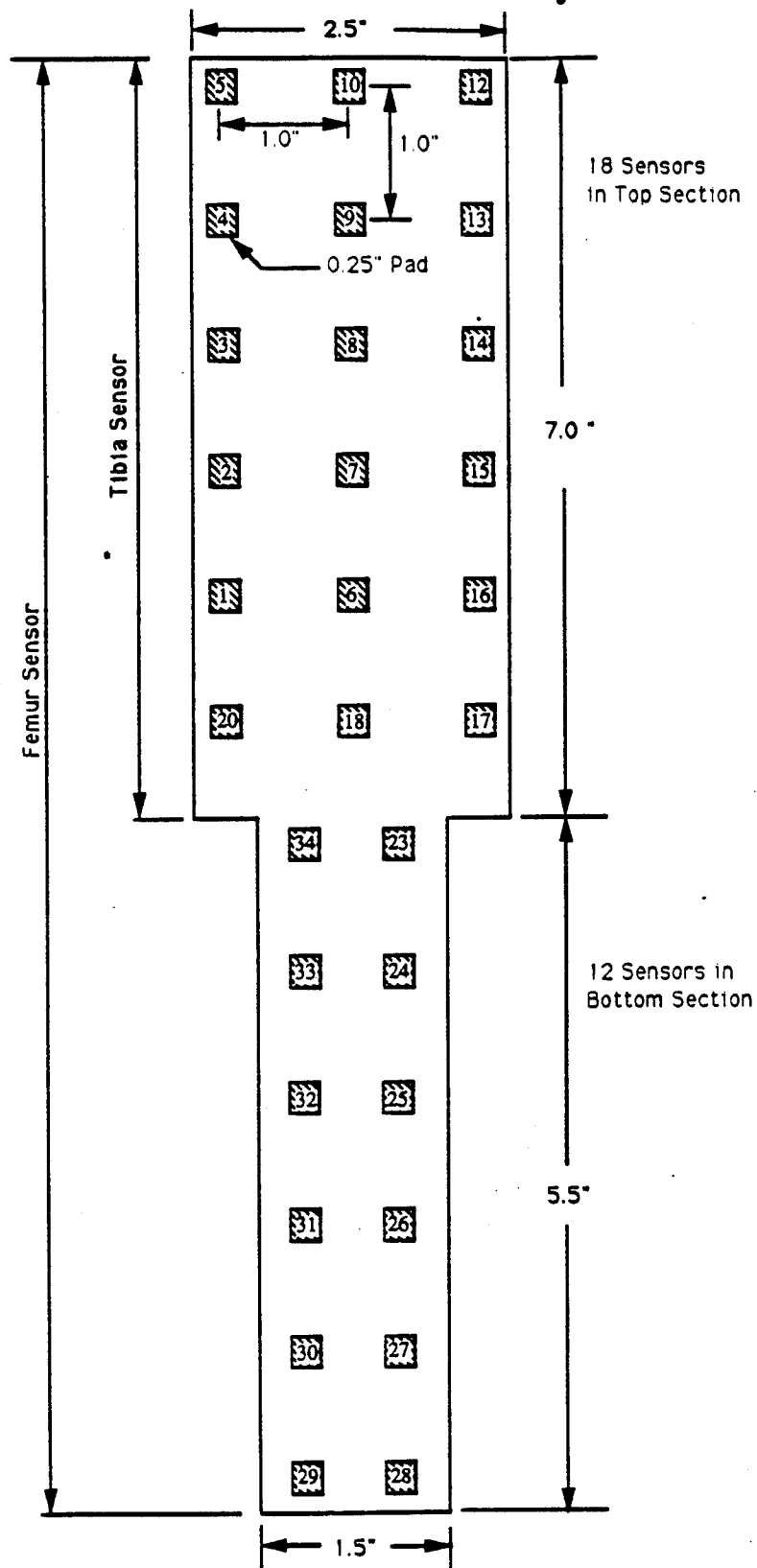


Figure 3.6.2-3. ABC Man Tactile Foil Layout.

Table 3.6.2-1. Junction Box M Hook-Up

Table 3.6.2-2. Junction Box K Hook-Up

HOOK-UP TABLES

(with Letter F=Femur and T=Tibia)

Orange Box #	Sensor #
M2	Ground Common
M4	18F
M6	16F
M8	14F
M10	12F
M12	10F
M14	8F
M16	6F
M18	4F
M20	2F
M22	1F
M24	3F
M26	5F
M28	7F
M30	9F
M32	13F
M34	15F
M36	17F
M38	23F
M40	25F
M42	27F
M44	29F
M46	31F
M48	33F
M50	EMPTY

Orange Box #	Sensor #
K2	1T
K4	3T
K6	5T
K8	7T
K10	9T
K12	20F
K14	13T
K16	15T
K18	17T
K20	20T
K22	2T
K24	4T
K26	6T
K28	8T
K30	10T
K32	12T
K34	14T
K36	16T
K38	18T
K40	34F
K42	32F
K44	30F
K46	28F
K48	26F
K50	24F

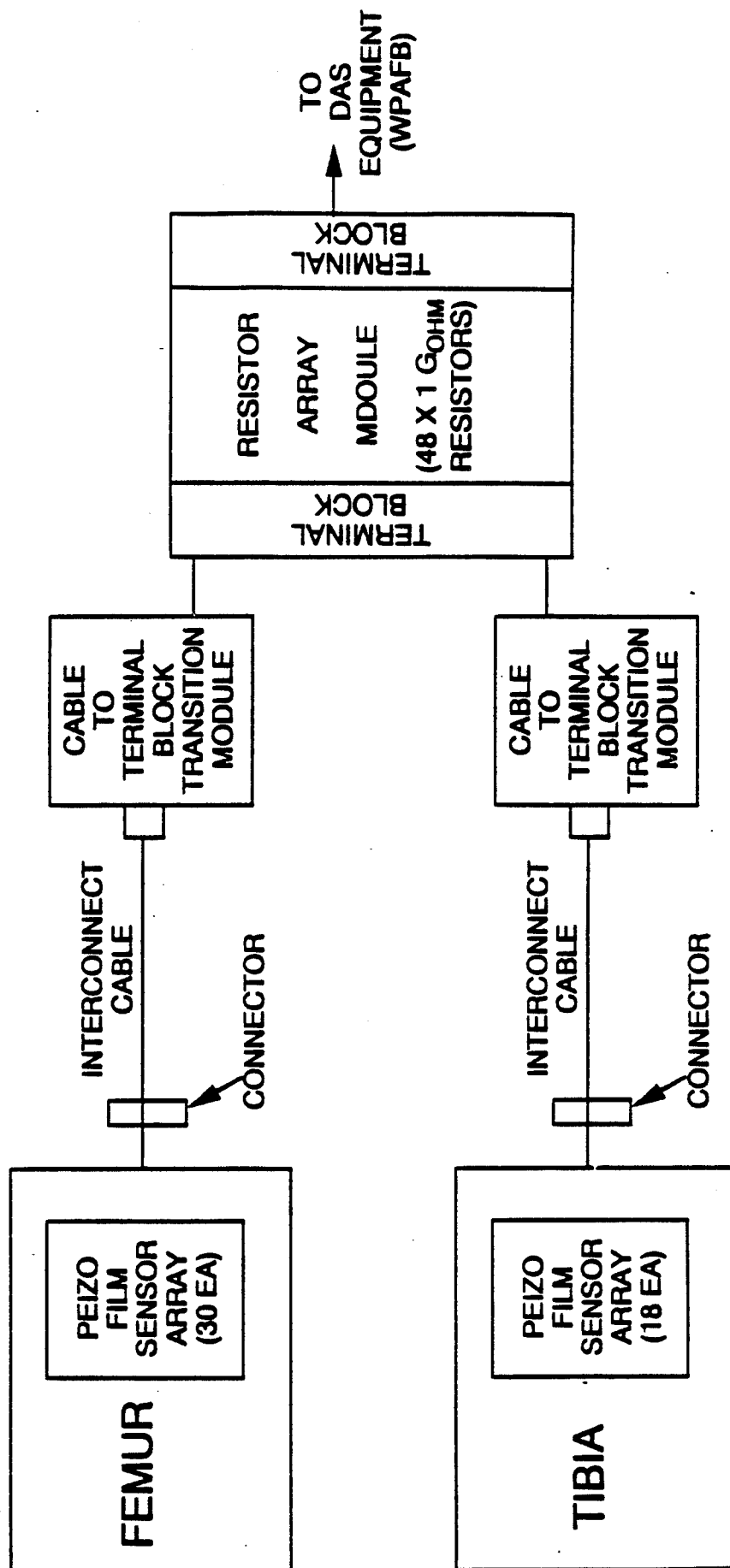


Figure 3.6.2-4. Flesh Instrumentation Hook-Up to DAS Schematic.

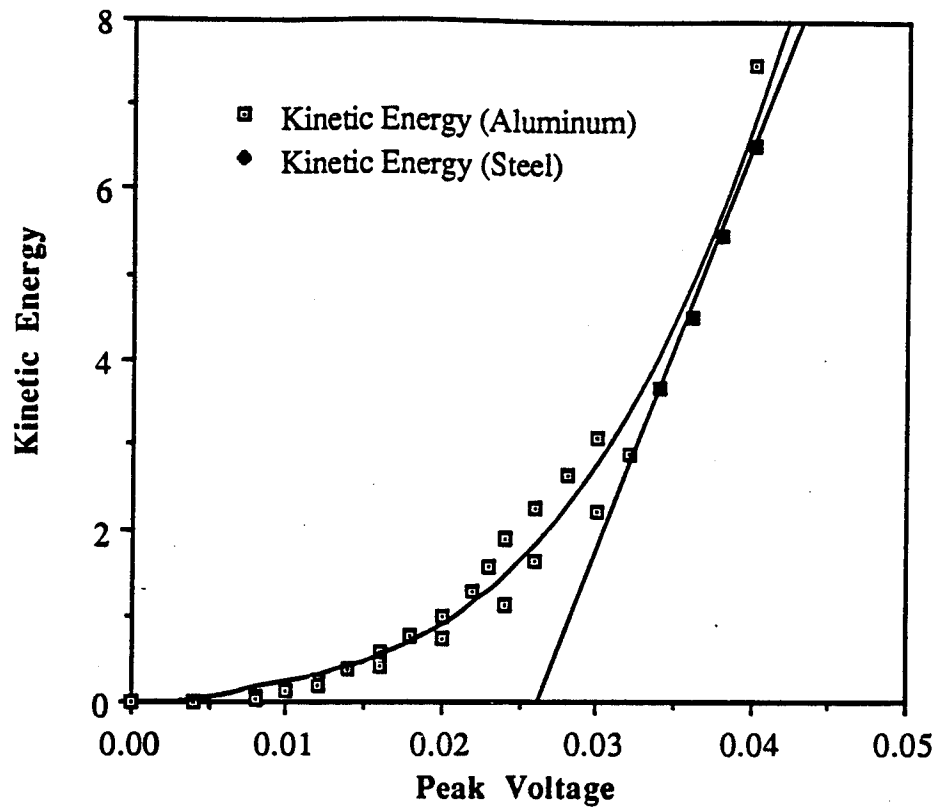


Figure 3.6.2-5. Femur Impact Data & Calibration Curves.

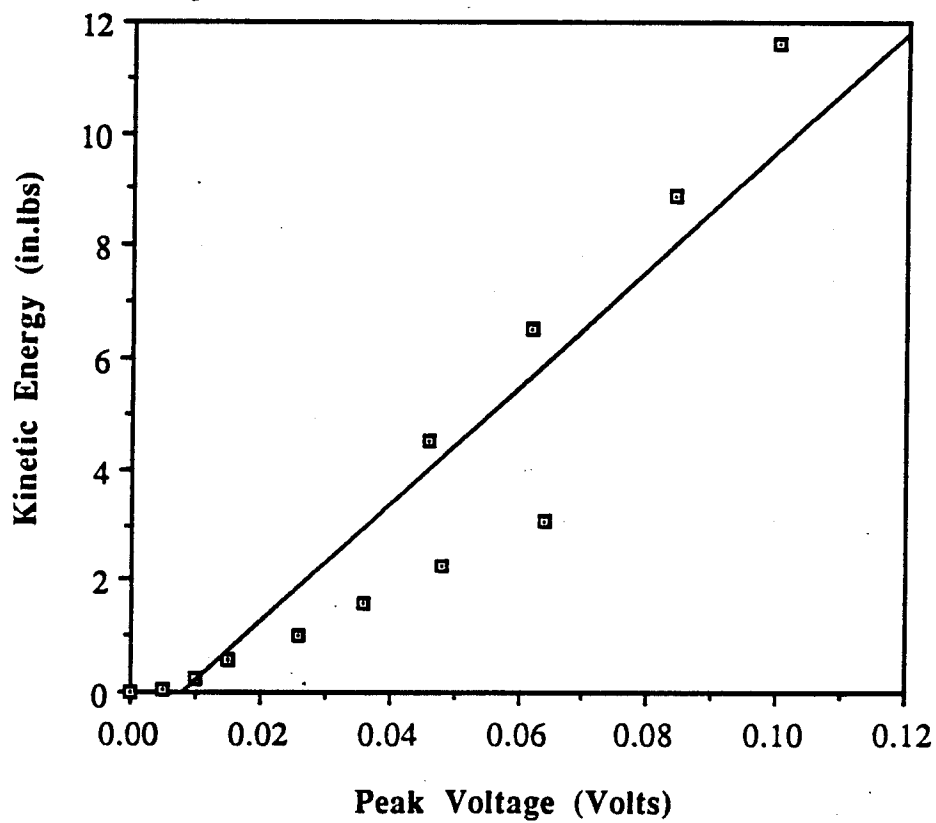


Figure 3.6.2-6. Tibia Impact Data & Calibration Curves.

Femur (low): K.E. (in/lbs) = $-0.16189 + 55.842V - 3250.3V^2 + 153700V^3$

Femur (high): K.E. (in/lbs) = $-12.552 + 475.65V$ $V > 0.039$ Volts

Tibia : K.E. (in/lbs) = $-0.84788 + 105.11V$

Calibration of the embedded sensor arrays for any arbitrary impact is a complex issue because it involves a combination of nonlinear inertial and nonlinear material property characteristics. It should be noted that the actual impact energy could vary significantly from the impact energy predicted by the above equations because of these nonlinear effects. Inspection of Figure 3.6.2-4 shows a good match between experimental data and curve fit calibration curves. However, Figure 3.6.2-5 shows more scatter between experimental data and the calibration curve. This is due in large part to the non-linear material characteristics of the flesh, which in this case are much more evident due to the small thickness of flesh between the sensor and the bone. This coupled with the rate change due to the difference of inertia between the different masses used during the impact tests caused the scatter in the data. The tibia flesh was relatively thin compared to the femur flesh. The tibia sensor response would produce a higher output for higher strain rate change inherent in the steel and aluminum inertial masses (i.e. the load/determination response is directly effected by the tibia bone under the sensor). The femur flesh on the other hand has a relatively uniform response independent of the mass of the impactor because of the compliance of the thick flesh.

3.7 Dynamic Sled Test

A series of dynamic sled tests were conducted at the Armstrong-Laboratory sled test facility. The tests were conducted using a full scale 50 percentile Hybrid III manikin. The Hybrid III manikin had a "standard" left leg and the new ABC Man right leg. Figure 3.7-1 shows the test setup. Due to the limited number of data channels on the sled system Data Acquisition System (DAS) only the femur and tibia strain gage and accelerometer data were taken. Also there were no impacts on the flesh during the tests so the flesh tactile foil array was unnecessary in this test case. Figure 3.7-2 shows a close up view of the ABC Man leg in the sled. The multi colored flat cables are the Femur and Tibia data wires.

The sled tests were conducted at peak G accelerations ranging from 5 to 20 Gs as shown in Table 3.7-1.

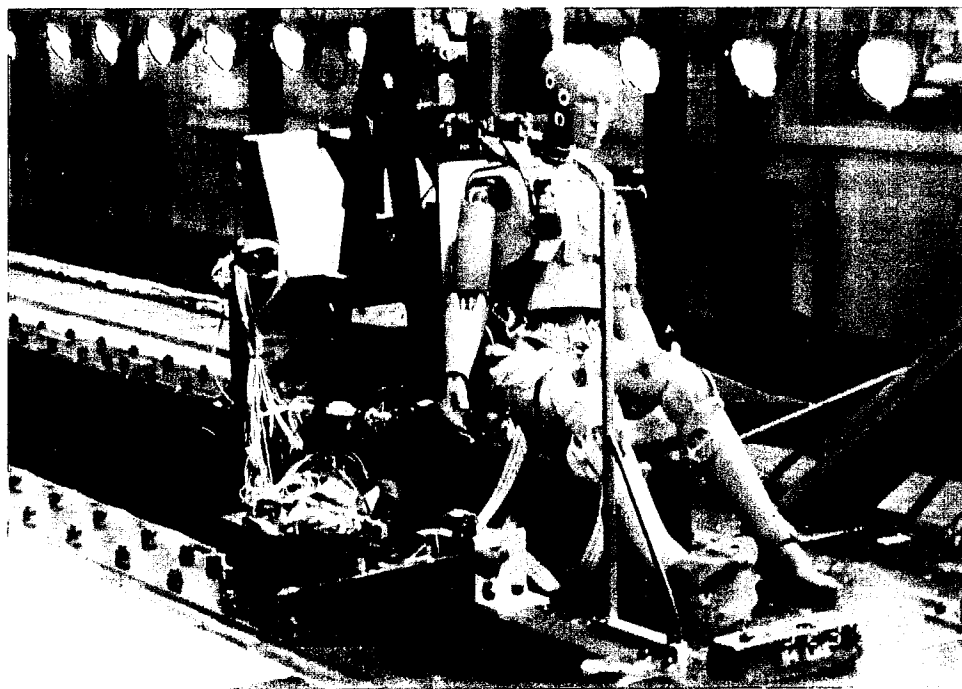


Figure 3.7-1. Armstrong-Laboratory ABC Man Sled Test Setup.

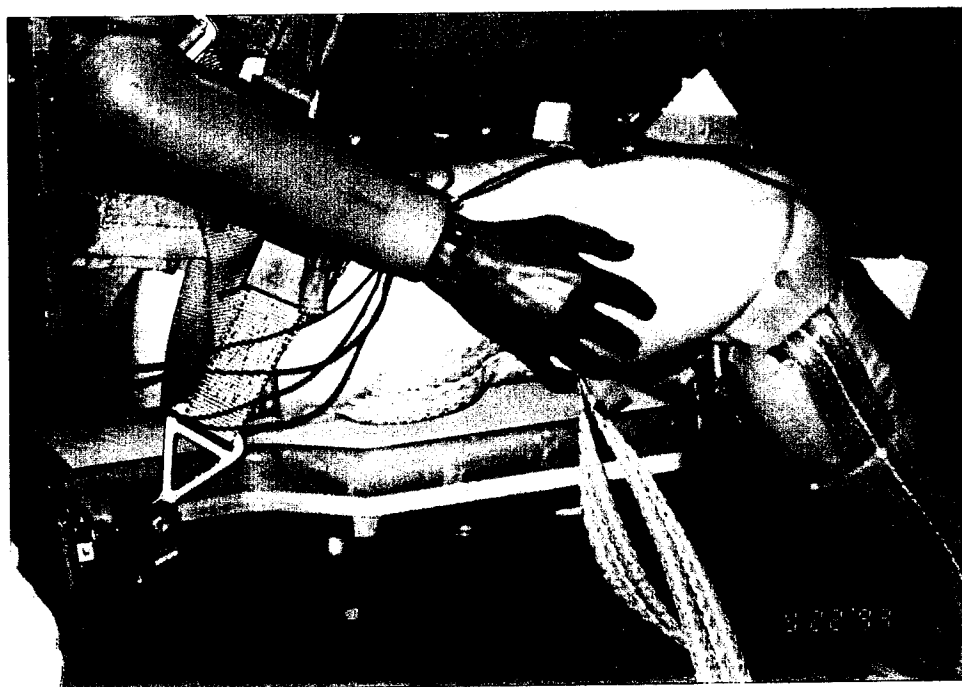


Figure 3.7-2. On-Sled ABC Man Leg Prior to Testing.

Table 3.7-1. Full Scale Sled Test Matrix

Test No.	Planned Peak G	Actual Peak G
1 (4637)	5	5.5
2 (4638)	7.5	7
3 (4639)	10	8.5
4 (4641)	12.5	10.0
5 (4542)	15	15
6 (4643)	20	20

The tests were conducted by accelerating the manikin backward using a hydraulic ram to accelerate the sled. On-board high speed black and white visual and infrared cameras were used to record movement of the dummy. Infrared markers were placed on the chest, right and left upper leg and on the proximal tibia of the ABC man leg. These markers, seen as triangular shapes and small white squares in Figures 3.7-1 and 3.7-2, were tracked by the on-board infrared camera to give relative in-plane locations during the tests. An off-board video camera was also used to record the real time tests. Another test involving a swing arm with light diodes was "piggybacked" with this test but had no impact on the Hybrid III data (see swing arm in lower middle right side of sled in Figure 3.7-1).

In addition to the camera data, the sled acceleration history and the ABC Man strain gage and accelerometer data were taken during each test. The Hybrid III manikin was securely strapped into the sled seat with a "standard" aircraft harness. Although the harness was as tight as possible, there was relative motion between the seat and the pelvis during the tests. This motion was up to an estimated 4-5 inches based on the post test on-board film. This relative motion caused a significant jerk of the manikin during the acceleration as the manikin "slammed" into the harness. All data from the sled tests except the film footage are presented in Appendix B by test number. The following discussion is a representative summary of specific tests and can be applied to all tests taking into account the variation in peak G accelerations.

General Observation

The standard Hybrid III and ABC Man leg gross movements were similar. In the first series of tests it was noticed that the ABC Man leg had a lateral motion in addition to the vertical motion. It was determined that this was due to the slight difference in the ABC Man flesh

geometry and the standard Hybrid III leg. The standard Hybrid III femur flesh is made in three segments while the ABC Man flesh is a single pedestrian unit which caused the lap belt to sit differently on each leg. The initial ABC Man leg lateral movement was solved by placing the ABC Man leg foot slightly (~ 6 inches) outboard. All tests went smoothly and were completed in one day. There were no significant channel drop outs during the tests.

The long bone strain gage and accelerometer data were converted by the Armstrong Laboratory DAS to local accelerations and forces or moments based on the calibration data. A review of the post-test long bone forces and accelerations indicated that the force histories were out of phase with the acceleration profiles. In some cases, high accelerations produced very little load or vice versa. Figures 3.7-3 and 3.7-4 show the effect for the 20G acceleration tests. It was believed that this inconsistency was due to the accelerometers and strain gages were measuring the accelerations and forces in the relatively stiff long bone segments; however, the majority of the load came from the mass of the flesh as shown in Table 3.7-2.

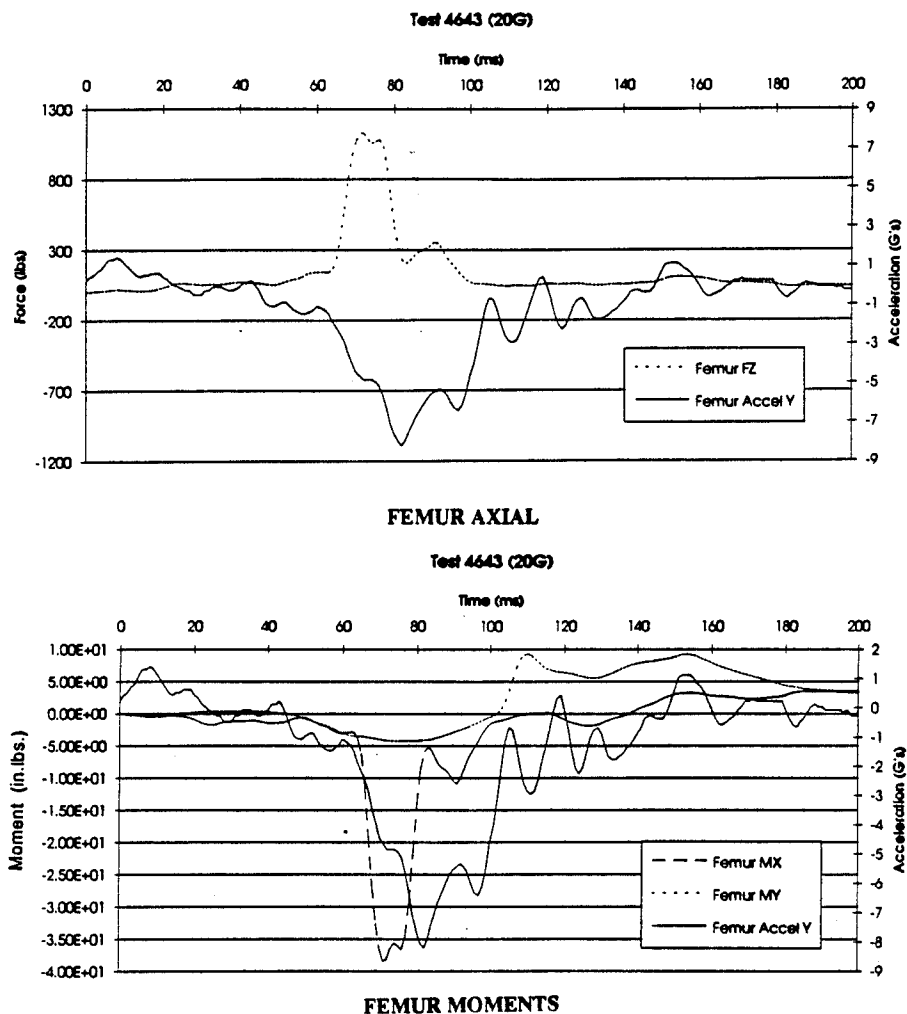


Figure 3.7.3. Load and Acceleration Histories for the 20g Sled Test.

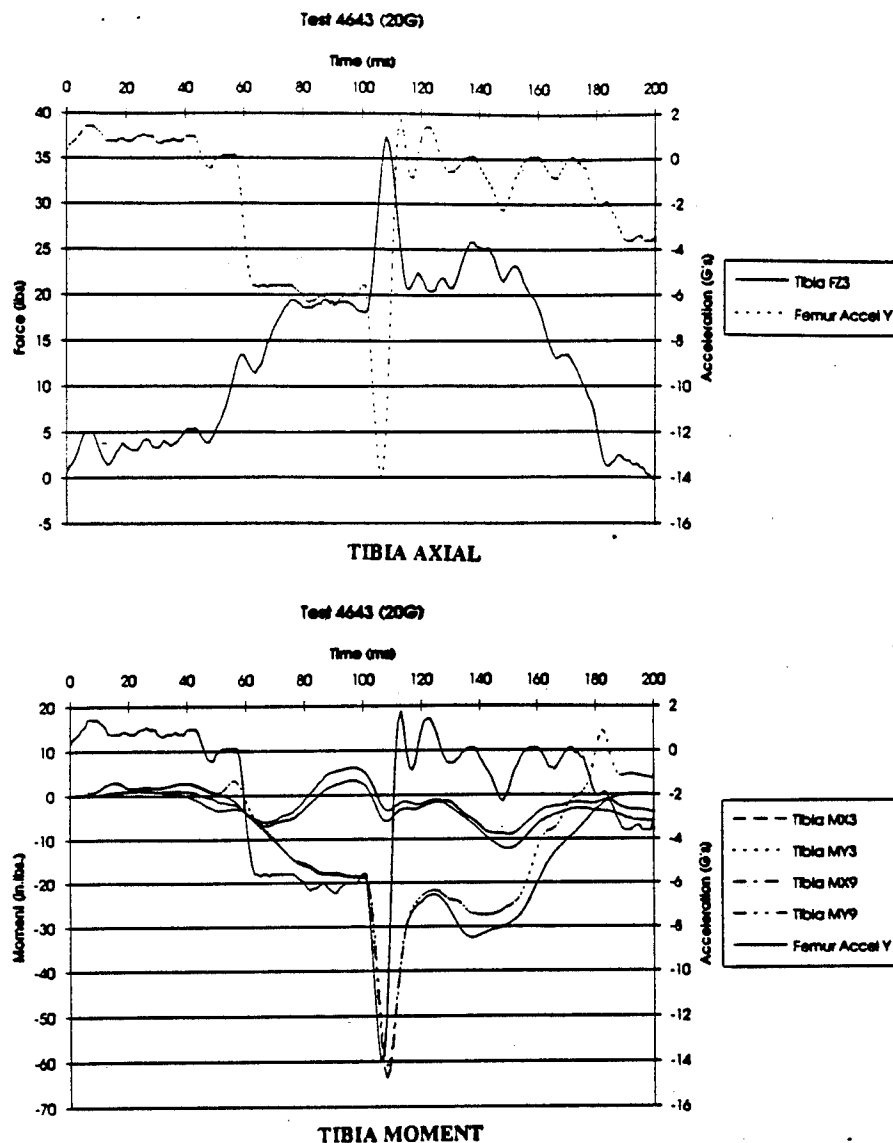


Figure 3.7.4. Load and Acceleration Histories for the 20g Sled Test.

Table 3.7-2. Mass Breakout of ABC Man Leg Segments

Segment	Long Bone Mass	Flesh Mass	Percent of Total	
			Bone	Flesh
Femur	1.069 Kg (2.36 lbs)	8.14 Kg (17.94 lbs)	11.6%	88.4%
Tibia	0.684 Kg (1.51 lbs)	3.71Kg (8.19 lbs)	15.6%	84.4%

Because the flesh material was significantly heavier than the bone ($\approx 8.5x$), it would contribute the majority of the load induced on the bone from a given acceleration profile. In addition, the compliance of the flesh was much less than that of the bone. Because of these effects, it was conceivable that out-of-phase non-intuitive response could be realized. If this were true, then it implies that in order to achieve accurate load histories that not only must the total segment mass be accurate, but that the mass must be accurately distributed and with the correct relative

compliance. In order to test this theory a detailed analysis was conducted on the 20G acceleration test.

3.7.1 20G Sled Test Analysis

A detailed analysis of the 20G Sled test data was performed to understand the complicated dynamic response seen in the acceleration and load histories recorded during the tests. In order to accomplish this, two dynamic finite element models (FEM) of the ABC Man leg were developed: one model consisted of a "Lumped Mass" configuration where the total flesh and bone mass was rigidly applied to the skeletal beam elements, the other model consisted of a distributed mass configuration where the flesh mass was separate from the bone with independent compliance. The output of these two models were compared to the actual sled test data.

Because the post test analyses were more complicated than anticipated, the dynamic FEMs had to incorporate several simplifying assumptions including: forcing function at the pelvis taken from the sled test video, approximate flesh and bone geometry, and sliding flesh on the femur only. However, within these limitations, the FEM showed that the dynamic response of the flesh relative to the bone had a significant impact on the overall response of the ABC Man leg. The resource limitations of the contract allowed for only a detailed analysis of the 20G test.

3.7.1.1 "Lumped Flesh" Finite Element Analysis

The "Lumped Mass" model consisted of 2-D beam elements with the mass of the flesh, bone and hardware lumped into the beam. A time sequence of this model is shown in Figure 3.7.1-1. This model was developed to investigate the effects of lumping the mass rigidly on the bone, this which be similar to the current Hybrid III design where most of the segment mass is in the bone and not in the flesh.

Figure 3.7.1-2 show the displacement and acceleration output from this model. The x and y coordinates are in the global reference frame with x being horizontal along initial femur directions and y being vertical to the sled. In this figure, at approximately 0.11 sec the tibia (foot) reaches the fully extended position which causes a "ringing" in the accelerations for the femur and tibia. Figure 3.7.1-3 shows the same data but plotted in the local coordinates relative to each bone. The hip x is the horizontal movement of the pelvis. Again, when the tibia rotates to full extension, a discrete ringing occurs in the system. This was also observed in the test data but to a much lesser extent. Figure 3.7.1-4 compares the predicted local anterior-posterior (transverse) accelerations and global displacements (y) of the femur with the actual test data.

BEAM4 DEFORMATION HISTORY

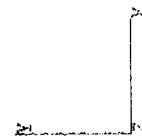
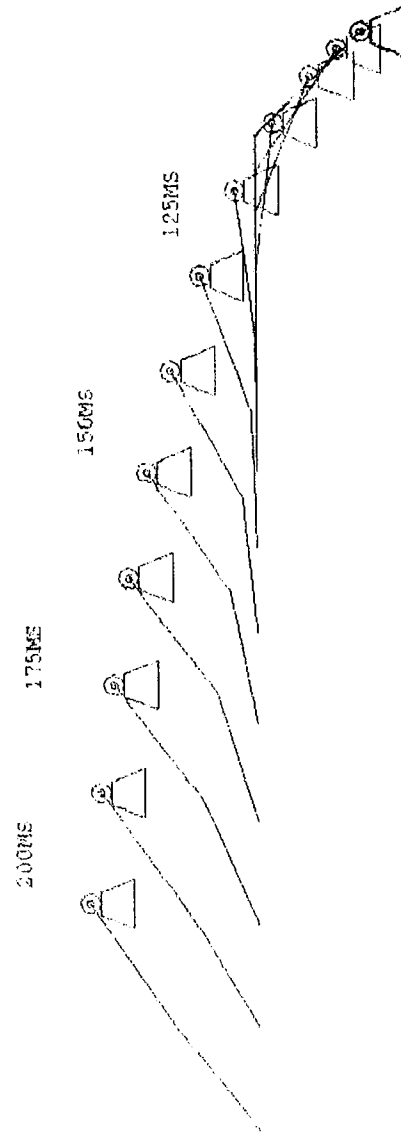


Figure 3.7.1-1. "Lumped Mass" Finite Element Model Depicting Segment Motion, Model is Moving from Right to Left.

20G Finite Element Results (Flesh Mass Lumped into Leg)

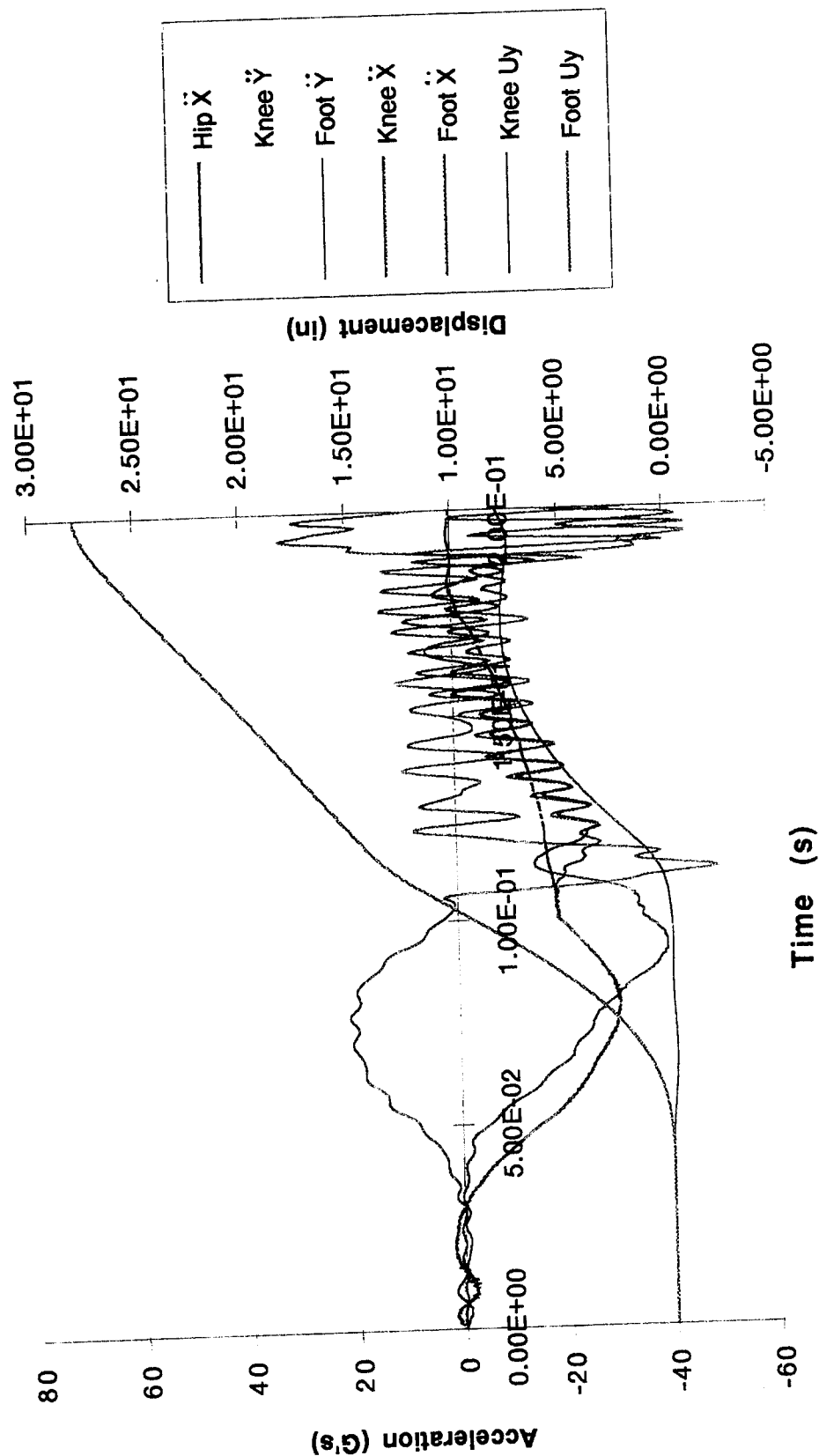


Figure 3.7.1-2. Acceration and Displacement Histories for "Lumped Mass" Model in Global Coordinates.

20G Finite Element Results (Flesh Mass Lumped into Leg)

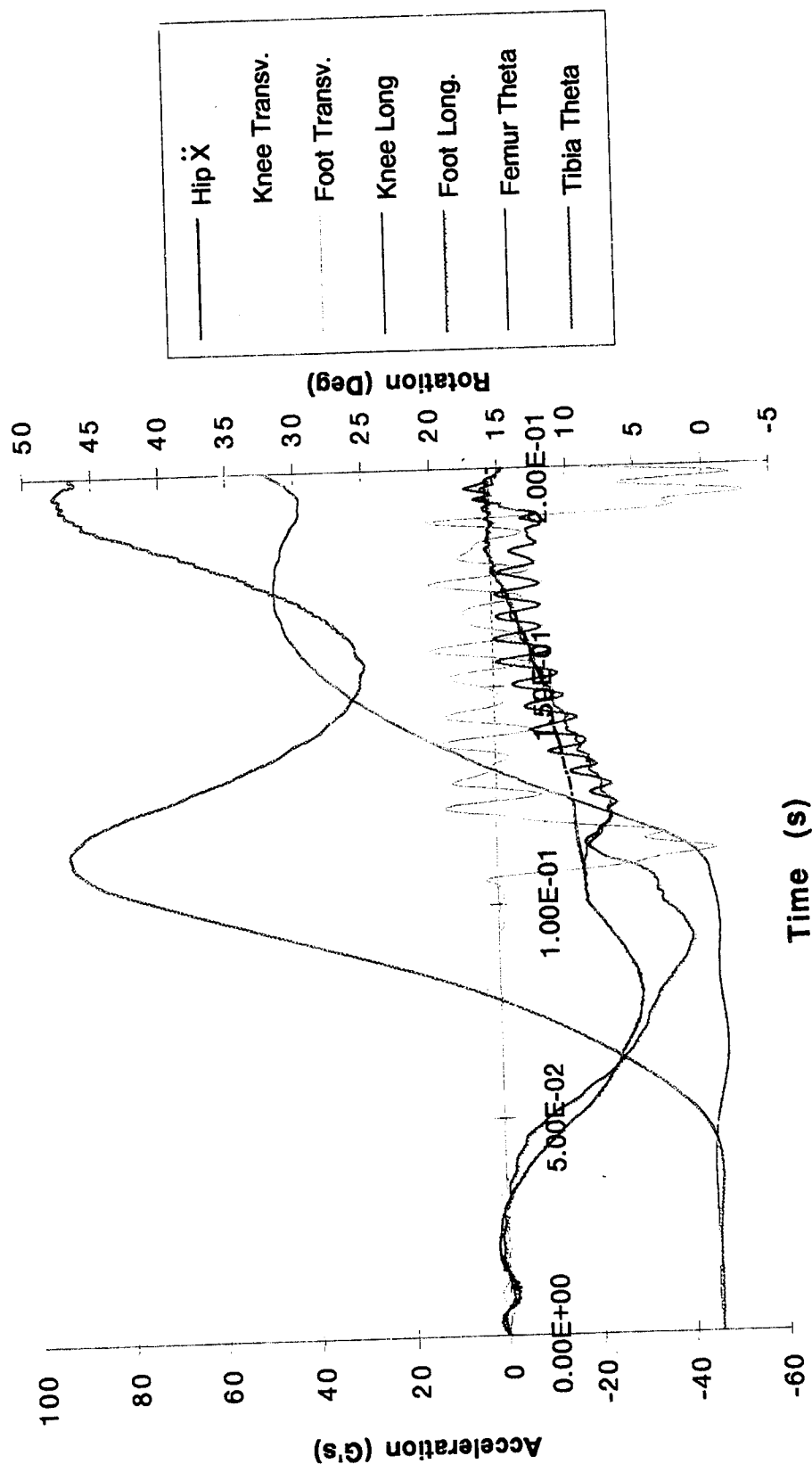


Figure 3.7.1-3. Accelerations and Rotations of "Lumped Mass" Model in Local Relative Coordinates.

20G Femur Acceleration Vertical Results (Flesh Mass Lumped into Leg)

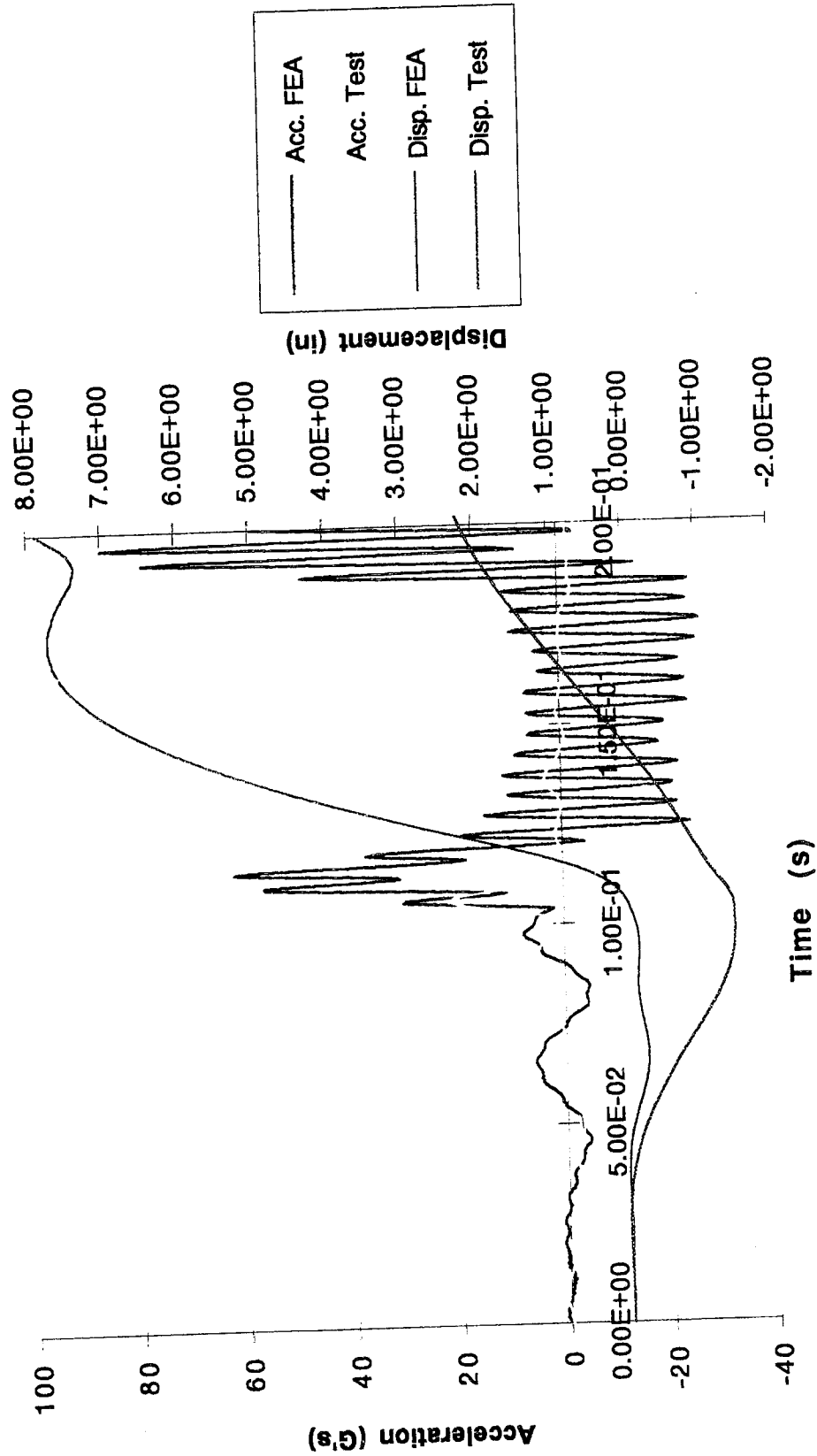


Figure 3.7.1-4. Comparison of Lumped Mass Accelerations and Displacement

Both the displacement and accelerations show consistent responses between the predicted and actual. The major variation in displacement is probably due to the way the seat was modeled. In the "real test" the dummy slid forward and had a slight rotation of the hip which would cause an increase in initial downward motion of the femur. The FEM however, modelled the initial motion as only horizontal. Any downward motion of the femur could occur as a compression of the flesh. The acceleration difference can be explained by the relatively hard knee stop in the FEM which caused an acceleration overshoot and subsequent ringing.

3.7.1-2 Distributed Flesh Finite Element Model

The Distributed Flesh FEM, shown in Figures 3.7.1-5a and 3.7.1-5b distributed the flesh longitudinally and axially along the skeletal segments to simulate both the geometry and compliance of the real flesh. In this model, the segment mass was more realistically distributed with the heavy compliant flesh surrounding a stiff light bone. The flesh was modelled with plane stress elements and the bone with 2-D beam elements.

The displacement and acceleration output (in global coordinates) of the model is shown in Figure 3.7.1-6. The right side scale is in inches and the foot and knee displacements (U_y) are also shown in global coordinates.

The effect of the compliant flesh "sloshing around" can be seen by comparing Figures 3.7.1-6 and the lumped mass acceleration in Figure 3.7.1-2. Although the global displacements are similar, there is a marked difference in the acceleration histories especially after the tibia is fully extended. The distributed flesh acts as a damper to the excessive ringing shown in the lumped mass model. This same effect is seen in the local acceleration response shown in Figure 3.7.1-7.

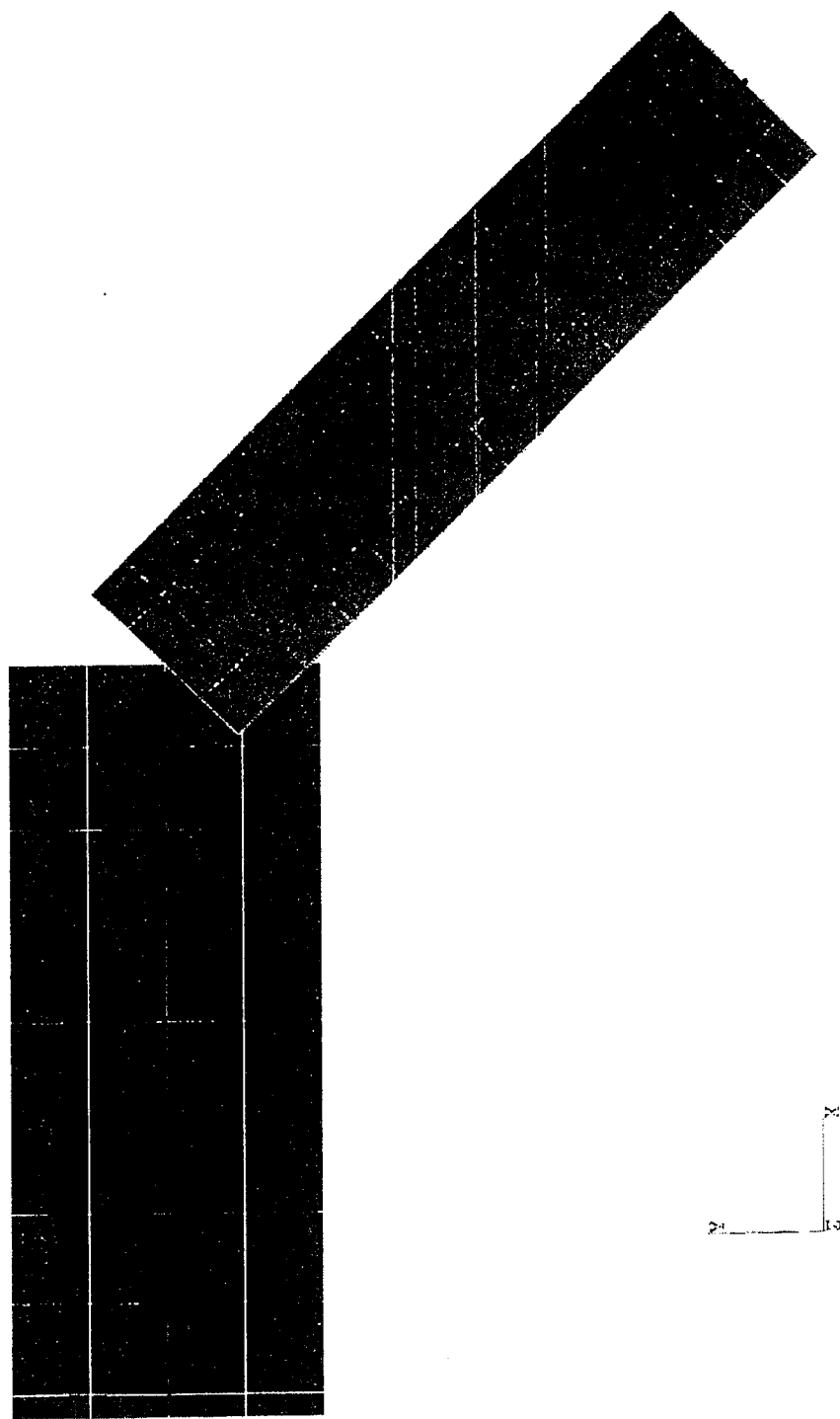
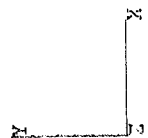
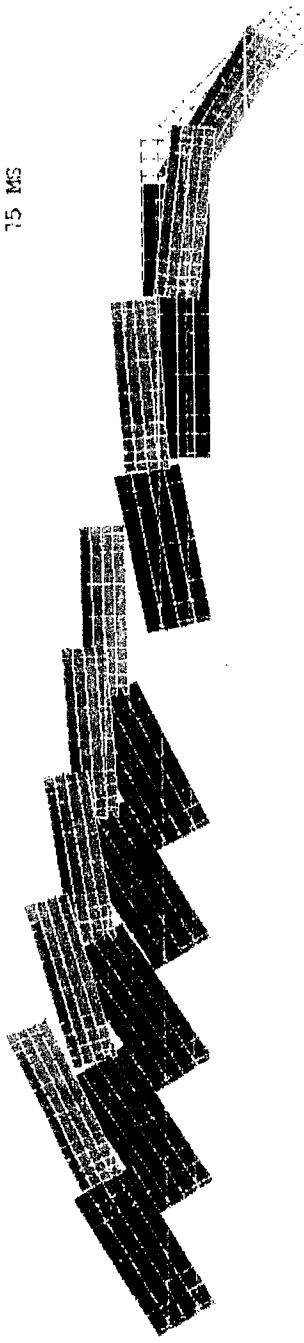


Figure 3.7.1-5a. Distributed Mass Flesh Finite Element Model.

ELSH1

ACTUAL DEFORMED SHAPE

200 MS 128 MS 175 MS 163 MS 150 MS 125 MS 100 MS 75 MS



AEC MAN FLESH DYNAMIC MODEL 1 22:07:00 97 114
ABRQUS V5.3-1 30-DEC-93
PROCEDURE 12 TIME STEP 1 INCREMENT 888
1. ANIMATE 6. ANIMATE 7. NEW CASE 8. END

Figure 3.7.1-5b. Dynamic Motion of Distributed Flesh Finite Element Model
(Model Motion is from Right to Left)

20G Finite Element Results (Leg Including Flesh)

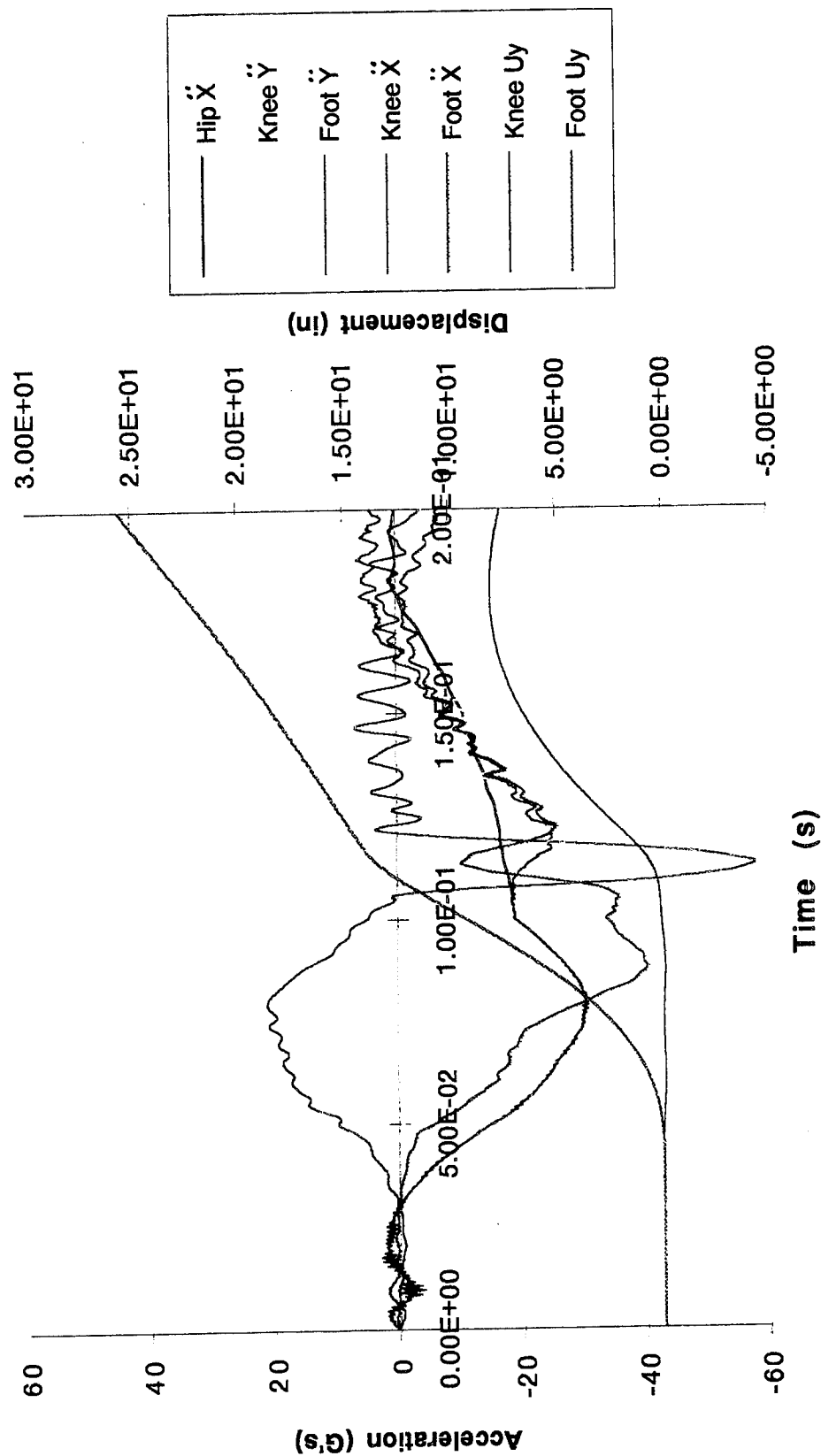


Figure 3.7.1-6. Distributed Mass Acceleration and Displacement Histories.

Finite Element Results (Distributed Flesh) 20G Sled Test (4643)

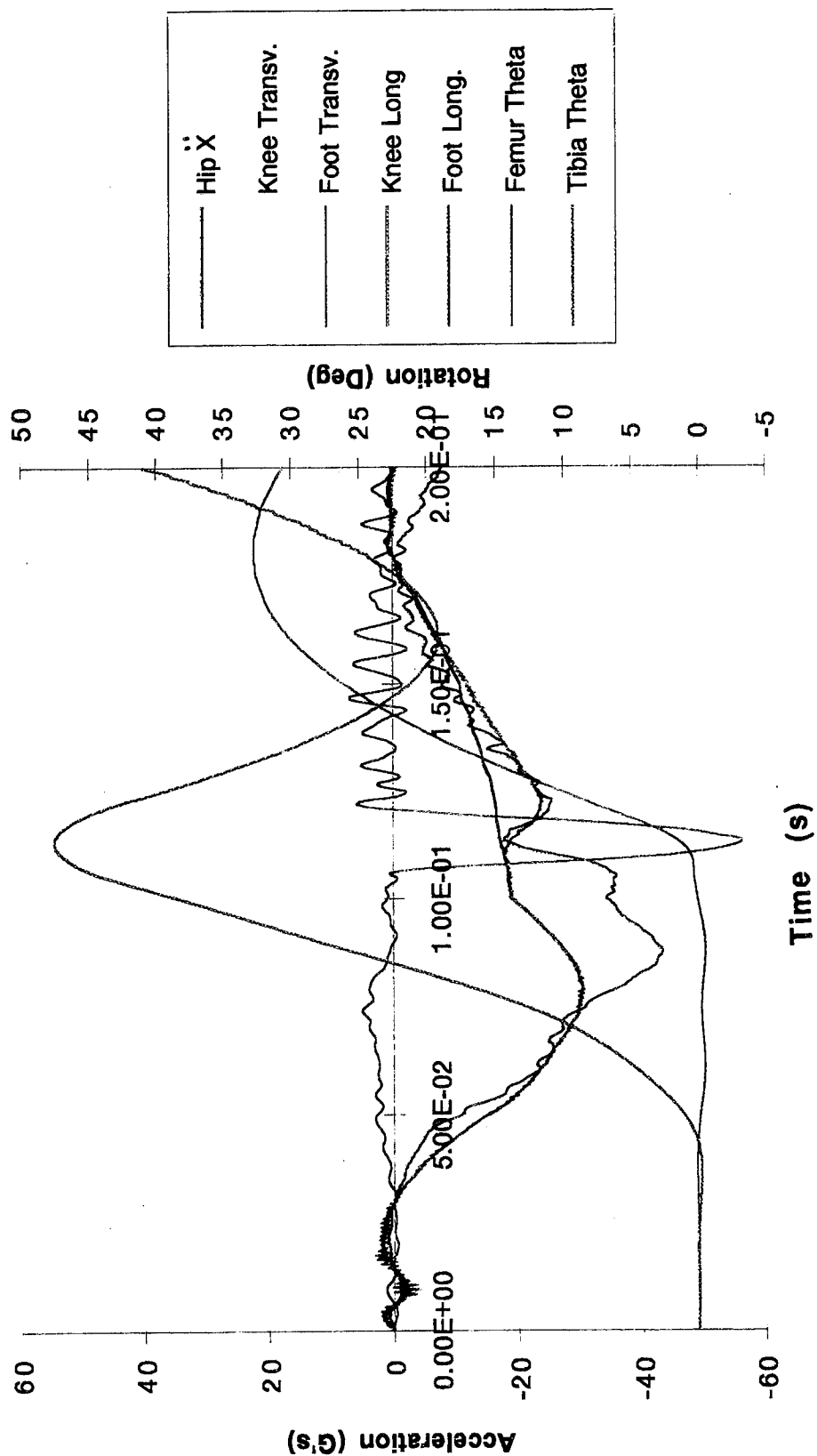


Figure 3.7.1-7. Distributed Flesh Mass Acceleration and Angular Rotation Histories

A comparison of the distributed mass FEM and the actual test data for the femur is shown in **Figure 3.7.1-8**. There is much better agreement between the distributed mass results and the test data than between the lumped mass model (**Figure 3.7.1-4**) and the test data. The predicted peak accelerations and maximum displacements are larger than the measured, which is likely due to the initial boundary conditions and assumptions as discussed for the lumped mass model. Clearly the overall response of the distributed mass model more closely reflects the actual data than the lumped mass model (**Figure 3.7.1-4**).

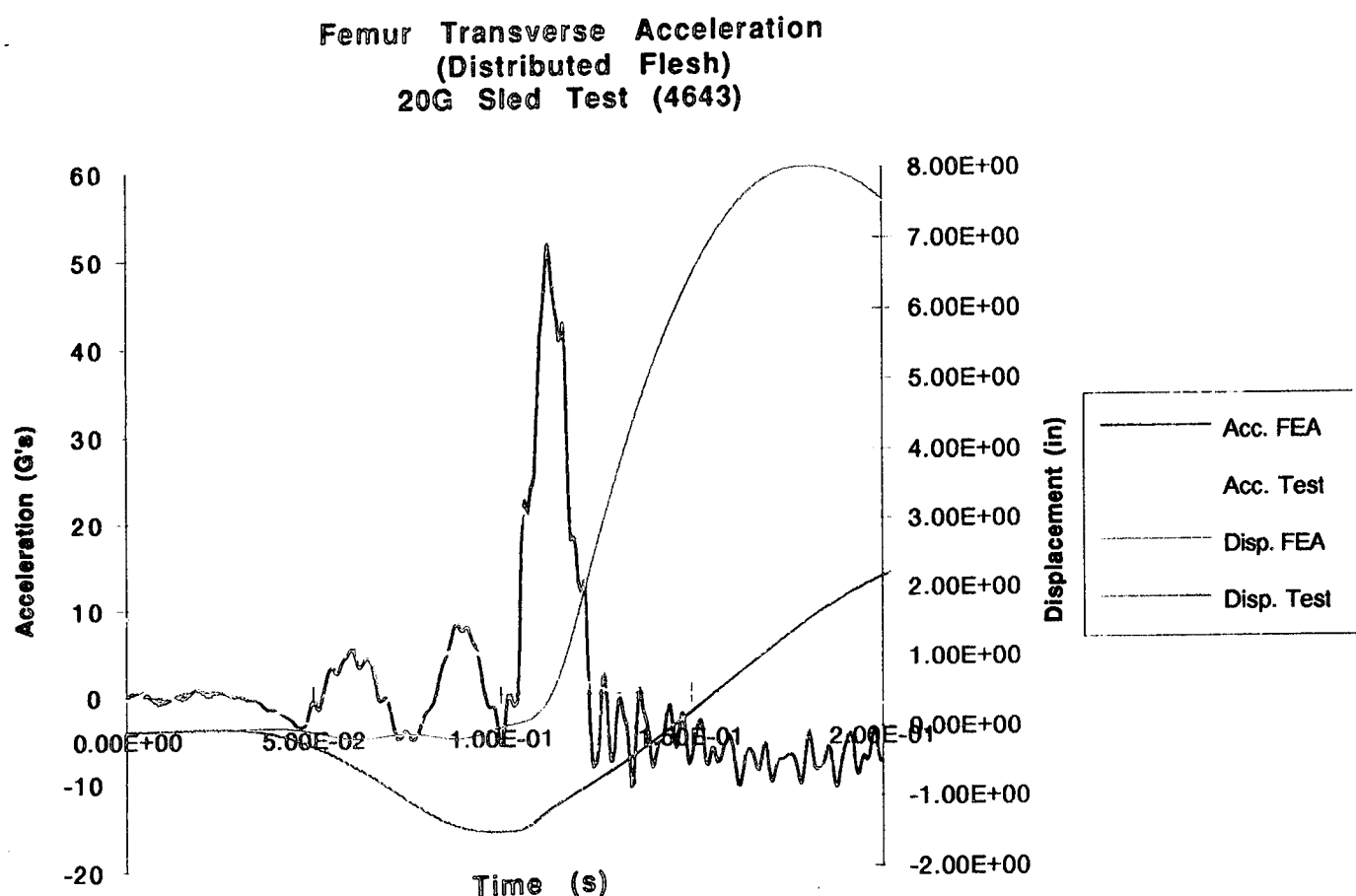


Figure 3.7.1-8. Comparison of Distributed Mass FEM Accelerations and Displacements to Actual Test Data.

The difference in response between the two models, lumped mass and distributed mass, shows that the correct mass distribution and correct relative compliance between the skeletal and flesh components is necessary to accurately model the true load/acceleration time histories of human occupants in dynamic environments.

3.7.1.3 Loads Analysis

Both the lumped mass and distributed mass FEMs were used to predict sectional loads for use in assessing the effect of the distributed mass. Figure 3.7.1-9 shows the sectional forces for the lumped mass model and Figure 3.7.1-10 shows the sectional forces for the distributed model. In both models the measured and predicted forces followed the same trends, however, the distributed mass model had a loading profile which more closely resembled the actual data indicating the importance of the flesh mass distribution.

From observing the video footage of the 20G sled test, significant displacement of the flesh relative to the bone was noticed on the standard Hybrid III leg positioned on the left side of the dummy. The standard Hybrid III leg flesh is lighter and has a similar stiffness to the Skin Flex III flesh. Although not visible in the video, it can be inferred that the flesh on the right leg (Skin Flex III), due to its higher mass, would deflect more than the Hybrid III leg. The flesh for both the femur and tibia is attached to the bone by positioning the flesh around the bone and fastening the zipper. Under heavy loading, the flesh can slide along the bone being only supported by the thickened ends of the bone and bone/flesh interface friction. In an effort to model this behavior a finite element model was developed to allow this sliding between the bone and the flesh elements of the femur to occur. Figure 3.7.1-11 shows the difference between the axial force in the bone due to the fixed versus the sliding flesh. The axial force in the sliding flesh case is up to 50% higher because all of the mass of the accelerating flesh must be transferred through the entire bone. This effect could be demonstrated in the tibia flesh/bone interface if it was allowed to slide as well. Taking this effect into consideration, the analysis of the axial loads would be very close to the actual measured axial loads.

The bending moment data were difficult to correlate and not fully understood. The predicted bending moments were much higher than the bending moment calculated based on the test results. This could have been due in part because the dynamic FEM used straight beams to model the skeletal segments when as, particularly in the femur, the long bones were complex compound curves. In addition, the complex coupling between the compliant flesh and rigid bone may have had a canceling effect on the overall moment loads as the femur and tibia locked and rebounded. Unfortunately the resources available in this program prevented a more detailed study of this possibility.

**Actual vs FEA Forces and Moments in Femur
(Lumped Flesh)
20G Sled Test (4643)**

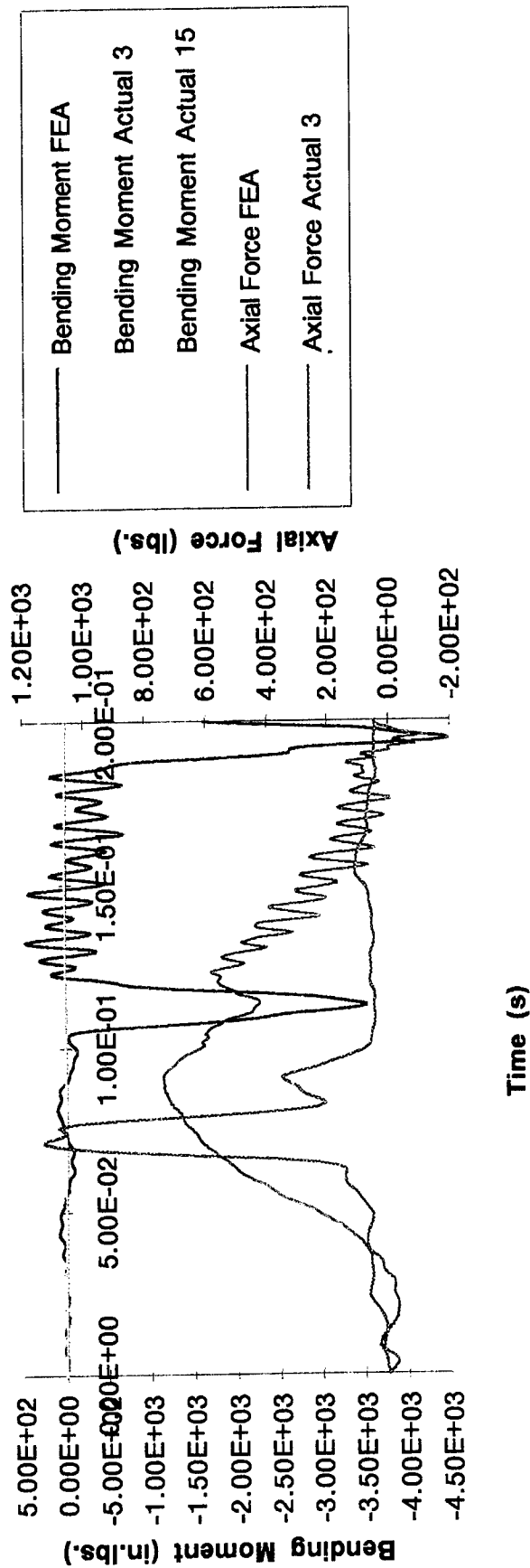


Figure 3.7.1-9. Section Forces and Moments in the Lumped Finite Element Model Compared with Actual Test Results.

**Actual vs FEA Forces and Moments in Femur
(Distributed Flesh)
20G Sled Test (4643)**

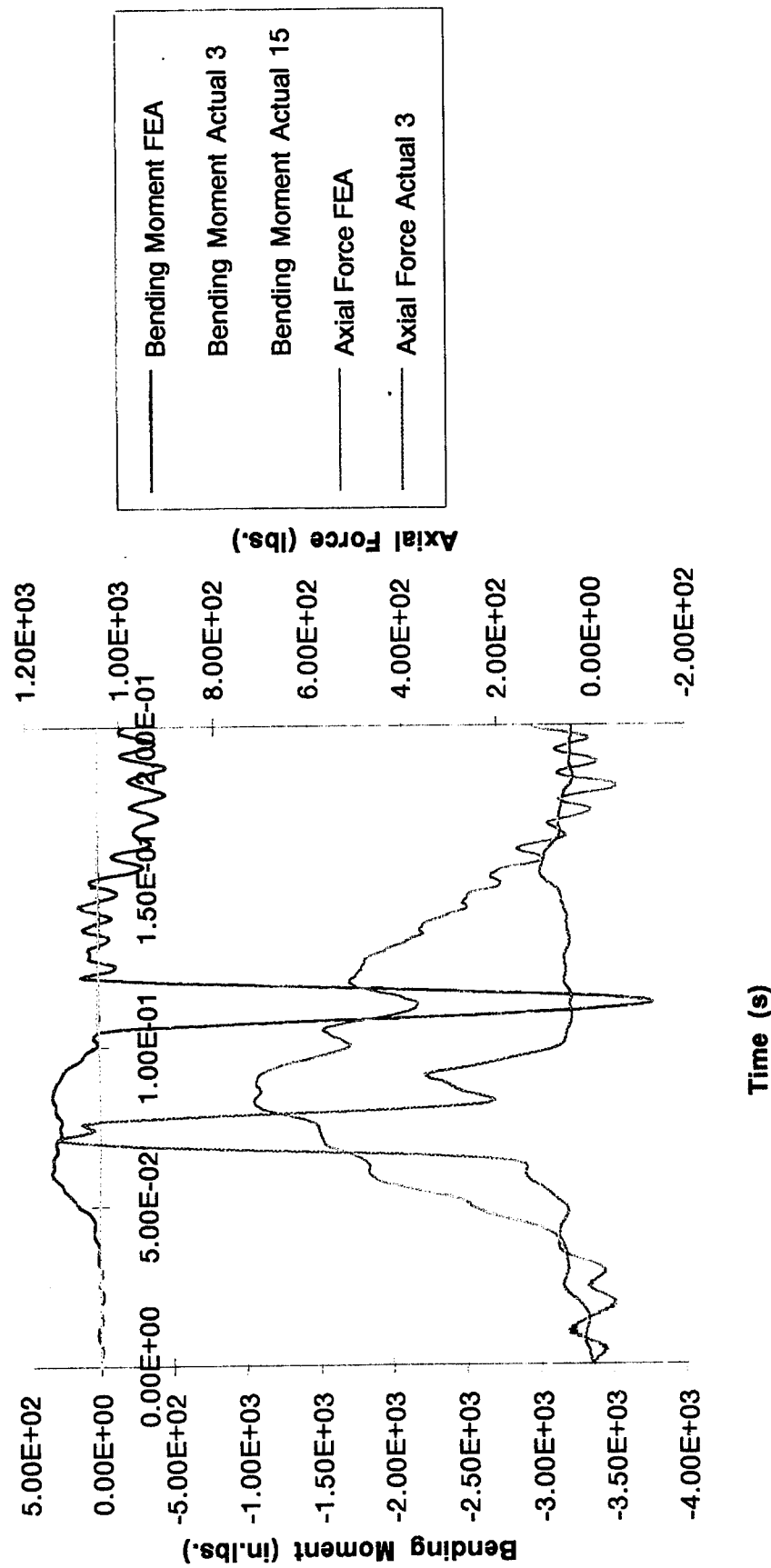


Figure 3.7.1-10. Distributed Flesh Mass Finite Element Model Section Forces and Moments Compared to Test Data.

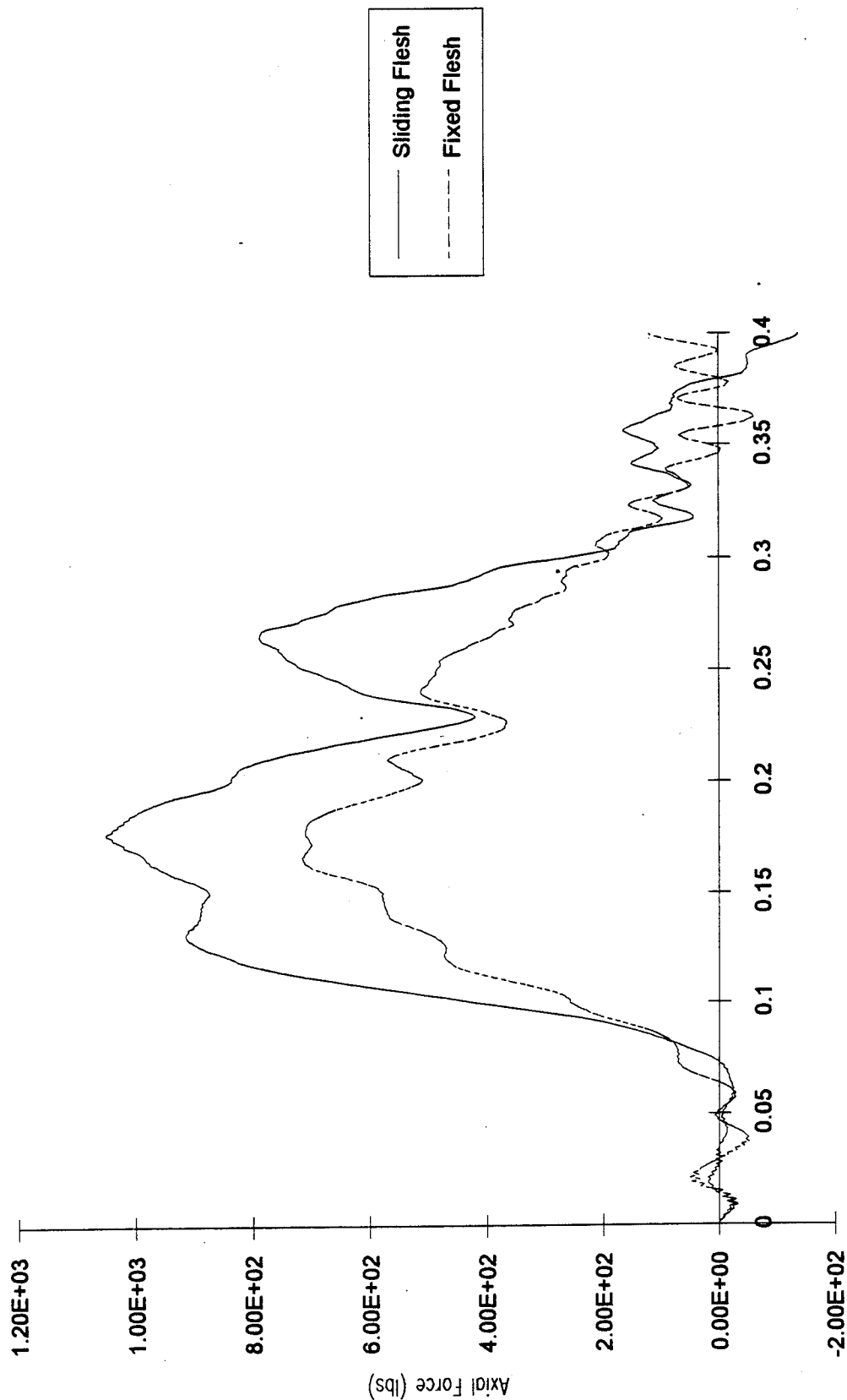


Figure 3.7.1-11. Comparison of Distributed Flesh Mass and Axial Sliding and Fixed Bone Interface Showing an Increase in Axial Load due to the Relative Moment of the Flesh.

THIS PAGE LEFT BLANK INTENTIONALLY

4.0 Discussion of Results

The successful conclusion of the ABC Man Phase II research demonstrated the ability to design, develop and fabricate biofidelic long bone and flesh segments which have a similar mass and geometry to *in vivo* human leg segments. Specifically, this research provided the proof-of-concept demonstration that:

- 1) Advanced composites can be used to develop bone segments for human test manikins which have a mass and geometry similar to human bones but can withstand the high loads experienced during dynamic testing,
- 2) A synthetic polymer could be successfully alloyed to produce the correct, complimentary flesh density for the skeletal segments while maintaining the correct tactile feel and tear strength,
- 3) Sensors could be successfully embedded in both the composite long bones and the flesh. The long bone sensors were foil strain gages and multiple single axis accelerometers. The flesh sensors were piezoresistive foil gages that measure local impact load histories.

4.1 Long Bone Structural Design

The long bone segment design was driven by the requirement to achieve a bone mass as close as possible to that of *in vivo* human bone yet withstand the extremely high loads experienced during testing. These loads, shown in Table 4.1-1, were developed by Wright Laboratory and represent loads predicted for an ejection from a high speed aircraft into a 600 Knot wind blast.

These design criteria were strength critical and required a very high specific strength material. Table 4.1-2 gives a summary of the baseline composite materials for the skeletal segments. Detailed finite element analyses for both the femur and tibia were developed to quantify and expand the closed form structural analysis. These analysis showed that a biofidelic mass and geometric femur and tibia could be developed and that advance composite structures could be used in all areas except the proximal femur neck. Bending loads induced interlaminar shear stresses which required the use of a titanium end fitting at the proximal femur neck. A titanium insert was also used at the ankle but to only provide an interface with the existing Hybrid III foot. Figure 4.1-1 shows a solid shaded image of the 3-D finite element models for both the femur and tibia.

Table 4.1-1. ABC Man Femur and Tibia Design Loads

Femur Load Case		Magnitude
1	Tension	4500 lb
2	Compression	8640 lb
3	Torsion	4500 in-lb
4	Bending	1623 lb*
* Transverse Cantilever Load (Moment Arm = 14 Inches)		
Tibia Load Case		Magnitude
1	Tension	3000 lb
2	Compression	3000 lb
3	Torsion	4500 in-lb
4	Bending	5250 lb*

Table 4.1-2. Baseline Skeletal Materials for ABC Man Long Bone Segments.

Material	Key Parameter	Rational for Selection
Toray T1000G Carbon Fiber	950 Ksi Ult Strength	Highest Strength and toughness fiber available
Amoco 1908 Epoxy Resin	6% Strain to Failure	Provides adequate ductility to enforce first fiber failure micromechanics allowing full strength of T1000G fibers to be achieved

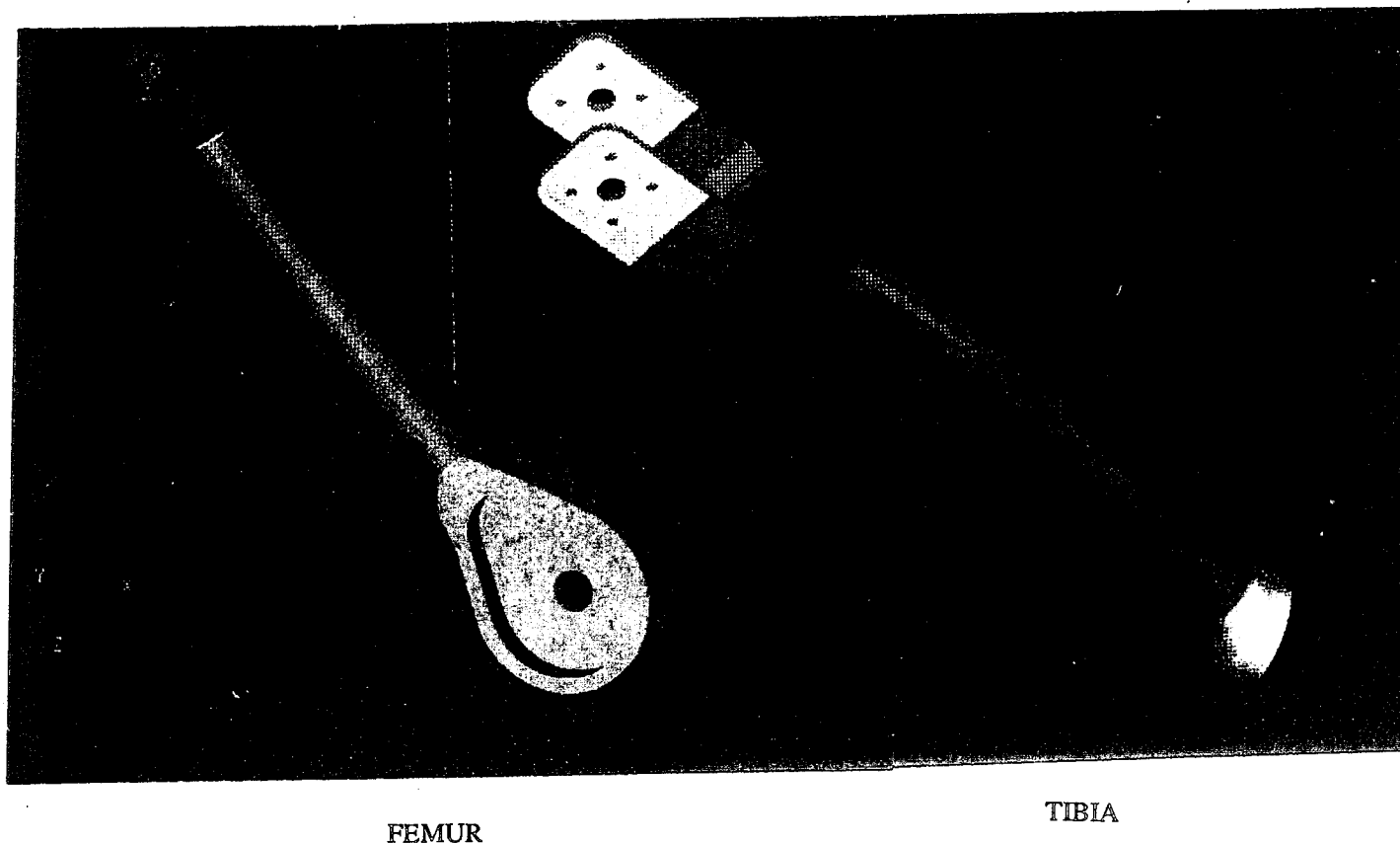


Figure 4.1-1. Final 3-D Finite Element Model of the ABC Man Femur and Tibia.

A summary of the structural analysis results is given in **Table 4.1-3**.

The structural analysis used a 1.5 factor of safety which gave all positive margins for both the femur and tibia designs except for a highly localized region in the femur titanium neck. This was not considered critical because if the maximum load was reached it would yield locally with a very small permanent set [1.27 Mils, (0.032mm)]. It should be noted that although there was a 1.5x factor of safety, the analysis assumed that the fibers were relatively well aligned. If this were not the case, as will be discussed later in Section 4.4, the strength would be reduced in proportion to the fiber misalignment or buckling.

Table 4.1-3. 3-D Finite Element Analysis Summary for ABC Man Long Bone Segments.

LOAD CASE	FIBER STRAIN MARGIN OF SAFETY			INSERT MARGIN OF SAFETY
	0 ° FIBER	+ - 45 ° FIBER	90 ° FIBER	TITANIUM
TENSION	+ 2.47	> 5	> 5	+ 0.87
COMPRESSION	+ 0.81	> 5	+ 0.81	- 0.01*
BENDING	+ 0.28	+ 0.48	+ 0.69	+ 4.19
TORSION	+ 4.08	+ 1.70	> 5	+ 0.75

Femur Analysis Summary

LOAD CASE	FIBER STRAIN MARGIN OF SAFETY			INSERT MARGIN OF SAFETY
	0 ° FIBER	+ - 45 ° FIBER	90 ° FIBER	TITANIUM
TENSION	+ 2.68	+ 3.02	> 5	+ 1.33
COMPRESSION	+ 2.68	+ 3.02	> 5	+ 1.33
BENDING	+ 0.89	+ 1.28	+ 1.59	+ 0.78
TORSION	+ 0.91	+ 0.29	+ 0.71	+ 3.32

Tibia Analysis Summary

4.2 Instrumentation

One of the objectives of the ABC Man research was to investigate the ability and effectiveness of embedding sensors into the long bone and flesh segments. In order to accomplish this, a series of foil strain gages and accelerometers for the long bones and impact sensors for the flesh was investigated.

4.2.1 Long Bone Sensors

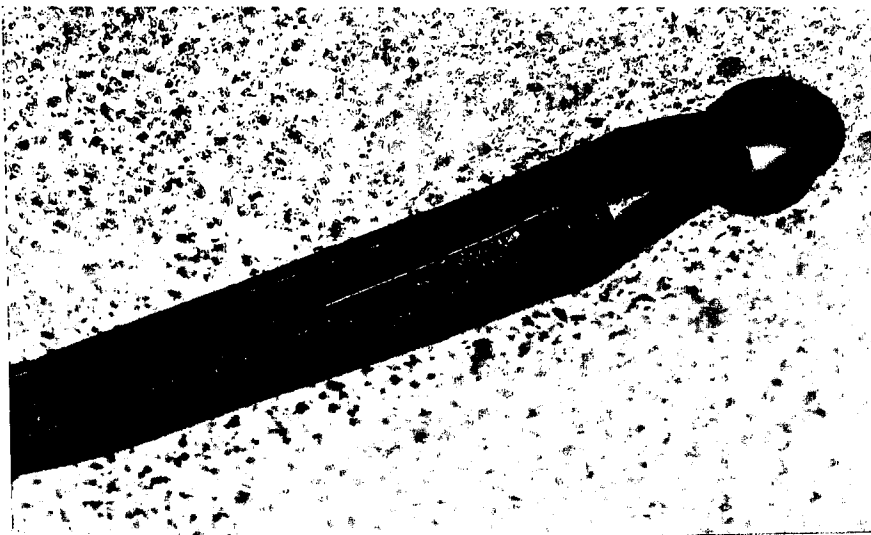
Based on panel coupon tests, it was determined that the fiber optic lead, foil gage leads and solder joints were too fragile to confidently survive the high pressures and differential fiber movement during net molding processing and subsequent handling during testing. In addition, a rather complex linearizing circuit was needed for the fiber optic gages to extract meaningful strain data. Because of these findings, the Post Embedded Gage (PEG) methodology was developed for the long bone gages. A summary of the advantages of the PEG methodology was given in Table 4.2.1-1. The experience with the foil and fiber optic cables breaking at the exit of the composite coupon and the requirement by the Air Force for a quick disconnect capability lead to the use of embedded/surface mount connectors placed on the lateral-proximal section of each bone segment. As shown in Figure 4.2.1-1 this configuration had the advantage of being rigidly attached to the bone with no exposed wires however, care during fabrication had to be used to keep the resin from "wicking" up into the connector and coating or clogging the pins. In addition, if there was a faulty signal, it was difficult to tell if there was a bad connection at the connector or a problem with the gage. It is recommended that future connectors be placed on a "pig tail" extending several inches from the long bone. Making a solder connection inside the PEG layer from the lead wires to an external cable would minimize any potential for wire damage and would make the connector accessible without limiting its quick disconnect capabilities. This approach was used successfully on the flesh.

4.2.2 Flesh Instrumentation

The instrumentation for the flesh was a piezoresistive foil sensor which outputs a voltage in response to an applied displacement or stress. The particular sensor selected for the ABC Man program was a Kynar piezoresistive polymer film on a mylar substrate manufactured by AMP sensors. The sensor produces a linear output versus energy or momentum and can be custom fabricated with any grid size or sensor geometry. Figure 4.2.2-1 shows a typical sensor voltage output as a function of impact velocity.

Table 4.2.1-1. Long Bone Sensor Summary

Sensor	Advantage	Disadvantage
Embedded Fiber Optic	Fast response, high sensitivity	Fragile optic cable (net molding processing), requires complex signal processing
Embedded Foil Gage	Good response characteristics well understood behavior, adequate sensitivity	Fragile solder connectors for net molding processing
PEG Foil Gages	Good response, mature technology, high reliability	Requires semi or fully cured substrate
Piezoresistive Accelerometers	Small profile, rugged high sensitivity	Single axis requires multiple gages



Femur PEG Connectors



Tibia PEG Connectors

Figure 4.2.1-1. Photographs of Femur and Tibia On-Board Quick Disconnect Connectors.

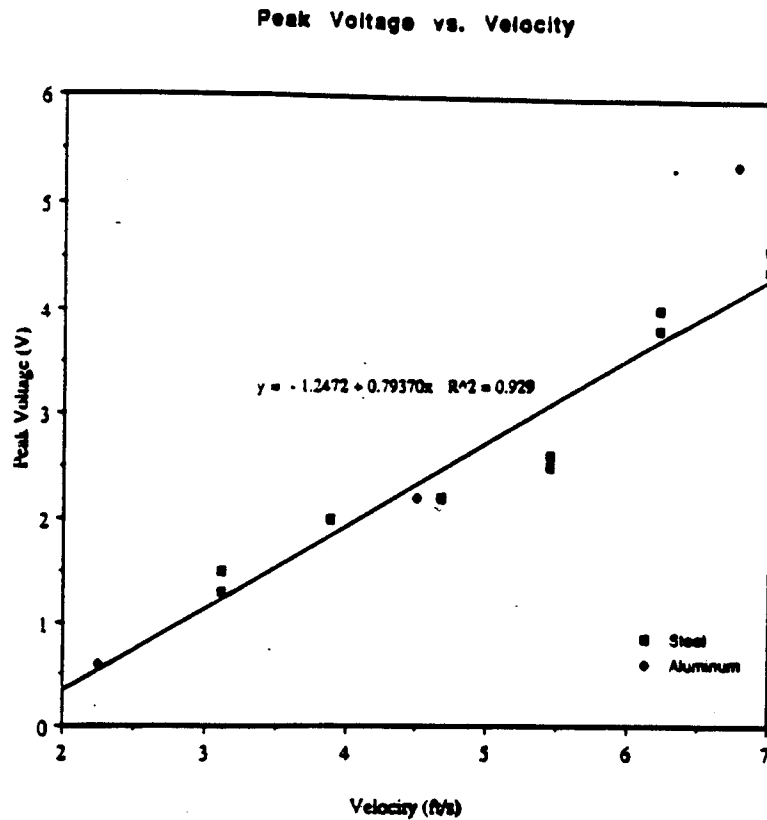


Figure 4.2.2-1. Flesh Tactile Foil Sensor Output as a Function of Impact Velocity.

After a series of coupon tests and discussions with the Air Force, a specific sensor layout, shown in Figure 4.2.2-2, with 1/4 (6.35mm) square pads on 1.0" (25.4mm) centers was selected. This distribution would provide approximately a 0.5 inch (12.7mm) resolution.

For commonality in manufacturing of the femur and tibia sensor panels, each sensor was fabricated as a full femur/tibia sensor panel. This layout was designed so that the entire sensor panel would fit the femur and the top 18 sensors, shown in Figure 4.2.2-2, could be cut to fit the tibia. Figure 4.2.2-3 is a scaled flesh tactile foil fabrication layout. The sensor pads and ribbon connector leads were fabricated as a single unit which could be cut to accommodate the tibia or femur layout. As noted in Section 3.1.2, and shown in Figure 4.2.2-3, flesh instrumentation backplane and sensor pads were bonded with a z-axis interlayer to form a flexible circuit board. The wires coming off of the circuit board were manufactured as a straight ribbon cable. Routing the ribbon cable was achieved by folding the ribbon cable onto itself to form the appropriate angle (the femur and tibia angles are different) between the exit from the tactile array to the exit

of the bone segment connectors flesh access hold as shown in Figure 4.2.2-4. The ribbon cable was terminated with a Berg connector. The tactile foil sensor circuit board was installed in the flesh by gluing the sensor into the femur or tibia pocket and bonding a flesh cap over the pocket to enclose the entire sensor. Figure 4.2.2-5 shows the femur and tibia sensor in place prior to bonding the flesh covering.

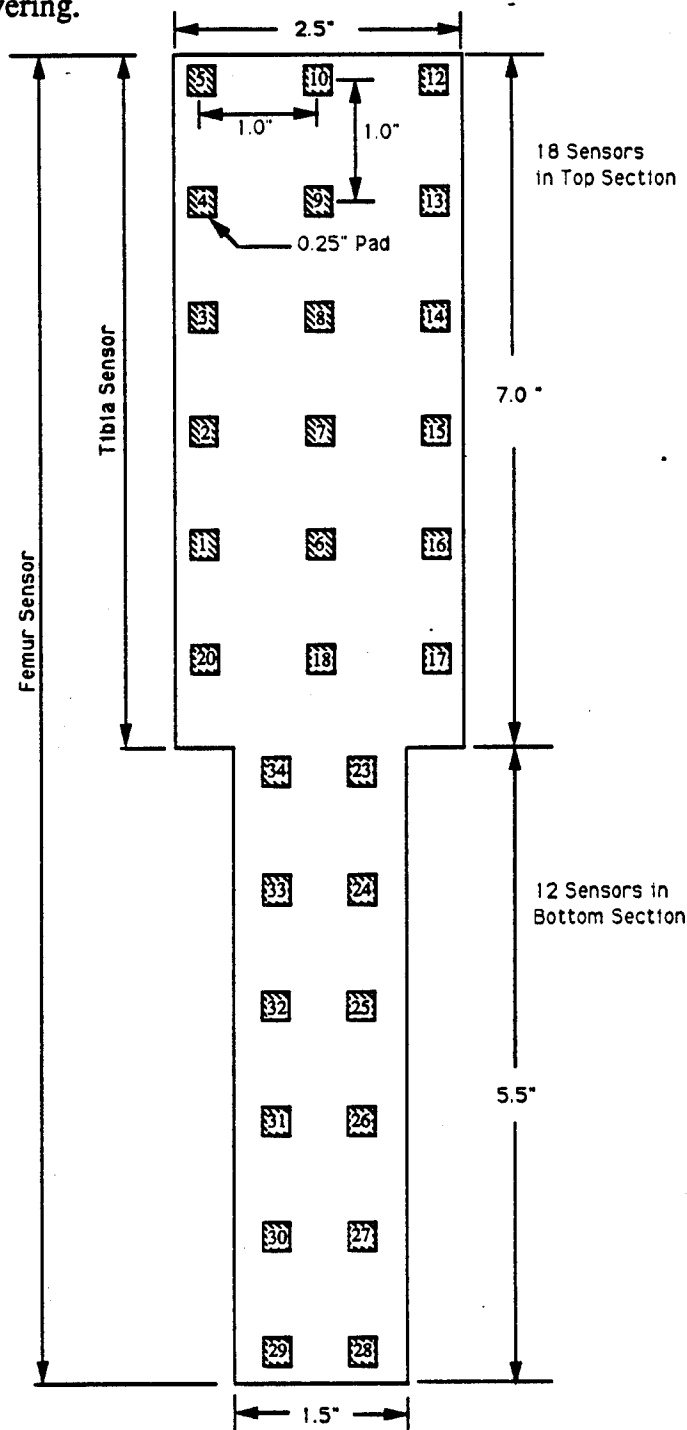


Figure 4.2.2-2. Layout for Flesh Sensors.

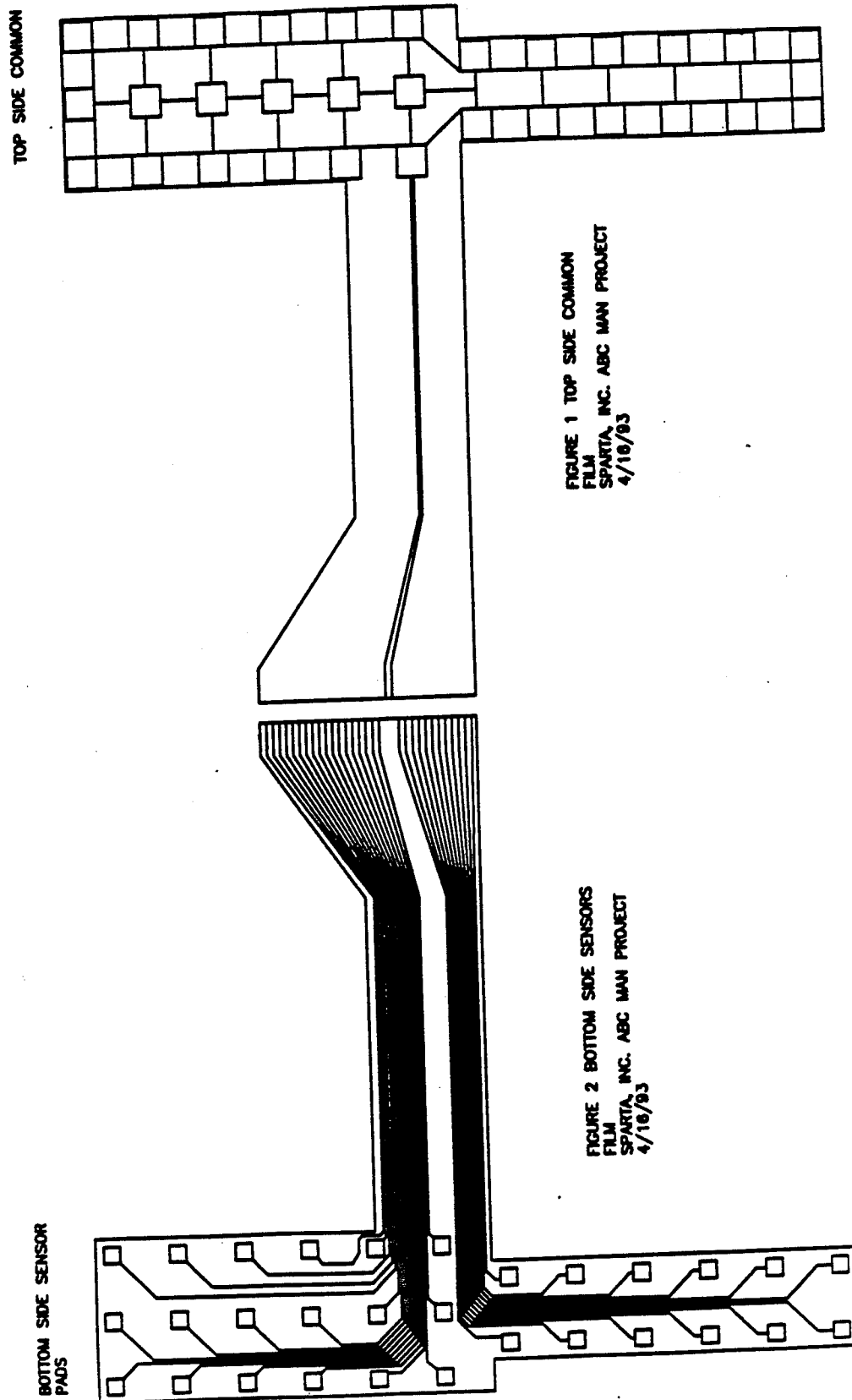


Figure 4.2.2-3. Scaled Tactile Foil Sensor Layout.

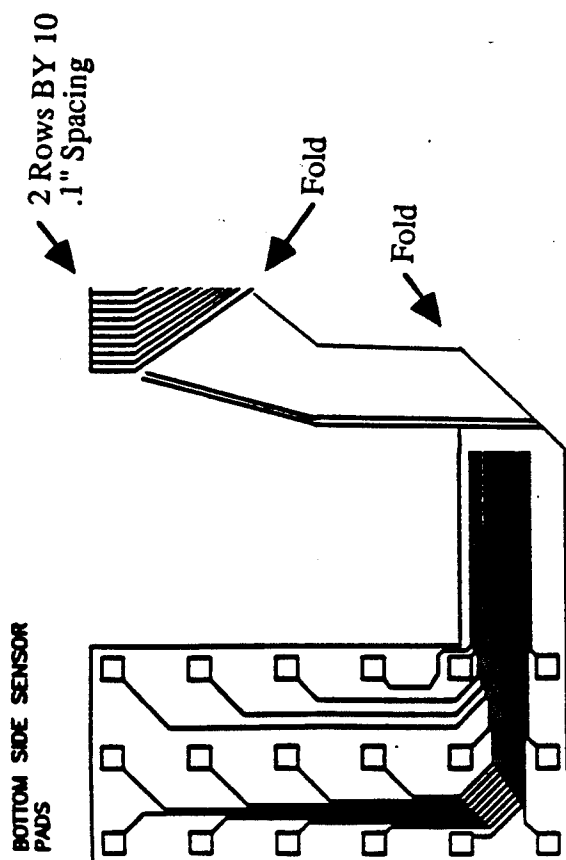
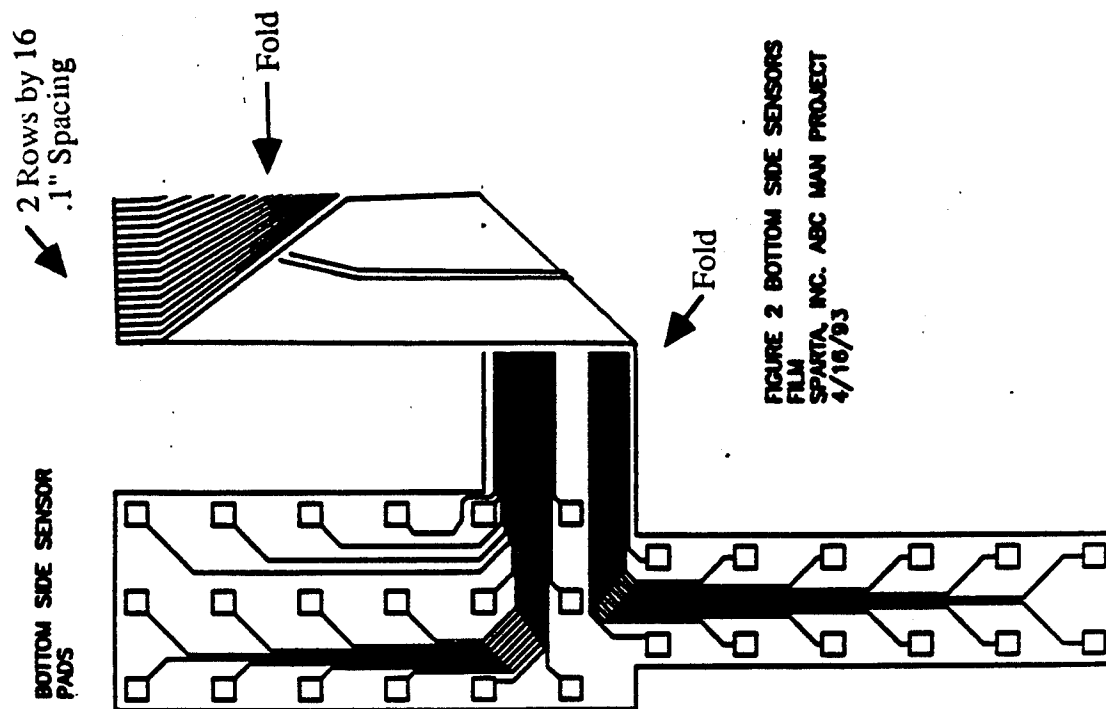
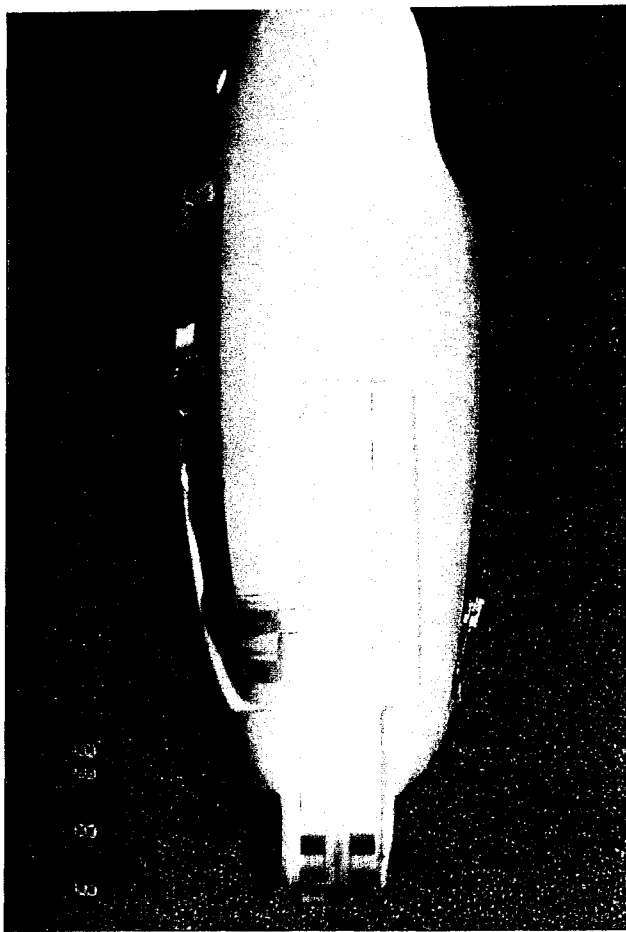
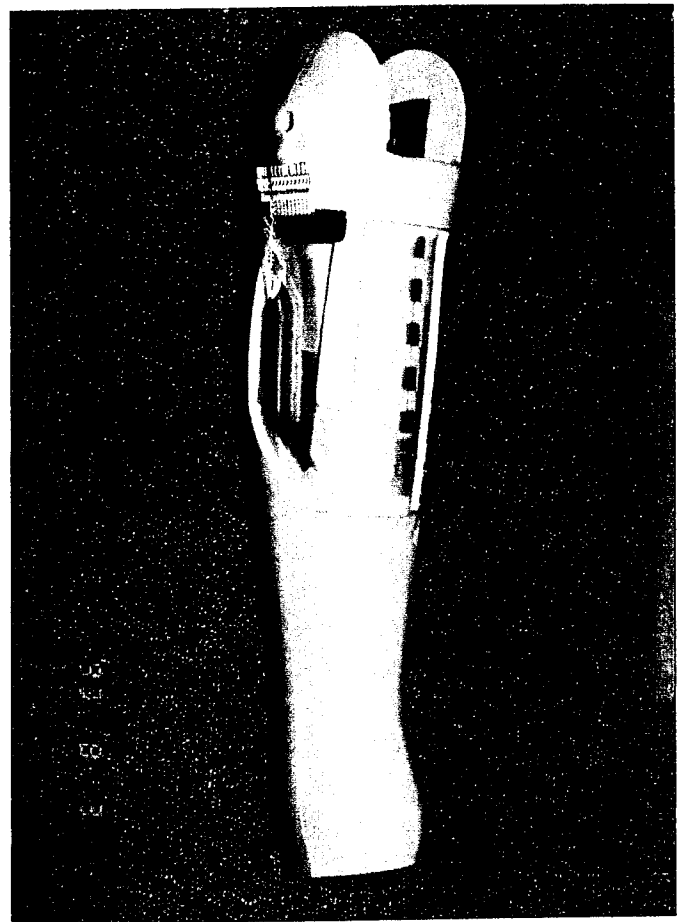


Figure 4.2.2-4. Tactile Foil Sensors Showing Folded Installation.



Femur Showing Placement of
Tactile Foil Sensor



Tibia Showing Placement of
Tactile Foil Sensor

Figure 4.2.2-5. Placement of Tactile Foil Sensors in the ABC Man Femur and Tibia Flesh.

A flexible ribbon cable was connected to the sensor circuit board leads with a Berg pinned connector inside the flesh pocket. The ribbon cable exited the flesh at the proximal end on the lateral side with an approximately a 6 inch (152mm) external lead to a pinned connector. Although this configuration was suitable and worked for the purpose of the ABC Man program, it is felt by the authors that a more suitable flesh sensor installation would be to mold the sensor in place. This could be accomplished by bonding the sensor to a "flesh" pad which could be placed in the mold and then molded over. This would likely give a more durable and reproducible sensor placement as well as have a higher esthetic quality.

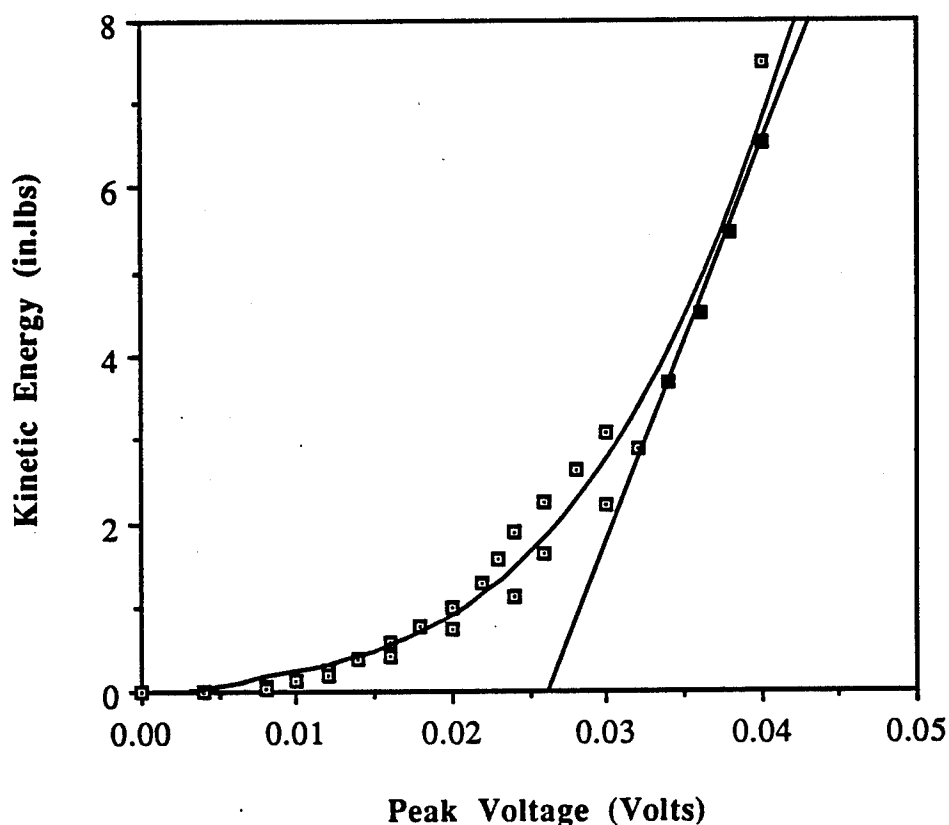
4.3 Static and Dynamic Test Results

4.3.1 Calibration Tests

The long bone accelerometers were calibrated at the factory and the calibration data were supplied with the accelerometers. The PEG strain gages however required a set of calibration tests to quantify specific gage readings with a known load.

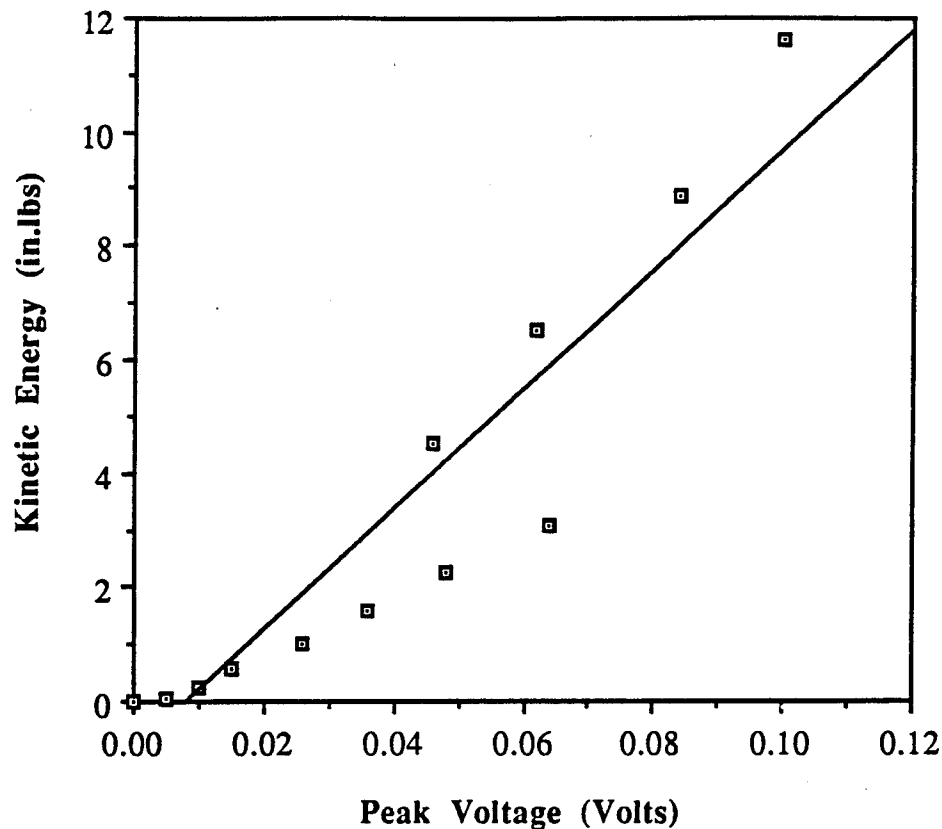
Both the femur and tibia were subjected to a series of axial and bending loads. The strain gage readings were taken as a function of the applied load. This load-strain history along with the finite element analysis was used to derive force and moment coefficients for the femur and tibia respectively. This data were reported in Section 3.6.3.

The tactile foil calibration was accomplished by impacting the actual flesh with a known mass at a given pull back distance (height). In order to obtain the correct sensor response, the calibration test were conducted with the long bone inside the flesh. This gave a calibration curve for the femur and tibia (see Figure 4.3.1-1). It is interesting to note that the femur curve, with its thick flesh between the sensor and bone, is well behaved. However, the tibia data shows a difference between the heavy steel impactor versus the lighter aluminum impactor.



Femur Flesh Sensor Calibration Data

Figure 4.3.1-1. Tactile Foil Calibration Curves for the ABC Man Flesh.



Tibia Flesh Sensor Calibration Data.

Figure 4.3.1-1. Tactile Foil Calibration Curves for the ABC Man Flesh.

This difference is believed to be due to the inertial rebound effect of the relatively thin tibia skin against the bone and reflects the inertial driven velocity of the steel vs. aluminum impactor. For a given impact energy the heavier steel impactor would not slow down as much as the aluminum mass thereby giving a higher voltage output. This effect is not seen in the femur because the thick femur flesh "smooths" out the impact response, providing a consistent calibration curve.

4.3.2 Sled Test Results

The sled test results, described in Section 3.7, showed that the mass distribution between the bone and flesh segments could have a significant effect on the response of the body segment. The initial look at the sled test data showed loads from the strain gages were apparently inconsistent with the segment acceleration data. Further investigation into this response (which included two additional dynamic finite element models) revealed that the coupling between the stiff lightweight bones and the soft heavy flesh caused an out-of-phase load-acceleration history. Figure 4.3.2-1 compares the acceleration history of the femur for a stiff flesh (lumped) and a soft flesh (distributed) mass compared to the actual test data. From the figure, the acceleration profile

of the distributed soft flesh more closely matched the actual test data. As would be expected, the acceleration profiles are a function of the mass distribution and the relative compliance of the flesh and bone mass.

20G Femur Acceleration Comparison of Lumped vs Distributed F

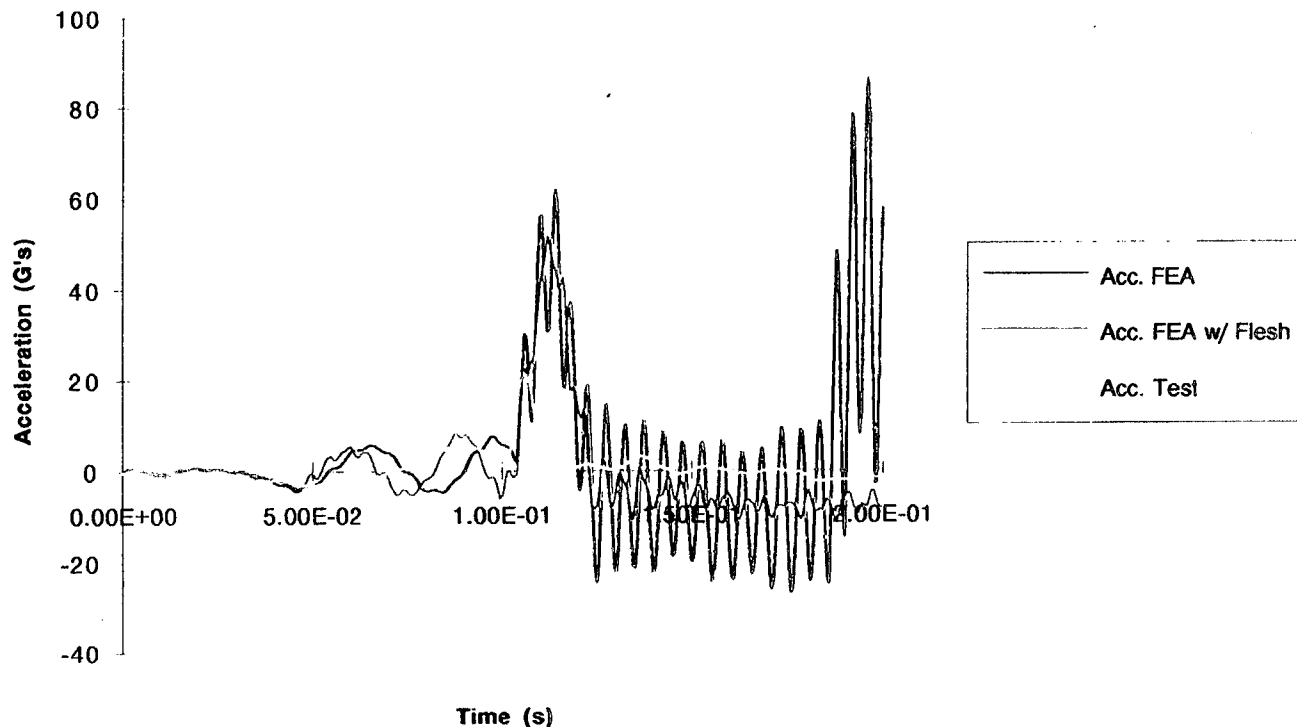


Figure 4.3.2-1. Comparison of Actual Acceleration Test Data with Predicted Data for Stiff Segment Mass (Ass. FEA) and Soft Flesh Distributed Mass (FEM with Flesh).

The effect of the soft flesh of the femur on the loads is shown in **Figure 4.3.2-2**. Although the profiles are not exact due to the simplifying modelling assumption discussed in Section 3.7, the load trends show a definite effect of the increased load due to the soft flesh sliding on the long bone. The peak force of 1100 lbs is very close to the measured peak load of about 1200 lbs. The model also predicted the rebound load (second, lower peak). Unfortunately, the fidelity of the model did not allow a closer approximation of the peak load profile, but does demonstrate the contribution of the flesh mass. **Figure 4.3.2-3** shows the tibia load response. The actual test data are much less than the predicted loads, however, as the model was refined

i.e., lumped mass to distributed mass, the predicted loads started to approach the test data. Due to the complexity of the model, it was not possible to put the true sliding flesh on the tibia. However, based on the femur results, if this was taken into account the predicted load would be very close to the test loads. **Figure 4.3.2-4** shows a deformed plot (5x magnification) of the femur/tibia finite element model at full extension. In this figure, it can be seen that the flesh has a definite axial deformation and loads the respective long bone at the distal end of each long bone. The line on the far left is the exposed beam of the upper femur which resulted from the flesh sliding distally. In addition, there are radial deformations of the flesh which cause a coupling between the bending and axial loads in each long bone.

As can be seen from the above data, the compliance and mass of the flesh has a significant effect on the acceleration and load profile experienced by the skeletal segment. There is a definite coupling between the flesh reactions and the dynamic environment to the overall displacement and load history experienced by the test manikin or human occupant. If the majority of the segment mass is in the skeletal segment, as in current test manikins, inaccurate load, accelerations, and position histories will be obtained. In order to accurately simulate a true human response, it is necessary to have an accurate mass distribution and relative compliance between the skeletal components and the flesh components.

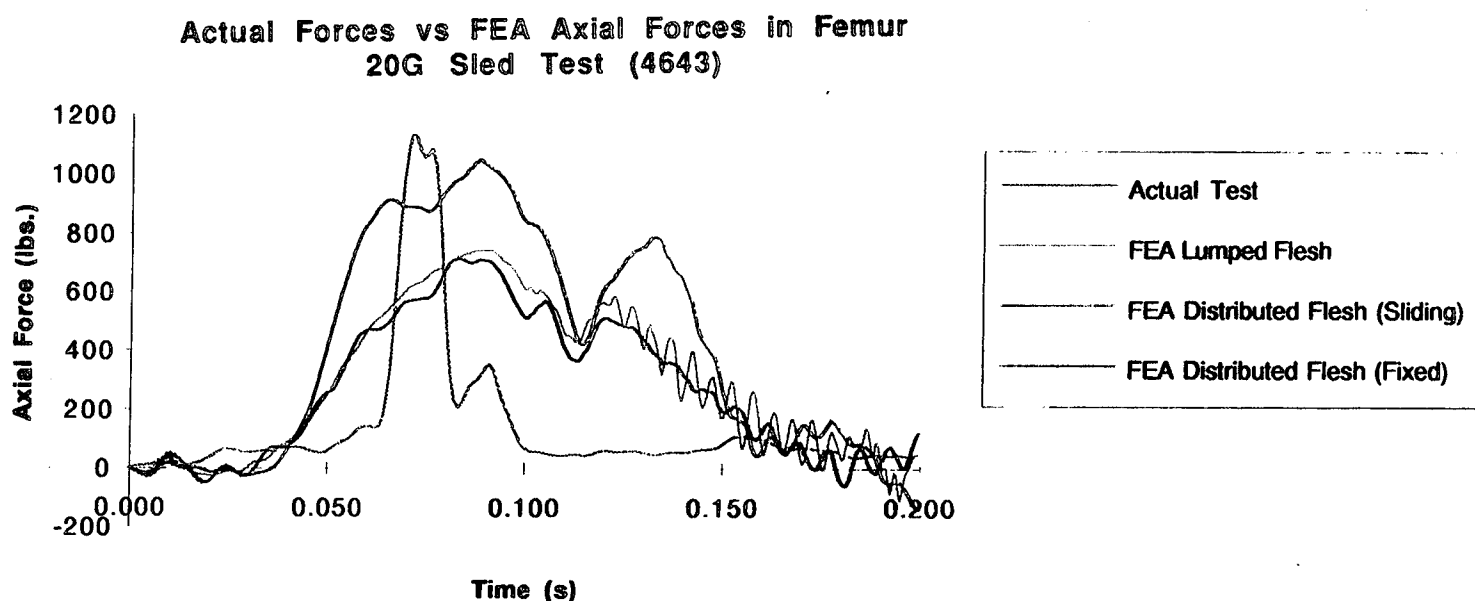


Figure 4.3.2-2. Comparison of Femur Loads Showing the Effect of the Soft Sliding Flesh on the Stiff Bone.

Actual Forces vs FEA Axial Forces in Tibia 20G Sled Test (4643)

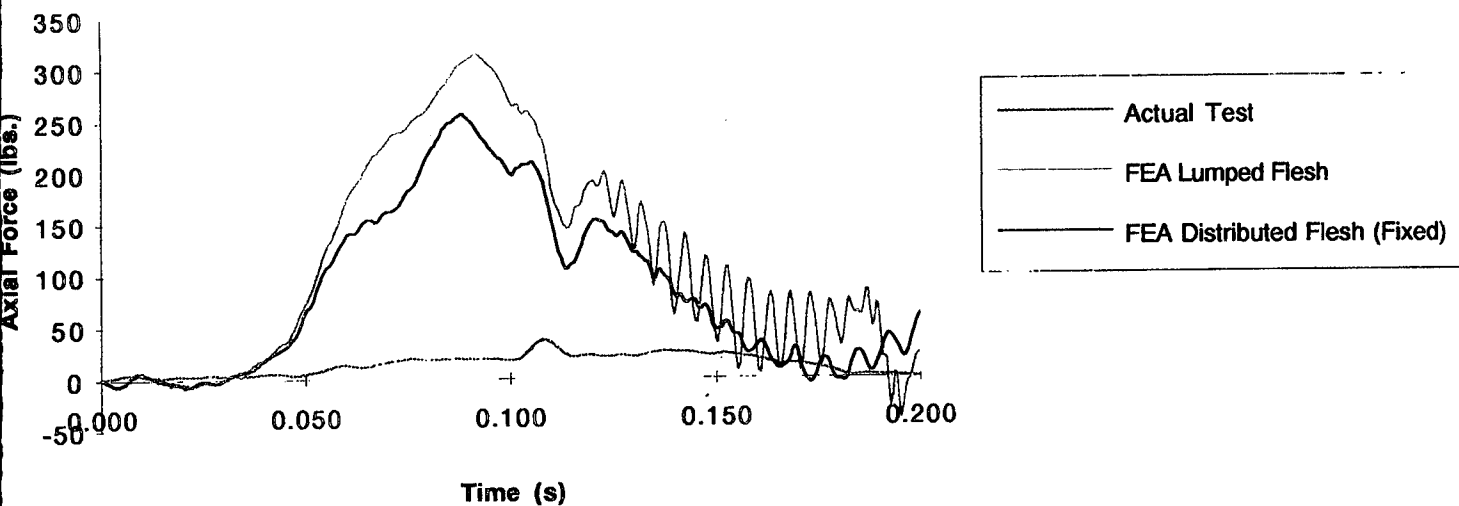


Figure 4.3.2-3. Comparison of Soft Flesh on the Tibia Loads with Test Loads (Not True Sliding Flesh Included in these Calculations).

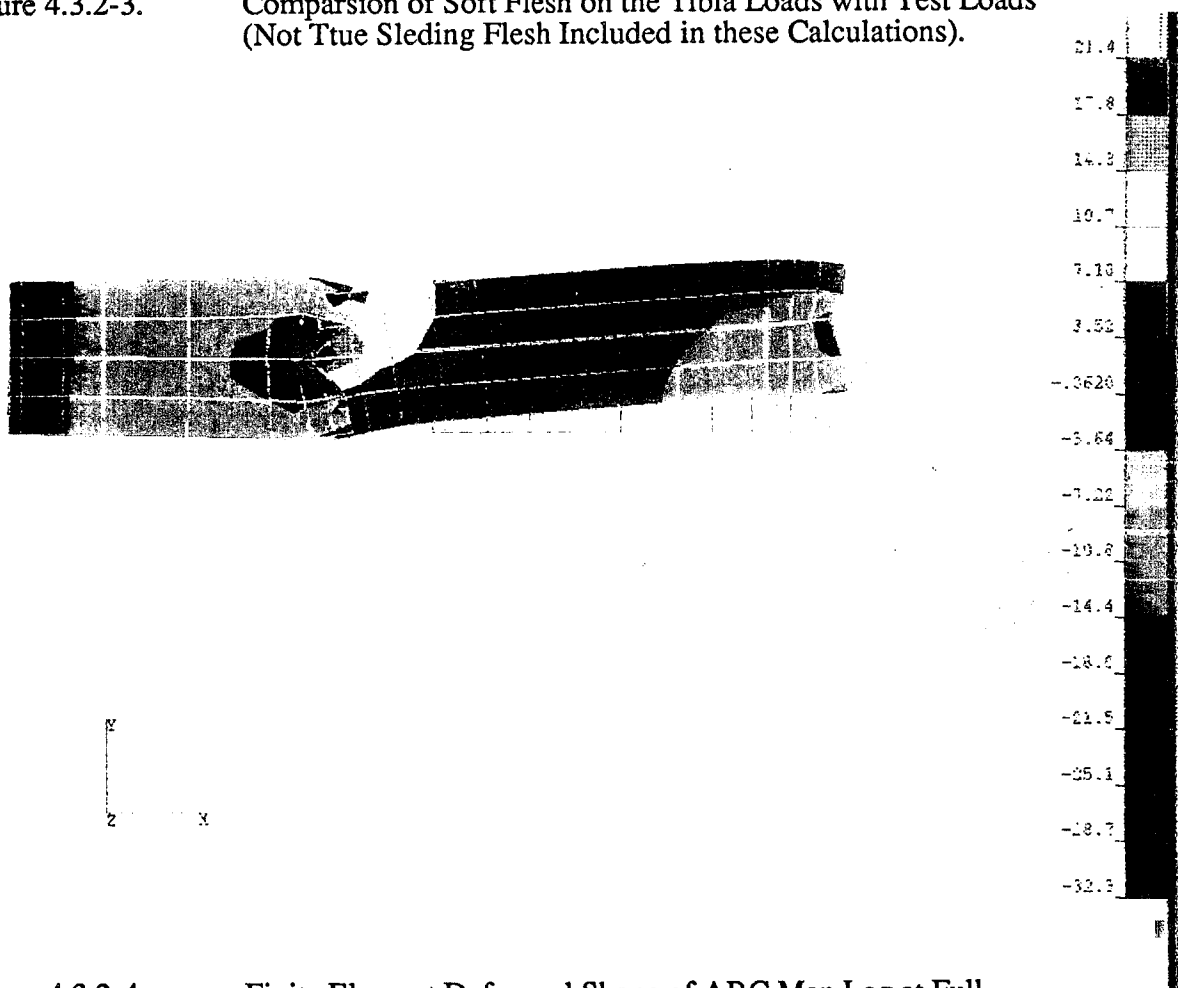


Figure 4.3.2-4. Finite Element Deformed Shape of ABC Man Leg at Full Extension with Distributed Sliding Flesh.

5.0 REFERENCES

1. Foster, King J., Kortge, J. O.; Wolawin, J. J., "Hybrid III - A Biochemically Based Crash Test Dummy," Safety Research and Development Laboratory, Environmental Activities Staff, General Motors Corporation.
2. Tennant, J. A., Jensen, R. J. Potter, R. A., "GM-ATD 502 Anthropomorphic Test Dummy Development and Evaluation"; Report on the Fifth International Technical Conference on Experimental Safety Vehicles, Long, England, June, 1974.
3. Anthropomorphic Test Dummies Handbook; Humanoid Systems, Carson California, Nov. 1986.
4. Higgins, M.A., Roberts, E. O., "The USAF's Crest Program"; Safe Journal, Vol. 15, No. 3, Aerospace Medical Division CREST Advanced Development Program Office, Wright-Patterson AFB.
5. "Materials Engineering, Materials Selector 1990", Penton Publishing, December 1989.
6. SPARTA, Inc. in-house data base.
7. Moreno White; Dan Jacobson; "Composite Materials for Manikin Skeletal Components"; Phase I SBIR Final Report; SPARTA, Inc.; Prepared for Biomechanics Branch, Biodynamics and Bioengineering Division, Armstrong Aerospace Medical Laboratory, Human Systems Division, Wright-Patterson AFB, Ohio; May 21, 1990; Contract No. F33615-88-C-0548 Item No. 001.
8. Personal Communications with Mr. M. K. Bebe, Humanetics, Inc., Norwalk, OH.
9. Composite Skin and Embedded Fiberoptic Pressure Sensors, D. Mitchell, 1991.
10. Non Destructive Testing of Composite Structures using Embedded Optical Fibers a Mechanical Interaction Model, D. Engrand, 1990.
11. Embedded Fiberoptic Pressure and Temperature Sensors Enable Cure Monitoring of Pultruded Composite Materials, D. Cable, 1990.
12. A Program to Compute Strain Transformations in Composite Materials, R. Ahmed, 1990.
13. Development of Intelligent Structures, J. Scragg, 1990.
14. Current Status and Future Prospects of Smart Composite Materials, R. Davidson, 1990.
15. Strain and Dynamic Measurement Using Fiberoptic Sensors Embedded into Graphite/Epoxy Tubes, D. Dehart, 1989.
16. Measurement of Physical parameters in Composite Materials using Embedded Fiberoptic Sensors, E. Saaki, 1989.
17. Composite Integrity Monitoring, R. Rudd, 1989.
18. Laboratory Feasibility Study of a Composite Embedded Fiberoptic Sensor for Measurement of Structural Vibrations, C. Dube, 1988.

19. Resistance Foil Strain Gage Technology as Applied to Composite Materials, M. Tuttle, 1985.
20. Embedded Gage Impact Study, S. Schramm, 1984.
21. Residual Stress in Angle Plied Laminates and their Effects on Laminate Behavior, C. Chamis, 1978.
22. Lamination Residual Stresses in Fiber Composites, I. Daniel, 1975.
23. Strain Gage Techniques for Internal Strain Measurements in Boron-Epoxy Composite, R. Egger, 1973.
24. Fiber Optic Smart Structures and Skins II, SPIE Proceedings, Volume 1170, 1989, pp. 143-149.
25. C.Y. Warner, M.G. Wille, S.R. Brown, S. Nilsson, H. Mallander, and M. Kock; "A Load Sensing Face Form for Automotive Collision Dummy Instrumentation" Proceedings - SAW International Congress and Exposition, Detroit Mich. Feb. 24-28 1986. SAE publication No. 860197.
26. D.L. Allsop, C.Y. Warner, M.G. Wille, D.C. Schneider, and A.M. Nahum; "Facial Impact Response - A Comparison of the Hybrid III Dummy and Human Cadaver" Proc. 32nd Stapp Car Crash Conference, Oct. 1988. SAE Publication No. 881719.
27. T.R. Perl, S.N. Nilsson, I. Planath, and M.G. Wille; "Deformable Load Sensing Hybrid III Face", Proc. 33rd Stapp Car Crash Conf., Oct. 1989, SAE Publication No. 892427.
28. I. Planath and S. Nilsson; "Testing and Evaluation of a Hybrid III Load Sensing Face", *Accident Analysis & Prevention* 21 (5): 483-492, 1989.

APPENDIX A

**Letter of Support from a Potential
Commercial User of ABC Man
Developed Technology**

April 6, 1990

Captain Chris Taylor
Modeling and Analysis Board
Biodynamics and Bioengineering Division
AAMRL/BBM
Wright Patterson AFB, Ohio 45433-6573

RE: Industry Support for the SPARTA Phase II SBIR
"Advanced Biofidelic Composite Manikin" Proposal

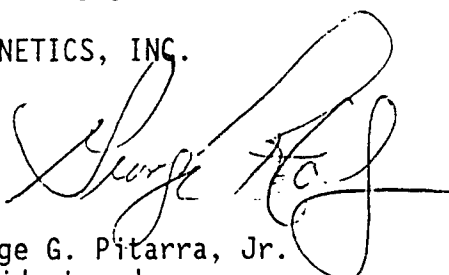
Dear Capt. Taylor:

Humanetics is involved in the development and sale of advanced anthropomorphic test manikins for a wide variety of commercial and aerospace applications for a variety of customers including GM, Ford, Chrysler, and DoD (Air Force, Army). As a team member on the proposed Phase II SBIR and a participant in the initial Phase I program, we are well aware of the scope of the proposed research effort. We believe that if the proposed Phase II program is successful, it would lead to highly improved biofidelic response in test manikins under dynamic loading such as experienced in crash or ejection seat scenarios. There is a recognized need in our industry for test dummies which more accurately reflect true human response and to accurately measure this response in dynamic situations. If the Phase II program proposed by SPARTA is successful, we would be highly interested in incorporating this technology in our advanced test manikins. We have reviewed the proposed concept with several of our major customers (GM, Ford, Chrysler, Air Force) and have determined that there is a significant interest on their part in using these advanced test dummies in their own programs.

We believe that the successful outcome of the proposed Phase II program would present a quantum jump in the advancement of anthropomorphic simulation. We highly encourage you to favorably consider funding the entire proposed program.

Very truly yours,

HUMANETICS, INC.



George G. Pitarra, Jr.
President and
Chief Executive Officer

Encl.

cc: Mr. Moreno White/SPARTA, Inc.
Lt. Eric Spittle

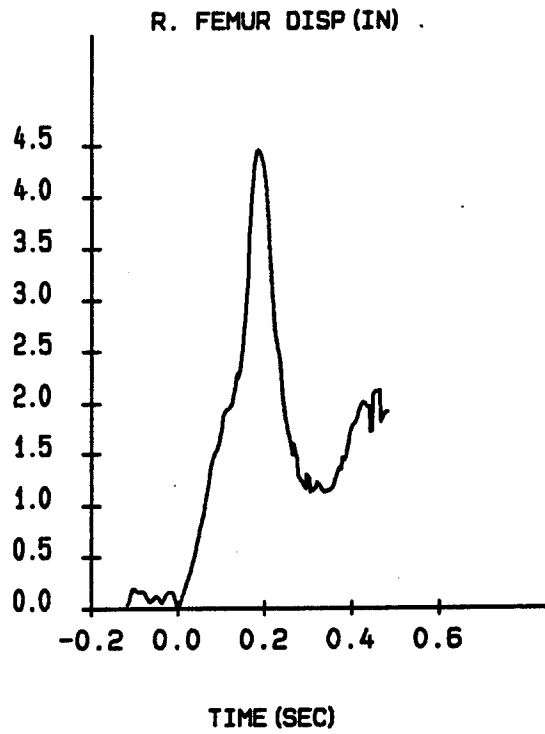
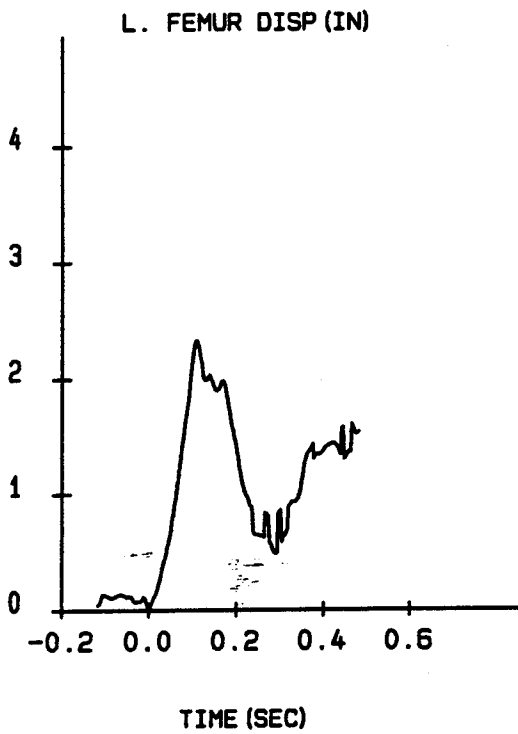
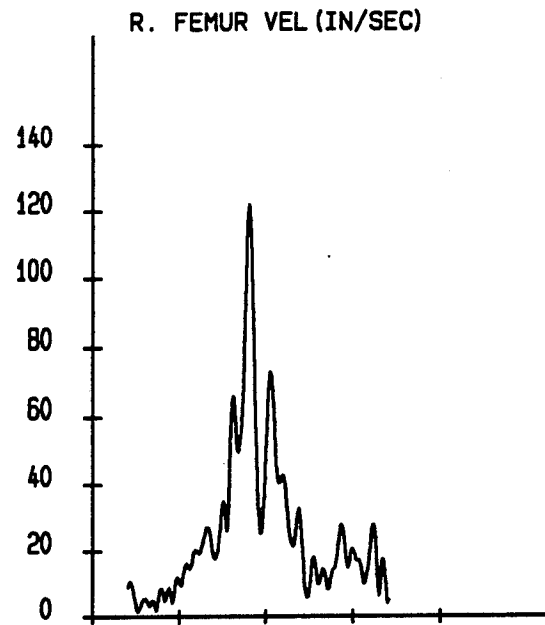
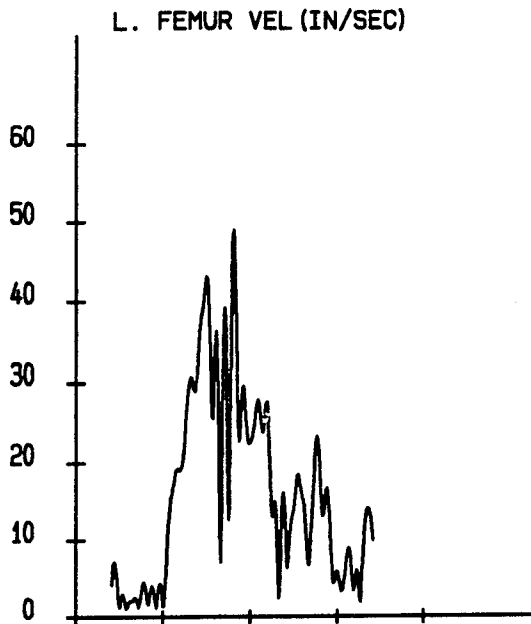
APPENDIX B

Sled Test Data

TEST 1 (4637) 5.5 G

SPARTA -GX

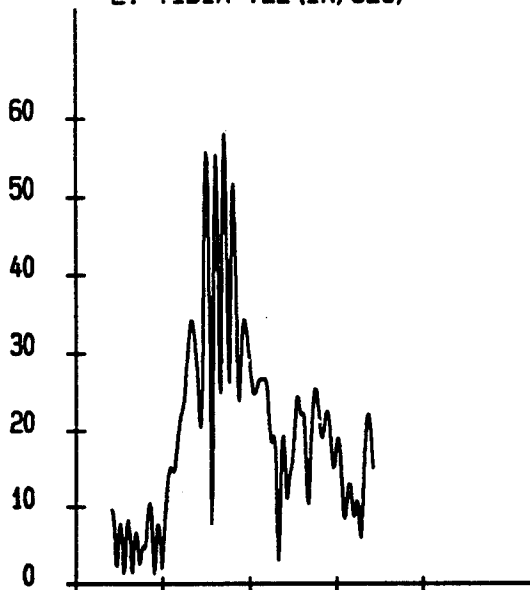
TEST: 4637 DATE: 23-SEP-1993 SUBJ: HB3-50 CELL: A



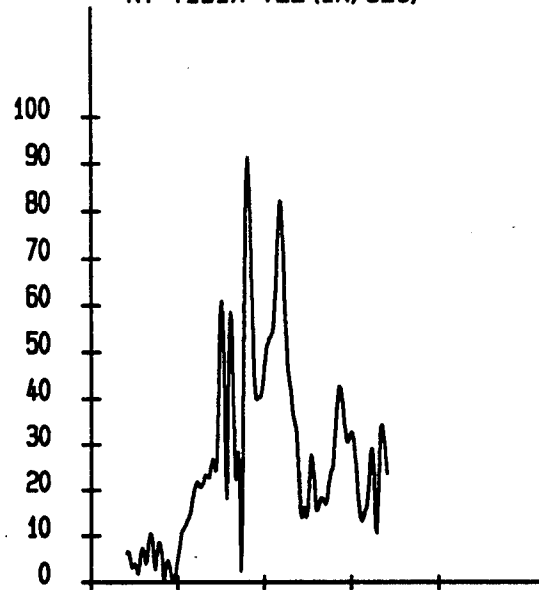
SPARTA -GX

TEST: 4637 DATE: 23-SEP-1993 SUBJ: HB3-50 CELL: A

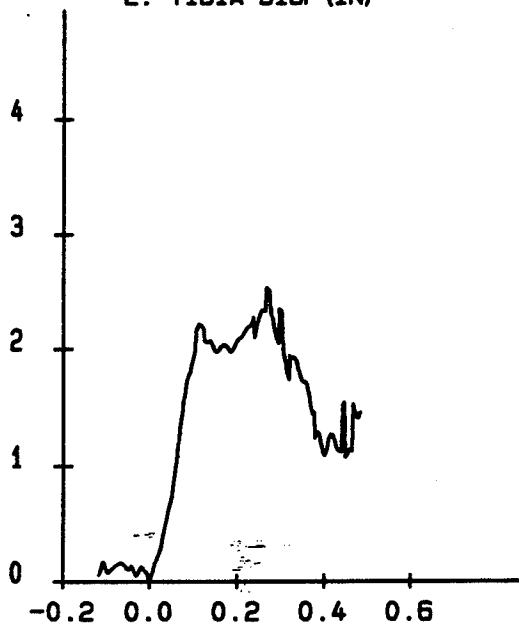
L. TIBIA VEL (IN/SEC)



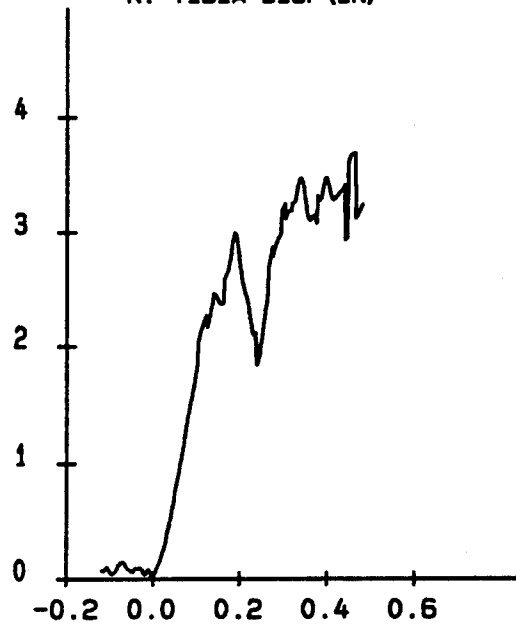
R. TIBIA VEL (IN/SEC)



L. TIBIA DISP (IN)



R. TIBIA DISP (IN)

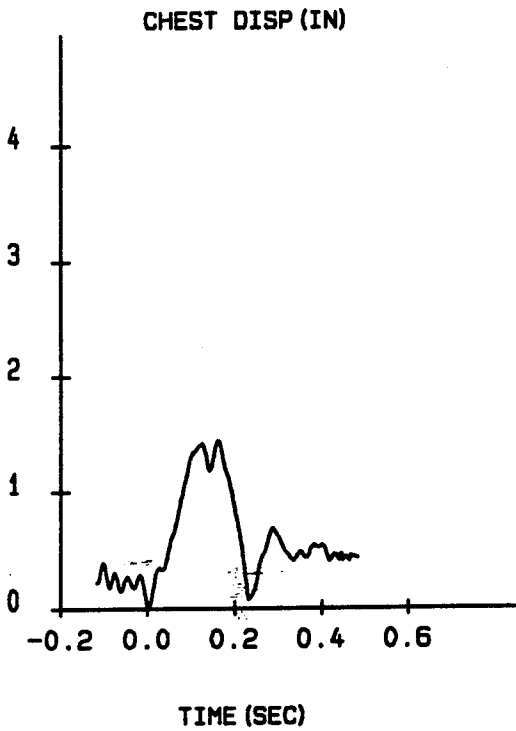
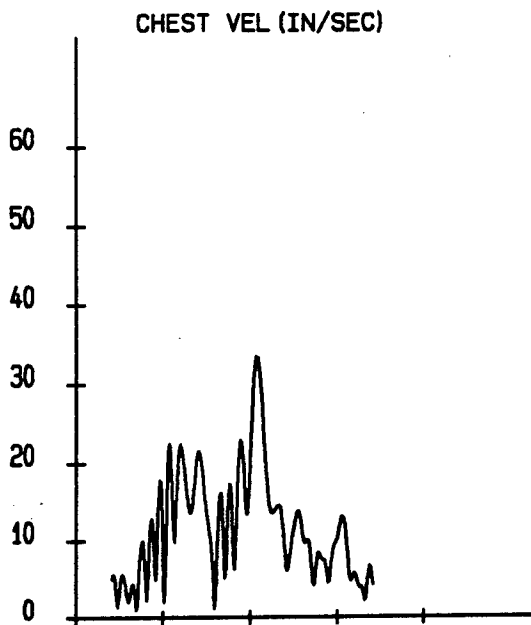


TIME (SEC)

TIME (SEC)

SPARTA -GX

TEST: 4637 DATE: 23-SEP-1993 SUBJ: HB3-50 CELL: A



SPARTA -GX

TEST: 4637 DATE: 23-SEP-1993 SUBJ: HB3-50 CELL: A

RELIABILITY FACTORS (IN)

TARGET DESCRIPTION	MAXIMUM	MINIMUM	AVERAGE	STANDARD DEVIATION	AT MAX DISPLACEMENT
1 L. FEMUR	0.2520	0.0009	0.0678	0.0442	0.0102
2 R. FEMUR	1.1273	0.0004	0.3018	0.3510	0.1317
3 L. TIBIA	0.2101	0.0009	0.0750	0.0459	0.0672
4 R. TIBIA	0.1831	0.0007	0.0679	0.0424	0.0364
5 CHEST	0.3303	0.1293	0.2091	0.0383	0.1586

TARGET	MAXIMUM	TIME(SEC)	MINIMUM	TIME(SEC)
L. FEMUR				
POSITION(IN)				
X AXIS	22.5736	0.1080	20.3210	0.0000
Y AXIS	4.8880	0.4660	3.3873	0.0220
Z AXIS	7.4233	0.2660	6.0946	0.1220
VELOCITY(IN/SEC)	48.8915	0.1620	1.3929	0.0000
ACCELERATION(G)	7.4363	0.1540	0.3561	0.4720
DISPLACEMENT(IN)				
X AXIS	2.2526	0.1080	0.0000	0.0000
Y AXIS	1.3978	0.4660	-0.1029	0.0220
Z AXIS	0.4866	0.2660	-0.8421	0.1220
RESULTANT	2.3339	0.1080	0.0000	0.0000
R. FEMUR				
POSITION(IN)				
X AXIS	23.4968	0.1760	20.9436	0.0000
Y AXIS	-3.2046	0.1920	-8.0614	0.4640
Z AXIS	9.5341	0.0840	6.2860	0.1760
VELOCITY(IN/SEC)	121.8895	0.1620	4.0608	0.4800
ACCELERATION(G)	15.9106	0.1820	0.3741	0.3040
DISPLACEMENT(IN)				
X AXIS	2.5532	0.1760	0.0000	0.0000
Y AXIS	3.1254	0.1920	-1.7315	0.4640
Z AXIS	1.0166	0.0840	-2.2315	0.1760
RESULTANT	4.4481	0.1840	0.0000	0.0000

SPARTA -GX
 TEST: 4637 DATE: 23-SEP-1993 SUBJ: HB3-50 CELL: A

TARGET	MAXIMUM	TIME(SEC)	MINIMUM	TIME(SEC)
L. TIBIA				
POSITION(IN)				
X AXIS	27.8851	0.1140	25.5354	0.3040
Y AXIS	5.4314	0.4460	3.6565	0.1040
Z AXIS	5.0496	0.2660	2.4455	0.4820
VELOCITY(IN/SEC)	57.9483	0.1420	3.0410	0.2660
ACCELERATION(G)	10.4465	0.1100	0.4074	0.1900
DISPLACEMENT(IN)				
X AXIS	2.2068	0.1140	-0.1430	0.3040
Y AXIS	1.4933	0.4460	-0.2815	0.1040
Z AXIS	2.4686	0.2660	-0.1356	0.4820
RESULTANT	2.5301	0.2660	0.0000	0.0000
R. TIBIA				
POSITION(IN)				
X AXIS	29.7736	0.1400	27.3315	0.0000
Y AXIS	-3.8801	0.1900	-9.8287	0.4640
Z AXIS	5.5252	0.3020	2.2324	0.1720
VELOCITY(IN/SEC)	91.5300	0.1620	2.4358	0.1460
ACCELERATION(G)	13.8567	0.1800	0.3112	0.0520
DISPLACEMENT(IN)				
X AXIS	2.4422	0.1400	0.0000	0.0000
Y AXIS	2.2902	0.1900	-3.6584	0.4640
Z AXIS	3.0166	0.3020	-0.2762	0.1720
RESULTANT	3.6861	0.4640	0.0000	0.0000
CHEST				
POSITION(IN)				
X AXIS	13.4772	0.1600	12.0028	0.3820
Y AXIS	1.6897	0.4720	0.7505	0.2860
Z AXIS	20.3697	0.1160	19.4550	0.2380
VELOCITY(IN/SEC)	33.4088	0.2140	1.1016	0.1180
ACCELERATION(G)	4.6167	0.1660	0.0862	0.4380

SPARTA -GX

TEST: 4637 DATE: 23-SEP-1993 SUBJ: HB3-50 CELL: A

TARGET	MAXIMUM	TIME(SEC)	MINIMUM	TIME(SEC)
CHEST				
DISPLACEMENT(IN)				
X AXIS	1.2272	0.1600	-0.2473	0.3820
Y AXIS	0.2647	0.4720	-0.6746	0.2860
Z AXIS	0.8438	0.1160	-0.0708	0.2380
RESULTANT	1.4345	0.1600	0.0000	0.0000

SPARTA -GX

TEST: 4637 DATE: 23-SEP-1993 SUBJ: HB3-50 CELL: A

Note: Invalid samples are interpolated.

Samples 1145 through 1164 of the L. FEMUR target are invalid.
Invalid sample range occurred from 0.1200 seconds to 0.1580 seconds.

Samples 1167 through 1170 of the L. FEMUR target are invalid.
Invalid sample range occurred from 0.1640 seconds to 0.1700 seconds.

Samples 1175 through 1177 of the L. FEMUR target are invalid.
Invalid sample range occurred from 0.1800 seconds to 0.1840 seconds.

Samples 1180 through 1185 of the L. FEMUR target are invalid.
Invalid sample range occurred from 0.1900 seconds to 0.2000 seconds.

Samples 1163 through 1171 of the R. FEMUR target are invalid.
Invalid sample range occurred from 0.1560 seconds to 0.1720 seconds.

Samples 1184 through 1188 of the R. FEMUR target are invalid.
Invalid sample range occurred from 0.1980 seconds to 0.2060 seconds.

Samples 1195 through 1288 of the R. FEMUR target are invalid.
Invalid sample range occurred from 0.2200 seconds to 0.4060 seconds.

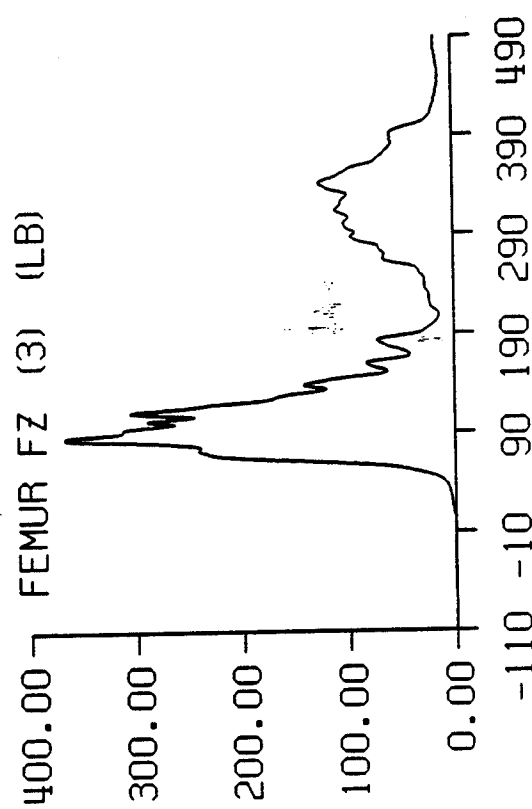
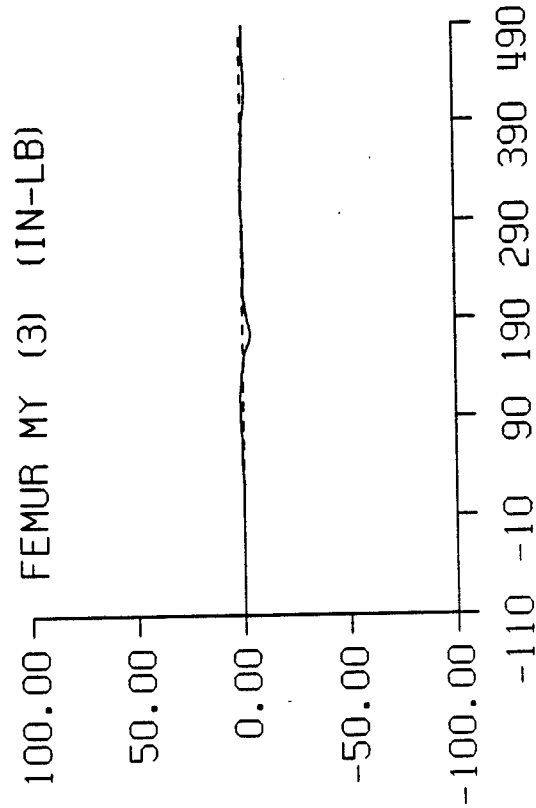
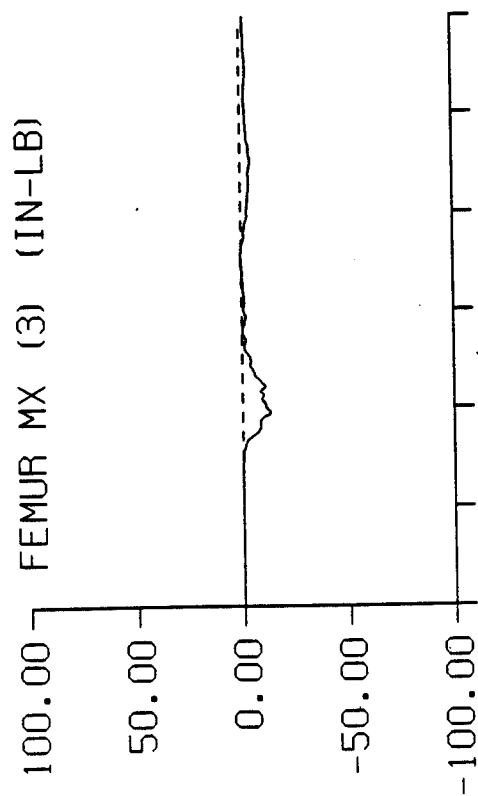
Samples 1161 through 1166 of the R. TIBIA target are invalid.
Invalid sample range occurred from 0.1520 seconds to 0.1620 seconds.

Sample number 1128 of target 6 is invalid.
Invalid sample 1128 occurred at 0.0860 seconds.

SPARTA -GX STUDY TEST: 4637

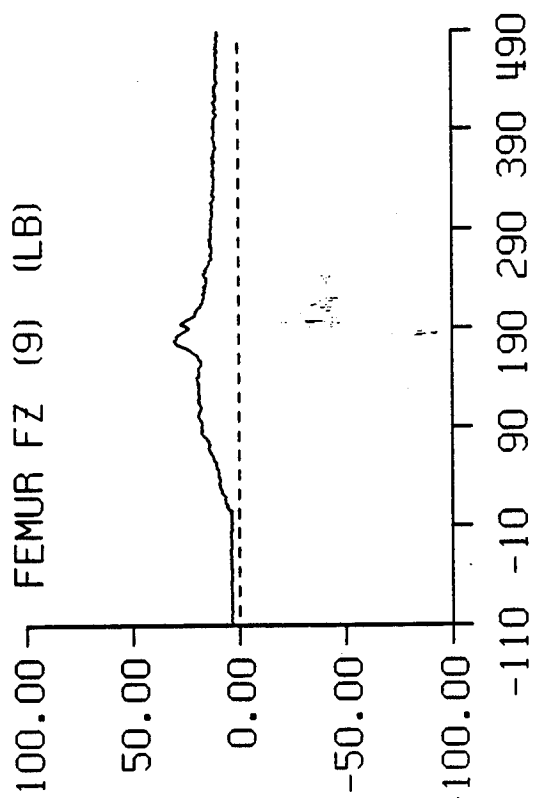
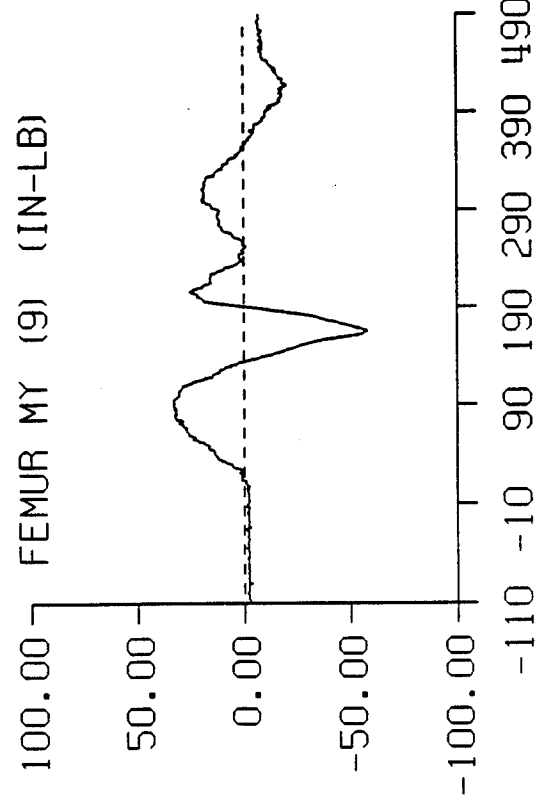
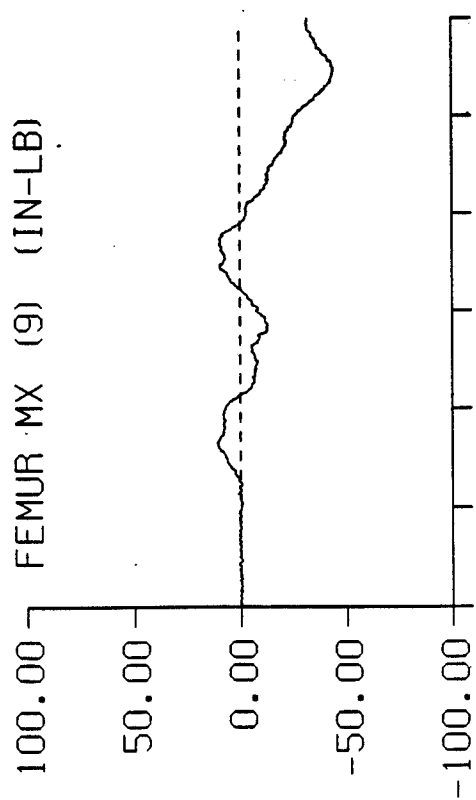
DATA ID	IMMEDIATE PREIMPACT	MAXIMUM VALUE	MINIMUM VALUE	TIME OF MAXIMUM	TIME OF MINIMUM
REFERENCE MARK TIME (MS)				-118.	
FEMUR					
MX (3) (IN-LB)	0.01	0.29	-12.84	243.	85.
MY (3) (IN-LB)	-0.01	1.32	-3.71	108.	174.
FZ (3) (LB)	0.38	367.07	0.08	85.	1.
MX (9) (IN-LB)	-0.03	10.62	-44.13	51.	433.
MY (9) (IN-LB)	-2.16	32.82	-58.21	79.	165.
FZ (9) (LB)	3.51	30.33	3.15	177.	5.
MX (15) (IN-LB)	0.06	1.40	-5.56	252.	437.
MY (15) (IN-LB)	0.06	2.49	-6.69	109.	172.
FZ (15) (LB)	5.99	35.78	3.36	172.	437.
MX (21) (IN-LB)	0.53	11.96	-45.89	83.	429.
MY (21) (IN-LB)	-1.17	55.07	-17.85	267.	171.
FZ (21) (LB)	1.70	54.82	1.62	182.	0.
TIBIA					
MX (3) (IN-LB)	0.03	10.77	-2.65	200.	164.
MY (3) (IN-LB)	0.02	10.21	-9.86	89.	174.
FZ (3) (LB)	0.94	11.08	-3.11	174.	75.
MX (9) (IN-LB)	0.00	9.23	-2.30	200.	162.
MY (9) (IN-LB)	0.06	10.40	-10.15	90.	174.
FZ (9) (LB)	1.94	8.93	1.67	159.	191.

SPARTA -GX STUDY TEST: 4637



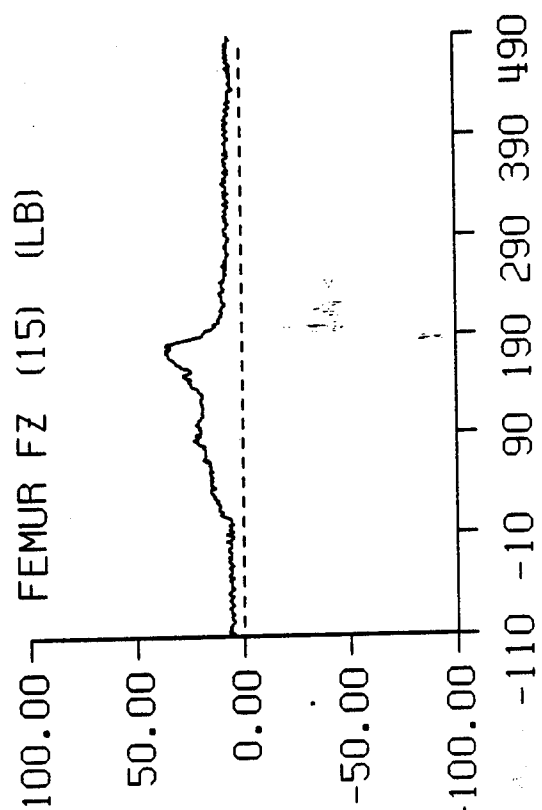
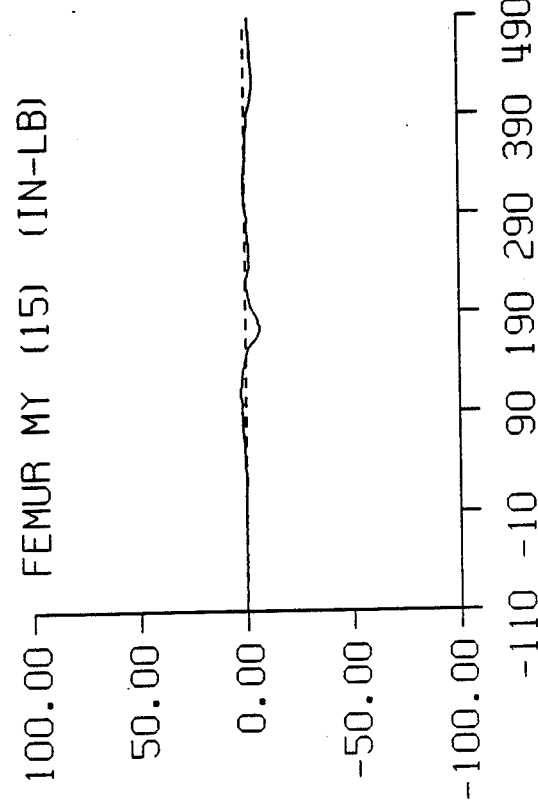
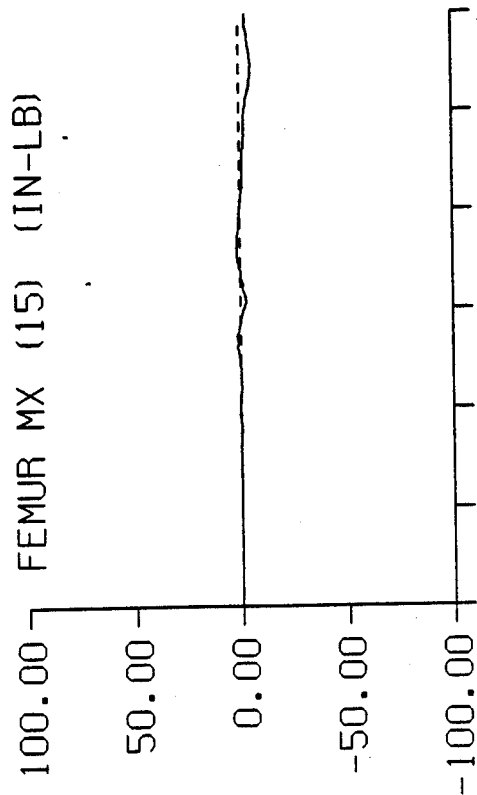
TIME IN MILLISECONDS

SPARTA -GX STUDY TEST: 4637



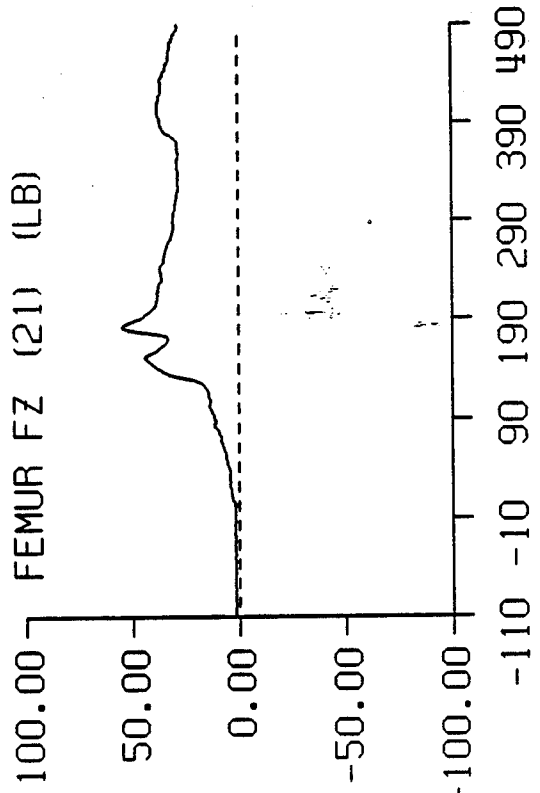
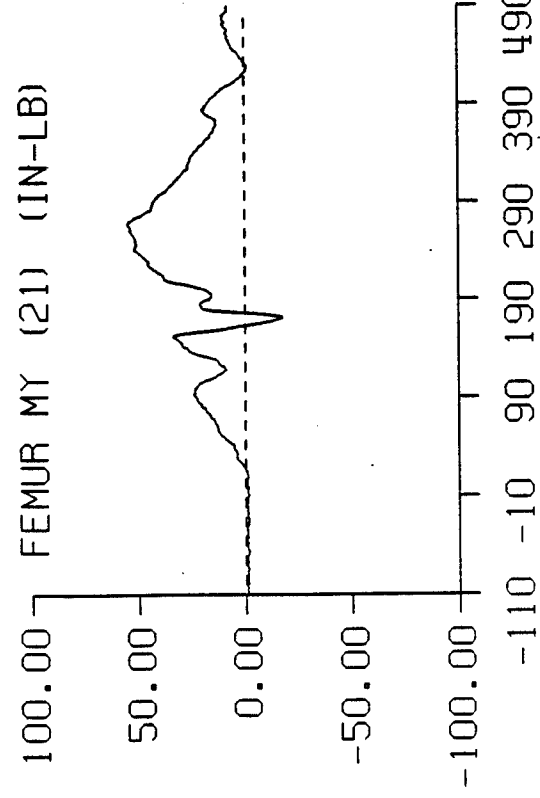
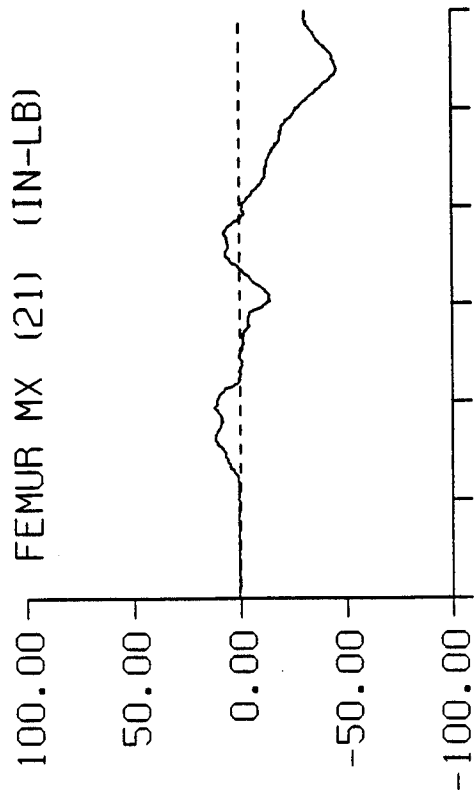
TIME IN MILLISECONDS

SPARTA -GX STUDY TEST: 4637



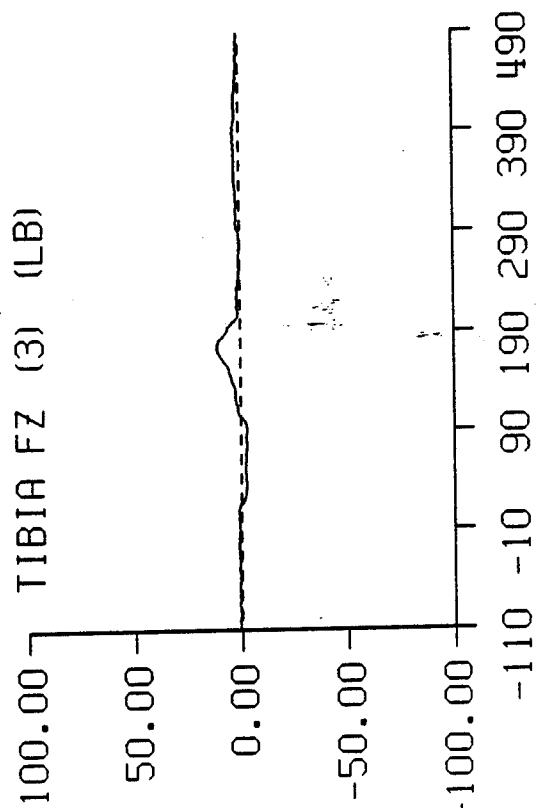
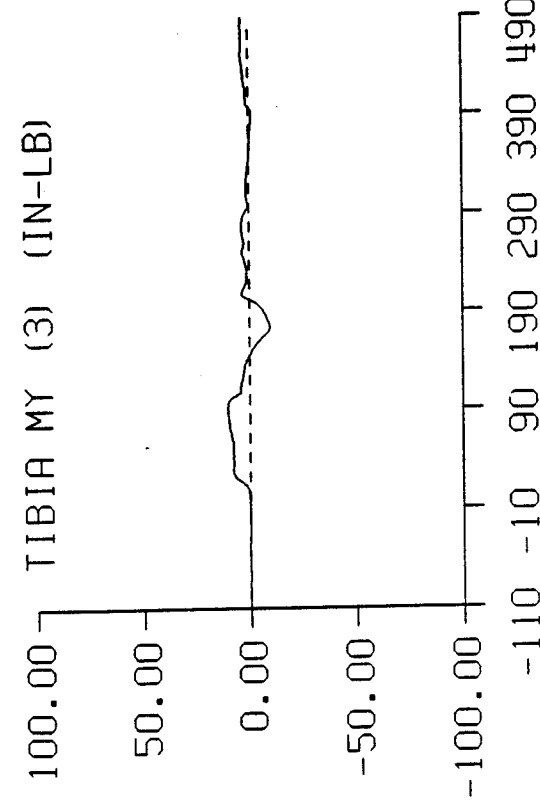
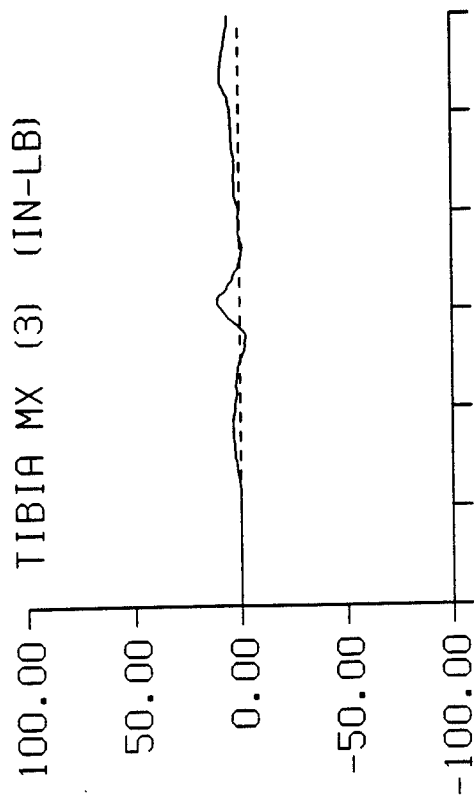
TIME IN MILLISECONDS

SPARTA -GX STUDY TEST: 4637



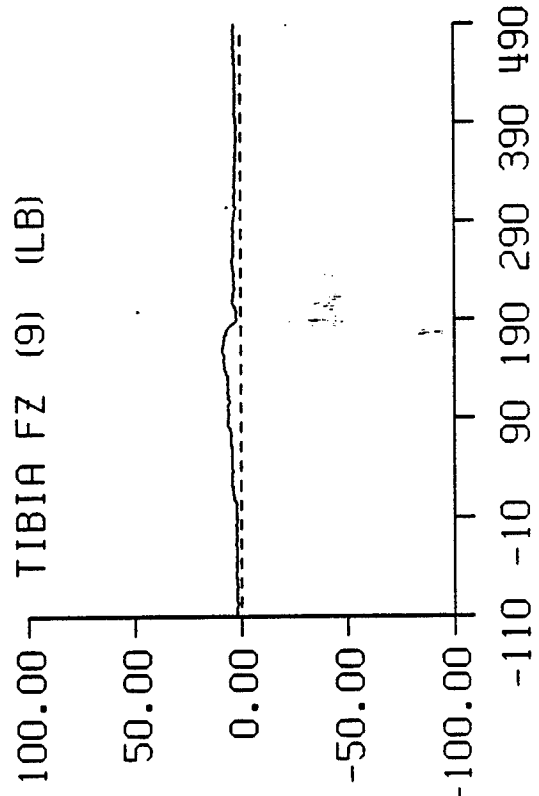
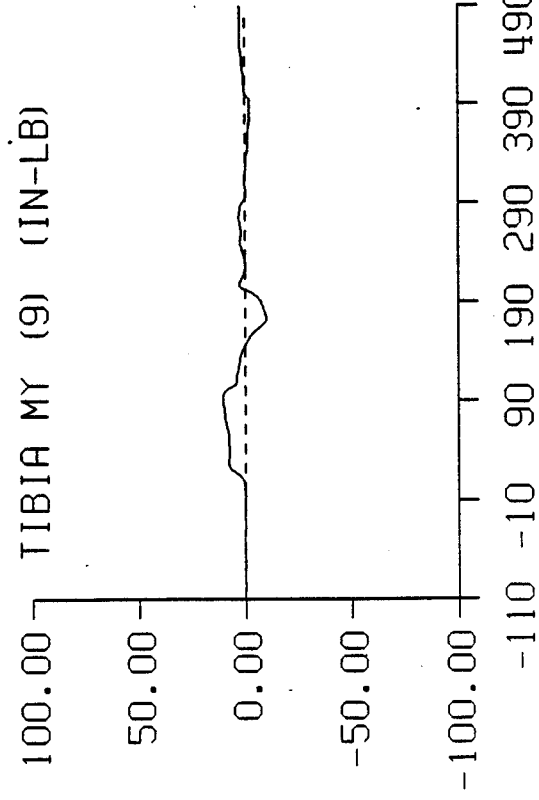
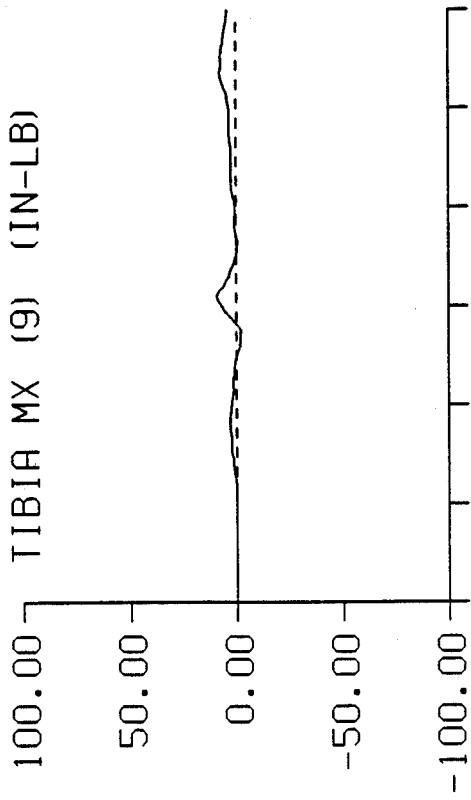
TIME IN MILLISECONDS

SPARTA -GX STUDY TEST: 4637



TIME IN MILLISECONDS

SPARTA -GX STUDY TEST: 4637



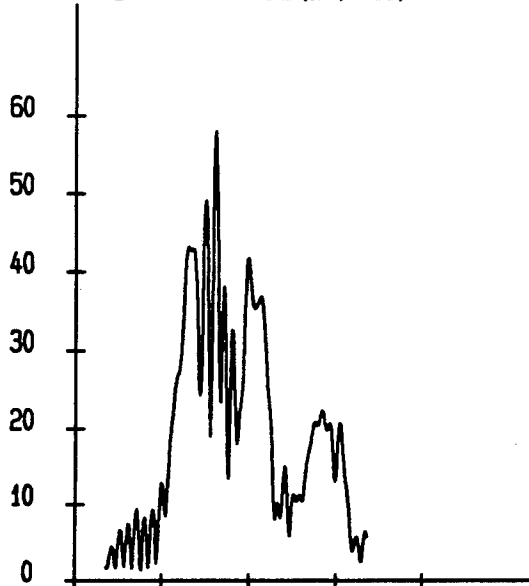
TIME IN MILLISECONDS

TEST 2 (4638) 7.0 G

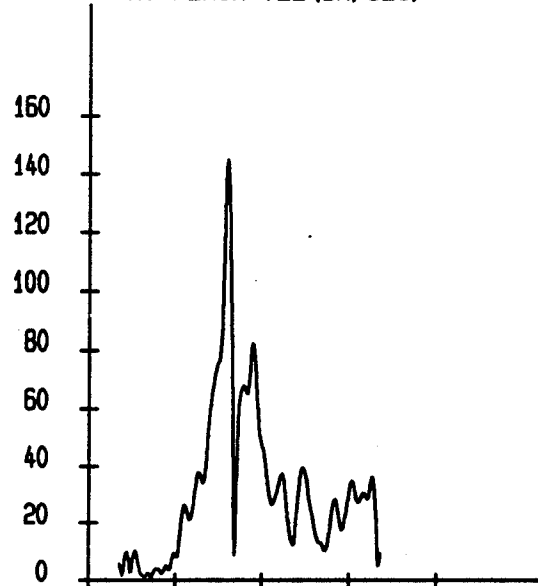
SPARTA -GX

TEST: 4638 DATE: 23-SEP-1993 SUBJ: HB3-50 CELL: B

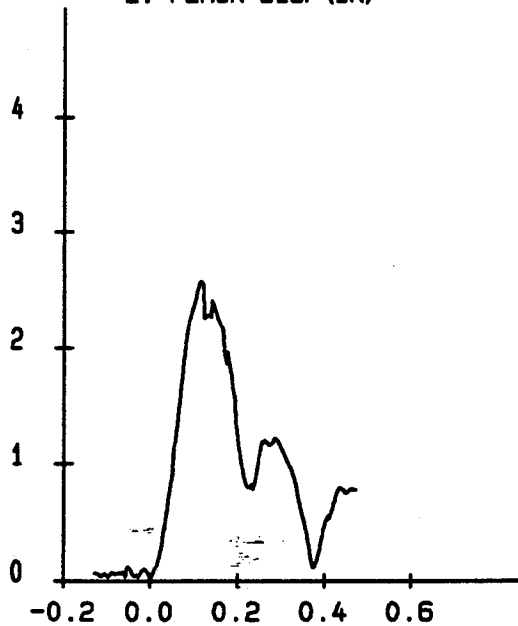
L. FEMUR VEL (IN/SEC)



R. FEMUR VEL (IN/SEC)

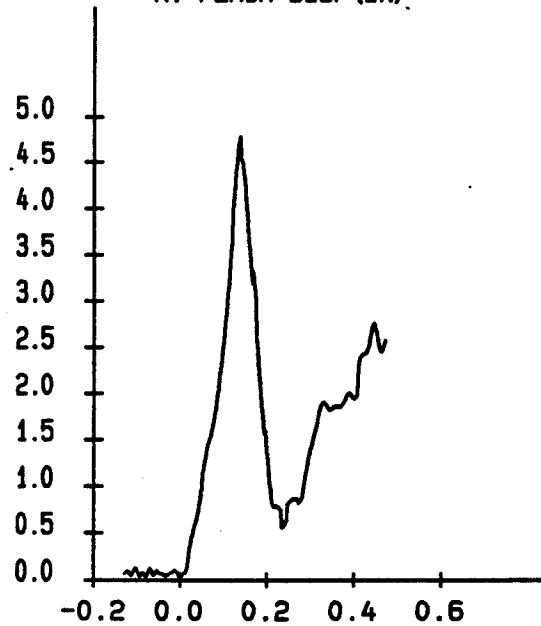


L. FEMUR DISP (IN)



TIME (SEC)

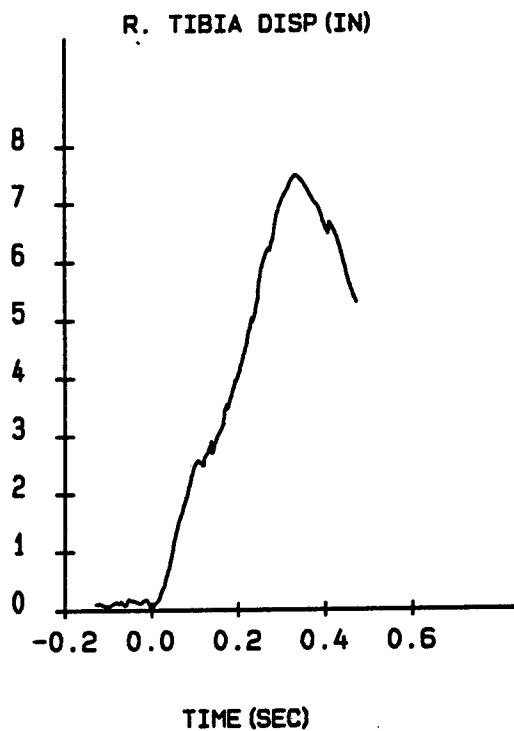
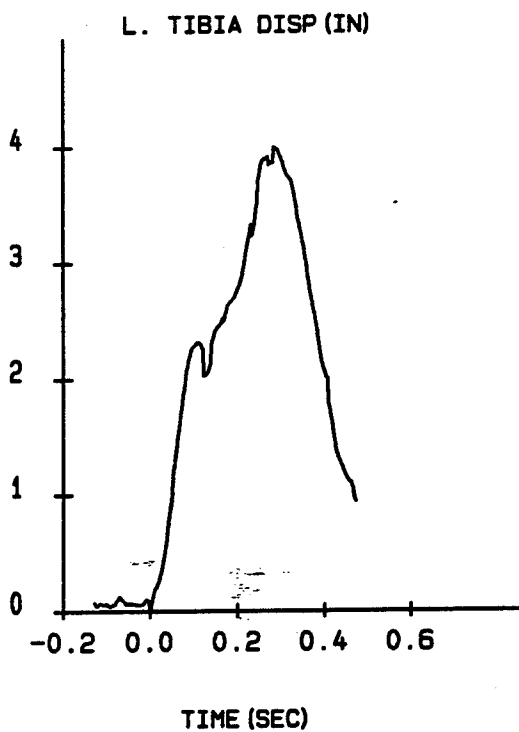
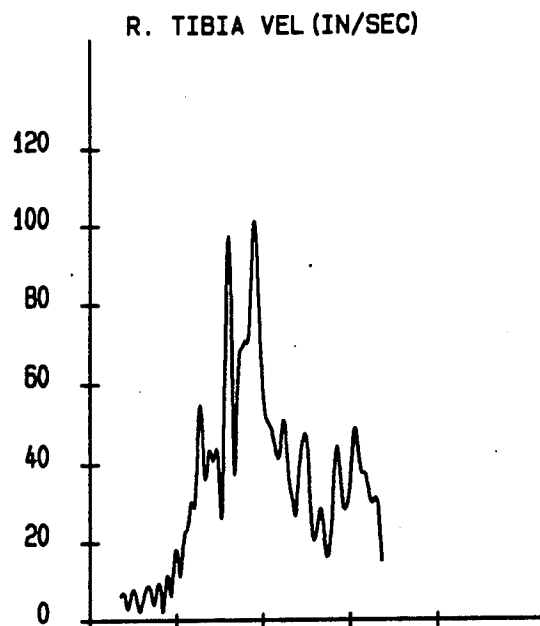
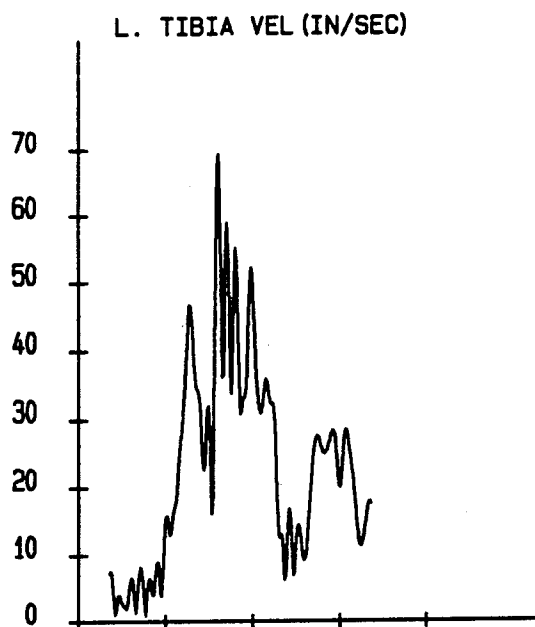
R. FEMUR DISP (IN)



TIME (SEC)

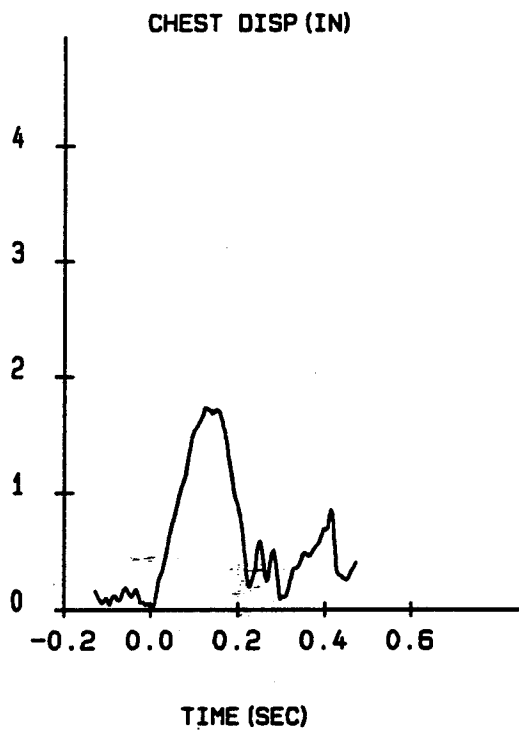
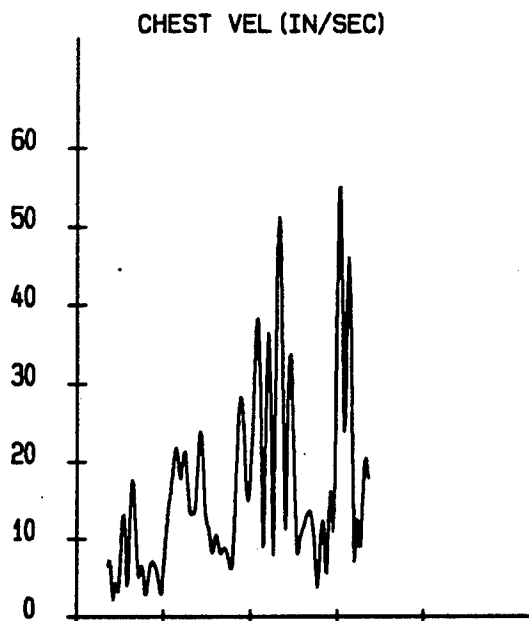
SPARTA -GX

TEST: 4638 DATE: 23-SEP-1993 SUBJ: HB3-50 CELL: B



SPARTA -GX

TEST: 4638 DATE: 23-SEP-1993 SUBJ: HB3-50 CELL: B



SPARTA -GX
TEST: 4638 DATE: 23-SEP-1993 SUBJ: HB3-50 CELL: B

RELIABILITY FACTORS (IN)					
TARGET DESCRIPTION	MAXIMUM	MINIMUM	AVERAGE	STANDARD DEVIATION	AT MAX DISPLACEMENT
1 L. FEMUR	0.3115	0.0002	0.0599	0.0540	0.1434
2 R. FEMUR	0.2444	0.0020	0.1109	0.0555	0.1218
3 L. TIBIA	0.1376	0.0014	0.0481	0.0301	0.0652
4 R. TIBIA	0.1806	0.0012	0.0983	0.0439	0.1635
5 CHEST	0.4631	0.0013	0.1761	0.1035	0.1975

TARGET	MAXIMUM	TIME(SEC)	MINIMUM	TIME(SEC)
L. FEMUR				
POSITION(IN)				
X AXIS	22.4092	0.1400	19.7293	0.2820
Y AXIS	6.4291	0.4080	5.1309	0.1120
Z AXIS	7.8494	0.2860	5.7583	0.1180
VELOCITY(IN/SEC)	58.0159	0.1220	2.4453	0.4580
ACCELERATION(G)	10.7268	0.1080	0.0958	0.4120
DISPLACEMENT(IN)				
X AXIS	2.2899	0.1400	-0.3900	0.2820
Y AXIS	0.3476	0.4080	-0.9506	0.1120
Z AXIS	1.1565	0.2860	-0.9346	0.1180
RESULTANT	2.5707	0.1140	0.0000	0.0000
R. FEMUR				
POSITION(IN)				
X AXIS	24.0512	0.1400	20.5337	0.3260
Y AXIS	-2.3985	0.1380	-7.9366	0.4440
Z AXIS	9.9071	0.3260	6.1357	0.1400
VELOCITY(IN/SEC)	145.0635	0.1200	5.0890	0.4680
ACCELERATION(G)	21.6275	0.1340	0.4404	0.3660
DISPLACEMENT(IN)				
X AXIS	2.9829	0.1400	-0.5345	0.3260
Y AXIS	2.9089	0.1380	-2.6292	0.4440
Z AXIS	1.3696	0.3260	-2.4018	0.1400
RESULTANT	4.7797	0.1380	0.0000	0.0000

SPARTA -GX

TEST: 4638 DATE: 23-SEP-1993 SUBJ: HB3-50 CELL: B

TARGET	MAXIMUM	TIME(SEC)	MINIMUM	TIME(SEC)
L. TIBIA				
POSITION(IN)				
X AXIS	27.5716	0.0980	24.5056	0.2820
Y AXIS	7.2097	0.4080	5.6196	0.1120
Z AXIS	6.2035	0.2860	2.1900	0.1000
VELOCITY(IN/SEC)	69.3025	0.1200	6.2701	0.2740
ACCELERATION(G)	10.3462	0.1060	0.3144	0.3660
DISPLACEMENT(IN)				
X AXIS	2.2296	0.0980	-0.8364	0.2820
Y AXIS	0.8627	0.4080	-0.7274	0.1120
Z AXIS	3.9398	0.2860	-0.0738	0.1000
RESULTANT	3.9962	0.2860	0.0000	0.0000
R. TIBIA				
POSITION(IN)				
X AXIS	30.0768	0.1080	25.9741	0.3800
Y AXIS	-3.5993	0.1380	-9.8120	0.4300
Z AXIS	9.3421	0.3260	2.3645	0.1160
VELOCITY(IN/SEC)	101.2211	0.1800	11.4119	0.0080
ACCELERATION(G)	14.1800	0.1320	0.6921	0.3680
DISPLACEMENT(IN)				
X AXIS	2.5515	0.1080	-1.5512	0.3800
Y AXIS	1.7365	0.1380	-4.4762	0.4300
Z AXIS	6.8875	0.3260	-0.0902	0.1160
RESULTANT	7.4864	0.3320	0.0000	0.0000
CHEST				
POSITION(IN)				
X AXIS	13.4705	0.1540	11.6870	0.4080
Y AXIS	1.6938	0.1540	0.2738	0.4160
Z AXIS	20.6093	0.1220	19.2002	0.2800
VELOCITY(IN/SEC)	55.0116	0.4060	3.8488	0.3540
ACCELERATION(G)	10.6460	0.2540	0.0556	0.0840

SPARTA -GX

TEST: 4638 DATE: 23-SEP-1993 SUBJ: HB3-50 CELL: B

TARGET	MAXIMUM	TIME(SEC)	MINIMUM	TIME(SEC)
CHEST				
DISPLACEMENT (IN)				
X AXIS	1.3426	0.1540	-0.4409	0.4080
Y AXIS	0.6761	0.1540	-0.7439	0.4160
Z AXIS	1.0497	0.1220	-0.3594	0.2800
RESULTANT	1.7309	0.1260	0.0000	0.0000

SPARTA -GX

TEST: 4638 DATE: 23-SEP-1993 SUBJ: HB3-50 CELL: B

te: Invalid samples are interpolated.

mples 1136 through 1152 of the L. FEMUR target are invalid.
valid sample range occurred from 0.0920 seconds to 0.1240 seconds.

mples 1159 through 1165 of the L. FEMUR target are invalid.
valid sample range occurred from 0.1380 seconds to 0.1500 seconds.

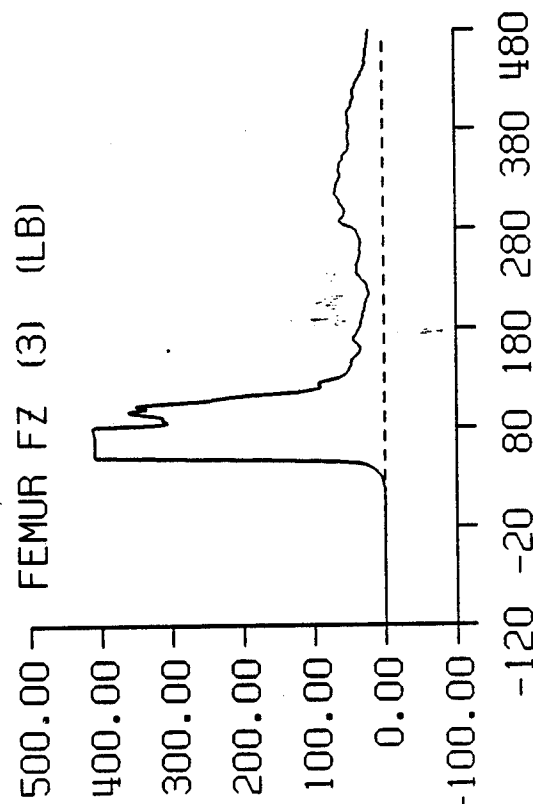
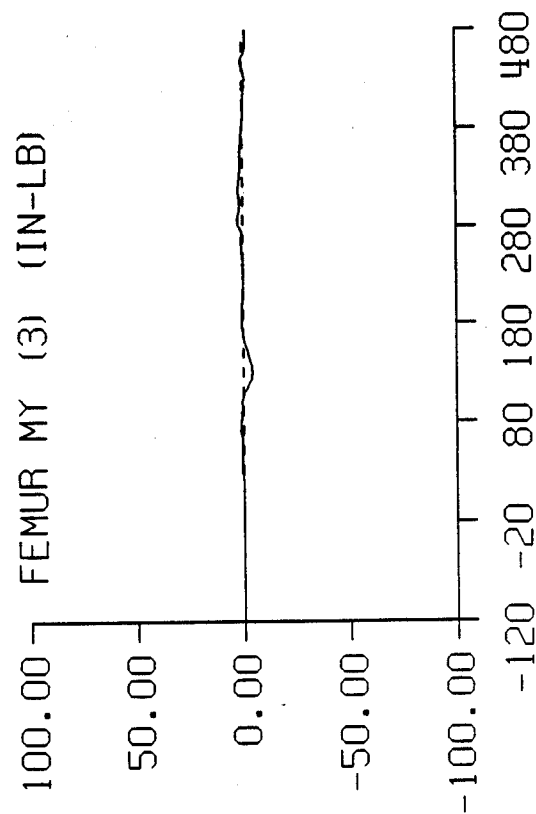
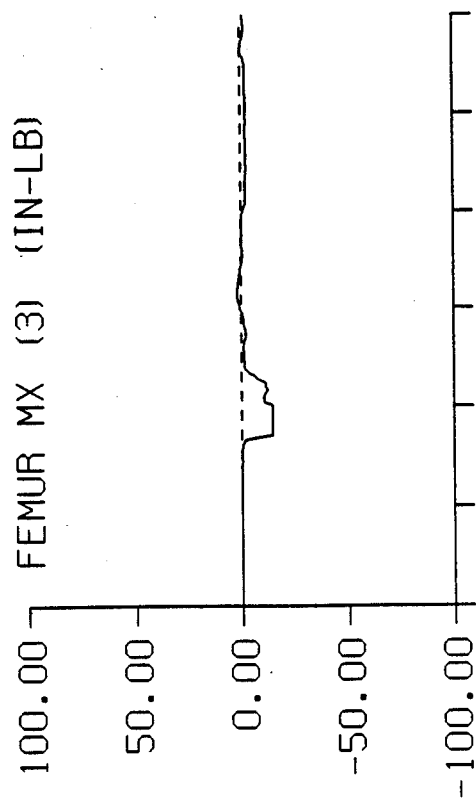
mples 1150 through 1157 of the R. FEMUR target are invalid.
valid sample range occurred from 0.1200 seconds to 0.1340 seconds.

mples 1201 through 1326 of the CHEST target are invalid.
valid sample range occurred from 0.2220 seconds to 0.4720 seconds.

SPARTA -GX STUDY TEST: 4638

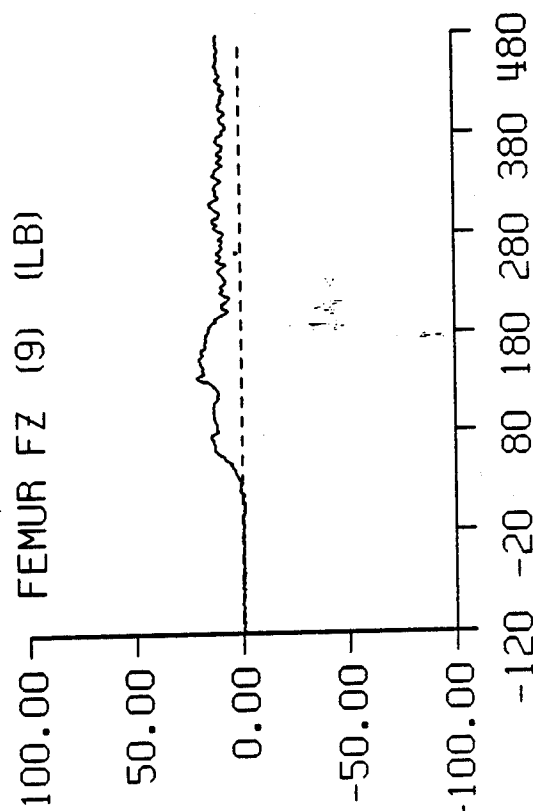
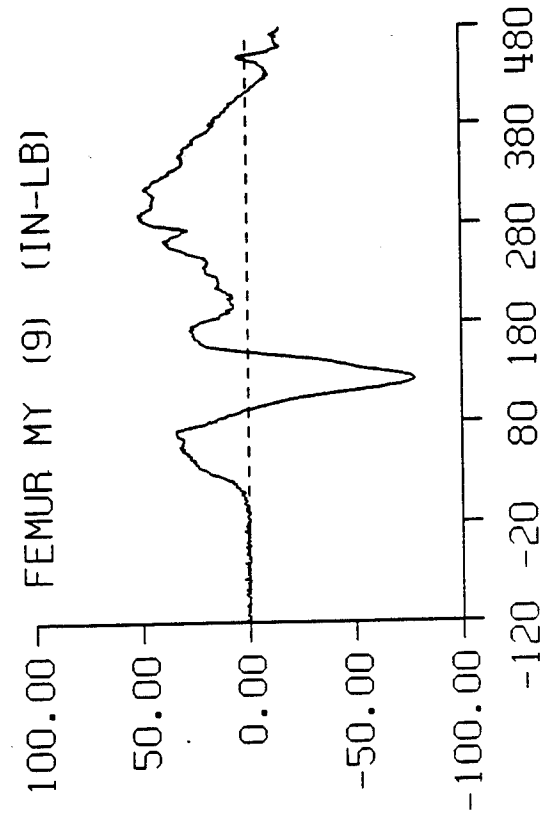
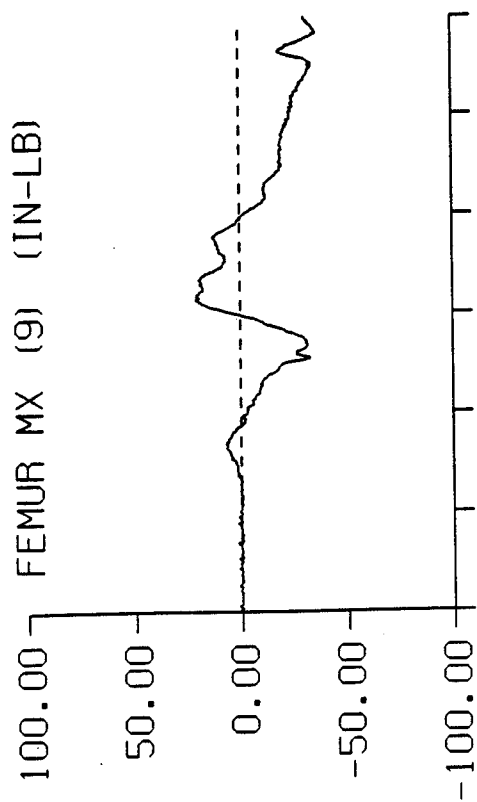
DATA ID	IMMEDIATE PREIMPACT	MAXIMUM VALUE	MINIMUM VALUE	TIME OF MAXIMUM	TIME OF MINIMUM
REFERENCE MARK TIME (MS)				-128.	
FEMUR					
MX (3) (IN-LB)	0.00	1.92	-14.51	195.	51.
MY (3) (IN-LB)	0.00	2.34	-4.44	285.	129.
FZ (3) (LB)	-0.18	411.74	-0.57	81.	2.
MX (9) (IN-LB)	0.12	21.06	-36.24	194.	464.
MY (9) (IN-LB)	0.26	51.39	-78.48	290.	122.
FZ (9) (LB)	-0.61	20.87	-1.60	135.	0.
MX (15) (IN-LB)	-0.03	4.47	-4.21	193.	153.
MY (15) (IN-LB)	0.05	4.99	-8.13	284.	131.
FZ (15) (LB)	-1.09	22.69	-5.09	124.	387.
MX (21) (IN-LB)	-0.14	20.64	-36.89	193.	466.
MY (21) (IN-LB)	0.22	59.56	-34.48	199.	130.
FZ (21) (LB)	-0.42	54.68	-1.27	143.	39.
TIBIA					
MX (3) (IN-LB)	-0.02	11.94	-7.76	151.	194.
MY (3) (IN-LB)	0.02	7.62	-14.36	31.	131.
FZ (3) (LB)	-0.22	11.75	-5.24	132.	32.
MX (9) (IN-LB)	-0.01	10.01	-6.28	152.	193.
MY (9) (IN-LB)	0.01	7.48	-14.74	30.	444.
FZ (9) (LB)	-0.25	7.13	-3.68	105.	282.

SPARTA -GX STUDY TEST: 4638



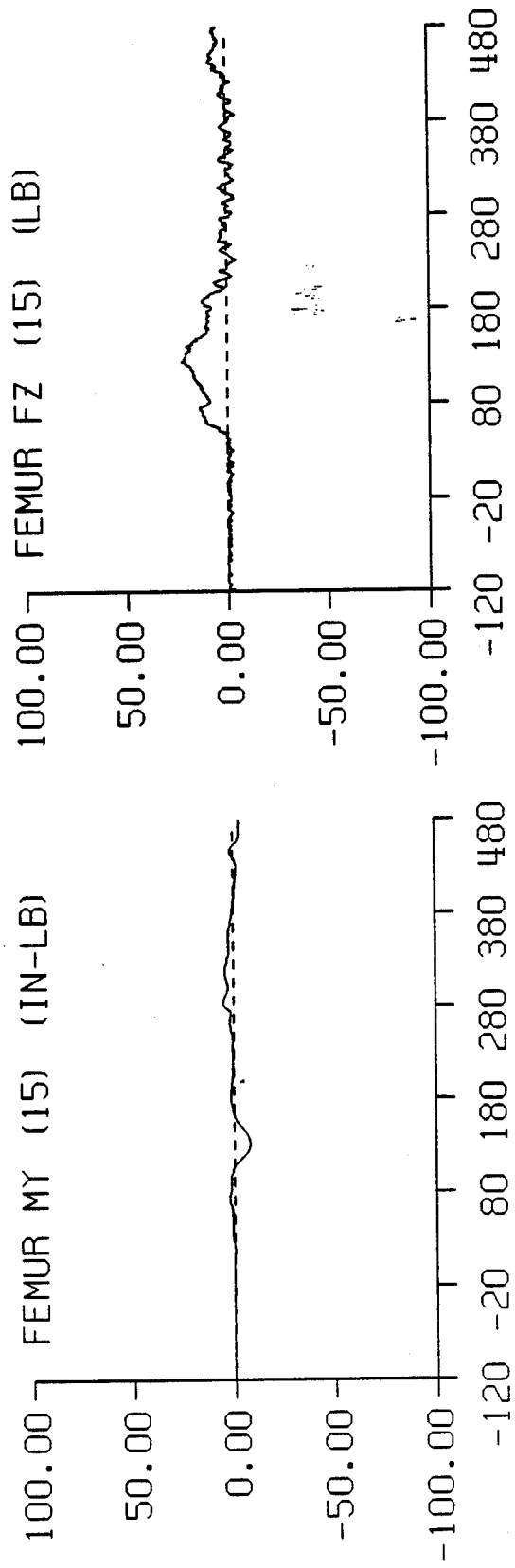
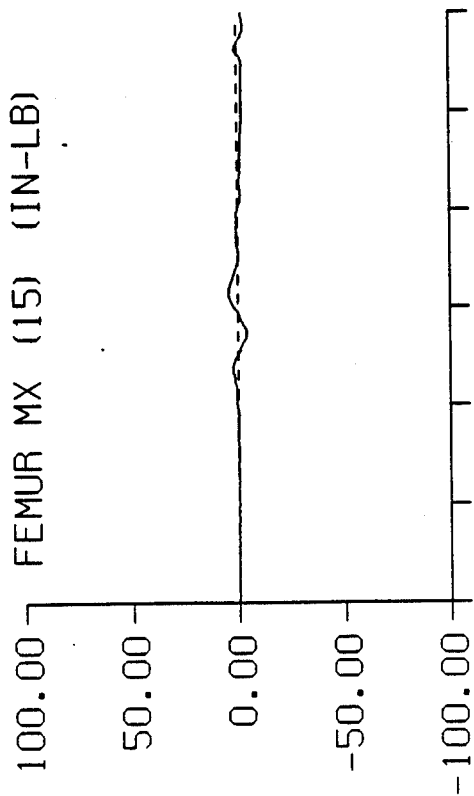
TIME IN MILLISECONDS

SPARTA -CX STUDY TEST: 4638



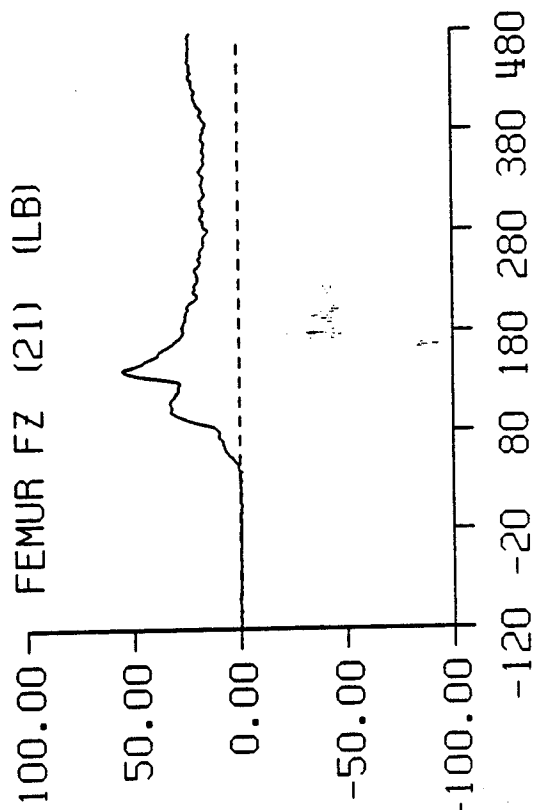
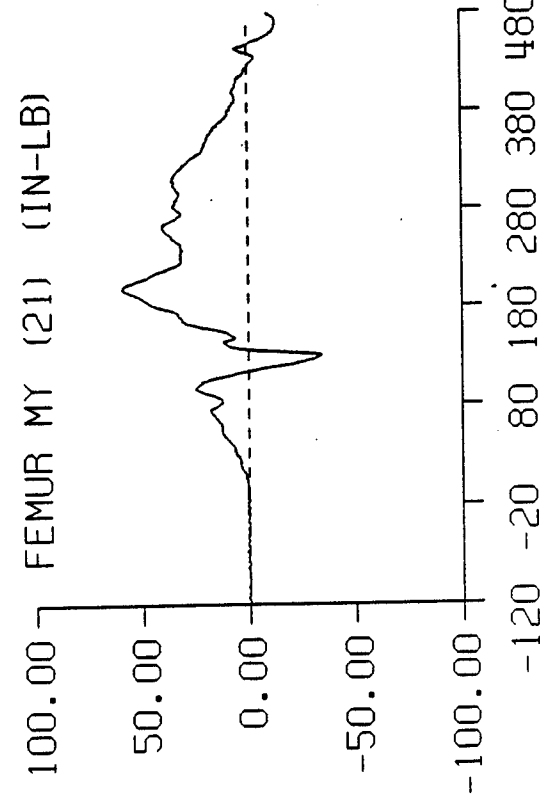
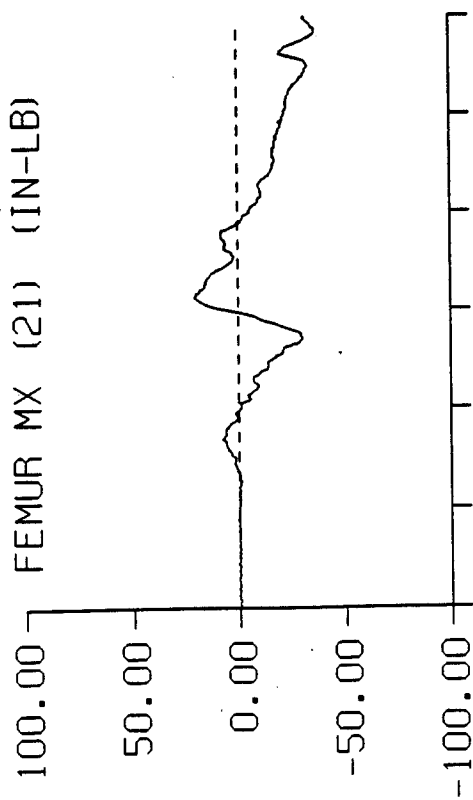
TIME IN MILLISECONDS

SPARTA -GX STUDY TEST: 4638



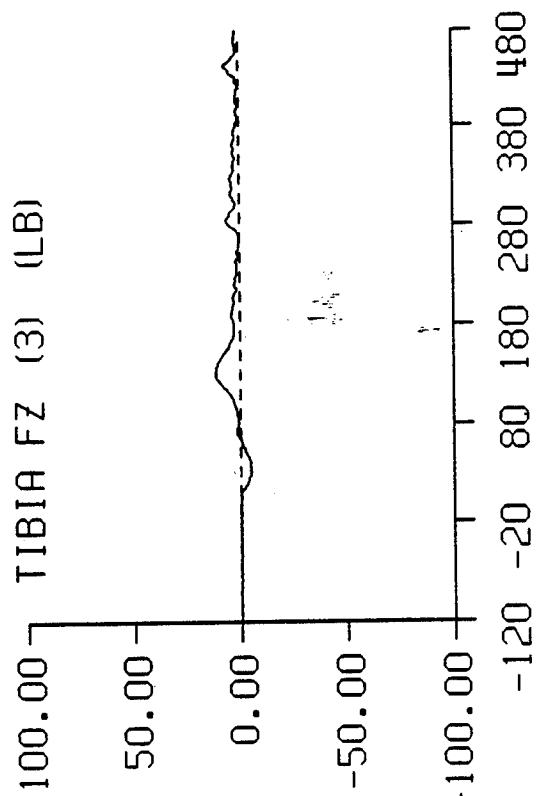
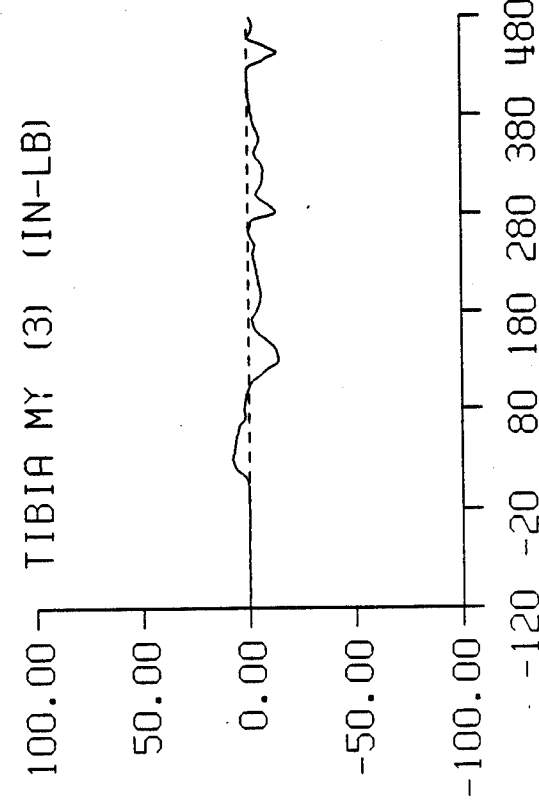
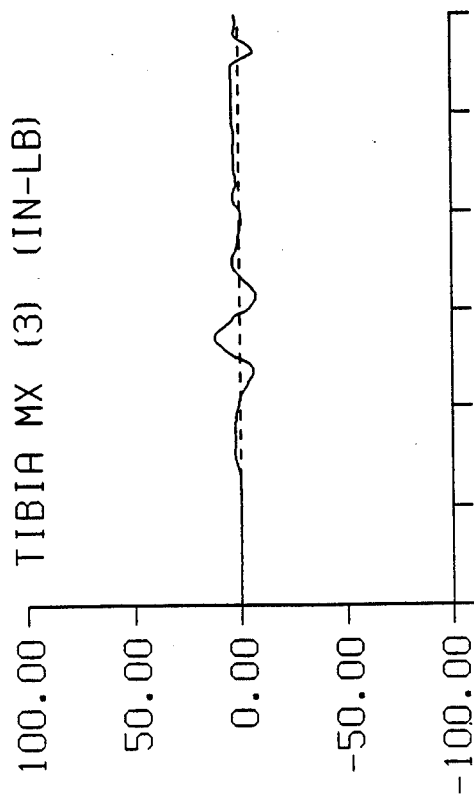
TIME IN MILLISECONDS

SPARTA -GX STUDY TEST: 4638



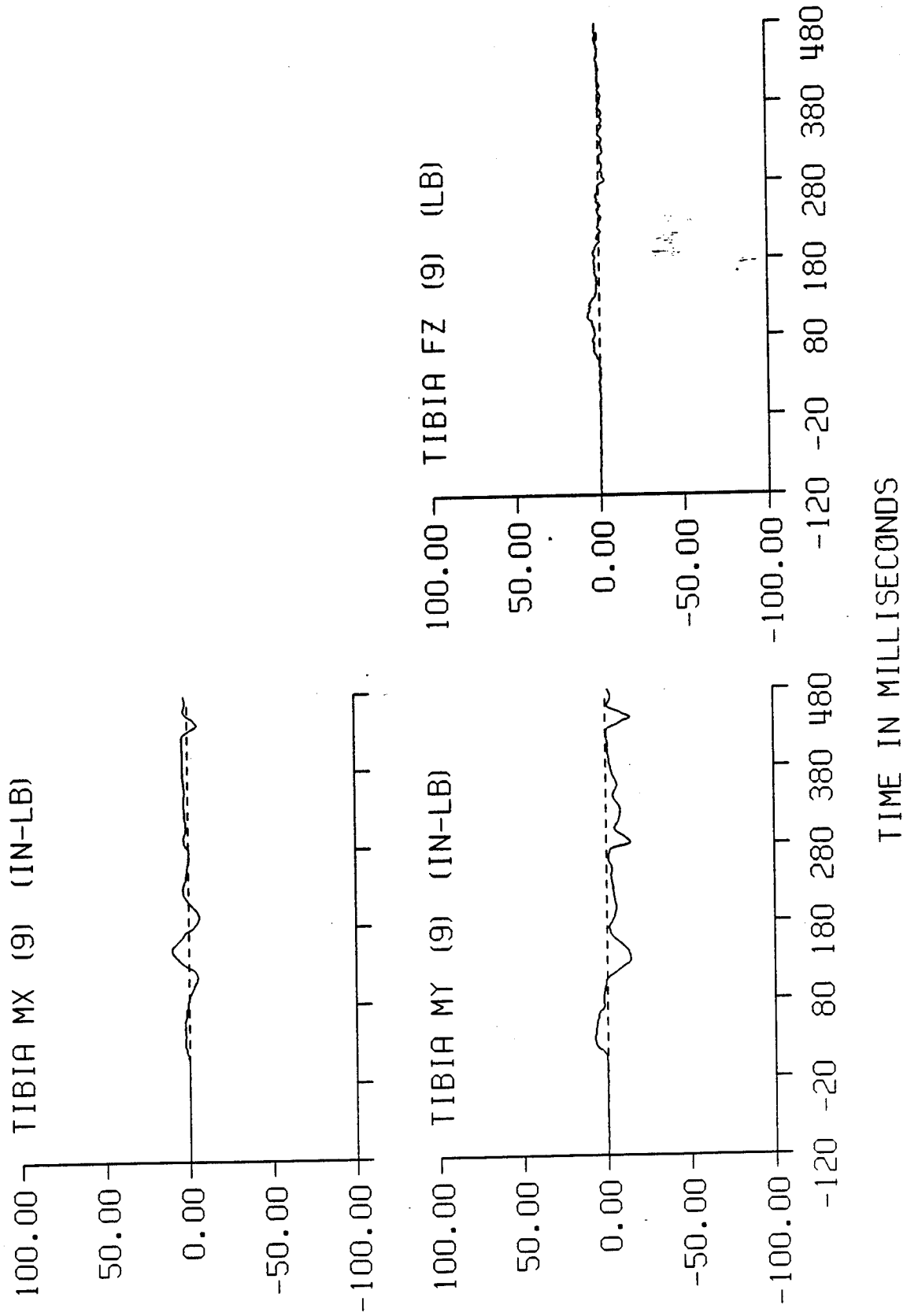
TIME IN MILLISECONDS

SPARTA -GX STUDY TEST: 4638



TIME IN MILLISECONDS

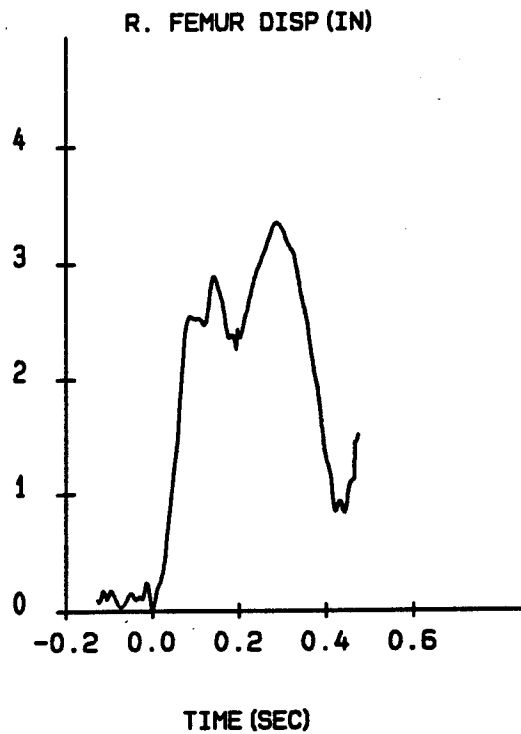
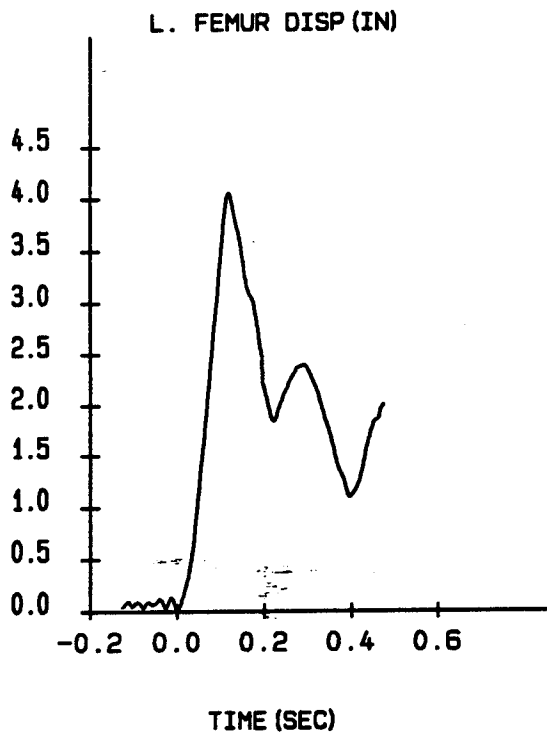
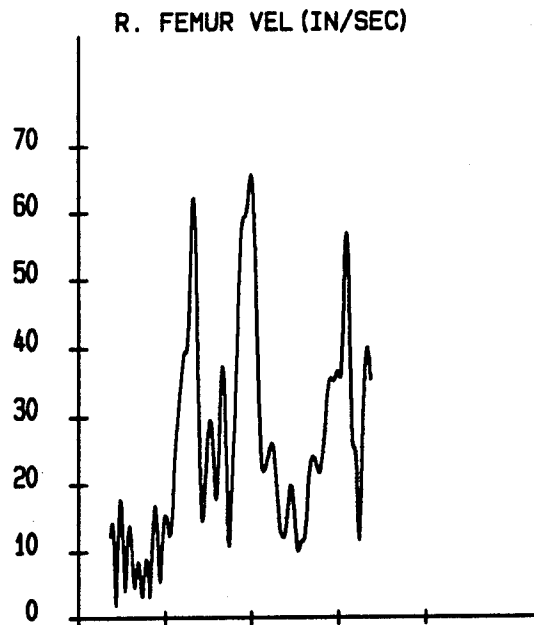
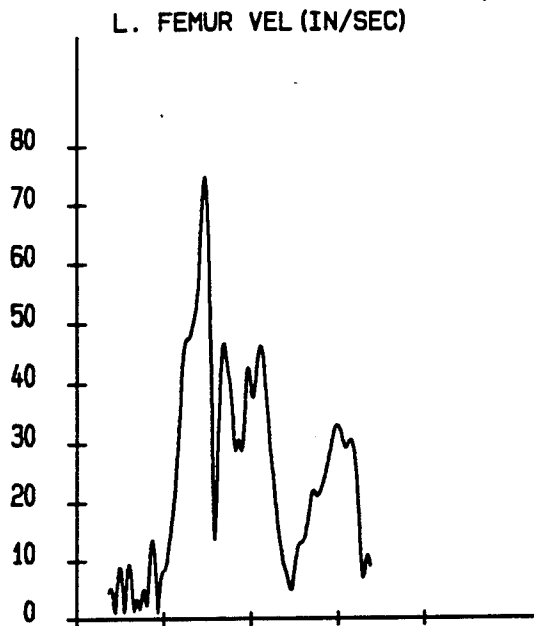
SPARTA -GX STUDY TEST: 4638



TEST 3 (4639) 8.5 G

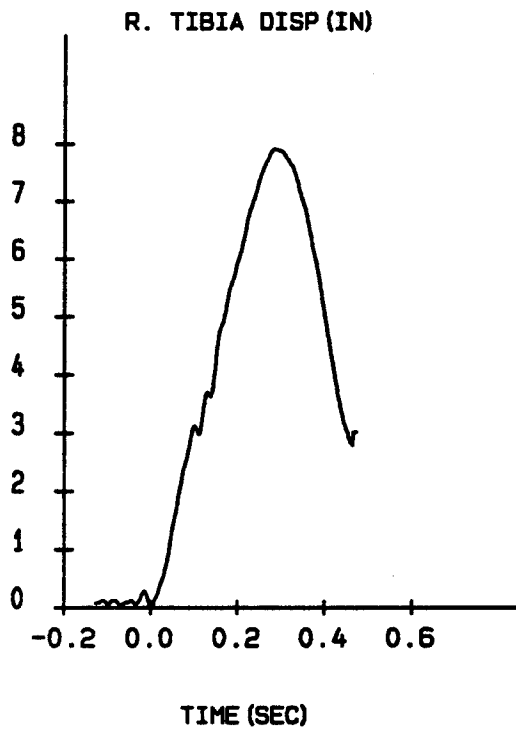
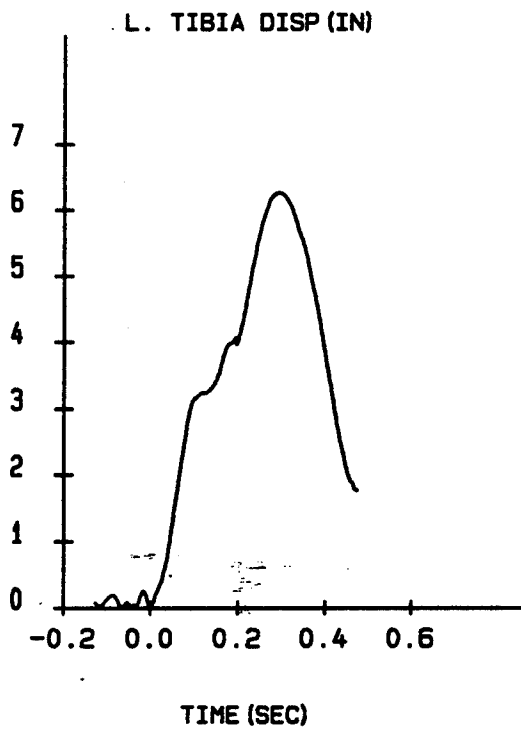
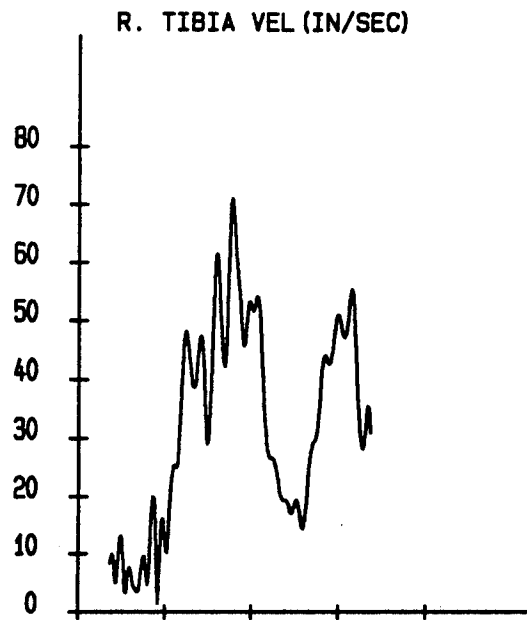
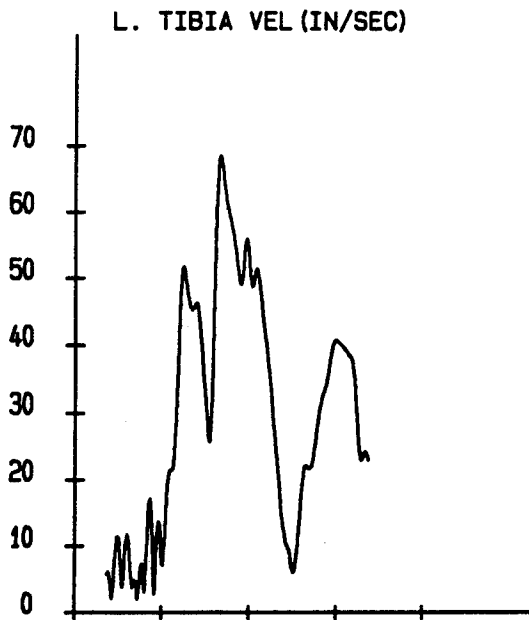
SPARTA -GX

TEST: 4639 DATE: 23-SEP-1993 SUBJ: HB3-50 CELL: C



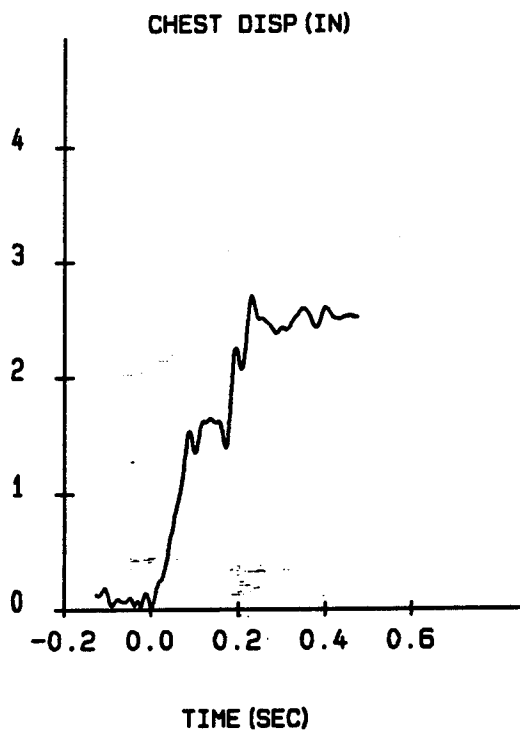
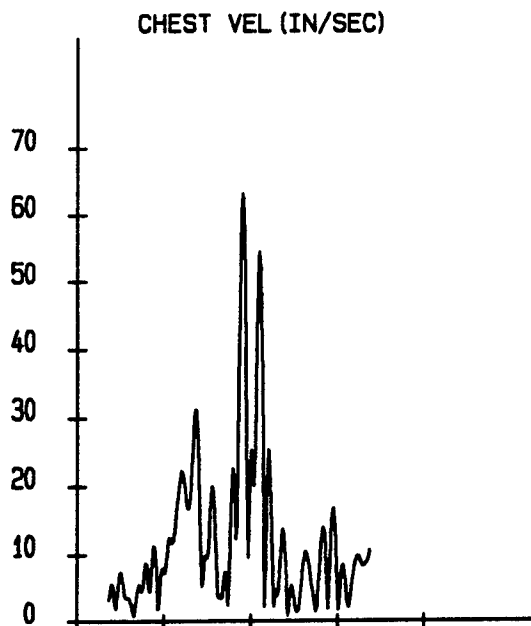
SPARTA -GX

TEST: 4639 DATE: 23-SEP-1993 SUBJ: HB3-50 CELL: C



SPARTA -GX

TEST: 4639 DATE: 23-SEP-1993 SUBJ: HB3-50 CELL: C



SPARTA -GX

TEST: 4639 DATE: 23-SEP-1993 SUBJ: HB3-50 CELL: C

RELIABILITY FACTORS (IN)

TARGET DESCRIPTION	MAXIMUM	MINIMUM	AVERAGE	STANDARD DEVIATION	AT MAX DISPLACEMENT
1 L. FEMUR	0.2210	0.0032	0.0709	0.0382	0.1363
2 R. FEMUR	0.1970	0.0009	0.0550	0.0384	0.0965
3 L. TIBIA	0.1495	0.0000	0.0732	0.0388	0.1062
4 R. TIBIA	0.1692	0.0004	0.0639	0.0367	0.0772
5 CHEST	0.3919	0.1061	0.2432	0.0708	0.3692

TARGET	MAXIMUM	TIME(SEC)	MINIMUM	TIME(SEC)
L. FEMUR				
POSITION(IN)				
X AXIS	23.1137	0.1200	19.5793	0.0000
Y AXIS	6.7709	0.4640	5.0528	0.2480
Z AXIS	9.4714	0.2900	5.6613	0.1140
VELOCITY(IN/SEC)	74.7636	0.0940	4.9892	0.2920
ACCELERATION(G)	11.1667	0.1120	0.0875	0.3960
DISPLACEMENT(IN)				
X AXIS	3.5344	0.1200	0.0000	0.0000
Y AXIS	0.2684	0.4640	-1.4497	0.2480
Z AXIS	1.9186	0.2900	-1.8916	0.1140
RESULTANT	4.0539	0.1160	0.0000	0.0000

R. FEMUR				
POSITION(IN)				
X AXIS	24.1500	0.0860	20.9820	0.2880
Y AXIS	-4.0411	0.1960	-6.8297	0.4740
Z AXIS	10.0594	0.2920	6.4984	0.1180
VELOCITY(IN/SEC)	65.8143	0.1980	10.0454	0.3060
ACCELERATION(G)	7.2202	0.0820	0.6593	0.3920
DISPLACEMENT(IN)				
X AXIS	2.5024	0.0860	-0.6655	0.2880
Y AXIS	1.5579	0.1960	-1.2307	0.4740
Z AXIS	3.2262	0.2920	-0.3348	0.1180
RESULTANT	3.3430	0.2860	0.0000	0.0000

SPARTA -GX

TEST: 4639 DATE: 23-SEP-1993 SUBJ: HB3-50 CELL: C

TARGET	MAXIMUM	TIME(SEC)	MINIMUM	TIME(SEC)
L. TIBIA				
POSITION(IN)				
X AXIS	27.7885	0.1000	24.2566	0.3120
Y AXIS	7.5007	0.4640	5.4193	0.2540
Z AXIS	8.8030	0.2980	2.2714	0.1100
VELOCITY(IN/SEC)	68.5636	0.1320	6.0392	0.3020
ACCELERATION(G)	9.9433	0.1120	0.4903	0.4140
DISPLACEMENT(IN)				
X AXIS	3.0952	0.1000	-0.4367	0.3120
Y AXIS	0.2846	0.4640	-1.7969	0.2540
Z AXIS	6.0562	0.2980	-0.4754	0.1100
RESULTANT	6.2650	0.2960	0.0000	0.0000
R. TIBIA				
POSITION(IN)				
X AXIS	30.2485	0.0980	26.7113	0.2900
Y AXIS	-4.8895	0.1960	-8.2397	0.4740
Z AXIS	9.4588	0.2920	1.6482	0.0000
VELOCITY(IN/SEC)	71.1660	0.1540	10.2650	0.0040
ACCELERATION(G)	5.8236	0.0960	0.1549	0.4000
DISPLACEMENT(IN)				
X AXIS	2.7931	0.0980	-0.7441	0.2900
Y AXIS	1.7717	0.1960	-1.5785	0.4740
Z AXIS	7.8105	0.2920	0.0000	0.0000
RESULTANT	7.9027	0.2860	0.0000	0.0000
CHEST				
POSITION(IN)				
X AXIS	14.0774	0.3500	12.1000	0.0000
Y AXIS	3.0831	0.2300	1.2299	0.0020
Z AXIS	20.6880	0.0840	19.6605	0.0020
VELOCITY(IN/SEC)	63.1144	0.1800	0.7948	0.2860
ACCELERATION(G)	8.0903	0.1660	0.0898	0.2720

SPARTA -GX

TEST: 4639 DATE: 23-SEP-1993 SUBJ: HB3-50 CELL: C

TARGET	MAXIMUM	TIME(SEC)	MINIMUM	TIME(SEC)
CHEST				
DISPLACEMENT(IN)				
X AXIS	1.9774	0.3500	0.0000	0.0000
Y AXIS	1.8524	0.2300	-0.0007	0.0020
Z AXIS	1.0255	0.0840	-0.0020	0.0020
RESULTANT	2.7111	0.2300	0.0000	0.0000

SPARTA -GX

TEST: 4639 DATE: 23-SEP-1993 SUBJ: HB3-50 CELL: C

Note: Invalid samples are interpolated.

Samples 1129 through 1154 of the L. FEMUR target are invalid.
Invalid sample range occurred from 0.0800 seconds to 0.1300 seconds.

Samples 1158 through 1160 of the L. FEMUR target are invalid.
Invalid sample range occurred from 0.1380 seconds to 0.1420 seconds.

Samples 1163 through 1164 of the L. FEMUR target are invalid.
Invalid sample range occurred from 0.1480 seconds to 0.1500 seconds.

Samples 1136 through 1153 of the R. FEMUR target are invalid.
Invalid sample range occurred from 0.0940 seconds to 0.1280 seconds.

Samples 1145 through 1148 of the R. TIBIA target are invalid.
Invalid sample range occurred from 0.1120 seconds to 0.1180 seconds.

Samples 1153 through 1155 of the R. TIBIA target are invalid.
Invalid sample range occurred from 0.1280 seconds to 0.1320 seconds.

Sample number 1159 of the R. TIBIA target is invalid.
Invalid sample 1159 occurred at 0.1400 seconds.

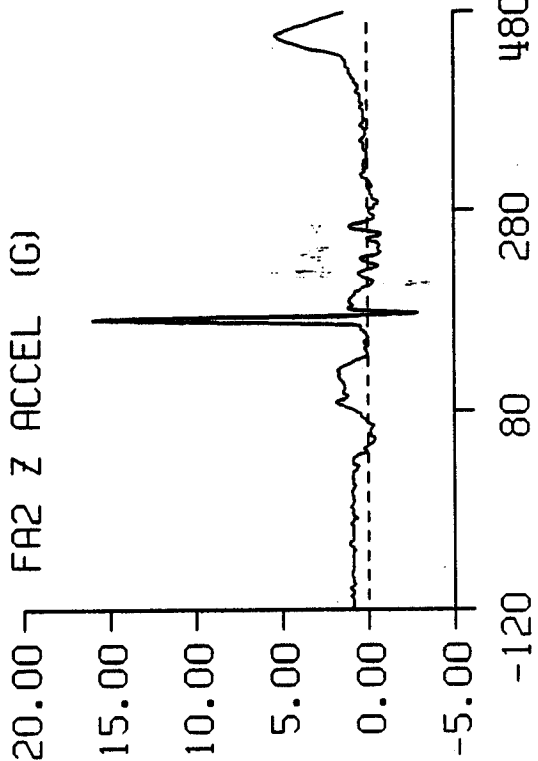
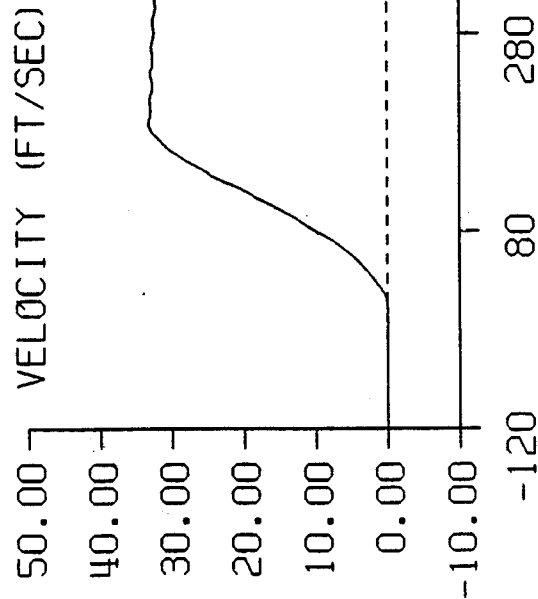
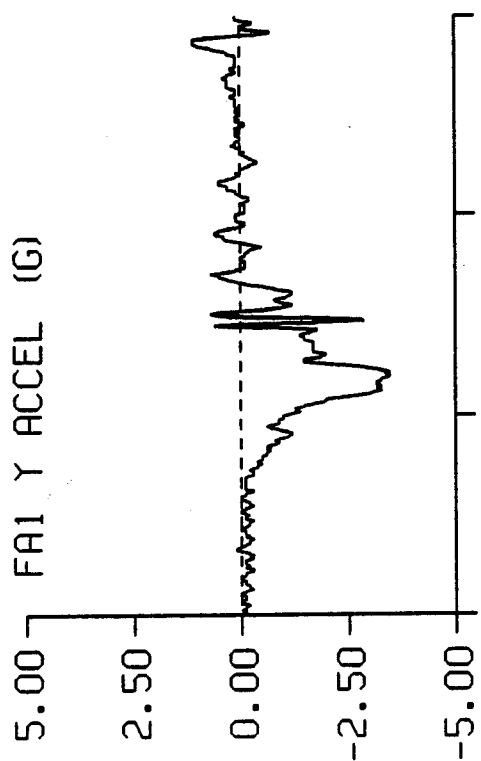
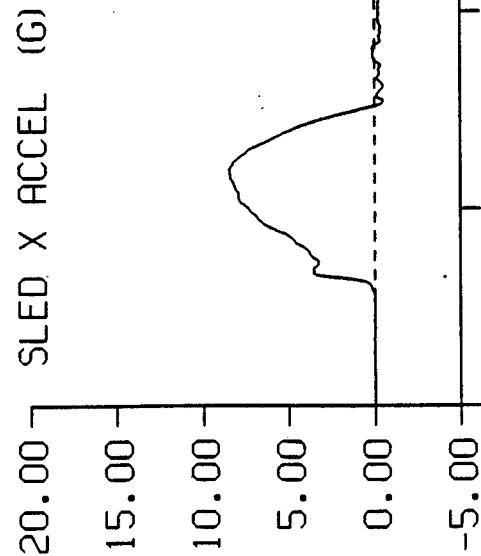
Samples 1163 through 1165 of the R. TIBIA target are invalid.
Invalid sample range occurred from 0.1480 seconds to 0.1520 seconds.

Samples 1180 through 1326 of the CHEST target are invalid.
Invalid sample range occurred from 0.1820 seconds to 0.4740 seconds.

test 4639 cell c

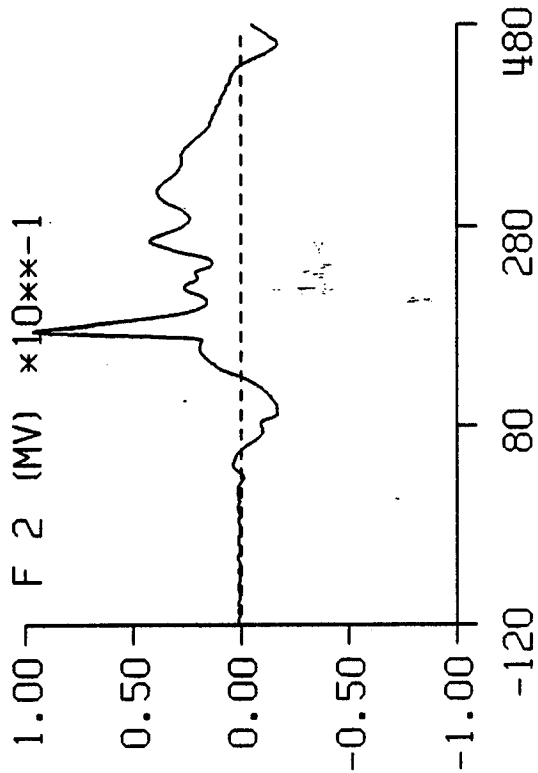
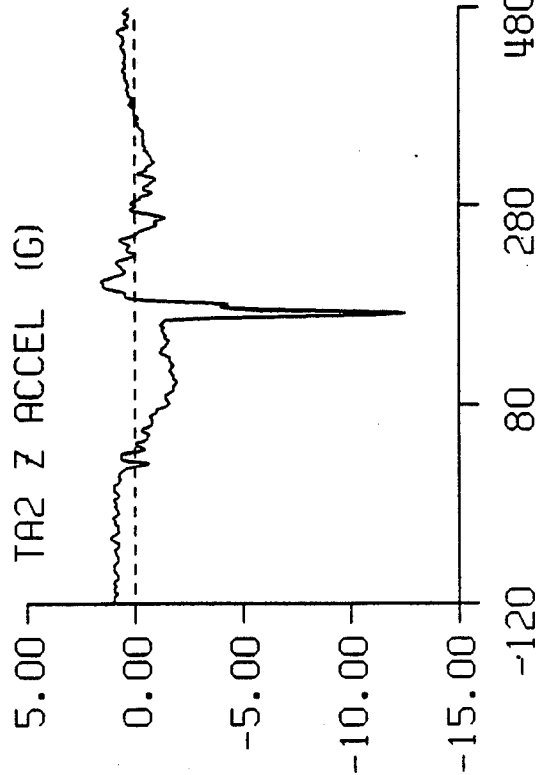
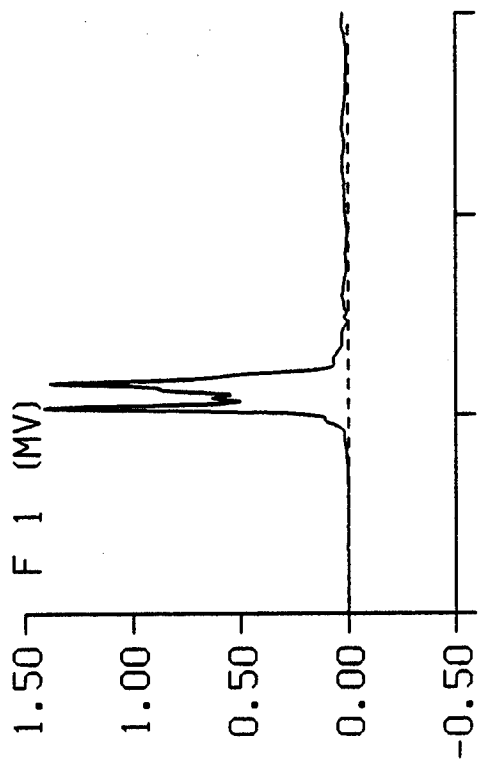
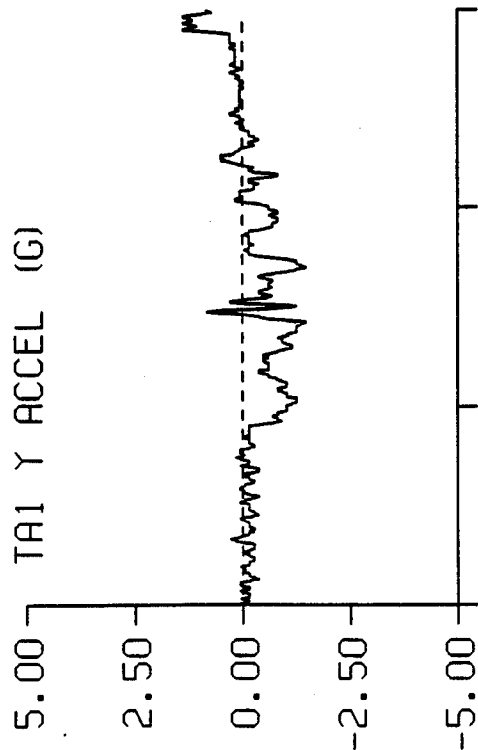
CHANNEL	MAXIMUM VALUE	MINIMUM VALUE	TIME OF MAXIMUM	TIME OF MINIMUM
IMPACT RISE TIME			116.0	
IMPACT DURATION			185.0	
VELOCITY CHANGE	32.80			
SLED X ACCEL (G)	8.45	-0.52	116.0	189.0
F 1 (MV)	1.41	0.00	87.0	3.0
F 2 (MV)	0.10	-0.02	175.0	91.0
F 3 (MV)	0.04	-0.01	172.0	471.0
F 4 (MV)	0.02	-0.03	469.0	174.0
F 5 (MV)	0.05	-0.08	462.0	175.0
F 6 (MV)	0.03	-0.03	90.0	175.0
F 7 (MV)	0.02	-0.01	468.0	224.0
F 8 (MV)	0.05	-0.02	175.0	92.0
F 9 (MV)	0.02	-0.01	126.0	470.0
F 10 (MV)	0.01	-0.02	467.0	221.0
F 11 (MV)	0.02	-0.03	89.0	175.0
F 12 (MV)	0.03	-0.01	88.0	174.0
F 13 (MV)	0.02	-0.03	467.0	170.0
F 14 (MV)	0.09	-0.02	174.0	91.0
F 15 (MV)	0.04	-0.02	170.0	469.0
F 16 (MV)	0.01	-0.02	467.0	85.0
F 17 (MV)	0.03	-0.08	93.0	174.0
F 18 (MV)	0.02	-0.02	88.0	175.0
F 19 (MV)	0.03	0.00	75.0	224.0
F 20 (MV)	0.07	0.00	175.0	2.0
F 21 (MV)	0.02	0.00	172.0	468.0
F 22 (MV)	0.02	-0.02	466.0	223.0
F 23 (MV)	0.04	-0.04	91.0	175.0
F 24 (MV)	0.02	-0.01	88.0	469.0
FA1 Y ACCEL (G)	1.09	-3.47	452.0	119.0
FA2 Z ACCEL (G)	16.02	-2.92	171.0	178.0
TA1 Y ACCEL (G)	1.37	-1.47	460.0	164.0
TA2 Z ACCEL (G)	1.57	-12.54	203.0	172.0
T 1 (MV)	0.08	-0.02	172.0	472.0
T 2 (MV)	0.24	-0.03	173.0	27.0
T 3 (MV)	0.03	-0.03	468.0	221.0
T 4 (MV)	0.00	-0.02	29.0	172.0
T 5 (MV)	0.02	-0.16	26.0	173.0
T 6 (MV)	0.02	-0.06	244.0	174.0
VELOCITY (FT/SEC)	33.20	-0.06	189.0	0.0
T 7 (MV)	0.11	-0.03	172.0	471.0
T 8 (MV)	0.24	-0.03	173.0	27.0
T 9 (MV)	0.03	-0.04	467.0	169.0
T 10 (MV)	0.01	-0.05	26.0	173.0
T 11 (MV)	0.04	-0.38	27.0	173.0
T 12 (MV)	0.03	-0.28	245.0	173.0

TEST 4639 CELL C



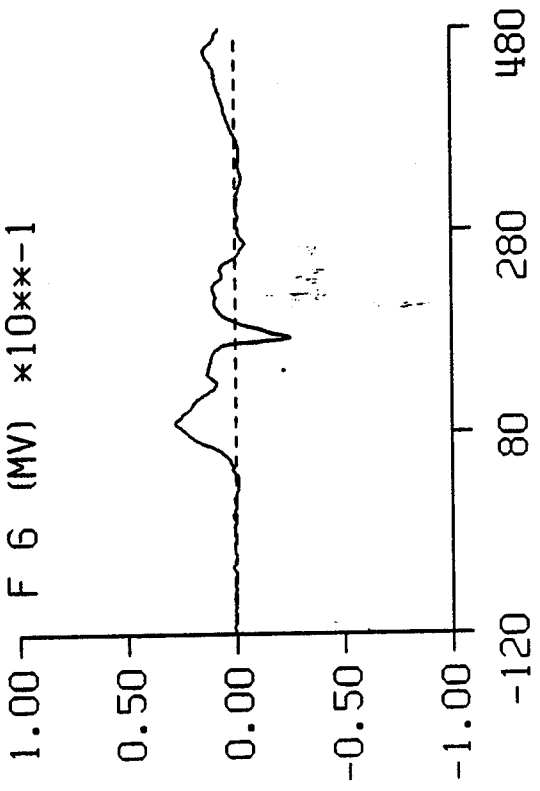
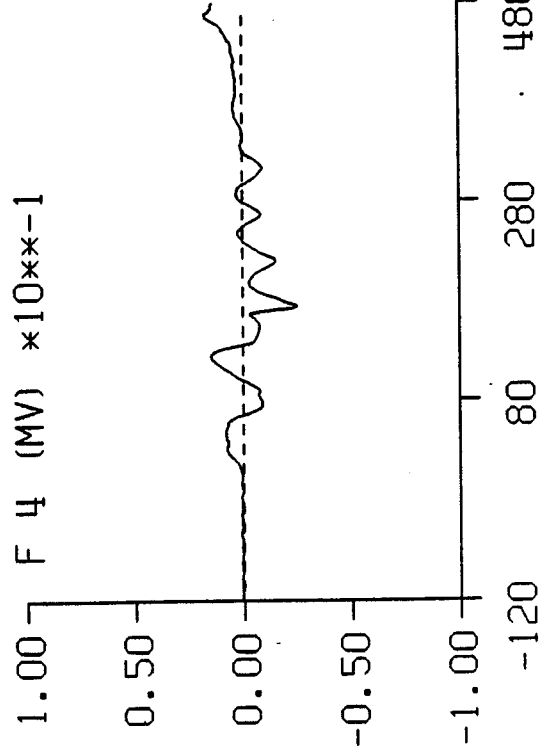
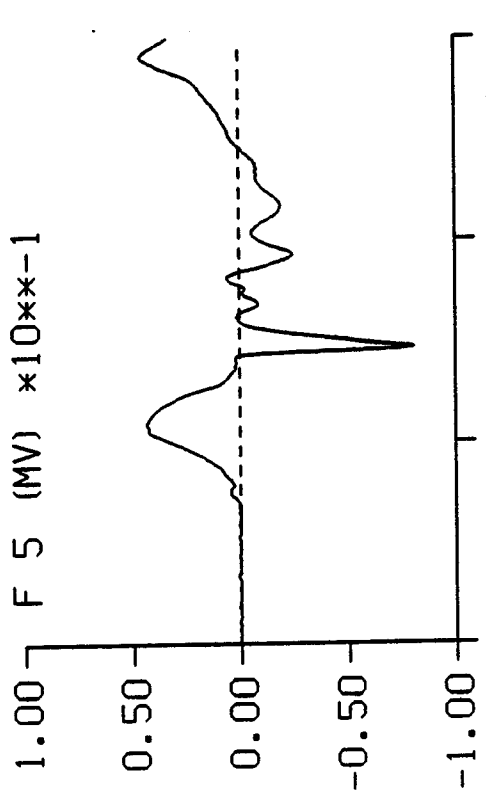
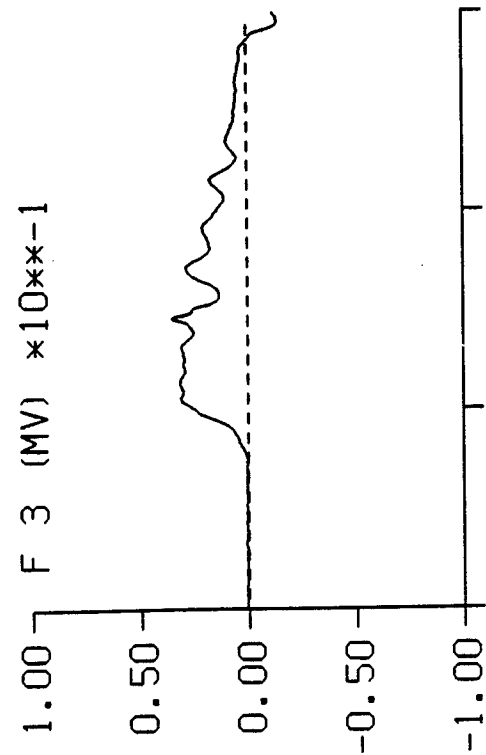
TIME IN MILLISECONDS

TEST 4639 CELL C



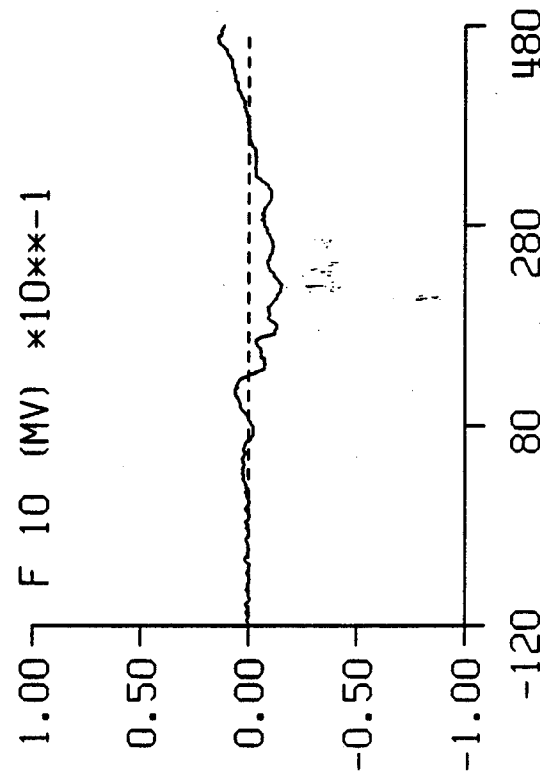
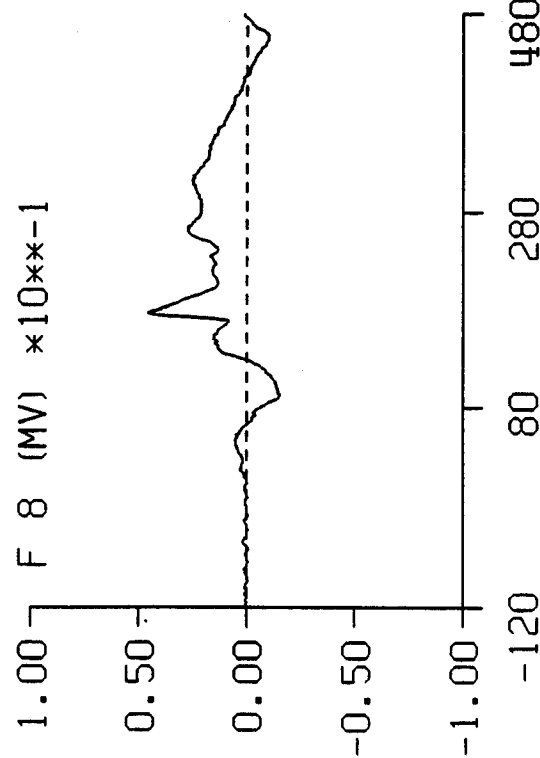
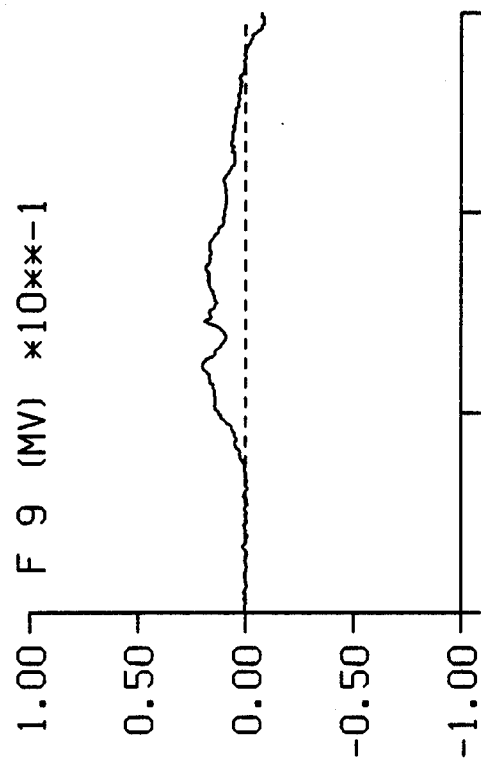
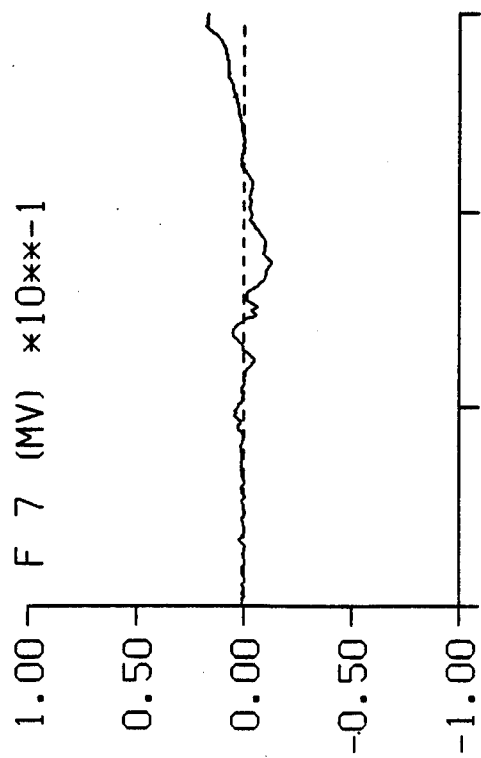
TIME IN MILLISECONDS

TEST 4639 CELL C.



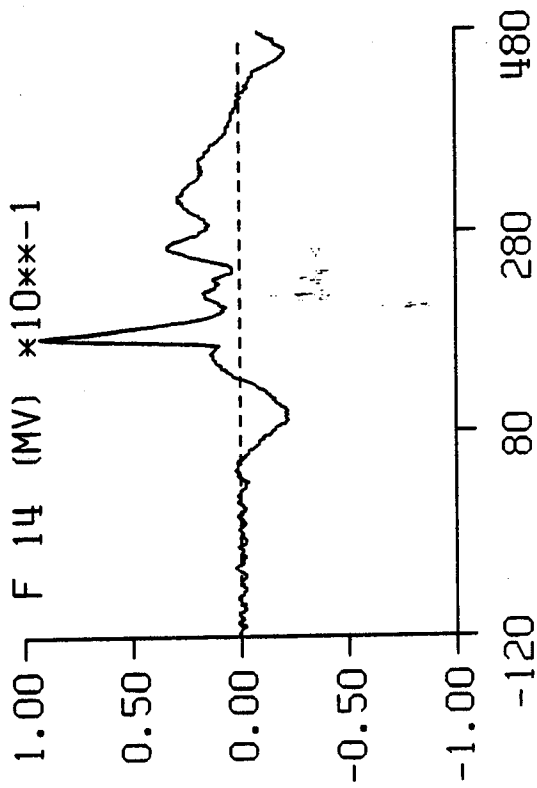
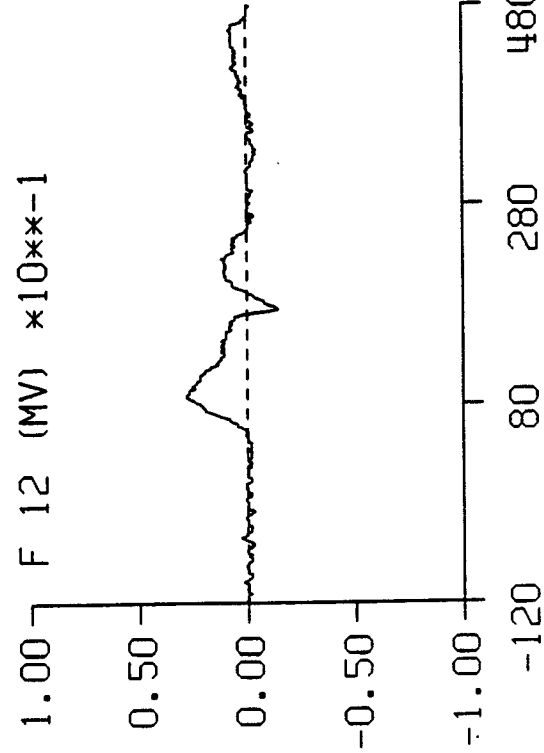
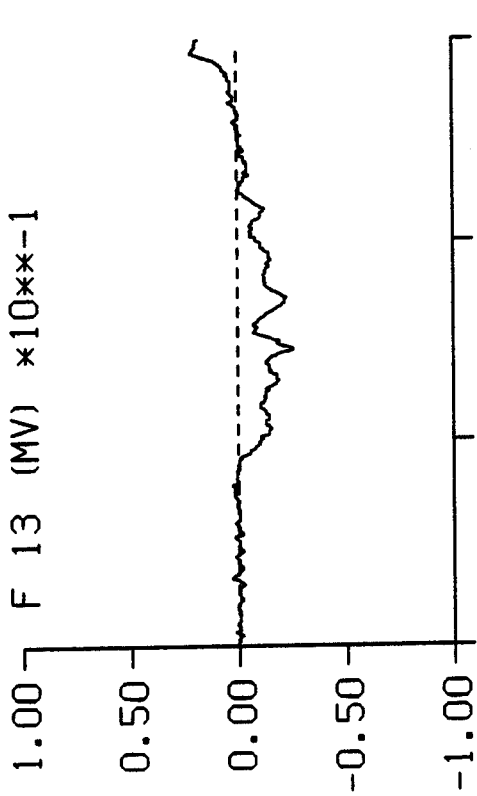
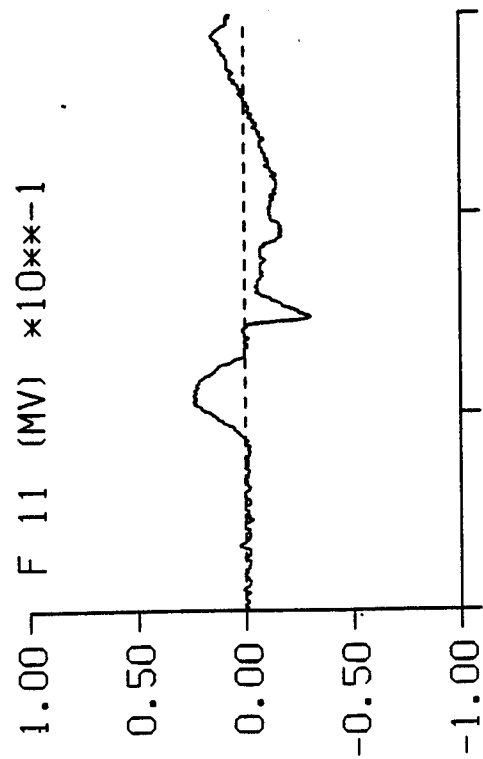
TIME IN MILLISECONDS

TEST 4639 CELL C



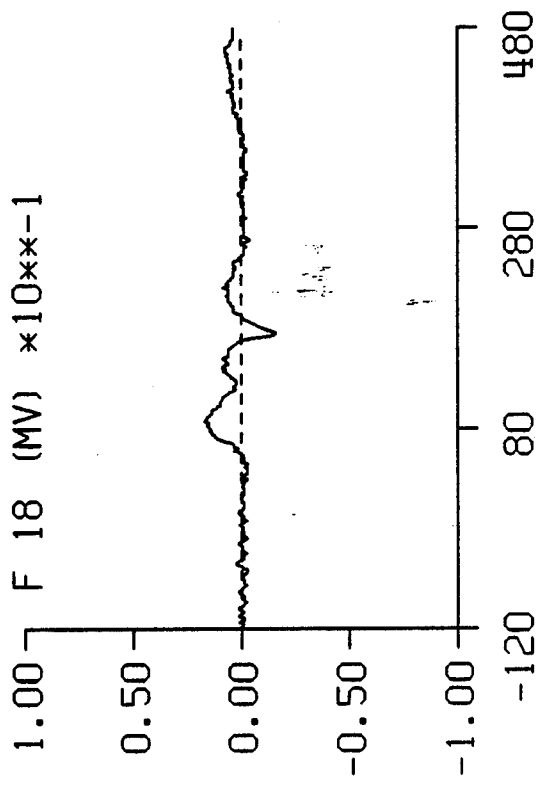
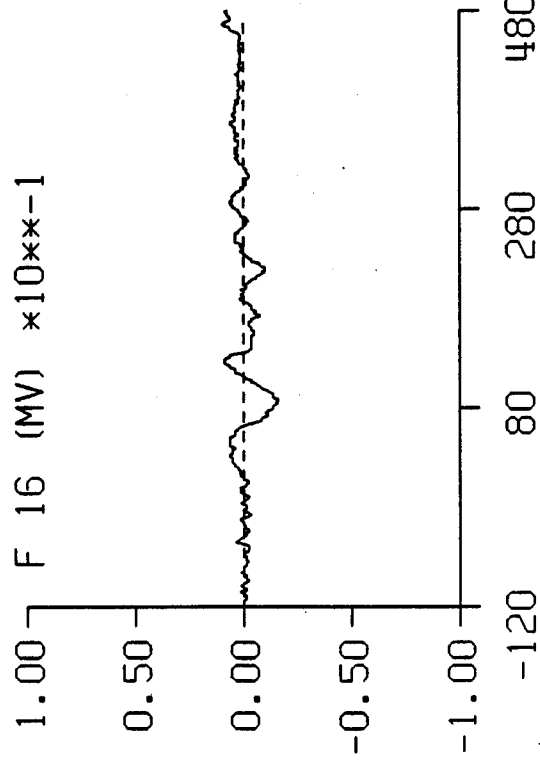
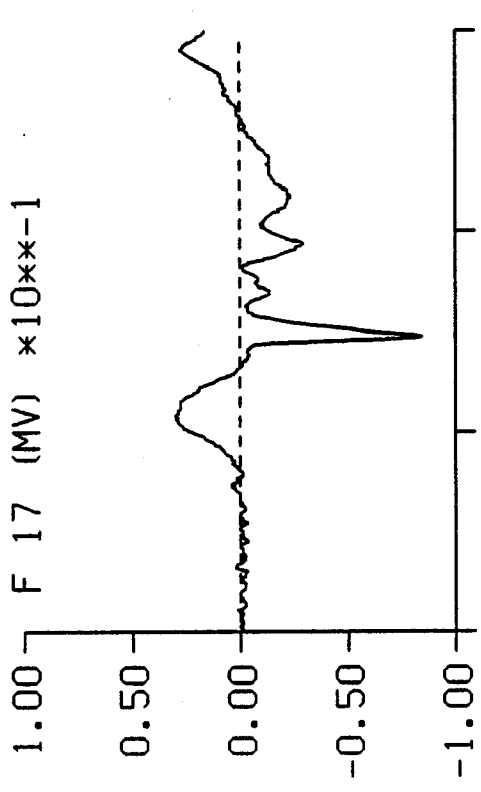
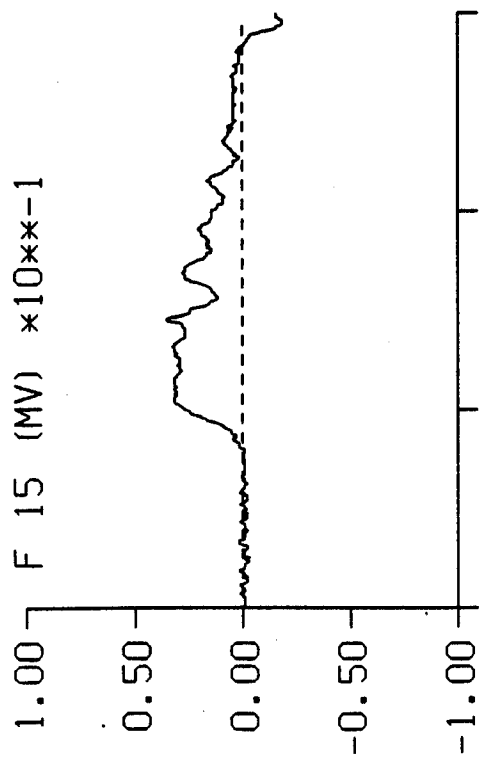
TIME IN MILLISECONDS

TEST 4639 CELL C



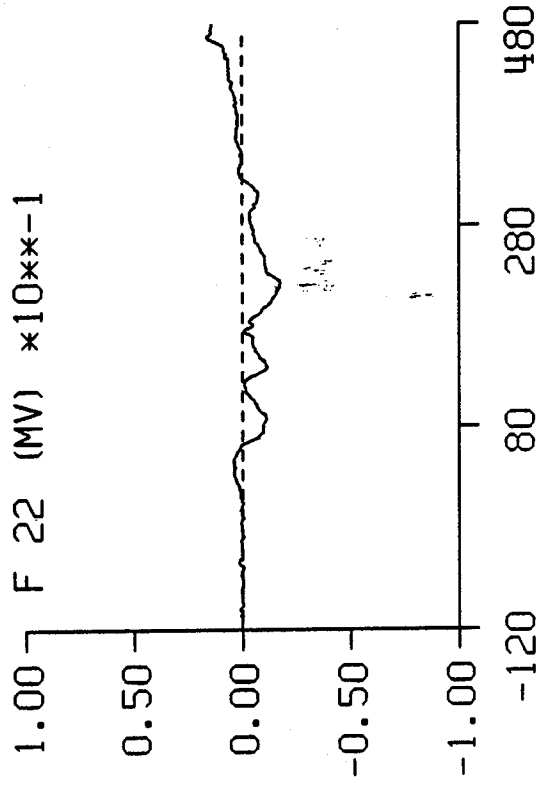
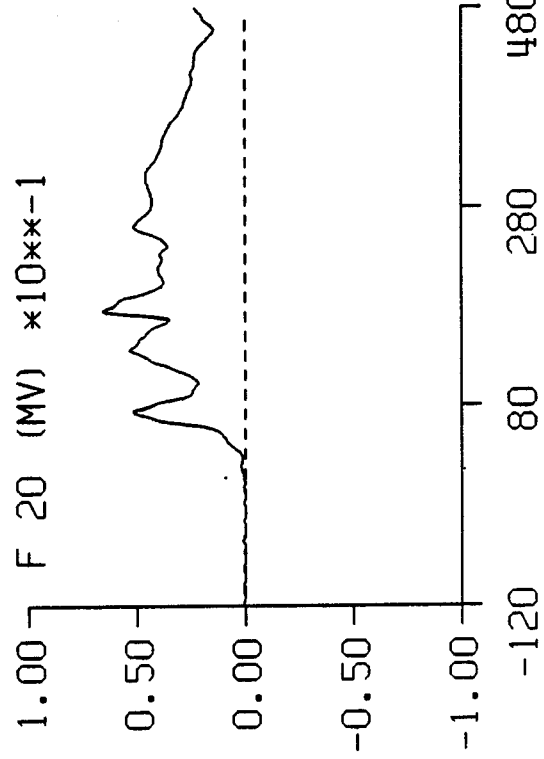
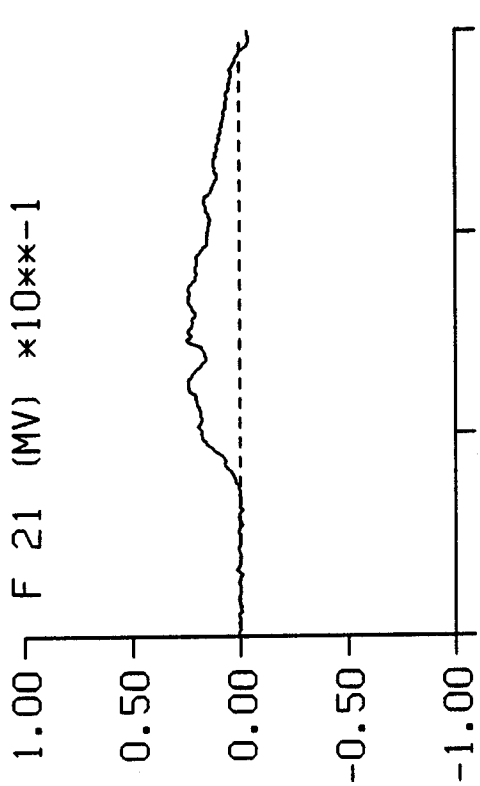
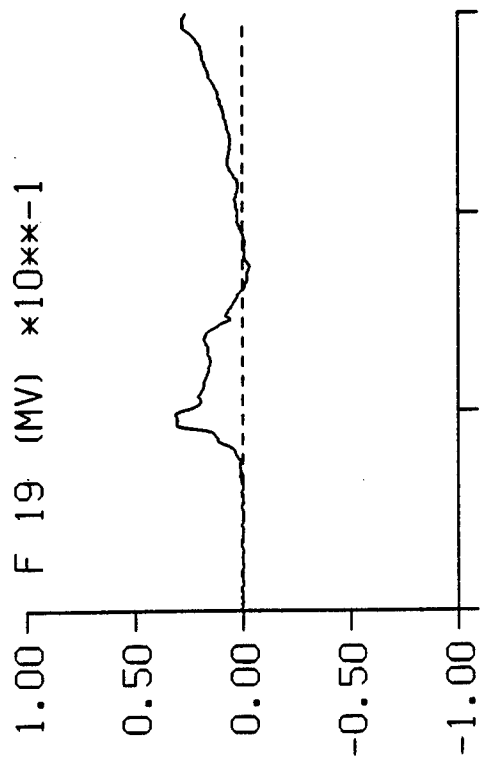
TIME IN MILLISECONDS

TEST 4639 CELL C



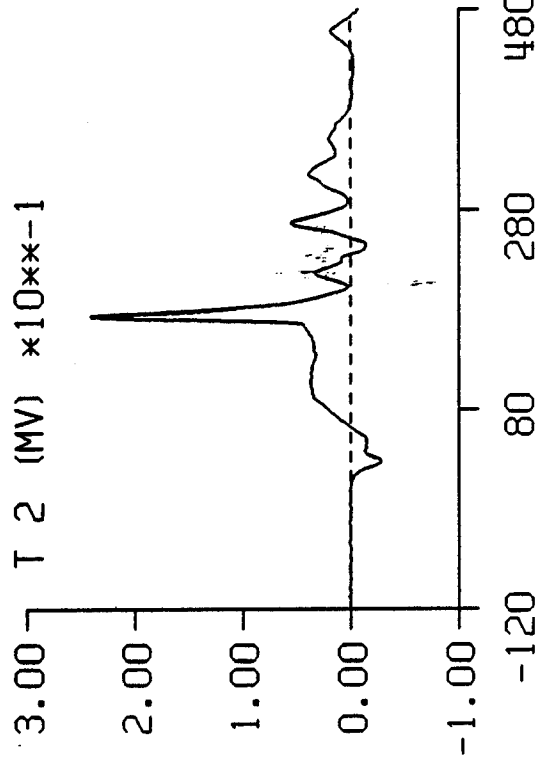
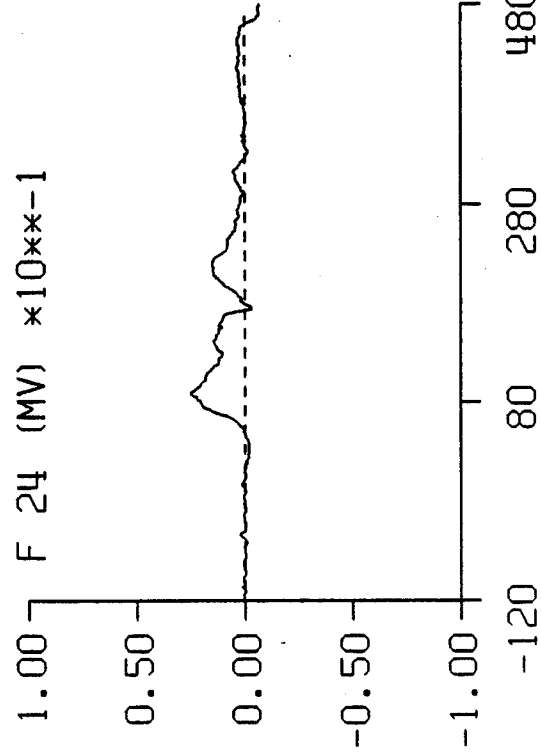
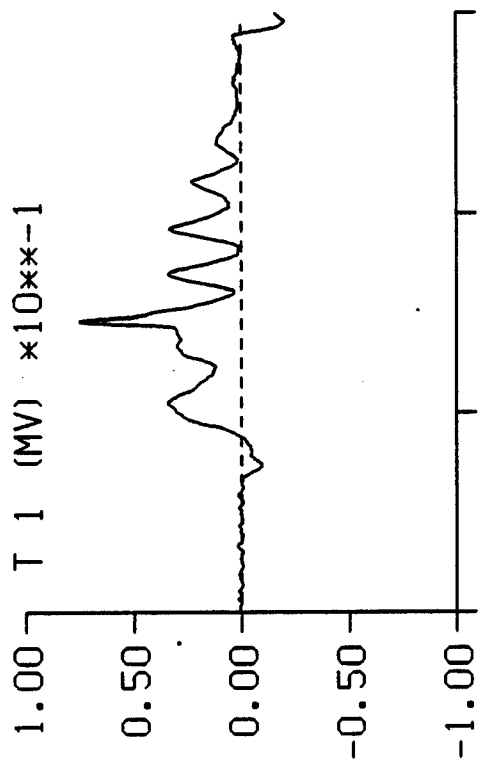
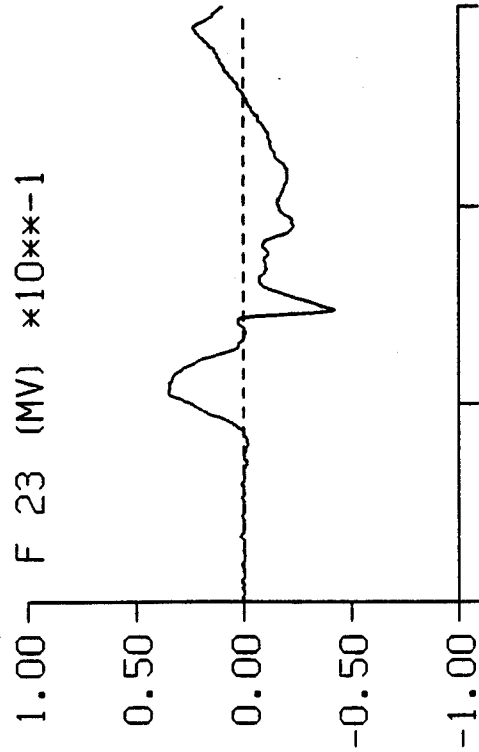
TIME IN MILLISECONDS

TEST 4639 CELL C



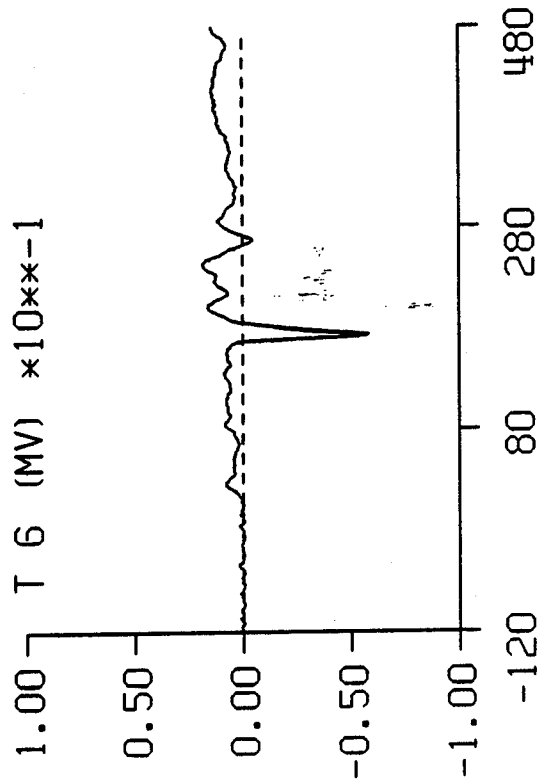
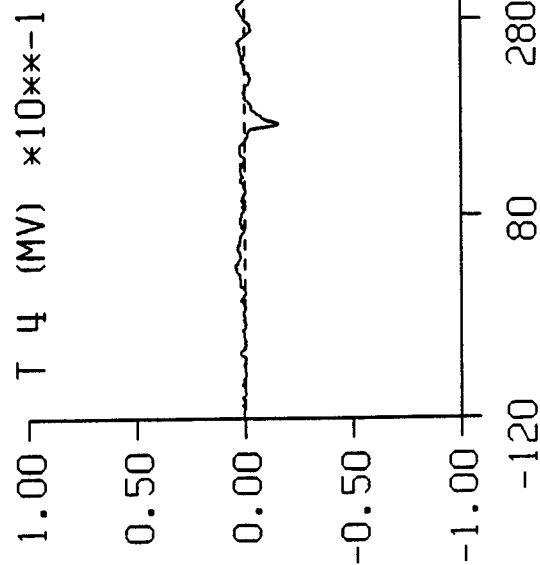
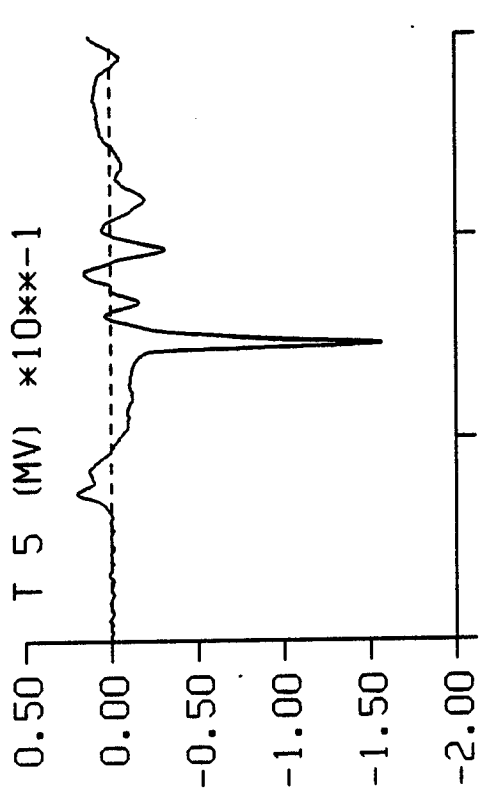
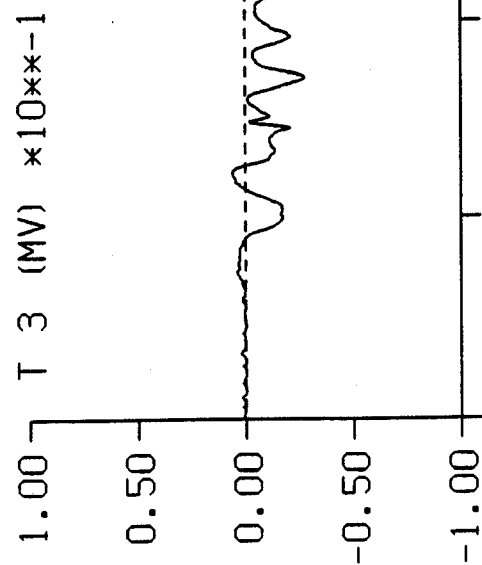
TIME IN MILLISECONDS

TEST 4639 CELL C



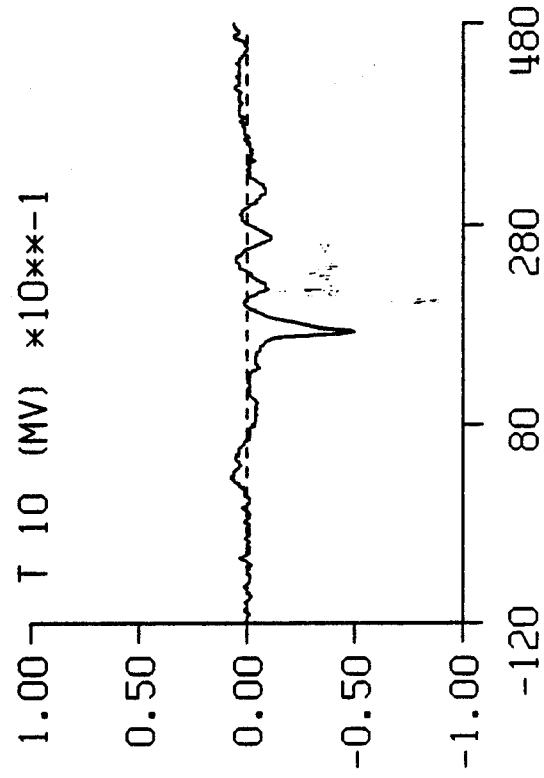
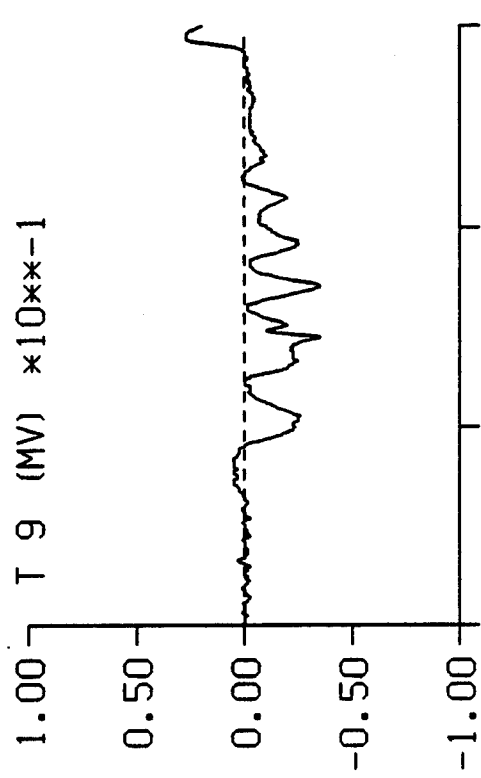
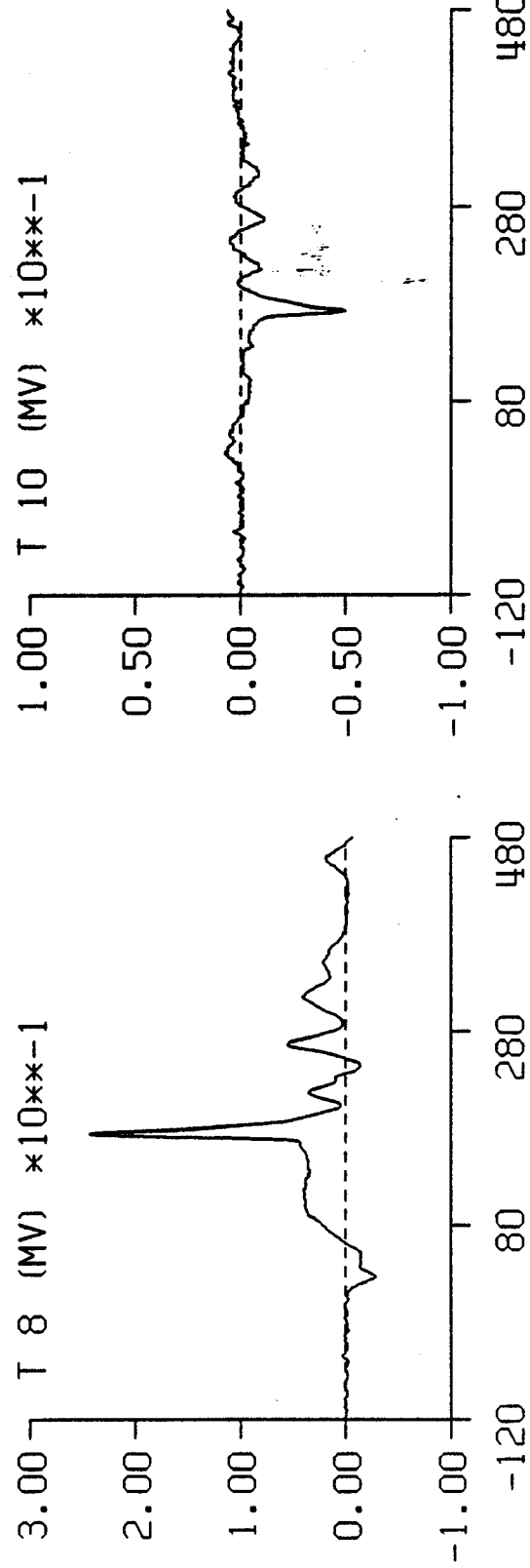
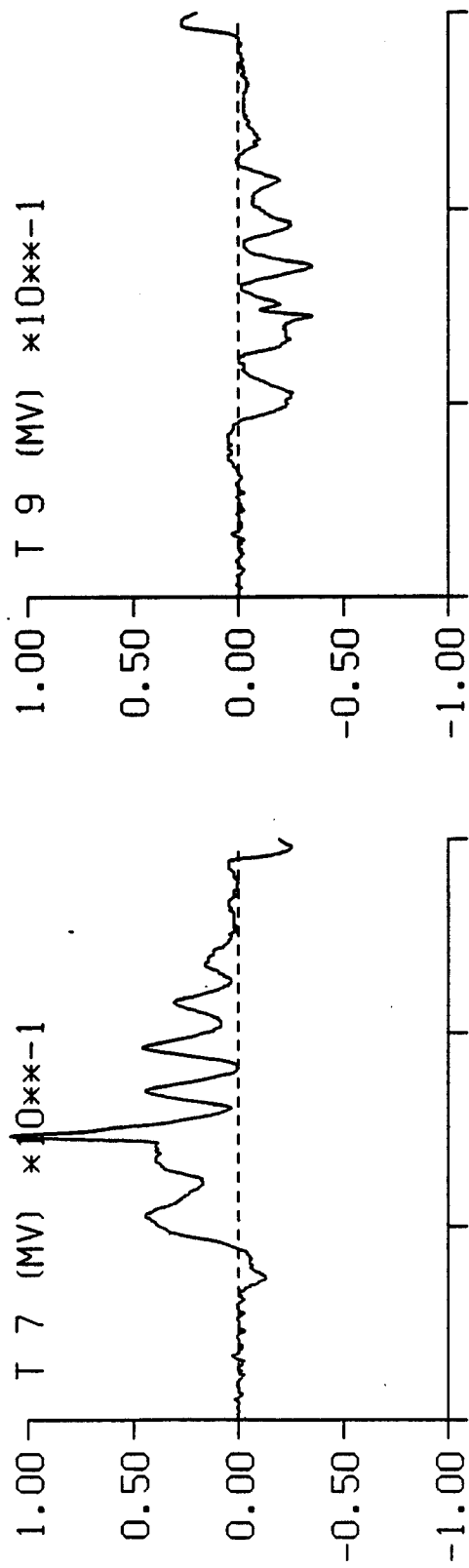
TIME IN MILLISECONDS

TEST 4639 CELL C

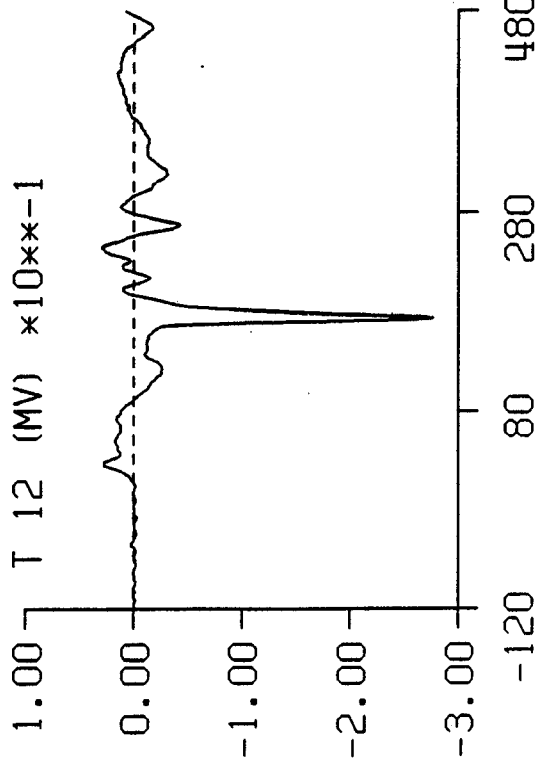
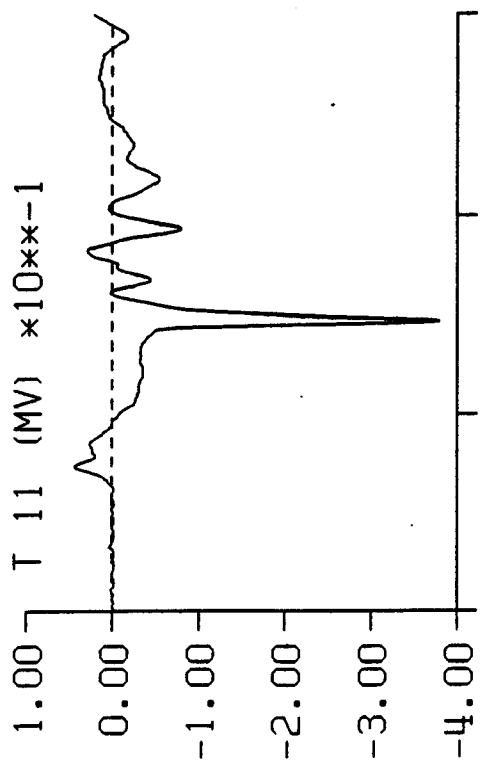


TIME IN MILLISECONDS

TEST 4639 CELL C



TEST 4639 CELL C

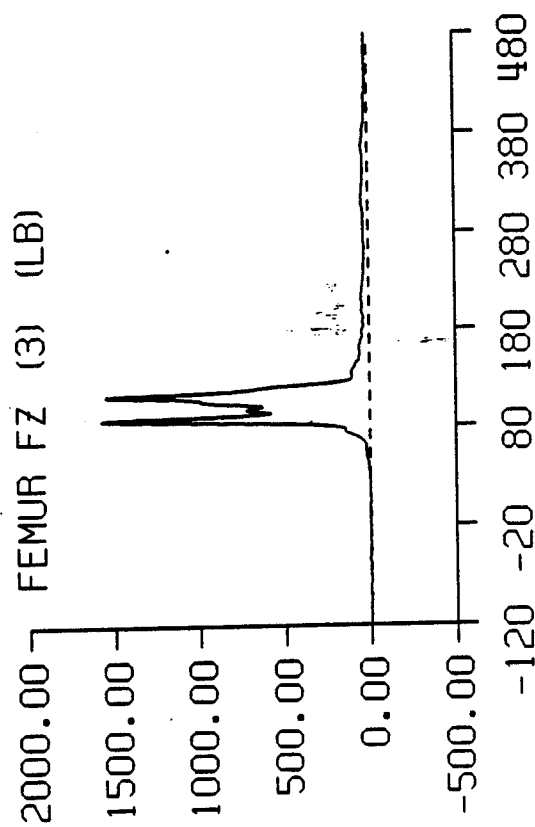
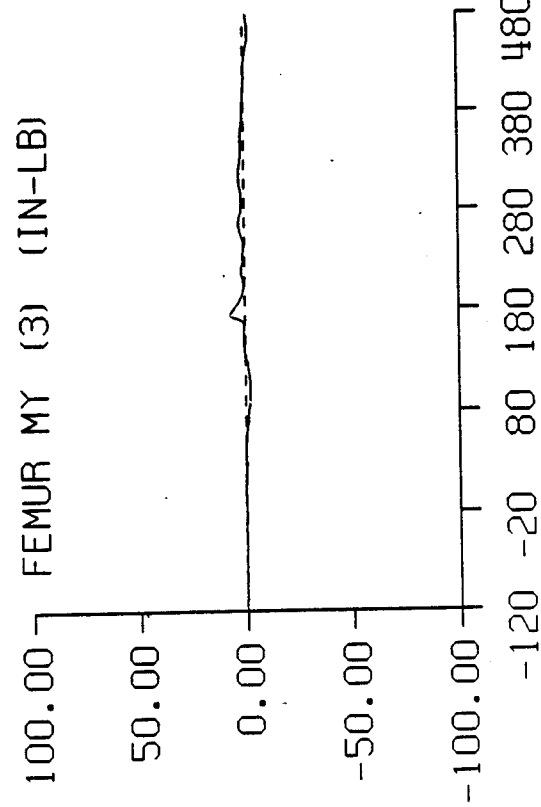
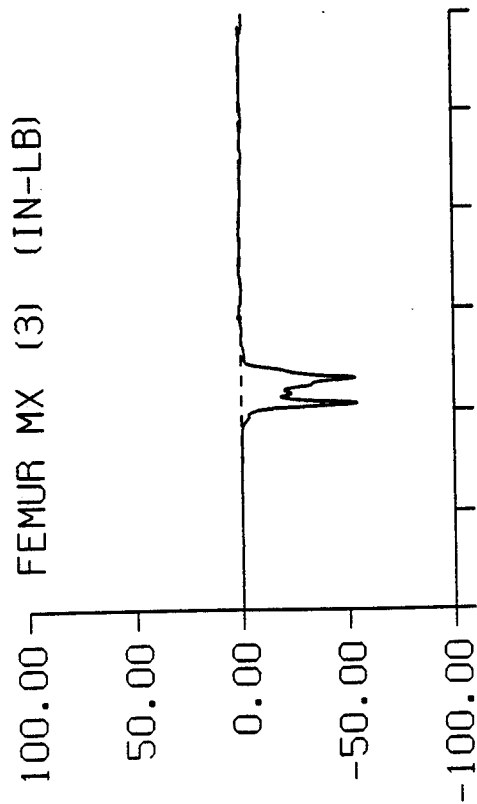


TIME IN MILLISECONDS

SPARTA -GX STUDY TEST: 4639

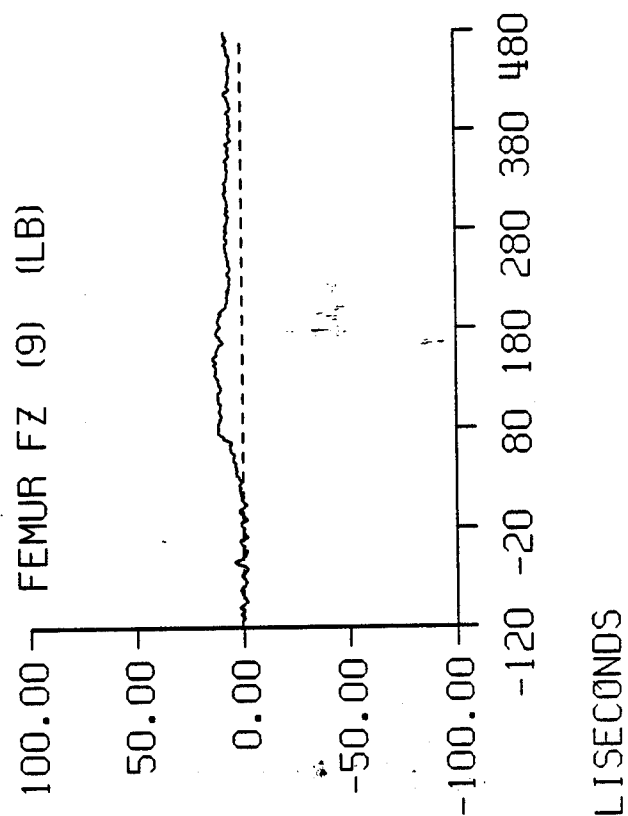
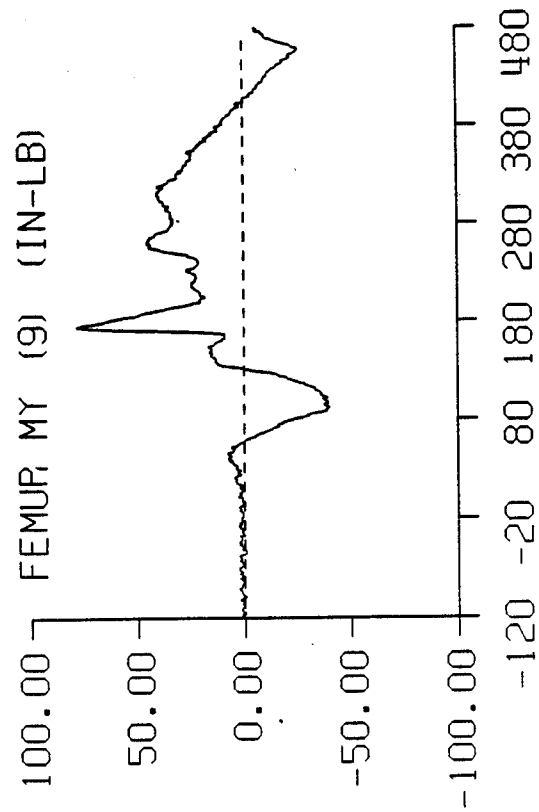
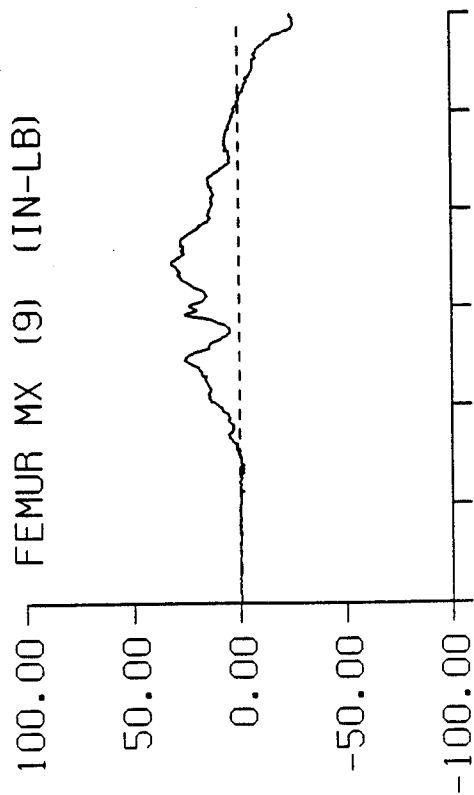
DATA ID	IMMEDIATE PREIMPACT	MAXIMUM VALUE	MINIMUM VALUE	TIME OF MAXIMUM	TIME OF MINIMUM
REFERENCE MARK TIME (MS)				-126.	
FEMUR					
MX (3) (IN-LB)	0.07	1.31	-54.83	172.	87.
MY (3) (IN-LB)	0.02	7.03	-2.47	175.	462.
FZ (3) (LB)	-0.75	1576.95	-2.75	87.	3.
MX (9) (IN-LB)	-0.43	31.84	-26.72	224.	470.
MY (9) (IN-LB)	1.17	78.60	-40.45	175.	92.
FZ (9) (LB)	-0.55	13.68	-1.85	150.	4.
MX (15) (IN-LB)	-0.05	4.93	-3.14	170.	469.
MY (15) (IN-LB)	0.00	14.40	-4.27	174.	97.
FZ (15) (LB)	-1.79	19.40	-2.59	112.	4.
MX (21) (IN-LB)	-0.19	26.89	-31.88	224.	468.
MY (21) (IN-LB)	0.13	66.23	-2.31	176.	31.
FZ (21) (LB)	-0.05	55.99	-0.70	75.	4.
TIBIA					
MX (3) (IN-LB)	0.01	4.51	-9.09	472.	172.
MY (3) (IN-LB)	-0.02	4.76	-39.38	27.	173.
FZ (3) (LB)	0.08	20.27	-2.11	174.	28.
MX (9) (IN-LB)	0.00	3.53	-9.17	471.	171.
MY (9) (IN-LB)	0.01	4.91	-41.95	27.	173.
FZ (9) (LB)	-0.53	4.50	-7.39	96.	173.

SPARTA -GX STUDY TEST: 4639

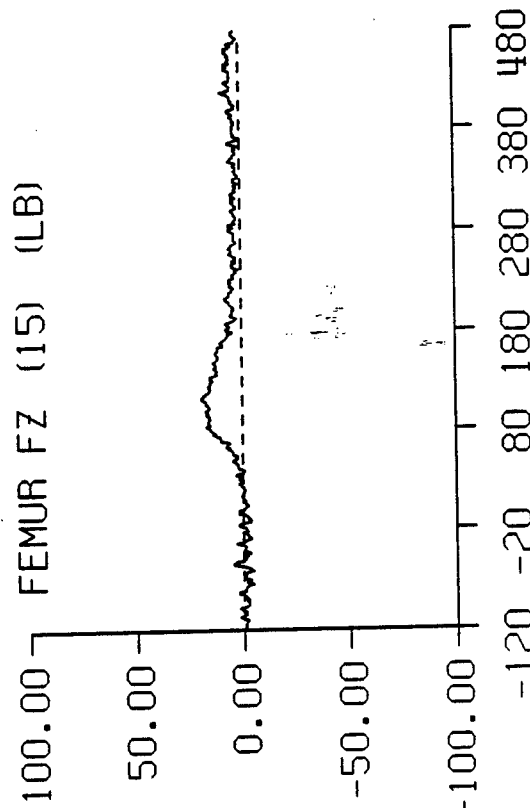
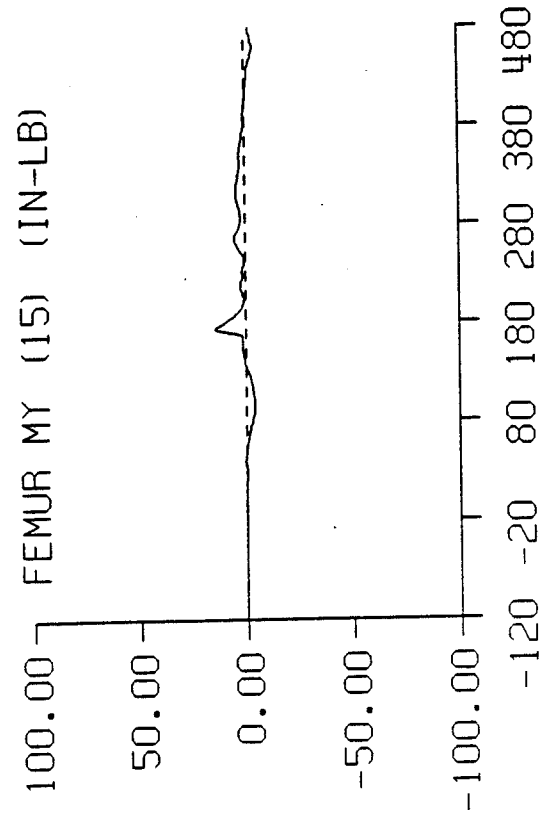
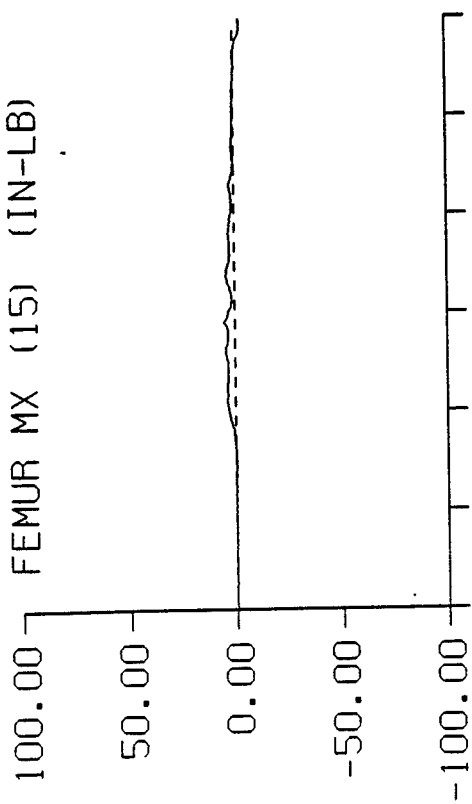


TIME IN MILLISECONDS

SPARTA -GX STUDY TEST: 4639

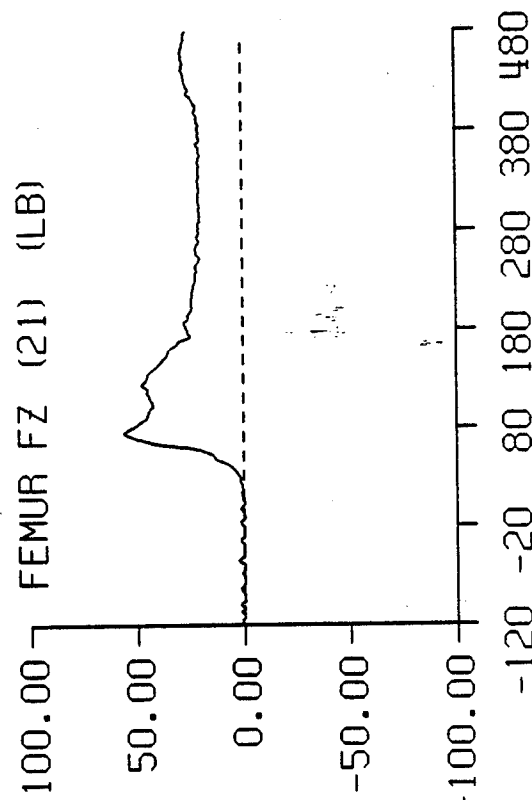
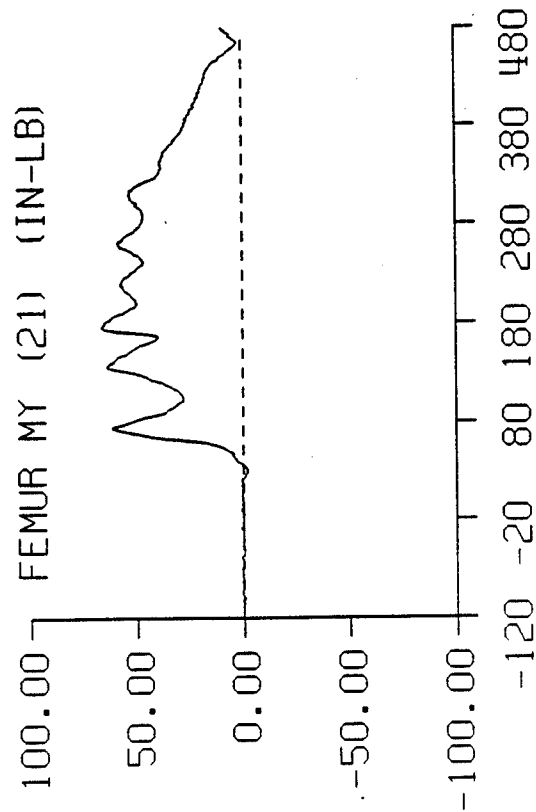
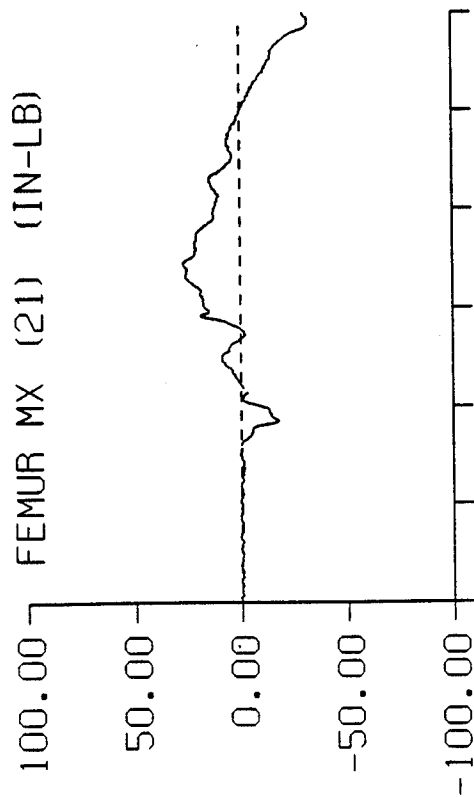


SPARTA -GX STUDY TEST: 4639



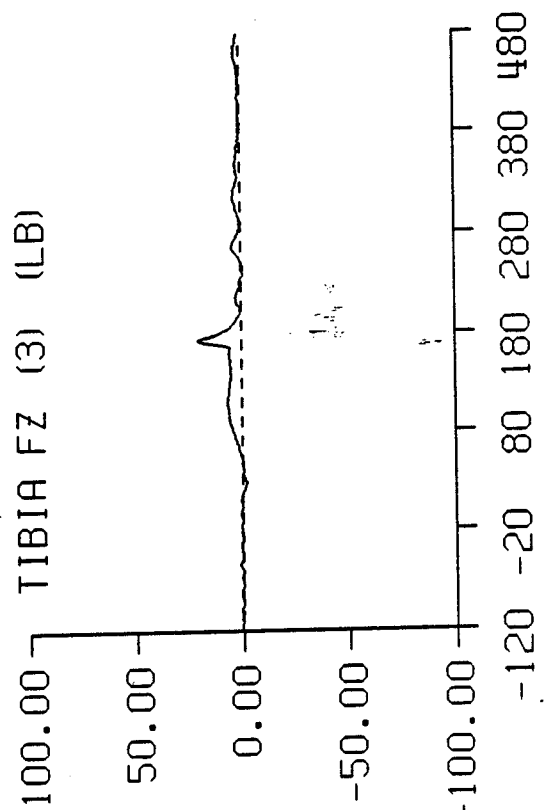
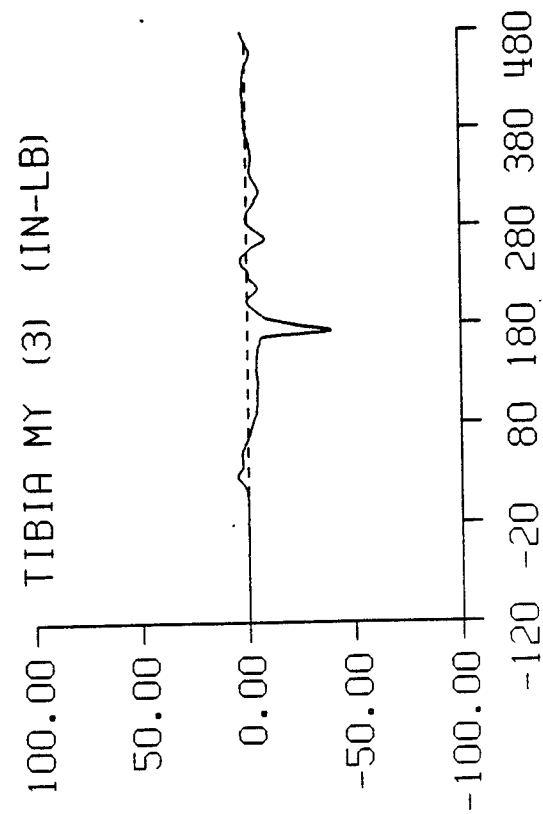
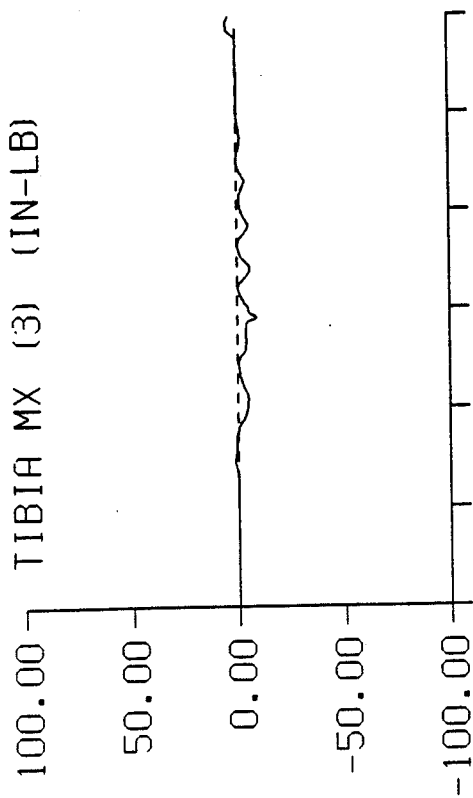
TIME IN MILLISECONDS

SPARTA -GX STUDY TEST: 4639



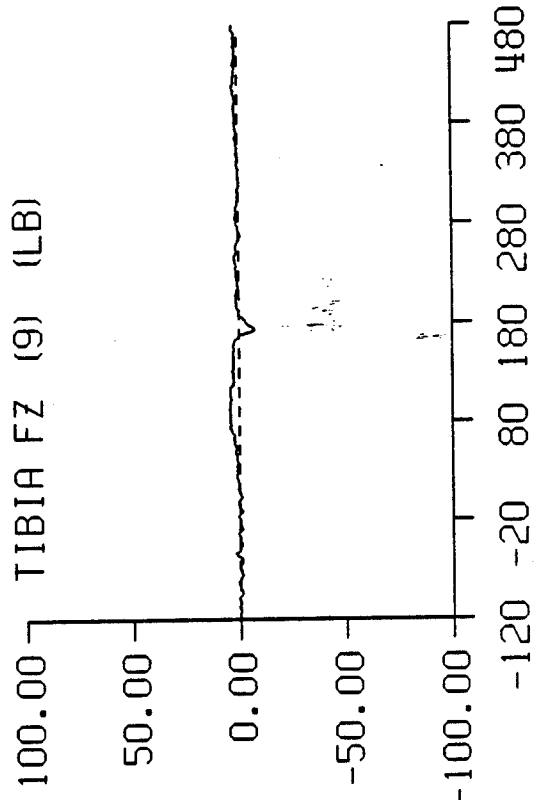
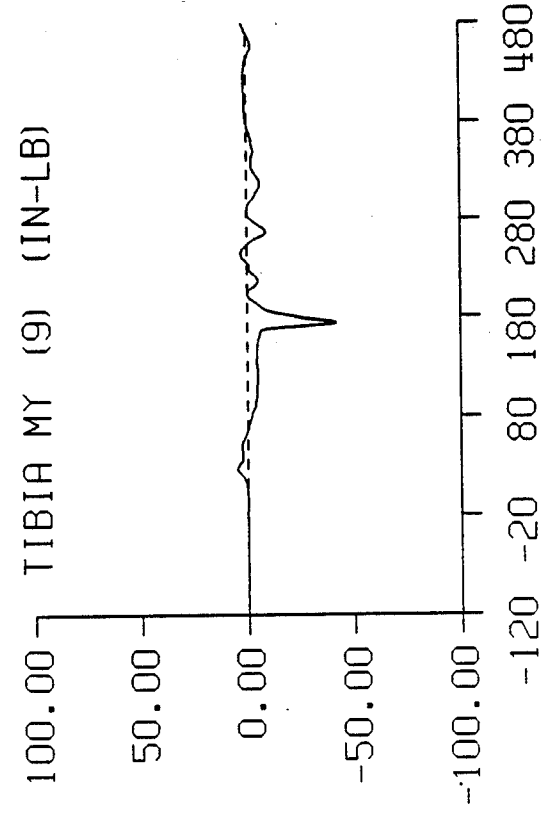
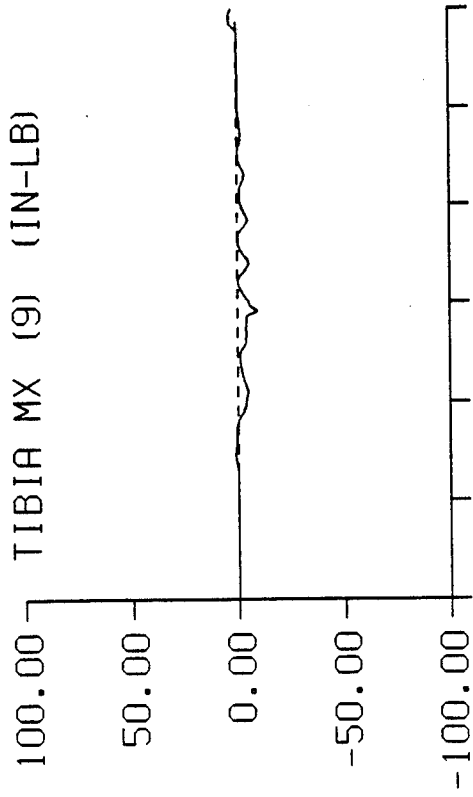
TIME IN MILLISECONDS

SPARTA -GX STUDY TEST: 4639



TIME IN MILLISECONDS

SPARTA -CX STUDY TEST: 4639



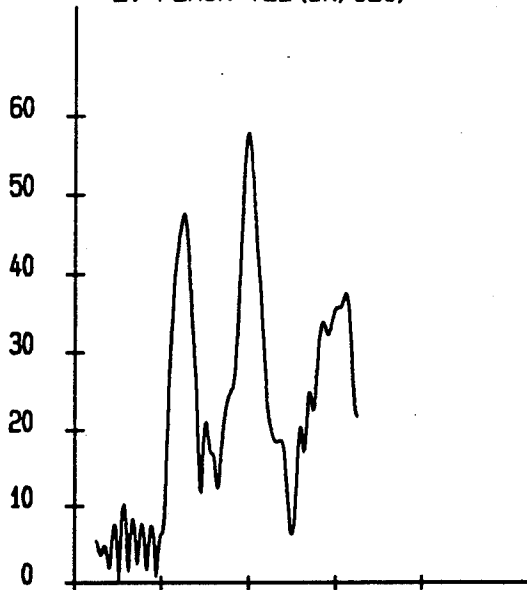
TIME IN MILLISECONDS

TEST 4 (4641) 10.0 G

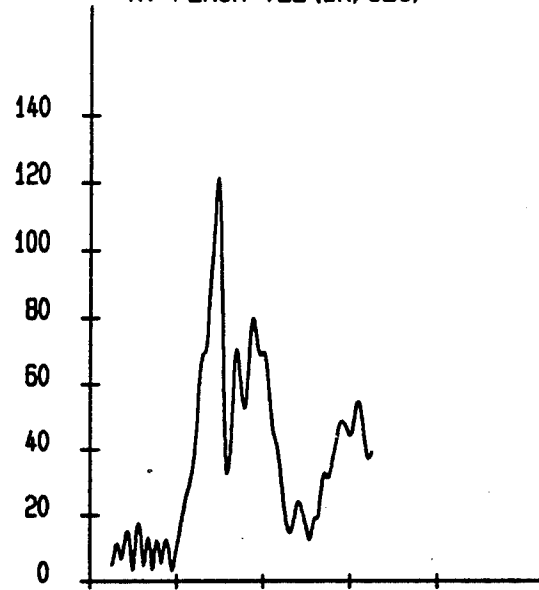
SPARTA -GX

TEST: 4641 DATE: 24-SEP-1993 SUBJ: HB3-50 CELL: D

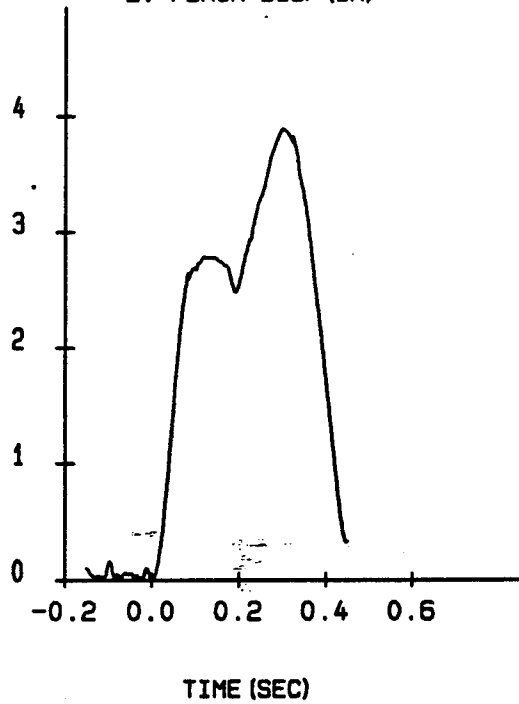
L. FEMUR VEL (IN/SEC)



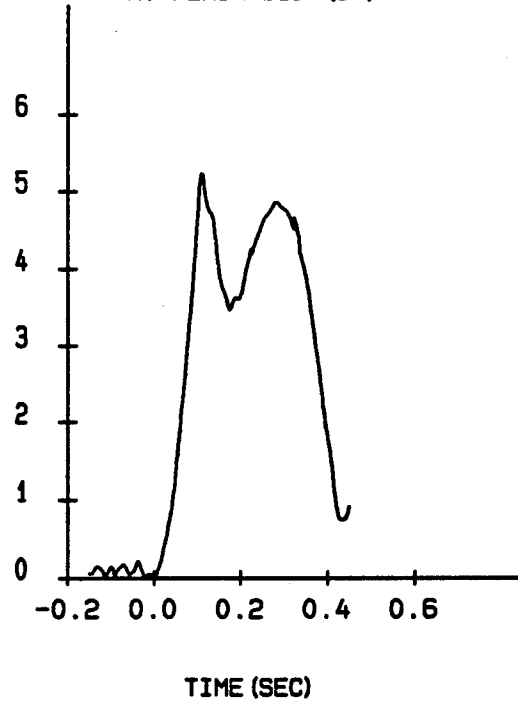
R. FEMUR VEL (IN/SEC)



L. FEMUR DISP (IN)

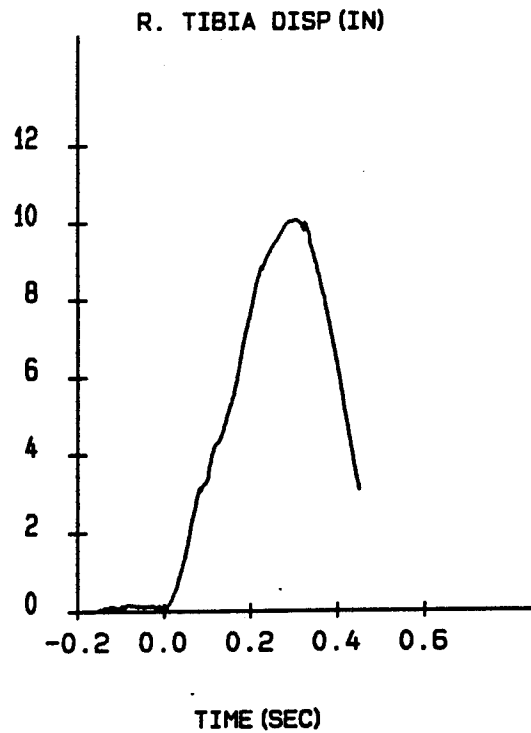
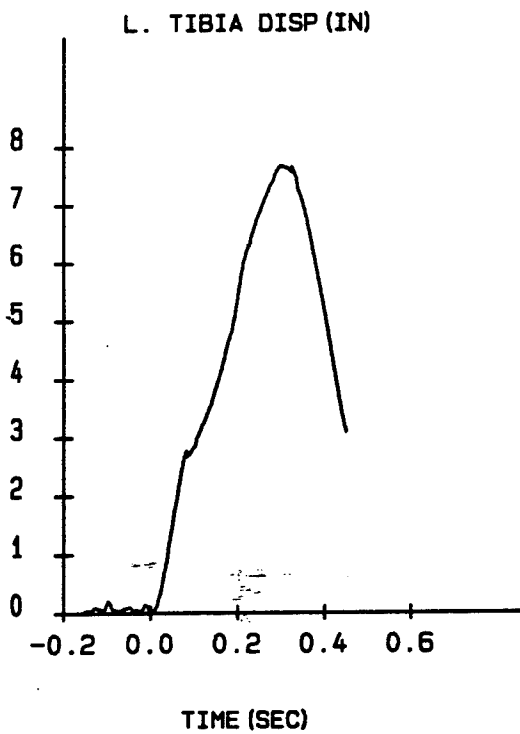
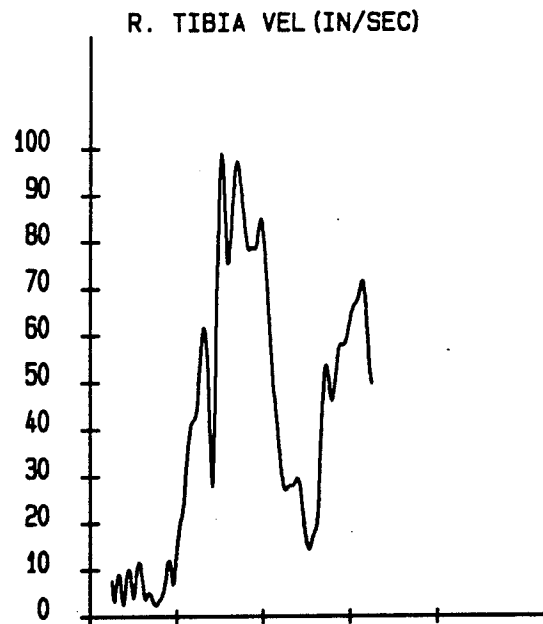
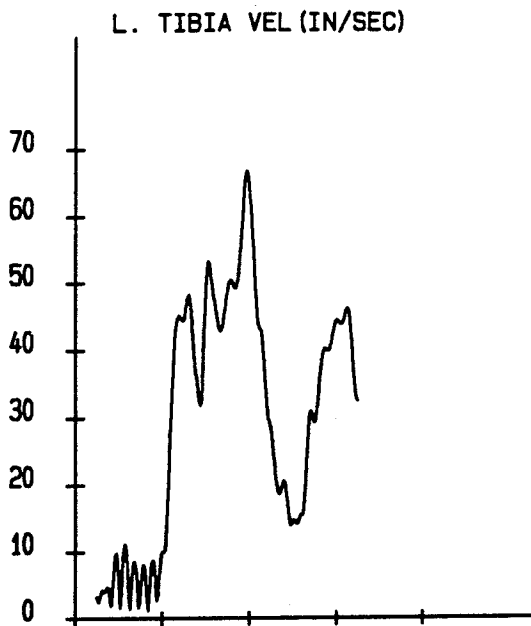


R. FEMUR DISP (IN)



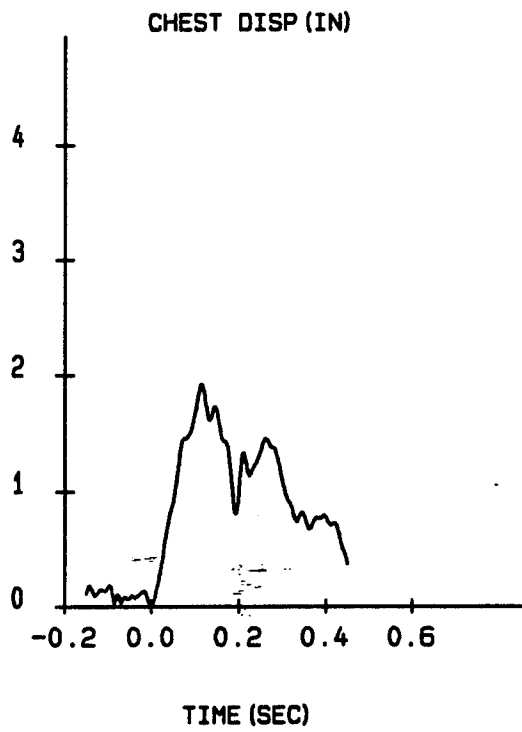
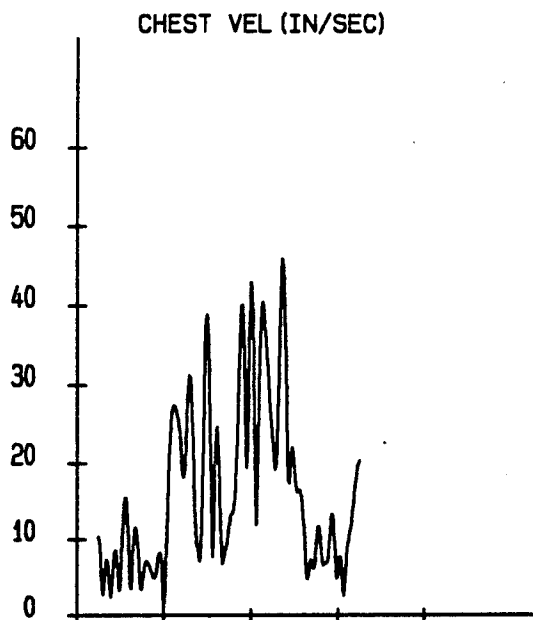
SPARTA -GX

TEST: 4641 DATE: 24-SEP-1993 SUBJ: HB3-50 CELL: D



SPARTA -GX

TEST: 4641 DATE: 24-SEP-1993 SUBJ: HB3-50 CELL: D



SPARTA -GX
TEST: 4641 DATE: 24-SEP-1993 SUBJ: HB3-50 CELL: D

RELIABILITY FACTORS (IN)					
TARGET DESCRIPTION	MAXIMUM	MINIMUM	AVERAGE	STANDARD DEVIATION	AT MAX DISPLACEMENT
1 L. FEMUR	0.2351	0.0028	0.0882	0.0617	0.1753
2 R. FEMUR	0.2288	0.0079	0.1011	0.0526	0.1931
3 L. TIBIA	0.2434	0.0018	0.1113	0.0766	0.2120
4 R. TIBIA	0.2514	0.0008	0.1102	0.0776	0.2298
5 CHEST	0.3266	0.0817	0.2061	0.0440	0.1996

TARGET	MAXIMUM	TIME(SEC)	MINIMUM	TIME(SEC)
L. FEMUR				
POSITION(IN)				
X AXIS	23.2134	0.1040	19.9241	0.2740
Y AXIS	7.2527	0.4500	5.4701	0.2700
Z AXIS	9.6019	0.3240	5.8179	0.0840
VELOCITY(IN/SEC)	57.7866	0.1980	6.3501	0.0000
ACCELERATION(G)	4.5034	0.0700	0.0443	0.4180
DISPLACEMENT(IN)				
X AXIS	2.6885	0.1040	-0.6008	0.2740
Y AXIS	0.0643	0.4500	-1.7184	0.2700
Z AXIS	3.5866	0.3240	-0.1974	0.0840
RESULTANT	3.8814	0.3000	0.0000	0.0000
R. FEMUR				
POSITION(IN)				
X AXIS	25.4964	0.1040	19.9577	0.2720
Y AXIS	-2.9928	0.1360	-6.3457	0.0160
Z AXIS	11.8414	0.3240	5.9973	0.1020
VELOCITY(IN/SEC)	121.3010	0.0960	9.8977	0.0000
ACCELERATION(G)	15.4892	0.1100	0.2289	0.1440
DISPLACEMENT(IN)				
X AXIS	3.7169	0.1040	-1.8217	0.2720
Y AXIS	3.2627	0.1360	-0.0902	0.0160
Z AXIS	3.7171	0.3240	-2.1271	0.1020
RESULTANT	5.2257	0.1100	0.0000	0.0000

SPARTA -GX

TEST: 4641 DATE: 24-SEP-1993 SUBJ: HB3-50 CELL: D

TARGET	MAXIMUM	TIME(SEC)	MINIMUM	TIME(SEC)
L. TIBIA				
POSITION(IN)				
X AXIS	27.8593	0.0820	23.5766	0.2740
Y AXIS	8.1861	0.0400	5.8110	0.2400
Z AXIS	9.4371	0.3240	2.0076	0.0240
VELOCITY(IN/SEC)	66.7479	0.1940	9.9417	0.0000
ACCELERATION(G)	5.6509	0.0900	0.2484	0.4200
DISPLACEMENT(IN)				
X AXIS	2.6988	0.0820	-1.5838	0.2740
Y AXIS	0.0676	0.0400	-2.3075	0.2400
Z AXIS	7.3510	0.3240	-0.0785	0.0240
RESULTANT	7.6692	0.3000	0.0000	0.0000
R. TIBIA				
POSITION(IN)				
X AXIS	30.9957	0.1140	25.7834	0.2740
Y AXIS	-3.2320	0.2240	-7.3550	0.0160
Z AXIS	12.0486	0.3240	2.3950	0.0860
VELOCITY(IN/SEC)	98.9411	0.1020	14.1803	0.0000
ACCELERATION(G)	11.9320	0.0880	0.6363	0.3940
DISPLACEMENT(IN)				
X AXIS	3.1127	0.1140	-2.0997	0.2740
Y AXIS	4.0032	0.2240	-0.1199	0.0160
Z AXIS	9.3721	0.3240	-0.2815	0.0860
RESULTANT	10.0612	0.3040	0.0000	0.0000
CHEST				
POSITION(IN)				
X AXIS	13.4501	0.1140	11.9487	0.0000
Y AXIS	2.2828	0.1120	0.2824	0.2820
Z AXIS	20.8192	0.1220	19.2365	0.2680
VELOCITY(IN/SEC)	45.8412	0.2720	0.9550	0.0000
ACCELERATION(G)	9.4482	0.1880	0.4837	0.3500

SPARTA -GX

TEST: 4641 DATE: 24-SEP-1993 SUBJ: HB3-50 CELL: D

TARGET	MAXIMUM	TIME(SEC)	MINIMUM	TIME(SEC)
CHEST				
DISPLACEMENT(IN)				
X AXIS	1.5014	0.1140	0.0000	0.0000
Y AXIS	1.0699	0.1120	-0.9305	0.2820
Z AXIS	0.5913	0.1220	-0.9915	0.2680
RESULTANT	1.9235	0.1140	0.0000	0.0000

SPARTA -GX

TEST: 4641 DATE: 24-SEP-1993 SUBJ: HB3-50 CELL: D

te: Invalid samples are interpolated.

mples 1153 through 1161 of the L. FEMUR target are invalid.
valid sample range occurred from 0.1040 seconds to 0.1200 seconds.

mples 1165 through 1167 of the L. FEMUR target are invalid.
valid sample range occurred from 0.1280 seconds to 0.1320 seconds.

mples 1155 through 1163 of the R. FEMUR target are invalid.
valid sample range occurred from 0.1080 seconds to 0.1240 seconds.

mples 1164 of the R. TIBIA target is invalid.
valid sample 1164 occurred at 0.1260 seconds.

mples 1189 through 1195 of the CHEST target are invalid.
valid sample range occurred from 0.1760 seconds to 0.1880 seconds.

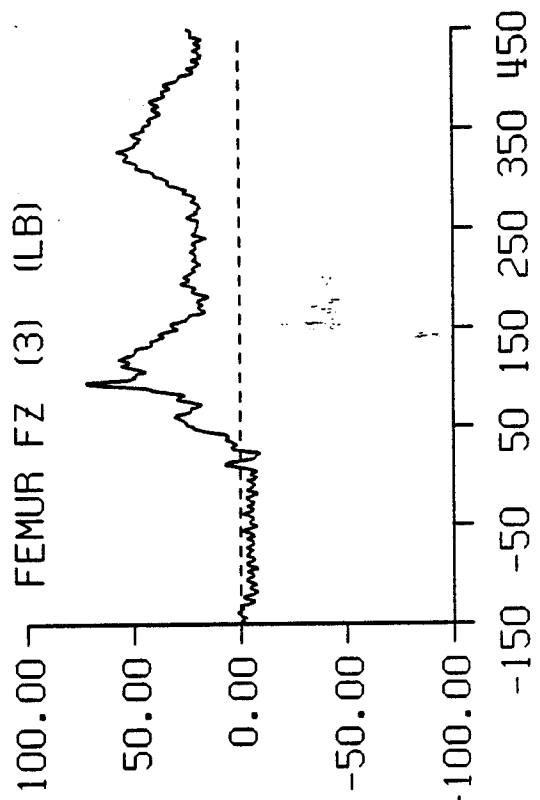
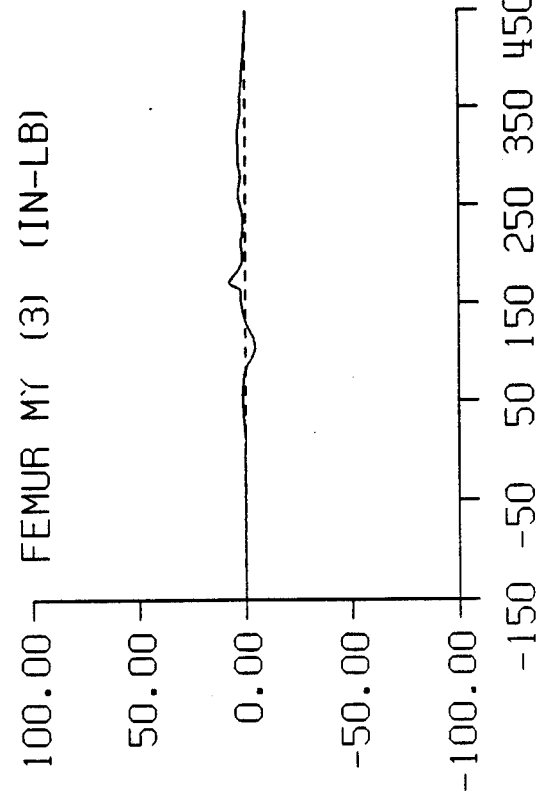
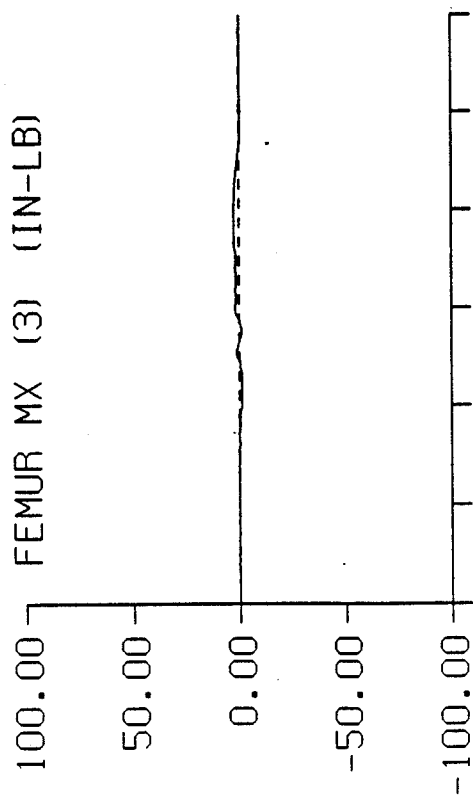
mples 1202 through 1236 of the CHEST target are invalid.
valid sample range occurred from 0.2020 seconds to 0.2700 seconds.

mples 1292 through 1295 of the CHEST target are invalid.
valid sample range occurred from 0.3820 seconds to 0.3880 seconds.

SPARTA -GX STUDY TEST: 4641

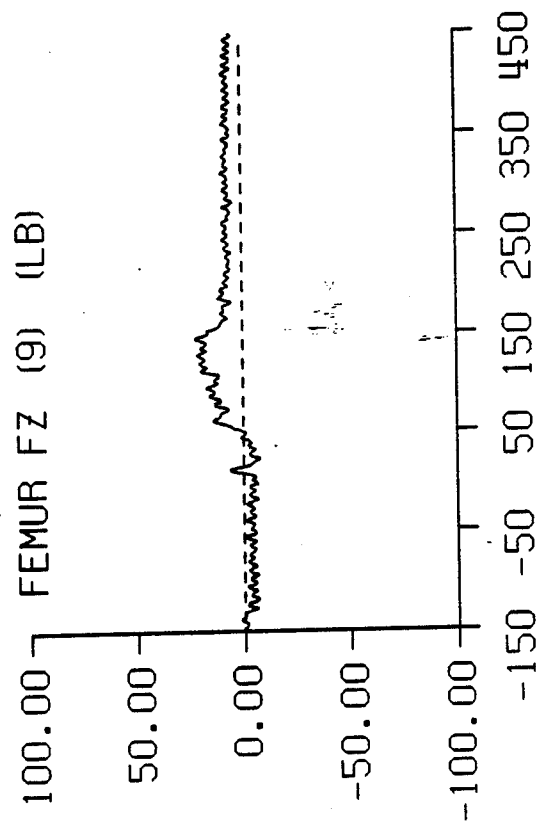
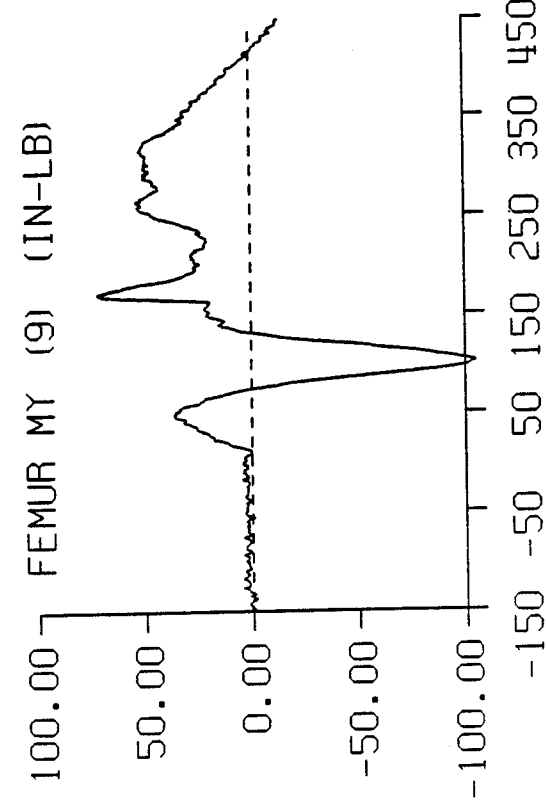
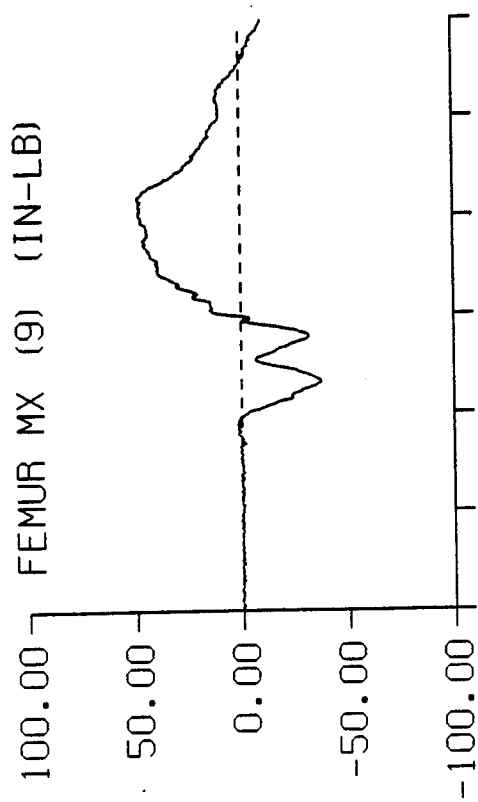
DATA ID	IMMEDIATE PREIMPACT	MAXIMUM VALUE	MINIMUM VALUE	TIME OF MAXIMUM	TIME OF MINIMUM
REFERENCE MARK TIME (MS)				-150.	
FEMUR					
MX (3) (IN-LB)	0.14	2.53	-1.27	241.	62.
MY (3) (IN-LB)	0.03	7.41	-4.72	171.	105.
FZ (3) (LB)	-5.28	72.38	-9.31	95.	23.
MX (9) (IN-LB)	-0.33	48.32	-37.62	267.	81.
MY (9) (IN-LB)	2.37	72.00	-104.98	172.	101.
FZ (9) (LB)	-3.98	21.94	-7.74	145.	23.
MX (15) (IN-LB)	-0.11	4.87	-1.59	260.	81.
MY (15) (IN-LB)	0.03	14.27	-8.03	171.	106.
FZ (15) (LB)	-6.23	32.47	-13.85	111.	32.
MX (21) (IN-LB)	-0.82	45.90	-49.47	266.	80.
MY (21) (IN-LB)	0.06	80.65	-6.51	176.	104.
FZ (21) (LB)	-2.95	77.56	-5.16	112.	22.
TIBIA					
MX (3) (IN-LB)	0.04	6.53	-9.66	124.	167.
MY (3) (IN-LB)	-0.02	13.92	-40.06	94.	170.
FZ (3) (LB)	-1.33	17.89	-6.09	170.	31.
MX (9) (IN-LB)	-0.01	3.02	-11.43	124.	167.
MY (9) (IN-LB)	0.03	5.15	-41.13	38.	170.
FZ (9) (LB)	-2.35	13.60	-11.57	87.	170.

SPARTA -GX STUDY TEST: 4641



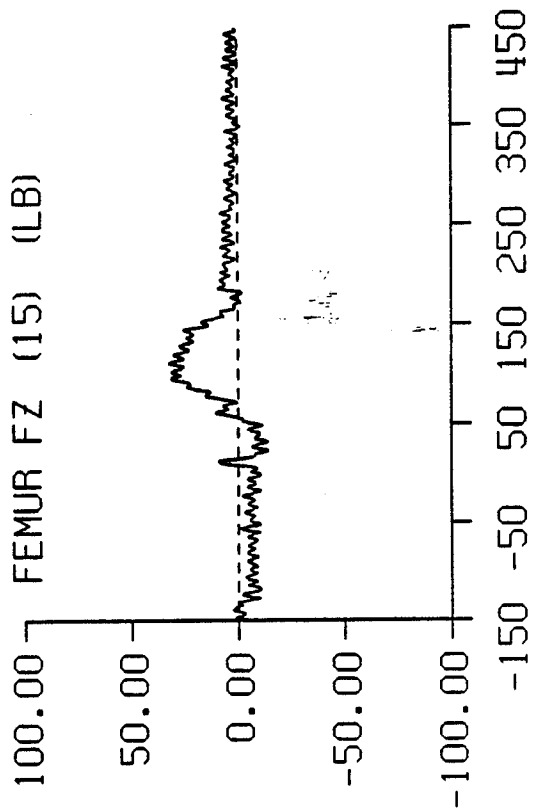
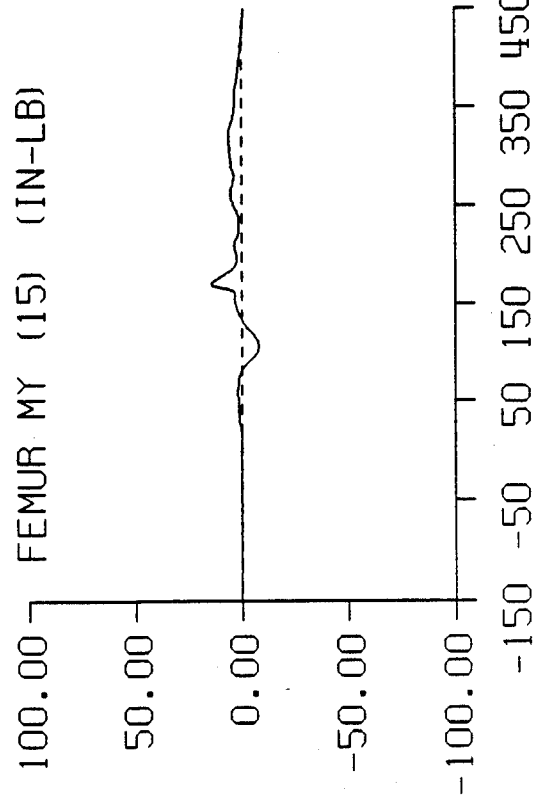
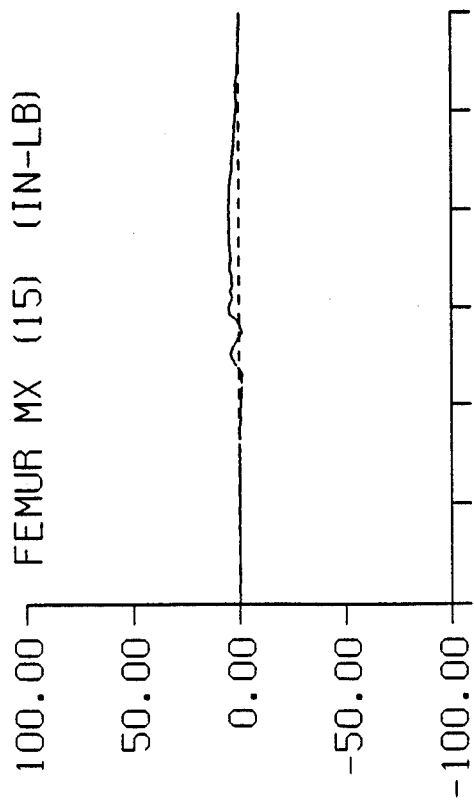
TIME IN MILLISECONDS

SPARTA -GX STUDY TEST: 4641



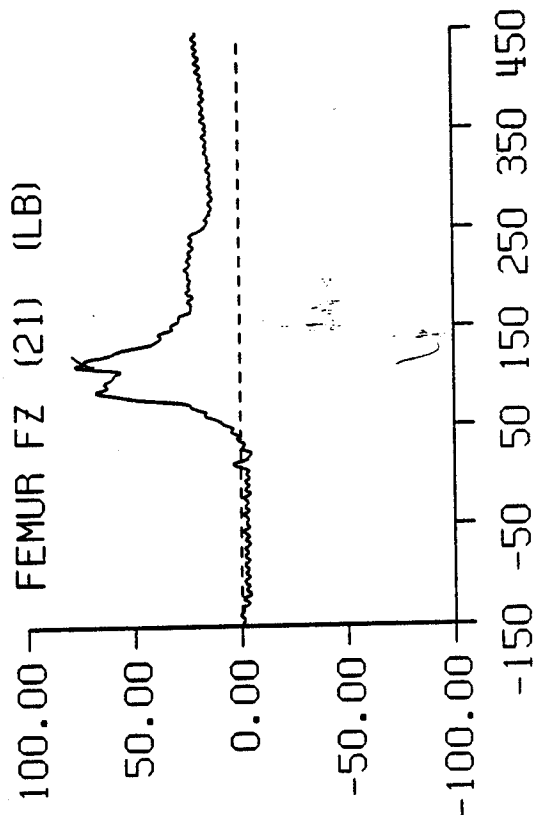
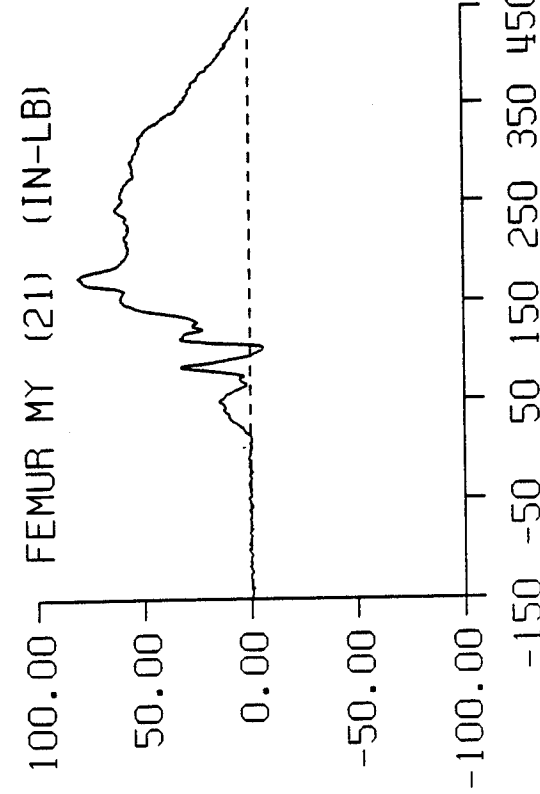
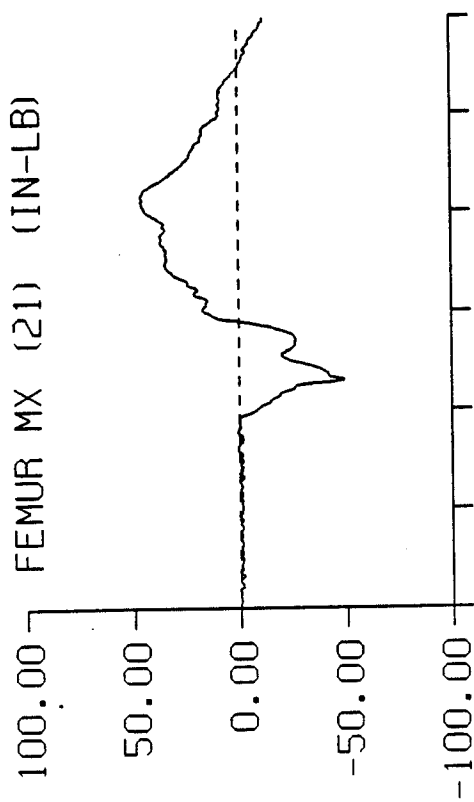
TIME IN MILLISECONDS

SPARTA -GX STUDY TEST: 4641



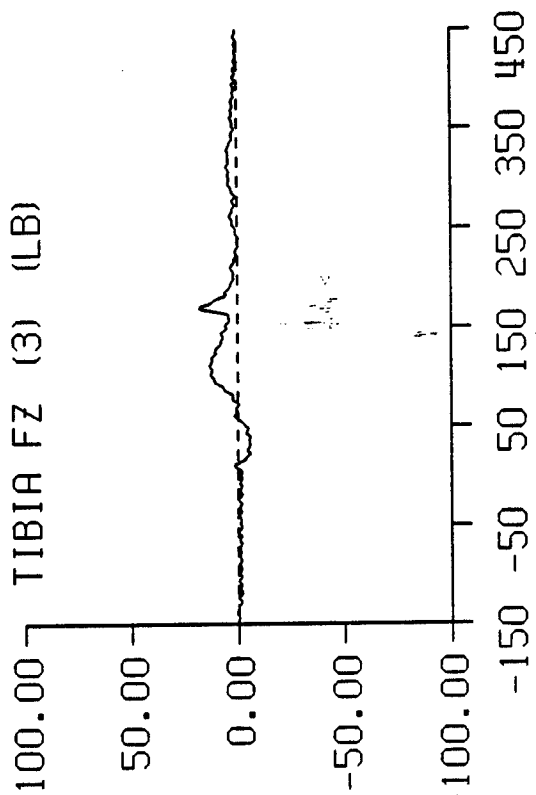
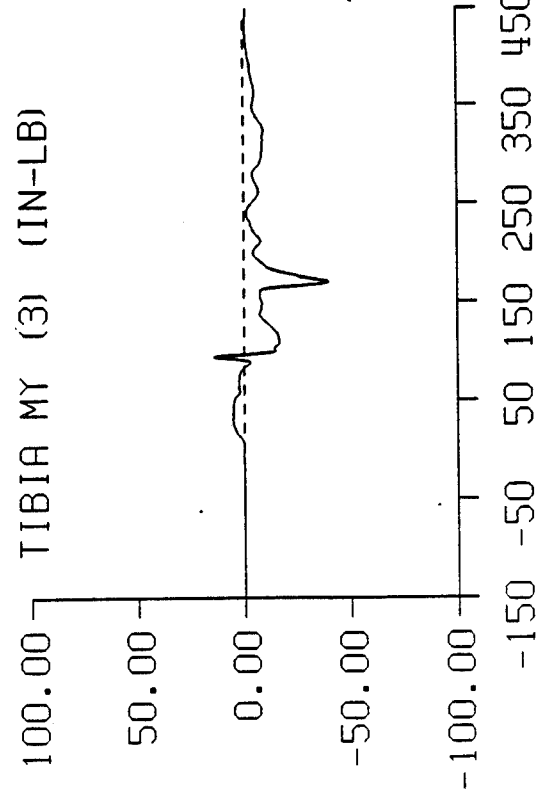
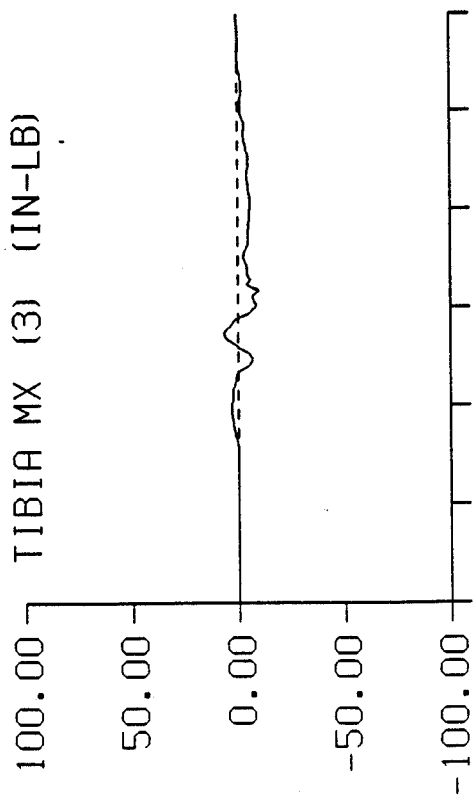
TIME IN MILLISECONDS

SPARTA -CX STUDY TEST: 4641



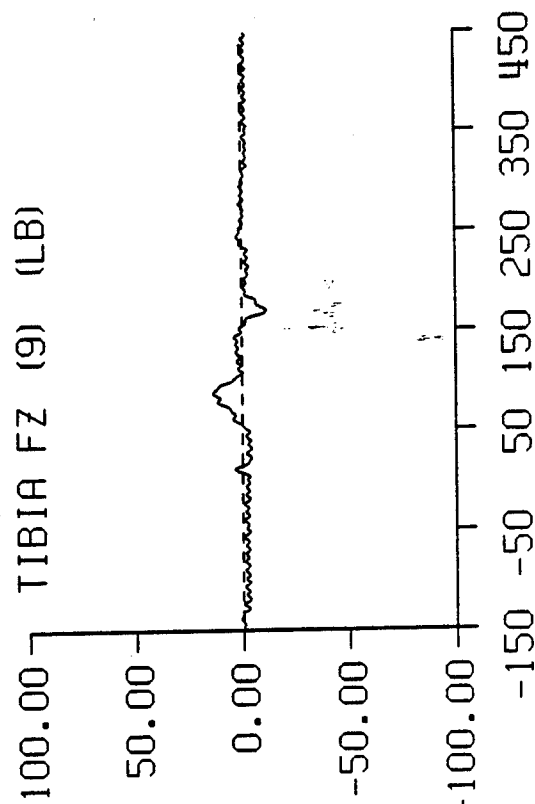
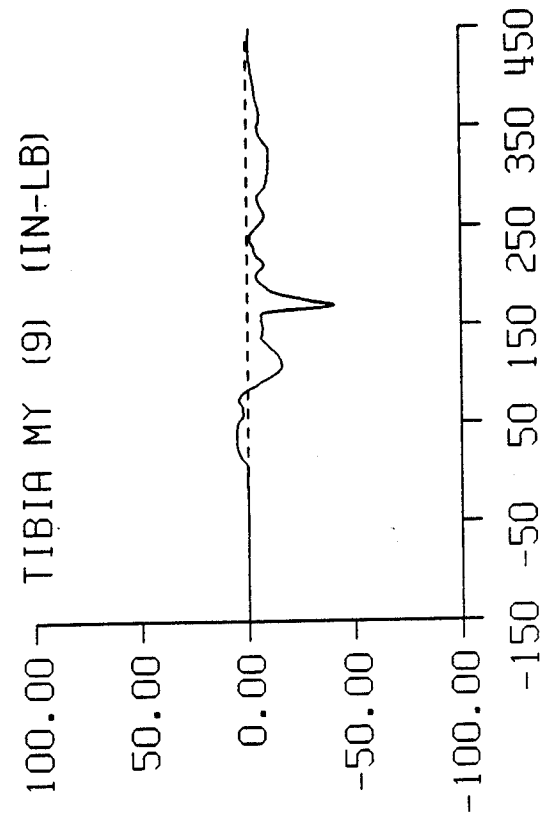
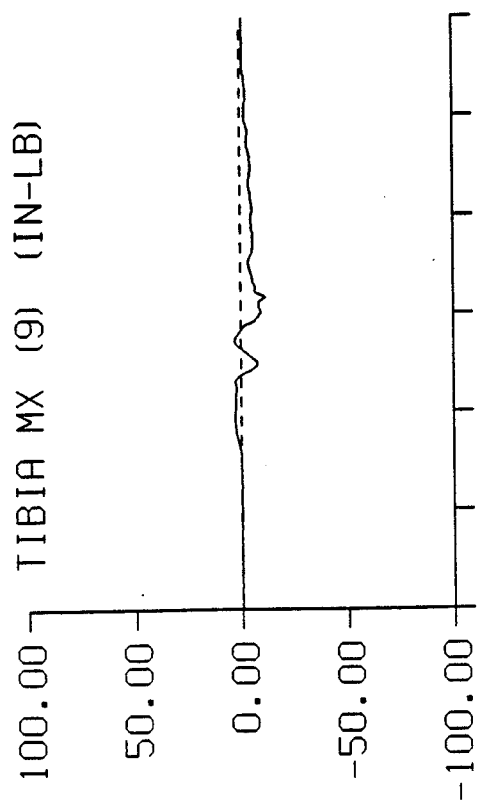
TIME IN MILLISECONDS

SPARTA -GX STUDY TEST: 4641



TIME IN MILLISECONDS

SPARTA -GX STUDY TEST: 4641

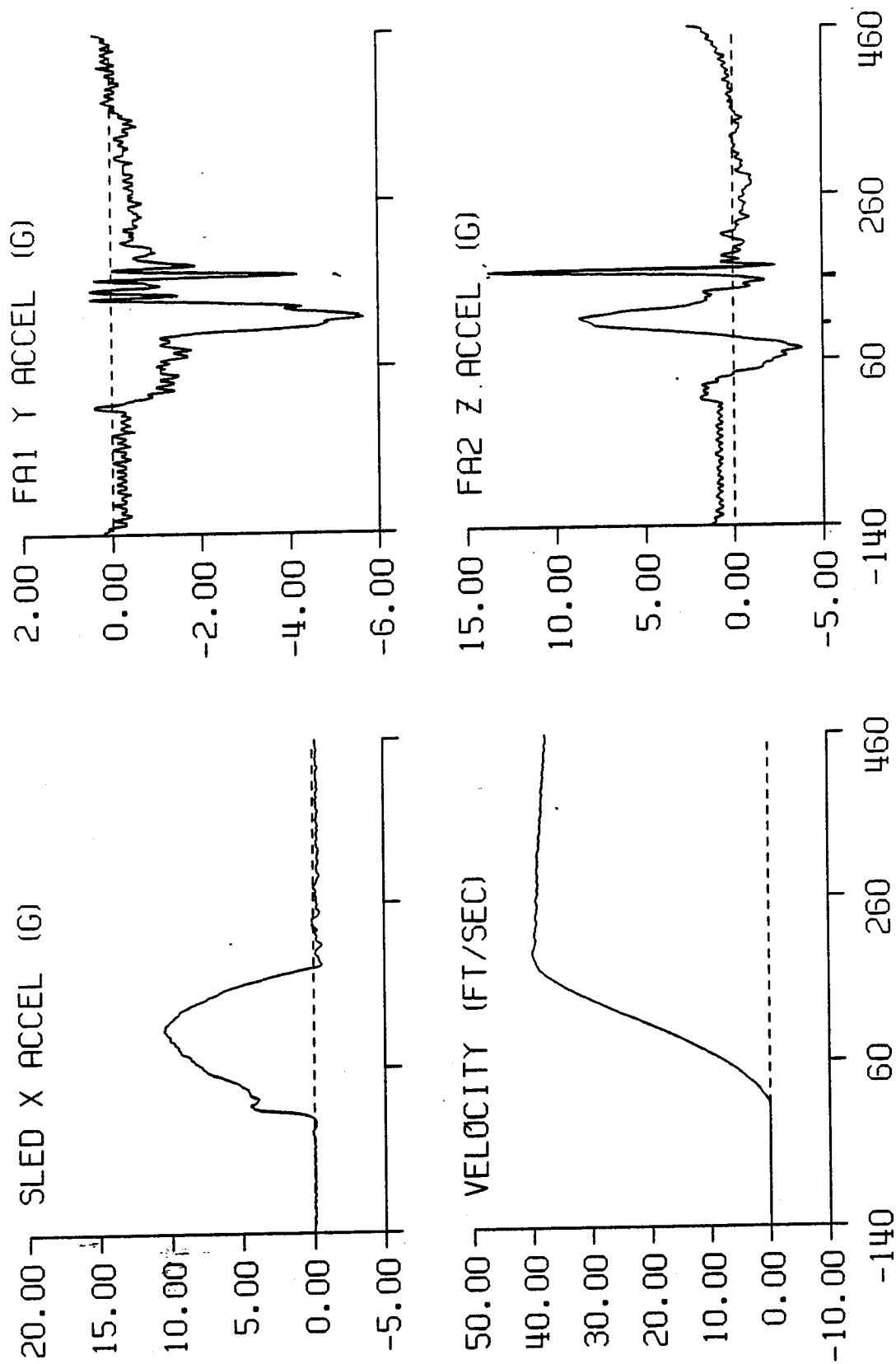


TIME IN MILLISECONDS

TEST 4641 CELL D

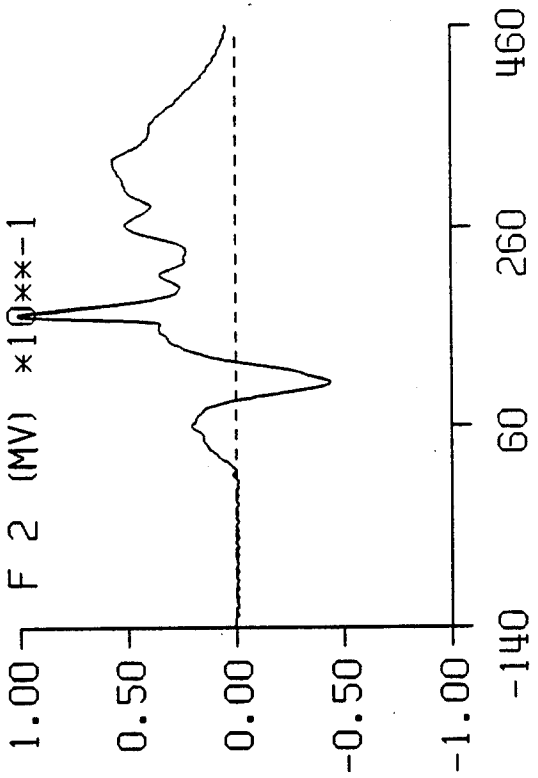
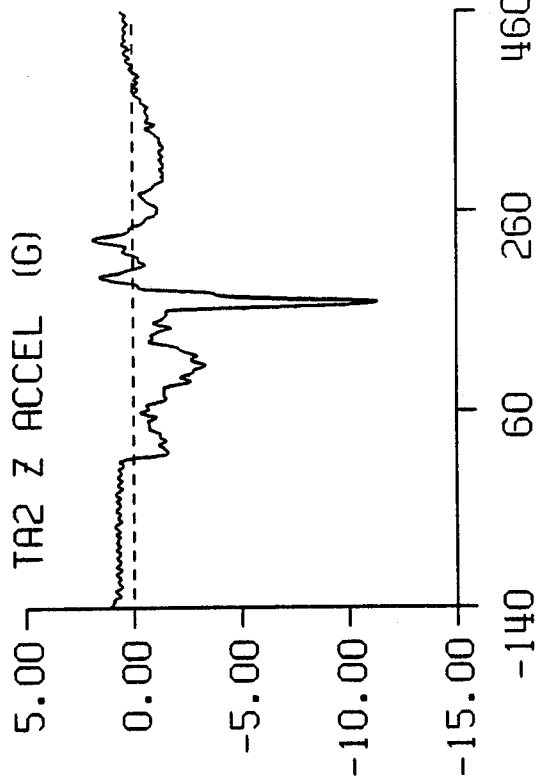
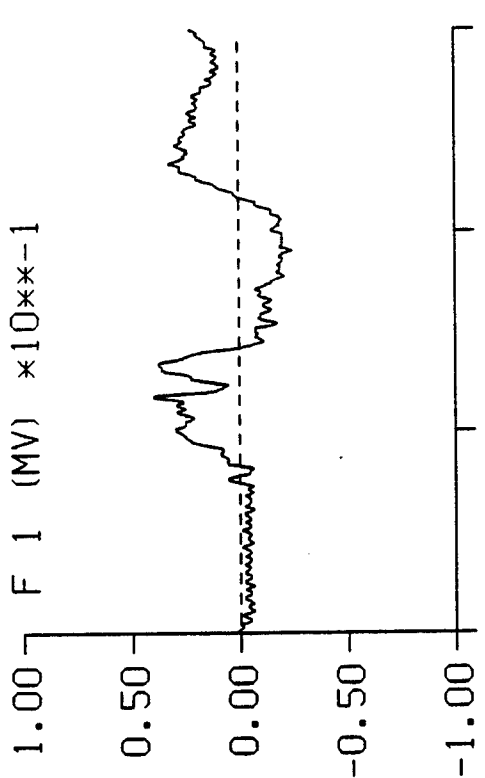
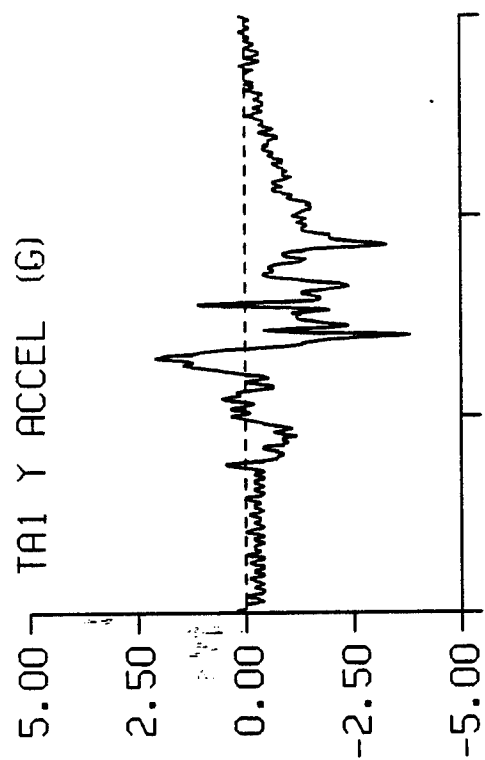
CHANNEL	MAXIMUM VALUE	MINIMUM VALUE	TIME OF MAXIMUM	TIME OF MINIMUM
IMPACT RISE TIME			105.0	
IMPACT DURATION			181.0	
VELOCITY CHANGE	39.24			
SLED X ACCEL (G)	10.48	-0.62	105.0	208.0
F 1 (MV)	0.04	-0.02	93.0	241.0
F 2 (MV)	0.10	-0.04	171.0	104.0
F 3 (MV)	0.04	0.00	244.0	71.0
F 4 (MV)	0.05	-0.04	121.0	171.0
F 5 (MV)	0.08	-0.09	105.0	171.0
F 6 (MV)	0.04	-0.02	97.0	171.0
F 7 (MV)	0.03	-0.02	128.0	266.0
F 8 (MV)	0.04	-0.05	171.0	100.0
F 9 (MV)	0.03	-0.01	245.0	81.0
F 10 (MV)	0.03	-0.02	120.0	175.0
F 11 (MV)	0.06	-0.03	101.0	172.0
F 12 (MV)	0.04	-0.02	95.0	48.0
F 13 (MV)	0.02	-0.03	126.0	216.0
F 14 (MV)	0.09	-0.05	170.0	106.0
F 15 (MV)	0.04	-0.01	144.0	31.0
F 16 (MV)	0.04	-0.03	120.0	93.0
F 17 (MV)	0.06	-0.09	104.0	171.0
F 18 (MV)	0.03	-0.01	96.0	32.0
F 19 (MV)	0.05	-0.02	80.0	266.0
F 20 (MV)	0.07	-0.01	171.0	101.0
F 21 (MV)	0.03	0.00	261.0	0.0
F 22 (MV)	0.03	-0.02	122.0	231.0
F 23 (MV)	0.08	-0.04	101.0	171.0
F 24 (MV)	0.03	-0.02	97.0	125.0
FA1 Y ACCEL (G)	0.48	-5.68	142.0	119.0
FA2 Z ACCEL (G)	13.80	-3.81	167.0	72.0
TA1 Y ACCEL (G)	2.08	-3.83	118.0	140.0
TA2 Z ACCEL (G)	1.83	-11.33	231.0	168.0
T 1 (MV)	0.07	-0.02	168.0	40.0
T 2 (MV)	0.24	-0.04	170.0	31.0
T 3 (MV)	0.05	-0.03	121.0	154.0
T 4 (MV)	0.01	-0.01	118.0	168.0
T 5 (MV)	0.20	-0.17	94.0	170.0
T 6 (MV)	0.04	-0.08	94.0	170.0
VELOCITY (FT/SEC)	40.01	0.03	191.0	0.0
T 7 (MV)	0.10	-0.03	168.0	39.0
T 8 (MV)	0.24	-0.04	170.0	31.0
T 9 (MV)	0.04	-0.07	83.0	165.0
T 10 (MV)	0.01	-0.05	61.0	169.0
T 11 (MV)	0.05	-0.37	75.0	170.0
T 12 (MV)	0.03	-0.28	239.0	170.0

TEST 4641 CELL D



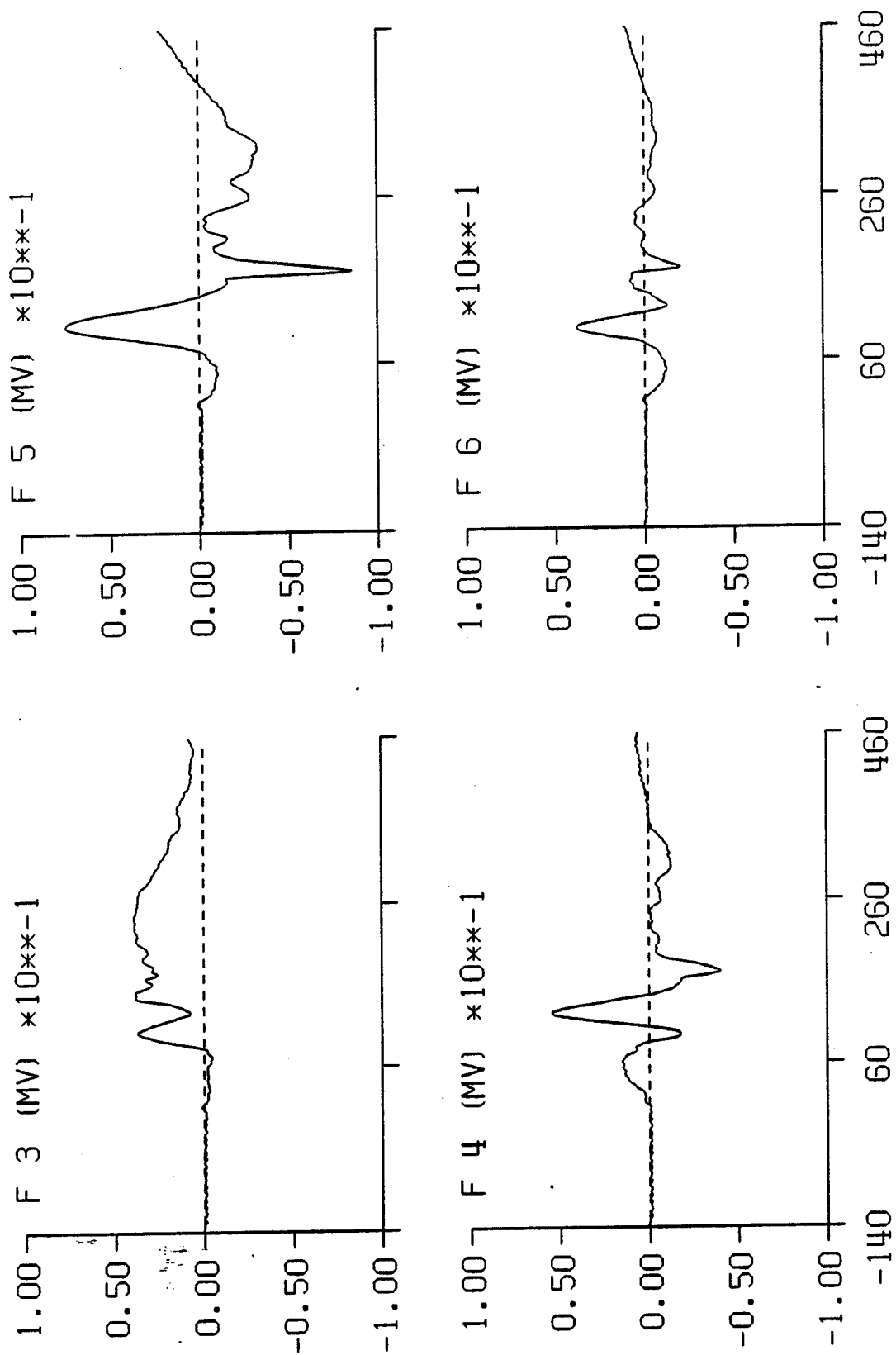
TIME IN MILLISECONDS

TEST 4641 CELL D

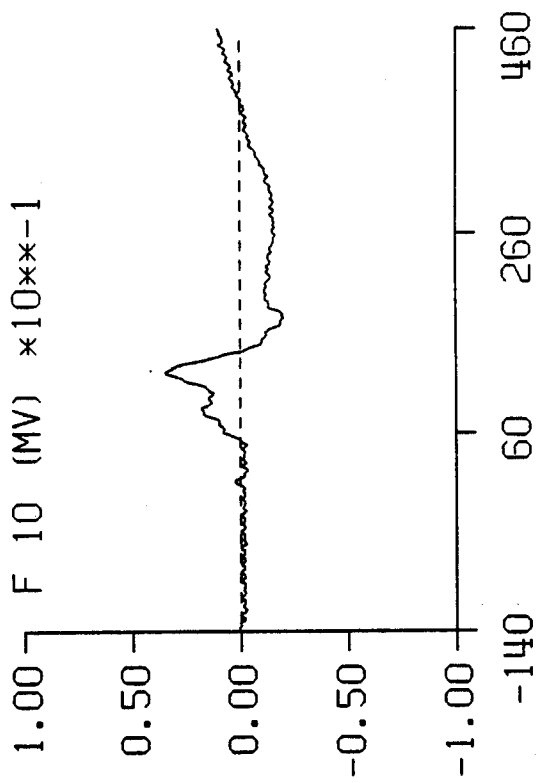
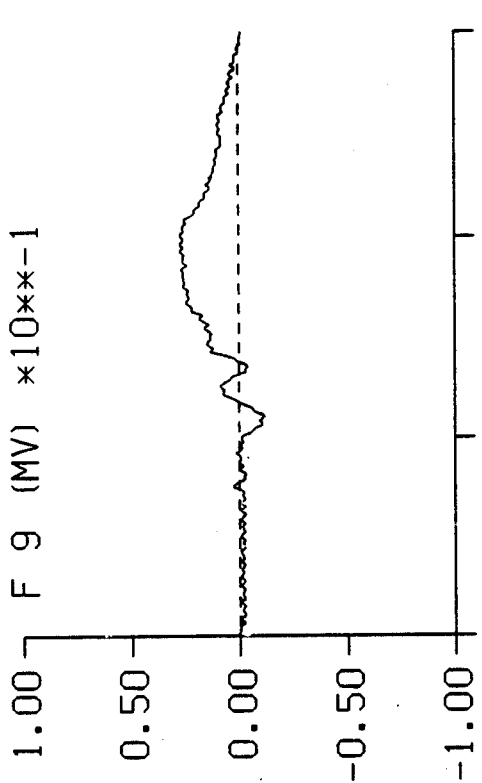
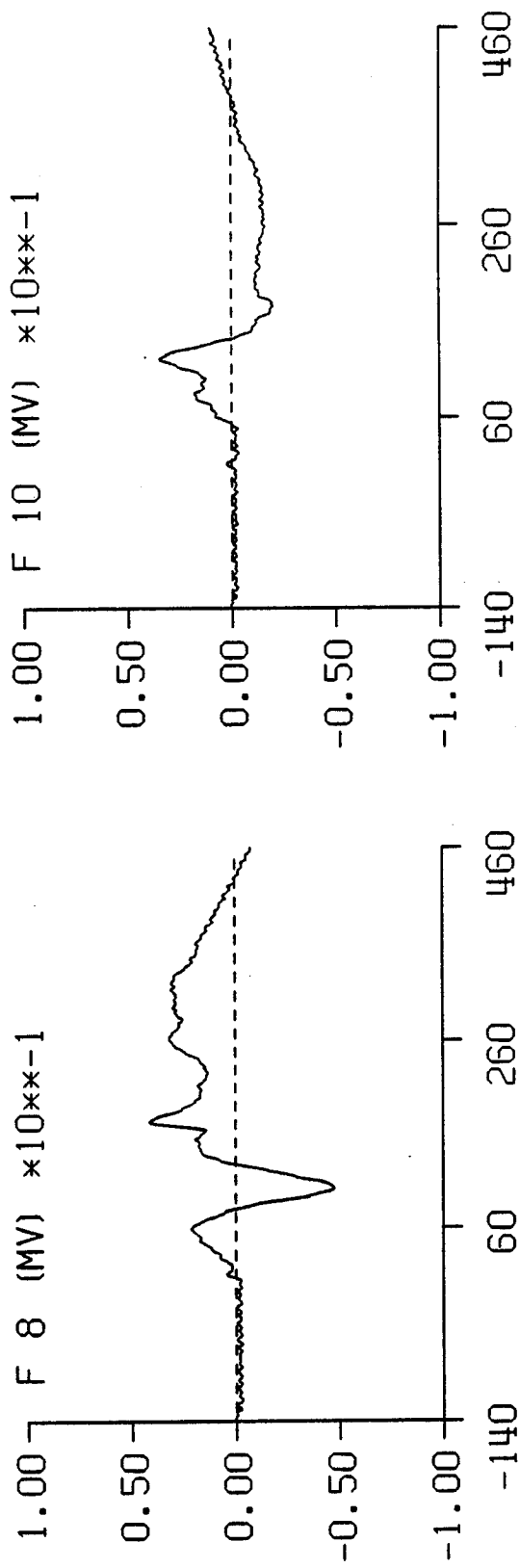
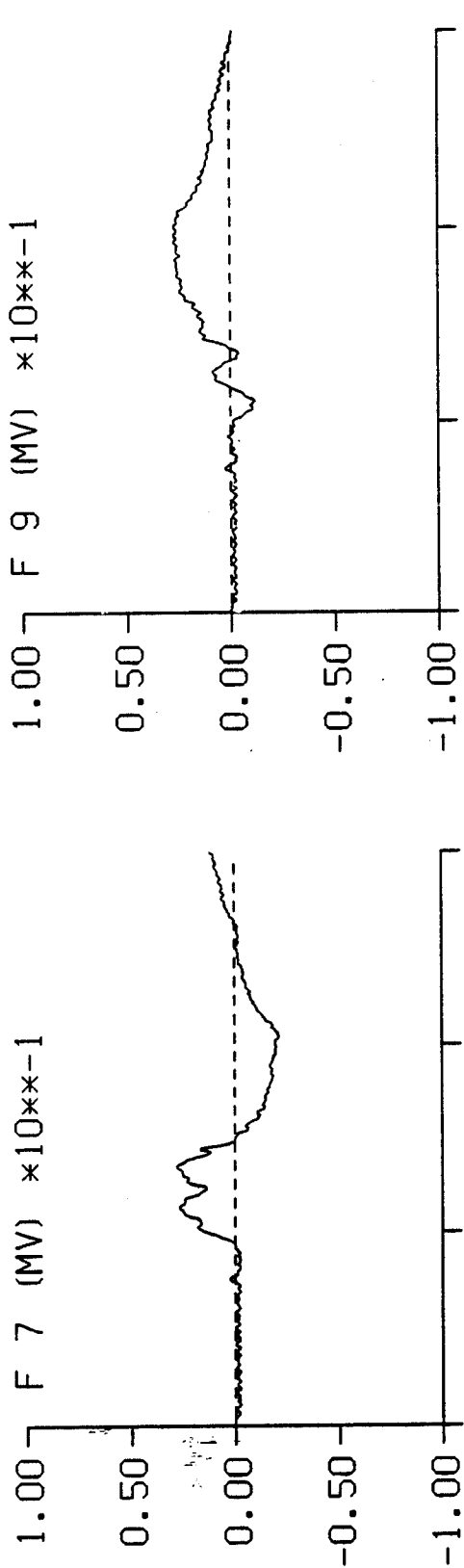


TIME IN MILLISECONDS

TEST 4641 CELL D

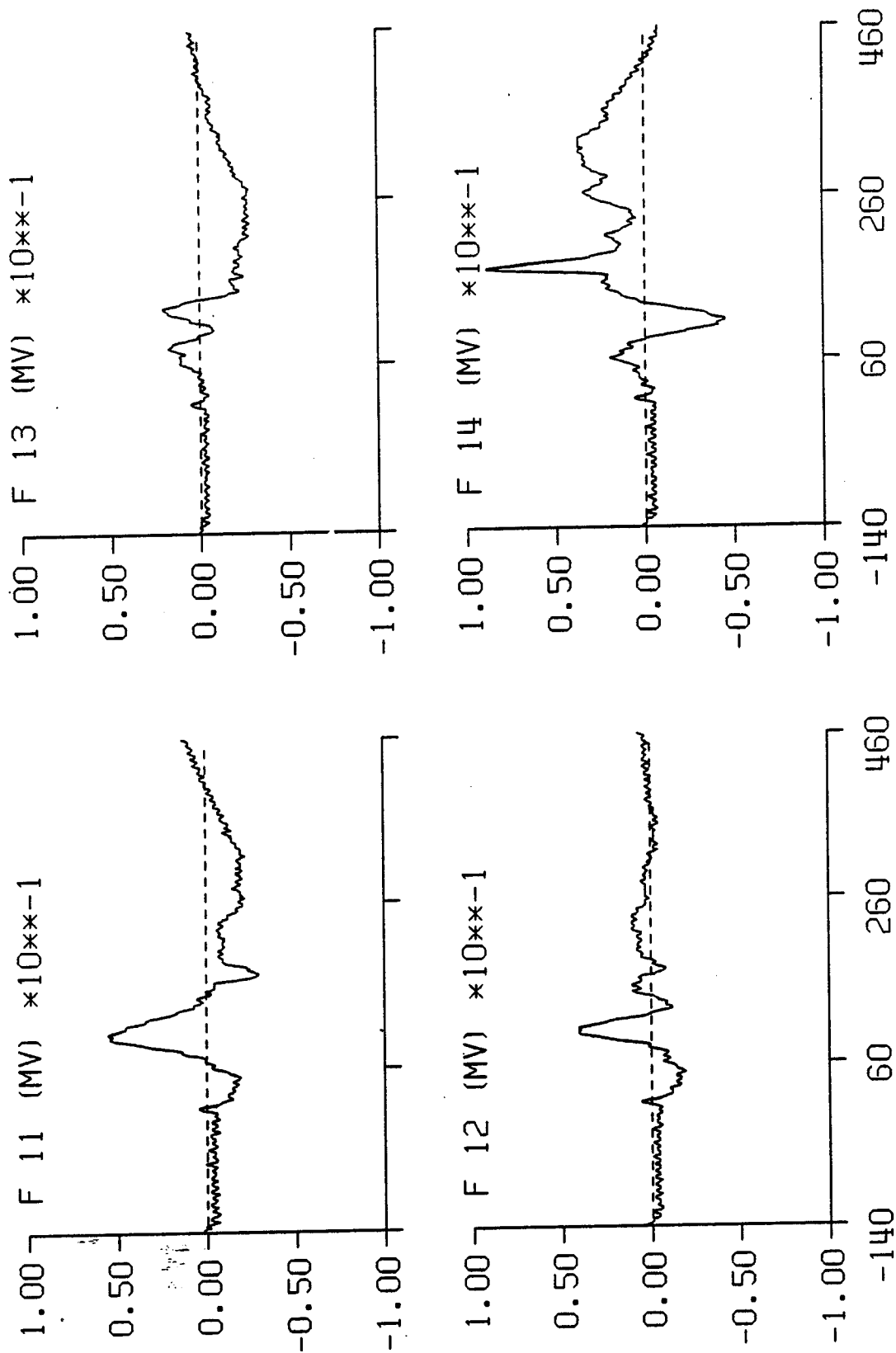


TEST 4641 CELL D



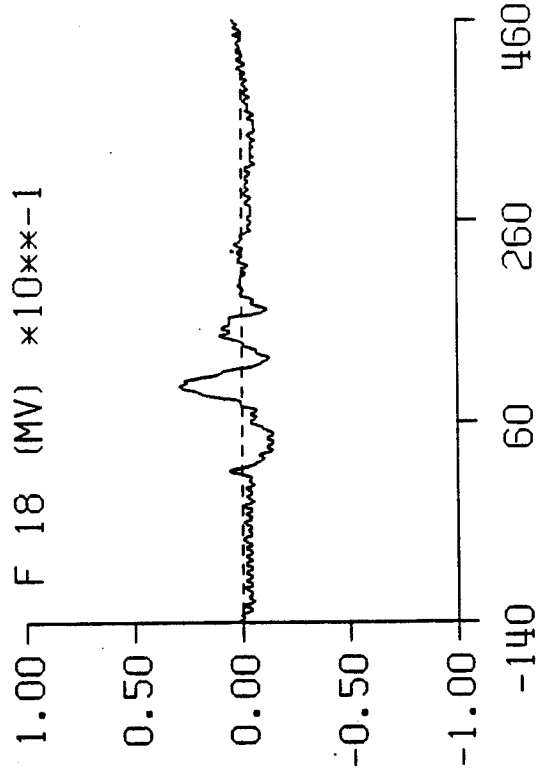
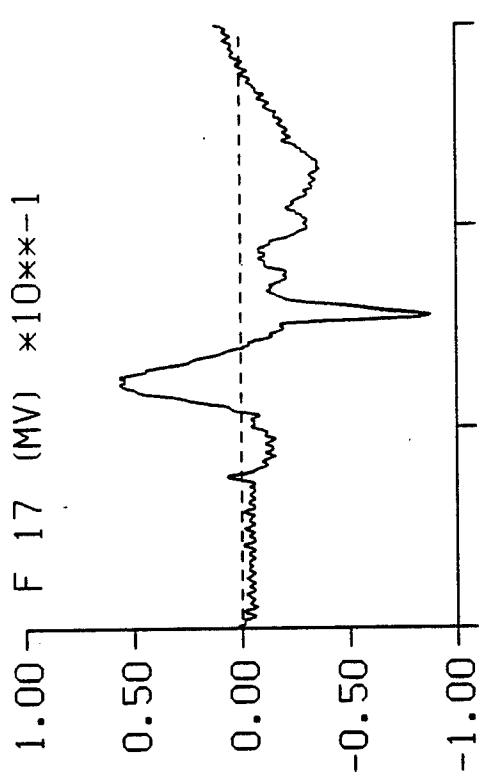
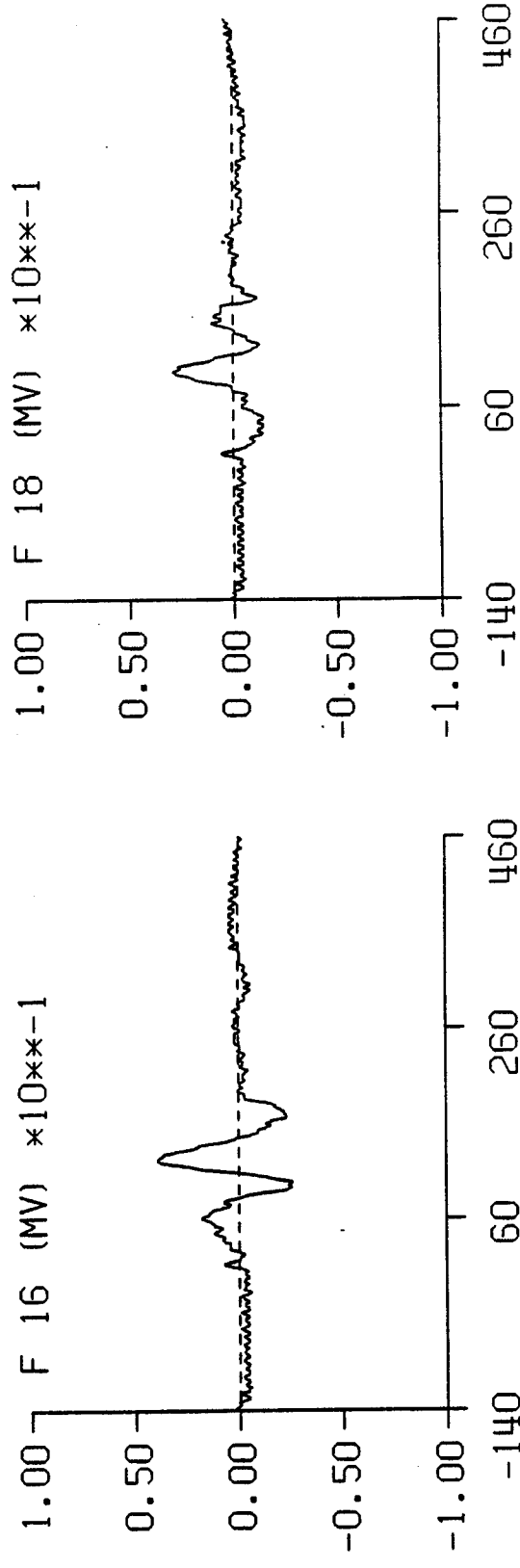
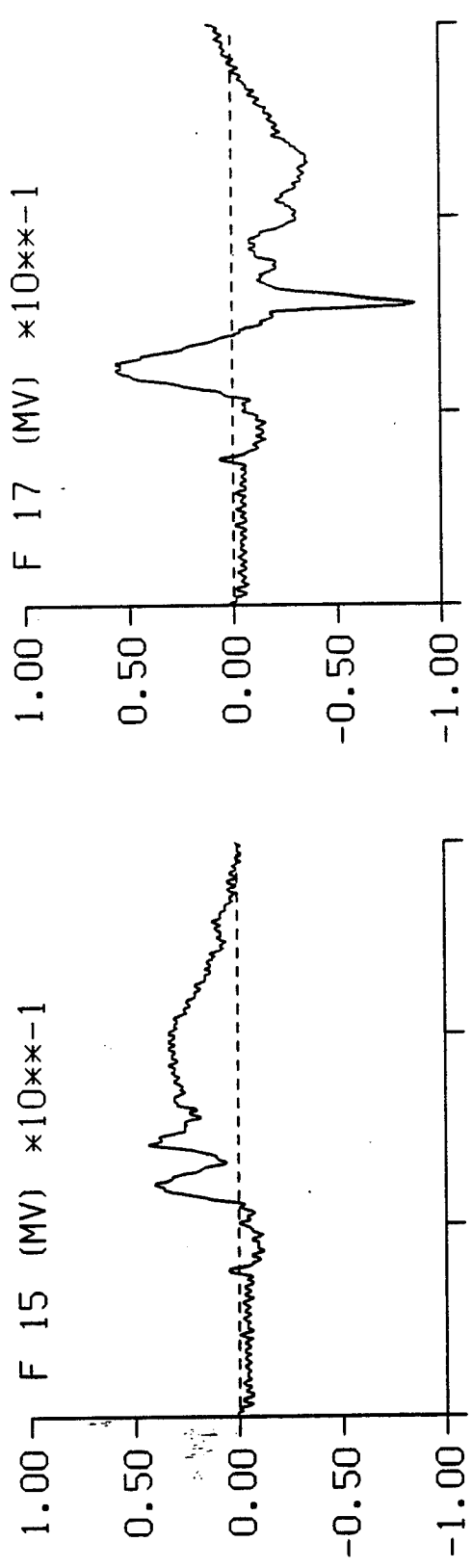
TIME IN MILLISECONDS

TEST 4641 CELL D



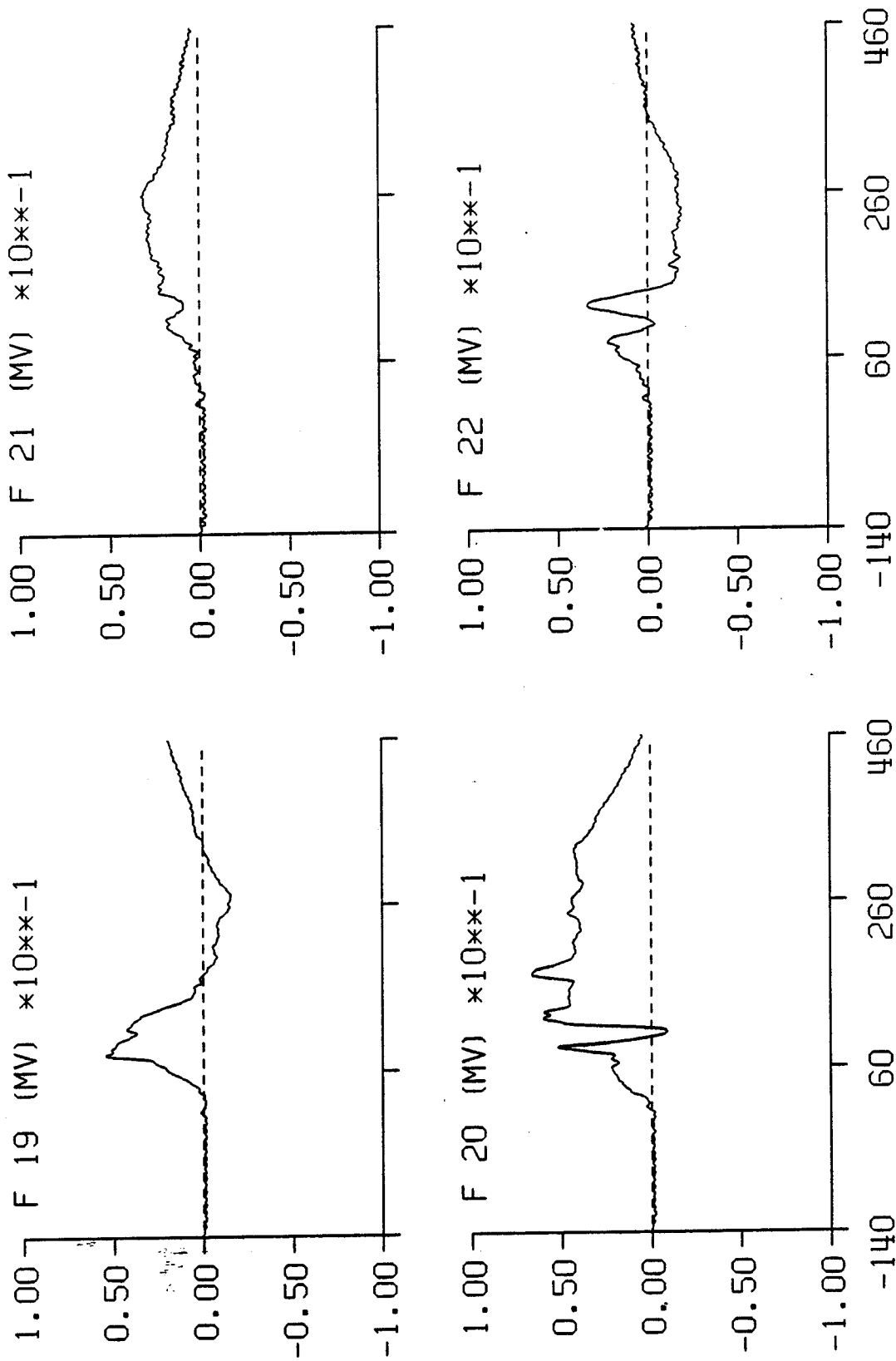
TIME IN MILLISECONDS

TEST 4641 CELL D

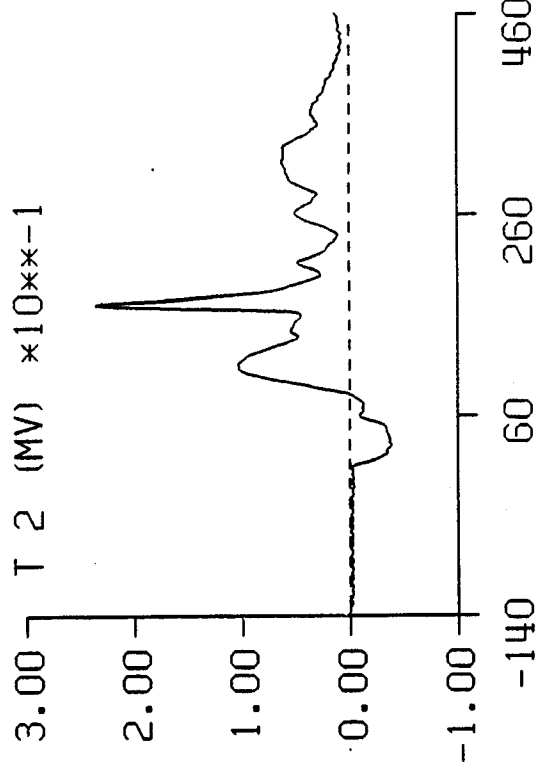
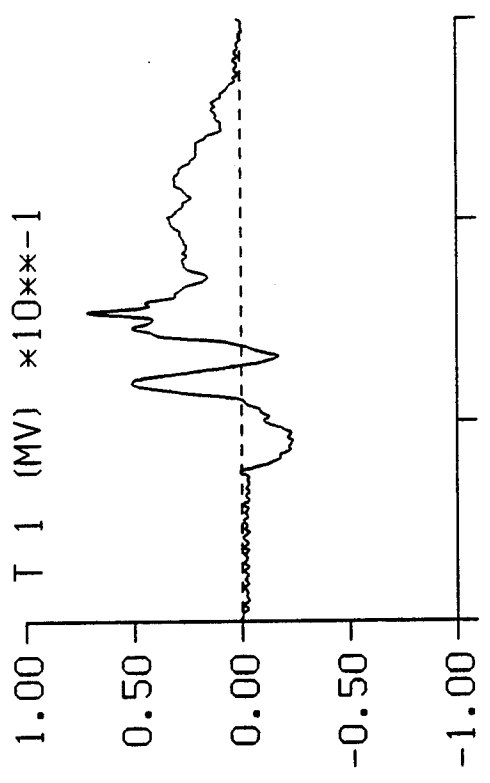
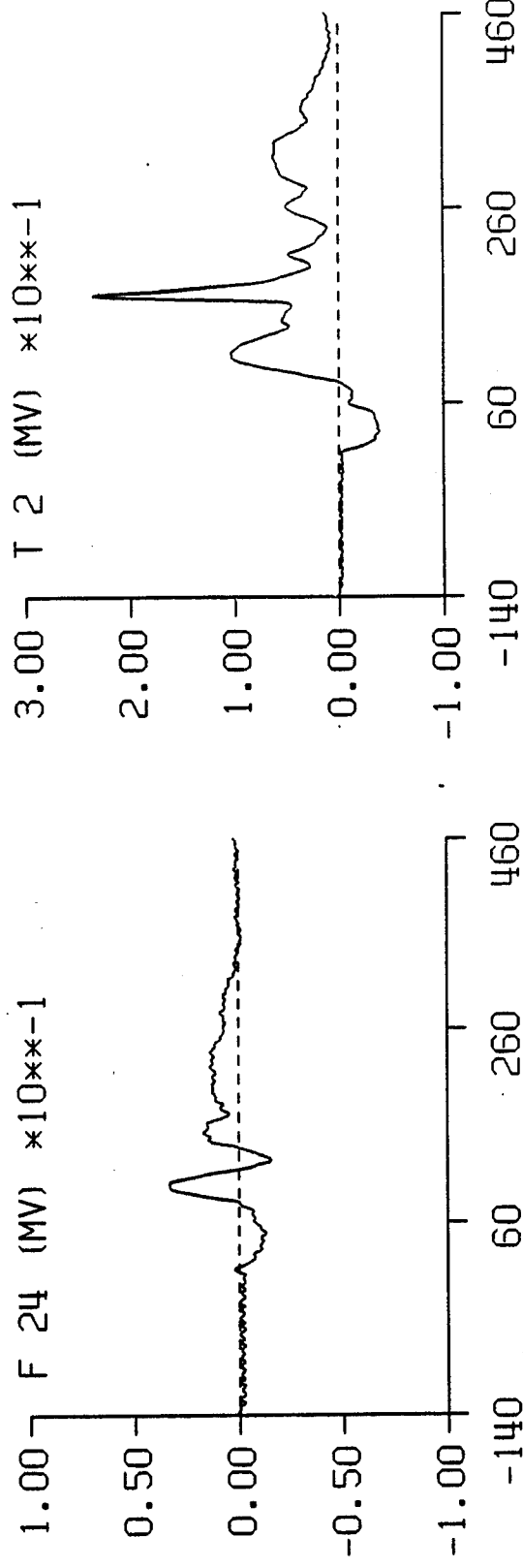
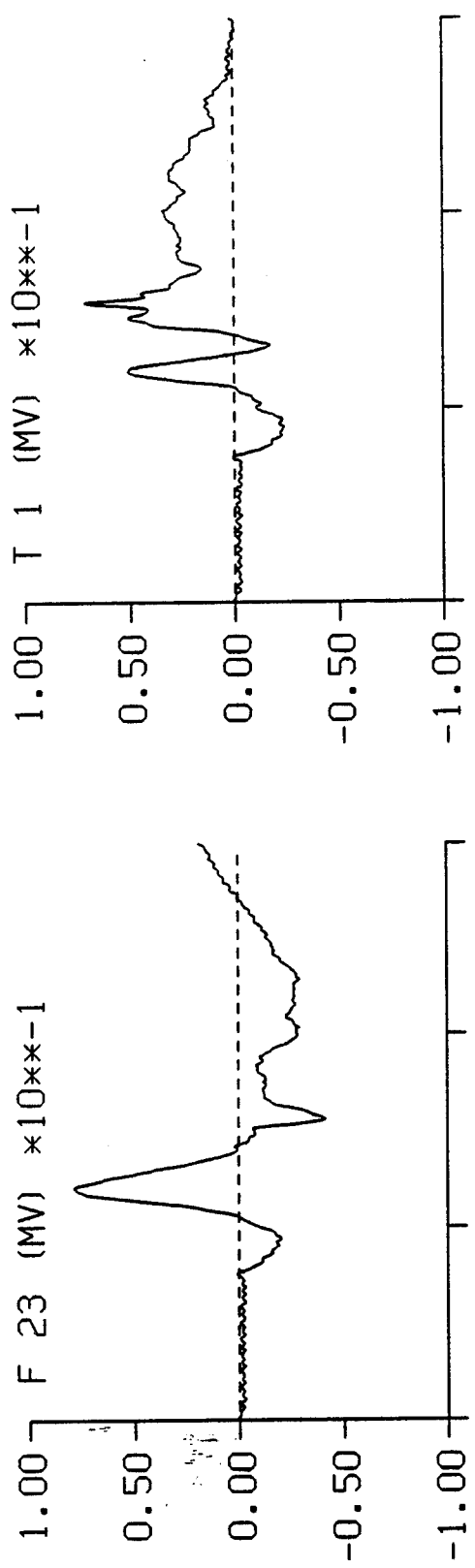


TIME IN MILLISECONDS

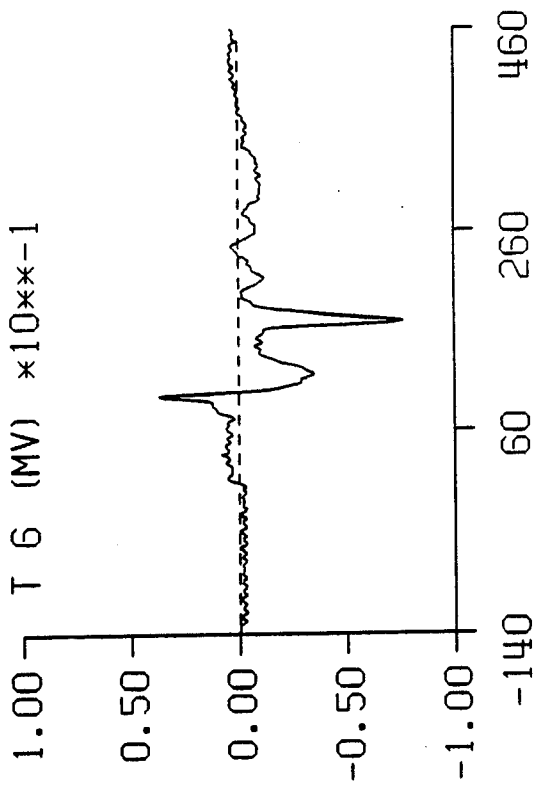
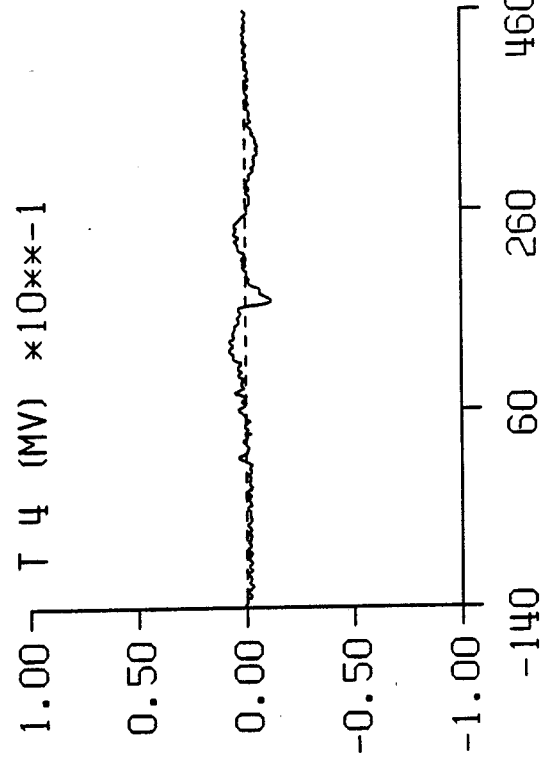
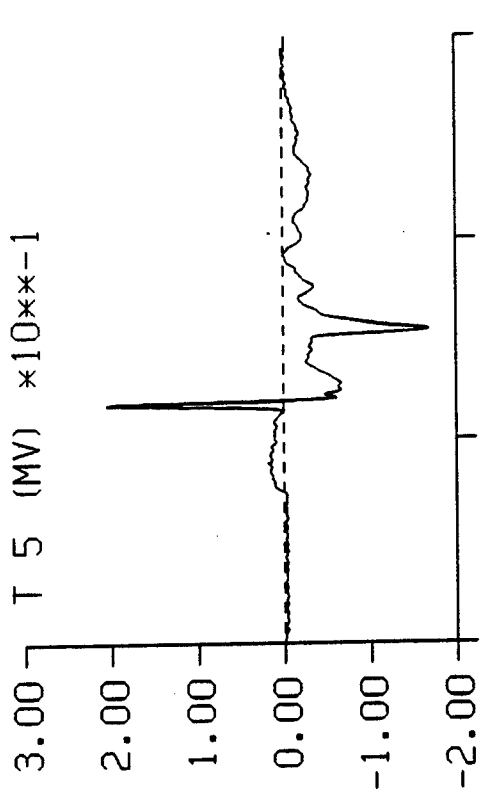
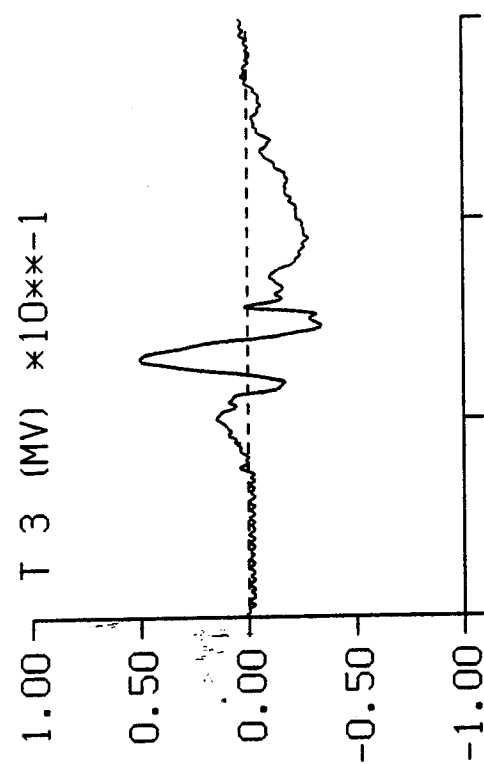
TEST 4641 CELL D



TEST 4641 CELL D

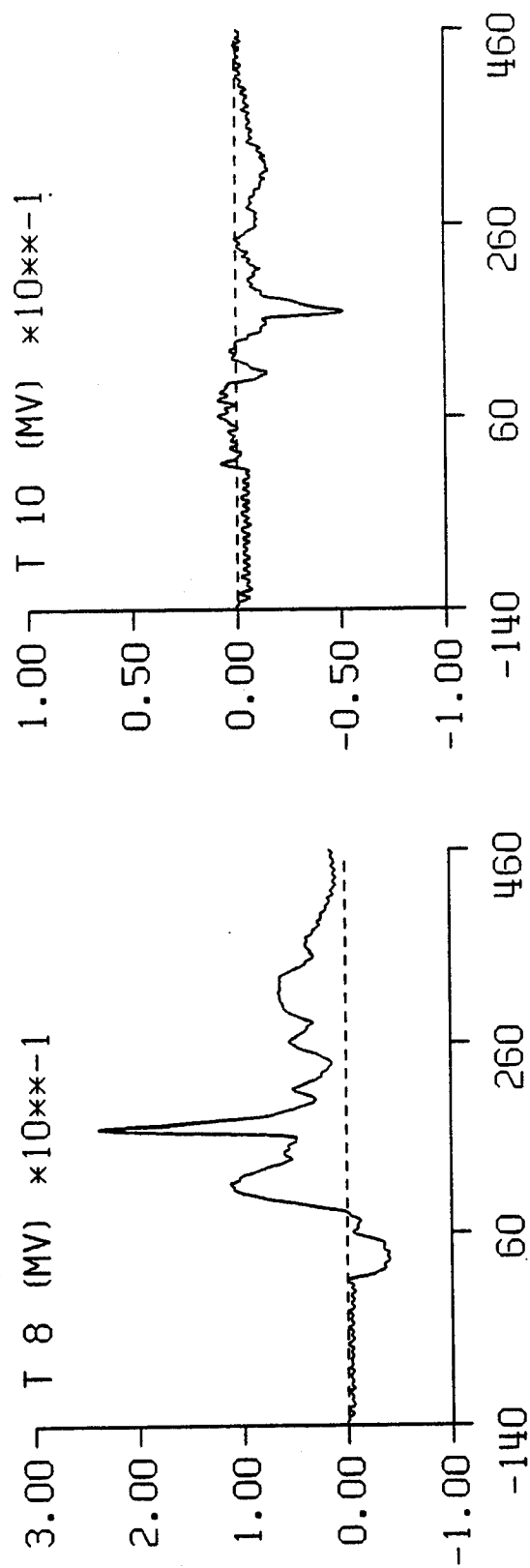
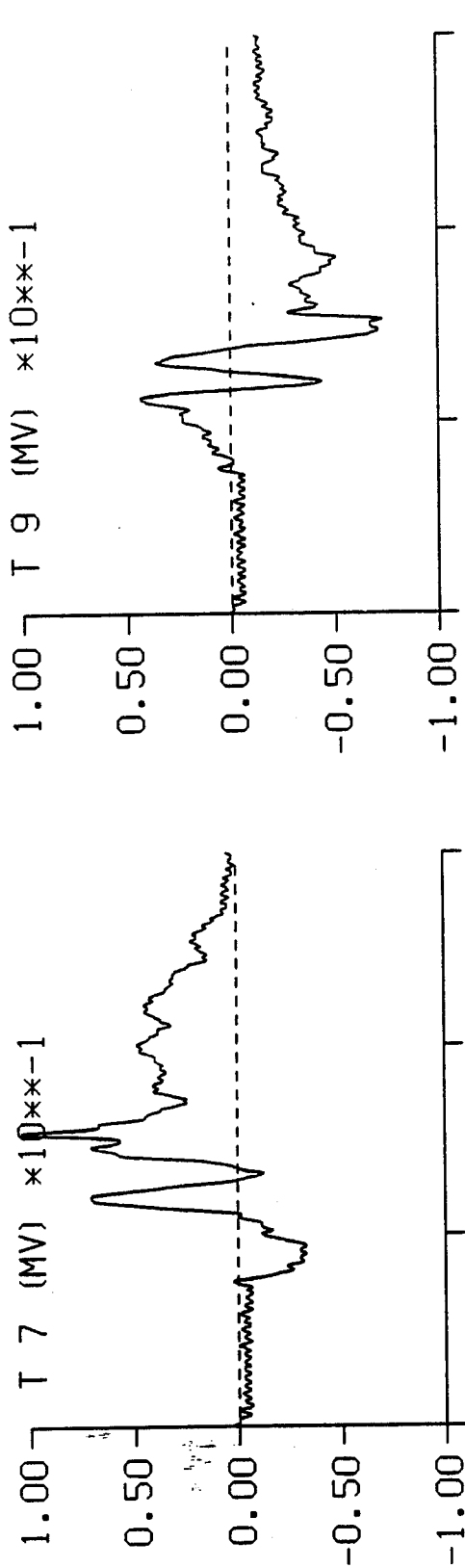


TEST 4641 CELL D



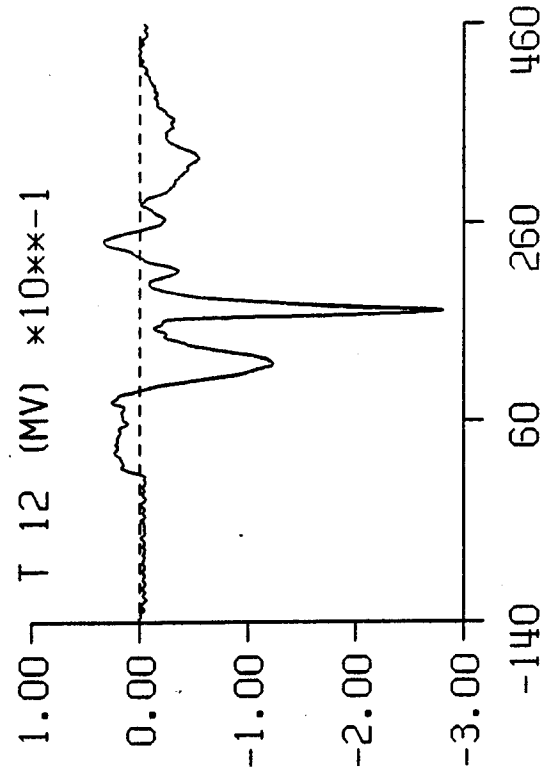
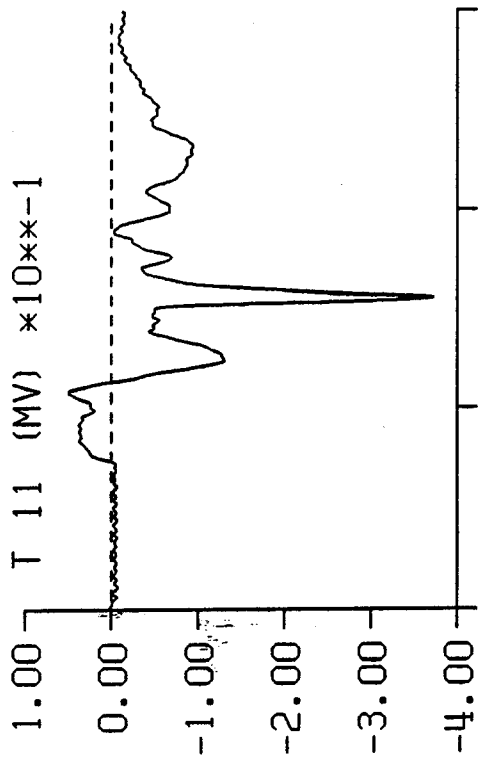
TIME IN MILLISECONDS

TEST 4641 CELL D



TIME IN MILLISECONDS

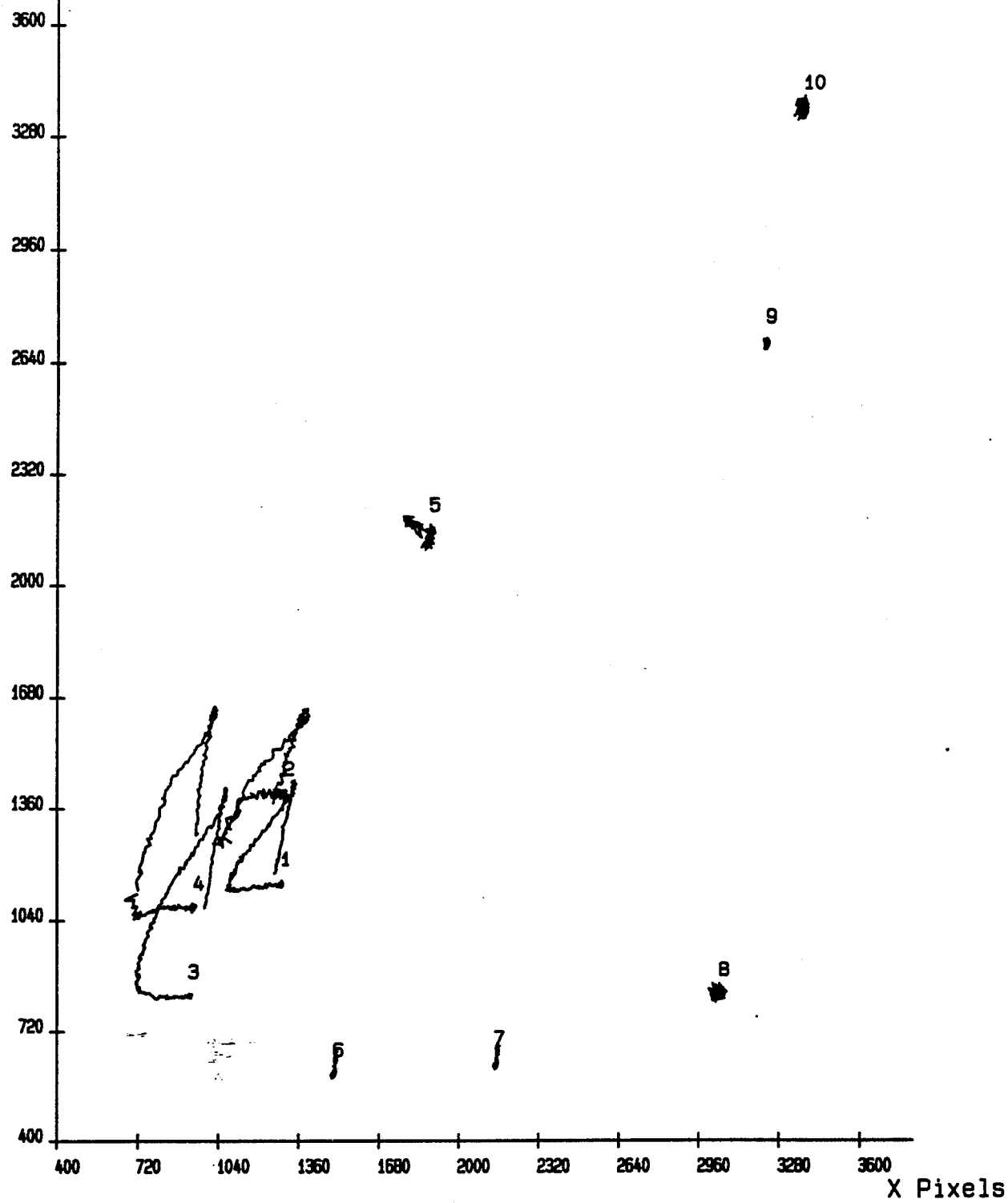
TEST 4641 CELL D



TIME IN MILLISECONDS

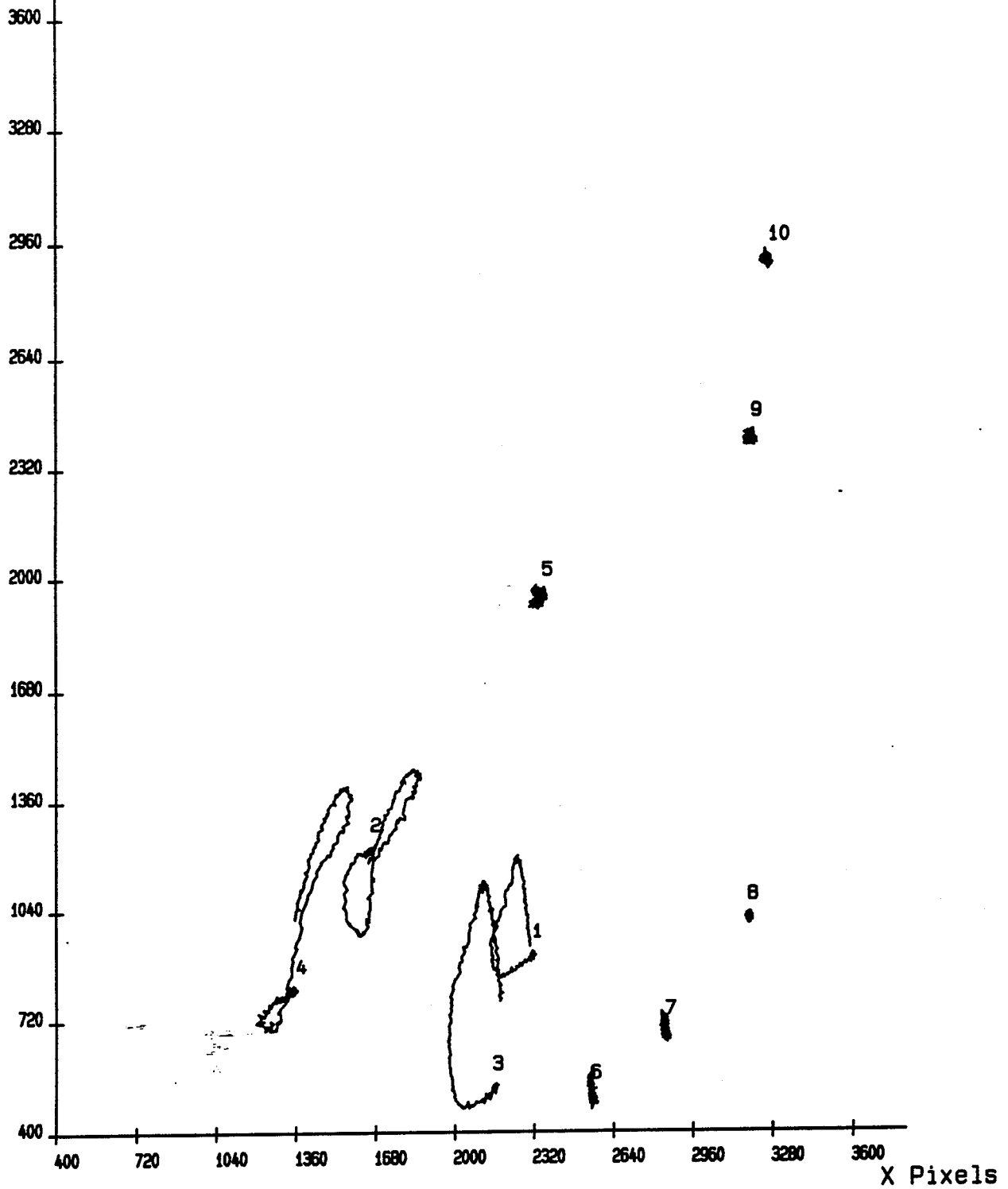
Test DATA-4641HAC.RUN Camera 1

Y Pixels



Test DATA-4641HAC.RUN Camera 2

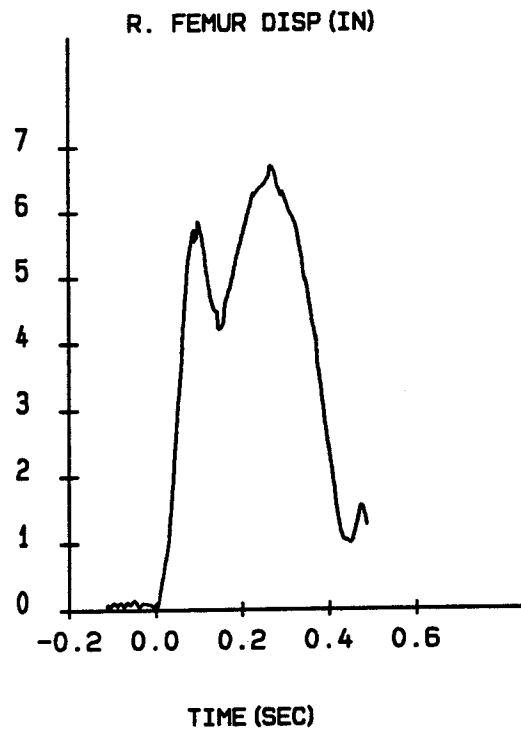
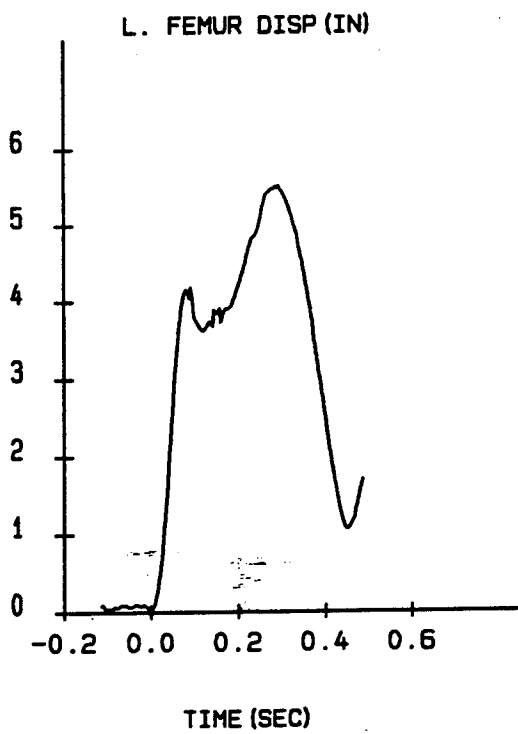
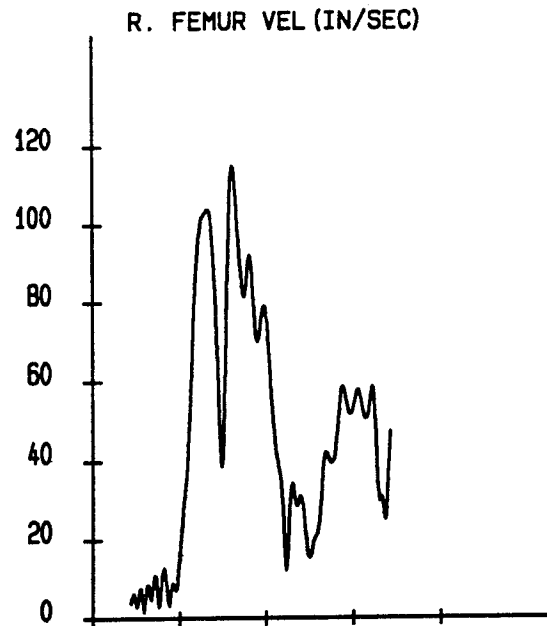
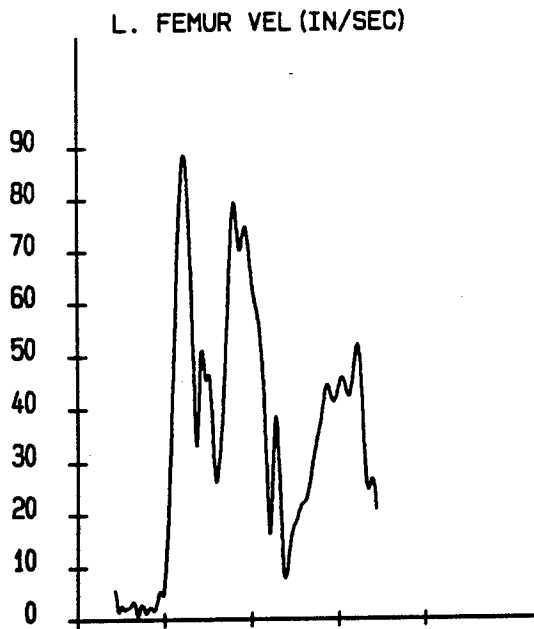
Y Pixels



TEST 5 (4642) 15.0 G

SPARTA -GX

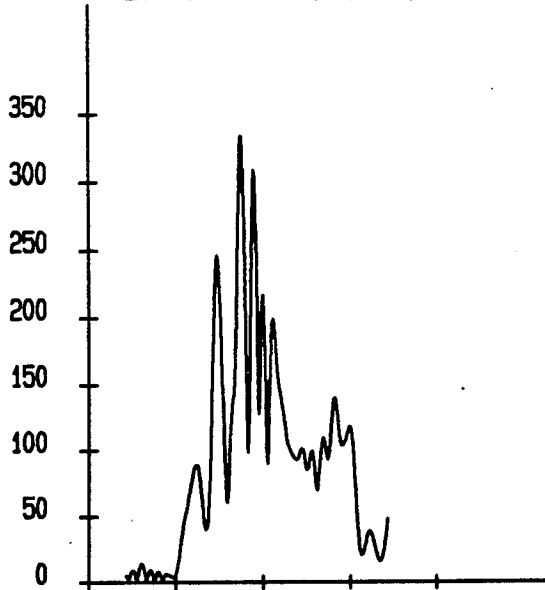
TEST: 4642 DATE: 24-SEP-1993 SUBJ: HB3-50 CELL: E



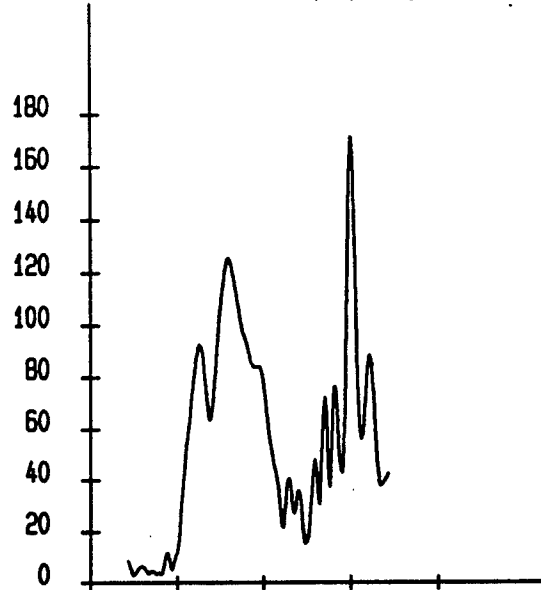
SPARTA -GX

TEST: 4642 DATE: 24-SEP-1993 SUBJ: HB3-50 CELL: E

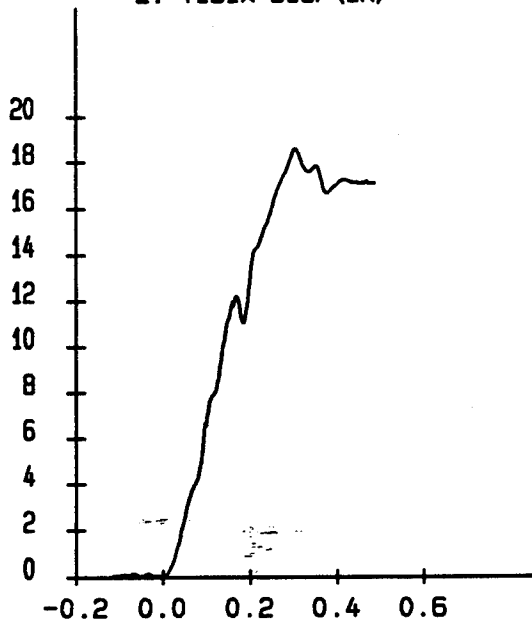
L. TIBIA VEL (IN/SEC)



R. TIBIA VEL (IN/SEC)

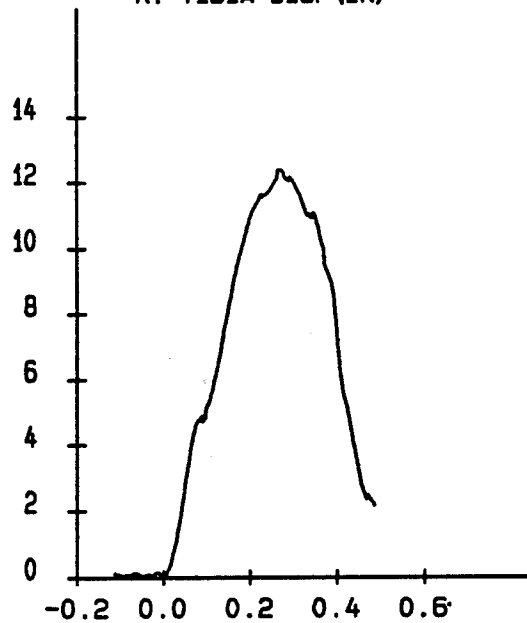


L. TIBIA DISP (IN)



TIME (SEC)

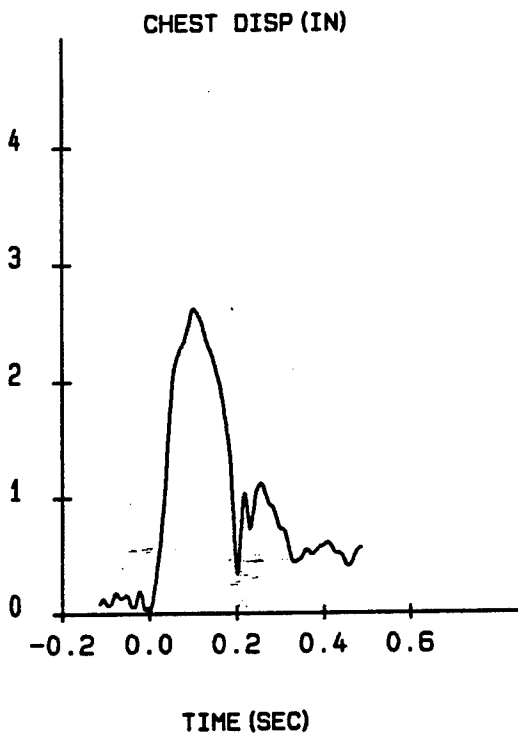
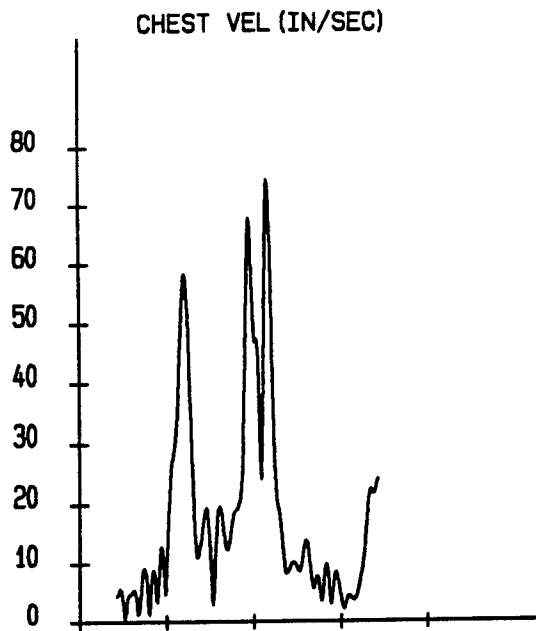
R. TIBIA DISP (IN)



TIME (SEC)

SPARTA -GX

TEST: 4642 DATE: 24-SEP-1993 SUBJ: HB3-50 CELL: E



SPARTA -GX

TEST: 4642 DATE: 24-SEP-1993 SUBJ: HB3-50 CELL: E

RELIABILITY FACTORS (IN)

TARGET DESCRIPTION	MAXIMUM	MINIMUM	AVERAGE	STANDARD DEVIATION	AT MAX DISPLACEMENT
1 L. FEMUR	0.2282	0.0002	0.0958	0.0573	0.1321
2 R. FEMUR	0.2528	0.0013	0.1170	0.0597	0.1333
3 L. TIBIA	1.6141	0.0007	0.3819	0.3434	0.4696
4 R. TIBIA	0.9792	0.0035	0.2044	0.1948	0.1807
5 CHEST	0.3569	0.0103	0.2111	0.0713	0.2102

TARGET	MAXIMUM	TIME(SEC)	MINIMUM	TIME(SEC)
L. FEMUR				
POSITION(IN)				
X AXIS	24.1932	0.0800	18.8960	0.2580
Y AXIS	8.9061	0.4860	4.9940	0.2380
Z AXIS	11.3907	0.2920	5.5879	0.0720
VELOCITY(IN/SEC)	88.4951	0.0440	7.1022	0.0000
ACCELERATION(G)	10.8365	0.0720	0.2464	0.3980
DISPLACEMENT(IN)				
X AXIS	4.0876	0.0800	-1.2096	0.2580
Y AXIS	1.6591	0.4860	-2.2529	0.2380
Z AXIS	5.1085	0.2920	-0.6943	0.0720
RESULTANT	5.5098	0.2920	0.0000	0.0000
R. FEMUR				
POSITION(IN)				
X AXIS	26.1496	0.0780	18.8794	0.2540
Y AXIS	-2.2206	0.0980	-5.7858	0.0000
Z AXIS	12.9512	0.2760	5.9154	0.0940
VELOCITY(IN/SEC)	115.2234	0.1220	12.3437	0.2460
ACCELERATION(G)	14.5460	0.1000	0.4155	0.4100
DISPLACEMENT(IN)				
X AXIS	4.6802	0.0780	-2.5900	0.2540
Y AXIS	3.5652	0.0980	0.0000	0.0000
Z AXIS	5.3018	0.2760	-1.7339	0.0940
RESULTANT	6.6968	0.2660	0.0000	0.0000

SPARTA -GX

TEST: 4642 DATE: 24-SEP-1993 SUBJ: HB3-50 CELL: E

TARGET	MAXIMUM	TIME(SEC)	MINIMUM	TIME(SEC)
L. TIBIA				
POSITION(IN)				
X AXIS	31.0668	0.1380	11.0461	0.4160
Y AXIS	8.3955	0.0440	-1.6603	0.1680
Z AXIS	17.1899	0.2980	2.0682	0.0640
VELOCITY(IN/SEC)	333.9969	0.1480	6.4555	0.0000
ACCELERATION(G)	55.8408	0.1620	0.7034	0.4480
DISPLACEMENT(IN)				
X AXIS	6.2160	0.1380	-13.8047	0.4160
Y AXIS	0.1531	0.0440	-9.9028	0.1680
Z AXIS	15.0396	0.2980	-0.0821	0.0640
RESULTANT	18.5864	0.3040	0.0000	0.0000
R. TIBIA				
POSITION(IN)				
X AXIS	31.9040	0.0760	24.7992	0.2560
Y AXIS	-2.3622	0.2440	-6.9490	0.4860
Z AXIS	13.6679	0.2780	2.2659	0.0000
VELOCITY(IN/SEC)	171.3809	0.4000	11.9819	0.0000
ACCELERATION(G)	15.0181	0.4140	0.3684	0.3700
DISPLACEMENT(IN)				
X AXIS	4.4206	0.0760	-2.6842	0.2560
Y AXIS	4.3317	0.2440	-0.2552	0.4860
Z AXIS	11.4020	0.2780	0.0000	0.0000
RESULTANT	12.3770	0.2680	0.0000	0.0000
CHEST				
POSITION(IN)				
X AXIS	14.1558	0.0960	11.7751	0.4860
Y AXIS	2.0558	0.1000	0.0305	0.2600
Z AXIS	21.0524	0.1040	19.1598	0.2460
VELOCITY(IN/SEC)	74.4544	0.2320	2.2348	0.4060
ACCELERATION(G)	12.6747	0.2200	0.2321	0.4300

SPARTA -GX

TEST: 4642 DATE: 24-SEP-1993 SUBJ: HB3-50 CELL: E

TARGET	MAXIMUM	TIME(SEC)	MINIMUM	TIME(SEC)
CHEST				
DISPLACEMENT (IN)				
X AXIS	2.0634	0.0960	-0.3172	0.4860
Y AXIS	1.2458	0.1000	-0.7794	0.2600
Z AXIS	1.0653	0.1040	-0.8273	0.2460
RESULTANT	2.6251	0.1000	0.0000	0.0000

SPARTA -GX
TEST: 4642 DATE: 24-SEP-1993 SUBJ: HB3-50 CELL: E

Note: Invalid samples are interpolated.

Sample number 1218 of the L. FEMUR target is invalid.
Invalid sample 1218 occurred at 0.0700 seconds.

Samples 1221 through 1229 of the L. FEMUR target are invalid.
Invalid sample range occurred from 0.0760 seconds to 0.0920 seconds.

Sample number 1232 of the L. FEMUR target is invalid.
Invalid sample 1232 occurred at 0.0980 seconds.

Samples 1234 through 1237 of the L. FEMUR target are invalid.
Invalid sample range occurred from 0.1020 seconds to 0.1080 seconds.

Samples 1224 through 1232 of the R. FEMUR target are invalid.
Invalid sample range occurred from 0.0820 seconds to 0.0980 seconds.

Samples 1230 through 1242 of the L. TIBIA target are invalid.
Invalid sample range occurred from 0.0940 seconds to 0.1180 seconds.

Samples 1259 through 1262 of the L. TIBIA target are invalid.
Invalid sample range occurred from 0.1520 seconds to 0.1580 seconds.

Samples 1305 through 1336 of the L. TIBIA target are invalid.
Invalid sample range occurred from 0.2440 seconds to 0.3060 seconds.

Samples 1349 through 1353 of the L. TIBIA target are invalid.
Invalid sample range occurred from 0.3320 seconds to 0.3400 seconds.

Samples 1368 through 1426 of the L. TIBIA target are invalid.
Invalid sample range occurred from 0.3700 seconds to 0.4860 seconds.

Sample number 1231 of the R. TIBIA target is invalid.
Invalid sample 1231 occurred at 0.0960 seconds.

Samples 1355 through 1381 of the R. TIBIA target are invalid.
Invalid sample range occurred from 0.3440 seconds to 0.3960 seconds.

Samples 1257 through 1265 of the CHEST target are invalid.
Invalid sample range occurred from 0.1480 seconds to 0.1640 seconds.

Samples 1282 through 1426 of the CHEST target are invalid.
Invalid sample range occurred from 0.1980 seconds to 0.4860 seconds.

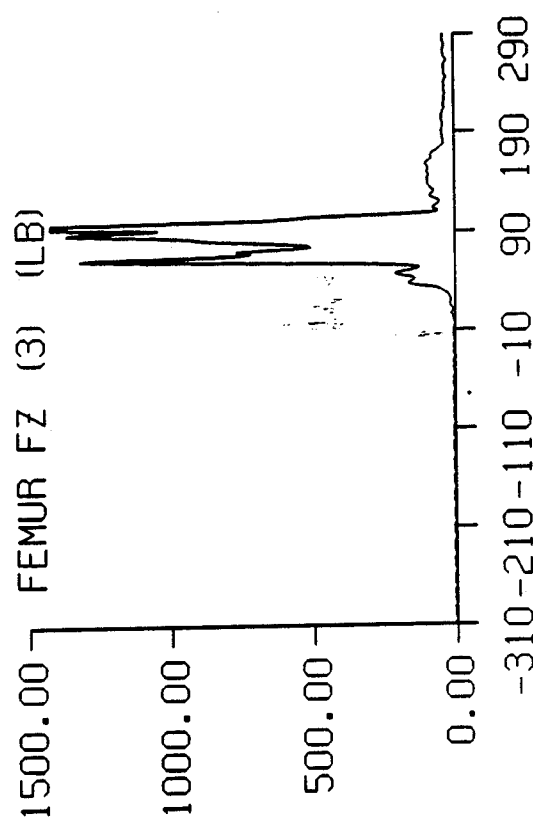
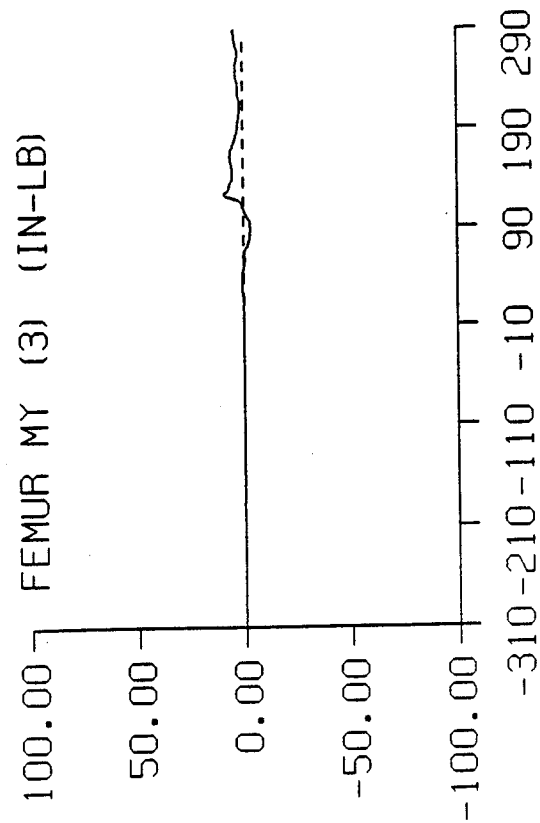
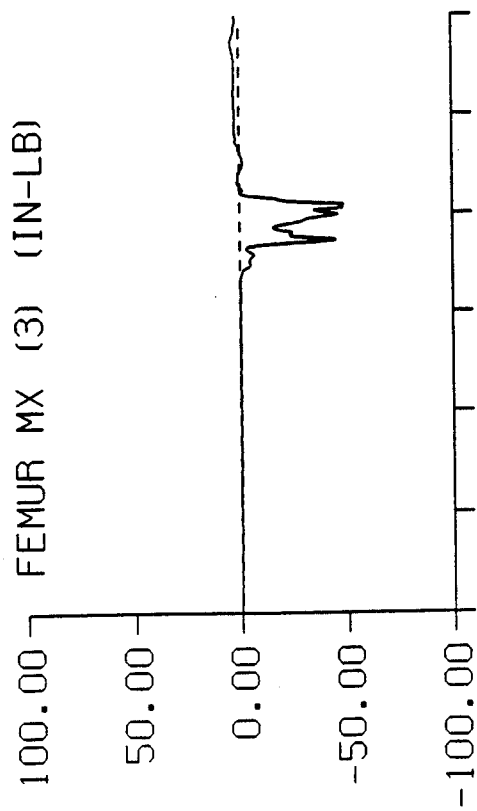
Sample number 1323 of target 6 is invalid.
Invalid sample 1323 occurred at 0.2800 seconds.

Sample number 1328 of target 6 is invalid.
Invalid sample 1328 occurred at 0.2900 seconds.

SPARTA -GX STUDY TEST: 4642

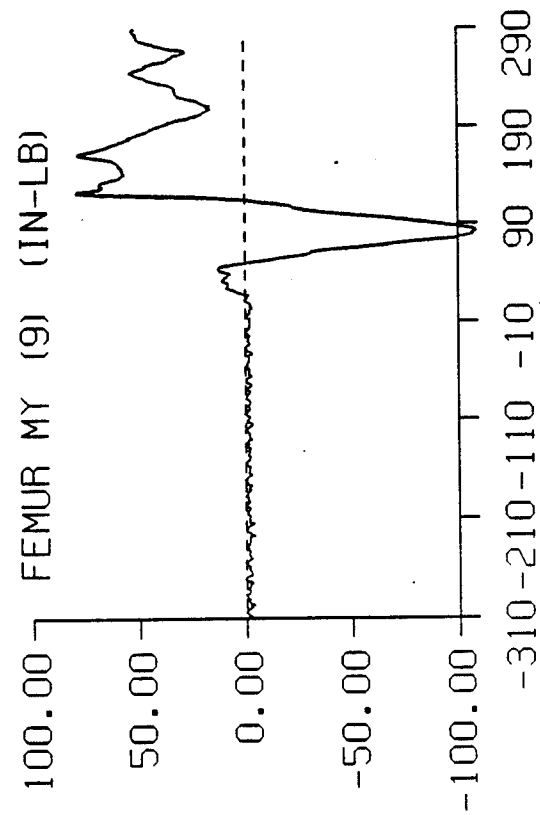
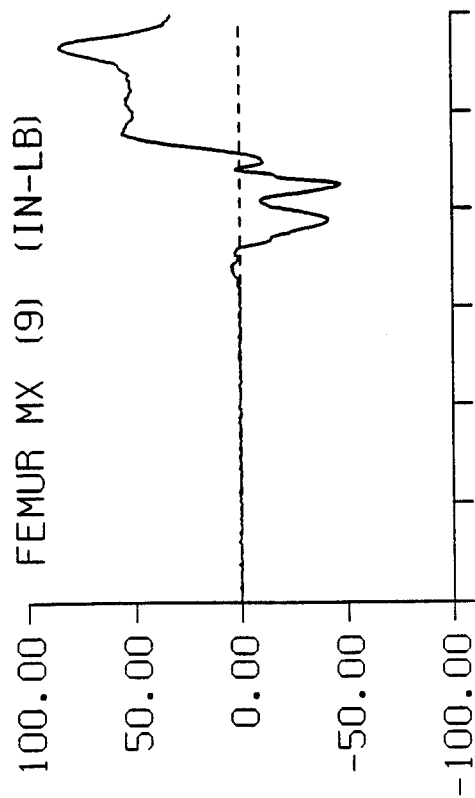
DATA ID	IMMEDIATE PREIMPACT	MAXIMUM VALUE	MINIMUM VALUE	TIME OF MAXIMUM	TIME OF MINIMUM
REFERENCE MARK TIME (MS)				-314.	
FEMUR					
MX (3) (IN-LB)	-0.08	4.01	-48.57	264.	99.
MY (3) (IN-LB)	0.01	8.95	-3.47	123.	89.
FZ (3) (LB)	4.06	1422.47	4.77	95.	11.
MX (9) (IN-LB)	0.36	84.39	-47.39	257.	115.
MY (9) (IN-LB)	-1.51	79.54	-108.90	123.	82.
FZ (9) (LB)	3.79	38.62	4.50	125.	2.
MX (15) (IN-LB)	0.04	8.36	-0.32	262.	111.
MY (15) (IN-LB)	0.03	16.42	-8.20	122.	81.
FZ (15) (LB)	5.55	45.27	7.06	84.	0.
MX (21) (IN-LB)	1.08	78.37	-39.24	258.	78.
MY (21) (IN-LB)	-1.20	85.08	-40.90	163.	81.
FZ (21) (LB)	2.15	63.92	2.71	94.	0.
TIBIA					
MX (3) (IN-LB)	-0.03	6.78	-12.06	103.	163.
MY (3) (IN-LB)	0.04	55.24	-51.31	180.	122.
FZ (3) (LB)	1.24	32.08	0.70	122.	214.
MX (9) (IN-LB)	-0.12	5.19	-13.77	271.	121.
MY (9) (IN-LB)	0.05	3.52	-53.62	15.	122.
FZ (9) (LB)	1.70	34.61	-1.02	269.	122.

SPARTA -GX STUDY TEST: 4642

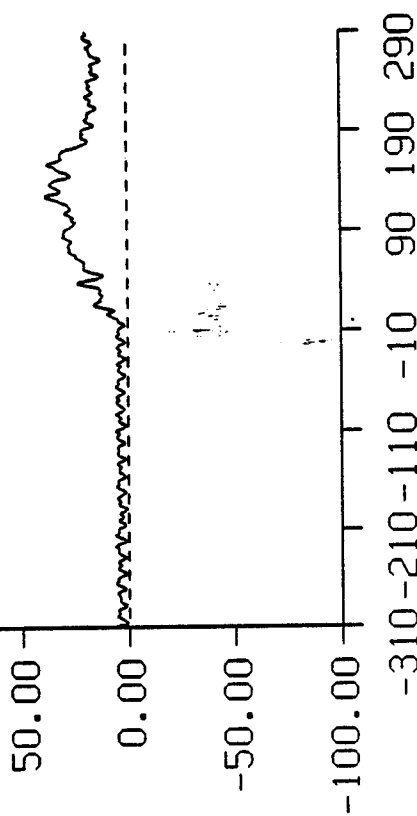


TIME IN MILLISECONDS

SPARTA -GX STUDY TEST: 4642

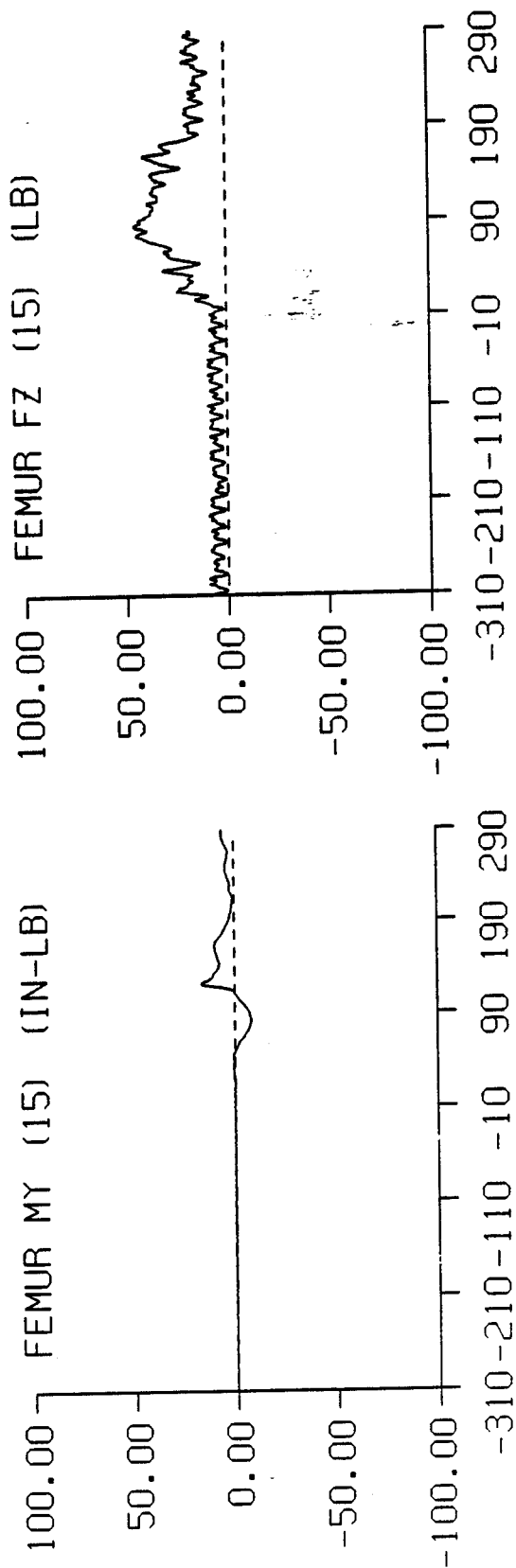
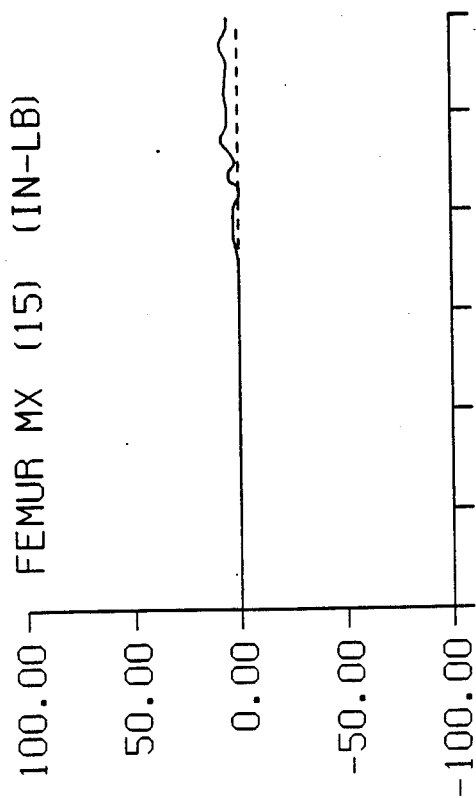


FEMUR FZ (9) (LB)



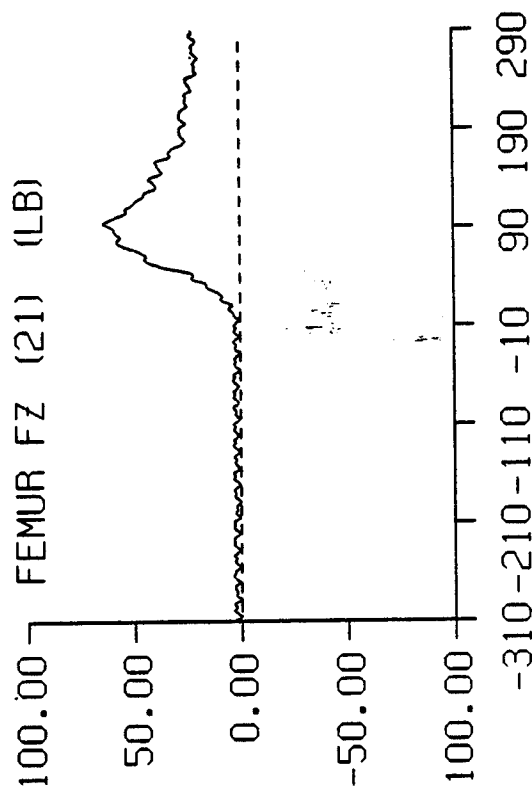
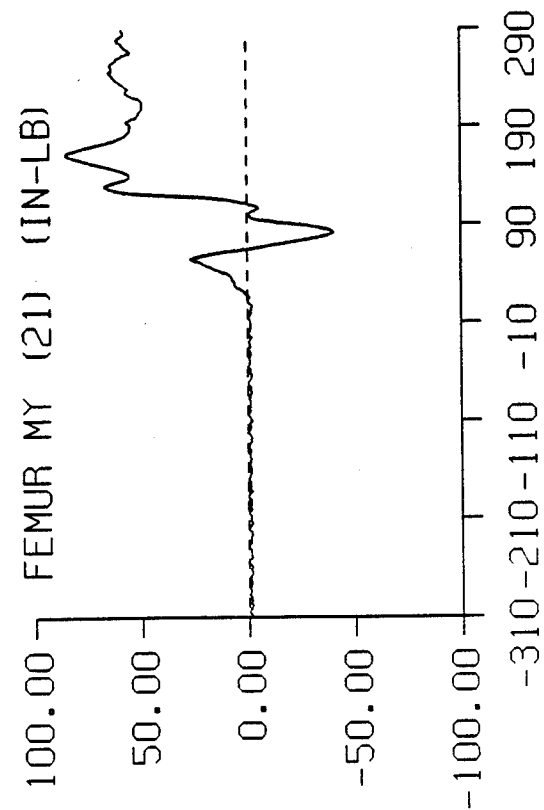
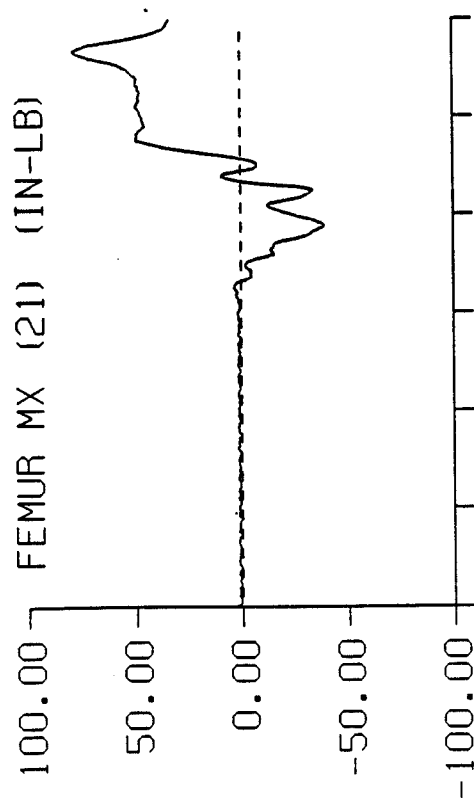
TIME IN MILLISECONDS

SPARTA -GX STUDY TEST: 4642



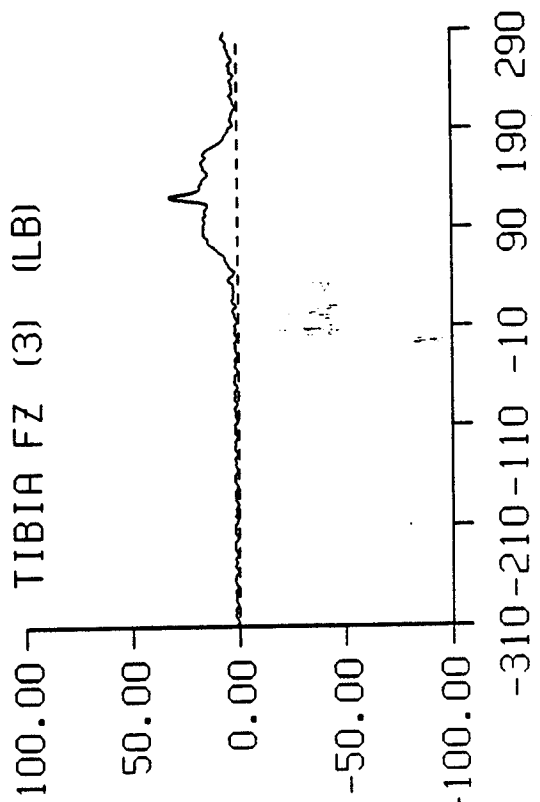
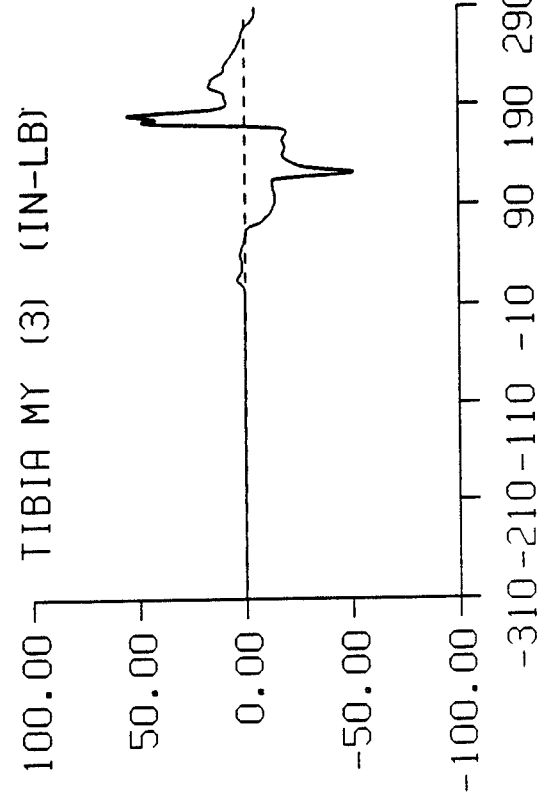
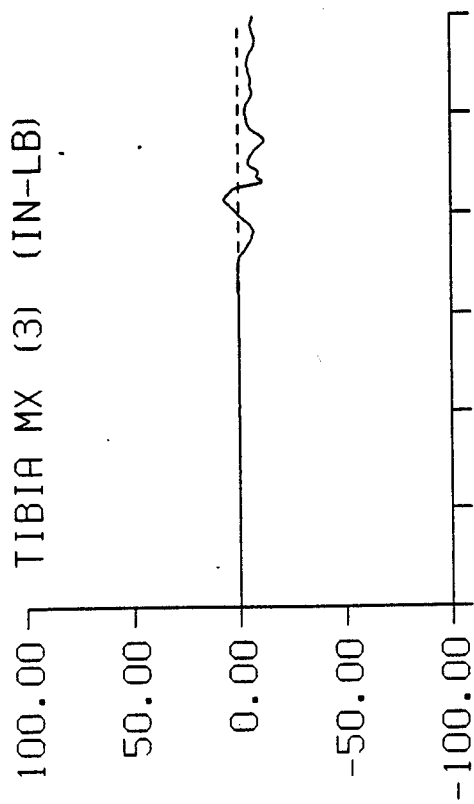
TIME IN MILLISECONDS

SPARTA -GX STUDY TEST: 4642



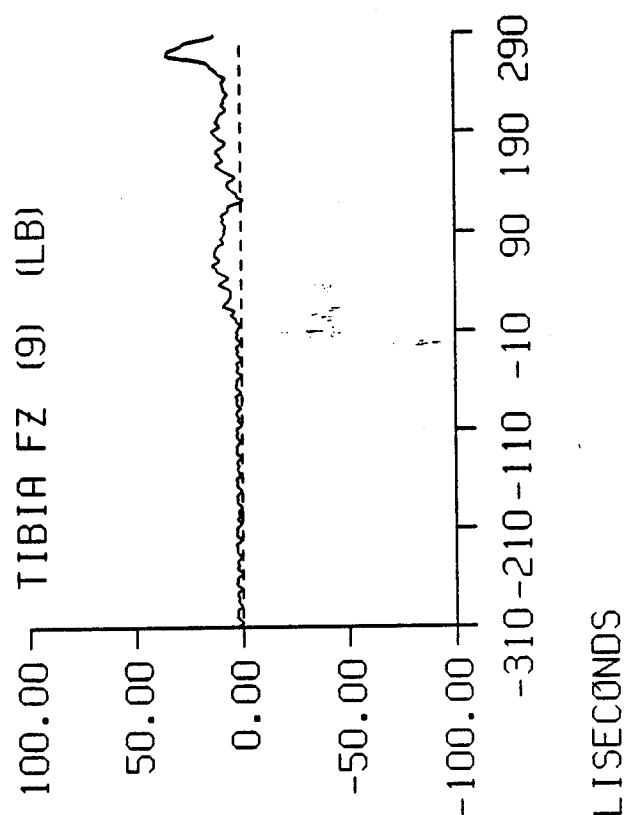
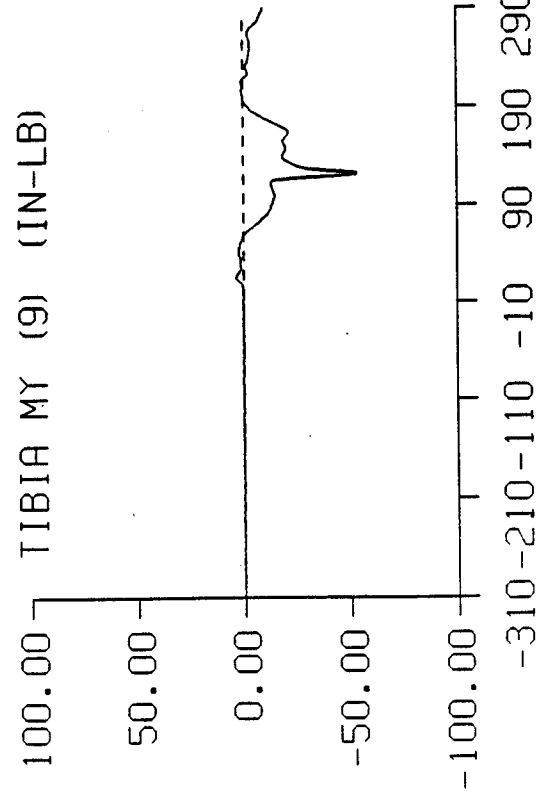
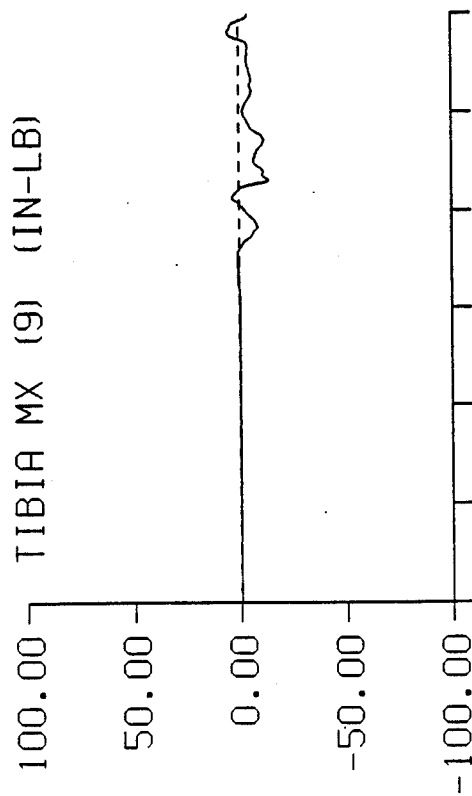
TIME IN MILLISECONDS

SPARTA -CX STUDY TEST: 4642



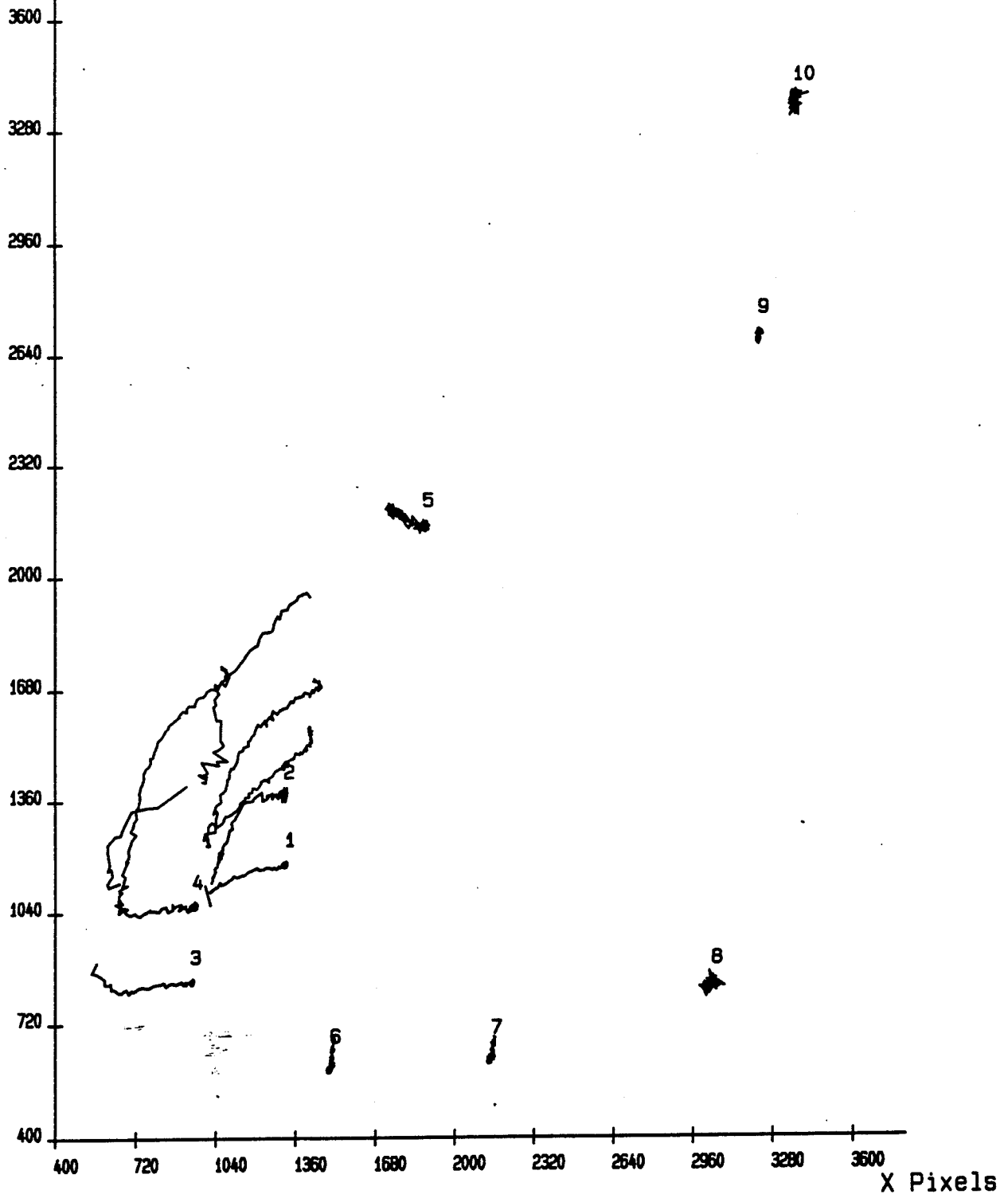
TIME IN MILLISECONDS

SPARTA -GX STUDY TEST: 4642



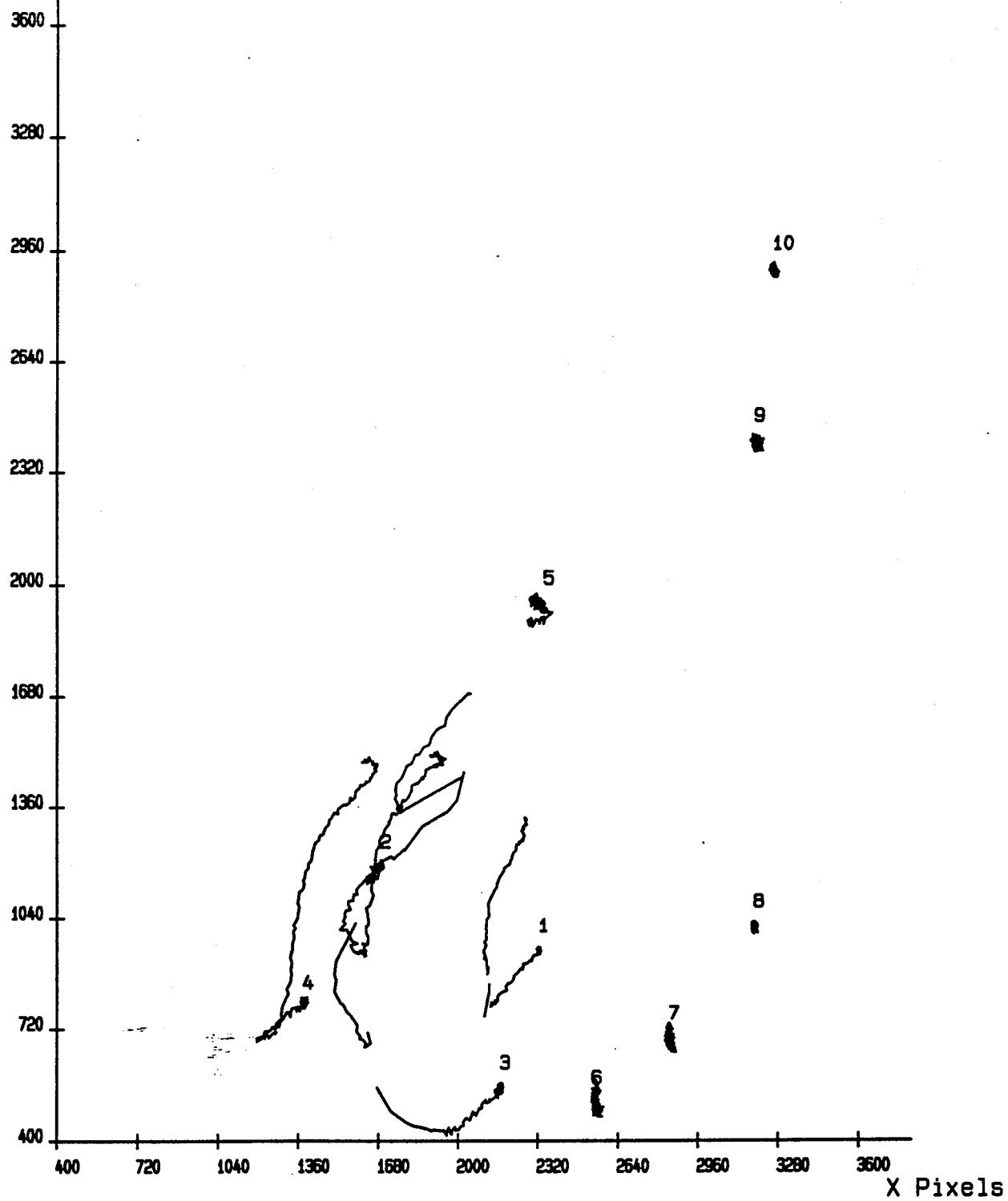
Test DATA-4642HAC.RUN Camera 1

Y Pixels



Test DATA-4642HAC.RUN Camera 2

Y Pixels

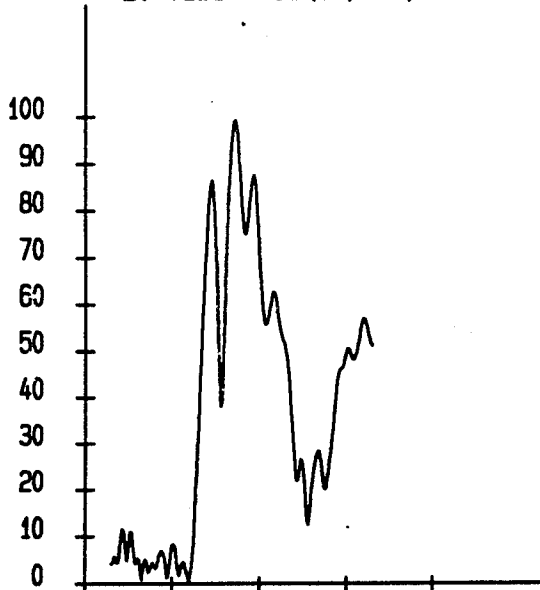


TEST 6 (4643) 20.0 G

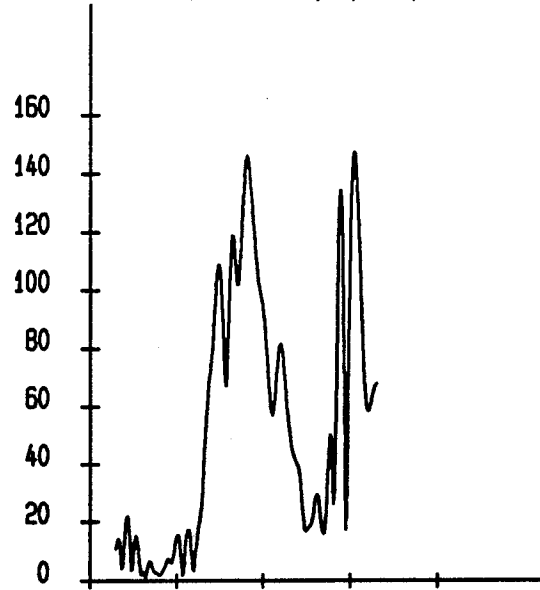
SPARTA -GX

TEST: 4643 DATE: 24-SEP-1993 SUBJ: HB3-50 CELL: F

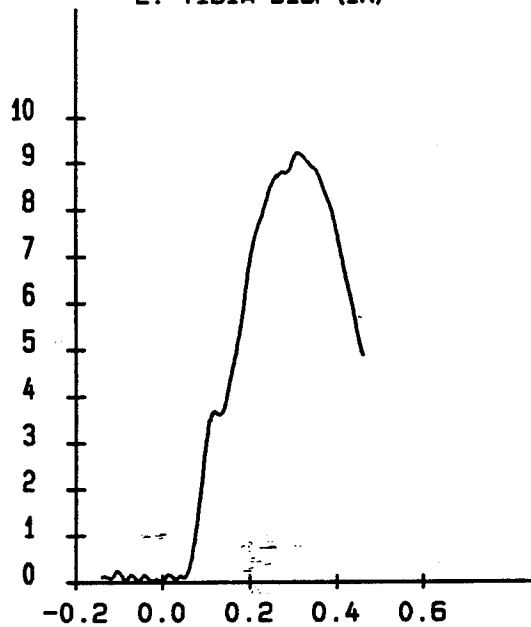
L. TIBIA VEL (IN/SEC)



R. TIBIA VEL (IN/SEC)

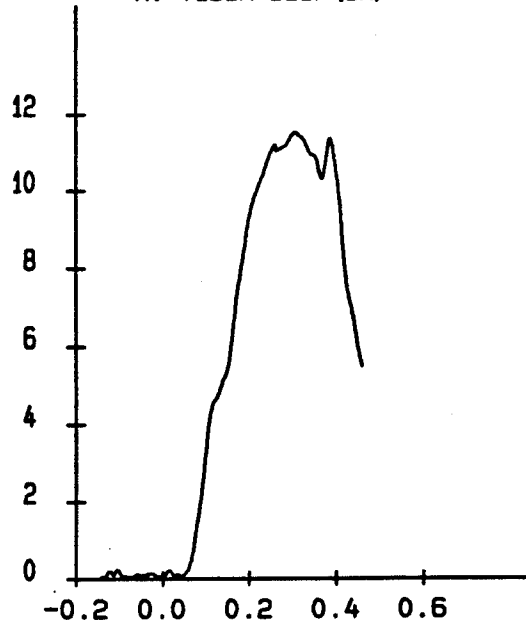


L. TIBIA DISP (IN)



TIME (SEC)

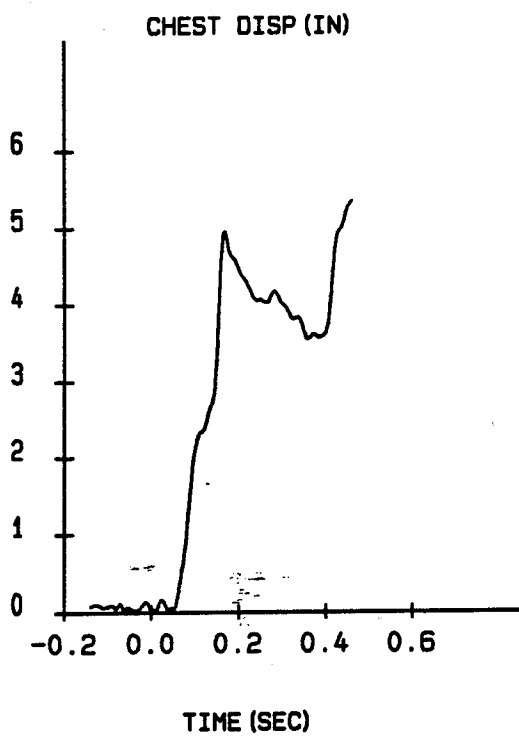
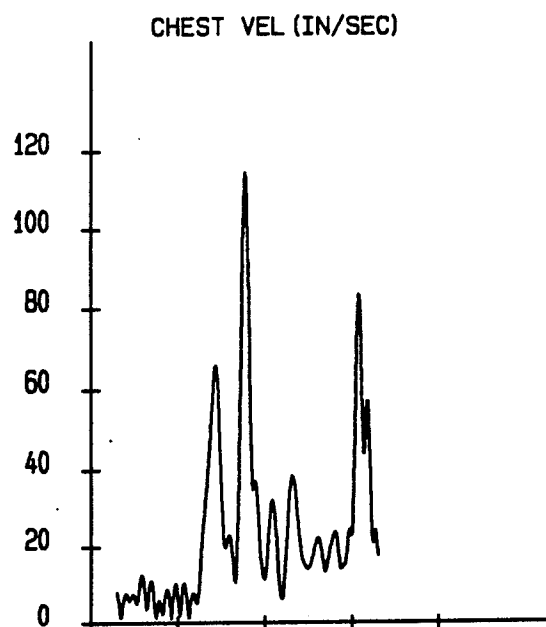
R. TIBIA DISP (IN)



TIME (SEC)

SPARTA -GX

TEST: 4643 DATE: 24-SEP-1993 SUBJ: HB3-50 CELL: F



SPARTA -GX
 TEST: 4643 DATE: 24-SEP-1993 SUBJ: HB3-50 CELL: F

RELIABILITY FACTORS (IN)

TARGET DESCRIPTION	MAXIMUM	MINIMUM	AVERAGE	STANDARD DEVIATION	AT MAX DISPLACEMENT
1 L. FEMUR	0.2471	0.0003	0.1129	0.0670	0.1733
2 R. FEMUR	0.2852	0.0008	0.1431	0.0784	0.2151
3 L. TIBIA	0.3480	0.0023	0.1404	0.1016	0.2343
4 R. TIBIA	0.8938	0.0011	0.2103	0.1924	0.2787
5 CHEST	0.6232	0.0156	0.2355	0.1089	0.6232

TARGET	MAXIMUM	TIME(SEC)	MINIMUM	TIME(SEC)
L. FEMUR				
POSITION(IN)				
X AXIS	24.0291	0.1240	19.0957	0.3280
Y AXIS	8.1299	0.4600	5.1527	0.2680
Z AXIS	10.6689	0.3140	5.3733	0.1260
VELOCITY(IN/SEC)	94.3331	0.0920	2.4888	0.0360
ACCELERATION(G)	11.0917	0.1180	0.2490	0.4380
DISPLACEMENT(IN)				
X AXIS	3.9450	0.1240	-0.9883	0.3280
Y AXIS	1.2305	0.4600	-1.7467	0.2680
Z AXIS	4.3241	0.3140	-0.9715	0.1260
RESULTANT	4.6856	0.3100	0.0000	0.0000
R. FEMUR				
POSITION(IN)				
X AXIS	26.5401	0.1220	19.5555	0.2940
Y AXIS	-1.5406	0.3060	-5.1526	0.0520
Z AXIS	12.4755	0.2560	5.6149	0.1340
VELOCITY(IN/SEC)	134.7883	0.1580	5.0717	0.0240
ACCELERATION(G)	18.2016	0.1400	0.2532	0.3280
DISPLACEMENT(IN)				
X AXIS	4.9454	0.1220	-2.0392	0.2940
Y AXIS	3.5766	0.3060	-0.0353	0.0520
Z AXIS	4.9569	0.2560	-1.9038	0.1340
RESULTANT	6.1688	0.2980	0.0000	0.0000

SPARTA -GX

TEST: 4643 DATE: 24-SEP-1993 SUBJ: HB3-50 CELL: F

TARGET	MAXIMUM	TIME(SEC)	MINIMUM	TIME(SEC)
L. TIBIA				
POSITION(IN)				
X AXIS	28.7227	0.1160	22.7557	0.3300
Y AXIS	8.9379	0.4600	5.2141	0.2660
Z AXIS	10.9201	0.3120	2.0934	0.1040
VELOCITY(IN/SEC)	99.1864	0.1440	0.2998	0.0380
ACCELERATION(G)	13.7088	0.1120	0.2339	0.2340
DISPLACEMENT(IN)				
X AXIS	3.6660	0.1160	-2.3010	0.3300
Y AXIS	1.5769	0.4600	-2.1469	0.2660
Z AXIS	8.7900	0.3120	-0.0367	0.1040
RESULTANT	9.2162	0.3100	0.0000	0.0000
R. TIBIA				
POSITION(IN)				
X AXIS	32.1758	0.1200	25.7511	0.3000
Y AXIS	0.0597	0.3880	-6.4138	0.0840
Z AXIS	12.6475	0.3100	2.2155	0.1040
VELOCITY(IN/SEC)	147.2181	0.4080	1.8283	0.0140
ACCELERATION(G)	31.1867	0.3920	0.6286	0.0260
DISPLACEMENT(IN)				
X AXIS	4.5470	0.1200	-1.8777	0.3000
Y AXIS	6.2895	0.3880	-0.1839	0.0840
Z AXIS	10.2765	0.3100	-0.1554	0.1040
RESULTANT	11.5110	0.3060	0.0000	0.0000
CHEST				
POSITION(IN)				
X AXIS	16.8052	0.1680	11.9681	0.0220
Y AXIS	2.3810	0.1360	0.9572	0.4040
Z AXIS	21.5419	0.1700	16.2315	0.4600
VELOCITY(IN/SEC)	114.4129	0.1540	1.4034	0.0240
ACCELERATION(G)	15.8001	0.1680	0.3513	0.2660

SPARTA -GX
TEST: 4643 DATE: 24-SEP-1993 SUBJ: HB3-50 CELL: F

TARGET	MAXIMUM	TIME(SEC)	MINIMUM	TIME(SEC)
CHEST				
DISPLACEMENT(IN)				
X AXIS	4.7419	0.1680	-0.0952	0.0220
Y AXIS	0.7731	0.1360	-0.6507	0.4040
Z AXIS	1.4267	0.1700	-3.8837	0.4600
RESULTANT	5.3411	0.4600	0.0000	0.0000

SPARTA -GX
TEST: 4643 DATE: 24-SEP-1993 SUBJ: HB3-50 CELL: F

Note: Invalid samples are interpolated.

Samples 1280 through 1287 of the L. FEMUR target are invalid.
Invalid sample range occurred from 0.1160 seconds to 0.1300 seconds.

Samples 1290 through 1291 of the L. FEMUR target are invalid.
Invalid sample range occurred from 0.1360 seconds to 0.1380 seconds.

Samples 1285 through 1288 of the R. FEMUR target are invalid.
Invalid sample range occurred from 0.1260 seconds to 0.1320 seconds.

Samples 1288 through 1292 of the R. TIBIA target are invalid.
Invalid sample range occurred from 0.1320 seconds to 0.1400 seconds.

Samples 1414 through 1427 of the R. TIBIA target are invalid.
Invalid sample range occurred from 0.3840 seconds to 0.4100 seconds.

Samples 1306 through 1452 of the CHEST target are invalid.
Invalid sample range occurred from 0.1680 seconds to 0.4600 seconds.

Sample number 1262 of target 6 is invalid.
Invalid sample 1262 occurred at 0.0800 seconds.

Samples 1269 through 1270 of target 6 are invalid.
Invalid sample range occurred from 0.0940 seconds to 0.0960 seconds.

Sample number 1384 of target 6 is invalid.
Invalid sample 1384 occurred at 0.3240 seconds.

Samples 1387 through 1388 of target 6 are invalid.
Invalid sample range occurred from 0.3300 seconds to 0.3320 seconds.

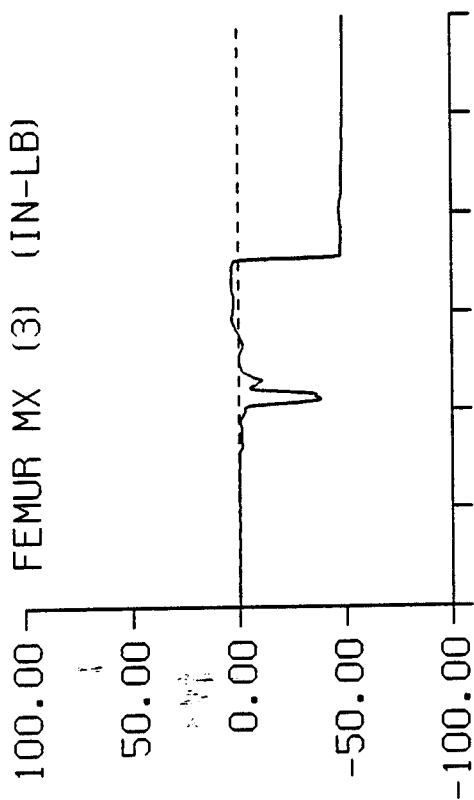
Sample number 1397 of target 6 is invalid.
Invalid sample 1397 occurred at 0.3500 seconds.

SPARTA -GX STUDY TEST: 4643

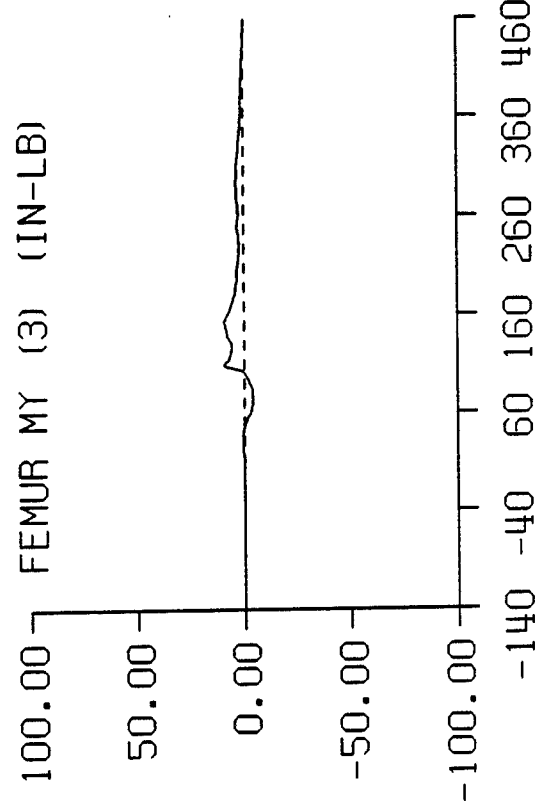
DATA ID	IMMEDIATE PREIMPACT	MAXIMUM VALUE	MINIMUM VALUE	TIME OF MAXIMUM	TIME OF MINIMUM
REFERENCE MARK TIME (MS)				-140.	
FEMUR					
MX (3) (IN-LB)	-0.19	3.54	-49.48	197.	434.
MY (3) (IN-LB)	-0.01	9.31	-4.25	110.	74.
FZ (3) (LB)	8.02	1464.06	1.06	263.	0.
MX (9) (IN-LB)	0.34	62.36	-757.36	192.	453.
MY (9) (IN-LB)	-4.04	212.54	-128.67	149.	76.
FZ (9) (LB)	7.06	376.92	1.72	278.	0.
MX (15) (IN-LB)	0.13	7.37	-1.10	152.	125.
MY (15) (IN-LB)	0.00	18.13	-8.00	109.	74.
FZ (15) (LB)	11.92	64.47	3.10	279.	0.
MX (21) (IN-LB)	1.35	74.96	-86.97	257.	59.
MY (21) (IN-LB)	-2.00	108.41	-45.80	148.	79.
FZ (21) (LB)	4.34	96.21	1.17	58.	0.
TIBIA					
MX (3) (IN-LB)	-0.02	6.21	-12.20	97.	149.
MY (3) (IN-LB)	0.06	15.70	-61.00	242.	108.
FZ (3) (LB)	2.20	37.41	-0.17	108.	199.
MX (9) (IN-LB)	0.01	3.35	-9.02	97.	150.
MY (9) (IN-LB)	0.13	3.94	-63.64	240.	108.
FZ (9) (LB)	3.87	19.61	-1.86	58.	108.

SPARTA -CX STUDY TEST: 4643

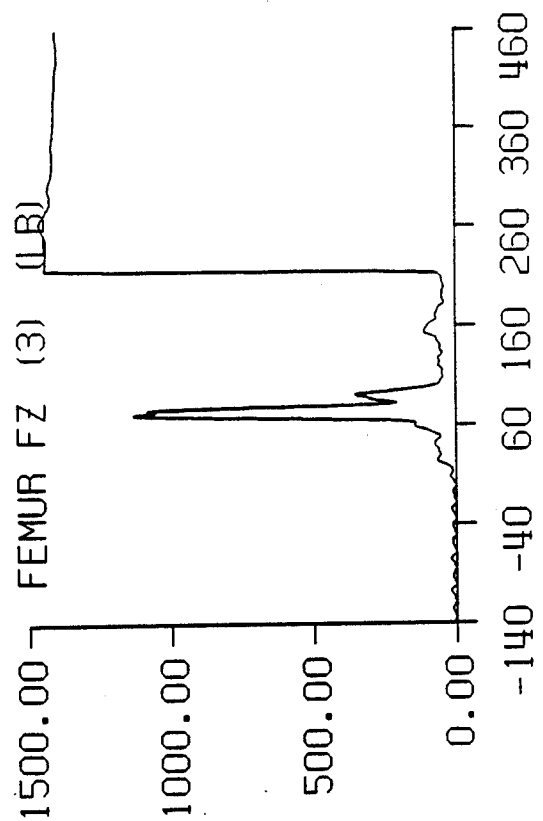
FEMUR MX (3) (IN-LB)



FEMUR MY (3) (IN-LB)

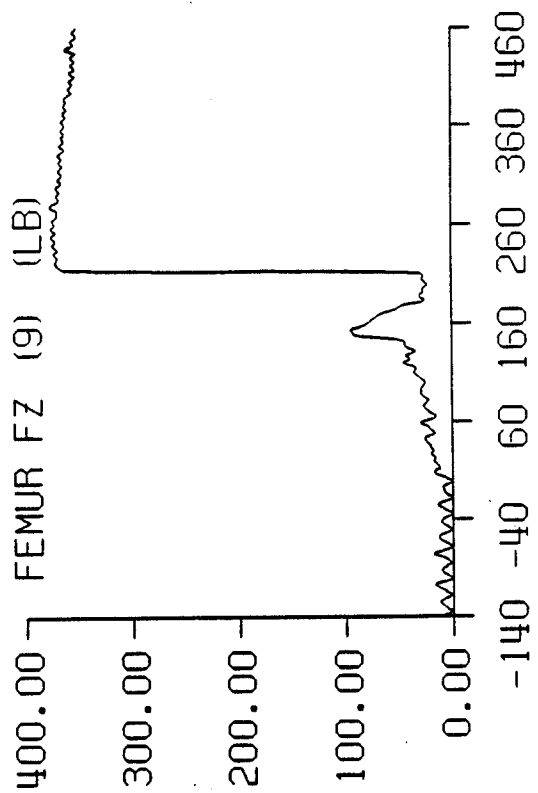
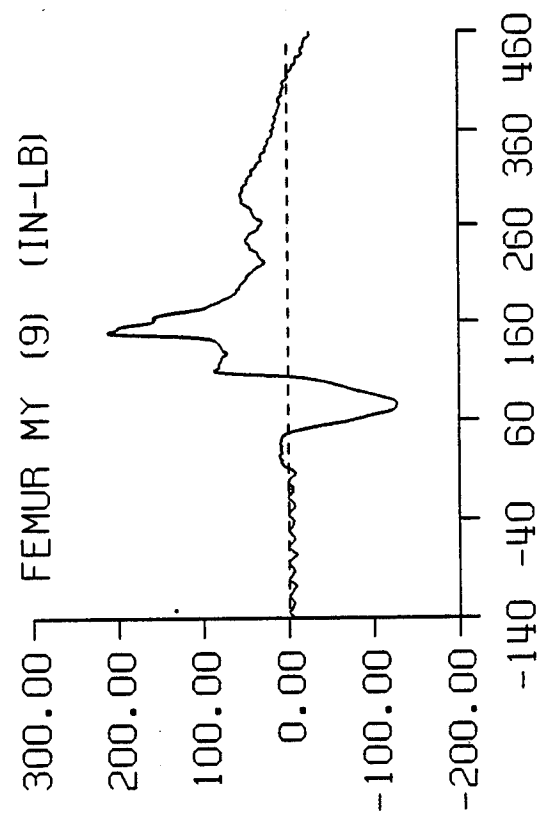
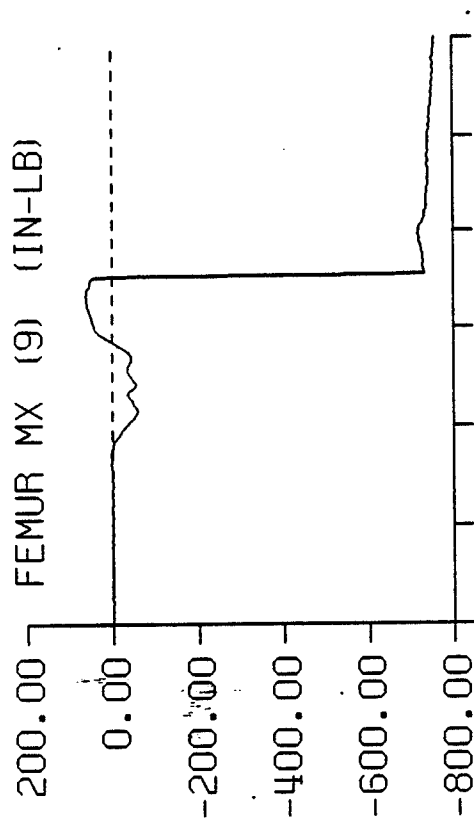


FEMUR FZ (3) (LB)



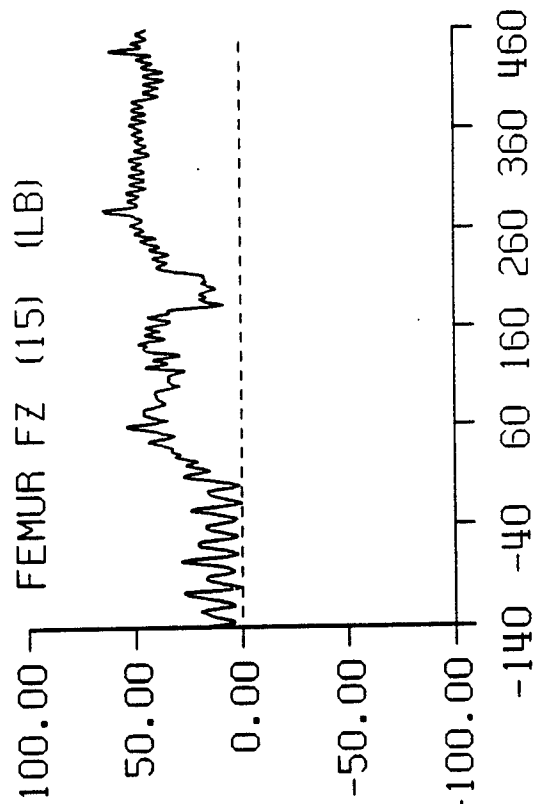
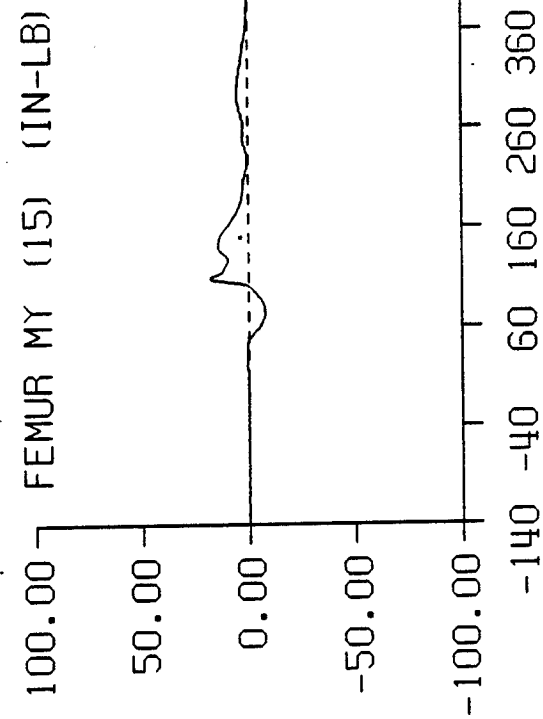
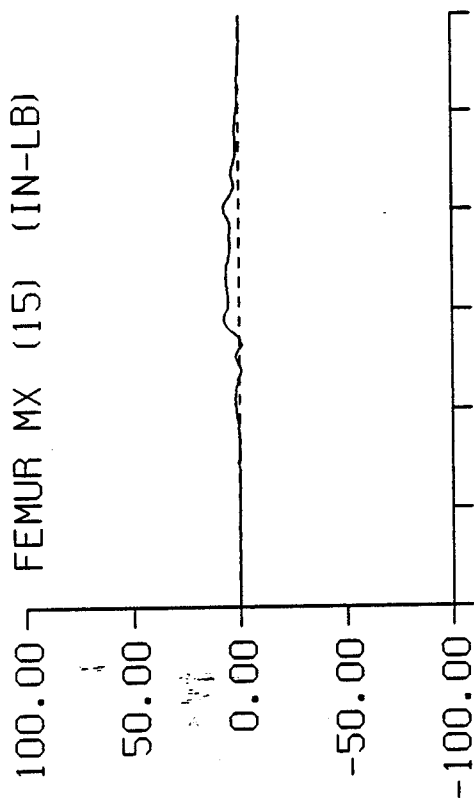
TIME IN MILLISECONDS

SPARTA -GX STUDY TEST: 4643



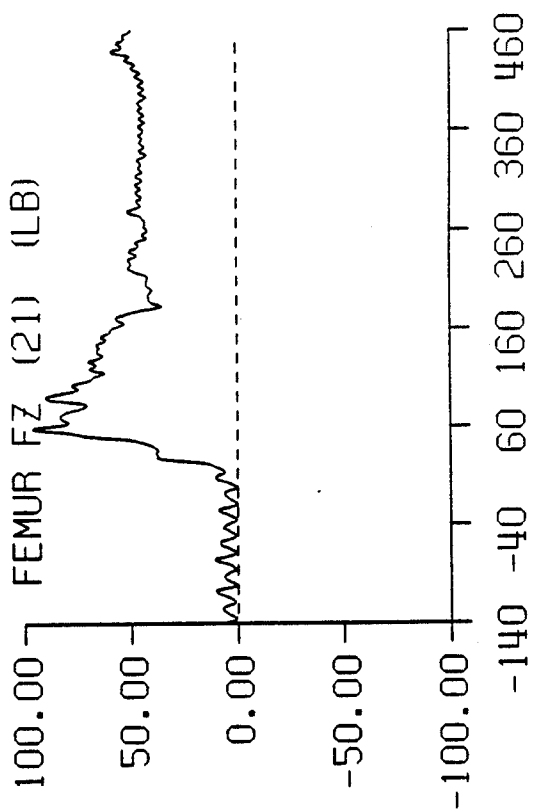
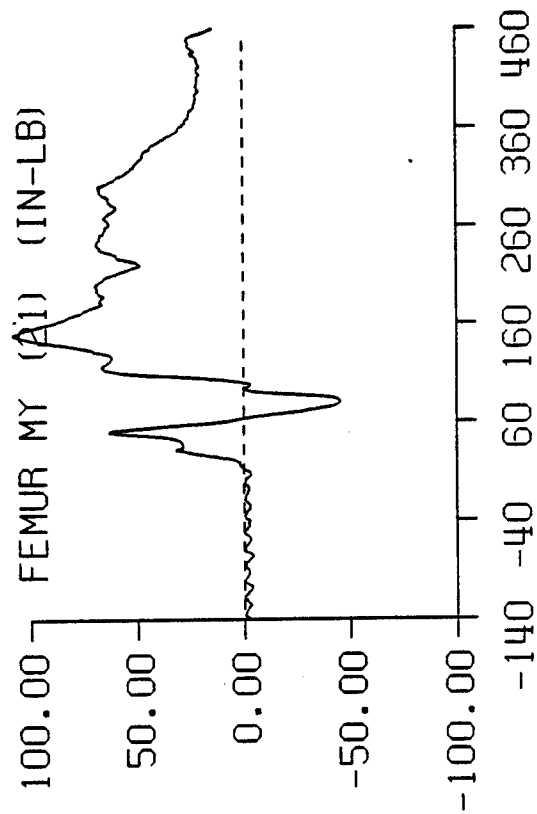
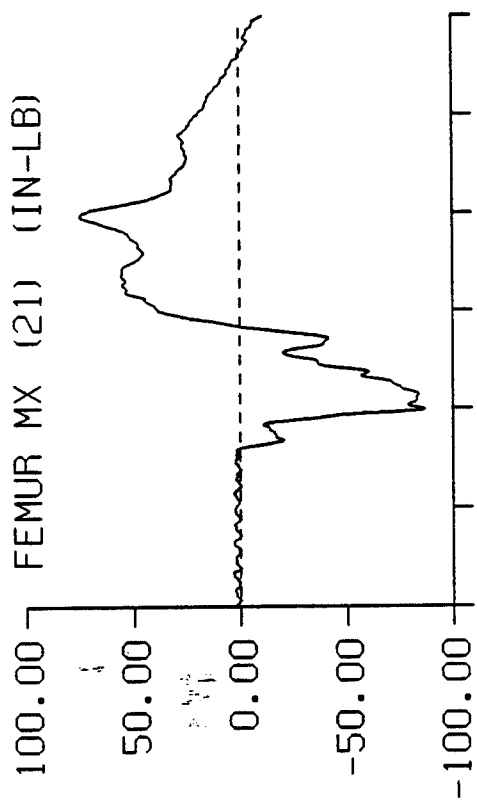
TIME IN MILLISECONDS

SPARTA -GX STUDY TEST: 4643



TIME IN MILLISECONDS

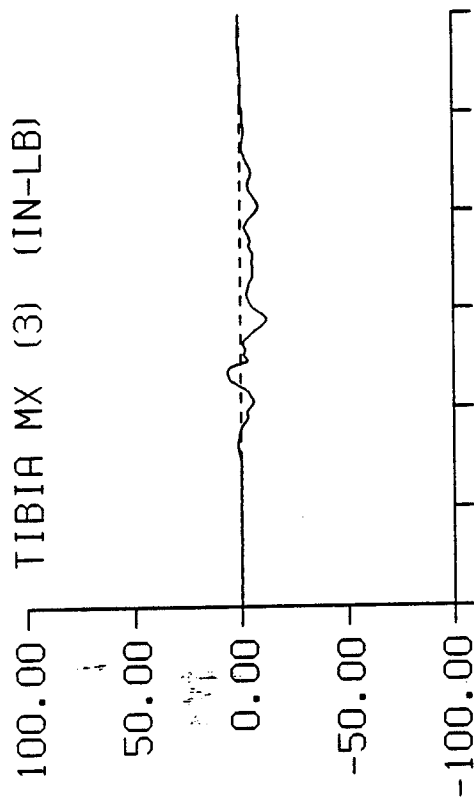
SPARTA -GX STUDY TEST: 4643



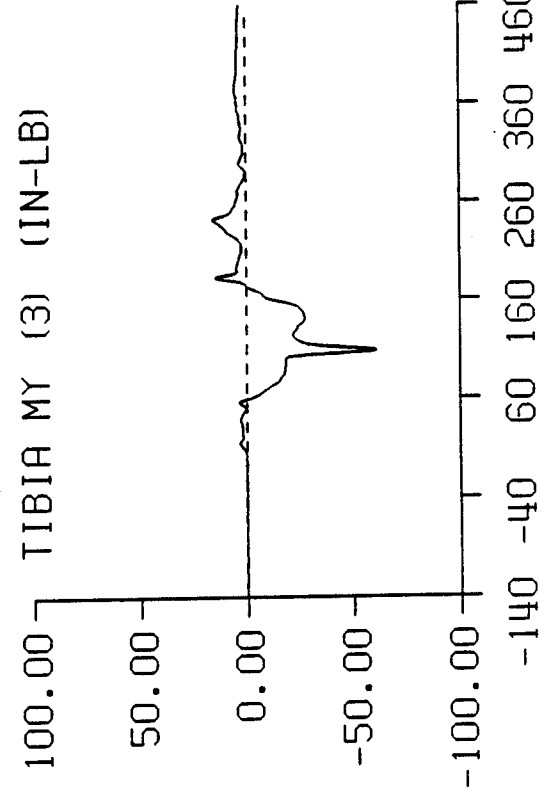
TIME IN MILLISECONDS

SPARTA -GX STUDY TEST: 4643

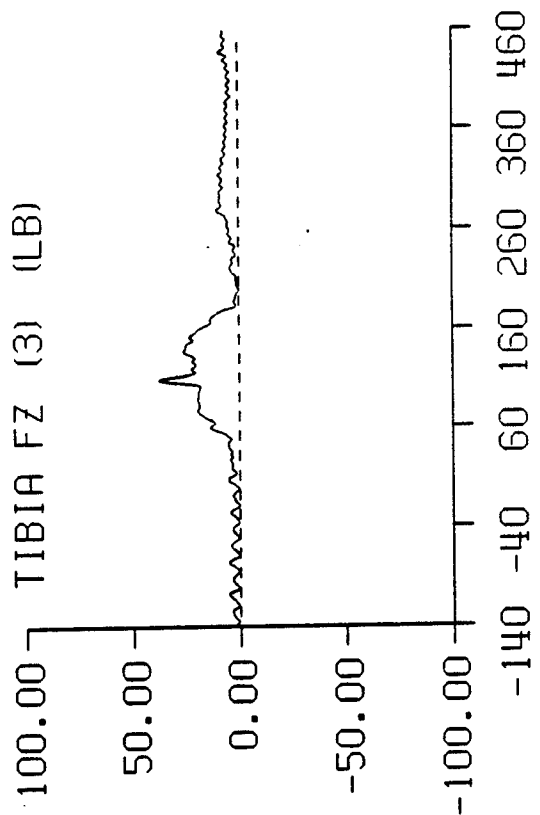
TIBIA MX (3) (IN-LB)



TIBIA MY (3) (IN-LB)



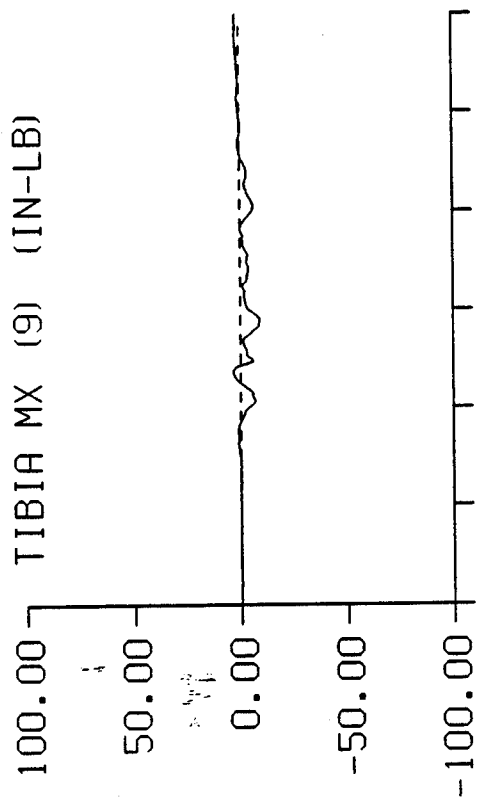
TIBIA FZ (3) (LB)



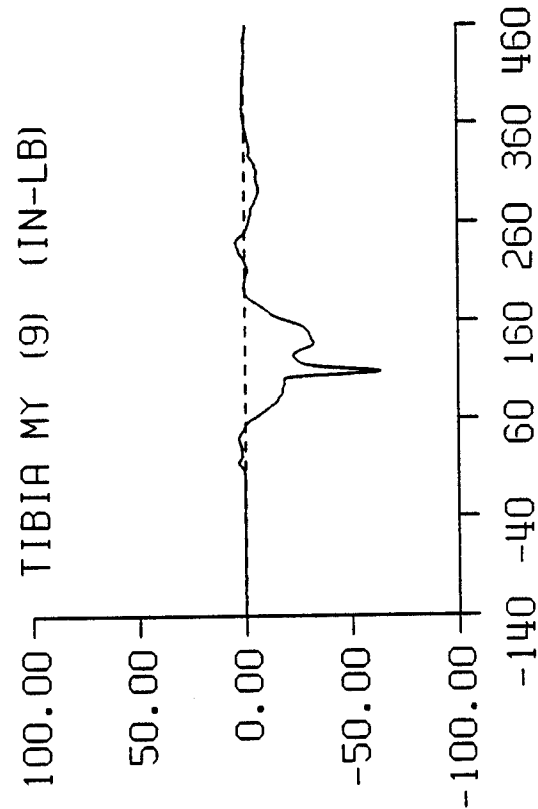
TIME IN MILLISECONDS

SPARTA -GX STUDY TEST: 4643

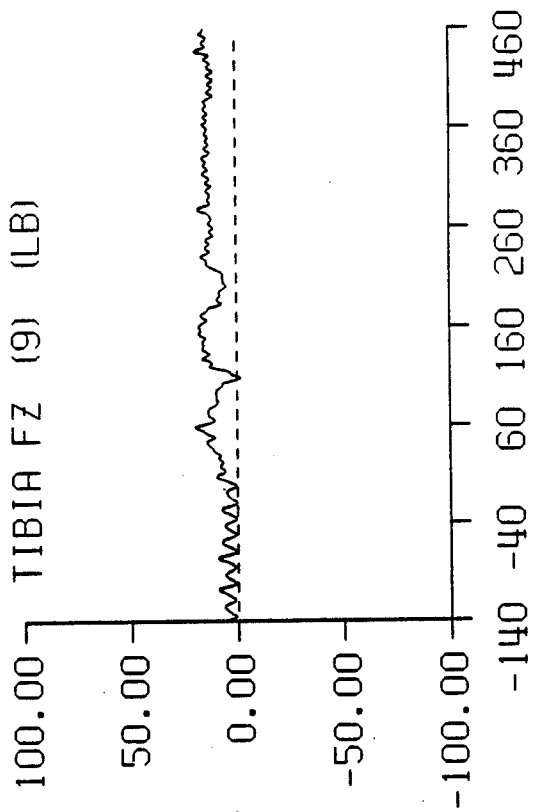
TIBIA MX (9) (IN-LB)



TIBIA MY (9) (IN-LB)



TIBIA FZ (9) (LB)

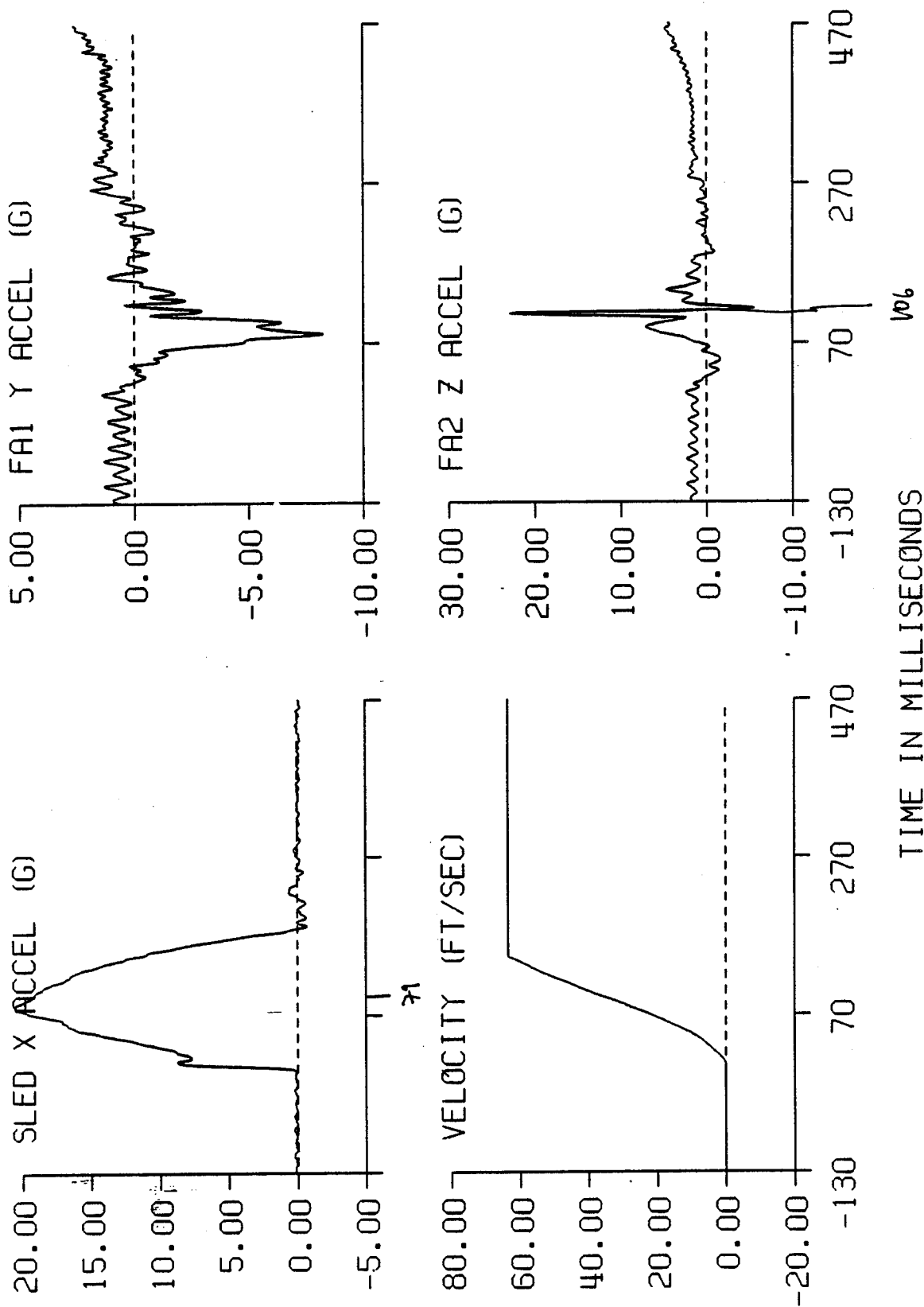


TIME IN MILLISECONDS

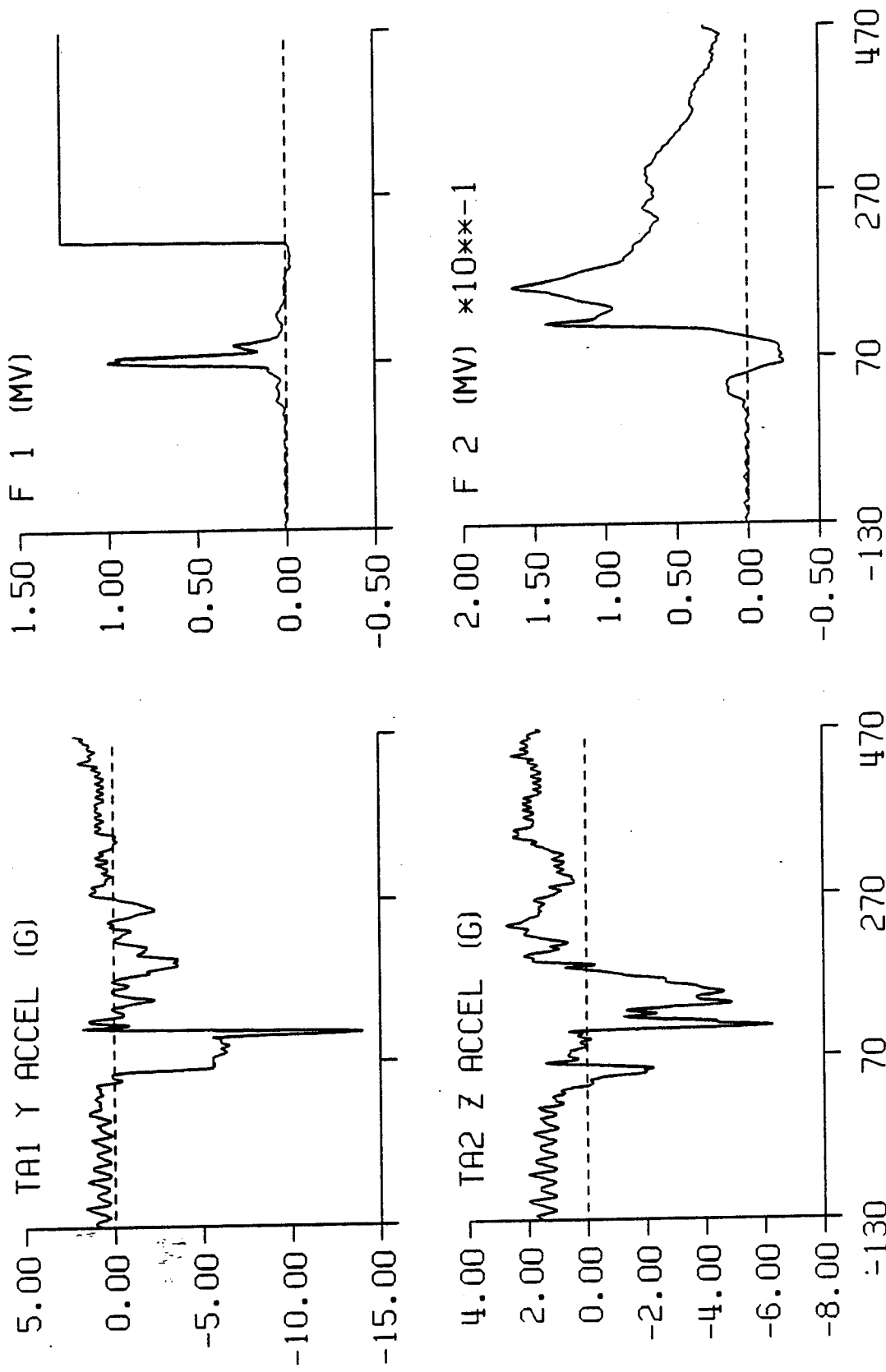
TEST 4643 CELL F

CHANNEL	MAXIMUM VALUE	MINIMUM VALUE	TIME OF MAXIMUM	TIME OF MINIMUM
IMPACT RISE TIME			79.0	
IMPACT DURATION			179.0	
VELOCITY CHANGE	74.67			
SLED X ACCEL (G)	20.53	-0.69	79.0	181.0
F 1 (MV)	1.27	-0.03	216.0	185.0
F 2 (MV)	0.17	-0.03	154.0	63.0
F 3 (MV)	0.09	0.00	154.0	0.0
F 4 (MV)	0.05	-0.04	93.0	149.0
F 5 (MV)	0.09	-0.09	75.0	110.0
F 6 (MV)	0.03	-0.04	68.0	109.0
F 7 (MV)	0.75	-0.02	214.0	184.0
F 8 (MV)	0.19	-0.05	149.0	70.0
F 9 (MV)	0.05	-0.01	255.0	68.0
F 10 (MV)	0.04	-0.02	90.0	148.0
F 11 (MV)	0.07	-0.02	76.0	109.0
F 12 (MV)	0.04	-0.03	74.0	108.0
F 13 (MV)	0.04	-0.03	438.0	199.0
F 14 (MV)	0.13	-0.03	109.0	66.0
F 15 (MV)	0.07	0.00	262.0	0.0
F 16 (MV)	0.04	-0.02	93.0	66.0
F 17 (MV)	0.07	-0.09	74.0	109.0
F 18 (MV)	0.03	-0.02	59.0	107.0
F 19 (MV)	0.10	-0.01	59.0	258.0
F 20 (MV)	0.09	-0.03	144.0	79.0
F 21 (MV)	0.06	0.00	256.0	0.0
F 22 (MV)	0.04	-0.02	96.0	198.0
F 23 (MV)	0.10	-0.04	75.0	148.0
F 24 (MV)	0.03	-0.02	152.0	108.0
FA1 Y ACCEL (G)	2.81	-8.22	471.0	82.0
FA2 Z ACCEL (G)	22.95	-5.56	106.0	113.0
TA1 Y ACCEL (G)	2.19	-14.01	470.0	106.0
TA2 Z ACCEL (G)	2.70	-6.27	232.0	106.0
T 1 (MV)	0.10	0.00	151.0	97.0
T 2 (MV)	0.37	-0.02	108.0	241.0
T 3 (MV)	0.06	-0.03	95.0	265.0
T 4 (MV)	0.08	0.00	82.0	0.0
T 5 (MV)	0.16	-0.25	182.0	108.0
T 6 (MV)	0.02	-0.11	58.0	108.0
VELOCITY (FT/SEC)	63.46	-0.16	143.0	6.0
T 7 (MV)	0.14	0.00	150.0	14.0
T 8 (MV)	0.39	-0.01	108.0	14.0
T 9 (MV)	0.06	-0.03	95.0	66.0
T 10 (MV)	0.04	-0.05	173.0	108.0
T 11 (MV)	0.05	-0.56	239.0	108.0
T 12 (MV)	0.07	-0.44	240.0	108.0

TEST 4643 CELL F

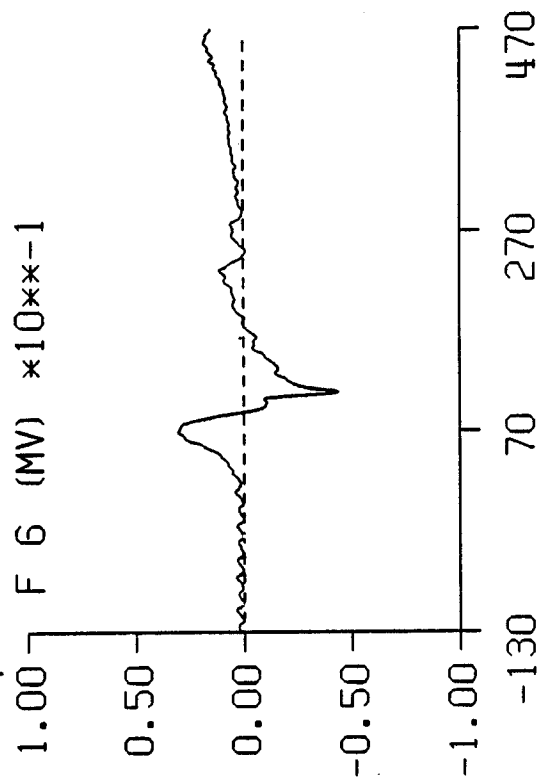
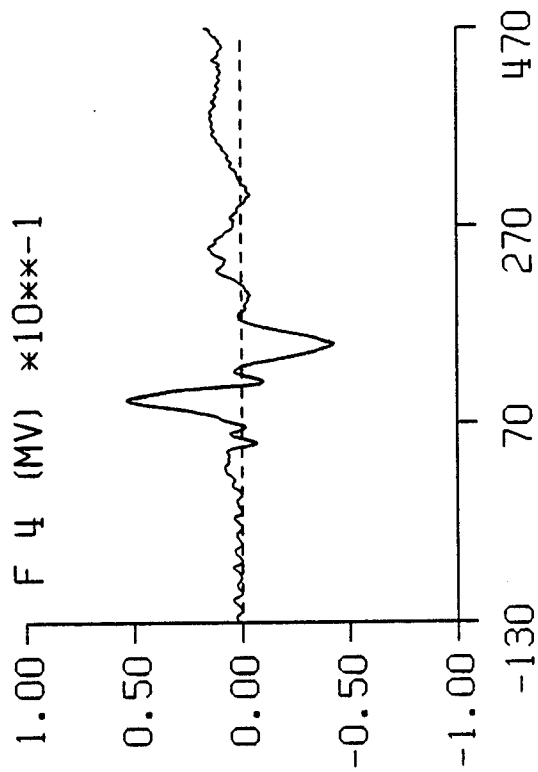
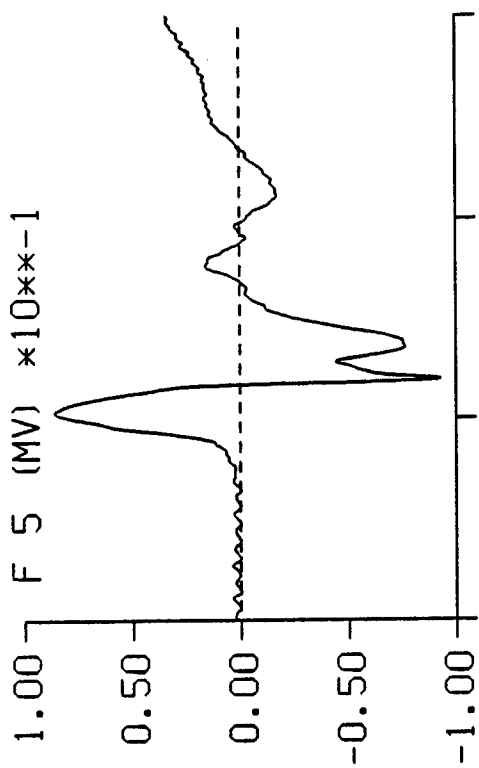
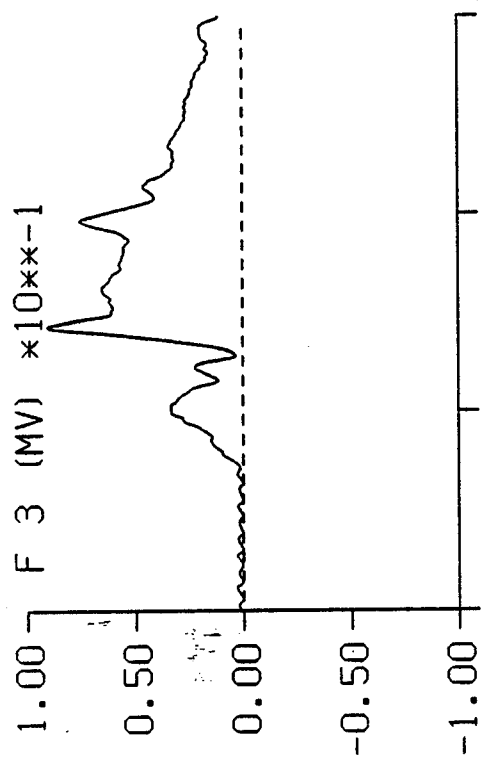


TEST 4643 CELL F



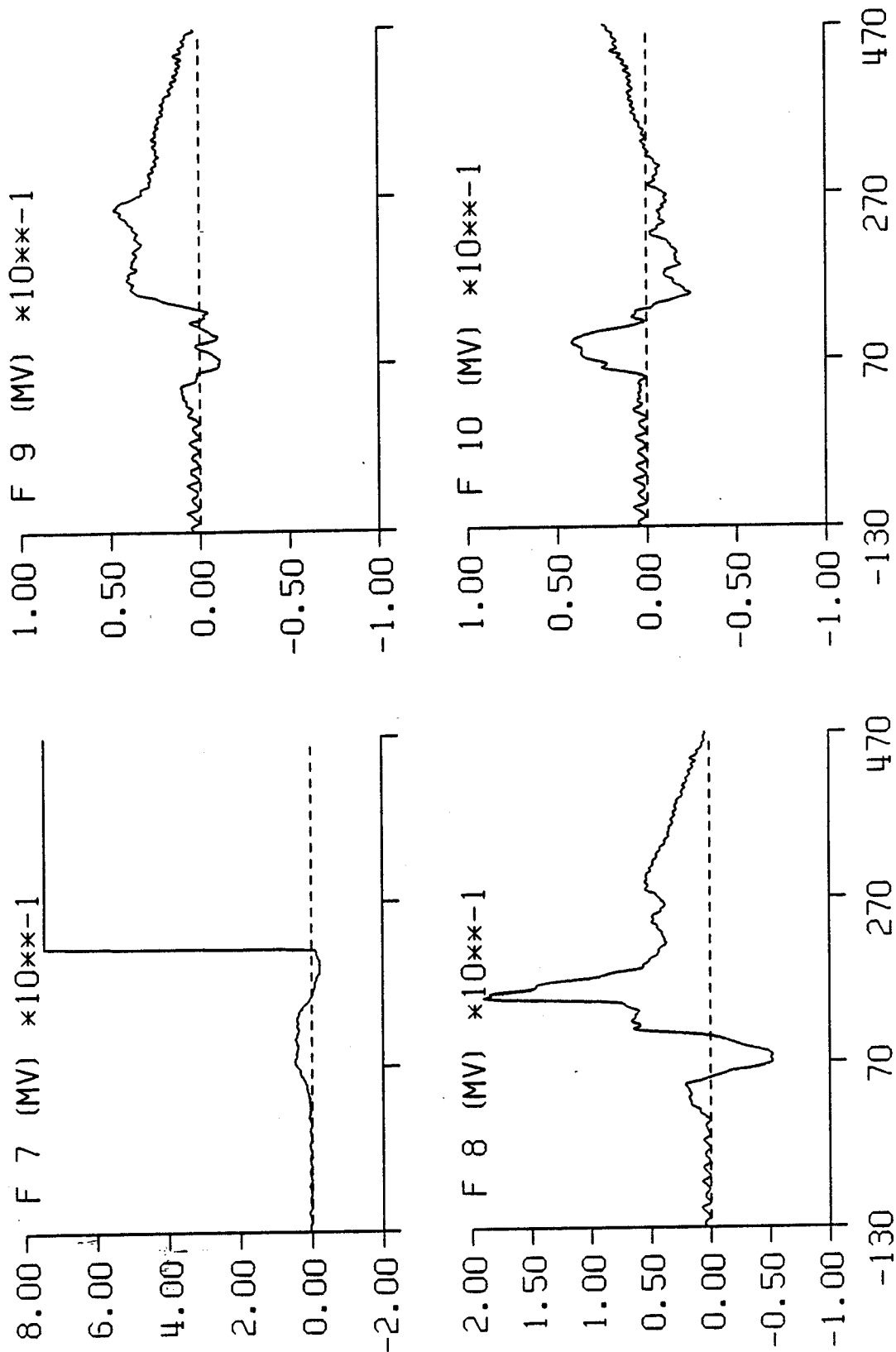
TIME IN MILLISECONDS

TEST 4643 CELL F



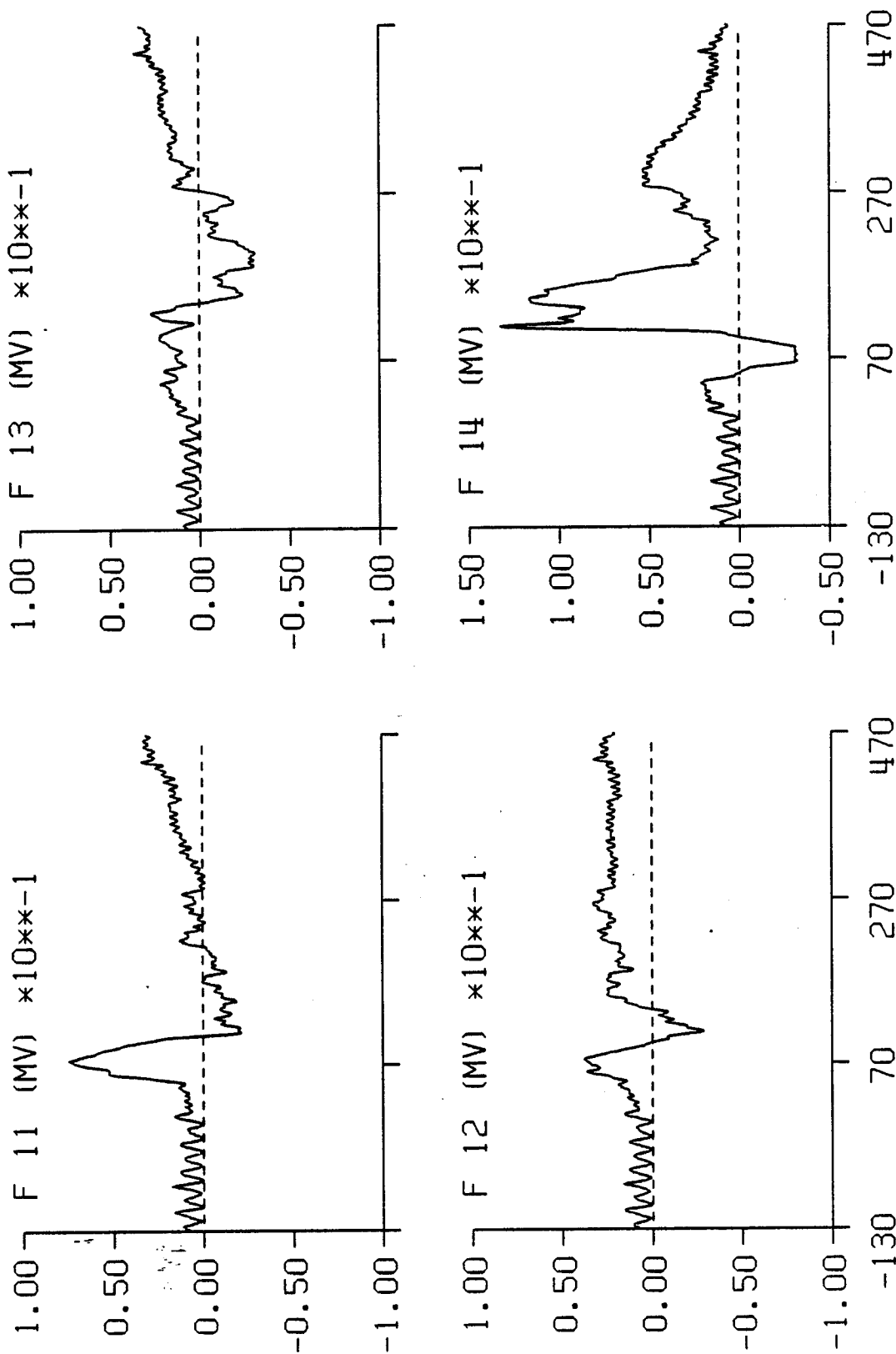
TIME IN MILLISECONDS

TEST 4643 CELL F



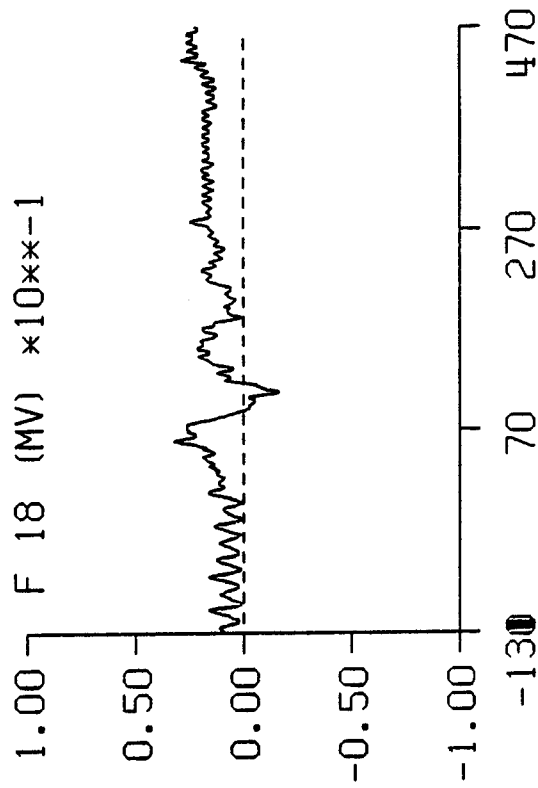
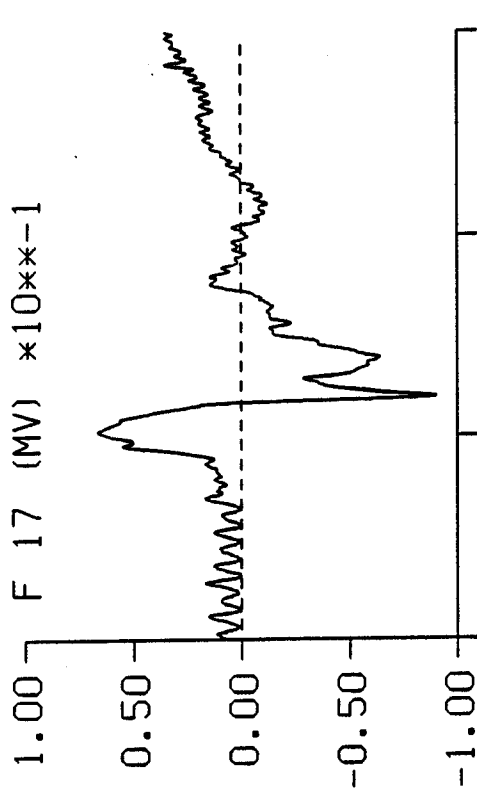
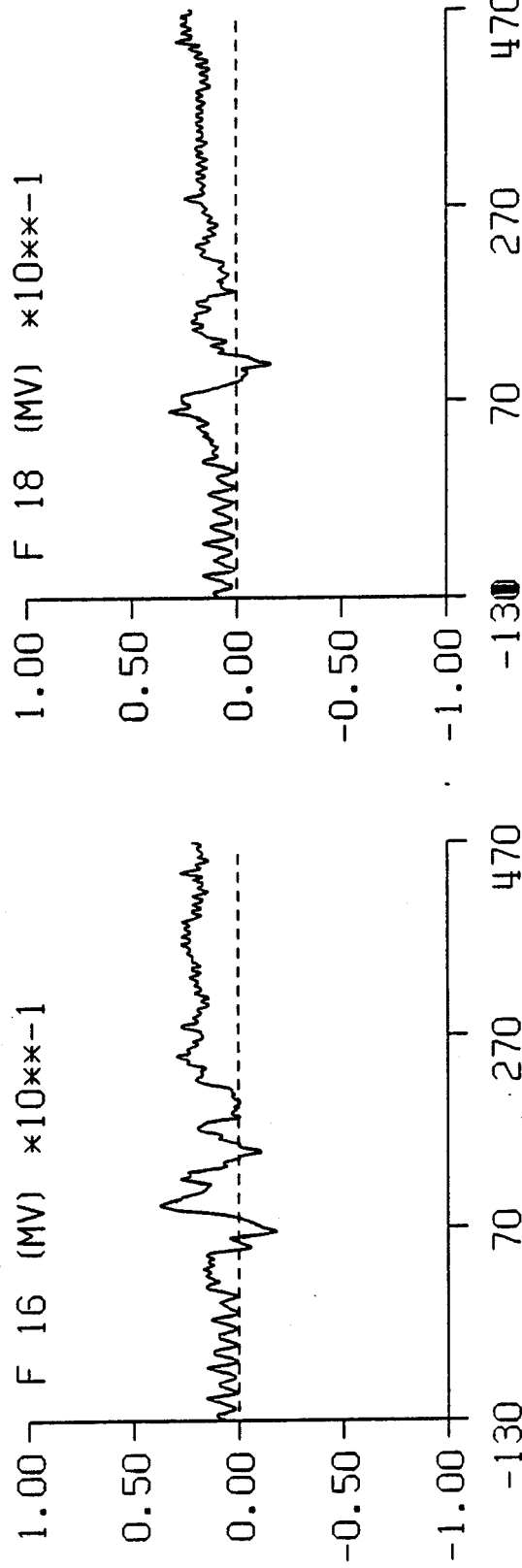
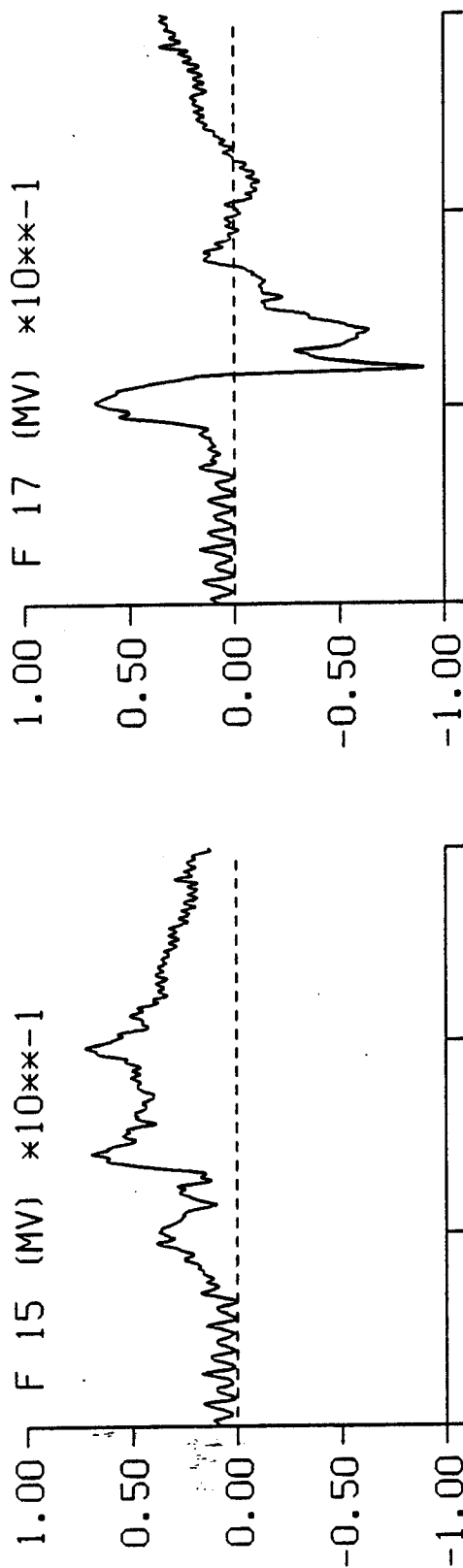
TIME IN MILLISECONDS

TEST 4643 CELL F



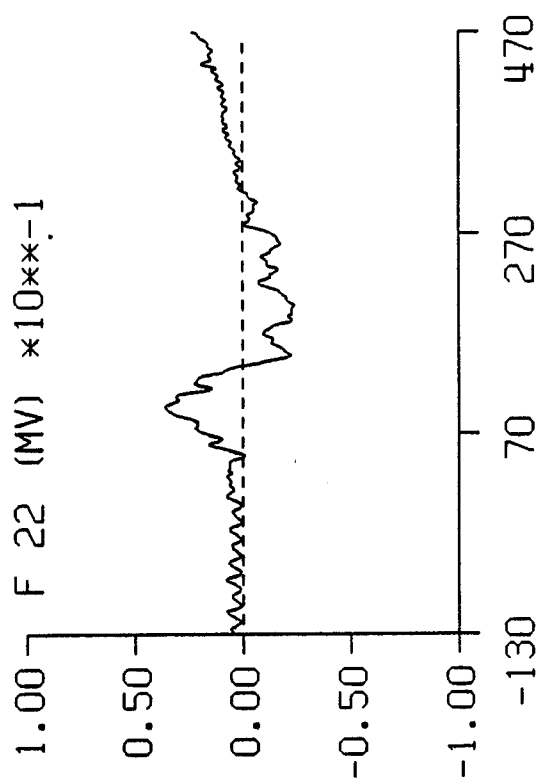
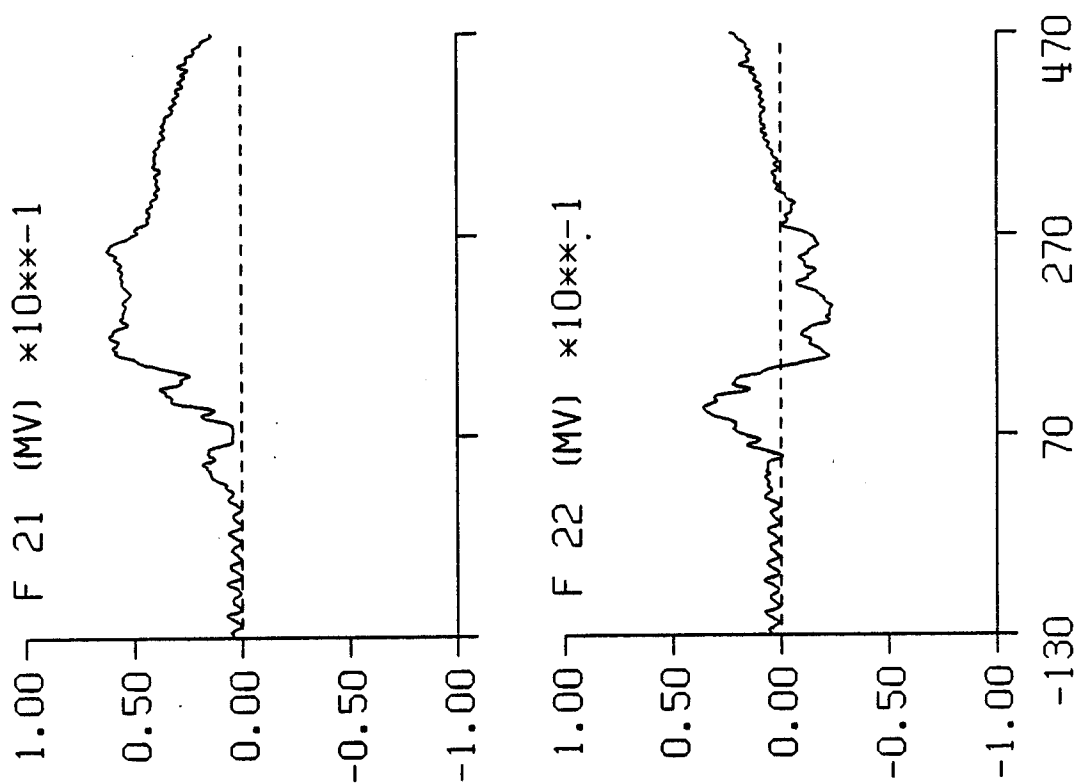
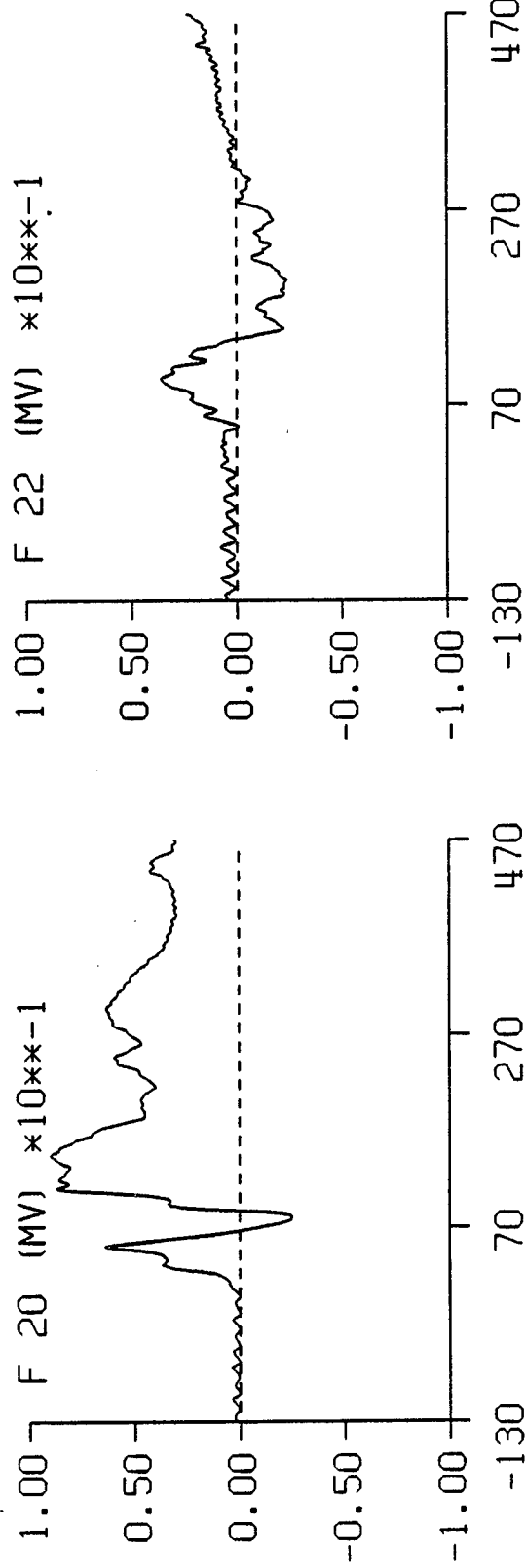
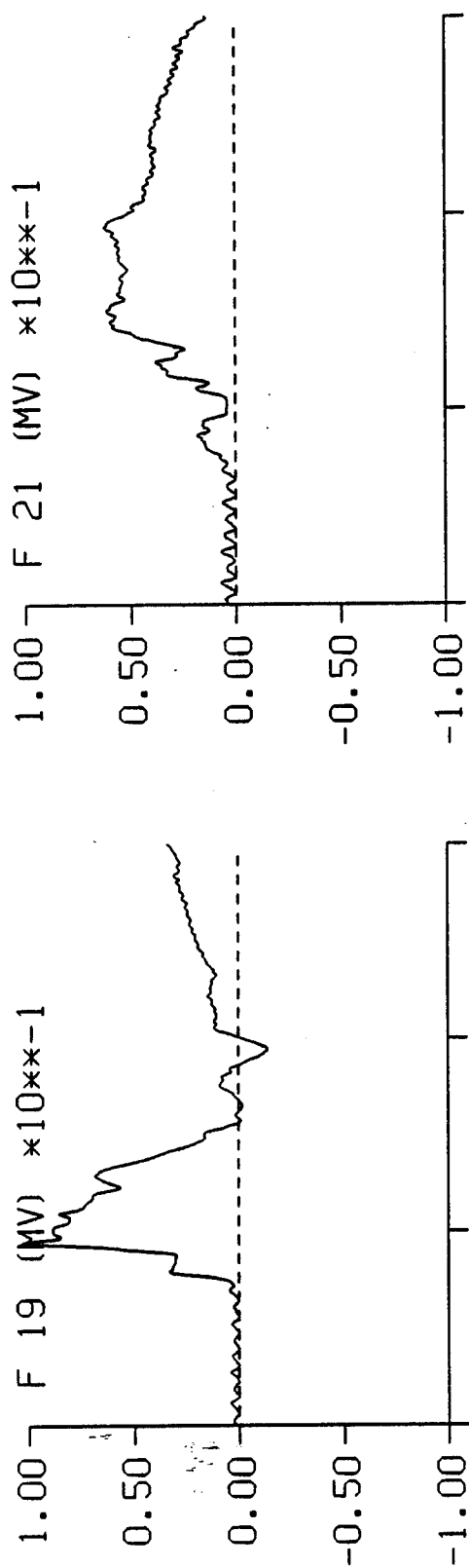
TIME IN MILLISECONDS

TEST 4643 CELL F

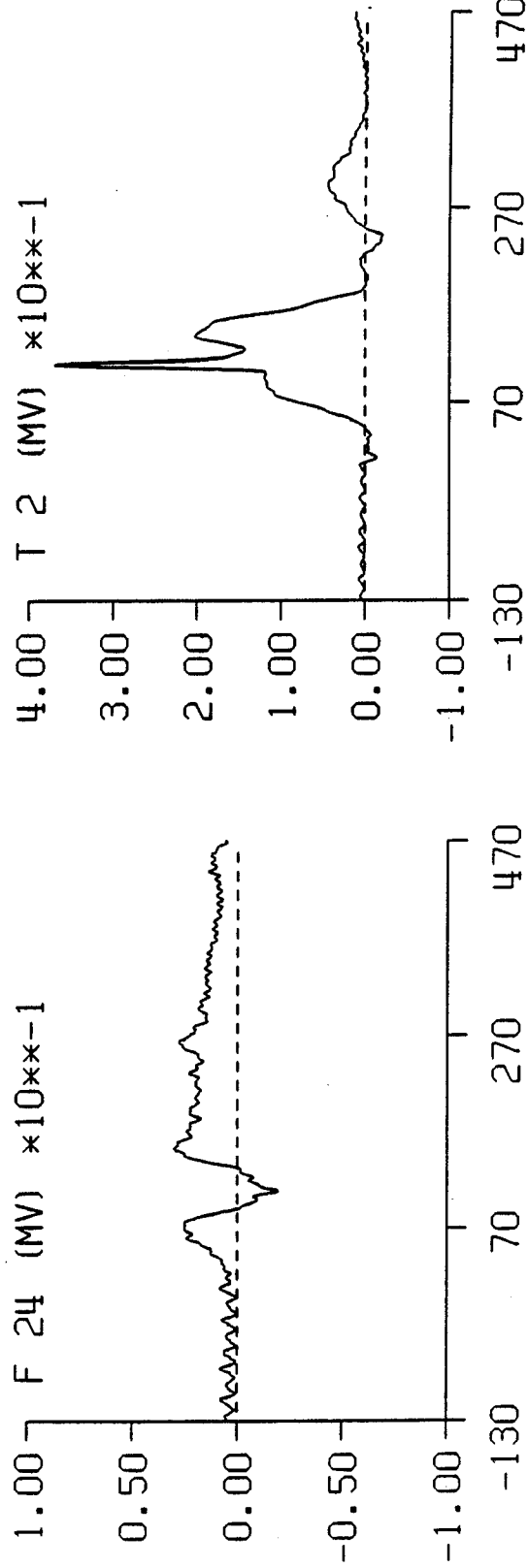
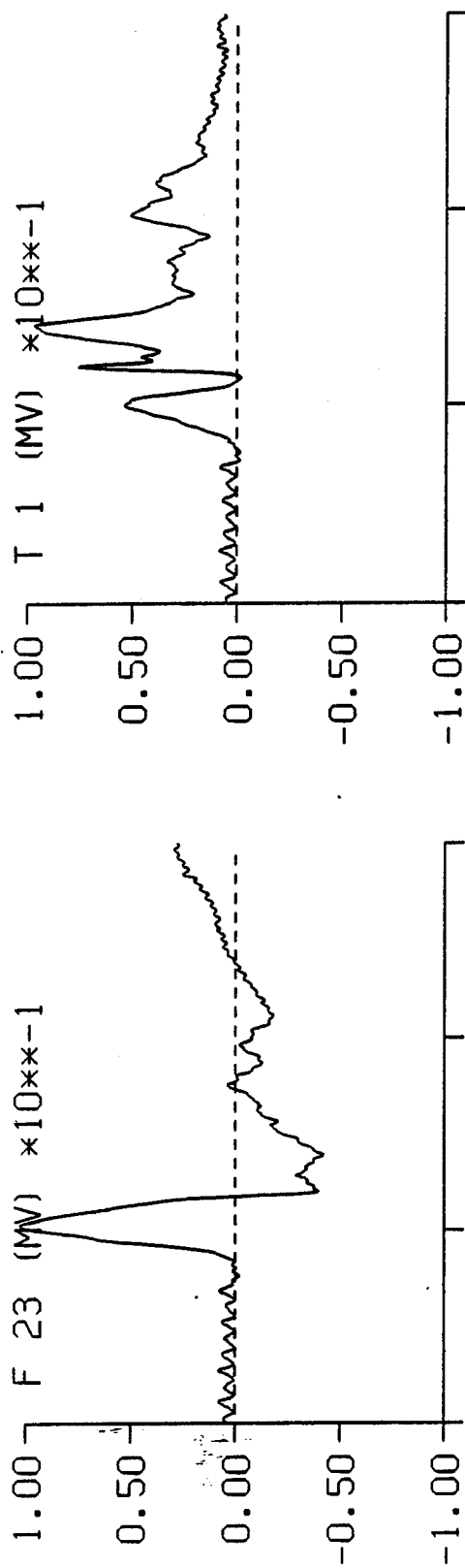


TIME IN MILLISECONDS

TEST 4643 CELL F

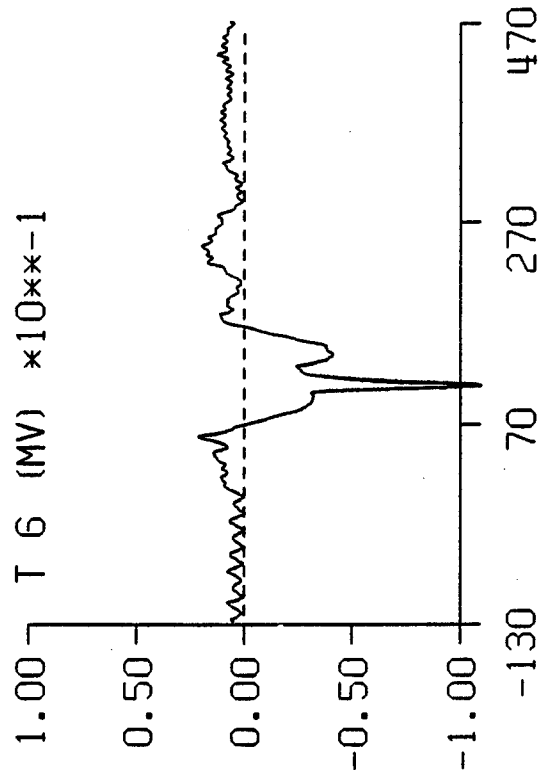
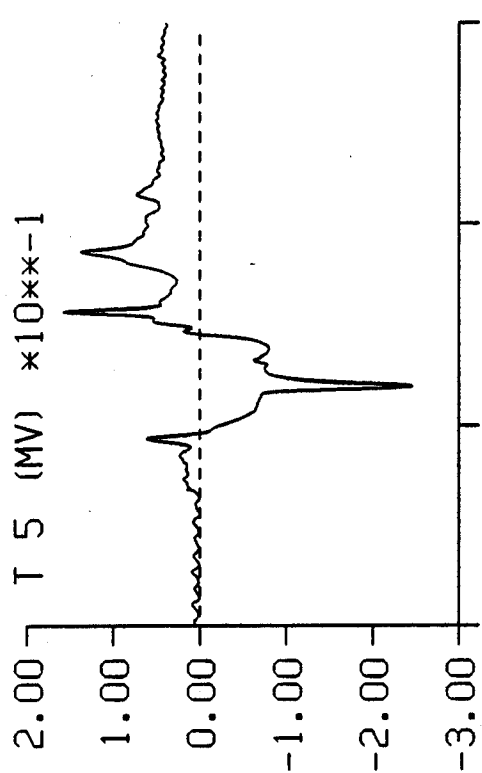
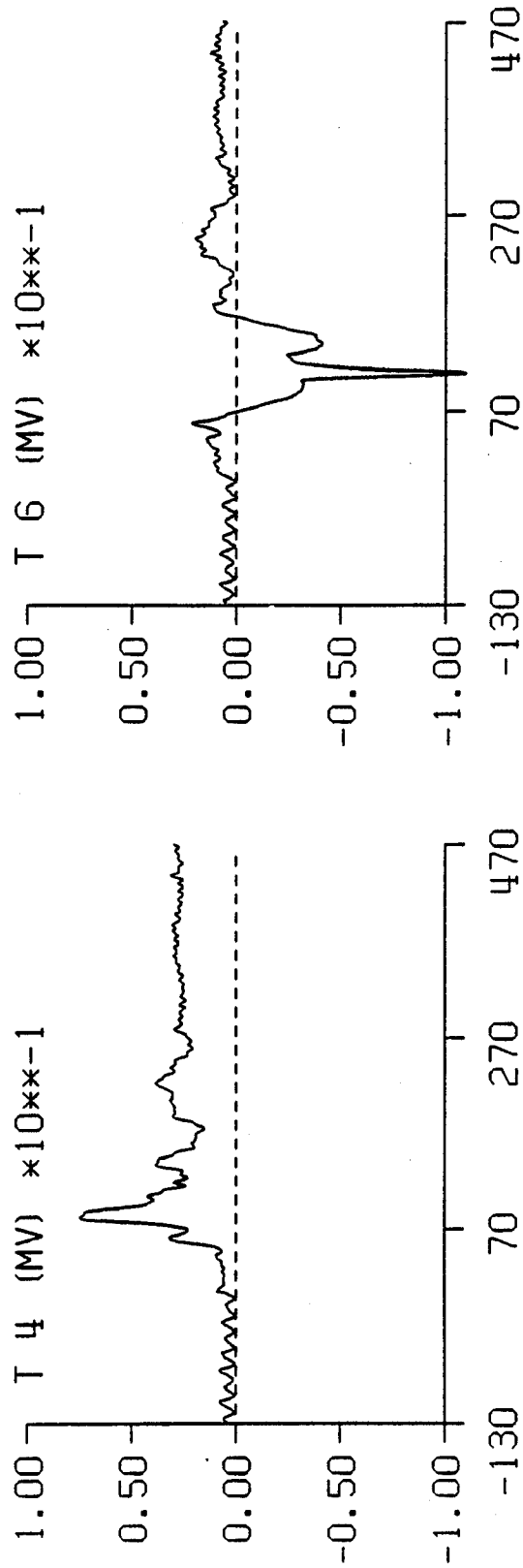
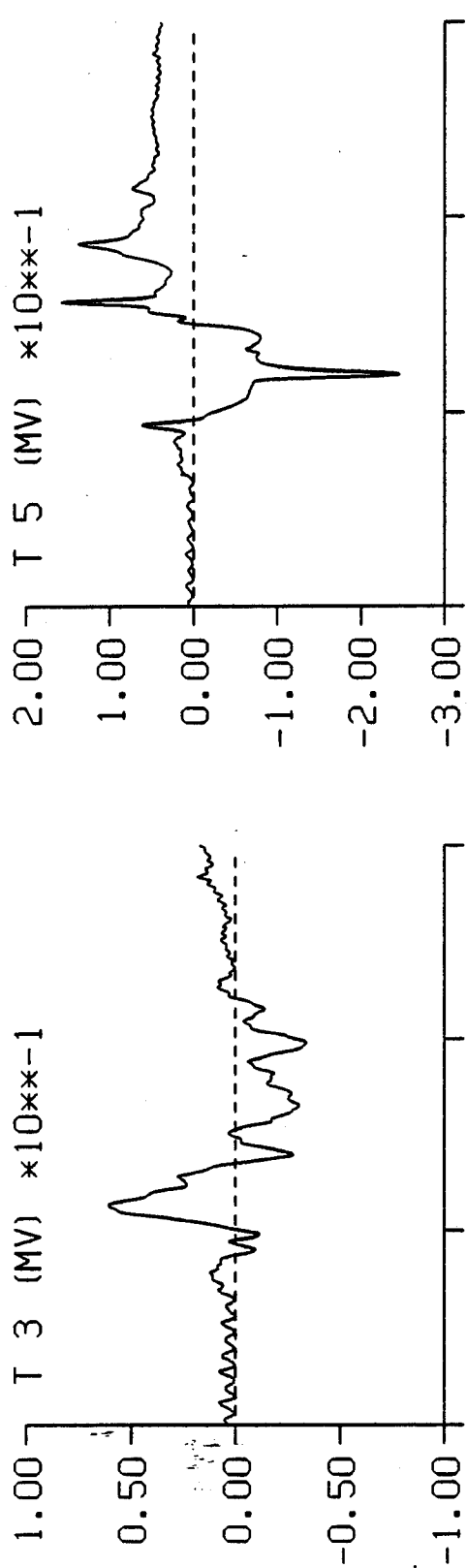


TEST 4643 CELL F



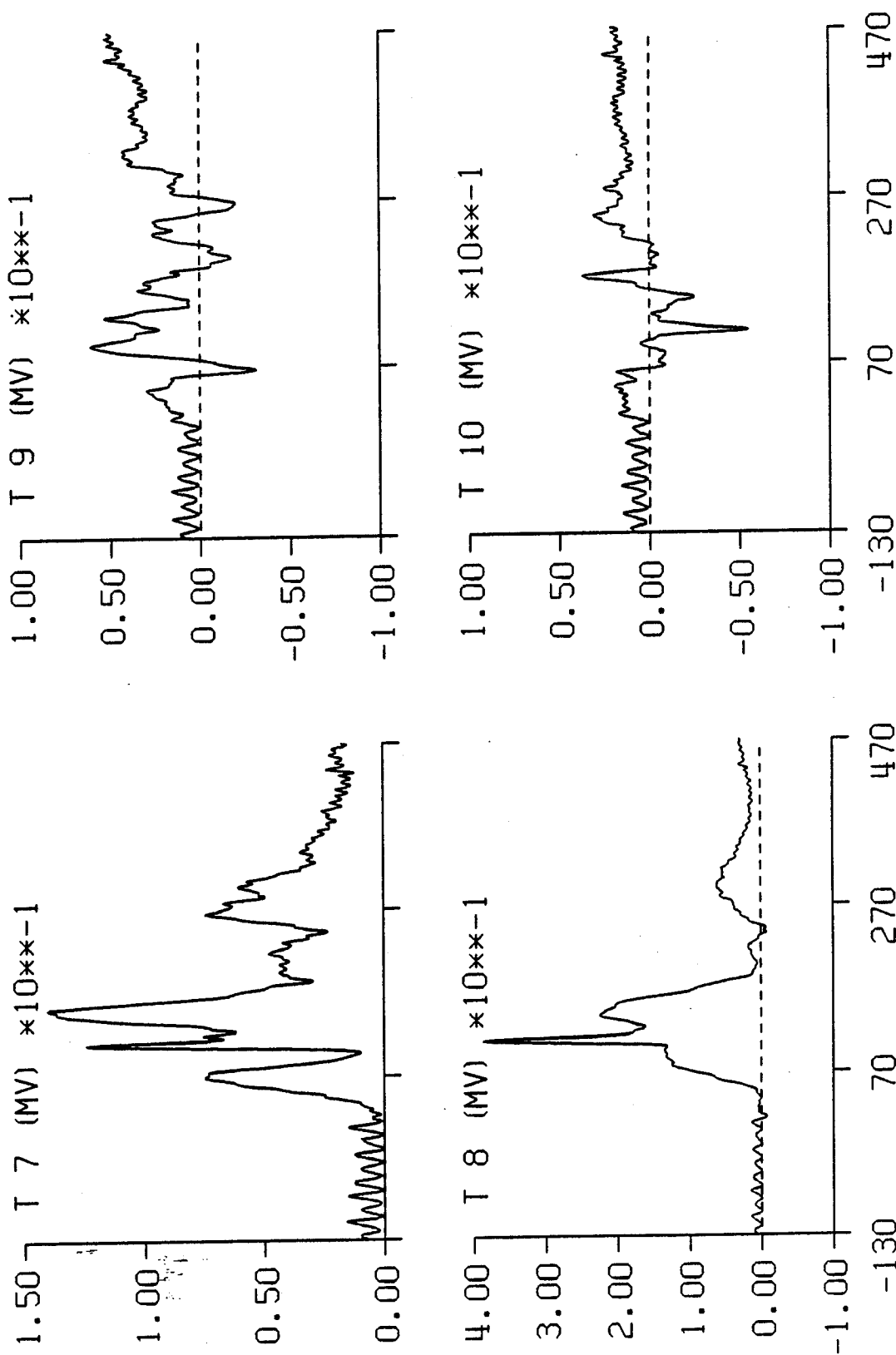
TIME IN MILLISECONDS

TEST 4643 CELL F



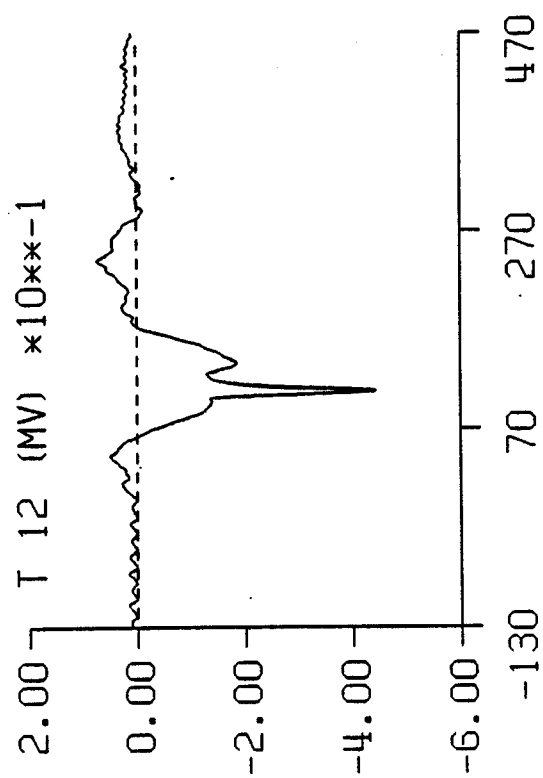
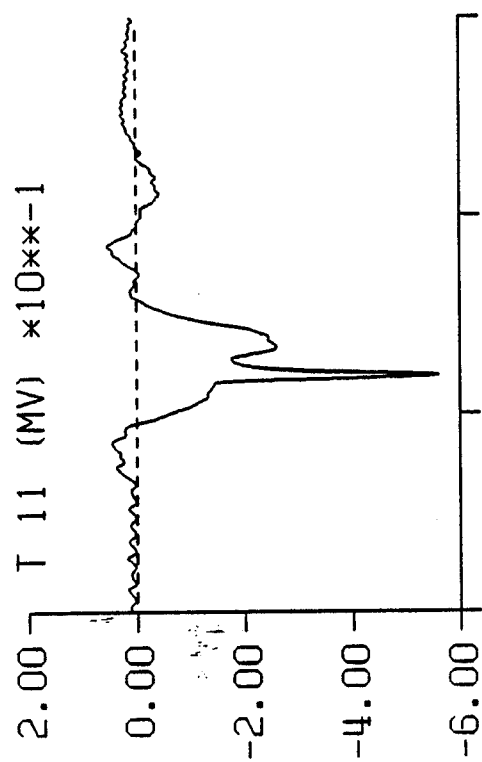
TIME IN MILLISECONDS

TEST 4643 CELL F



TIME IN MILLISECONDS

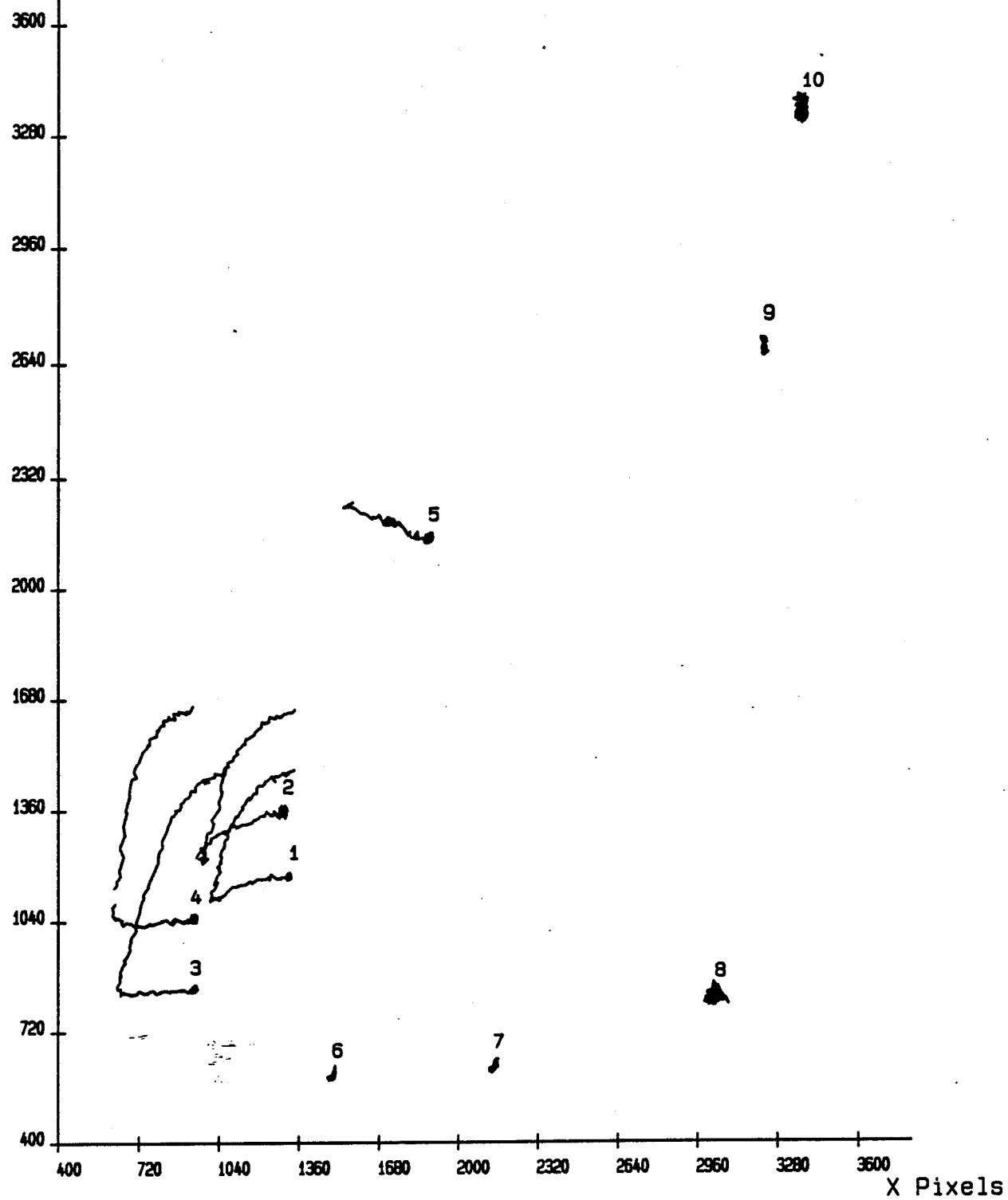
TEST 4643 CELL F



TIME IN MILLISECONDS

Test DATA-4643HAC.RUN Camera 1

Y Pixels



Test DATA-4643HAC.RUN Camera 2

Y Pixels

